THE AUSTENITISATION AND DECARBURISATION OF HIGH SILICON SPRING STEELS

A thesis submitted in fulfilment
of the requirements for the Degree
of
Doctor of Philosophy in Engineering
at the University of Canterbury

by

Chris Mardon

University of Canterbury
Christchurch, New Zealand.

1998

ABSTRACT

The 1970's saw the demand for more fuel efficient vehicles. This necessitated lighter automobiles, and was partly attained by lowering the weight of the coil springs used for the suspensions of these vehicles. Substantial weight reductions were achieved with new steels such as SUP7, with their elevated carbon and silicon contents allowing the springs to operate at higher stresses. However, these steels are prone to decarburisation during spring manufacture, which sharply reduces the sag resistance and the fatigue strength of the springs. The literature pertaining to the decarburisation of high silicon spring steels is limited, despite the subsequent reduced sag and fatigue properties.

The research detailed in this thesis was therefore undertaken to investigate the decarburisation of spring steels with 0 to 3wt.% silicon for a range of temperatures and heat treatment atmospheres. The austenitisation of these steels was also investigated to provide complementary information. Austenitisation and decarburisation heat treatments were undertaken with 0, 1 and 3wt.% silicon experimental steels, and the commercially available 2wt.% silicon SUP7 and SUP7NV steels. These five steels have similar carbon, manganese and chromium contents.

Two dimensional austenite growth occurred for the different steels, with the austenite grain shape inherited from the initial ferrite grain structure. The austenitisation accelerated with increasing temperature, with the higher silicon steels exhibiting faster transformation kinetics at comparable intercritical fractional superheat temperatures due to the higher Ac_1 and Ac_3 temperatures. The austenite growth was controlled by the substitutional diffusion of the alloy elements at low intercritical temperatures, and by carbon diffusion through the austenite at higher temperatures. This resulted in the faster transformation of ferrite/spheroidal cementite initial microstructures than pearlitic microstructures at low intercritical temperatures, and the opposite at higher temperatures. Austenite nucleated earlier in ferrite/spheroidal cementite initial microstructures when the cementite particles were located predominantly on the ferrite grain boundaries of the initial structures rather than within the ferrite grains. The austenite growth eventually became faster for the latter structure.

An increasing silicon content up to 2wt.% increased the rate of carbon removal at comparable temperatures. Multiple linear regression analysis demonstrated that the mass of carbon removed during decarburisation increased with silicon contents up to 2wt.%, with temperature, and with p_{H_2O}/p_{H_2} ratios of 0.01 to 0.25, while manganese decreased the decarburisation. However, slower decarburisation resulted for the 3% Silicon steel, especially at higher temperatures and lower p_{H_2O}/p_{H_2} ratios, where a dense oxide layer strongly inhibited carbon removal. The decarburisation of the 1% Silicon, SUP7 and SUP7NV steels was fastest at their respective Ac_3 temperatures. Columnar free ferrite grain structures were obtained for the 0% Silicon and SUP7 steels, compared with equiaxed grains for the 1% Silicon, SUP7NV and 3% Silicon steels.

The decarburisation of SUP7 was fastest when the specimen was heated in the furnace with the heat treatment atmosphere already established, while slower decarburisation resulted when the specimens were annealed in inert atmospheres prior to the introduction of the decarburisation atmosphere. Different initial SUP7 microstructures influenced the carbon release kinetics as the specimens heated to temperature. Prolonged decarburisation of SUP7 and SUP7NV at 900°C yielded decreasing free ferrite depths after 4hr, despite continued carbon removal from the steel.

This research contributes to the understanding of the austenitisation and decarburisation of spring steels. The information obtained is directly applicable to automobile coil spring production, but is also pertinent to the austenitisation and decarburisation of steel.

ACKNOWLEDGEMENTS

I would like to say a grateful thankyou to the following who have assisted in my research:

BHP New Zealand Steel for their generous financial assistance from 1993 to 1995.

Geoff *"Danger Mouse"* **Leathwick** for obtaining *"anything and everything"* that I required.

Ken Brown and **Otto Bolt** for their *"mass production"* of countless test specimens.

Mike Flaws, **Dave Healy**, **Hugh Mobbs** and **Kevin Stobbs** for *"valuable"* materials support.

Eric Cox and **Ron Tinker** for supplying the *"related incidentals"*.

Julian Phillips for helping construct *"salt baths Mark I, II, III, IV, V, VI, VII and VIII"*.

Paul *"SMF"* **Southward** for his *"skills on the computer"*.

The various *"Chunky Chipmunk"* postgrad guys and gals for *"advice and entertainment"*.

John Smaill for being there when I started, being there when I finished, and making sure that I *"did the bits in-between"*.

Thomas *"Sleeve"* and *"Sex is Short Stay Hard Reebonk"* **Mackenzie** *for "making me look outside the sphere and not be afraid to be different"*.

Mum, **Dad**, **Simon** and **Rachael** in Nelson for their question *"when will I finish"*.

Finally, and most importantly, to *"Princess"* **Joy** who has provided me with untold love and care over the past two years as I have struggled forward in the *"quest for extra letters after my name"*. Thank you so very much.

Never ever give up.
If you fail 99 times,
try a 100th time,
because if you keep trying despite always failing,
you will eventually succeed.

Dr Chris Mardon

This thesis is presented in acknowledgment of the financial support for

C. A. Mardon from 1993 to 1995 by BHP New Zealand Steel Limited.

C.A. Mardon
Recipient of the BHP
New Zealand Steel
Scholarship 1993-1995

Dr. J. S. Smaill
Supervisor
Department of Mechanical
Engineering
University of Canterbury

Professor J. K. Raine
Head of Department
Department of Mechanical
Engineering
University of Canterbury

TABLE OF CONTENTS

LIST OF FIGURES

LIST OF TABLES

NOMENCLATURE

a	activity
a_c	carbon activity
a_g, a_s	gas and steel carbon activities
a_{Si}	silicon activity
a_{SiO_2}	SiO_2 activity
A	surface area (cm^2, m^2)
Ac_1, Ac_3	austenite formation temperatures upon heating
A_{cem}	total cementite particle area (m^2) μ
A_P	area of cementite lamellae
c_c	carbon concentration in the steel specimen (g/g or mol/cm^3)
$c_{c,G1}$	carbon concentration of the steel surface (g/g)
c_g	carbon concentration at the steel surface
$c_{c,o}$, $c_{c,t}$	carbon concentration at the steel surface for t=0 and t respectively
C_s, c_s	carbon concentration in the steel surface (wt.%)
$C_{interval}$	average carbon content over each interval (wt.%)
C_o	initial concentration at time t_o
CO	carbon monoxide concentration (vol.%)
$C_{p_{salt}}$	molar heat capacity of salt ($JK^{-1}mol^{-1}$)
$C_{p_{steel}}$	molar heat capacity of steel ($JK^{-1}mol^{-1}$)
$C_{removed}$	average carbon content removed over each interval
C_x	carbon content at a distance x from the steel surface (wt.%)
$\bar{C}_{gas}$	mean gas composition (vol. %)
$C.F.$	correction factor
d_{cem}	diameter of the cementite particle (m) μ
d_{eq}	equivalent area diameter of the spherical particles (m) μ
$d_{template}$	diameter of template circles (m) μ
D	diffusion coefficient for carbon in steel (cm^2/s, cm^2/min)
D	mean effective ferrite grain diameter

D_b	grain boundary diffusivity
D_d	lattice dislocation diffusivity
$D_{effective}$	effective diffusion coefficient of carbon in ferrite (cm^2/s)
D_{H_2O}	diffusion coefficient of water in hydrogen (m^2/s)
D_l	lattice diffusivity
D_o	diffusion coefficient for an infinitely high temperature (cm^2/s)
D_s	surface diffusivity
D_α	diffusion coefficient of carbon in ferrite for a Fe-C steel (cm^2/s)
E	activation energy of the reaction (J/kg)
E_c	critical excitation potential (keV)
E_o	accelerating voltage (kV)
EDS	**E**nergy **D**ispersive **S**pectroscopy
erfc	complimentary error function
f	fraction of austenite transformed (vol.%)
f_c	activity coefficient of carbon
$f_c(gr)$	activity coefficient of carbon relative to graphite
F.S.	fraction between the Ac_1 and Ac_3 temperatures
G	austenite growth rate (μm/s)
$G_{C\alpha}$	mean ASTM ferrite columnar grain size
G_α	mean ASTM ferrite grain size
G_γ	mean ASTM austenite grain size
J	mass flow density (g/cm^2s)
K	constant
$k,\ k_o,\ K$	reaction rate coefficient (cm/s, $mol/cm^2.min.atm$, $mol/cm^2.min.atm^2$)
K	equilibrium constant
K	reaction coefficient
K_c	reaction coefficient for grain boundary corner nucleation
K_e	reaction coefficient for grain boundary edge nucleation
K_s	reaction coefficient for grain boundary surface nucleation
$l_{effective}$	element effective heating length (mm)
l_{rod}	length of threaded rod (m)

$\bar{l}_\alpha$, $\bar{l}(\alpha)$	mean lineal intercept length of the ferrite grains
$\bar{l}_\gamma$	mean lineal intercept length of the austenite grains (m, mm, μ)
L	test specimen length (cm)
L_{ti}	circle or horizontal test line length for the i^{th} field
m	constant
m	mass of steel sample
m_c	mass of carbon removed (g)
m_{gas}	mass of gas evolved (g)
$m_{interval}$	mass of carbon removed over each interval (g)
$m_{H_2O(consumed)}$	mass of water consumed (g)
m_{salt}	mass of salt (kg)
m_{steel}	mass of steel (g)
$\dot{m}_{H_2}$	hydrogen mass flow rate (kg/s)
$\dot{m}_{H_2O}$	mass flow rate of diffusing water (kg/s)
Mr_C	molecular mass of carbon (g/n)
Mr_{H_2O}	molecular mass of water (18g/n)
Mr_{gas}	molecular mass of gas (g/n)
mV_{inlet},	inlet transducer pressure (mV)
mV_{outlet}	outlet transducer pressure (mV)
n	number of fields measured
n	reaction exponent
n_C	number of moles of carbon removed during decarburisation
n_{CO}, n_{CH_4}	number of moles of carbon monoxide and methane evolved
$n_C(total)$	total number of moles of carbon removed during decarburisation
n_{gas}	moles of gas evolved
N	total number of cementite particles
N_A	number of grains per unit area
N_{icem}	number of cementite having a size within the i^{th} interval range
N_T	number of lamellae intersections

N_V	number of grains per unit volume (no./mm^3)
$N_{i\gamma}$	number of austenite grains intercepted by the test circle for the i^{th} field
$N_{Li}(\gamma)$	number of austenite grains intercepted per unit length of test circle for the i^{th} field
$\dot{N}$	nucleation rate (no./mm^{3}s)
$\bar{N}_L(\gamma)$	mean number of austenite grain intercepts per unit length of test circle for n fields measured
$\bar{N}_\alpha$	average value of the number of ferrite grains intercepted by the test circle
p	component partial pressure (atm)
P	absolute pressure (atm.)
$P_c(i)$	cementite point fraction for the i^{th} field
P_{Ar}	argon pressure (kPa)
$P_{atmospheric}$	atmospheric pressure at STP (Pa)
P_{CO}	partial pressure of carbon monoxide (Pa)
P_{H_2}	partial pressure of hydrogen (Pa)
P_{H_2O}	partial pressure of water (Pa)
p_{H_2O} / p_{H_2}	water to hydrogen pressure ratio
P_i	point count for the i^{th} field
P_{inlet}, P_{outlet}	inlet and outlet transducer pressures (kPa)
$P_i(\alpha)$	number of grain boundaries intersected by the test lines for the i^{th} field
$P_{Li}(\alpha)$	number of ferrite grain boundary intersections per unit length of test lines
$P_M(i)$	martensite point fraction
P_P	perimeter of lamellae
P_{SiO}	partial pressure of SiO (Pa)
P_T	total number of test grid points
$P_\alpha(i)$	ferrite point fraction in the i^{th} field
$\bar{P}_L$	mean number of grain boundaries intersected per unit length of test line

$\bar{P}_L(\alpha)$	mean number of ferrite grain boundary intersections per unit length of test lines for n fields
$\bar{P}_\alpha$	average ferrite point fraction
Q	activation energy (J)
R	ideal gas constant (J/kgK)
R	minimum particle size for EDS (μm)
R	radius of largest austenite nodule (μm)
RE	relative error (wt.%C)
R_{th}	radius of the threaded hole (cm)
R_i	radius of austenite core after decarburisation (cm)
R_o	original radius of test specimen (cm)
R_o	universal gas constant (8315J/kgmolK)
R_{rod}	radius of threaded rod (m)
$R_{specimen}$	radius of test specimen (m)
s	standard deviation
SEM	**S**canning **E**lectron **M**icroscope
SF	shape factor
S_v	grain boundary surface area per unit volume
S_{vex}	surface area per unit volume in the extended structure
t	transformation time (s, min)
t	95% confidence interval multiplier
t , $t_{specimen}$	thickness of test specimen (m)
t_d	decarburisation time (s)
	thickness of specimen (m)
$t_{0.5}$	time for 50% transformation (s)
T	temperature (°K)
T_{Ac_1} , T_{Ac_3}	Ac_1 and Ac_3 transformation temperatures (°C)
T_{HT}	heat treatment temperature at a fractional superheat (°C)
T_i	initial temperature of test specimens (°K)
T_{inlet}, T_{outlet}	inlet and outlet transducer temperatures (°C)
T_m	melting temperature (°K)

$T_{saltafter}$	salt temperature after addition of test specimens (°K)
$T_{saltbefore}$	salt temperature before addition of test specimens (°K)
V	volume of the steel specimen (cm^3)
$V_{CO}(Range2)$	CO range 2 concentration (vol.%)
$V_{CO}(Range3)$	CO range 3 concentration (vol.%)
$V_{CO_2}(Range3)$	CO_2 range 1 concentration (vol.%)
V_{gas}	volume of gas liberated (cm^3)
$V_{interval}$	volume of steel over which carbon is removed for each interval (cm^3)
V_{steel}	volume of steel over which carbon is removed (cm^3)
V_v	fraction of austenite formed (vol.%)
V_{vcem}	cementite volume fraction (%)
V_{vex}	volume fraction in the extended structure
$V_{vgraphite}$	graphite volume fraction (%)
$V_{v\alpha}$	ferrite volume fraction (%)
$V_{v\gamma}$	austenite volume fraction (%)
$\dot{V}$	decarburisation atmosphere gas flow rate
$\dot{V}_{H_2}$	hydrogen volume flow rate (m^3/s)
$\dot{V}_{H_{2\max}}$	maximum hydrogen flow rate (m^3/s)
$wt.\%C_{graphite}$	graphite contribution to bulk steel carbon content (wt.%)
x	distance from steel surface
x_d	decarburisation depth (cm)
$x_d(i)$	decarburisation depth for the i^{th} iteration (mm)
$x_d(i-1)$	decarburisation depth for the $(i-1)^{th}$ iteration (mm)
$x_{recorder}$	pen recorder height (mm)
α	coefficient of thermal expansion (K^{-1})
α	ferrite
γ	austenite
β	mass transfer coefficient (cm/s)
$\left\lfloor \frac{\delta c}{\delta x} \right\rfloor$	carbon concentration gradient

$\left[\frac{\delta c_c}{\delta x}\right]_{x=0}$	carbon gradient at the surface (mol/cm^4)
δ	sample thickness
Δg^o	standard free energy change
$\frac{dn_c}{dt}$	number of moles of carbon diffusing into the steel specimen
v	atomic diffusion volume
ν	reaction rate (mol/cm^{2}s)
ν_c	reaction rate (%/min)
ρ	density of steel (g/cm^3)
ρ_{gas}	density of gas (kg/m^3)
$\rho_{graphite}$	density of graphite (g/cm^3)
ρ_{iron}	density of iron (g/cm^3)
σ_r	random pearlite interlamellar spacing (μ m)
σ_t	true pearlite interlamellar spacing (μ m)
$95\%CI$	95% confidence interval
$95\%CI_{cem}$	cementite 95% confidence interval (vol.%)
$95\%CI_{\gamma}$	austenite 95% confidence interval (vol.%)
$\%C_{bulk}$	bulk steel carbon content (wt.%)
$\%C_{cem}$	cementite carbon content (wt.%)
$\%H_2O$	mean water consumption (%)
$\%C_{asat}$	saturated ferrite carbon content (wt.%)
$\%C_{\gamma}$	austenite carbon content (wt.%)
$\%RA$	percent relative accuracy
$\%i^{th}$ interval	percentage of total cementite particles present falling within the i^{th} size interval
%C removed	austenite carbon concentration – mean ferrite carbon concentration (in wt.%.)
$\phi_{heatingelement}$	diameter of heating element (mm)

CHAPTER 1

INTRODUCTION

1.1 Fundamentals of spring steels

Steel springs of widely varying types, shapes and sizes are used in a multitude of domestic and engineering applications, ranging from delicate hairsprings for instrument meters to buffer springs for railroad equipment. Smaller springs are invariably manufactured by coiling from wire in a cold state, while larger springs are manufactured by coiling at elevated temperatures. Typical spring steels include carbon steels, silicon and manganese containing steels, alloy steels, and stainless steels. Springs made from these steels must be capable of storing and reversibly releasing energy. After repeated load application, the springs must retain their original shape and dimension.

Prabhudev[1] identified three major requirements of spring steels, these being:

1) "A high yield strength in the vicinity of 210 MPa, or, more accurately, a high proportional limit so that the spring does not show any appreciable set in service;
2) A high fatigue strength under alternating and fluctuating stresses, with a reserve for occasional or more frequent overloads;
3) An adequate plastic range to form the springs."

These requirements can be fulfilled by steels with higher carbon and alloying element contents, in conjunction with the appropriate heat treatment. Spring failure is invariably by fatigue, with stress raisers acting as the nuclei for failure[1]. A high fatigue strength is achieved by using spring steels in a hard, high strength condition. Therefore, springs are hardened and tempered. The heat treatments used to facilitate this are crucial to the performance of the springs. In the hardened condition, the steel should be completely martensitic in order to attain the maximum yield strength, and so avoid excessive set in service[1].

1.2 Modern automobile suspension spring steels

Both front and rear suspension systems in modern automobiles utilise steel coil springs in conjunction with shock absorbers[2]. These two components act in a complimentary fashion to reduce the transmission of road surface vibration into the vehicle structure and the passengers within. The principal function of the springs is to isolate the vibration while that of the shock absorber is to dampen the oscillation in the spring. The vertical load on a coil spring creates torsional and shear stresses[3], as illustrated schematically in Figure 1.1. Table 1.1 lists the characteristics of typical automobile coil springs.

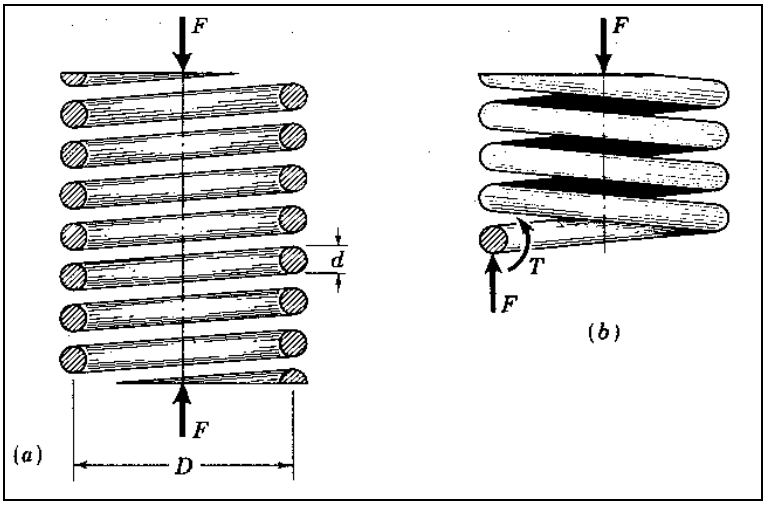

Figure 1.1 Schematic illustration of a coil spring showing (a) axial loading, and (b) the free-body diagram (from Ref. 3).

Table 1.1 Characteristics of typical automobile suspension coil springs (From Ref 4).

CHARACTERISTIC	TYPICAL PROPERTY
Outside diameter	160mm
Free height	394-445mm
Height (under static loading)	286mm
Weight	4.6-5.1kg
Load	2500-4500N
Spring rate (load/displacement)	17.5-35N/mm

Modern automobile suspension spring steels owe their development and implementation to the fuel crises of the 1970's, and the subsequent demand for more fuel efficient vehicles. This necessitated lighter automobiles, and was partly achieved by lowering the weight of the coil springs used for the suspensions of these vehicles[5]. Two important performance characteristics of coil springs are the sag resistance and fatigue strength[6]. The coil springs must be able to withstand the automobile weight without incurring too much sag[7]. During the service life of the automobile, the springs progressively sag, due to microyielding under sustained and cyclic loadings[7]. The fatigue strength of the spring is important as spring failure is invariably by fatigue[1,6], and usually initiates at the surface where the stresses are highest[8]. Both the sag resistance and fatigue strength are dependent on the hardness and by association, the yield strength of the steel[1,8,9].

When attempts were made to reduce the weight of the springs, the sag phenomenon became more significant[7]. Consequently, new steels with elevated carbon and silicon contents were developed with improved sag resistance[10], thus achieving substantial spring weight reductions. Utilisation of lighter springs requires the springs to operate at higher stresses[7,11], with a 5% increase in the operational stress level decreasing the mass of the spring by 11%[12]. However, the higher stresses caused the sag phenomenon to become more prevalent[7]. Sagging can be more effectively resisted by a finer distribution of precipitates, which act as barriers to dislocation motion[7]. The higher carbon content increases the carbide fraction, while the increased silicon content yields a finer carbide size and spacing[10], which gives a higher resistance to microyielding and therefore an enhanced sag resistance.

One of the spring steels developed in response to the fuel crises was SUP7. The chemical composition of SUP7, and the SAE 5160 steel it replaced, are given in Table 1.2.

Table 1.2 Chemical composition of SAE 5160[1] and SUP7[13] spring steels.

Designation	C (wt.%)	Si (wt.%)	Mn (wt.%)	Cr (wt.%)
SAE 5160	0.56 - 0.64	0.20 - 0.35	0.75 - 1.00	0.70 - 0.90
SUP7	0.55 - 0.65	1.80 - 2.20	0.70 - 1.00	0.20

Alloy additions are made to increase the sag resistance and fatigue strength of spring steels by increasing the hardness. There are three mechanisms by which alloy additions increase the hardness, these being:

1) Solution strengthening;
2) Precipitation strengthening;
3) Grain refinement.

The addition of silicon and manganese enhance the sag resistance of spring steels. Both elements are strong solution strengthening elements, while silicon also refines the shape and dispersion of the carbides precipitated during tempering. Assefpour-Dezfuly[9] found that although silicon additions of up to 2.5wt% improved the sag resistance, the optimum content was 1.5wt%, due to the detrimental effect of silicon on the surface decarburisation of the steel. Carbon was also found to improve the sag resistance of spring steels, while chromium reduced the sag resistance in Si-Cr, Si-Cr-Mo, and Si-Cr-V steels[5,9].

Precipitation strengthening usually involves the precipitation of M_3C, M_2C, and MC carbides, where the MC carbide is the most effective in strengthening the steel. Both vanadium and niobium form MC type carbides, with these being V_4C_3 and NbC respectively. Vanadium and niobium carbides can also exhibit a grain refining effect, with these carbides found to impede the grain coarsening upon hot rolling and austenitising prior to the coiling operation during spring manufacture[9].

Grain coarsening decreases the toughness and strength, and therefore lowers the sag resistance. The grain refining effect of vanadium and niobium results from carbides existing at the austenite grain boundaries impeding the growth of the austenite grains during austenitisation. The fine grain structure and the carbides preciptiated during tempering in the vanadium/niobium steels improve the sag resistance by obstructing the dislocation motion. As precipitation strengthening and grain refinement by vanadium and niobium carbides is supposedly independent of solution strengthening by silicon, silicon steels with vanadium and niobium additions can exhibit these three strengthening effects simultaneously.

Microalloying elements of vanadium and niobium have been thought to improve the sag resistance of spring steels by grain refinement of the prior austenite grains through grain boundary pinning at the austenitising temperature, and by the precipitation of a fine dispersion of vanadium and niobium carbides during tempering[5,14], resulting in secondary hardening. However, Assefpour-Dezfuly[9] stated that no improvement in the sag resistance was obtained from microalloy additions of vanadium and niobium. The improved sag resistance instead arose from subtle effects of varying hardness levels and prior austenite grain size, as well as small but significant differences in critical elements such as silicon of these steels relative to the conventional steels.

Secondary precipitation first requires vanadium and niobium carbides to be taken into solution during the austenitisation process, usually at 1100°C or higher. Secondly, for any significant hardening to be induced, the subsequent tempering treatment should be carried out at temperatures higher than approximately 550°C. For such high austenitising temperatures, rapid grain coarsening occurs as the vanadium and niobium carbides are dissolved, culminating in a lower sag resistance, while at tempering temperatures above 550°C, the desired hardness level of 50HRC or higher are not achievable. Assefpour-Dezfuly concluded that no advantages were apparent with vanadium and niobium alloy additions, especially as the sag resistance of the SAE 9261 steel containing 2.0 to 2.2wt% silicon was found to be as good as any of the microalloyed steels[9].

Alternatives to traditional steel coil springs appeared in the 1980's with the construction of springs from fibre reinforced plastic composites[2,4,15]. Mallick[2] developed a stacked spring comprising several elliptic spring elements constructed from unidirectional E-glass fibre reinforced epoxy tapes. Due to the higher strength-to-weight ratio than steel, this composite elliptic spring weighs only 50% of steel coil springs. Springs comprising corrugated strips of fibre reinforced plastic clamped between mounting plates which weigh 30% of traditional steel units were also developed[15]. These springs are also considerably cheaper to manufacture than steel coil springs as only one manufacturing operation is required, compared with up to twelve operations for steel springs.

1.3 Manufacture and heat treatment of automobile suspension springs

The general manufacturing processes involved in the production of automobile suspension springs, from forging of the bar stock in the steel mill, through to the presetting of the springs, are illustrated in Figure 1.2. Forging of the bar stock occurs at a maximum temperature of 1050°C, and concludes at 850°C. Decarburisation and surface scale arising from the forging operation are removed by a peeling operation, subsequently followed by an austenitisation heat treatment in a neutral atmosphere at approximately 900°C. Coiling of the springs follows austenitisation, and is undertaken at 820 to 860°C. After coiling, the springs are cooled to approximately 100°C, then heated uniformly and thoroughly to the hardening temperature of approximately 820 to 860°C. The soaking time at the hardening temperature is determined on the basis of 90s for each mm diameter, and is concluded by an oil or water quench. The springs are tempered at 400 to 550°C immediately following the hardening operation in either a salt bath or forced air-circulating furnace. This is necessary to avoid cracking upon hardening.

Surface decarburisation can occur during the coiling and hardening operations. As the hardness and yield strength are dependent upon the carbon content of carbon and low alloy steels[16], a decarburised layer is intrinsically weaker than the core and thus has a lower fatigue strength[17]. 0.19mm surface decarburisation reduced the fatigue life of a 0.60wt.%C/ 1.80wt.%Si/0.85wt.%Mn SUP6 spring steel to half that of the non-decarburised value[18]. This reduced fatigue life was attributed to the lower yield strength and the greater surface roughness of the decarburised layer, where fatigue crack initiation and development is confined to surface grains[19-21].

The sharp stress concentrations such as oxidised ferrite grain boundaries present in the decarburised layer, and cracks arising during quenching due to different thermal expansion coefficients of austenite in the core and ferrite at the surface, result in high stresses in the microvolumes adjoining the surface defects, therefore lowering the sag resistance[22]. However, the surface finish only affects the yield strength and hence the fatigue strength for surface roughnesses greater than approximately 5μm for a wide range of steels[23]. Gildersleeve[17] found that the fatigue limit of a 0.37wt.%C/0.30wt.%Si/1.39wt.%Mn EN 16 steel is independent of decarburisation depth up to 1mm. However, the fatigue limit increased linearly with

increasing surface carbon content and microhardness. The maximum tolerable decarburisation of finished springs in the quenched and tempered condition is 0.15mm plus one percent of the bar diameter[24].

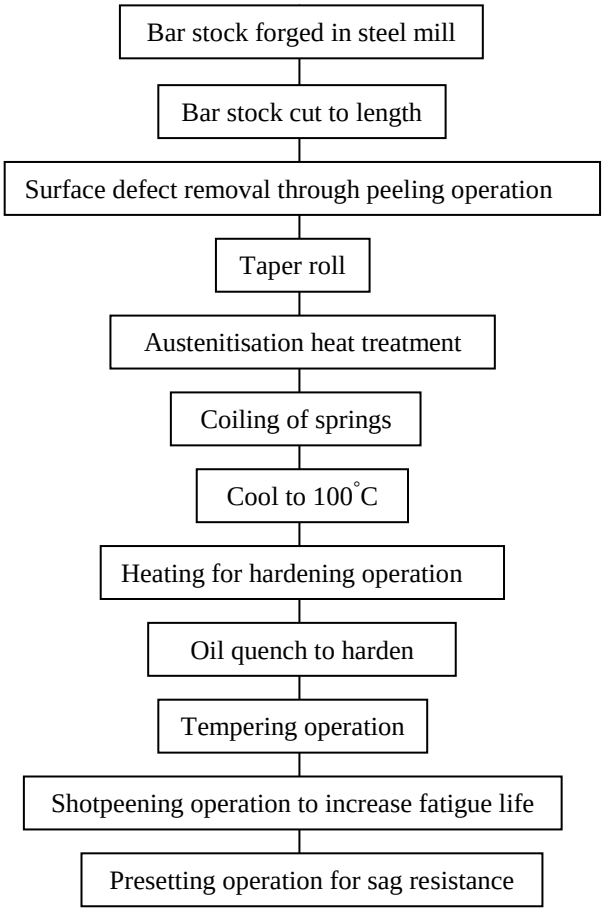

Figure 1.2 General automobile spring manufacturing processes.

The effect of a slight amount of decarburisation can be removed by a shotpeening operation after the springs are tempered[25,26]. Shotpeening involves the bombardment of a surface with smal pieces of rounded shot, and introduces compressive residual stresses into the surface and immediate subsurface layers[27]. Since a surface crack will not easily initiate in, or propagate through, an area under compression, an improvement in the fatigue strength is obtained. The mean fatigue limit of EN 16 steel increased by 42% through shotpeening[17]. This higher fatigue limit also coincided in a shift of the fatigue initiation site from the surface to a subsurface location. This initiation occurred predominantly at Al_2O_3 inclusions. Sato[18] also demonstrated that the fatigue life of a SUP6 spring steel with small amounts of decarburisation can be

increased by various types of shotpeening operations. However, for a decarburisation depth of 0.19mm, the different methods yielded similar fatigue lives of half that of the non-decarburised spring.

Silicon/manganese spring steels such as SUP7 are prone to deep decarburisation[5,9]. The depth of decarburised layers has also been found[5] to be strongly related to the carbon activity of the steel, with a reduced level of decarburisation obtainable through a lower carbon activity of the steel. Silicon increases the activity of carbon, while chromium and vanadium lower the carbon activity. Si-Cr-V steels were found to be more resistant to decarburisation than SUP7, primarily due to a lower silicon content. The Si-Cr-V steels also contain chromium and vanadium, which decrease the carbon activity, and therefore the extent of decarburisation.

The final operation in the spring manufacture involves presetting the springs, which increases their fatigue lives by introducing residual compressive stresses into the springs. Presetting also reduces the sag occurring during the service life of the springs[12]. Values of 1225 and 1080MPa are typical for the ultimate tensile and 0.2% proof stresses, along with 9% elongation[1].

1.4 Scope and outline of thesis

Tens of millions of automobiles are manufactured annually, with the coil springs used for their suspension systems produced from steels such as SUP7. The worldwide market for coil springs was estimated to be £1.6 billion[15] (New Zealand $5.2 billion for September 1998 exchange rates[28]) in 1986. With each spring weighing approximately 5kg[4], it is readily apparent that a considerable amount of steel is used annually for the manufacture of coil springs. The two most important operational parameters for springs are the sag resistance and the fatigue strength. Both are influenced by the tensile strength of the spring, and are substantially reduced by any decarburisation. Decarburisation arising from the heat treatments during the manufacture of the springs is of considerable importance due to the susceptibility of SUP7 to decarburisation.

Given the investment in spring manufacture, it is surprising that relatively little research has been undertaken into the austenitisation and decarburisation of spring steels such as SUP 7.

The focus has instead been on selecting the appropriate steel composition for maximum sag resistance and fatigue strength, while minimising the influence of decarburisation through suitable heat treatments, and shotpeening and presetting operations.

Consequently, a better understanding and therefore more accurate modelling of the mechanisms controlling the austenitisation and decarburisation of spring steels is of significance. From this knowledge, the rolling conditions in the steel mill, as well as the spring manufacturing conditions, could be optimised to reduce the decarburisation of these steels. Furthermore, the wastage associated with the current practice of peeling bar stock prior to spring manufacture could be reduced, and the premature failure of the finished product due to the decarburisation arising from spring manufacture addressed.

A comprehensive literature search demonstrated that the austenitisation of plain carbon and manganese steels is well documented, as is the decarburisation of low carbon electrical steels. However only limited information was found for the austenitisation or decarburisation of steels with compositions similar to those used for automobile spring steels. Consequently, the author commenced this research with the intention of making a significant contribution to the understanding of the austenitisation and decarburisation of spring steels. The aims of this research were to:

1) Investigate and quantify the influence of silicon content, initial microstructure and temperature on the austenite nucleation and growth kinteics of 0 to 3wt.% silicon spring steels;
2) Investigate and quantify the influence of silicon content, gas atmosphere composition, temperature and initial microstructure on the decarburisation of 0 to 3wt.% silicon spring steels.

The relevant literature existing for austenitisation, decarburisation and diffusion in steel is detailed in Chapters 2, 3 and 4 respectively.

In addition to the commercially available SUP7 and SUP7NV spring steels, three other steels were produced. These had silicon contents of approximately 0, 1 and 3 wt.%, with otherwise similar chemical analyses to SUP7. This gave five steels with silicon contents ranging from 0

to 3wt.% from which the austenitisation and decarburisation of spring steels could be investigated.

Chapter 5 details the experimental programs undertaken for the austenitisation and decarburisation heat treatments. Short and long duration austenitisation experiments were undertaken in salt bath and tube furnace test rigs respectively, with both developed specifically for this project. The tube furnace rig was also used for the decarburisation heat treatments. This experimental apparatus is described in Chapter 6. Chapter 7 is concerned with the experimental techniques developed for the heat treatments, and for the microstructural analysis, while the analytical techniques developed for the analysis of the heat treated specimens are detailed in Chapter 8.

The transformation of the five steels with various initial structures to austenite at different temperatures is investigated in Chapter 9. Decarburisation experiments were undertaken for SUP7 using a range of experimental conditions, with the effects of initial structure, heat treatment temperature, atmosphere composition and prior austenitisation quantified. This experimentation is described in Chapter 10, while the decarburisation of different silicon steels is detailed in Chapter 11. Chapter 12 presents the conclusions obtained from this research, with the recommendations for future research detailed in Chapter 13.

This research was undertaken in order to make a significant contribution to the current understanding of the austenitisation and decarburisation of spring steels, and therefore improve automobile coil spring production. However, it is hoped that the results obtained are more widely applicable to the austenitisation and decarburisation of steel in general.

CHAPTER 2

FORMATION OF AUSTENITE IN STEELS

Most commercial processes rely to some extent on the heat treatments that cause the steel to transform to austenite[29]. Austenitisation can be defined as the heat treatment of steel in the austenite region[30], and is undertaken for two reasons:

1) As a necessary precursor for heat treatment;
2) To chemically homogenise the steel so that the concentration gradients formed during solidification upon casting are minimised.

The austenitisation process commences with the formation of an austenite nucleus at a ferrite/cementite interface. The growth of this nucleus occurs at the moving interface where ferrite and cementite react to form austenite. The rate of this interaction is dependent on the dissolution rate of the cementite and the transformation rate of the ferrite in the austenite at the interface, and also upon the diffusion rate of the carbon atoms in the austenite. Since decarburisation is dependent on the diffusion of carbon from the phases present in the steel to the steel surface, an investigation into the austenitisation of spring steels is a necessary precursor to obtaining a detailed understanding of the decarburisation of these steels.

In most steels, the heating of ferrite/cementite steel structures results in the rapid transformation of ferrite to austenite. This transformation requires less than 1s for plain carbon steels[31], 3s for chromium steels[32], and 20s for complex steels with carbide forming elements[33], while the dissolution of carbides in the austenite proceeds much more slowly[34]. However, steels containing increased silicon and manganese contents require much longer for the initial structure to transform to austenite[35].

2.1 Nucleation and growth of austenite

The nucleation and subsequent growth of austenite from an initial structure comprising ferrite and iron carbide is influenced by the initial structure, the alloy content, and the austenitisation temperature to which that steel is subjected. The basic reaction involved in the austenitisation process is:

$$\text{ferrite} + \text{cementite} \rightarrow \text{austenite} \qquad (2.1)$$

Hillert[32] described mechanisms for the austenitisation of steels with different carbon contents, as illustrated in Figure 2.1. The remainder of this section details these austenitisation mechanisms. For a low carbon content, Figure 2.1(a), an austenite shell forms around a cementite particle soon after contact is established between an austenite nucleus and the particle, with the main reaction being the carbon diffusion through this shell. If the carbon diffusion through the austenite is the only reaction of importance, the shell can only grow until it has consumed all the carbon from the cementite particle in its centre. As the distance between cementite particles is large, there is only a very small chance that the austenite will come into contact with another particle. Therefore, further austenitisation will depend on the formation of new austenite nuclei, with each cementite particle requiring its own nucleus. If the nucleation rate is low, this process, rather than the rate of diffusion, may govern the overall reaction rate.

For realistic carbon contents, the distance between the cementite particles is not very large, with carbon diffusion in the ferrite matrix becoming important. A particle can then be dissolved by carbon diffusion through the ferrite phase to the austenite shell at a neighbouring particle, Figure 2.1(b). This reaction becomes more important at lower nucleation rates. At sufficiently high carbon contents, the cementite particles will be so close to each other that an austenite shell formed around one particle will invariably come into contact with the neighbouring particles before the particle in the centre is completely dissolved, Figure 2.1(c). The austenite region may then continue to grow indefinitely, or until it impinges on another austenite region. This reaction becomes important as the carbon content is increased above the Ac_3 line on the iron-carbon equilibrium diagram.

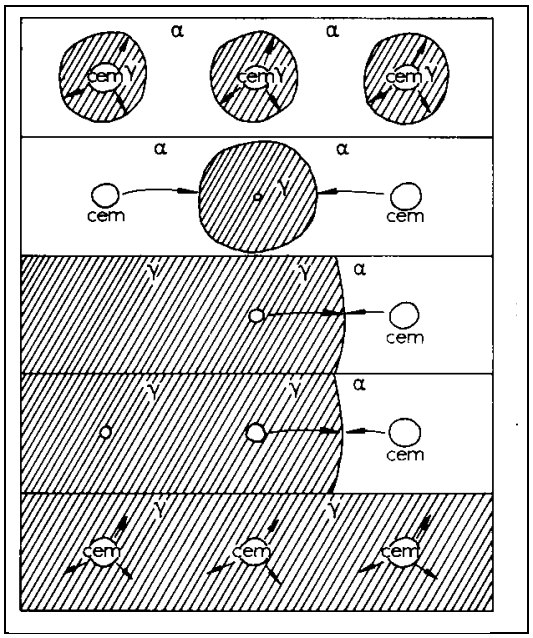

Figure 2.1 Mechanisms for the austenitisation of steel (from Ref. 32).

If the carbon content is considerably higher than the Ac_3 value, the austenite region can continue to grow with only partial dissolution of the cementite particles, Figure 2.1(d). The further advance of the austenite/ferrite interface is governed by

$$\text{ferrite} + \text{cementite} \rightarrow \text{austenite (in eqm. with ferrite)} + \text{cementite}, \qquad (2.2)$$

with the austenite having the carbon content required for equilibrium with ferrite. Far behind the austenite/ferrite interface, another reaction will continue where the remaining parts of the cementite particles will dissolve. Here,

$$\text{austenite (in eqm. with ferrite)} + \text{cementite} \rightarrow \text{austenite (high carbon)}. \qquad (2.3)$$

At a sufficiently high temperature, the ferrite phase may transform to austenite without any cementite dissolution, Figure 2.1(e). In the iron-carbon system, this occurs at approximately 910°C. The cementite dissolution will then occur completely inside an austenite matrix by:

$$\text{austenite (low carbon)} + \text{cementite} \rightarrow \text{austenite (high carbon)}. \qquad (2.4)$$

2.1.1 Low carbon steels

Speich[36] investigated austenite formation from ferrite in the absence of cementite in a 0.0004wt.% C zone-refined Fe-C steel, as well as in a Fe-0.013wt.%C steel. Possible nucleation sites for austenite in pure iron are illustrated in Figure 2.2(a). Austenite can nucleate either[36]:

1) In the matrix;
2) At grain boundary faces;
3) At grain boundary edges;
4) At grain boundary corners, which is not easily shown in two dimensions.

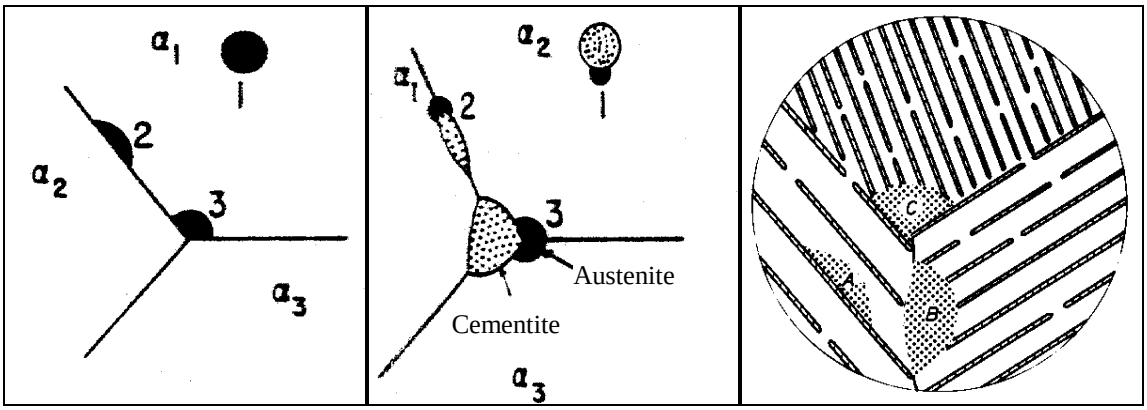

(a) **(b)** **(c)**

Figure 2.2 Possible nucleation sites for austenite in (a) ferrite, (b) spheroidal cementite (from Ref.36) and (c) pearlitic structures (from Ref. 38).

Nucleation for both the 0.0004wt.%C zone refined structure, and the Fe-0.013wt.%C steel occurred at the ferrite/ferrite grain boundaries. However, austenite nucleated at grain boundary faces, type 2 sites, in the zone refined structure, while grain boundary edges, type 3 sites, were favoured for the Fe-0.013wt.%C steel. The transformation of ferrite to austenite for the zone-refined steel was complete at 950°C in less than 10ms.

2.1.2 Pearlitic steels

The formation of austenite from higher carbon steels with pearlitic starting structures is well documented[36,37]. Speich[36] found that austenite nucleation occurred predominantly at cementite particles located in the boundaries between the pearlite colonies for a 0.77wt.%C steel, a 0.96wt.%C Fe-C steel, and a 0.96wt.%C/0.24wt.%Si/0.20wt.%Mn alloy. Similar nucleation sites were observed by Roosz for an eutectoid plain carbon steel[38], as illustrated in Figure 2.2(c). Austenite nucleation for lower carbon steels comprising approximately 0.1wt.%C and 1.5wt.%Mn is somewhat more contentious. Several investigators have determined that austenite formation initiated at cementite particles located on ferrite grain boundaries[39-41]. However, Navara[42] observed that austenite nucleation occurred along ferrite grain boundaries at manganese-rich regions.

Speich[36] concluded that the subsequent growth of the austenite was controlled by carbon diffusion. Upon completion of the austenitisation, lamellar carbides remained. These carbides eventually dissolved or spheroidised, depending on the carbon content and the temperature. Nehrenberg[37] found that within the Ac_1-Ac_3 temperature range, austenite grew freely in every direction for initially pearlitic structures, resulting in approximately equiaxed grain structures. This austenite growth was observed for hypoeutectoid, eutectoid, and hypereutectoid steels.

The very first austenite to form for a SAE 4140 steel with an initial structure of proeutectoid ferrite in prior austenite grain boundaries was located in this ferrite[37]. It was also observed that the last ferrite to transform to austenite did not exist as ferrite in the initial structure, but eventuated from pearlite colonies from which the carbon diffused as the heating progressed. The austenite present upon disappearance of the pearlite was not homogeneous, with residual cementite always found[43]. Generally the cementite particles exist as small isolated constituents imbedded in the matrix, but often they are lamellar in appearance. Furthermore, carbon concentration gradients exist in the austenite once these particles are no longer detectable as separate particles. Figure 2.3 illustrates the austenitisation and cementite dissolution phases for a 0.78wt.%C pearlitic steel.

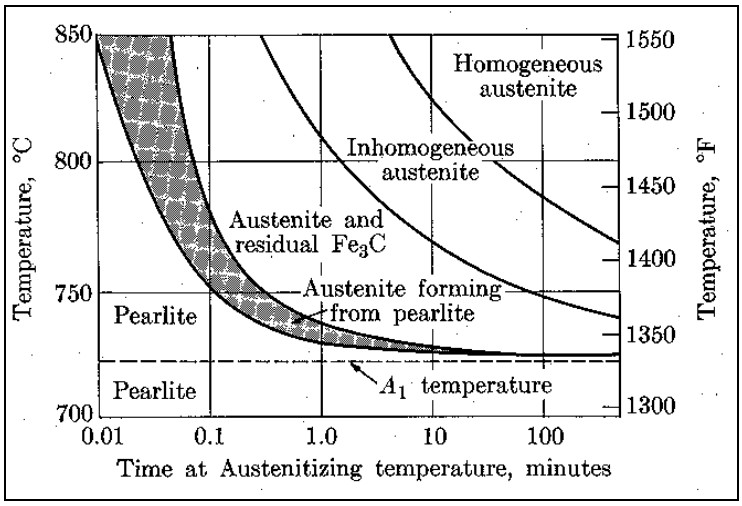

Figure 2.3 Time-temperature iso-transformation diagram for a 0.78wt.%C pearlitic steel (from Ref. 43).

2.1.3 Spheroidised steels

Nehrenberg[37] demonstrated that spheroidised structures are generally produced by either a high temperature transformation of inhomogeneous austenite, or by the tempering of martensite, with a fundamental difference between the resultant structures. In both structures, austenite nucleated at the ferrite boundaries, with the austenite growth confined to the ferrite grains in which the austenite started to grow. However, equiaxed austenite grains developed from the initial structure produced by a high temperature transformation, whereas the austenite transformation from the tempered martensite structure resulted in the austenite exhibiting directional growth, with the formation of equiaxed grains. This difference was attributed to the initial shape of the ferrite grains, where spheroidised structures produced by a high temperature transformation had equiaxed ferrite grains, while those of structures produced by tempering martensite were equiaxed.

The formation of austenite from spheroidised structures produced by the tempering of martensite was investigated by Speich[36] for 0.77 and 0.96 wt.%C Fe-C steels, and a 0.96wt.%C/0.24wt.%Si/0.20wt.%Mn alloy, with all the carbides located in the ferrite/ferrite grain boundaries. Austenite was found to nucleate at the junction between a cementite particle and two ferrite grains, type 3 sites in Figure 2.2(b). Therefore, the density of carbides in the ferrite grain boundaries essentially controls the number of nucleation events.

A fine grained tool steel with 0.95wt.%C/0.29wt.%Si/1.13wt.%Mn/0.59wt.%Cr/0.49wt.% W/0.20wt.%V comprising an initial ferrite/globular cementite structure exhibited a change in the nucleation mechanism with an increase in the austenitising temperature[33]. At 760°C, the austenite nucleated predominantly at grain boundaries, while at 800 and 820°C, the mechanism shifted to edge and corner nucleation. Site saturation occurred from 760 to 820°C, where the nucleation rates for the grain boundary nucleated phase transformations were sufficiently high that the potential nucleating sites were exhausted early in the transformation. The reaction was further controlled by growth.

The austenite film nucleated at cementite particles located on the ferrite grain boundaries grew until the carbide was completely enveloped. Further austenite growth occurred by carbon diffusion through the austenite envelope from the dissolving carbide to the ferrite/austenite boundary. Eventually the austenite regions impinged, with the carbide dissolution occurring until the carbide was either completely dissolved, or the austenite achieved its equilibrium carbon content. The presence of alloying elements reduced the growth rate of the austenite envelope near the eutectoid temperature by a factor of ten relative to the Fe-C steels, but by less at higher temperatures[36].

Molinder[31] demonstrated that the transformation of a hypereutectoid ferrite/cementite structure to an austenite/cementite structure can be divided into three periods, where:

1) The initial structure remains untransformed, with embryo for austenite nuclei formed;
2) The ferrite transforms to austenite with concurrent rapid carbide dissolution. The speed of carbide dissolution is such that the carbon content of the austenite increases even though the amount of austenite is also rapidly increasing;
3) Further carbide dissolution occurs in the austenite, until the carbide is completely dissolved, or the equilibrium carbon content for the austenitising temperature is attained.

For a 1.27 wt.% carbon steel, period 1 was only observed at 750°C[31], while period 2 was observed to its full extent at 750 and 775°C. At 900°C, period 2 was completed within 0.1s. It was presumed that at 750, 775, and 800°C, the carbon content of the austenite to first form was close to that of the Ac_3 value, increasing to 0.55 to 0.60wt.%C when the remaining ferrite

disappeared. The rate of carbide solution was then much slower in period 3 than during period 2. Nemoto[44] found that the cementite dissolution in ferrite was almost completely prevented by 0.5wt.%Mn. However, manganese has less influence on the cementite dissolution once the growing austenite grain came into contact with it.

2.2 Austenite formation and carbide dissolution kinetics

2.2.1 Austenite transformation

From experimental measurements of the transformation of ferrite to austenite, the isothermal transformation to austenite can be analysed by the Avrami rate equation[45] that describes the relationship between the austenite fraction formed, and the transformation time:

$$f = 1 - \exp(-Kt^n) \tag{2.5}$$

where f = fraction of austenite formed;

t = transformation time in s;

K = reaction coefficient;

n = the reaction exponent.

Equation (2.5) may be written in the form

$$\log\ln\left(\frac{1}{1-f}\right) = \log K + n\log t \tag{2.6}$$

From equation (2.6), log ln [1/(1-f)] can be plotted against log t, with the reaction exponent n given by the slopes of the resulting graphs. Figure 2.4(a) illustrates the austenite fraction versus the logarithm of time at different austenitising temperatures for a 0.95 wt.% carbon tool steel[33], from which the log ln [1/(1-f)] versus log t plot of Figure 2.4(b) was obtained.

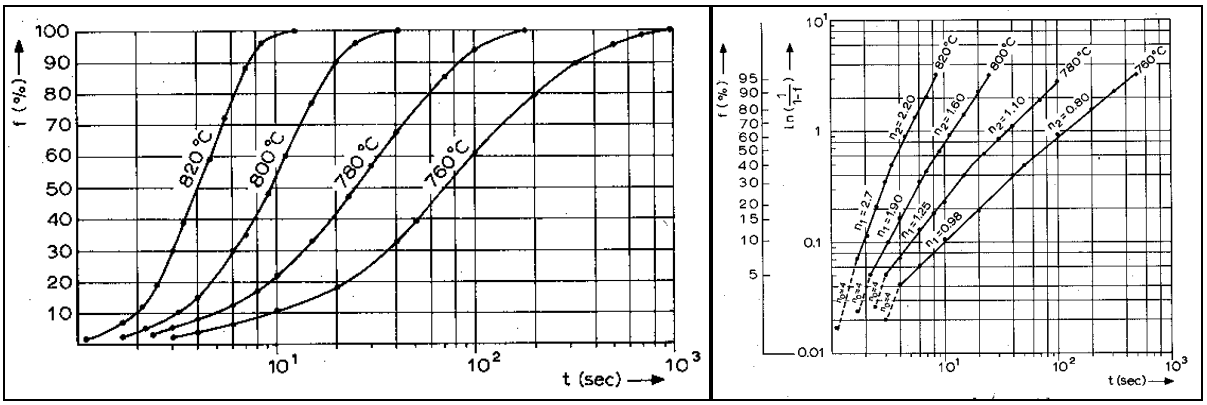

(a) **(b)**

Figure 2.4 Influence of temperature on austenitisation kinetics of a 0.95 wt.%C tool steel for (a) amount of austenite versus log t at different austenitising temperatures, and (b) log ln [1/(1-*f*)] versus log (from Ref. 33).

The reaction exponent varied with transformation temperature, and exhibited changes for each temperature in the vicinity of about 5 and 40% transformation. Dirnfeld[33] attributed the first change to the fraction of boundary area of edge length transformed being larger than the volume fraction transformed, and suggested that after 40% transformation, more alloying elements such as chromium and manganese were dissolved in the austenite matrix. Karmazin[35] investigated the austenitisation of a 0.80wt.%C/2.02wt.%Si/2.06wt.%Mn/ 1.05wt.%Cr steel for initial globular cementite structures in a ferrite matrix produced by the high temperature transformation of austenite, and by the tempering of martensite. For both structures the ferrite to austenite transformation was considerably slower than that of lower silicon and manganese steels[31-33], with the via austenite transformation requiring 1 hour, and the via martensite 15 hours, Figure 2.5. As the carbon release kinetics from the cementite into the space surrounding the dissolving cementite particles were the same, it was concluded that the difference kinetics of the ferrite to austenite transformation were associated with the different matrix properties surrounding the cementite particles.

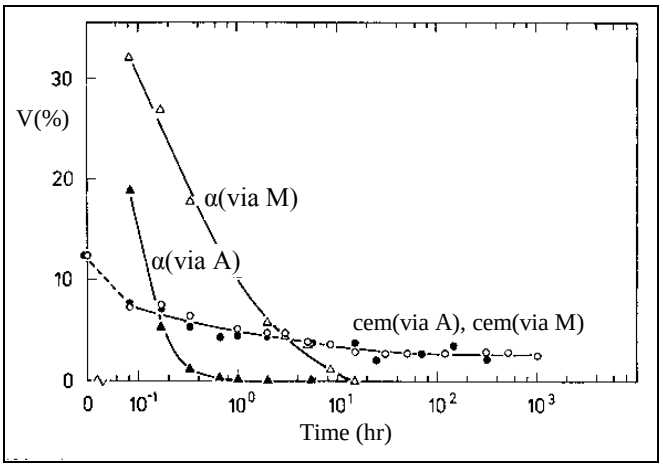

Figure 2.5 Decrease in the ferrite volume fraction during austenitisation of a 0.80wt.%C/2.02wt.%Si/2.06wt.%Mn/1.05wt.%Cr steel at 820°C (from Ref. 35).

The austenite layer adjacent to the retreating cementite inherits a high concentration of carbide forming elements, but no silicon, from the cementite. This lowers the carbon activity in this layer. In the opposite layer of the austenite shell next to the ferrite/austenite boundary, a low content of carbide forming elements in conjunction with slightly greater than 2.0wt.%Si is inherited from the initial ferrite, which increases the local carbon activity. Consequently, the driving force for carbon diffusion across the austenite shell from the dissolving cementite to the ferrite/cementite boundary, and therefore the ferrite to austenite boundary movement, is decreased. During the ferrite/austenite interface movement, partitioning of the alloying elements between ferrite and austenite increases the silicon content of ferrite, while decreasing the manganese content. Since silicon is a ferrite stabiliser, while manganese is an austenite stabiliser, the partitioning of silicon and manganese further retards the austenitisation of the steel.

The initial via austenite structure has most of the cementite particles located inside ferrite grains, while almost all the cementite particles are located on the grain boundaries for the via martensite structure. With the diffusion of alloying elements along grain boundaries being significantly greater than by volume diffusion, the via martensite structure will exhibit a greater redistribution of silicon and manganese during the formation of the austenite network, and therefore a greater ferrite stabilisation. Consequently, the ferrite to austenite

transformation is retarded more in the initially martensitic structure than in the initially austenitic structure.

Various authors[36,46,47] have established that the austenitic growth front advances with constant velocity in all directions in spheroidised carbon and alloy steels. Dirnfeld[33] found that a constant growth rate occurred up to about 30% transformation in a spheroidised hypereutectoid low alloy steel.

2.2.2 Carbide dissolution

Figure 2.6(a) illustrates the continuation of cementite dissolution in a 1.27 wt.% C steel well after transformation of the ferrite to austenite[31]. Figure 2.6(b) demonstrates the increasing austenite carbon content upon transformation of the ferrite, due to the continued carbide dissolution in the austenite. Figure 2.5 also illustrates that carbide dissolution continued well after all the ferrite had transformed to austenite in the hypereutectoid steel investigated by Karmazin[35].

Speich[36] determined that once austenite nucleated in pearlitic 0.77 and 0.96wt.%C Fe-C steels and alloys, the growth of austenite was controlled by the rate of carbon diffusion in the austenite. Judd and Paxton[46] concluded that growth of the austenite front in spheroidised structures was controlled by the rate of carbon diffusion through the austenite envelope upon nucleation of austenite at carbides, and the subsequent complete enveloping of the carbide by the austenite. The third period of the ferrite/cementite to austenite/cementite transformation, where the ferrite to austenite transformation is complete, involves a gradual dissolution of carbides in the austenite. Molinder[31] found that the activation energy calculated for this period was substantially higher than that required for carbon diffusion to be the governing factor, being 840kJ/mole versus 145kJ/mole for carbon diffusion in austenite.

He concluded, therefore, that the rate controlling factor was the interface reaction at the carbide/austenite interface. Dirnfeld[33] investigated the transformation of a spheroidised structure to one containing undissolved carbides in an austenitic structure for a fine grained tool steel, with the calculated activation energy coinciding with the value required for interface controlled growth at the ferrite/austenite interface.

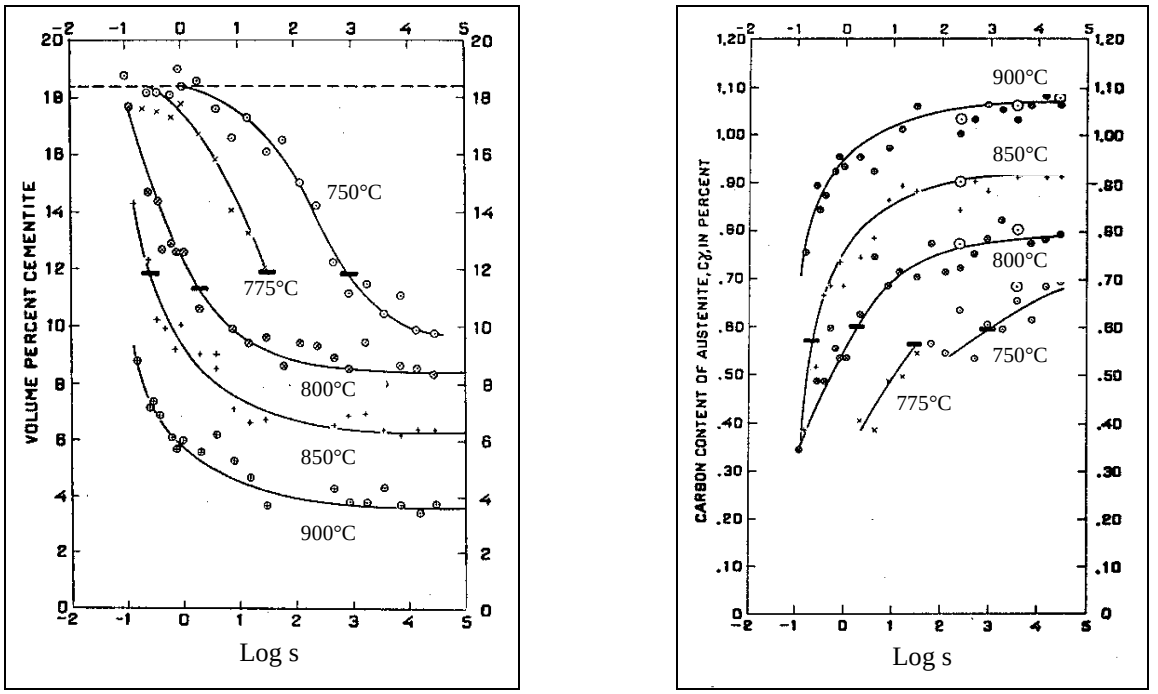

(a) **(b)**

Figure 2.6 Transformation kinetics for a 1.27 wt.%C steel illustrating (a) cementite volume fraction as a function of log t for different austenitising temperatures, and (b) carbon content of austenite versus log t at different austenitising temperatures. – indicates the time when the ferrite dissolution was completed. (from Ref. 31).

2.3 Influence of alloying elements on austenitisation

Several investigators[32,48,49] have determined that for manganese and chromium alloy steels, these elements concentrate first in the cementite, but they diffuse into the austenite together with the carbon at a later stage in the transformation. Hultgren[50-52] investigated the function of alloy elements on various transformations in steels, and distinguished between two cases in the transformation of austenite, where:

1) The transformation occurred without the redistribution of alloying elements;
2) The transformation only occurred as the alloying elements were being redistributed between the various phases involved in the transformation.

Svoboda[53] investigated the partitioning of alloying elements between ferrite, austenite, and cementite in a low alloy steel containing higher silicon and manganese contents, as illustrated in Figure 2.7. Chromium is generally a stronger carbide-forming element than manganese, but the content of these elements in cementite is dependent on whether cementite was in equilibrium with ferrite or austenite. For temperatures below the eutectoid zone where ferrite and cementite were in equilibrium, the cementite manganese concentration was considerably greater than that of chromium. At temperatures above the eutectoid zone where cementite coexisted with austenite, this relationship was reversed. Within the eutectoid zone, manganese showed a preference for austenite, and silicon for ferrite. The chromium concentration was not significantly different in ferrite and austenite.

Karmazin[54] determined that chromium was mainly located in the carbides, with the rest uniformly distributed in the matrix. Manganese was also present in the carbides, but the majority was dissolved in the martensite matrix. Silicon was dissolved entirely in the matrix, with a preference for ferrite. These observations are in accordance with the recognised austenite stabilisation and weak carbide forming tendency of manganese and the ferrite stabilisation of silicon[35,55].

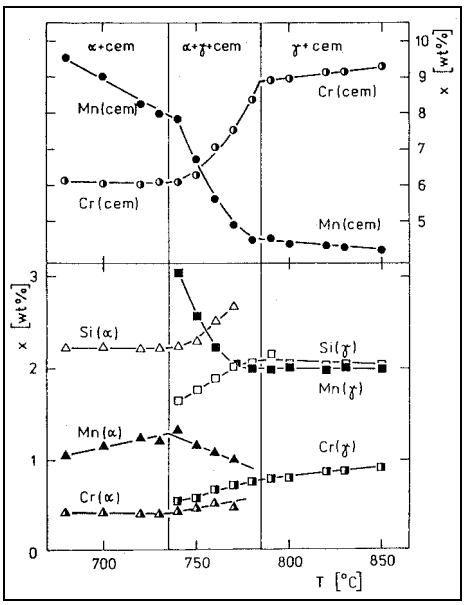

Figure 2.7 Influence of annealing temperature on the partitioning of alloying elements for a 0.80wt.%C/2.06wt.%Mn/2.02wt.%Si/1.05wt.%Cr steel (from Ref. 53)

Speich[39] separated austenite formation from ferrite/pearlite initial structures for 0.06-0.20wt.%C/1.5wt.%Mn steels into three stages:

1) Very rapid austenite growth into pearlite until pearlite dissolution was completed;
2) Slower austenite growth into ferrite at a rate controlled by carbon diffusion in austenite at high temperatures of approximately 850°C, and by manganese diffusion in ferrite or along grain boundaries at low temperatures of approximately 750°C;
3) Very slow final equilibration of ferrite and austenite at a rate controlled by manganese diffusion in austenite.

These three stages were also observed by other researchers for similar steels[56,57]. The development of dual phase structures were investigated for a 0.11wt.%C/0.73wt.%Si/ 1.60wt.%Mn steel from a homogeneous ferrite/pearlite initial structure[58]. No measurable silicon partitioning was observed. However, substantial manganese partitioning to the lamellar cementite plates occurred, as illustrated in Figure 2.8(a). Figure 2.8(b) illustrates significant manganese redistribution between the ferrite and martensite during the austenitisation process.

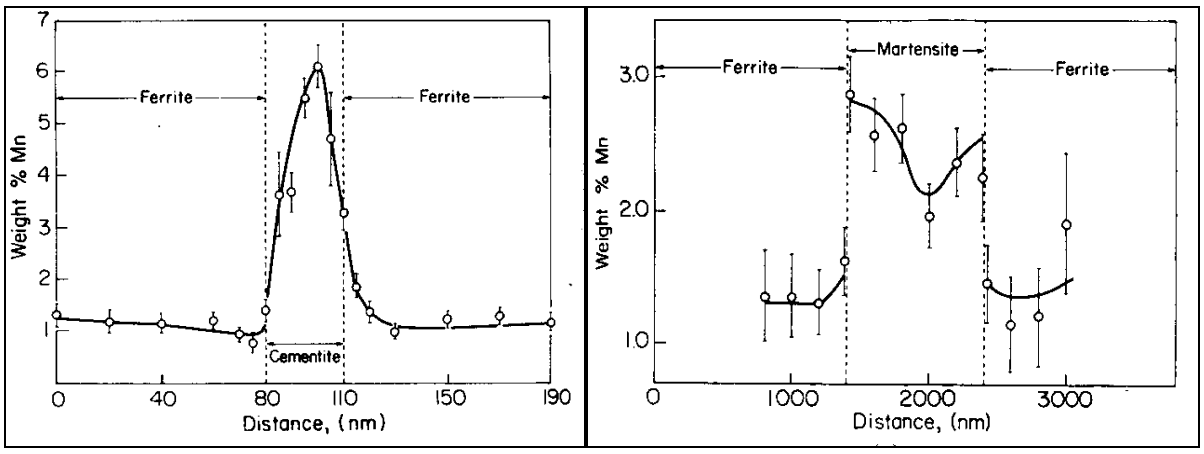

(a) **(b)**

Figure 2.8 Manganese concentration profiles for a 0.11wt.%C/0.73wt.%Si/1.60wt.%Mn steel across (a) a thin cementite plate of the initial structure, and (b) a martensite shell at a ferrite/ferrite interface after 2hr at 769°C (from Ref.58).

This chapter detailed the literature pertaining to the austenitisation of steel in terms of the influence of composition, microstructure and temperature on the austenite formation and

concurrent cementite dissolution. An investigation into the decarburisation of steel requires information pertaining to carbon diffusion through steel as a function of composition and microstructure. Since this information is available from an austenitisation investigation, the austenitisation literature of this chapter preceded the decarburisation literature of Chapter 3.

CHAPTER 3

DECARBURISATION OF STEELS

3.1 Introduction

Decarburisation involves carbon removal from the steel surface, and often occurs during commercial heat treatments when the carbon potential, or carbon activity, of the furnace atmosphere falls below that necessary to sustain the surface carbon content for temperatures above approximately 500°K[67]. Carbon removal initiates at the steel surface/furnace atmosphere interface, with carbon removed from the steel matrix at the surface, and from any carbide intersecting the surface. This creates a carbon concentration gradient in the steel specimen, resulting in carbon diffusion from the interior to the surface of the steel.

The carbon content at the surface of a decarburised component can range from just below the bulk steel content to virtually zero, with the carbon concentration gradient dependent on the local carbon content of the steel. The local carbon concentration in the steel is a function of the alloy element concentration, the phases that are present, the temperature with the associated solubility for these given phases, and the solubility product for the carbide precipitates in the presence of the given phases. The local carbon content is also influenced by the extent of the ferrite to austenite transformation upon heating the steel to temperature, and the presence of any undissolved carbide particles.

Several different mechanisms contribute to the carbon transport through the steel to the surface. Carbon transport can occur in the steel by diffusion in the bulk, along dislocations and other defects, as well as along grain boundaries. In addition to the diffusion of carbon through the steel, the rate and extent of decarburisation is a function of the oxidising potential of the heat treatment atmosphere, and the subsequent formation of any oxide layers. The carbon activity of the furnace atmosphere establishes the minimum surface carbon content to which the steel can be decarburised, and also influences the rate of decarburisation. Any decarburisation arising in the production of springs is of importance, due to the reduction in sag resistance and fatigue strength of the springs.

3.2 Decarburisation of plain carbon steels

Decarburisation can lead to a gradual lowering of the carbon content throughout a structure, or a step change in composition if a phase change accompanies the carbon removal. The decarburisation phases and associated equilibrium carbon contents can be predicted from the Fe-C equilibrium diagram[59], Figure 3.1. The carbon activity of the furnace atmosphere at the gas/steel interface determines the minimum carbon content to which the steel surface can be decarburised. If the carbon activity of the furnace atmosphere is zero, the steel can be theoretically decarburised to give a final structure containing no carbon. In reality however, small carbon contents remain[60,61].

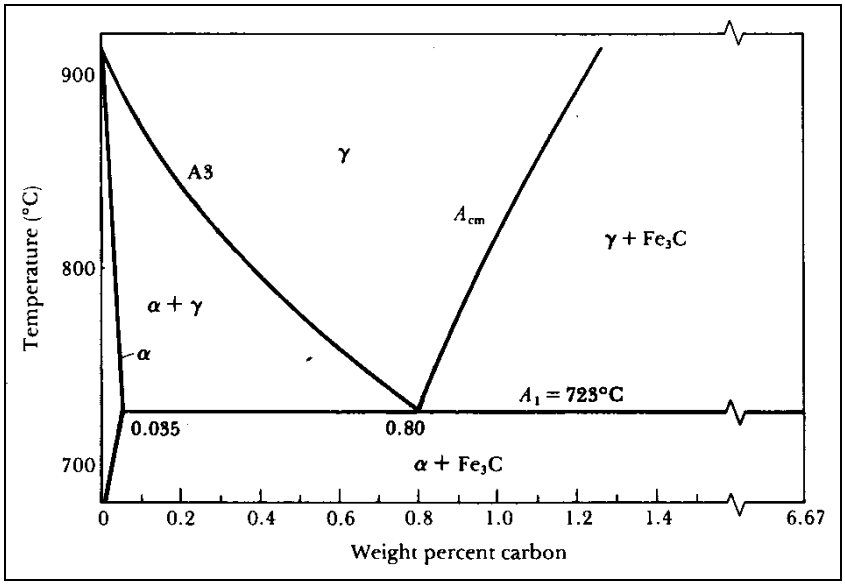

Figure 3.1 Left-hand portion of the Fe-C equilibrium diagram (from Ref. 62).

3.2.1 Decarburisation in the intercritical temperature range

Decarburisation within the intercritical temperature range results in carbon removal from the ferrite/austenite dual phase region, with the subsequent formation of a surface ferrite layer. Figure 3.2(a) illustrates the carbon concentration profile for this situation, based on a diffusion-controlled process with the inward motion of the ferrite/ferrite plus austenite interface. It is assumed that Fick's second law applies to the ferrite and ferrite/austenite, and that there are equilibrium conditions at the ferrite/ferrite plus austenite interface phases[63]. C_s

denotes the surface carbon content, while C_{sat} is the ferrite saturation carbon content at the interface between the ferrite and ferrite/austenite phases. At the interface there is a step change in the carbon content from C_{sat} to the initial bulk steel content, C_o. As carbon diffusion in ferrite is considerably greater than in austenite, carbon removal from the ferrite/austenite two phase structure will result in a surface layer of ferrite separated from the two-phase region by a sharply defined interface.

3.2.2 Decarburisation at the Ac_3 temperature

There is a specific temperature for each carbon content where the initial non-decarburised structure of the steel will be just austenitic. Carbon removal will result in a phase change at the surface from austenite to ferrite, with a lowering in the carbon content to the saturation value for ferrite. This is illustrated in Figure 3.2(b), with diffusion controlled decarburisation assumed.

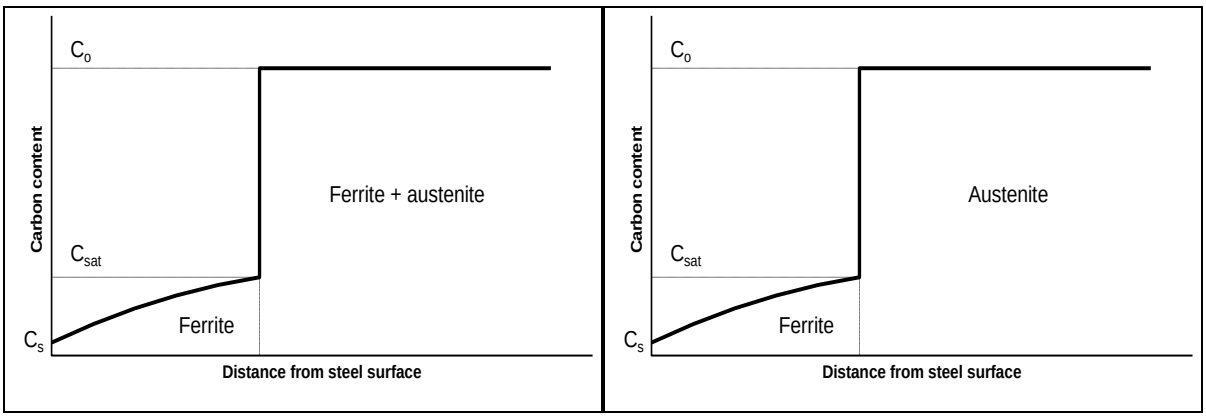

(a) **(b)**

Figure 3.2 Carbon profiles assuming diffusion controlled decarburisation with the formation of a surface ferrite layer for (a) decarburisation in the ferrite/austenite two phase region, and (b) decarburisation at the Ac_3 temperature (from Ref 63).

3.2.3 Decarburisation above the Ac_3 temperature

At temperatures greater than the Ac_3 value for a steel, carbon removal for diffusion controlled decarburisation will initially result in a concentration profile being established in the

austenite, with the carbon concentration increasing from the surface to the centre of the steel. For temperatures lower than approximately 910°C, there will be a phase change from austenite to ferrite when the surface carbon content reaches that specified by the Ac_3 value. Further decarburisation will result in a surface ferrite layer separated from an austenitic core, with a concentration gradient in the austenite, Figure 3.3. For temperatures above 910°C, the steel remains austenitic when decarburised.

One of the earlier studies[64] into decarburisation was undertaken for an eutectoid steel at 690 to 925°C. At temperatures above 730°C, a free ferrite surface layer formed from the initial structure, and had a columnar grain structure. Pennington[64] suggested that these grains could only be formed in the intercritical range at the point where austenite was being converted into ferrite at a fairly uniform temperature, and only when the rate of decarburisation was sufficiently high. For low carbon steels, two conditions must exist simultaneously for columnar growth to occur[65]:

i) Decarburisation must occur between the Ac_1 and Ac_3 temperatures;
ii) The cementite distribution in the steel prior to decarburisation must be as a uniformly dispersed grain boundary network.

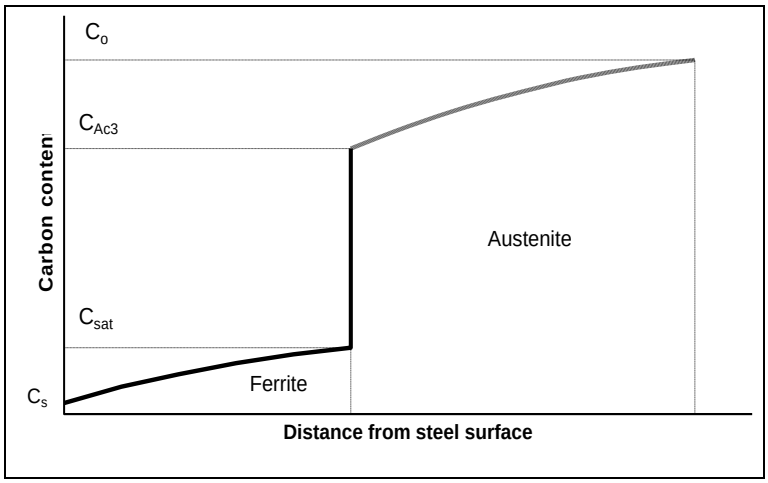

Figure 3.3 Carbon profile assuming diffusion controlled decarburisation above the Ac_3 temperature, but below 910°C, with the formation of a surface ferrite layer (from Ref 63).

Marder[66] demonstrated that the grain structure obtained during the decarburisation of low carbon steels is also dependent on the carbon content. Decarburisation of a 0.02wt.%C steel within the ferrite/austenite two phase region at 788°C yielded equiaxed ferrite grains. However, a columnar grain structure was obtained when decarburising a 0.06wt.%C steel at the same temperature. Upon decarburising within the two phase region, the cementite and surrounding ferrite transformed to austenite, with the austenite pinning the ferrite grain boundaries, and therefore preventing abnormal grain growth. Decarburisation progressed as a front moving from the surface inward, with the carbon rich austenite particles preventing grain growth until decarburisation eliminated the austenite. This yielded directional grain growth from the surface inward, and the subsequent columnar morphology. Complete decarburisation prior to columnar grain growth into the bulk of the specimen was not necessary, with the advancement of the grain dependent upon a reduction of pinning points below a certain minimum[66].

During the decarburisation of a eutectoid steel at 730°C, the austenite at the ferrite/austenite interface had a carbon content greater than the minimum austenite content of 0.75wt.% even after 6hr[64]. Consequently, there was not enough surface exposed on a planar interface for the transformation of austenite to ferrite upon carbon removal to occur sufficiently rapidly to satisfy the demands for diffusion. Therefore the planar interface was destroyed, with ferrite particles existing well into the austenite. The austenite was found to be broken up into many pieces with more surface in contact with the ferrite, as opposed to existing as one piece with a planar interface with ferrite.

The minimum austenite carbon content at 760°C is 0.50wt.%. Upon decarburisation of the eutectoid steel with a bulk steel carbon content of 0.83wt.%[64], the initial carbon removal was directly from the austenite, with the carbon content remaining above the Ac_3 value of 0.50wt.%. However, the carbon content in the surface layer was soon lowered to 0.50wt.%. Once it reached this value, the austenite transformed to ferrite, with the surface carbon content now 0.026wt.%. A distinct ferrite layer was present after 30min for the 0.83wt.%C steel decarburised at this temperature[64].

As the decarburisation temperature is further increased, the formation of a free ferrite layer will not necessarily occur immediately, with the free ferrite formation dependent on the bulk carbon content of the steel, and the speed of decarburisation. At 895°C, where the minimum

austenite carbon content is just 0.05wt.%, Pennington[64] demonstrated that no ferrite layer was present after 30min. This was due to carbon diffusion to the surface maintaining the austenite carbon content above the minimum value. However, ferrite formation was observed after 2hr, since carbon could not be supplied at the surface rapidly enough to maintain the surface content above this minimum value.

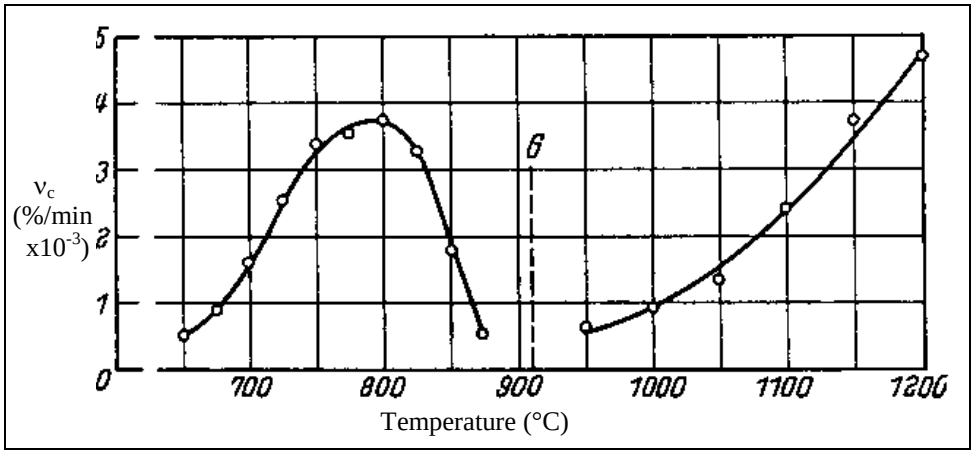

Figure 3.4 Dependence of decarburisation rate, ν_c, of a Fe/0.06wt.%C steel on the heat treatment temperature (from Ref. 67).

The influence of annealing temperature on the decarburisation rate of a low carbon steel is illustrated in Figure 3.4[67], with the wet hydrogen atmosphere yielding diffusion controlled decarburisation. The decarburisation rate is defined as

$$\nu_c = \frac{k}{m}\int_o^{t_d} \frac{CO}{t_d},$$

where ν_c = decarburisation rate in %/min;

k = a constant;

m = mass of the steel sample;

CO = carbon monoxide concentration in vol.%;

t_d = decarburisation time.

The decarburisation rate reached a maximum within the intercritical region at 800°C. The minimum decarburisation rate occurs at the Ac_3 temperature, and then increased at higher

temperatures in the austenite region. The decarburisation rates were similar at 800 and 1150°C.

3.2.4 Influence of alloying elements on decarburisation

Birks[68] considered the qualitative effect of alloying elements on decarburisation, where the alloying elements may influence the decarburisation due to their effect on the:

(i) Ferrite to austenite transformation temperature;
(ii) Activity of carbon in solution;
(iii) Diffusion coefficient of carbon in solution;
(iv) The oxidation characteristics of iron.

Birks also predicted the qualitative effects of some of the common alloying elements on the decarburisation[68], as summarised below.

Silicon

Silicon diffuses from the steel into the oxide scale, forming silica, SiO_2, and fayalite, Fe_2SiO_4, with both oxides reducing the scaling rate. Silicon also increases the carbon activity in solution, and therefore the tendency for carbon to diffuse to the scale/metal interface. Therefore, Birks[68] predicted that silicon would tend to increase decarburisation.

Manganese

Manganese concentrates in the oxide scale in the wustite, FeO, and magnetite, Fe_3O_4, oxides. The scaling rates are hardly affected, with any effect on the decarburisation restricted to the effect of manganese on carbon activity and diffusion. Since manganese is denuded in the surface layers of a steel, Birks[68] suggested that any effect of manganese on the decarburisation would be slight.

Chromium

Chromium concentrates in the oxide scale, forming spinel or R_2O_3 oxides, depending on its concentration. Chromium generally reduces the scaling rate. Chromium also reduces the carbon activity in solution, which tends to reduce carbon diffusion to the surface. Therefore,

the lower scaling rate would tend to increase the decarburisation rate, whereas the reduced carbon activity would tend to reduce it[68].

Nickel

Nickel concentrates in the metal at the oxide scale/metal interface, but may not greatly affect the scaling rate. However, the solubility of carbon in the surface layers may be reduced, thus restricting carbon diffusion and hence the decarburisation rate[68].

Copper

Copper concentrates in the metal at the oxide scale/metal interface. Due to the low solubility of copper in iron, a copper rich phase will form, reducing the decarburisation rate[68].

3.3 Decarburisation environments

Decarburisation commonly occurs at elevated temperatures in the presence of CO, CO_2, H_2, H_2O, and CH_4, which react with carbon at the steel surface and lower the carbon content. The decarburisation of steel occurs in hydrogen through the reaction of hydrogen with carbon by equation (3.1)[69-71].

$$[C] + 2H_2(g) = CH_4(g), \qquad (3.1)$$

where [C] = carbon in solution in iron.

Decarburisation with hydrogen is influenced by the furnace temperature, heat treatment duration, and the steel carbon content, and is slow because the speed of equation (3.1) is slow. CO_2 reacts with the steel to produce CO by equation 3.2[71,72].

$$[C] + CO_2(g) = 2CO(g). \qquad (3.2)$$

Water vapour is a potent decarburising agent, even for small water vapour concentrations. The decarburisation is strongly influenced by the water content of the gas and furnace, with decarburisation occurring by reaction (3.3)[64,69-71,73]. The decarburisation rate using water vapour is considerably greater than by hydrogen or CO_2[64,69-71]. The addition of hydrogen to water vapour facilitates the decarburisation as it determines the amount of oxidising agent

available[67]. The main role of hydrogen in the atmosphere is to maintain reducing conditions at the gas/steel interface. Decarburisation can also occur by the water gas reaction of (3.4)[69,71].

$$[C] + H_2O(g) = CO(g) + H_2(g) \quad (3.3)$$

$$CO(g) + H_2O(g) = CO_2(g) + H_2(g). \quad (3.4)$$

3.4 Decarburisation of higher silicon steels

Low carbon steels containing up to 3wt.%Si are commonly used in the electrical industry. These steels are decarburised to very low carbon contents in order to obtain desirable magnetic properties. The decarburisation is normally carried out in a moisturised hydrogen atmosphere with the predominant decarburisation reaction that of equation (3.3). In comparison, decarburisation with hydrogen by equation (3.1) has been found to be negligible[69]. Decarburisation of these steels is influenced by the silicon content, the furnace temperature, and by the composition of the decarburisation atmosphere.

3.4.1 Influence of alloy content

Wiesner[73] demonstrated that the silicon content and subsequent oxidation behaviour determined the decarburisation characteristics of low carbon steels with 0.5 to 3.0wt.%Si. Two different decarburisation profiles were exhibited, these being:

1) A non-linear decrease in carbon content with time;
2) A linear decrease in carbon content with time.

These decarburisation profiles are shown in Figures 3.5(a) and (b) respectively. The non-linear decarburisation profile corresponded to a high degree of decarburisation, and was obtained from the low silicon steels. However, the higher silicon steels exhibited less decarburisation, with a linear decrease in carbon. Modelling the non-linear decarburisation with a diffusion process yielded a diffusion coefficient an order of magnitude lower than for carbon diffusion in ferrite[73]. The low silicon steels formed a porous SiO_2 oxide structure when exposed to the heat treatment atmosphere which facilitated decarburisation by a delayed diffusion controlled process. The partial covering of the surface with SiO_2 resulted in longer diffusion paths, and the reduced permeability of the steel surface for carbon. At higher silicon

contents the formation of a compact thin but dense SiO_2 layer resulted in decarburisation controlled by a time law of zeroeth order typical of a time constant boundary layer process[73].

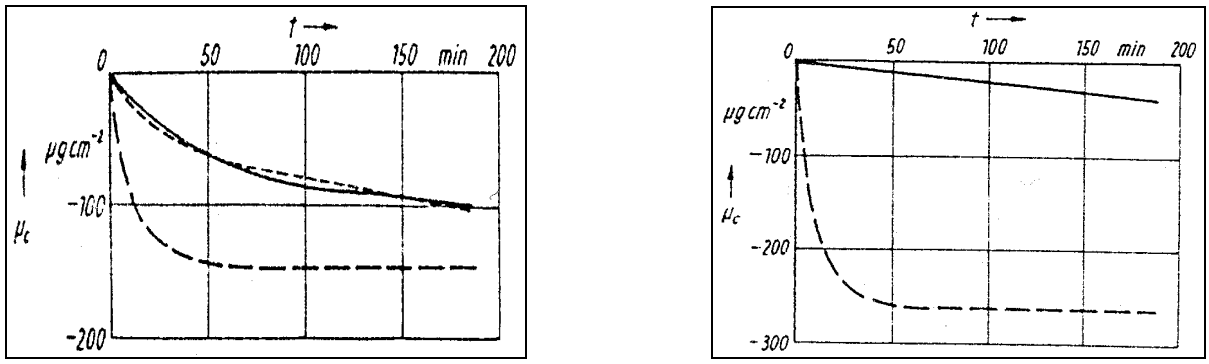

Figure 3.5 Decarburisation profiles of electrical steels at 850°C showing the mass change per area, μ_c, for (a) non-linear carbon content decrease with time, and (b) linear carbon content decrease with time. The dashed line denotes decarburisation controlled by carbon diffusion through ferrite (from Ref. 73).

Figure 3.6 illustrates that the decarburisation rate of low carbon steels increased with increasing silicon content[67].

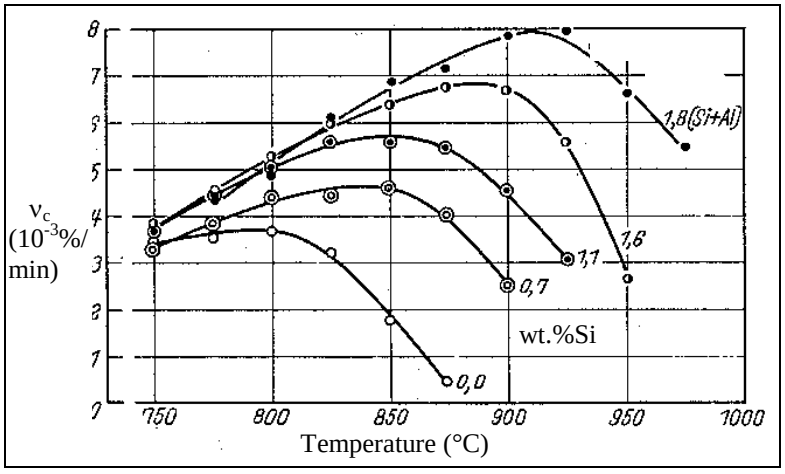

Figure 3.6 Influence of silicon content on decarburisation rate, ν_c, of low carbon steels (from Ref. 67).

Inwards diffusion of carbon atoms was observed during the vacuum annealing of 0.095wt.%C/2.06wt.%Si/1.01-2.04wt.%Mn[74] and 0.50-0.97wt.%C/2.07-3.03wt.%Si/1.02-2.53wt.%Mn[75] steels. Heat treating at 950 to 1,000°C in a 10^{-3}Pa vacuum resulted in the transformation of austenite to ferrite at the surface due to manganese depletion[75]. The manganese depletion was attributed to manganese evaporation, which increased the activity of the carbon atoms at the surface, resulting in carbon diffusion into the interior and an austenite to ferrite transformation[74]. Subsequent decarburisation in a wet hydrogen/argon atmosphere at 850°C resulted in the inward growth of the surface ferrite layer as columnar grains[74]. However, decarburisation at 700°C yielded columnar grains at the surface, with finer equiaxed ferrite grains further into the ferrite layer[74].

A similar austenite to ferrite transformation was observed during the oxidation of a Fe/6.6wt.%Si/16.1wt.%Mn/2.1wt.%Ni alloy in air[76]. This arose from the formation of a silica layer at the surface of the alloy. This caused the oxidation process to become selective to manganese, with the formation of a manganese oxide, MnO, layer on the surface of the silica layer[76,77]. Consequently, the metal near the scale/metal interface transformed from austenite to ferrite, with the subsequent growth of the ferrite layer controlled by the outward grain boundary diffusion of manganese through the ferrite layer to the oxidising surface[77].

3.4.2 Influence of temperature

Marini[78] investigated the decarburisation of a 0.054wt.%C/2.87wt.%Si steel at temperatures ranging from 790 to 930°C in a wet hydrogen atmosphere. Typical decarburisation profiles at 790 and 930°C are illustrated in Figure 3.7(a). The total carbon extracted from the steel was less at 930°C than at 790°C. This is also illustrated in Figure 3.7(b), where complete carbon release does not occur at temperatures higher than 830°C. The decarburisation of this steel was characterised by two distinct steps, as illustrated in Figure 3.7(a). During the heating of the steel specimen, a partial decarburisation occurred. Once the temperature reached approximately 700°C, the silicon reacted with the wet hydrogen atmosphere, resulting in external oxidation, and the formation of an impervious thin silica layer that inhibitted the decarburisation[79]. As the temperature further increased, the oxygen potential became suitable for internal oxidation of silicon, and the decarburisation recommenced. As the oxidised particles formed, the decarburisation rate decreased. Decarburisation finally ceased when a

critical volume fraction of silica formed. At 790°C, complete decarburisation of the steel occurred since the internal oxidation was non-blocking.

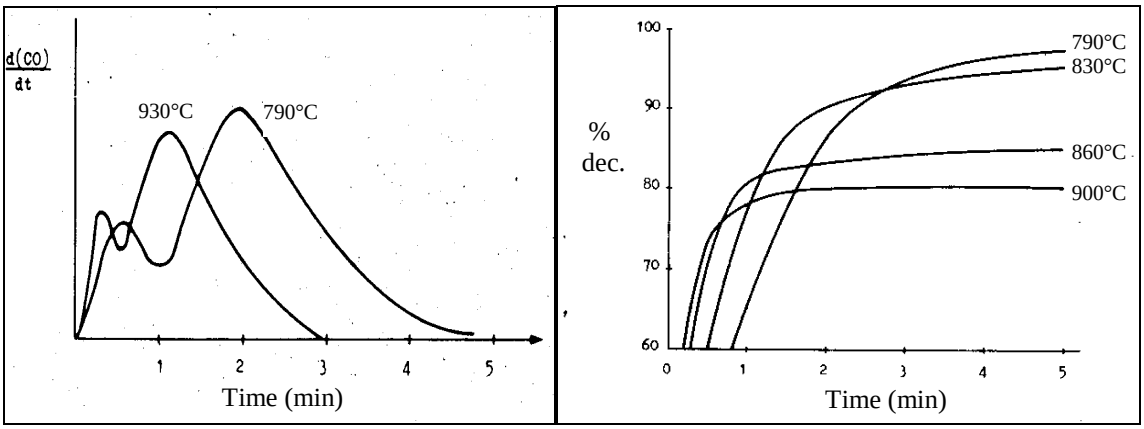

(a) **(b)**

Figure 3.7 Decarburisation of a 2.87wt.%Si electrical steel at p_{H_2O} / p_{H_2} =0.25 for (a) 790 and 930°C, and (b) 790 to 930°C (from Ref. 78).

Decarburisation of a low carbon 3wt.%Si steel at 800 and 1000°C at a dew point of 30°C resulted in the liberation of CO and CH_4, Figures 3.8(a) and (b) respectively[69]. No CO_2 was detected. The CO liberated at both temperatures was considerably greater than that of CH_4, indicating that equation (3.3) was the predominant decarburisation reaction. At 800°C, the CO profile exhibitted a single maxima. However, a second peak was also observed after approximately 20min at 1,000°C. The first peak was due to the formation of a silica layer as the specimen heated to temperature, which restrained the decarburisation. Further heating allowed the decarburisation to recommence, resulting in the second peak of Figure 3.8(b)[67,78].

3.4.3 Influence of decarburisation atmosphere

Electrical steels are predominantly decarburised in a wet hydrogen atmosphere, with carbon removal effected by equation (3.3). The oxidising potential of this atmosphere is described by the p_{H_2O} / p_{H_2} ratio, with the oxidising potential increasing as the water content, and therefore the p_{H_2O} / p_{H_2} ratio, increases. The desired hydrogen water content is generally obtained by bubbling hydrogen through water maintained at a specific temperature, in an attempt to saturate the hydrogen with water vapour at that temperature. The water temperature

determines the maximum possible water vapour pressure, with the saturation water vapour pressure increasing with temperature, from 0.0129kPa at –40°C to 101.35kPa at 100°C. The saturation water pressures at different temperatures are listed in Appendix D.

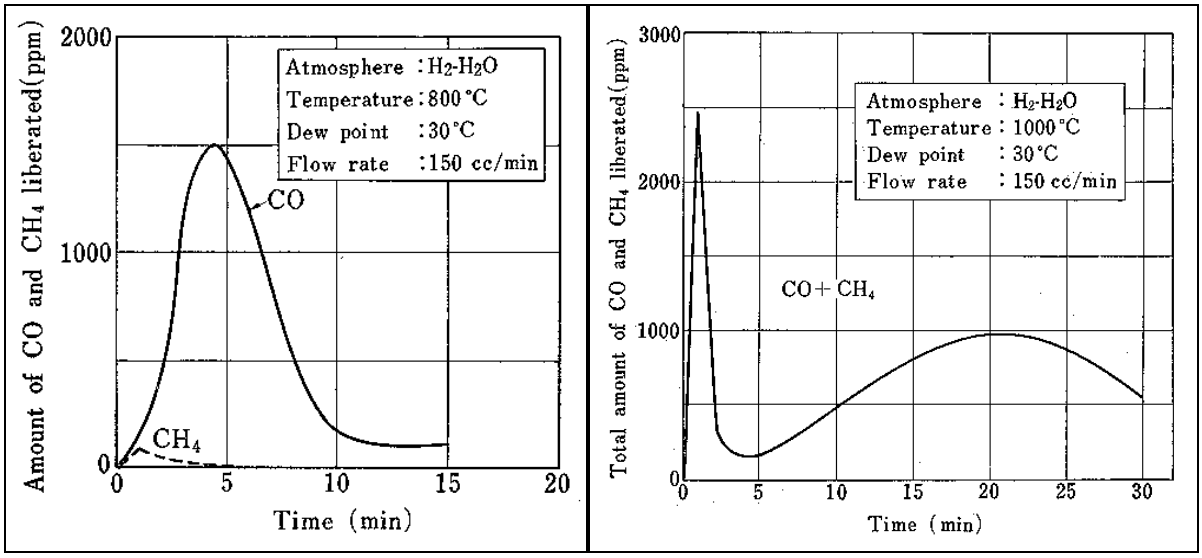

(a) **(b)**

Figure 3.8 Decarburisation of a 3wt.%Si electrical steel with a p_{H_2O} / p_{H_2} ratio of 0.04 (30°C dew point) at (a) 800°C, and (b) 1,000°C (from Ref. 69).

An increase in the p_{H_2O} / p_{H_2} ratio from 0.03 to 0.25 for the decarburisation of a 0.04wt.%C/0.68wt.%Si/0.31wt.%/Mn steel at 850°C doubled the decarburisation rate, Figure 3.9(a)[67]. However, when the p_{H_2O} / p_{H_2} ratio exceeded that necessary for oxidation of the iron matrix, a sharp decrease in the decarburisation rate resulted. This decrease was less pronounced with increasing silicon content from 0.7 to 2.5wt.% at 800°C, Figure 3.9(b). Marini[78] demonstrated that the percentage decarburisation of a 0.054wt.%C/2.87wt.%Si steel increased for p_{H_2O} / p_{H_2} ratios of up to 0.4, as illustrated in Figure 3.10. However, 100% decarburisation was not obtained above 830°C, regardless of the p_{H_2O} / p_{H_2} ratio. This was attributed to the eventual formation of a critical silica volume fraction that prevented full decarburisation[78].

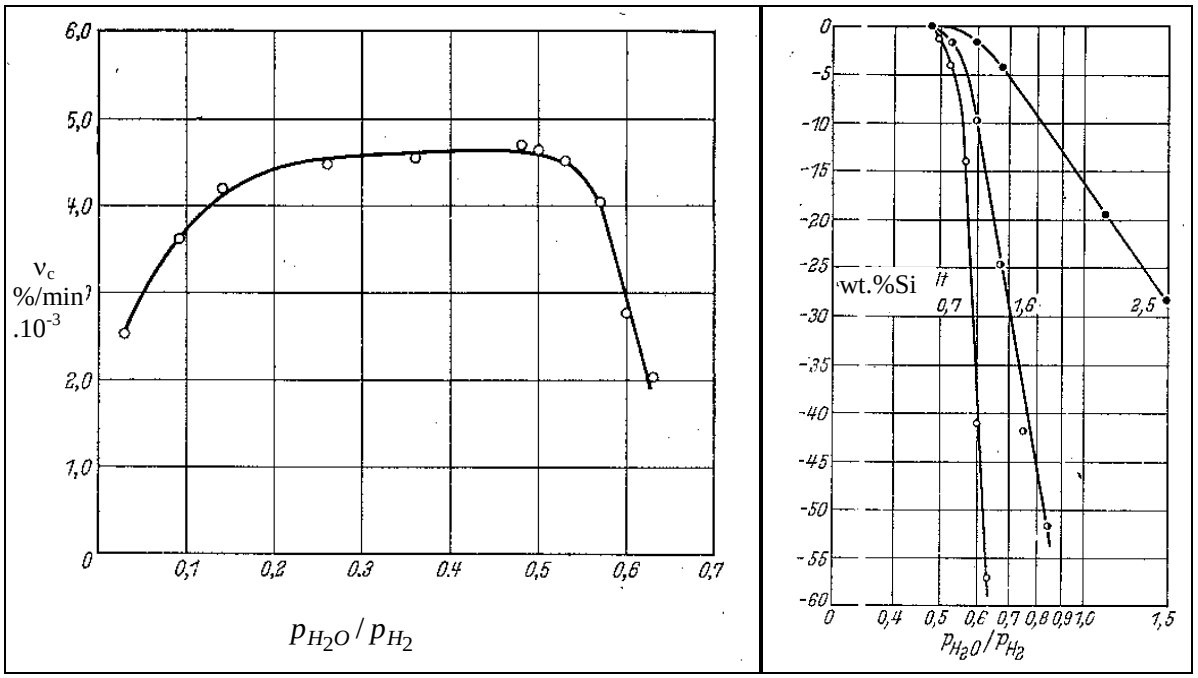

(a) **(b)**

Figure 3.9 (a) Dependence of the decarburisation rate on p_{H_2O} / p_{H_2} ratio for a 0.04wt.%C/0.68wt.%Si/0.31wt.%Mn steel at 850°C, and (b) influence of silicon content on the decrease in decarburisation rate at 800°C with increasing p_{H_2O} / p_{H_2} ratios above the oxidation limit (from Ref. 67).

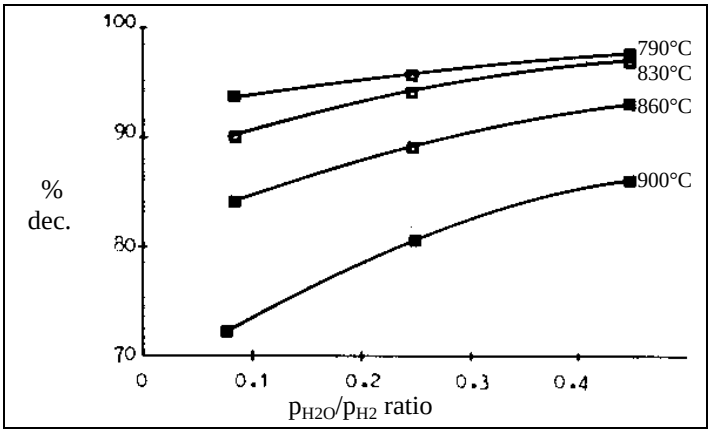

Figure 3.10 4min decarburisation of a 2.87wt.%Si steel as a function of p_{H_2O} / p_{H_2} ratio (from Ref. 78).

3.5 Oxidation of silicon steels

3.5.1 Fundamentals of oxidation

Oxidation involves the reaction of a metal with oxygen, with the oxide formation often influencing the decarburisation. The oxide may be[80]

1) Unstable, where oxidation does not occur;
2) Volatile, where oxidation occurs at a constant, relatively high rate;
3) One or more oxides which form a layer, or layers, at the metal surface.

The third occurrence is the most common. Surface oxide layers with a thickness of less than about 300nm are known as films, and as scales when their thickness exceeds this value and is more easily measured. Films usually decrease the rate of additional oxidation, and in cases, may be almost completely protective. The Pilling-Bedworth rule classifies thick oxide layers as either protective or non-protective, depending on the volume of the oxide[80]. From this rule, an oxide is protective if the volume of the oxide is at least as great as the volume of metal from which it formed. If the volume of the oxide is less than the volume of the metal from which it formed, the scale is not continuous, and is therefore comparatively ineffective in preventing the access of oxygen to the metal surface.

Metals that have non-protective oxide(s) tend to increase the weight of their scale at a linear rate, with the growth mechanism involving passage of gaseous oxygen through pores or fissures in the oxide film[80]. For the formation of a protective oxide on an exposed metallic surface, diffusion must occur through the scale for additional growth to occur, as illustrated schematically in Figure 3.11. The metal ion, M++, and the electrons then diffuse through the oxide layer to the oxygen surface. The electron aids in forming the oxygen ion, with this ion reacting near the oxygen surface with the metal ion to form the oxide, MO. In this case the oxidation rate should follow a parabolic law.

Parabolic growth is observed experimentally in many cases, with the oxidation of iron involving the simultaneous formation of two or more oxide layers. At high temperatures, three layers are formed, with the scale comprised largely of an inner layer of FeO, wustite. Fe_3O_4, magnetite, forms a middle layer, while Fe_2O_3, hematite, forms at the oxygen surface, with FeO and Fe_3O_4

growing by the mechanism described in Figure 3.11[80]. However, the oxidation of iron to Fe_2O_3 occurs by a different mechanism, as the oxygen is more mobile and diffuses inwards from the oxygen surface.

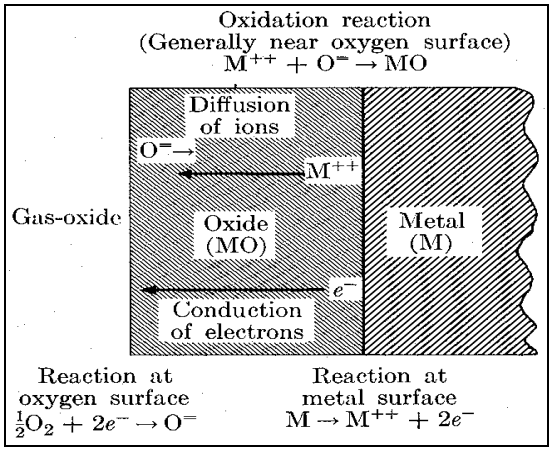

Figure 3.11 Oxidation of a metal through a protective oxide layer (from Ref. 80).

Some metals forming protective oxides have reaction rates that diminish more rapidly with time than predicted by a parabolic law. There are situations when an oxide layer approaches a constant thickness with increasing time, thus obeying an asymptotic law. In other cases, such as in the oxidation of iron at moderate temperatures, a logarithmic increase in the weight of the oxide occurs. The oxidation of an alloy, as opposed to a pure metal, involves several other features, including[80]:

1) The formation of a solid solution by the separate oxides;
2) The appearance of a multiphase scale;
3) The oxidation of only a single component in the alloy through selective oxidation.

When the oxides that form are highly soluble in each other, certain generalisations can be made about the oxidation behaviour of the alloy system[80]. For cation-deficient structures, the addition of a higher valence species tends to increase the oxidation rate, while additions of a lower valence species usually decrease the oxidation rate. However, for oxides with excess cations and electrons in interstitial positions, the reverse applies. For multiphase oxide scales consisting of more than one phase, the oxidation characteristics of the alloy are usually governed by the properties of that oxide phase which is continuous. With selective oxidation of one component at

the surface of an alloy, certain surface films decrease the oxidation rate if they are adherent, have poor electrical conductivity, and possess a complex crystal structure that hinders diffusion through them. A specific case of selective oxidation is that of internal oxidation.

Internal oxidation involves the oxidation of an alloying element beneath the surface of the base metal. This form of oxidation, which may occur in the absence of appreciable surface film or scale formation, usually requires that[80]:

a) The alloying element must have a greater affinity for oxygen than does the base metal;
b) Oxygen must diffuse rapidly in the base metal relative to the diffusion of the alloying element;
c) Scaling of the base metal must not be so rapid as to destroy the surface region in which internal oxidation is occurring.

For high temperature use, certain alloy steels are available that form protective scales while still very thin. Thin scales are unlikely to be detached from the surface as would thick scales. This is due to the internal compressional energy per unit area available for detachment being much smaller for thin scales than for thick scales, while there is no reduction in the energy required to detach a unit area for increasing scale thicknesses[81]. Both chromium and aluminium are commonly alloyed with steel to increase the oxidation resistance at high temperatures. Chromium and aluminium produce an oxide at the base of the film in close contact with the metal, and are thought to provide a barrier against the movement of cations from the metal into the oxide layer outside[81].

Oxidation rarely occurs by only one of the methods described. Combinations of two or three types of reaction may occur in turn or simultaneously in different parts of the oxide layer. The internal stresses in the oxide layer and the orientation of the oxide layer may vary with time or thickness, with discontinuous cracking or spalling of the oxide layer causing sudden changes in the reaction rate. With more than one oxide being stable under the oxidation conditions, a series of oxide layers are formed similar to that for iron.

3.5.2 Influence of heat treatment atmosphere

The decarburisation of steels containing up to 3wt.%Si in wet hydrogen atmospheres is an important industrial process. Since these atmospheres have an oxidising potential, oxidation of the steel occurs, often with a considerable influence on the decarburisation, with numerous investigations[67,69,73,78,82-85] undertaken into the oxidation and decarburisation of silicon steels. Various factors influence the diffusion of oxygen and silicon in iron, and therefore the oxidation characteristics. These factors include the[86]:

- Heat treatment temperature;
- Oxidising potential of the furnace atmosphere;
- Duration of the heat treatment;
- Time for the specimen to heat to the furnace temperature;
- Initial silicon content;
- Isomorphic iron structure;
- Available diffusion paths in the oxidation zone.

Tuck[82] found that two forms of scaling occurred during the oxidation of a low carbon 1.74wt.%Si steel, namely:

1) Protective scale formation;
2) Non-protective scale formation.

Logani[84] investigated the formation of a FeO-Fe_2SiO_4 scale on a ferritic 1.5wt.%Si steel exposed to a CO/CO_2 atmosphere at 1000°C. The oxidation of this alloy exhibitted an initial region of variable reaction rate, followed by a region of linear reaction behaviour. The initial growth of an oxide scale on a Fe-Si alloy often did not proceed uniformly over the surfaces. Instead, the nuclei of the more stable oxides appear in the metastable oxide films of the steel, and grew into well defined nodules during the early oxidation stages. This behaviour was pronounced in atmospheres of low oxygen potential at elevated temperatures.

Nucleation of the nodules occurred in the oxide film on the alloy grain boundaries, on threefold grain boundary intersections, and within the film covering the alloy grains. These nodules, which

comprised FeO, with fayalite, Fe_2SiO_4, as a minor constituent, had circular bases due to isotropic lateral growth. Only those nodules formed at boundaries and grain boundary intersections grew rapidly when exposed to a 50 vol.% CO_2 atmosphere. Their areal coverage increased rapidly, leading to complete coverage after 8hr. The nodules on the specimens exposed to the pure CO_2 atmosphere grew at a much faster rate than in the lower oxygen potential atmospheres, with complete coverage being obtained after about 30min[84].

Internal oxidation was exhibited in the alloy beneath the nodules. Oxide precipitates occurred within the alloy matrix and boundaries, with their size decreasing at an increasing distance from the alloy surface. Figure 3.12 illustrates that the external oxide grew at a linear rate, while the internal oxidation zone grew at a continuously decreasing rate, attaining a maximum penetration depth of approximately 50µm after 40hr. By then the external scale thickness was approximately 300µm.

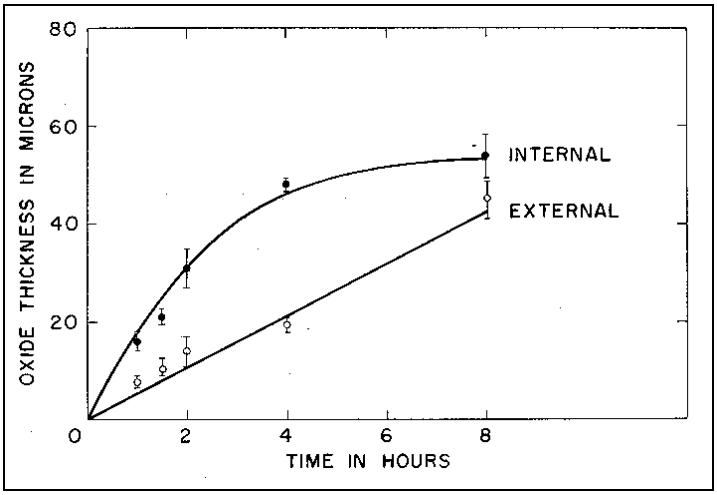

Figure 3.12 Growth kinetics of the external and internal oxidation zones of a 0.006wt.%C/1.74wt.%Si steel with a 50 vol.% CO_2 atmosphere at atmospheric pressure (from Ref. 84).

The oxidation rate of carbon and low alloy steels at higher temperatures is predominantly faster in steam than in air, and faster in air than in CO_2.. Tuck[82] found that a Fe/1.74wt.%Si steel oxidised many times faster in steam than in air. The oxide scale formed in air, Figure 3.13(a), comprised an outer part of silicon free alpha-Fe_2O_3. The inner portion of the scale, Fe_3O_4, comprised fine silica or fayalite particles, which were also present at the

hematite/magnetite interface. The absence of wustite formation suggests that the silica-rich layer formed in the early stages of oxidation effectively impeded the outward diffusion of iron ions.

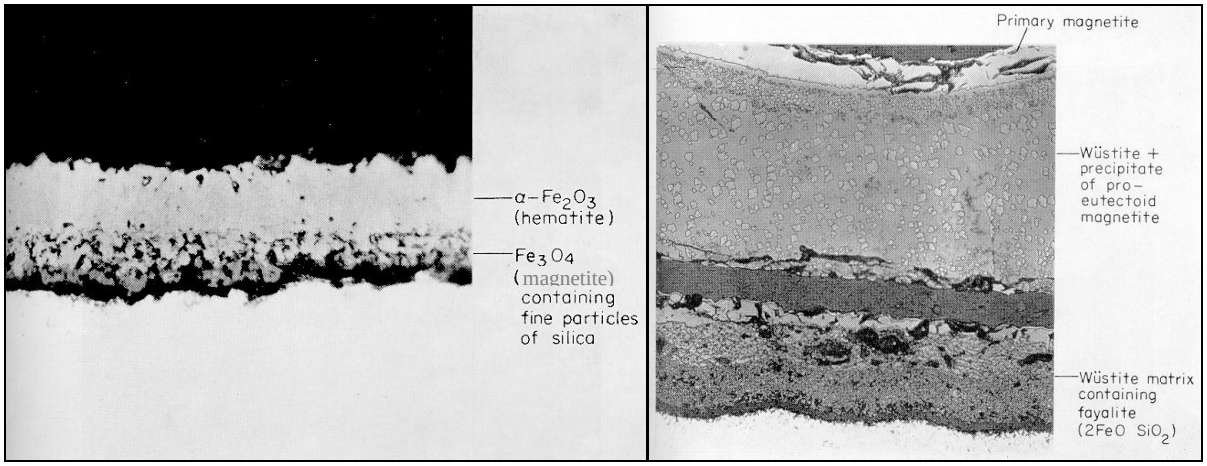

Figure 3.13 Scale structures for (a) 20hr at 980°C in still air, and (b) for 5hr at 934°C in CO_2 1,000x. (from Ref. 82).

Silicon was present in a wustite matrix as large fayalite particles after exposure to CO_2, Figure 3.13(b), instead of the fine silica or fayalite dispersion formed in air[82]. This silicon rich layer was incapable of preventing the outward diffusion of iron ions, which resulted in magnetite and wustite being maintained in the scale. Silicon, which is much less noble than iron, reacted with oxygen at suitable nucleation sites to form SiO_2. Concurrently, the iron in the surface layer, which is now denuded of silicon, also reacted with the oxide ions adsorbed on the surface. This resulted in the iron forming a layer of iron oxide or oxides outside the silica. As the reaction proceeded, silicon diffused to the surface of the metal and reacted with the oxygen dissolving into the alloy from the iron oxide. This allowed the silica layer to increase in thickness and extent, therefore hindering the further outward flow of iron ions. This process continued until the silica layer was sufficiently thick to prevent the outward diffusion of iron ions.

Consequently, the type of scale formed governs the subsequent oxidation of the alloy[82]. With CO_2 or steam atmospheres, the gas/scale phase boundary is rate determining, which results initially in linear scaling. As the supply of oxygen ions, by the decomposition of either CO_2 or

steam, is outweighed by the supply through the outward diffusion of iron ions, only wustite forms in the early stages. Thus, wustite and silica readily react to form fayalite. The fayalite formed presumably has vacancies in part of its lattice since the wustite from which it is formed has a cation-deficient structure. Consequently, iron ions can diffuse outwards through the fayalite layer. Furthermore, all the fayalite formation subsequent to the initial layer corresponding to the original metal surface is as discrete particles, rather than as a continuous layer. Therefore the wustite in which the fayalite particles are imbedded will provide ready diffusion paths for iron. In oxygen, the outer scale/gas phase boundary reaction is not rate-determining, with this reaction being much faster than the diffusion of iron through the silicon layer as it is formed. It has been suggested that either:

a) No wustite is formed outside the silica layer to allow the formation of fayalite; or
b) If wustite is formed, its existence is so short lived that it is converted to higher iron oxides before any fayalite-forming reaction can occur.

When wustite is present, it can readily react with the silica to produce fayalite, and also with the small quantity of alumina present in the steel. In the absence of wustite, the silica and alumina cannot react readily. For magnetite to react with silica, it would first have to be reduced to wustite, which is unlikely in the scale formed on Fe-Si alloys in oxygen.

Various oxidation reactions are possible for Fe-Si alloys. Yamazaki[69] considered the potential oxidation reactions (3.5) to (3.7) and constructed a relationship between p_{H_2O} / p_{H_2} ratio and temperature, Figure 3.14.

$$[Si] + 2H_2O(g) = SiO_2(s) + 2H_2(g) \quad (3.5)$$

$$[Fe] + H_2O(g) = FeO(s) + H_2(g) \quad (3.6)$$

$$[2Fe] + SiO_2(s) + 2H_2O(g) = Fe_2SiO_4(s) + 2H_2(g) \quad (3.7)$$

External oxidation involves oxides of reactive solutes such as silicon, manganese and aluminium in atmospheres reducing to iron, and mixed iron-solute oxides for atmospheres oxidising to iron. Internal oxidation arises when oxygen diffuses into the alloy and reacts with solute atoms, precipitating second phase oxides beneath the steel surface. The formation of external or internal oxidation is dependent on several interrelated factors, including alloy composition, annealing

temperature and oxygen potential of the atmosphere[87]. Factors which increase the oxygen flux into the alloy relative to the counter diffusion flux of reacting solute to the surface will favour internal oxidation. Factors having the opposite effect will favour external oxidation.

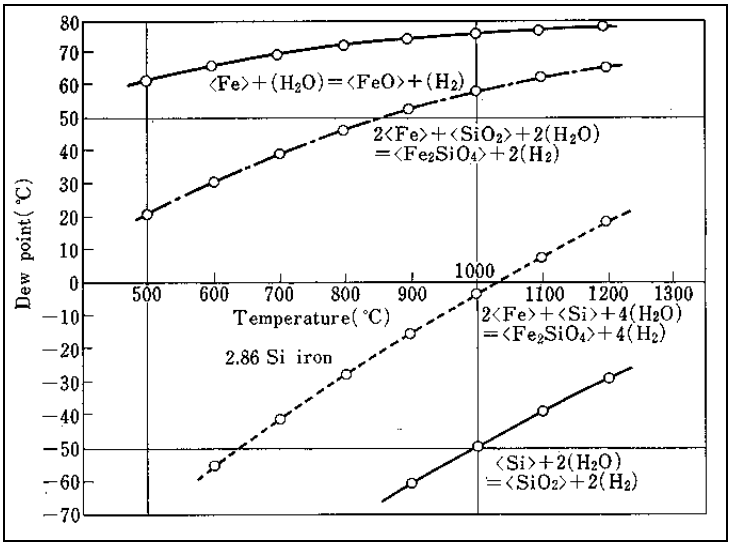

Figure 3.14 Relationships between p_{H_2O} / p_{H_2} ratio and temperature for the potential oxidation reactions of Fe-Si alloys (from Ref. 69).

Geiger[87] demonstrated that the transition from internal to external oxidation of a 0.024wt.%C/1.80wt.%Si steel occurred with increasing temperature. Figure 3.15(a) illustrates the influence of p_{H_2O} / p_{H_2} ratio on the weight gain of a Fe-3wt.%Si steel[85]. Below ratios of 0.02, the weight gain was approximately 5μg/cm^2. However, the weight gain increased rapidly with increasing p_{H_2O} / p_{H_2} ratios above this. The influence of p_{H_2O} / p_{H_2} ratio on the thickness of the SiO_2 layer forming on this steel is illustrated in Figure 3.15(b). Morito[85] concluded that external oxidation occurred below a p_{H_2O} / p_{H_2} ratio of 0.02, and internal oxidation above 0.025.

The silicon concentration across the oxidised layer of a Fe-3wt.%Si steel, Figure 3.16, demonstrates inner and outer zones[79], irrespective of the p_{H_2O} / p_{H_2} ratio. The outer zone, typically less than 50nm thick, was very rich in silicon and oxygen, with silicon mostly present as silica. The inner zone, typically 1-2μm thick, had much lower silicon and oxygen contents,

with silica particles precipitated in an iron matrix. The silicon enrichment of the outer zone was found to increase as the p_{H_2O} / p_{H_2} ratio decreased[79].

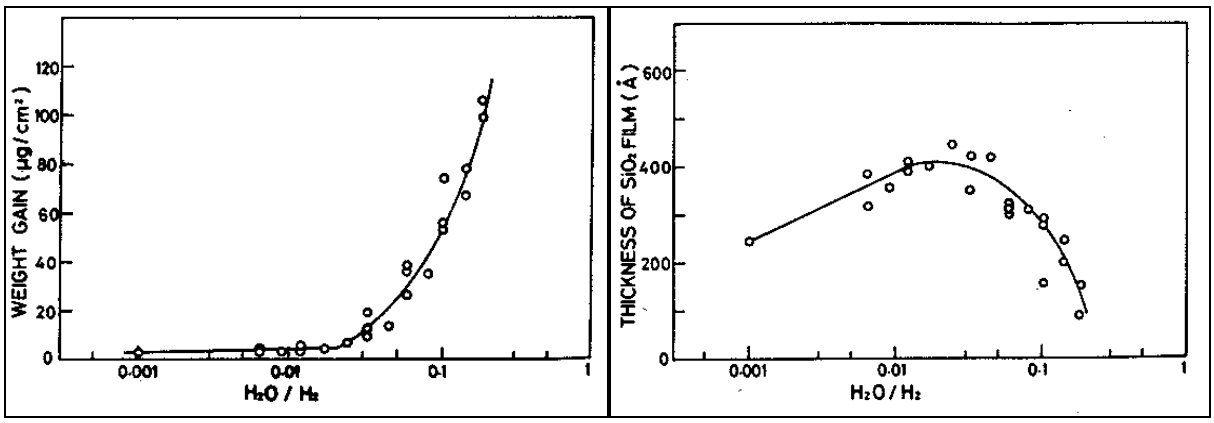

(a) **(b)**

Figure 3.15 Oxidation of a 0.021wt.%C/2.96wt.%Si steel for 1hr at 850°C illustrating the influence of p_{H_2O} / p_{H_2} ratio on (a) weight gain, and (b) thickness of SiO_2 layer (from Ref.79).

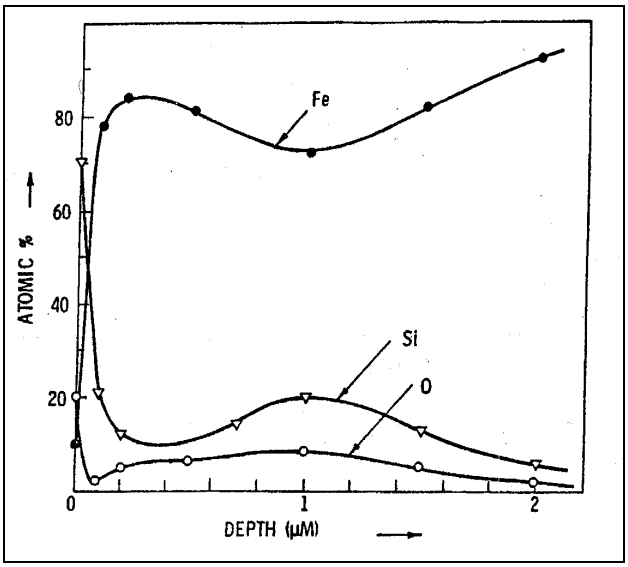

Figure 3.16 Alloy element concentration profile of oxidised layer for 10min decarburisation of a Fe-3wt.%Si steel at 801°C, p_{H_2O} / p_{H_2} =0.20 (from Ref. 79).

3.5.3 Influence of silicon content

The decarburisation of steels containing 0.5 to 3.0 wt.%Si at 850°C and p_{H_2O} / p_{H_2} ratios of 0.1 to 0.5 was investigated by Wiesner[73], with the influence of silicon content on the specific mass of oxide formed shown in Figure 3.17. The surface oxide was identified as SiO_2. From 0.4 to 2.0 wt.%Si, the oxide formation decreased linearly with increasing silicon content. However, the specific mass of SiO_2 formed remained constant for 2 to 3wt.%Si. The oxide structure was thick, uneven and porous for low silicon contents, and thin, even and dense, for high silicon contents.

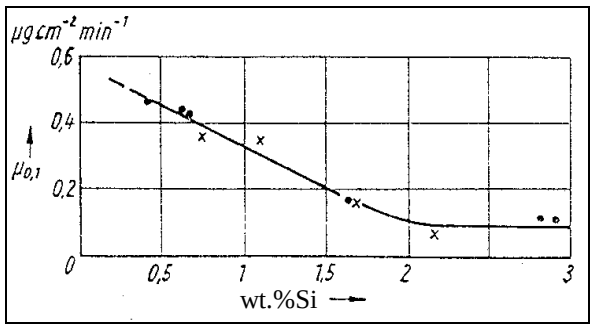

Figure 3.17 Influence of silicon content on the specific mass change, $\mu_{0,1}$, for SiO_2 formation during the decarburisation of electrical steels (from Ref. 73).

Alloys containing more than 3wt.%Si form a protective scale, since no internal oxidation occurs. In alloys with less than 3wt.%Si, internal oxidation can occur, with the scale being non-protective. Above a specific silicon content, usually slightly less than 3wt.%, the supply of silicon by the outward diffusion from the metal to the reaction front is more than enough to prevent any oxygen diffusion inwards to form iron oxide in areas denuded of silicon[82]. Logani[84] found that the concentration profile across the ferritic 1.5wt.% Fe-Si alloy illustrated in Figure 3.18 contained three distinct regions:

a) An alloy and internal oxidation zone;
b) A wustite/fayalite conglomerate layer;
c) An external wustite layer.

The local iron and silicon concentrations exhibited large fluctuations in the conglomerate layer. However, the iron concentration maxima corresponded to the iron concentrations in the external wustite layer, while the minima to a phase containing 70% wustite, this being the amount of wustite in fayalite. Furthermore, the silicon maxima occurred with iron minima, confirming that these regions were of high fayalite content, where the silicon content in fayalite is 13.8wt%. Wustite in the external layer contained a small amount of silicon, 0.01 to 0.02 wt.%, at the wustite/conglomerate interface. Figure 3.19(a) illustrates the silicon profile up to the internal oxidation zone/alloy interface. After 8hr, the silicon concentration had decreased from its initial concentration of 1.5wt.% to 0.5wt.% at the internal oxidation boundary. This minimum value decreases slowly with time to 0.2 wt.%Si after 40hr, Figure 3.19(b). Internal oxidation was evident for this alloy, with the initial stages of oxidation appearing to depend on three basic processes[84]:

a) The growth and crystallisation of an amorphous silica film;
b) The formation and growth of wustite/fayalite nodules;
c) The internal oxidation of silicon to form silicon precipitates in the alloy.

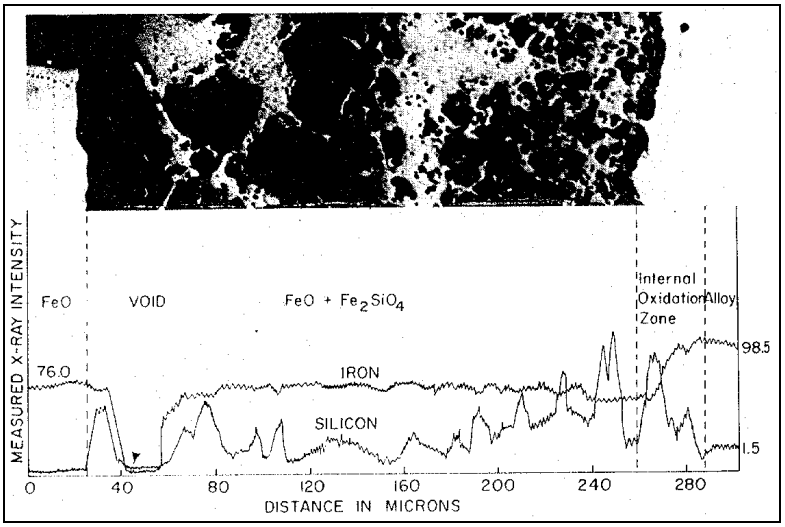

Figure 3.18 Silicon and iron concentration profiles for a ferritic Fe-1.5wt.%Si alloy across the scale and alloy for 24hr oxidation in 50 vol.% CO_2 at atmospheric pressure (from Ref. 84).

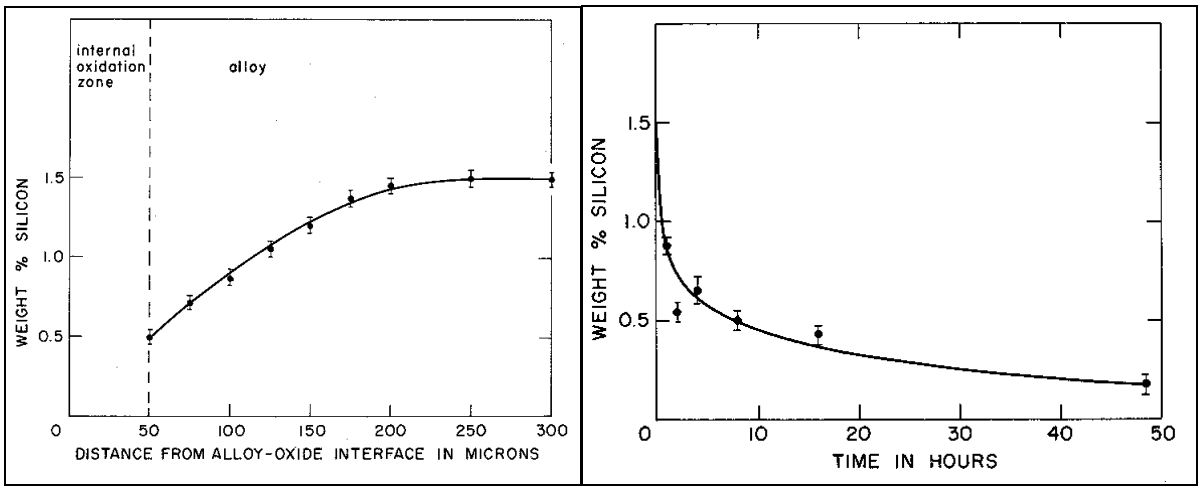

(a) **(b)**

Figure 3.19 Oxidation of a Fe-1.5wt.%Si steel in a 50 vol.% CO_2 atmosphere illustrating (a) silicon concentration profile up to the internal oxidation zone front after 8hr, and (b) variation of silicon concentration at the internal oxidation zone/alloy interface with time (from Ref. 84).

3.6 Mechanisms of decarburisation

Decarburisation is a complicated process that involves diffusion of atoms in the steel matrix, reactions at the surface of the steel, and gas diffusion in the furnace atmosphere from the steel surface to the bulk gas flow[88]. In a few cases, the rate of decarburisation is controlled by the transport in the gas phase, especially for low gas flow rates. At higher flow rates, the chemical surface reaction(s) often determine the course of the decarburisation, especially for thin specimens. For larger steel specimens, the rate of decarburisation is predominantly controlled by carbon diffusion through the steel. There are also many instances where neither the surface reactions nor the diffusion or transport alone controls the overall decarburisation process[88]. The steps involved in the decarburisation of a steel sheet by reaction 3.1 are illustrated schematically in Figure 3.20.

The rate at which this steel sheet decarburises is dependent on such system variables as the gas flow rate and composition, pressure, temperature, and the sheet thickness. The following steps are involved in the decarburisation process[89]:

1) Transport of hydrogen in the direction of the gas flow;

2) Transport of hydrogen normal to the surface of the steel;

3) Surface reaction(s), possibly occurring in several steps;

4) Diffusion of carbon from the interior to the surface of the steel;

5) Counter diffusion of CH_4 gas back into the gas stream.

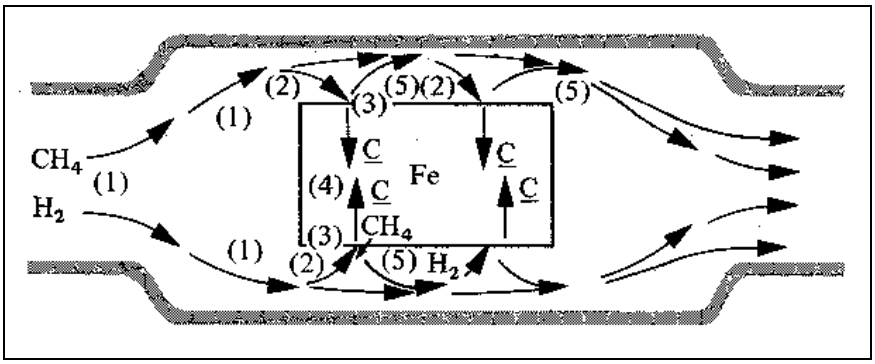

Figure 3.20 Steps involved in decarburisation of steel sheet by reaction (3.1) (from Ref. 89).

The first step involves supplying the required hydrogen to the steel by the gas flow into the furnace, and past the steel[89]. As the gas flows over the sheet, a velocity profile is established. If the reaction proceeds, the hydrogen is depleted at and near the solid-gas boundary. Consequently, step (2) involves diffusion with convection. Once the hydrogen has reached the steel surface, it reacts with the carbon atoms, step (3), which have diffused to the surface by step (4). Step (5) involves the gaseous reaction product (CH_4) diffusing back out into the gas flow, in order for the reaction to proceed. When one of these steps is considerably slower than the others, a limiting condition is obtained, and this rate-determining step determines the overall reaction rate. If none of the steps are significantly slower than the others, a more general condition of mixed control is achieved.

3.6.1 Thermodynamic principles

Fundamentally, the thermodynamics of the decarburisation reactions allow the extent of the decarburisation to be determined, while the kinetics describe the rate at which these reactions may proceed. The thermodynamics indicate which reactions will occur given the temperature and atmospheric parameters, and to what extent the steel will be decarburised. The equilibrium carbon contents in the various steel phases can be predicted, as can the influence

of alloying elements on the equilibrium structures. The thermodynamics of a reaction, for a system in a certain atmosphere at a specific temperature and pressure, can be investigated by considering the Gibbs free energy of the reaction[90]. A system comprising components A, B, and C could be envisaged to be controlled by the chemical reaction

$$A + 2B = 3C, \tag{3.8}$$

where A and C are gases;
B is a solid or liquid.

$$\text{Thus,} \quad \Delta g^o = -RT \ln\left[\left(\frac{p_C^3}{p_A}\right)\left(\frac{1}{a_B^2}\right)\right], \tag{3.9}$$

where Δg^o = the standard free energy change of reaction (3.8);
R = the ideal gas constant in J/kgK;
T = temperature in °K;
p_A, p_C = partial pressures of A, C in the gas mixture.
a = activity.

The term in brackets on the right hand side of equation (3.9) is known as the equilibrium constant K, where

$$K = \left[\left(\frac{p_C^3}{p_A}\right)\left(\frac{1}{a_B^2}\right)\right]. \tag{3.10}$$

For the free energy change of a reaction, it is necessary to define the standard states to which the free energy change is related[90]. Usually the standard state for gaseous components is defined as that of one atmosphere pressure, and of the pure phase for solid and liquid components. In a decarburisation environment comprising a steel specimen at elevated temperature in a specific decarburising atmosphere, two forms of equilibrium can exist. They are[90]:

1) Equilibrium between the gaseous environment and the steel specimen, namely gas-solid equilibrium;
2) Equilibrium between the phases, commonly ferrite and either ferrite/austenite or austenite, in the steel, namely solid-solid equilibrium.

The equilibrium in the gas phase is determined by the activity of the gas. Equation (3.10) can be re-written in terms of the activity of the gas phase to give:

$$a_B = \sqrt{\left(\frac{p_C^3}{p_A}\right)\left(\frac{1}{K}\right)}. \qquad (3.11)$$

In a decarburising environment the gas activity determines the minimum carbon content to which the steel can be decarburised, with this value being the equilibrium carbon content. Partial decarburisation in a certain range below and above the Ac_3 temperature can result in a structure with a ferritic case, and an austenitic or dual phase ferrite/austenite core. At the interface between these phases, an equilibrium exists. For binary Fe-C steels, the Fe-C equilibrium diagram can be used to calculate the carbon activities of the phases present, since the chemical activity of a saturated solid solution is unity[72]. Therefore, the carbon activity can be determined from the carbon concentration of the phase of interest divided by the saturation carbon content of that phase.

Of particular interest is the influence of the alloying elements on the chemical activities of the steel, and their subsequent influence on the decarburisation. Therefore, it is desirable to know the influence of some common alloying elements on the carbon activity. The carbon activity in austenite for alloy steels has been studied by equilibration with CH_4/H_2 and CO_2/CO gas atmospheres. However, decomposition of CH_4 and CO occurs[91], which can result in carbon deposition on the steel specimen for which the carbon activity is being determined. This lowers the carbon potential in the gas, corresponding to a lower carbon potential in the metal. The thermal decomposition of CO was found to give significantly higher carbon activities in CO_2/CO than in CH_4/H_2 gas atmospheres, with the legitimate source of activity data apparently being confined to that obtained from CH_4/H_2 gas atmospheres[91].

The temperature range for which carbon activity data obtained from CH_4/H_2 data can be accurately used is limited to 848°C. This is due to the reaction of hydrogen and silica in the silica tubes invariably used for these furnaces. In has been observed that there is a reduction of silica in the furnace tube above certain temperatures, with part of the silica thus generated vaporising and being absorbed by the sample[91]. Wada[92] investigated the activity coefficient of carbon in austenitic Fe-Mn-C, Fe-Si-C, Fe-Cr-C and Fe-V-C alloys at 848 to 1147°C, and found that the activity coefficient of carbon was diminished by manganese, and increased by silicon. It also increased with carbon at about the same rate as for the binary Fe-C system. Wada[92] found that the effect of the different alloying elements were additive. Therefore, for the Fe-Si-Mn-Cr-C alloy[92],

$$\log f_c[FeSiMnCrC] = \left(\frac{180 + 8.90\%Si}{T}\right)\%C + \left(0.041 + \frac{62.5}{T}\right)\%Si, \\ -\left(\frac{21.8}{T}\right)\%Mn - \left(\frac{102}{T} - 0.033\right)\%Cr, \qquad (3.12)$$

where f_c = the activity coefficient of carbon;

%C, %Mn, %Si = the alloy additions in wt.%.

Equation (3.12) which applies for 0 to 1wt.%C, 0 to 3wt.%Si, and 0 to 15wt.%Mn, was calculated with the infinitely dilute solution of pure carbon as the reference state. Usually, however, the activity of carbon is defined relative to graphite as the standard state. Equation (3.13)[92] therefore allows equation (3.12) to be converted to graphite as the standard state.

$$\log f_c(gr) - \log f_c(\%) = \frac{\Delta g_C^o}{4.576T}, \qquad (3.13)$$

where $f_c(gr)$= the activity coefficient of carbon relative to graphite.

The carbon activity, a_c, can be determined from

$$a_c = f_c\,[\%C]. \qquad (3.14)$$

3.6.2 Gas diffusion in the boundary layer

There are a few instances when transport in the gas phase influences the decarburisation. The most common situation involves decarburisation in a wet hydrogen atmosphere with a low water content. Here the diffusion of water molecules in the flowing boundary layer determines the speed of the reaction. The transport in gas mixtures is described by transport coefficients and equations[93,94]. For decarburisation limited by diffusion and convection through the boundary layer at the steel surface, equation (3.15) is obtained[95].

$$J = \rho.\beta\,(c_g - c_s), \qquad (3.15)$$

where J = mass flow density (g/cm^{2}s);

ρ = the density of steel in g/cm^3;

β = mass transfer coefficient in cm/s, which is a function of the velocities and the rate of diffusion in the gas phase;

c_g = the carbon concentration at the steel surface, a dimensionless parameter, g/g, corresponding to the carbon activity of the gas;

c_s = carbon concentration in the steel surface.

3.6.3 Surface reactions

In many cases, the chemical surface reactions determine the course of the reaction[88]. One instance of this involves the slow decarburisation in CH_4-H_2 gas atmospheres. The course of the chemical reactions are described by rate constants and rate equations which indicate the dependence of the reaction rate on variables such as the partial pressures of the gases, the carbon concentration, and the carbon activity. According to the Arrhenius rate equation,

$$K = k_o \exp\left(\frac{-E}{RT}\right), \qquad (3.16)$$

where k_o = reaction rate coefficient in cm/s;

E = activation energy of the reaction in J/kg.

The kinetic rate equations allow insights to be made into the atomic course of the reaction mechanics. The kinetic results, especially the rate constants, show a certain dispersion, and are generally less valid than transport and diffusion data. This is a consequence of such variables as the crystallographic orientation, the purity, roughness, lattice discontinuities, and any deformations at the surface, all of which can influence the chemical surface reactions strongly. However, the given kinetic values are useful in estimating the magnitude of the reaction rates and times. The mass flow density of carbon is described by the following general equation[96]:

$$J = \rho \sum_{\upsilon=1}^{n} \frac{k_\upsilon}{a_s m_\upsilon} (a_{g_\upsilon} - a_s) \qquad (3.17)$$

where J = mass flow density of carbon in g/cm^{2}s;

a_g, a_s = gas and steel carbon activities;

k = reaction rate coefficient;

m = 0 or 1, depending on the type of reaction.

For the carbon transfer from the steel to be calculated, it is necessary to know which reactions take place, the carbon activities in the gas phase, the reaction rate coefficients for all the reactions, and the surface carbon activity in the steel.

3.6.4 Diffusion in steel

There are many situations where diffusion in the steel determines the rate of decarburisation, especially in thick metal sheets. The diffusion of elements in steel are described by diffusion coefficients and diffusion equations[97,98]. Decarburisation within certain temperature ranges can result in the formation of free ferrite surface layers from initial ferrite/ferrite plus austenite or ferrite/austenite structures, as illustrated schematically in Figures 3.2 and 3.3. The thickness of the free ferrite increases for longer decarburisation times.

Jost[63] derived detailed equations to calculate the free ferrite layer thickness. This involved the assumption of diffusion controlled decarburisation with a moving interface, with the ferrite layer forming from the initial single or dual phase structures. These equations assumed equilibrium conditions at the ferrite/ferrite plus austenite or ferrite/austenite interfaces, with

Fick's second law applying for each phase. Smith[99] simplified these equations by assuming a linear carbon concentration profile in the ferrite due to the low solubility of carbon in ferrite, with the depth of the free ferrite layer calculated from equation 3.18.

$$x_d = \sqrt{\frac{2t_d C_{sat} D}{\left(C_o - \tfrac{2}{3} C_B\right)}}, \tag{3.18}$$

where x_d = thickness of the free ferrite layer in cm;
t_d = decarburisation time in s;
C_{sat} = saturation ferrite carbon content in wt.%;
C_o = initial carbon content in wt.%;
D = ferrite carbon diffusion coefficient in cm^2/s.

At temperatures exceeding approximately 910°C for Fe-C steels, carbon removal results in an austenite carbon concentration gradient in the steel, with no free ferrite formation. Fick's second law, equation 3.19, can then be used to estimate the distribution of carbon in the steel[68].

$$\frac{\partial C}{\partial t} = D\frac{\partial^2 C}{\partial x^2} \text{ for } x>0. \tag{3.19}$$

If it is assumed that decarburisation does not extend to the centre of the specimen, that the diffusion coefficient of carbon in austenite is independent of carbon content, and neglecting grain boundary diffusion of carbon, the solution to Fick's second law under these conditions is given by equation 3.20[68].

$$\frac{C_x - C_o}{C_s - C_o} = erfc\left[\frac{x}{2\sqrt{Dt_d}}\right], \tag{3.20}$$

where C_x = carbon concentration at a distance x from the steel surface in wt.%;
C_s = surface carbon content in wt.%;
x = distance from steel surface in cm;
$erfc$ = complimentary error function.

Situations also arise where the rate of decarburisation is not controlled solely by diffusion in the steel, or by the surface reactions. Instead, a case of mixed control occurs, where both diffusion and the surface reactions influence the rate of decarburisation. These situations are considered in detail by Geiger[89].

3.6.5 Kinetics of the decarburisation reactions

The decarburisation kinetics allow the rate at which various chemical surface reactions proceed to be determined, together with the rate determining step or steps of that reaction. The kinetics also allow the influence of concentration changes of the various constituents comprising the atmosphere on the decarburisation rate to be calculated. Consideration of the reaction rate may only be applied to one particular step at a time in a chemical reaction. Generally, any chemical reaction consists of several chains of reactions all proceeding simultaneously[97]. The decarburisation reactions of equations (3.1) to (3.4) comprise several steps, with the adsorption and desorption of molecules, the entrance and exit of atoms through the metal surface, and the reactions of adsorbed molecules and radicals having to be taken into account.

Often the course of a reaction sequence is controlled by one reaction step[88], which is known as the rate-determining step. The rate determining step of a reaction can be deduced from the rate law through a comparison of a theoretically expected rate law for a single step of an assumed mechanism with the experimentally determined rate law. Furthermore, if a specific reaction step determines the rate for a total reaction in one direction, then the corresponding reverse step determines the reaction rate for the reverse direction.

Only a fraction of the molecules that reach the surface are adsorbed. Even then, the rates of adsorption and desorption are usually of a much greater magnitude than the experimentally measured reaction rates. Therefore, the adsorption/desorption steps seldom limit the total reaction rate. The observed overall reaction rate can arise principally from one chain or sequence of steps, with one of these steps being responsible for the observed rate, since it is much slower than the others.

Situations also arise where the overall reaction has two slow steps, with neither of the steps sufficiently slow for the other to be considered fast in comparison[97]. At equilibrium, every

reaction step has the same rate as the reverse step, with this known as microscopic reversibility[88]. This only applies for reversible reactions that lead to equilibrium. Reactions (3.1) and (3.2) are reversible and lead to an equilibrium, where the rate of the forward and reverse reactions become equal at a specific carbon content. For reaction (3.3) the equilibrium is metastable, and only follows the given reaction in flowing gas atmospheres at low enough temperatures. For reaction (3.3) in stable equilibrium, the CH_4 and CO_2 and formation must also be considered. However, the reactions which lead to CH_4 and CO_2 formation can be disregarded under certain experimental conditions because they proceed much more slowly than those which lead to the metastable equilibrium of equation (3.3). For these fast reaction steps, microscopic reversibility can be assumed.

Hudson[100] demonstrated that decarburisation of a 0.11wt.%C/0.56wt.%Mn steel in dry and wet hydrogen followed a first order reaction with respect to the carbon content of the steel. This was despite the different decarburisation reactions for dry and wet hydrogen. The limiting decarburisation rate is given by diffusion theory, with the actual rate of this steel governed by the reaction rates involving carbon removal from the surface. Above 2.5vol.% water, the decarburisation rate approached the theoretical limiting rate of decarburisation. Mayer[67] found that diffusion controlled decarburisation occurred for 0 to 2.5wt.%Si low carbon steels in wet hydrogen atmospheres with p_{H_2O} / p_{H_2} ratios lower than that required for iron oxidation. Diffusion controlled decarburisation was also observed in moist hydrogen with no iron oxidation[70]. However, when oxidation occurred, the decarburisation rate was reduced, and became controlled by the chemical reaction on the steel surface.

For free ferrite formation during decarburisation of austenite, the temperature dependence of diffusion controlled decarburisation can be determined from the product of $D_\alpha C_\alpha$ [101]. D_α is the ferrite carbon diffusion coefficient and C_α the ferrite carbon solubility. With D_α increasing, but C_α decreasing, with increasing temperature above the Ac_1 temperature, the product reaches a maximum at 800°C for decarburisation in wet hydrogen. Increasing the silicon content raises the Ac_1 and Ac_3 transformation temperatures[102]. Mayer[67] confirmed that the temperature corresponding to the maximum product of $D_\alpha C_\alpha$ increased with increased silicon content.

Kaspersma[103] determined the following reactions to be the most important in a carburising furnace containing CO, CO_2, H_2, H_2O, N_2, and any hydrocarbons for a SAE 1010 steel heat treated in the austenitic phase region:

$$
\begin{aligned}
2CO &\xrightarrow{k_1} C + CO_2 && \text{(a)} \\
CO_2 + C &\xrightarrow{k_2} 2CO && \text{(b)} \\
H_2 + CO &\xrightarrow{k_3} C + H_2O && \text{(c)} \\
H_2O + C &\xrightarrow{k_4} H_2 + CO && \text{(d)} \\
CH_4 &\xrightarrow{k_5} C + 2H_2 && \text{(e)} \\
2H_2 + C &\xrightarrow{k_6} CH_4 && \text{(f)} \\
C_3H_8 &\xrightarrow{k_7} 3C + 4H_2 && \text{(g)}
\end{aligned}
\qquad (3.21)
$$

These reactions are based on carbon deposition at the steel surface when carbon diffusion is not a complicating factor. This was achieved through the use of a low carbon steel specimen 0.05mm thick that resulted in diffusion rapid enough to yield a uniform carbon profile within one minute at 900°C[104]. These reactions can be further broken down into a series of two or more simpler reactions. However, the overall reaction rates may be used for comparison without introducing any major errors. Therefore, the overall reaction rates for the above reactions are[103]:

$$
\begin{aligned}
V\frac{dc_c}{dt} &= Ak_1 p_{CO}^2 && \text{(a)} \\
V\frac{dc_c}{dt} &= -Ak_2 p_{CO}.a_c && \text{(b)} \\
V\frac{dc_c}{dt} &= Ak_3 p_{H_2} p_{CO} && \text{(c)} \\
V\frac{dc_c}{dt} &= -Ak_4 p_{H_2O}.a_c && \text{(d)} \\
V\frac{dc_c}{dt} &= Ak_5 p_{CH_4} && \text{(e)} \\
V\frac{dc_c}{dt} &= -Ak_6 p^2{}_{H_2}.a_c && \text{(f)} \\
V\frac{dc_c}{dt} &= Ak_7 p_{C_3H_8} && \text{(g)}
\end{aligned}
\qquad (3.22)
$$

where V = volume of the steel specimen in cm^3;

A = surface area of the steel specimen in cm^2;

c_c = carbon concentration in the steel specimen in mol/cm^3;

k = reaction rate coefficient in either $mol/cm^2.min.atm$ or $mol/cm^2.min.atm^2$;

t = time in min;

p = component partial pressure in atm;

a_c = carbon activity, which is a function of the percentage concentration of the carbon dissolved in the austenitic phase of the steel specimen.

The sum of equations 3.21(a) to (g) can be used to determine the carbon activity at equilibrium, where the net decarburisation or carburisation rate will be equal to zero. This calculation is only possible when the rate of diffusion is very small[103], and arises when the steel obtains the equilibrium carbon content, or the carbon concentration gradient becomes very small near the surface. In general, the rate of carbon diffusion at the steel surface can be represented by Fick's first law[103]:

$$\frac{dn_c}{dt} = -AD\left[\frac{\delta c_c}{\delta x}\right]_{x=0} \qquad (3.23)$$

where $\frac{dn_c}{dt}$ = number of moles of carbon diffusing into the steel specimen;

D = diffusion coefficient in cm^2/min;

$\left[\frac{\delta c_c}{\delta x}\right]_{x=0}$ = carbon gradient at the surface in mol/cm^4.

For the steel specimen,

$$\frac{dn_c}{dt} = V\left(\frac{dc_c}{dt}\right) \qquad (3.24)$$

Therefore, equations 3.22(a) to (g) may be applied to the steel specimen in conjunction with equation (3.23). Grabke[88] investigated the kinetics of the surface reactions occurring during the carburisation and decarburisation of steel. Carburisation and decarburisation in CH_4/H_2 atmospheres by equation (3.1) yielded equation (3.25) for low carbon concentrations.

$$\nu = \frac{\delta}{2}\frac{dc_c}{dt} = k_1^{'} p_{H_2}{}^{3/2}\left(c_{c,G1} - c_c\right), \qquad (3.25)$$

where ν = the reaction rate in mol/cm^{2}s;

δ = sample thickness;

$c_{c,G1}$ = carbon concentration of the steel surface in g/g;

c_C = carbon concentration at the steel surface in g/g.

Equation (3.25) can be integrated, giving:

$$\log\left[\frac{c_{c,G1} - c_{c,o}}{c_{c,G1} - c_{c,t}}\right] = \frac{2k_1^{'}}{2.3\delta}.p_{H_2}{}^{3/2}.t\,, \qquad (3.26)$$

where $c_{c,o}$, $c_{c,t}$ = the carbon concentration at the steel surface for t=0 and t respectively.

Equation (3.26), for a certain approximation to the equilibrium, allows the required reaction times to be calculated. For decarburisation in hydrogen, c_c=0 can be substituted into equation (3.26). Rate constants and activation energies are listed in Table 3.1.

Table 3.1 Rate constants and activation energies, in kJ/mol, of $K=k_o.exp(-E/RT)$ for decarburisation reactions (3.1) and (3.3) (from Ref. 88).

REACTION	K	k'
$CH_4(g)=[C]+2H_2(g)$	α-Fe 1.3×10^3 exp(-211/RT) mol/cm^{2}s.atm$^{1/2}$	α-Fe 5.3×10^{-3} exp(-57/RT) cm/s.atm$^{3/2}$
	γ-Fe 4.6×10^{-3} exp(-231/RT) mol/cm^{2}s.atm$^{1/2}$	γ-Fe 2.6×10^{-2} exp(-105/RT) cm/s.atm$^{3/2}$
$CO(g)+H_2(g)=[C]+H_2O(g)$	-	α-Fe 2×10^6 exp(-172/RT) cm/s
	-	γ-Fe 1×10^7 exp(-195/RT) cm/s

The decarburisation rate of austenite in CO/CO_2 gas atmospheres by reaction (3.2) was found to be proportional to p_{CO_2}, and independent of the carbon concentration near equilibrium[88]. Consequently, the oxygen exchange from CO_2 on the iron surface was rate determining. For small carbon concentrations, Grabke[88] obtained the following expression:

$$-\left(c_c - c_{c,o}\right) - c_{c,G1}\,\ln\left[\frac{c_{c,G1} - c_c}{c_{c,G1} - c_{c,o}}\right] = 2k_2' p_{CO_2}.t\,. \qquad (3.27)$$

Decarburisation occurring in wet hydrogen atmospheres by reaction (3.3) was found to be proportional to the carbon activity, and for small water contents, proportional to the p_{H_2O} / p_{H_2} ratio[88]. For low oxygen activity, as specified by the p_{H_2O} / p_{H_2} ratio, the rate equation of (3.28) applies.

$$v = k_3' \frac{p_{H_2O}}{p_{H_2}} a_c^{G1} - a_c\,. \qquad (3.28)$$

At higher oxygen activities, the rate equation is multiplied by an additional factor that incorporates the influence of the increasing saturation of the surface with adsorbed oxygen. This yields:

$$v = k_3 \frac{1}{1 + K_o p_{H_2O}/p_{H_2}}\, p_{CO} - k_3'' \frac{K_o p_{H_2O}/p_{H_2}}{1 + K_o p_{H_2O}/p_{H_2}}.a_c\,, \qquad (3.29)$$

The dependence of the decarburisation rate on the p_{H_2O} / p_{H_2} ratio is illustrated in Figure 3.21. From the rate constants, Table 3.1, and equation (3.29), the reaction rates and reaction times of reaction (3.3) can be determined. Integrating equation (3.29), after replacing carbon activities with carbon concentrations, yields

$$\log\frac{c_{c,G1} - c_{c,t}}{c_{c,G1} - c_{c,o}} = \frac{2}{2.3\delta} k_3' \frac{p_{H_2O}}{p_{H_2}}.t \qquad (3.30)$$

with this equation being applicable for p_{H_2O} / p_{H_2} ratios between 0.01 and 0.1. For lower p_{H_2O} / p_{H_2} ratios, the decarburisation is dominated by reaction (3.1). The decarburisation rate at higher p_{H_2O} / p_{H_2} ratios, which is limited by adsorbed oxygen, is in accordance with equation (3.29)[88].

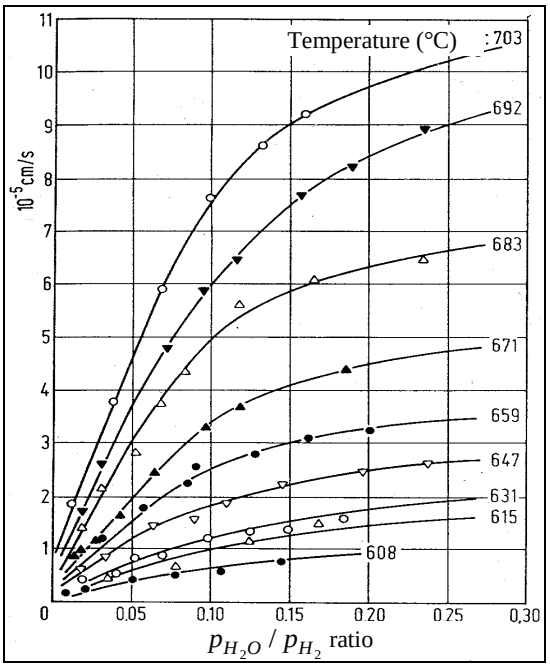

Figure 3.21 Dependence of the decarburisation rate in wet hydrogen mixtures divided by the carbon concentration, on the p_{H_2O} / p_{H_2} ratio (from Ref. 88).

As the part steps of equation (3.3) are rapid reactions, the association of CH_4, or of CO_2, in the flowing wet hydrogen mixture can usually be disregarded. The decarburisation with wet hydrogen mixtures occurs so rapidly that the reaction rate was found to be controlled by the diffusion of water in the flowing layer for the austenite region of steel specimens at high carbon concentrations. Only at high flow rates and less than 0.05wt.%C did the surface reaction predominate over the transport condition. Collin[95] determined the reaction rates of equations (3.1) and (3.2) to be 0.01 to 0.1 of the experimental values obtained, and concluded that the decarburisation reaction of (3.3) was the logical explanation of the experimentally determined reaction rates. This investigation involved decarburisation in $H_2/N_2/H_2O$ atmospheres, with the gas flow rate maintained at a sufficiently high value for the diffusion through the boundary layer to have no influence on the reaction rate. For a decarburisation environment, c_g=0, where

$$k' = \frac{6.31\text{x}10^5.\exp\left(-22{,}350/T\right) p_{H_2O}/\sqrt{p_{H_2}}}{1+5.6\text{x}10^6.\exp\left(-12{,}900/T\right) p_{H_2O}/\sqrt{p_{H_2}}}. \qquad (3.31)$$

The decarburisation of steel involves carbon diffusion through the steel, with carbon removed from the surface of the steel. Diffusion of alloying elements also occurs within the steel. There

are various mechanisms which facilitate diffusion, with the literature pertaining to the diffusion of carbon and other alloying elements in steel detailed in Chapter 4.

CHAPTER 4

DIFFUSION IN STEELS

Diffusion involves the transport of matter in the gaseous, liquid, and solid phases. The mechanism through which this diffusion occurs is dependent upon the thermal energy associated with each atom. The form of diffusion important in the heat treatment of steels is that of solid state diffusion, which is a function of the high frequency of vibration, 10^{12}Hz, of the atoms about their sites in the crystal lattice. At any point in time, a small percentage of the atoms will possess sufficient vibrational energy to jump from one lattice site to an adjacent site. As the temperature of the solid increases, the frequency at which an individual atom will possess sufficient vibrational energy to jump to another lattice site increases. This motion can either involve the movement of individual atoms within a lattice of similar atoms, self-diffusion, or the movement of solute atoms through a solvent lattice structure, inter-diffusion.

The decarburisation of steel involves the transport of carbon and other alloying elements. The diffusion of carbon through a steel often determines the decarburisation rate[64,70,71,99,100], with certain alloy elements modifying the rate at which carbon diffuses. Diffusion of alloying elements through the steel, as well as diffusion of various gaseous species into the steel, also influence the oxidation characteristics, and therefore the decarburisation behaviour. Diffusion can be defined as the movement of a species from a region of high concentration to a region of low concentration. Generally the rate of diffusion is proportional to the concentration gradient.

The diffusion of a species in a material is dependent on the temperature. It has been found empirically that the Arrhenius equation, equation 4.1, adequately describes the relationship between the diffusion coefficient and temperature[105-107]:

$$D = D_o \exp\left(-\frac{Q}{RT}\right) \qquad (4.1)$$

where D = the diffusion coefficient in cm^2/s;

D_o = the frequency factor in cm^2/s;

Q = the activation energy in J;

R = the universal gas constant of 8.32 J/mol°K;

T = absolute temperature in °K.

For self-diffusion in single crystals, the magnitude of the frequency factor is close to unity[108]. However, the frequency factor has been found to vary in alloys by twelve orders of magnitude, particularly for ferrous alloys[109]. The activation energy represents the energy expended when atoms of a dissolved element, or of a solvent, move from one equilibrium position in the crystal lattice to another. D_o and Q are related to the[108]:

- Preliminary heat treatment;
- Structure of the steel;
- Composition of the steel;
- Types and constants of the crystal lattice;
- Sizes of both the solvent and diffusing element atoms;
- Atomic bond energy;
- Numerous other physical variables of the solvent and diffusing substance.

The magnitudes of D_o and Q are influenced by the defects present in the crystal lattice of metals and alloys. An increase in the concentration of point imperfections such as vacancies through processes such as quenching and plastic deformation frequently increase the mobility of the atoms. This reduces the activation energy, while increasing the diffusion coefficient[108]. Diffusion is also influenced by other imperfections such as dislocations and foreign atoms. Dislocations particularly affect the mobility and diffusivity of atoms that form intersititial atoms. These atoms prefer to collect around dislocations where they form a Cottrell zone. The activation energy for diffusion of such atoms is much higher, and their mobility much smaller, than for diffusion in substitutional solutions. A theory of diffusion has been developed, based on the movement of atoms in a crystal lattice, which permits correlations to be established between diffusion and the physical constants of matter for every type of diffusion mechanism. A modern diffusion theory should satisfactorily explain:

a) The relationship between diffusion in a material, and the physical constants of the material;
b) The dependence of diffusion coefficients on temperature, pressure, and other external variables;
c) The dependence of diffusion on thermodynamic characteristics and composition of the alloys, and the influence of the specific chemical properties on both the diffusing and the solvent atoms on the diffusion;
d) The effect of a specific structure for a certain crystalline body on the diffusion.

4.1 Diffusion mechanisms

There are several mechanisms by which diffusion of various elements in a solid material are thought to occur[108]. These mechanisms include the:

1) Interstitial diffusion mechanism;
2) Vacancy mechanism;
3) Place exchange mechanism; and
4) Ring type mechanism.

4.1.1 Interstitial diffusion

The interstitial mechanism of diffusion arises when an atom passes from its interstitial site to one of its nearest neighbour interstitial sites without any permanent displacement of the matrix atoms[108]. This is illustrated in Figure 4.1(a). The atom can move to either an interstitial site in the crystal lattice or to a lattice vacancy. Atom 1, which is dislocated, moves towards its nearest neighbours, atoms 2, 3, and 4, and occupies the interstitial site illustrated by the dotted circle. As the atom acquires sufficient energy, the atom may then jump to a neighbouring interstitial site, position 5[108]. For this to occur, atoms 3 and 4 must deviate from their equilibrium positions, and move in the direction indicated by the arrows. The required amplitude of vibration of these atoms is large, and must exceed half the diameter of the diffusing atom. This required distortion of atoms 3 and 4 constitutes the barrier to an interstitial atom changing sites. Examples of the interstitial mechanism include the diffusion of carbon, nitrogen, hydrogen and boron in iron.

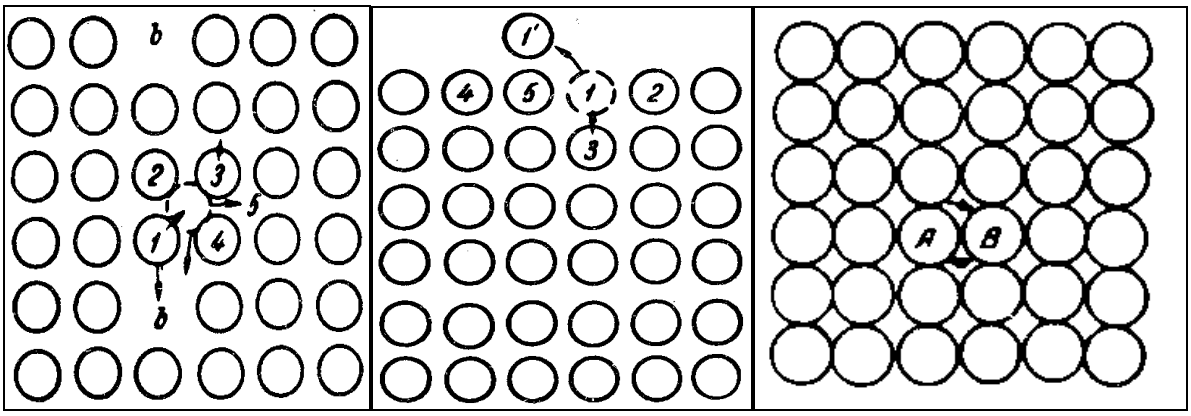

(a) **(b)** **(c)**

Figure 4.1 Illustration of (a) the interstitial and vacancy diffusion mechanisms, (b) vacancy formation, leading to the vacancy mechanism of diffusion, and (c) the place exchange diffusion mechanism (from Ref. 108).

Diffusion via the interstitial mechanism may occur during the diffusion of atoms in interstitial solid solutions and phases. For close packed lattices where the small interstitial atom is surrounded by numerous solvent atoms, there is a high probability that the vibrations of the solvent atoms will have a large amplitude. Consequently, there is a high probability that the large interatomic spacings necessary for the movement of the interstitial atoms will be generated. However, this probability decreases sharply with increasing atomic diameters due to only those atomic vibrations with an amplitude to create a gap sufficient for the passage of the diffusing atom being significant. The activation energy of diffusion also increases with increasing atom size[108].

This indicates that the same diffusion mechanism operates for carbon, nitrogen, hydrogen and boron where they form interstitial solid solutions, and their atoms diffuse along the interstices in the lattice. An increase in the solute atom diameter increases the distortions in the iron lattice produced when the diffusing atom jumps into the neighbouring empty interstitial sites. This greater deformation requires a larger activation energy, with the magnitude of the activation energy rising sharply as the diameter of the diffusing atoms approaches that of the solvent atoms.

4.1.2 Vacancy mechanism

Vacancy formation arises from the thermal motion of the atoms in the lattice. The vacancy mechanism of diffusion involves an atom on a site adjacent to a vacancy jumping into the vacancy[110], Figure 4.1(b). Atom 1 in Figure 4.1(b) acquires sufficiently more energy than its neighbours, with the bonds between atoms 1 and 2 being broken, and atom 1 leaving the surface row of atoms to occupy position 1'[108]. Thus, a vacancy appears at the site previously occupied by atom 1. Since the bond between atom 1 and 5 is unbroken, little energy is required for the vacancy to form as not all the bonds between atom 1 and its neighbours are broken. Vacancies also appear together with dislocated atoms, Figure 4.1(a). Consequently, the vacancy mechanism of diffusion is plausible, and has been established as the predominant mechanism in many metals and ionic compounds.

The energy required to move an iron atom into an adjacent vacancy is approximately equivalent to the energy required to move a carbon atom from one interstitial site to another in the same face centred cubic phase. However, iron diffuses much more slowly than carbon due to each carbon atom having several vacant nearest-neighbour sites, while the fraction of vacant iron sites is very small. Each iron atom must therefore wait an appreciable period before a vacancy becomes available. The possible cause of vacancy movement is as follows. In close packed metals and alloys, vacancies are surrounded by 8 or 12 atoms. Due to the random thermal vibrations, there is a high probability that any one of these atoms will acquire sufficient energy to leave its position in the lattice, and occupy a vacant site. Consequently, a vacancy will be on the former site of this atom, with the vacancy travelling in jumps through the crystal.

For iron at 1000°C, the period of time for which the vacancies occupies a specific site is very small, as they change places with lattice atoms 10^4 to 10^8 times a second[108]. If no concentration or stress gradients exist in the crystal, there is no preferred direction for vacancy movement. During a relatively long period of time, each vacancy changes place on average with the same amount of atoms in all directions in the crystal.

Real metals involve the formation and movement of a large number of vacancies in the lattice. In certain instances, vacancies may exhibit a preferred orientation in their motion, resulting in mass transfer. Technically the movement of vacancies arises from atoms "jumping". This gives the

concept of vacancy diffusion, where the formation and movement of vacancies is strongly dependent on the temperature[110,111]. An increased temperature raises the atomic mobility in metals and alloys, while the vacancy concentration also increases. Therefore, the heating of metals and alloys results in a simultaneous increase in the number of vacancies, and in their rate of position exchange with atoms, causing a sharp increase in the mobility of atoms.

4.1.3 Place exchange mechanism

The place exchange mechanism involves two atoms simultaneously leaving their equilibrium lattice positions, and exchanging places[112], Figure 4.1(c). For the place exchange mechanism to be possible, atoms A and B must simultaneously acquire sufficient energy for the deformation of the crystal lattice, and for the considerable compression of the atoms. The energy required for the atoms to move from one site to another is called the activation energy of diffusion. However, this mechanism fails to explain the diffusion in metals with close packed atomic structures[113].

4.1.4 Ring type mechanism

The ring type or annular mechanism is a further development of the place exchange mechanism. From energy considerations, it is more favourable for atoms to change positions within a group of atoms. Zener[114] showed that the minimum energy is required for the rotation of a ring consisting of four atoms, Figure 4.2(a). The lattice deformations produced are small, due to the atom movement occurring upon the rotation of the whole group of atoms. Such a rotation eliminates the counter movement of closely located atoms. Figures 4.2(b) and (c) show rings of four atoms for face centred cubic and body centred cubic atoms respectively. Various researchers attribute diffusion in body centred cubic metals and alloys which have close packed atomic structures to the annular diffusion mechanism.

4.2 Diffusion of carbon in steel

Carbon diffuses mainly along the grain boundaries in ferrite, and through the grains for austenite at high temperatures[108]. However, there are instances where the rate of grain boundary diffusion in austenite is also high[108]. An investigation into to the austenitisation of malleable cast iron illustrated that austenite mainly grows along ferrite grain boundaries[115], confirming the

considerable grain boundary diffusion of carbon in ferrite. This data indicates a higher mobility of carbon atoms along the grain boundaries than within the grains, due to the lower activation energy and the lower atomic packing density of the boundaries. As a result, a higher diffusion rate of carbon in fine grained iron than in coarse-grained structures is expected.

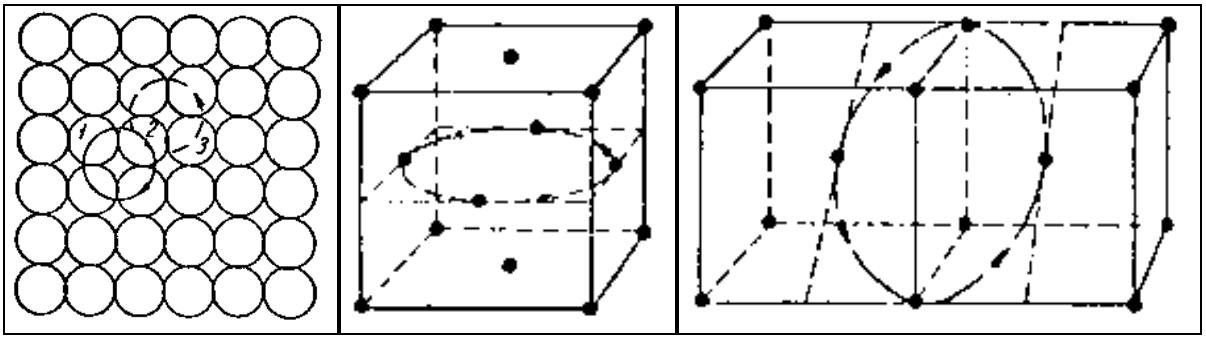

(a) **(b)** **(c)**

Figure 4.2 Schematic illustrations of annular diffusion for the (a) two-dimensional scheme, (b) face centred cubic lattice, and (c) body centred cubic lattice (from Ref. 108).

At a specific temperature, carbon diffusion in ferrite is much greater than in austenite. Ferrite has a lower activation energy for diffusion than austenite[116-121] due to its structural features, where the ferrite lattice is less closely packed than that of austenite. The coordination number and lattice atomic packing factor for ferrite are 8 and 0.68, and 12 and 0.74 for austenite. Ferrite has a much smaller lattice constant, $2.86\,\overset{o}{A}$, than austenite, $3.56\,\overset{o}{A}$. Therefore, the amplitude of vibration required for carbon atoms to jump from one interstitial site to a neighbouring site is much smaller in ferrite than in austenite, explaining the increased mobility of carbon atoms in ferrite. The lower ferrite carbon solubility compared to austenite may also enhance the carbon diffusivity, since any increase in concentration close to the solubility limit may produce a considerable increase in the diffusion coefficient of the solute atoms[108].

4.2.1 Influence of alloying elements on diffusion

The influence of alloying elements on the diffusion of interstitial atoms through steel is dependent upon[108]:

1) The alloying elements acting on the solvent metal, therefore distorting its lattice and increasing or decreasing the atomic bond energy in the solid solution, thus accelerating or decelerating carbon diffusion;
2) The alloying elements increasing or decreasing the thermodynamic activity of carbon, and so accelerating or decelerating its diffusion.

The jumping of a solute atom from one site in the crystal lattice to another by the intersitial diffusion mechanism is possible if the thermal vibrations create a large spacing between the atoms, and the interstitial atom is given a large impetus in the relevant direction[108]. As the extent of alloying increases, the activation energy increases, while the atom mobility decreases if the atoms of the alloying element are bonded to carbon and iron atoms. This reduces the fraction of larger amplitude vibrations, and therefore the magnitude of the diffusion coefficient. The maximum retarding of diffusion should occur when the austenite or ferrite is alloyed with carbide-forming elements that are capable of generating bonds with iron atoms, without distorting the crystal lattice significantly.

i) Diffusion of carbon in alloy ferrite

Silicon and nickel have little effect on the diffusion coefficient of carbon in ferrite for temperatures of 500 to 800°C[122]. Some reduction in the diffusion coefficient for a Fe-Si alloy, relative to non-alloyed ferrite, was noticed below 600°C. Between 500 and 800°C, carbide forming elements such as molybdenum and chromium reduce the carbon diffusion in ferrite. There are some situations where the carbon diffusion in ferrite is considerably lower if the ferrite is jointly alloyed with several elements[122-124].

ii) Diffusion of carbon in alloy austenite

The activity of carbon in steel increases with concentration. The diffusion of carbon in austenite increases with carbon content through the distortion of the crystal lattice, and the increased thermodynamic activity. Zhukov[125] qualitatively analysed the effect of some alloying elements on the thermodynamic activity of carbon in solid solutions. For a specific carbon content, an increased carbon activity occurs when its atoms are repelled by the alloy atoms. However, a

reduction in carbon activity occurs in austenite alloyed with carbide-forming elements due to the higher local bond energy of carbon atoms with the alloy atoms.

The bond energy between silicon and carbon atoms is smaller than between carbon and iron atoms, with the carbon atoms preferentially surrounded by iron atoms. This results in a repulsive action of silicon on carbon atoms in solid solutions, creating silicon atom regions depleted of carbon. This increases the silicon atom concentration in other regions of the alloy, thus raising its activity. A reduced carbon activity in austenite alloyed with chromium arises from the increased bond energy of carbon atoms with the chromium atoms.

The addition of chromium and manganese in ternary alloys increases the values of Q and D_o in austenite[126]. At any temperature, chromium decelerates the diffusion due to the increase in activation energy outweighing the increasing value of D_o. Manganese decreases the diffusion at temperatures below 1,100°K, but accelerates the diffusion somewhat at higher temperatures. Silicon has been found to influence the carbon diffusion only slightly in austenite, while aluminium slightly decreased the carbon diffusion in austenite. Blanter[126] made two conclusions about the effect of alloying elements on the carbon diffusion in austenite, namely:

1) Carbide forming elements usually decelerate carbon diffusion;
2) Elements that do not form carbides increase the carbon diffusion.

Silicon increased the carbon diffusion in austenite below 1,050°C in ternary Fe-C-Si steels, and slightly decreased it above 1,050°C[127]. Below 950°C, 1wt.%Si resulted in the largest increase in diffusion rate of silicon, nickel, cobalt, copper, aluminium and chromium relative to binary Fe-C alloys. Furthermore, silicon had a considerably greater inhibiting effect on diffusion than the other elements above 1,050°C.

Carbon diffusion in austenite for quaternary systems is lower than in ternary alloys. For alloys containing aluminium, cobalt or copper, the addition of 1.2wt%Si slightly reduces the mobility of atoms. For chromium alloys, the addition of silicon substantially decreases the atom mobility, reducing the relevant diffusion coefficients by an order of magnitude. This reduction mainly arises due to lower values of D_o, and is typical of alloys containing carbide forming elements. The retarding of diffusion for alloys containing 1.2wt.%Si, and about 1wt.% of another alloying

element can be arranged in a row where the last elements reduce the diffusion coefficient to a greater extent than the preceding elements:

Mn > Mo > V > W > Cr.

Therefore, chromium retards carbon diffusion in austenite to the greatest extent. The retarding effect caused by chromium is greater than that caused by manganese by a factor of 20.

4.2.2 High diffusivity paths

Any real crystalline material contains vacancies, interstitials, dislocations, free surfaces, and often grain boundaries, all which markedly influence the diffusion in the material. The mean jump frequency of an atom in these regions is considerably higher than that of an atom in the lattice. The rate of diffusion along grain boundaries is several orders of magnitude higher than diffusion within the grain volume. Several researchers[128-130] have established the ratio of grain boundary to volume diffusion at 10^3 to 10^5. This is a consequence of the looser packing and weaker bonding of the grain boundary atoms. Some researchers ascribe the higher rate of grain boundary diffusion to the higher vacancy concentration in the grain boundaries. The ratio of activation energy for grain boundary diffusion to that of volume diffusion for a series of metals was 0.6 to 0.7[131].

Grain boundary diffusion develops particularly well in metals and alloys after phase transformations[109,132-134]. Therefore, martensitic and polymorphic transformations of the ferrite-austenite type create numerous interfaces between the austenite grains, increasing the diffusion coefficients due to faster diffusion along the grain boundaries. Figure 4.3 illustrates the diffusion spectrum for face centred cubic metals[135], where T_m denotes the melting temperature. The surface diffusion data is averaged for a variety of surfaces for different metals, while the grain boundary diffusion data is averaged for a wide variety of large angle grain boundaries. The undissociated lattice dislocation diffusion data refer to discrete edge dislocations in small angle tilt boundaries and stacking fault ribbons. The dissociated lattice dislocation data refer to dislocations dissociated in that way. For temperatures significantly lower than T_m;

$$D_s > D_b \approx D_d(\text{undissociated}) > D_d(\text{dissociated}) > D_l, \qquad (4.2)$$

where D_s, D_b, D_d, D_l = surface, grain boundary, lattice dislocation and lattice diffusivities respectively.

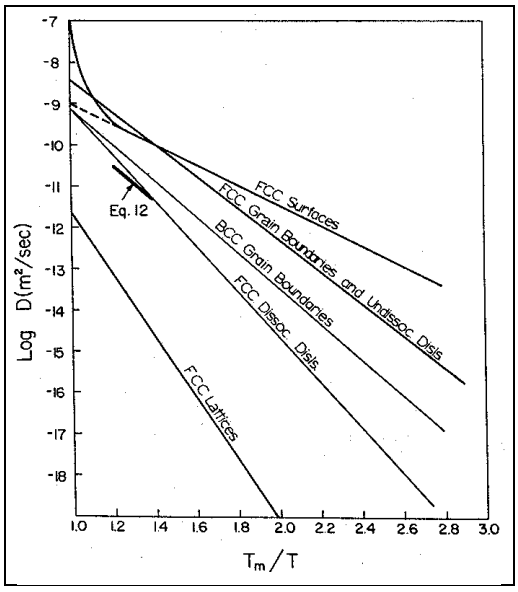

Figure 4.3 Diffusivity spectrum for metals (from Ref. 135).

Substitutional atoms generally diffuse more rapidly along grain boundaries than through the crystal lattice at temperatures appreciably below the melting point[135-139], producing a net diffusional transport of atoms along boundaries[140,141]. Grain boundaries also act as sources or sinks for diffusing atoms[142]. Balluffi[143] concluded that grain boundary diffusion occurs by a vacancy mechanism in the vast majority of boundaries, including small and large angle boundaries. The atom jumping occurs by vacancy exchange between a variety of sites in the core. An interstitial mechanism seems to be excluded due to the relatively high energy of formation of interstitials in most sites in the core.

Grain boundaries can be induced to migrate when solute atoms are diffused along them if the lattice diffusion length is relatively short[144], and is termed diffusion induced grain boundary migration, Figure 4.4. If solute atoms are diffused into a region of a boundary from some source, Figure 4.4(a), under conditions where the lattice diffusion length is relatively short, the boundary is observed to migrate at a velocity ν, leaving behind an alloyed zone in its wake. If solute atoms are diffused out of a boundary to some sink, Figure 4.4(b), the boundary is again observed to migrate. A zone with reduced alloy content is left in its wake.

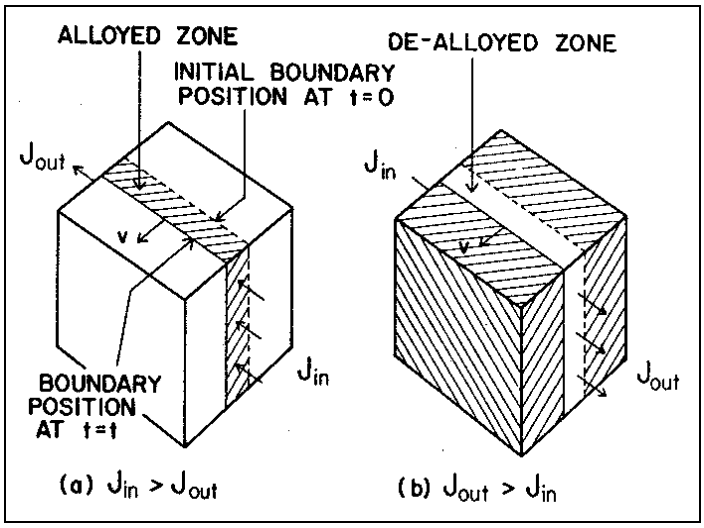

Figure 4.4 Diffusion grain boundary migration where (a) solute atoms are deposited during inward grain boundary diffusion, and (b) solute atoms are removed during outward grain boundary diffusion (from Ref. 144).

In a well annealed metal single crystal, any plane passing through the crystal will intercept 10^6 to 10^7 dislocations per cm^2. These randomly oriented dislocations in the single crystal increases the apparent diffusivity in all directions, while the grain boundaries increase the apparent diffusivity in the plane of the grain boundary.

Chapters 2, 3 and 4 have detailed the literature pertaining to the formation of austenite in steels, the decarburisation of steels, and the diffusion in steels. The remaining chapters are concerned with the original research undertaken for this project, with Chapter 5 detailing the experimental philosophy.

CHAPTER 5

EXPERIMENTAL PHILOSOPHY

5.1 Outline of research areas

This project originated from research that attempted to reduce the decarburisation of automobile coil springs during spring manufacture[145]. However, difficulties were encountered in trying to obtain uniform and repeatable decarburised layers during the heat treatments used for this research. This indicated that a better understanding of the decarburisation would allow heat treatments for minimised decarburisation. Consequently, a preliminary experimental program was undertaken for SUP7. This involved determining the Ac_3 transformation temperatures microscopically by thirty minute heat treatments at various temperatures, then producing and decarburising tapered needle test specimens at the Ac_3 temperature with various hydrogen and water decarburising atmosphered the existing experimental apparatus. However, the following experimental limitations were soon evident, where:

- Thirty minutes is insufficient for the initial room temperature structure to fully transform to austenite at the Ac_3 temperature;
- Little is known about the austenitisation and decarburisation of steels comprising typical spring steel carbon, silicon, manganese and chromium contents;
- The experimental apparatus gave a limited range of, and control over, the experimental decarburisation parameters.

It became apparent that the research necessary comprised two distinct topics, namely:

a) Transformation on heating from the initial to the equilibrium structure;
b) Decarburisation of the steels of interest.

The literature search of Chapters 2, 3, and 4 indicated that limited information exists for the influence of silicon on the austenitisation of steel. Furthermore, the literature pertaining to the

decarburisation of spring steels was also sparse, despite the detrimental effect of decarburisation on the sag and fatigue properties of automobile coil suspension springs. No detailed information for the decarburisation of higher carbon steels with elevated silicon contents could be obtained. The research undertaken into the influence of such factors as gas flow rates, specimen heating times, austenitisation prior to decarburisation, prior initial structure, and alloy content on the decarburisation processes appears to be less than rigorous, despite the fundamental importance of this information. Consequently, a detailed study into the austenitisation and decarburisation of varying silicon content spring steels was considered necessary to redress this lack of knowledge.

Two commercial spring steels, SUP7 and SUP7NV, were obtained, with their compositions listed in Table 5.1. These steels differ only in niobium and vanadium, with SUP7NV having higher contents of these two elements than SUP7. In order to investigate the influence of silicon on the austenitisation and decarburisation, three more steels comprising 0, 1, and 3wt.%Si, but otherwise similar chemical analyses to SUP7, were considered necessary. The desired alloy compositions of these steels, denoted by*, are given in Table 5.1.

Table 5.1 Desired composition of steels to be investigated.

DESCRIPTION	C	Si	Mn	Cr	V	Nb	Al	Cu
0% SILICON *	0.6	0.0	0.8	0.2	-	-	-	-
1% SILICON *	0.6	1.0	0.8	0.2	-	-	-	-
SUP7	0.60	1.94	0.77	0.19	0.005	-	0.033	0.01
SUP7NV	0.62	2.11	0.85	0.17	0.173	0.15	0.011	0.11
3% SILICON *	0.6	3.0	0.8	0.2	-	-	-	-

In order to comprehensively describe and quantify the austenitisation and decarburisation of varying silicon content spring steels, the proposed experimental procedure consisted of:

a) Production of the experimental steels;
b) Determination of the appropriate experimental variables of the austenitisation and decarburisation processes to be investigated;
c) Development of suitable experimental apparatus;
d) Development and application of suitable analytical techniques;

e) Undertaking the austenitisation and decarburisation heat treatments;
f) Analysis of the heat treated specimens;
g) Analysis of the experimental results.

The remainder of this chapter details the experimental parameters that were investigated. Chapter 6 focuses on the experimental apparatus, and Chapter 7 on the experimental techniques. The analytical techniques applied are described in Chapter 8, while the remaining chapters detail the results and conclusions obtained.

5.2 Description of research areas

5.2.1 Austenitisation investigation

Several factors influence the transformation of the steel from the initial structure to the equilibrium structure. The rate of transformation, final transformation structure, and composition of that structure, are influenced by the following parameters:

a) Heat treatment temperature relative to the Ac_1* and Ac_3 transformation temperatures;
b) Initial structure;
c) Alloy content.

The austenitisation kinetics are influenced by the alloy content of the steel, with elevated silicon and manganese levels greatly retarding the transformation to austenite. As silicon also modifies the carbon diffusion and oxidation characteristics during decarburisation, the austenitisation of spring steels with different silicon contents warrants investigation. An investigation into the austenitisation of two spring steels, SUP7 and SUP7NV, which differ with SUP7NV having higher niobium and vanadium contents is also appropriate, since considerable research into the effect of these microalloying elements on the physical and microstructural properties during spring manufacture has been undertaken[5-11].

* An eutectoid gap was observed during the course of the austenitisation experimentation. Therefore, the Ac_1 temperatures determined in Chapter 9 actually correspond to the Ac_1' temperatures for steels which exhibit eutectoid gaps. However, the term Ac_1 is often used instead of Ac_1' as it is generally quoted as the temperature at which austenite formation first occurs.

The initial steel microstructure influences the austenitisation kinetics. Pearlitic and spheroidal cementite structures transform at different rates, with the grain size, cementite size and cementite distribution influencing the transformation kinetics. The transformation kinetics are also dependent on the degree of superheat above the Ac_1 transformation temperatures of the different steels.

The aforementioned factors justified investigation due to the limited information available in the literature pertaining to spring steels with different silicon contents. This information is a necessary precursor to obtaining a detailed understanding of the decarburisation of these steels, where several different mechanisms contribute to the carbon transport through the steel to the surface. Carbon transport can occur by diffusion in the bulk, along dislocations and other defects, as well as along grain boundaries. The local carbon concentration in the steel is a function of the alloying element concentration, the phases that are present, the temperature with the associated solubility for these phases, and the solubility product for the carbide precipitates in the presence of the given phases. The majority of this information pertaining to the relationship between the austenitisation and these variables can be obtained from the proposed austenitisation investigation.

The austenitisation processes can be quantified by the measurement of the following physical and structural properties:

a) Initial alloy content of the steels;
b) Specification of the initial microstructure with respect to prior austenite grain size, pearlite interlamellar spacing, size and morphology of the ferrite grain structure, and cementite and graphite fraction, location, shape and size distribution;
c) Ferrite, austenite, cementite and graphite fractions, grain sizes, shapes and distribution;
d) Microalloy element partitioning amongst the various phases;
e) Microhardness of the various phases.

5.2.2 Decarburisation investigation

The following factors potentially influence the decarburisation of steel:

a) Alloy content;
b) Initial microstructure;
c) Heat treatment temperature relative to the Ac_1 and Ac_3 transformation temperatures;
d) Steel temperature and structure upon introduction of the decarburising atmosphere;
e) Concurrent austenite transformation and decarburisation;
f) Decarburisation atmosphere and gas flow rates;
g) Specimen geometry.

None of the above factors have been investigated in detail for the spring steels of interest, despite the reduction of the sag resistance and fatigue strength of automobile coil suspension springs due to decarburisation. The alloy content influences both the carbon diffusion through the steel, and the oxidation characteristics and subsequent carbon diffusion through any surface oxide layers. Investigation of the decarburisation of steels with different silicon contents allows the effect of silicon on the decarburisation to be quantified in terms of the:

- Influence on the diffusion coefficient of carbon in ferrite and austenite;
- Dissociation of the iron carbides;
- Formation of any oxide layers, and the subsequent influence on the carbon removal.

This would also eliminate the confusion as to whether silicon accelerates the decarburisation of medium carbon steels[146].

It is reasonable to expect that the initial microstructure of the steel prior to exposure to the heat treatment atmosphere will influence the decarburisation processes, especially if the decarburisation commences before the steel has obtained its equilibrium structure. This arises from the variation in grain shapes and sizes of different initial microstructures, as well as from the different locations of carbon rich sources such as cementite and austenite, and the subsequent dissolution to supply the carbon for decarburisation. The ongoing austenitisation to a final equilibrium structure could also influence the decarburisation. The majority of

decarburisation and diffusion studies are vague on the initial microstructural details, despite the potential influence on the decarburisation. Consequently, this research would allow the effect of the initial microstructure on the decarburisation to be established.

The decarburisation processes could also be dependent on the introduction of the decarburisation atmosphere relative to the steel specimen temperature as the specimen heats to temperature in the furnace, and on the extent of austenitisation. The heat treatment temperature, atmosphere, gas flow rate, and the test specimen geometry, can all influence the decarburisation. The decarburisation can be quantified through measurement of the following physical and structural properties:

a) Initial alloy content;
b) Specification of initial structure with respect to the prior austenite grain size, pearlite interlamellar spacing, size and morphology of the ferrite grain structure, and the cementite and graphite fractions, locations, and size distributions;
c) Free ferrite and partial decarburisation depths;
d) Oxide thicknesses;
e) Microalloy analysis of the oxide and decarburised structures;
f) Microhardness of the various phases.

5.3 Experimental design

5.3.1 Austenitisation experimentation

It is important that the austenitisation research specifies the effects of, and interrelationships between, the extent and kinetics of austenitisation in terms of alloy content, heat treatment temperature, and initial structure. Ideally this would involve the production of steels with different carbon, silicon and manganese contents. Heat treatments would be undertaken for each steel over a range of temperatures. Test specimens with different pearlitic and spheroidal cementite microstructures would be heat treated at each temperature for varying test durations. However, such an exhaustive investigation is not practical for this project due to the time and financial constraints imposed by the required number of heat treatments. Furthermore, the austenitisation investigation of spring steels is not the main aim of this

project. However, it is necessary due to the potential influence of austenitisation on the decarburisation. Consequently, this experimentation was limited to a manageable number of tests to give sufficient results from which meaningful conclusions could be drawn.

Rather than trying to investigate the interrelationships between all the alloying elements, silicon was chosen as the most important element. Silicon contents of 0 to 3wt.% are required, with the higher value corresponding to the silicon content where the oxidation and decarburisation characteristics of electrical steels exhibit marked differences relative to lower silicon contents. A greater experimental focus is placed on SUP7 than the other four steels due to its use for automobile coil suspension springs. Previous studies of the austenitisation of various steels involve different initial structures and heat treatment temperatures, which restricts comparisons between these steels. For the five steels to be investigated, the same heat treatment will yield different transformation structures and kinetics due to the different Ac_1 and Ac_3 transformation temperatures of the steels.

In order to facilitate a meaningful comparison of the steels, the following experimental criteria were established, which involve:

a) Identical prior austenitisation heat treatments for the production of the different initial microstructures;
b) Comparable heat treatment regimes for the production of the different initial microstructures;
c) Austenitisation heat treatments with the same superheats relative to the transformation temperatures;
d) Identical experimental procedure.

Production of the initial structures for each steel utilises the same initial austenitisation heat treatment of 12 hours at 900°C. The investigation of two pearlitic and three spheroidal cementite structures for SUP7 allows the influence of different initial structures to be quantified. The heat treatment regimes undertaken for the production of the initial structures are consistent among the steels. For example, one of the spheroidal cementite structures is produced for all steels by austenitising, quenching in water, and annealing for 96hr at 10°C

below the Ac_1 temperature. No attempt was made to obtain similar coarseness structures for the different steels due to the amount of experimentation necessary to achieve this.

Austenitisation heat treatments at the same temperatures for the different steels does not facilitate a totally meaningful comparison between the steels due to the different transformation temperatures. This could result, for example, in 100% austenite formation for one of the steels at one temperature, and no austenite formation for another. Therefore, austenitising at specific superheat temperatures relative to the Ac_1 and Ac_3 transformation temperatures for each steel allows the steels to be compared for their respective intercritical regions. Due to the temperature gap between the Ac_1 and Ac_3 temperatures being different for each steel, heat treatments within the Ac_1/Ac_3 interval were undertaken at the same "fractional superheat" for each steel. This heat treatment temperature, T_{HT}, is given by

$$T_{HT} = T_{Ac_1} + (F.S.)(T_{Ac_3} - T_{Ac_1}), \qquad (5.1)$$

where T_{HT} = heat treatment temperature at a fractional superheat in °C;

$F.S.$ = fractional superheat between the Ac_1 and Ac_3 temperatures;

T_{Ac_1}, T_{Ac_3} = Ac_1 and Ac_3 transformation temperatures in °C.

An identical experimental procedure is necessary for all the steels in terms of the test specimen size, austenitisation heat treatment procedure, quenching media, and post-heat treatment tempering. The experimental austenitisation program involved the sequence detailed below, with the heat treatments undertaken listed in Table 5.2.

- Production of the experimental steels;
- Forging of the cast ingots into 14mm diameter bar stock;
- Chemical analysis of the experimental steels;
- Theoretical calculation of the Ac_1 and Ac_3 transformation temperatures;
- Test specimen preparation for the determination of the transformation temperatures;
- Heat treatments to determine the transformation temperatures;
- Production of test specimens with different initial structures;
- Undertaking the austenitisation heat treatments;

- Preparation of the heat treated specimens for microstructural investigation;
- Analysis of the stereological and physical/microstructural properties;
- Analysis of the results.

5.3.2 Decarburisation experimentation

The same steels were used for the decarburisation investigation as were used for the austenitisation investigation. A direct comparison of the austenitisation and decarburisation processes necessitates the use of the same initial structures and heat treatment temperatures. A greater emphasis is placed on the decarburisation of SUP7 relative to the other steels. Several decarburisation parameters require investigation under reproducible experimental conditions, namely the:

- Type and composition of the heat treatment atmosphere;
- Heat treatment atmosphere gas flow rates;
- Test specimen geometry.

The predominant decarburisation atmospheres to be used comprise hydrogen with differing water vapour contents. The minimum gas flow rates were established experimentally, with flow rates greater than the minimum values used for the subsequent heat treatments. Cylindrical test specimens were used to simplify the preparation and analysis of the heat-treated specimens. The decarburisation experimentation undertaken is detailed in Table 5.3, with the experimental sequence being:

- Production of the test specimens with different initial structures;
- Undertaking the decarburisation heat treatments;
- Preparation of the heat treated specimens for microstructural investigation;
- Analysis of the decarburisation depths and physical/microstructural properties;
- Analysis of the results.

This chapter outlined the research areas pertaining to this project, and the experimentation for a detailed investigation into these areas. Chapter 6 subsequently details the experimental equipment developed for this project.

Table 5.2 Experimental austenitisation heat treatments.

DESCRIPTION	Transformation temperatures	Initial structures	Superheat fraction (%)	Superheat temperature		Test duration
				(relative to Ac_1, Ac_3)	(°C)	
0% SILICON	Ac_1, Ac_3	B*, D, F**	0.5	Ac_1+17°C	723	15min-96hr
		B, D, F	1	Ac_3	740	1min-16hr
1% SILICON	Ac_1, Ac_3	B, D, F	0.5	Ac_1+17°C	745	15min-96hr
		B, D, F	1	Ac_3	760	1min-16hr
SUP7	Ac_1, Ac_3	A, B, C, D, F	0.13	Ac_1+10°C	755	15min-192hr
		B, D, F	0.25	Ac_1+20°C	765	15min-96hr
		B, D	0.5	Ac_1+35°C	780	30s-192hr
		B, D	0.75	Ac_1+55°C	800	30s-192hr
		A, B, C, D, F	1	Ac_3	820	30s-4hr
SUP7NV	Ac_1, Ac_3	B, D, F	0.25	Ac_1+17°C	765	15min-96hr
		B, D, F	1	Ac_3	820	30s-2hr
3% SILICON	Ac_1, Ac_3	B, D, F	0.25	Ac_1+17°C	785	15min-96hr
		B, D, F	1	Ac_3	835	30s-4hr

* A,B denote air and furnace cooled initial pearlitic microstructures;

** C, D, F denote 12hr tempered martensite, 96hr tempered martensite and intercritical initial microstructures.

Table 5.3 Experimental decarburisation heat treatments.

DESCRIPTION	Initial structures	Superheat temperatures		Decarburisation atmosphere	Test specimen	Test duration
		(relative to Ac_1, Ac_3)	(°C)	p_{H_2O} / p_{H_2} ratio		
0% SILICON	B	Ac_1-56°C	650	0.05	5mm dia.x50mm	4hr
	B	Ac_1-6°C	700	0.05	5mm dia.x50mm	4hr
	B	Ac_3	740	0, 0.01, 0.05, 0.25, 0.5, 1.0, air	5mm dia.x50mm	4hr
	B	Ac_3+10°C	750	0.05	5mm dia.x50mm	4hr
	B	Ac_3+60°C	800	0.05	5mm dia.x50mm	4hr
	B	Ac_3+110°C	850	0.05	5mm dia.x50mm	4hr
	B	Ac_3+160°C	900	0.05	5mm dia.x50mm	4hr
1% SILICON	B	Ac_1-78°C	650	0.05	5mm dia.x50mm	4hr
	B	Ac_1-28°C	700	0.05	5mm dia.x50mm	4hr
	B	Ac_1+22°C	750	0.05	5mm dia.x50mm	4hr
	B	Ac_3	760	0, 0.01, 0.05, 0.25, 0.5, 1.0, air	5mm dia.x50mm	4hr
	B	Ac_3+40°C	800	0.05	5mm dia.x50mm	4hr
	B	Ac_3+90°C	850	0.05	5mm dia.x50mm	4hr
	B	Ac_3+140°C	900	0.05	5mm dia.x50mm	4hr

Table 5.3 (continued) Experimental decarburisation heat treatments.

DESCRIPTION	Initial structures	Superheat temperatures		Decarburisation atmosphere	Specimen geometry	Test duration
SUP7	B	Ac_1-95°C	650	0.05	5mm dia.x50mm	4hr
	B	Ac_1-45°C	700	0.05	5mm dia.x50mm	4hr
	B	Ac_1+5°C	750	0.05	5mm dia.x50mm	4hr
	As-supplied stock	Ac_1+55°C	800	0.05, 0.25	5mm dia.x80mm	5min-2hr
	B	Ac_1+55°C	800	0.05	5mm dia.x50mm	4hr
	A, B, C, D, F	Ac_3	820	0.05, 0.25	5mm dia.x15mm	15min-24hr
	A, B, C, D, F	Ac_3	820	0, 0.01, 0.05, 0.25, 0.5, 1.0, air	5mm dia.x50mm	4hr
	B	Ac_3	820	0.25	12mm dia.x20mm	2.5-15min
	B	Ac_3+20°C	850	0.05	5mm dia.x50mm	4hr
	B	Ac_3+80°C	900	0.05	5mm dia.x50mm	4hr
SUP7NV	B	Ac_1-98°C	650	0.05	5mm dia.x50mm	4hr
	B	Ac_1-48°C	700	0.05	5mm dia.x50mm	4hr
	B	Ac_1+2°C	750	0.05	5mm dia.x50mm	4hr
	B	Ac_1+52°C	800	0.05	5mm dia.x50mm	4hr
	B	Ac_3	820	0, 0.01, 0.05, 0.25, 0.5, 1.0, air	5mm dia.x50mm	4hr
	B	Ac_3+30°C	850	0.05	5mm dia.x50mm	4hr
	B	Ac_3+80°C	900	0.05	5mm dia.x50mm	4hr
3% SILICON	B	Ac_1-120°C	650	0.05	5mm dia.x50mm	4hr
	B	Ac_1-70°C	700	0.05	5mm dia.x50mm	4hr
	B	Ac_1-20°C	750	0.05	5mm dia.x50mm	4hr
	B	Ac_1+30°C	800	0.05	5mm dia.x50mm	4hr
	B	Ac_3	835	0, 0.01, 0.05, 0.25, 0.5, 1.0, air	5mm dia.x50mm	4hr
	B	Ac_3+15°C	850	0.05	5mm dia.x50mm	4hr
	B	Ac_3+65°C	900	0.05	5mm dia.x50mm	4hr

CHAPTER 6

EXPERIMENTAL APPARATUS

6.1 Introduction

A comprehensive investigation into the austenitisation and decarburisation of spring steels necessitated the development of the following experimental heat treatment apparatus:

a) A neutral salt bath with accurate temperature control for short duration austenitisation heat treatments;
b) A heat treatment furnace with accurate temperature control and the provision of an inert annealing environment for longer duration austenitisation heat treatments;
c) A furnace with accurate temperature control for decarburisation heat treatments with the provision of an inert annealing atmosphere, controlled insertion of the test specimens, monitoring and control of the decarburisation atmosphere and gas flow rate, and monitoring of the exhaust gases.

This chapter details the design philosophy behind, and the development of, the experimental heat treatment apparatus constructed for this project.

6.2 Salt bath

6.2.1 Design philosophy

Austenitisation heat treatments of less than fifteen minutes for 5mm diameter test specimens in an air furnace were impractical due to the time required to heat the specimens to the operating temperature. Preliminary experimentation established that approximately 10min was required for 5mm diameter specimens to heat to within 5°C of the tube furnace temperatures. Consequently, tests shorter than 15min were not undertaken in the tube furnace.

Several other media impart greater rates of heat energy transfer, and therefore faster heating rates, than air furnaces[108]. These include molten metal, fluidised bed, and salt bath furnaces, with Figure 6.1 comparing the heating rates for the different media. The use of a molten metal such as lead was quickly rejected due to the safety implications, while a fluidised bed furnace was not considered due to the apparent complexity of construction. The heat treatment of test specimens in the holes of a metallic block[35] was considered briefly, but not undertaken.

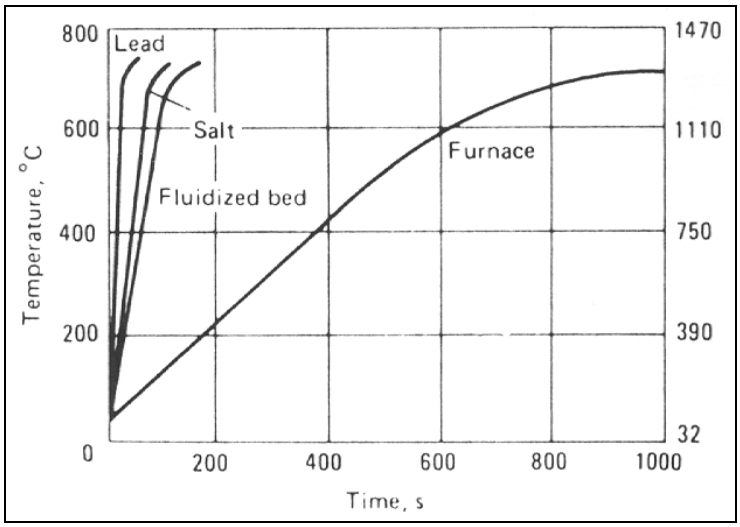

Figure 6.1 Comparison of heating rates for 16mm diameter steel bars in lead, salt bath, fluidised bed, and conventional air furnaces (from Ref. 147).

Consequently, a salt bath furnace was constructed for the short duration austenitisation heat treatments. An initial attempt was made with an existing air furnace into which a salt pot was inserted. However, large temperature gradients throughout the salt pot, and the regular burnout of the furnace heating element caused this option to be abandoned. It did however yield an approximate heating time of 30s to within 5°C of 800°C. This resulted in the design and development of a dedicated salt bath furnace with the following performance criteria:

- An inert molten salt environment for heat treatments at 650 to 1,000°C;
- Accurate temperature control;
- A method of melting the salt;
- Heating sources that will not be destroyed by the molten salt;

- A sufficient volume of salt to limit the drop in the salt temperature to less than 5°C upon insertion of the test specimens.

Considerable difficulty was encountered in constructing the salt bath due to the propensity of molten salt to short out heating elements. Various contact heating arrangements were tried, but all failed after the salt had been molten for a short period of time. The molten salt appeared to creep up and over the walls of the steel salt container, and eventually come into contact with the heating elements, with rapid corrosion and subsequent premature failure of the elements. However, success was obtained utilising radiative heating elements, as detailed in Section 6.2.2.

6.2.2 Salt bath layout

There are two possible salt bath layouts, which comprise either an externally heated furnace, or an immersed electrode furnace. Externally heated furnaces have a heat source external to the salt pot, while electrodes are immersed in the salt for the immersed electrode furnace. Externally heated furnaces are easily restartable, while immersed electrode furnaces are not recommended for intermittent operation due to the requirement of an external heat source to melt the salt before the electrodes can be utilised. However, an externally heated salt bath is less adaptable to close and uniform temperature control than an immersed electrode furnace due to the dissipation of heat by convection, which creates temperature gradients within the salt. Furthermore, the temperature lag between the salt thermocouple and the recovery time of the furnace may result in over- and under-shooting of the desired temperature by 14°C[147].

In immersed electrode furnaces the molten salt is heated by the passage of alternating current through the electrodes. A heating effect is generated by the resistance buildup to the passage of current through the salt. The heat is quickly dissipated by a downward stirring action created by the current between the electrodes, allowing temperature control to within 3°C throughout the salt pot. As the heat is generated within the salt, overshooting is easily avoided.

The dual requirements of accurate temperature control with uniform temperature throughout the salt pot, and easy startup for intermittent operation resulted in the design of a combined externally heated/immersed electrode furnace. A salt comprising 55% barium chloride, 25%

sodium chloride and 20% potassium chloride yielded an approximate melting temperature of 600°C, and the desired operating range of 650 to 1,000°C[1]. The addition of 2.5% boric acid rectified the salt by reacting with the oxides and oxychlorides that formed. This yielded a sludge that was periodically removed. Design of the furnace required a size sufficient to limit the temperature drop to 5°C upon addition of the test specimens. This yielded a minimum pot volume of 1,250cm^3, as calculated in Appendix A.

The maximum salt pot size was limited by the power availability of the heat sources. Earlier attempts to modify an existing furnace for the salt bath heat treatments demonstrated that a 1kW heat input was sufficient to yield molten salt at 800°C. A single phase external heating source can provide a maximum of 2.3kW, with a further 1kW from the immersed electrodes connected to a 1kW single phase transformer. Given a similar insulation layout to that of the air furnace, a salt pot of approximately 4,000cm^3 could be heated to the required temperature with the heat sources available. However, a rectangular salt pot with the internal dimensions of 148 by 68 by 160mm depth was fabricated from 6mm mild steel plate, giving a volume of 1,600cm^3.

Figures 6.2 and 6.3 illustrate the salt bath layout. Four Globar Type SGR Silicon Carbide Electric Heating Elements were wired, single phase, in series with the recommended element layout around the salt pot[148]. The use of radiative heating elements meant that the molten salt overflow could not come into contact with the elements, thus preventing premature failure of the elements. The element size was chosen to yield 2.3kW without overloading the elements, as detailed in Appendix B. Stainless steel reflectors allowed the heat energy transfer from the heating elements to the salt pot to be maximised.

An additional direct heat input into the salt of up to 1kW was provided by two mild steel electrodes wired to a 1kW single phase transformer which converted the line voltage to 5V AC. The recommended sloped back wall salt pot arrangement[147] was modified to give a rectangular salt pot with the electrodes sloping inwards from the top to the bottom of the salt pot. This resulted in a bottom heating effect in the salt pot, with better circulation and uniform temperature of the molten salt. The 14mm square cold leg of the electrodes are connected to the transformer by 200A arc welding cable, while 8mm^2 mild steel lengths were used for the hot leg of the electrodes. The element and electrode layout around the salt pot is illustrated in

Figure 6.2 Layout of salt bath furnace.

Figure 6.3 Salt bath element and electrode layout.

Figure 6.3. The salt pot, heating elements, and electrodes are supported and insulated within a mild steel container fabricated from 6mm plate by a combination of 12 to 25mm thick KAO and Hotboard insulation boards.

6.2.3 Salt bath furnace control

The controller illustrated in Figure 6.4, and the control equipment of Figure 6.5, controls the salt bath temperature. The transformer and controllers are contained inside a housing fabricated from 1.2mm thick sheet aluminium. The salt was melted by the silicon carbide heating elements which are controlled by a Watlow Series 935 Temperature Controller connected to a chromel/alumel thermocouple welded to the outside of the salt pot. The salt pot temperature was monitored with a second chromel/alumel thermocouple welded to the outside of the salt pot, which is connected to a 306 Digital Thermometer.

The power input to the heating elements was controlled by a custom built power controller, and monitored by a Yew Model 2433 Clip-On AC Power Meter. The salt temperature was measured by an immersed calibrated chromel/alumel thermocouple probe, which is connected to a calibrated Comark 5000 Digital Thermometer. The immersed electrodes are brought into operation once the salt began to melt. The power input into the salt, which was dependent on the molten salt volume, was controlled by a 0 to 260V variac. The power input from the electrodes is also monitored by the Yew power meter. The electrodes were controlled by a RKC Series RE-48 Temperature Controller connected to the calibrated thermocouple probe. Once the salt was molten, the four elements were controlled by the Watlow controller to give a salt pot wall temperature equal to the desired salt temperature. Temperature gradients of less than 5°C in the molten salt were verified for all the heat treatment temperatures, with the salt temperature corresponding to that displayed on the Comark Digital Thermometer.

6.3 Austenitisation heat treatment rig

The austenitisation heat treatment rig of Figure 6.6 was developed for test durations of 15min and longer, and is based around a Nabertherm R7019 Tube Furnace with a 125mm hot zone and a 70mm internal diameter ceramic tube liner. A 61mm internal diameter grade 316L stainless steel tube is contained inside the ceramic tube, with mild steel end caps connecting

the tube inlet and outlet to the plumbing. The plumbing system comprised ¼ inch outside diameter brass and stainless steel tubing, in conjunction with a variety of swagelok fittings.

The argon gas flow path for the austenitisation heat treatments is illustrated schematically in Figure 6.11. Industrial grade argon* passes through Labclear and Oxyclear gas filters to reduce the water and oxygen impurities to less than 50vppb. Once the ambient atmosphere was flushed with argon, heat treatments of 192hr were undertaken with minimal decarburisation.

6.4 Decarburisation heat treatment rig

6.4.1 Design philosophy

Preliminary decarburisation experimentation was undertaken with the existing experimental apparatus at the start of this project[150], which involved bubbling hydrogen through water in two glass conical flasks into the Nabertherm tube furnace via nylon tubing. However, it soon became apparent that this apparatus gave a limited range of, and control over, such experimental parameters as the hydrogen gas flow rates and p_{H_2O} / p_{H_2} ratios.

Of the three common decarburisation atmospheres, namely hydrogen/methane, carbon monoxide/carbon dioxide, and water/hydrogen, atmospheres comprising water and hydrogen were utilised. This atmosphere is commonly used for commercial decarburisation heat treatments of electrical steels, invariably yielding decarburisation rates considerably in excess of those generated by the other two atmospheres. Consequently, a new decarburisation test rig was designed and developed to achieve the following performance criteria:

- Accurate temperature control over the hot zone;
- Provision of an inert argon annealing atmosphere;
- Water/hydrogen gas atmospheres with a range of hydrogen flow rates and p_{H_2O} / p_{H_2} ratios;
- Dilution of water/hydrogen atmospheres with argon to increase the p_{H_2O} / p_{H_2} ratios;

* 99.99% argon with less than 30vppm water and 10vppm oxygen. The nominal composition is given in Appendix D[149].

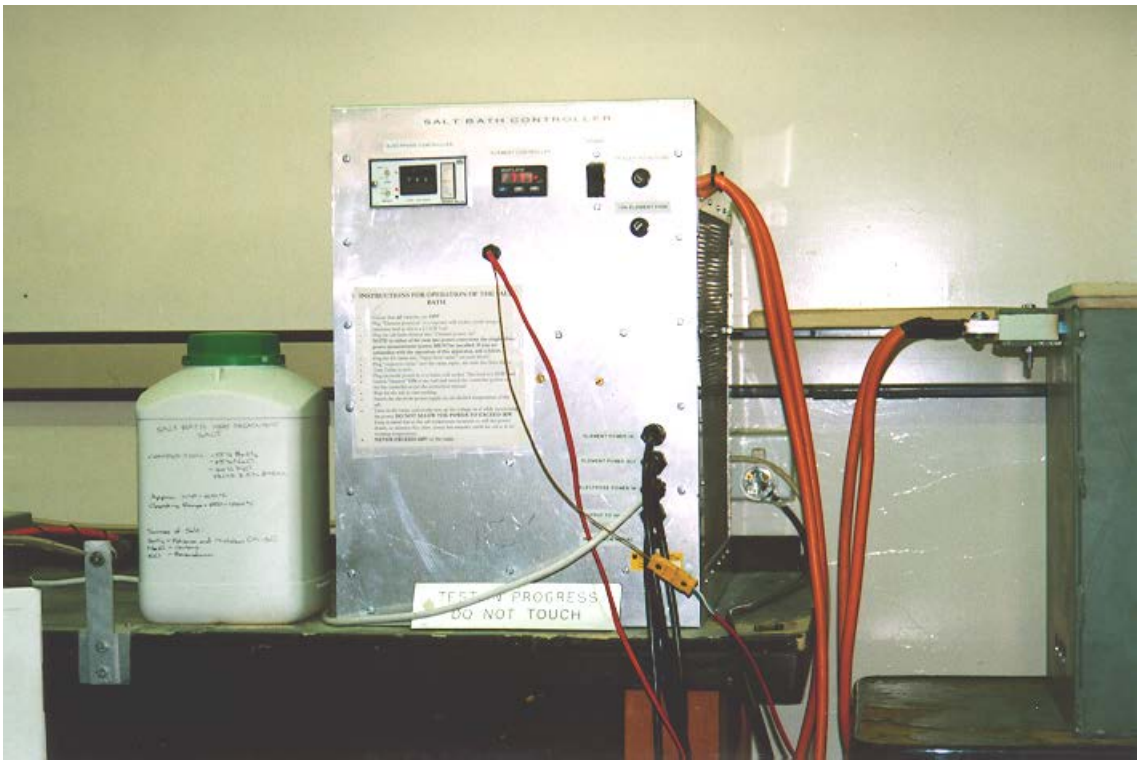

Figure 6.4 Salt bath controller.

Figure 6.5 Salt bath control equipment.

- The ability to insert test specimens into the hot zone once the required furnace atmosphere is attained;
- Continuous monitoring of the exhaust gases to determine the decarburisation kinetics;
- Monitoring of the pressure inside the tube furnace.

6.4.2 Test rig layout

The decarburisation test rig is based around the Nabertherm tube furnace illustrated in Figure 6.6. The increasing saturation water vapour pressures with temperature allow the generation of water/hydrogen decarburisation atmospheres comprising different water contents. Either industrial or zero grade hydrogen* was bubbled through the first water container maintained at the temperature where saturation of the hydrogen gas flow with water yields the water partial pressure necessary for the desired p_{H_2O} / p_{H_2} ratio. This hydrogen/water flow was then bubbled into the second water container, which was maintained at the temperature of the first water container to ensure saturation of the hydrogen gas flow with water. The hydrogen flow through the two water baths is illustrated schematically in Figure 6.7, with the relationship between the water temperature and p_{H_2O} / p_{H_2} ratio detailed in Appendix D.

Figure 6.8 illustrates the water baths used to saturate hydrogen with water vapour in the two water containers. The pressure regulated hydrogen flows through a M Series Nupro Vernier Valve, a 0 to 2,000cm^3/min Platon Hydrogen Gap Meter, a 100 by 360 by 60mm hydrogen/argon mixing chamber fabricated from 6mm aluminium plate, and into the first water container. This water container comprises a 215 by 140 by 80mm deep aluminium box containing approximately 1,000cm^3 of water. Each water container is enclosed in a 420 by 320 by 210mm high 21 litre polypropylene box filled with water, which acts as a water bath. The water bath was maintained at the desired water temperature by an electric heating element immersed in the water, and controlled by a 0 to 260V variac. Perspex covers reduced the heat losses from the two water baths.

* Nominal compositions given in Appendix D[149].

A combination of one-quarter inch outside diameter brass, stainless steel and copper plumbing was used for the test rig, in conjunction with swagelok fittings. Condensation in the plumbing between the two water baths was prevented by a silicon heating wire connected to a 0 to 260V variac insulated around the plumbing, which maintained the plumbing wall temperature at approximately 5°C higher than that of the two water baths. The water/hydrogen atmosphere from the first water container was bubbled into the second water container, with the water bath maintained at the desired temperature by a 450W Thermomix 1419 Stirrer yielding temperatures of 20 to 70°C. This gave a p_{H_2O} / p_{H_2} range of 0.024 to 0.44 for a water/hydrogen flow.

A lower p_{H_2O} / p_{H_2} ratio of 0.01 was attained by the addition of ice to the water baths to give a water temperature of 6°C. Higher p_{H_2O} / p_{H_2} ratios were achieved with the addition of an argon flow due to the decarburisation environment inside the furnace remaining at atmospheric pressure, while the water partial pressure is fixed by the water container temperature. Consequently, an increase in the argon partial pressure results in a lower hydrogen partial pressure, and therefore a higher p_{H_2O} / p_{H_2} ratio. A direct hydrogen path into the tube furnace also permits heat treatments in a dry hydrogen atmosphere.

The maximum gas flow rates are determined by the amount of gas that can be saturated in the two water containers, with a value of 3,000cm^3/min calculated for a water temperature of 70°C, Appendix D. The volume of water in the second water container has to be sufficient to allow the generation of a water/hydrogen atmosphere throughout the longest test at the highest water contents and gas flow rates. For a 24hr test with a 2,000cm^3/min hydrogen gas flow rate at a water temperature of 60°C, 527mL of water is transported, Appendix F. This corresponds to about half the volume contained in the second water container.

Condensation in the plumbing from the second water bath to the tube furnace was prevented by a silicon heating wire connected to a 0 to 260V variac insulating the plumbing, with the wall temperature maintained at approximately 5°C higher than that of the water baths. The temperatures at various positions in the water baths and associated plumbing were monitored by chromel/alumel thermocouples connected to a five point RKC Series RE-48 digital readout. The plumbing connects a 61mm internal diameter 316L stainless steel tube,

Figure 6.6 Austenitisation/decarburisation test rig.

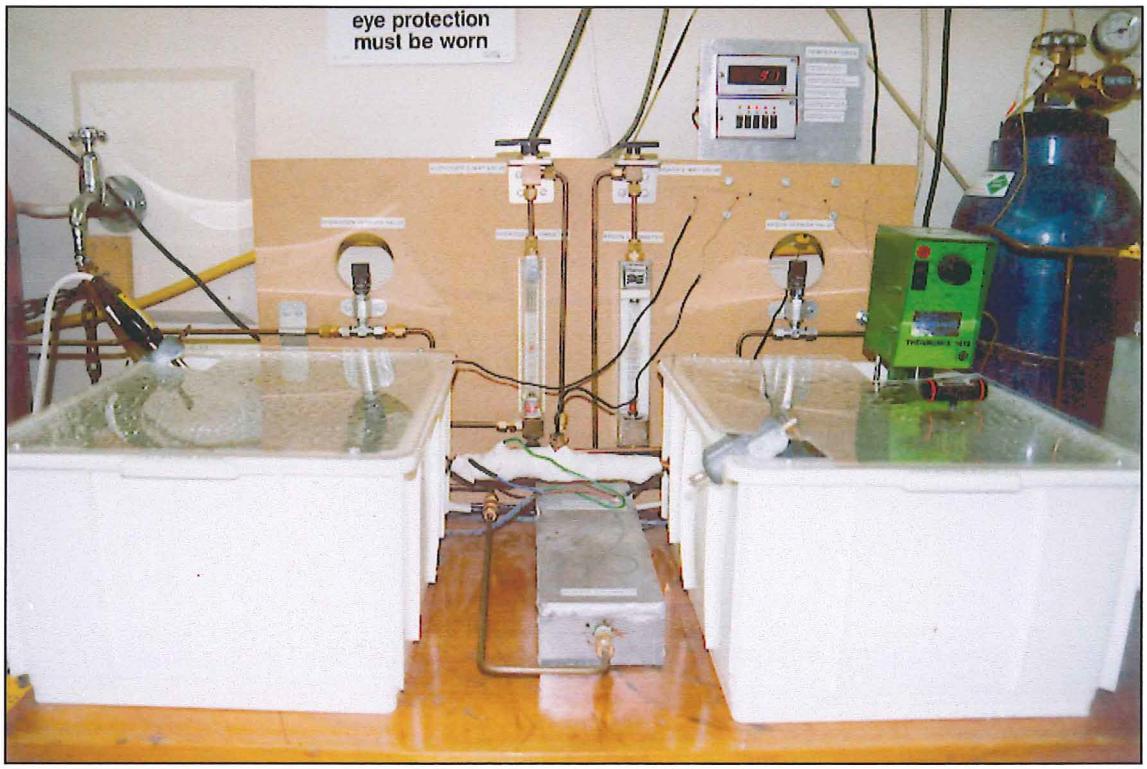

Figure 6.8 The water baths used to saturate hydrogen with water.

contained within a 70mm internal diameter ceramic lining tube, via a mild steel end cap. The test specimens were inserted and removed by disconnecting the quick connect joint separating the plumbing between the second water bath and the end cap, and unscrewing the end cap.

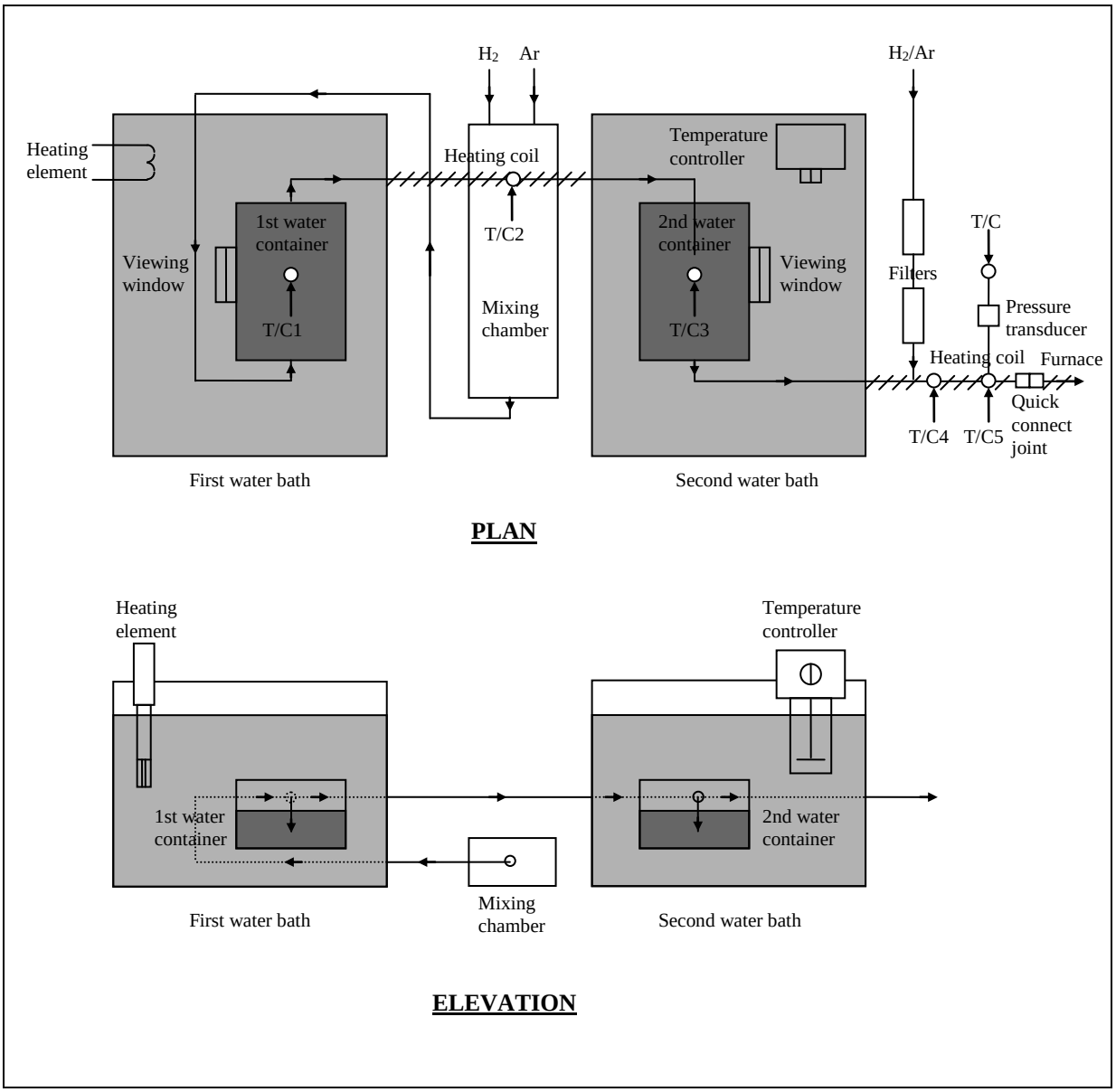

Figure 6.7 Schematic illustration of the generation of a water/hydrogen decarburisation atmosphere.

Hydrogen was either bubbled through the water baths, or flowed directly into the furnace through the Labclear and Oxyclear gas purifiers to give a purified hydrogen atmosphere. Argon was supplied from a 0 to 15L/min Cigweld rotameter directly into the tube furnace, or into the water baths via a M Series Nupro Vernier Valve. Alternative hydrogen and argon gas

flow routes were provided by a combination of two- and three-way valves. The furnace gas atmosphere exhausted from the tube furnace by one of two routes.

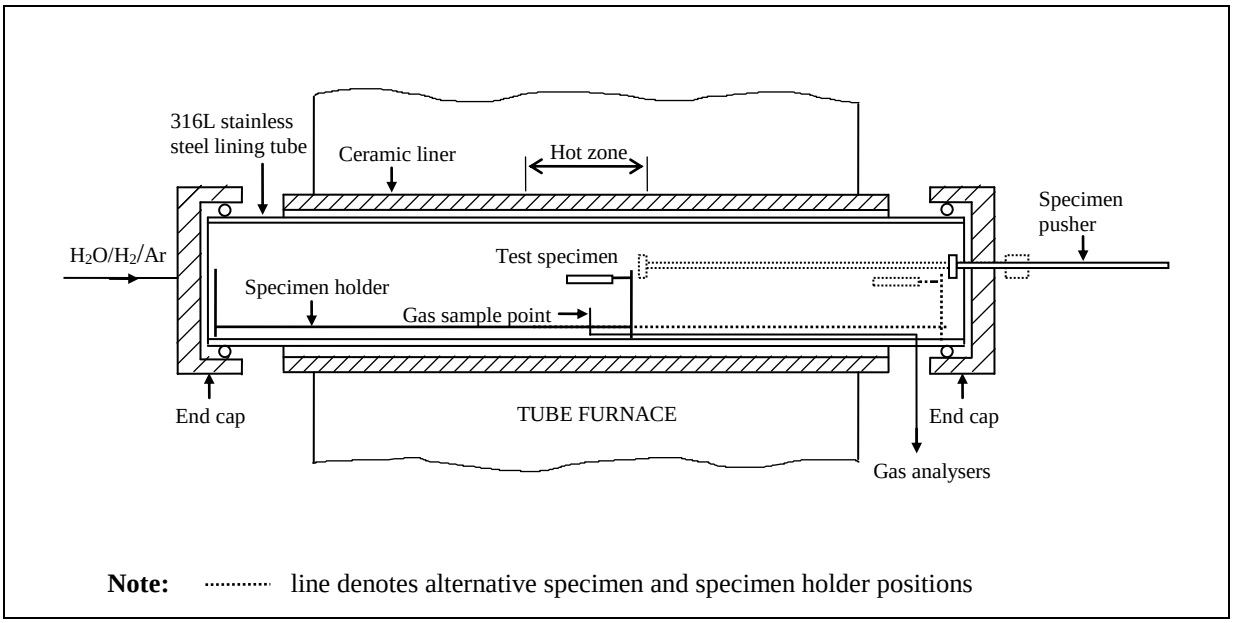

Figure 6.9 Schematic illustration of the tube furnace hot zone arrangement.

The first flow route was through the right hand mild steel end cap connecting the tube furnace to the plumbing, where the gas was bubbled into two glass cylindrical flasks, and the hydrogen combusted at the end of the plumbing by a custom built ignition coil spark igniter. The alternative gas path, for sampling of the exhaust gases in the hot zone, involved a 6mm outside diameter stainless steel tube located in the hot zone. This is illustrated schematically in Figure 6.9. The gas passed through a tapping point for discrete gas sampling, a Norgren water trap, and a 7 micron Nupro filter.

Previous research into the decarburisation of electrical steels with water/hydrogen environments has established that the main gas forming during carbon removal is carbon monoxide. Carbon dioxide and methane, although usually present in lower concentrations, are also commonly monitored. In order to determine the presence of these gases, and to establish their respective concentrations, the gas passed successively through a Beckman Model 864 Non-Dispersive Infrared Carbon Monoxide Analyser, a Carbon Dioxide Horiba Model PIR-2000 General Purpose Infrared Gas Analyser, and a Methane Horiba Model PIR-2000 General Purpose Infrared Gas Analyser. The decarburisation gas then flowed from the methane gas analyser into the water traps. The layout of the exhaust gas analysers is illustrated in Figure

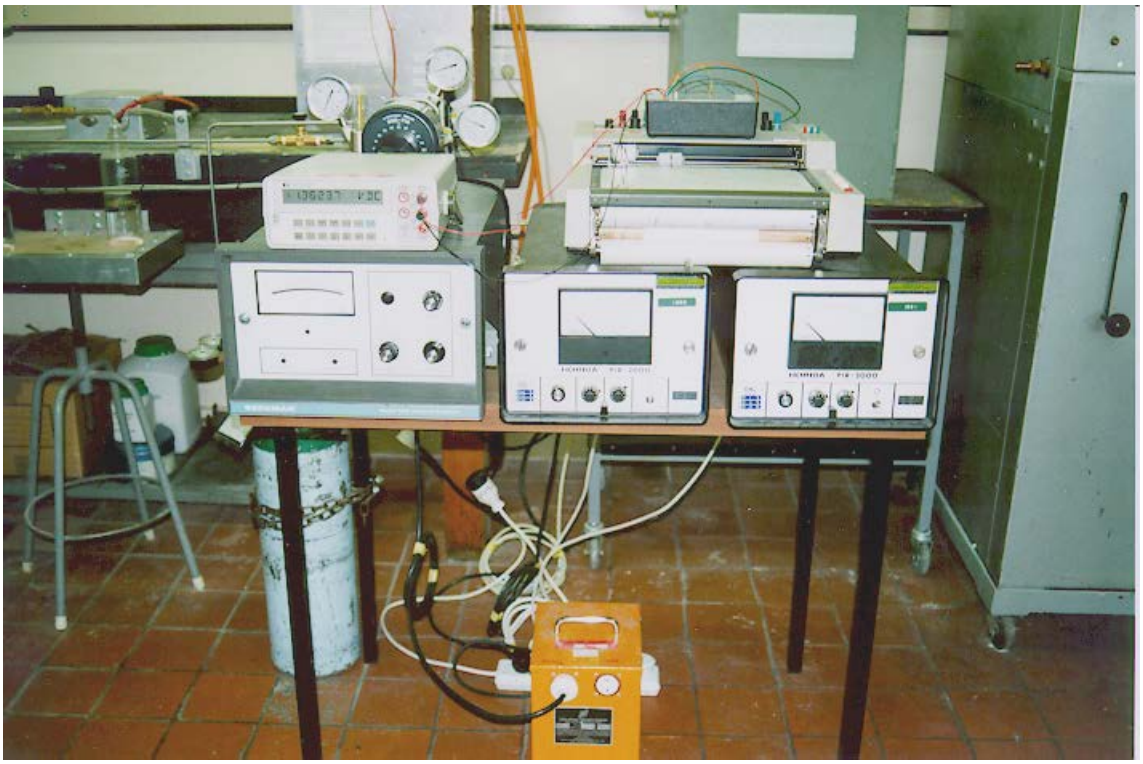

Figure 6.10 Exhaust gas analysis apparatus.

6.10. The output of the analysers was monitored by a Sekonic SS-250F three pen chart recorder.

Zero grade hydrogen with greater than 99.995 vol.% hydrogen, and less than 5vppm water, 5vppm oxygen, 0.5vppm carbon monoxide, and 1vppm carbon dioxide, Appendix C, was used for the decarburisation experiments involving monitoring of the exhaust gas. Zero grade hydrogen was necessary since the maximum specified carbon monoxide and carbon dioxide contents of industrial grade hydrogen, 5vppm and 100vppm respectively, would have had too large an effect on the carbon monoxide and carbon dioxide concentrations measured by the respective gas analysers.

The test specimens were inserted into the hot zone by the pusher rod arrangement of the right hand end cap, Figure 6.9. The inlet and exit tube furnace pressures were measured by MPX200AP Motorola pressure transducers enclosed in insulating plastic containers. The pressure transducer temperatures were measured by chromel/alumel thermocouples connected to a 306 Digital Thermometer, with the pressure measured in mV on a 3468A Hewlett Packard digital multimeter. The schematic layout of the decarburisation test rig is shown in Figure 6.11.

This chapter detailed the experimental apparatus developed for the heat treatments undertaken in this project. Chapter 7 subsequently describes the experimental techniques used in this project.

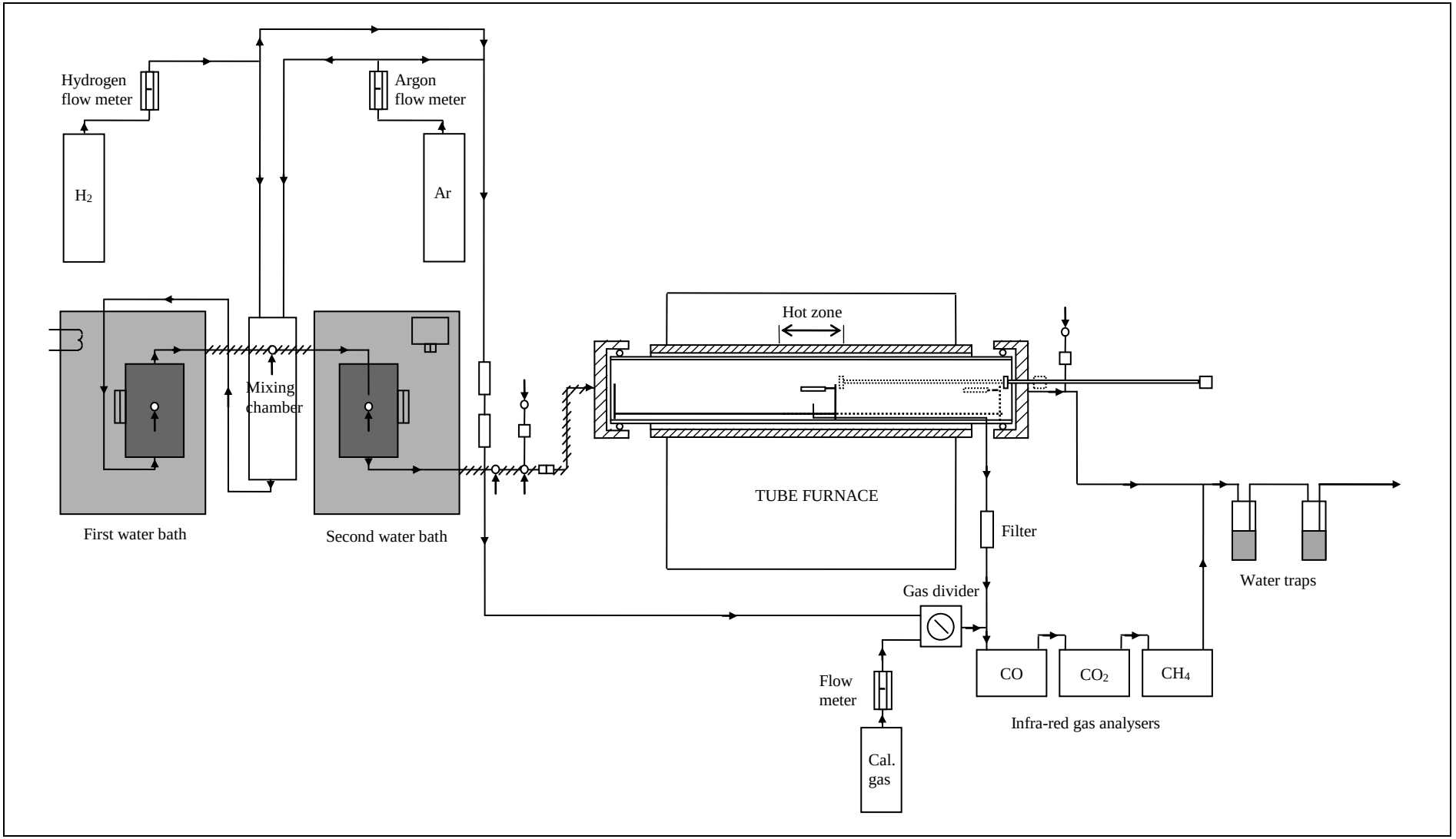

Figure 6.11 Schematic layout of the austenitisation/decarburisation test rig.

CHAPTER 7

EXPERIMENTAL TECHNIQUES

7.1 Introduction

Various experimental techniques were developed and used in this research. Specific methodologies were required for the production of the experimental steels, preparation of the test specimens for the austenitisation and decarburisation heat treatments, and the heat treatments themselves. Further methods involving the preparation of the heat treated test specimens for image analysis, decarburisation and oxidation layer thickness measurements, quantitative electron microscopy, and microhardness measurements were necessary. This chapter describes the experimental techniques utilised in this project.

7.2 Production of the experimental steels

The production of three steels with the desired alloy contents, Table 7.1, was undertaken with a Pantech 15kg 40kW Induction Hoist Tilting Furnace. The alloy additions required to achieve the desired steel compositions were calculated, as detailed in Appendix G. These alloy additions are listed in Table 7.2.

Table 7.1 Target experimental steel compositions.

DESCRIPTION	C (wt.%)	Si (wt.%)	Mn (wt.%)	Cr (wt.%)
0% SILICON	0.6	0.0	0.8	0.2
1% SILICON	0.6	1.0	0.8	0.2
3% SILICON	0.6	3.0	0.8	0.2

Prior to heating the induction furnace to temperature, the graphite addition was placed at the bottom of the furnace steel liner, and the furnace half filled with 100mm lengths of the 25mm diameter reinforcing bar. The furnace power was gradually increased to the operational value of 36kW, with the remainder of the reinforcing bar added as the steel melted. Lime was added

to the furnace, followed by the alloy additions just before pouring, and more lime. At a molten steel temperature of approximately 1,600°C, the slag was scraped off and the steel poured into a mould, yielding 14kg ingots. 14mm diameter bars were forged from the ingots at a temperature of 1,000 and 1,100°C. 20mm long lengths were cut from the ends of each bar and sent to Pacific Steel for spark spectrographic analysis. The presence of manganese segregration patterns inherited from the solidification processes is possible, which would result in banded initial microstructures. Manganese segregration patterns cannot be eliminated, except by long annealing times at high temperatures, namely 24hr at 1,300°C[151]. This was not practical, and so any banded structures were tolerated. The extent of any banding was not assessed quantitatively.

Table 7.2 Alloy additions for the production of the experimental steels.

DESCRIPTION	ADDITION (kg) Reinforcing bar	Graphite	Low C Fe-Cr	Fe-Mn	Fe-Si
0% SILICON	13.5	0.1428	0.0199	0.1264	-
1% SILICON	13.5	0.1449	0.0201	0.1298	0.1769
3% SILICON	13.5	0.1500	0.0207	0.1023	0.5044

7.3 Preparation of test specimens

The test specimens produced for the austenitisation and decarburisation heat treatments are illustrated in Figure 7.1. Heat treatments were initially carried out on 12mm diameter by 10mm test specimens, which were produced from 14mm diameter by 100mm lengths of bar stock held 12 hours at 900°C, and then either air cooled, or quenched. These specimens were used to determine the Ac_1 and Ac_3 temperatures of the steels. The Ac_1 and Ac_3 temperatures were estimated from the theoretical equations of Andrews[102], reproduced as equations (7.1) and (7.2). The theoretically determined Ac_1 and Ac_3 transformation temperatures are given in Table 7.3.

$$Ac_1 = 723 - 10.7Mn - 16.9Ni + 29.1Si + 16.9Cr + 290As + 6.38W, \qquad (7.1)$$

where the compositional limits for the application of this equation are:

Table 7.3 Theoretical Ac_1 and Ac_3 transformation temperatures calculated from the formulae of Andrews[102] for the steels investigated.

	Composition (wt.%)														
DESCRIPTION	**C**	**Si**	**Mn**	**Cr**	**V**	**Nb**	**Al**	**Cu**	**N**	**P**	**S**	**Mo**	**Sn**	**Ac_1 (°C)**	**Ac_3 (°C)**
0% SILICON	0.62	0.06	0.94	0.23	0.003	-	0.001	0.22	0.0105	0.031	0.034	0.013	0.026	717	739
1% SILICON	0.61	1.24	1.09	0.21	0.005	-	0.015	0.22	0.0091	0.022	0.021	0.008	0.018	749	788
SUP7	0.60	1.94	0.77	0.19	0.005	-	0.033	0.01	-	0.017	0.008	0.001	0.002	774**	844**
SUP7NV	0.62	2.11	0.85	0.17	0.173	0.15	0.011	0.11	-	0.018	0.025	0.011	0.009	778	850
3% SILICON	0.58	3.05	0.78	0.18	0.007	-	0.028	0.22	0.014	0.022	0.019	0.011	0.018	805	888

****** The Ac_1 and Ac_3 temperatures for a 9260 steel are 743 and 816°C respectively[152].

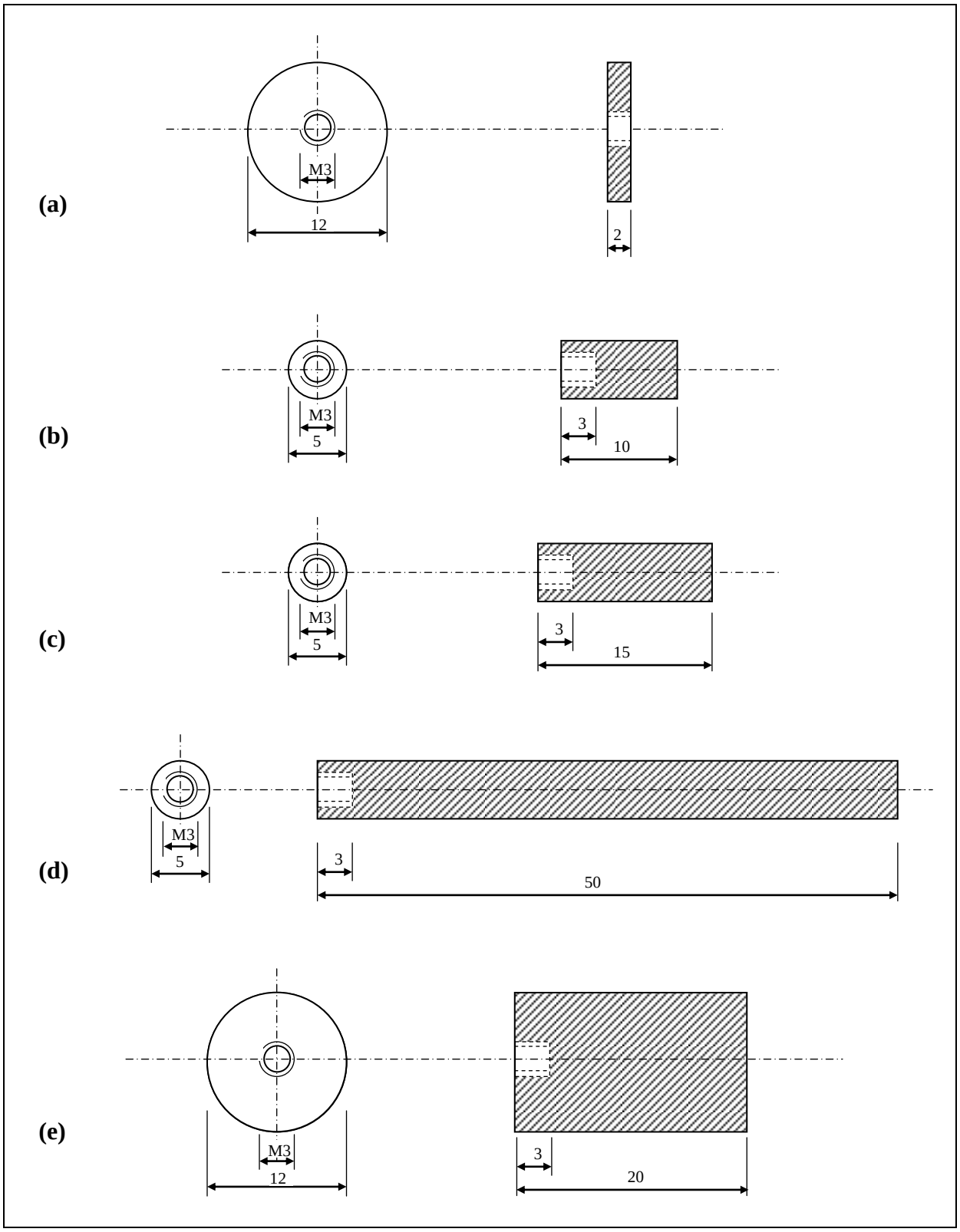

Figure 7.1 Test specimens prepared for (a) salt bath austenitisation heat treatments, (b) tube furnace austenitisation heat treatments, and (c), (d) and (e) decarburisation heat treatments. SCALE: 2:1

C : 0.08 - 1.43wt.%;	Mn : 0.04 - 1.98wt.%;	Ni : 0.00 - 5.00wt.%;
Si : 0.06 - 1.78wt.%;	Cr : 0.00 - 4.48wt.%;	V : 0.00 - 2.51wt.%;
Mo : 0.00 - 2.61wt.%;	As : 0.00 - 0.072wt.%;	W : 0.00 - 4.10wt.%.

$$Ac_3 = 910 - 203\sqrt{C} - 15.2Ni + 44.7Si + 104V + 31.5Mo + 13.1W - 30Mn - 11Cr - 20Cu + 700P + 400Al + 120As + 400Ti, \quad (7.2)$$

where the compositional limits for the application of this equation are:

C : 0.08 - 0.59wt.%;	Mn : 0.04 - 1.98wt.%;	Ni : 0.00 - 5.00wt.%;
Si : 0.09 - 1.78wt.%;	Cr : 0.00 - 4.48wt.%;	V : 0.00 - 0.70wt.%;
Mo : 0.00 - 1.05wt.%;	As : 0.00 - 0.072wt.%;	W : 0.00 - 4.10wt.%.

The theoretical Ac_1 and Ac_3 temperatures calculated from equations 7.1 and 7.2 for the steels investigated are plotted as a function of silicon content in Figure 7.2. This illustrates the increase in the transformation temperatures with increasing silicon content. The experimental determination of the Ac_1 and Ac_3 temperatures is detailed in Section 9.2.1.

Preliminary heat treatments were necessary to produce different initial microstructures. These were prepared by a prior austenitisation of the 14mm diameter by 100mm bar stock lengths for 12 hours at 900°C in the Nabertherm tube furnace. Two different pearlitic structures were obtained by first furnace cooling the bar stock in 20min to 5°C above the experimentally determined Ac_3 temperature. Air cooled pearlitic specimens were then produced by removing the bar stock from the tube furnace and air cooling, while furnace cooled pearlitic specimens were produced by furnace cooling at 25°C/hr to 600°C, and then turning the furnace off and cooling to ambient temperature.

Two different spheroidal cementite structures were produced by quenching the 14mm diameter bar stock from the austenitising temperature into either water or oil at room temperature, then tempering the resultant martensite structures for 12 and 96hr respectively at 10°C below the experimentally determined Ac_1 temperatures. The heat treatments were completed by air cooling. Through various combinations of subcritical and intercritical heat

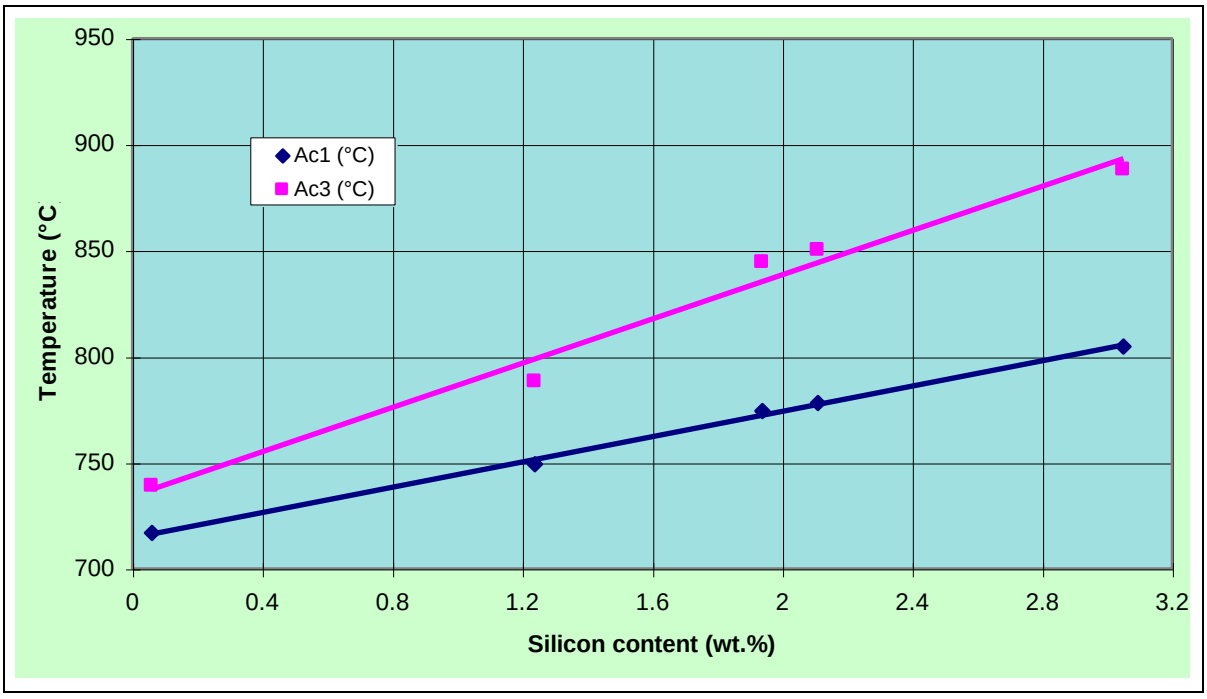

Figure 7.2 Influence of silicon content on the theoretically determined Ac_1 and Ac_3 temperatures for the steels investigated.

treatments, two further spheroidal cementite structures were produced. These heat treatments are summarised in Table 7.4.

A variety of test specimens were machined from the heat treated bar stock, as illustrated in Figure 7.1. 12mm diameter by 2mm salt bath heat treatment specimens, and 5mm diameter by 10mm tube furnace austenitisation specimens were machined to a fine turned finish, while 5mm diameter by 15 and 50mm, and 12mm diameter by 20mm decarburisation specimens were ground to a fine finish.

Table 7.4 Heat treatment regimes for production of the initial microstructures.

DESCRIPTION	HEAT TREATMENT
A) Air cooled	12hr at 900°C, furnace cooled to Ac_3+5°C, air cooled.
B) Furnace cooled	12hr at 900°C, furnace cooled to Ac_3+5°C, furnace cooled at 25°C/hr to 600°C, furnace turned off and cooled to ambient temperature.
C) 12hr tempered martensite	12hr at 900°C, water quenched. Tempered for 12hr at Ac_1-10°C, air cooled.
D) 96hr tempered martensite	12hr at 900°C, water quenched. Tempered for 96hr at Ac_1-10°C, air cooled.
E) Via austenite	12hr at 900°C, water quenched. Reheated for 30min at a 0.45 fractional superheat above the Ac_1 temperature, furnace cooled as rapidly as possible to Ac_1-10°C, held 18hr at Ac_1-10°C, furnace cooled at 10°C/hr for 3hr, air cooled.
F) Intercritical	12hr at 900°C, air cooled. Reheated for 6hr at Ac_1-10°C, held 1hr at a 0.45 fractional superheat above the Ac_1 temperature, furnace cooled as rapidly as possible to Ac_1-5°C, held 18hr at Ac_1-5°C, furnace cooled at 2°C/hr for 20hr, air cooled.

7.4 Salt bath austenitisation heat treatments

Prior to the salt bath heat treatments, the salt bath had to be heated to the operational temperature. This involved setting the furnace temperature to 200°C, with the power input to the elements limited to 2kW by the Yew power controller. The heating rate was controlled by the Auto-Tune function on the Watlow temperature controller. The furnace was allowed to stabilise at this temperature, before the same procedure was repeated for 100°C increments up to 600°C.

The furnace temperature was then set to 650°C, where the salt began to melt. Upon melting, its volume decreased and further salt was added to maintain the salt level. Once the salt had melted, the immersed electrodes were brought into operation, with the electrode power input controlled by the 0 to 260V variac. The molten salt was gradually heated to the desired operational temperature by using the maximum electrode and element power inputs. The specified furnace temperature was obtained by setting the two temperature controllers at the appropriate values to give the desired temperature, as displayed on the Comark Digital Thermometer. The furnace was then allowed to stabilise at the selected temperature. The times for the test specimens to heat to within 5°C of the furnace temperature once inserted into the molten salt were determined by a chromel/alumel thermocouple welded to the end of the specimen, which was connected to the 306 Digital Thermometer. This yielded heating times of approximately 20 ± 5s, with the heat treatments accurate to ± 5C.

The test specimens were screwed onto a 3mm diameter 316 stainless steel threaded rod and inserted into the molten salt at the operating temperature for the required test duration, plus the heating time to within 5°C of the operating temperature. For heat treatments involving the same test with different initial microstructures, the different specimens were heat treated simultaneously by screwing the specimens onto the same threaded rod. Following each heat treatment, the specimens were quenched into water at room temperature, rinsed in ethanol, and dried under a hot air stream. The specimens were then tempered for 1hr at 250°C in a Gallenkamp CR25 electric air furnace to improve the contrast between the martensite and the matrix for subsequent image analysis[36].

7.5 Tube furnace austenitisation heat treatments

Prior to undertaking austenitisation heat treatments, the Nabertherm tube furnace was heated to the desired temperature and allowed to stabilise over a period of a day. The hot zone temperature was calibrated prior to testing with a calibrated platinum/rhodium thermocouple connected to a RKC DP-200 Digital Readout. This gave hot zone temperatures accurate to within ± 5°C. The heating times to within 5°C of the tube furnace temperature, maintained at the respective Ac_3 temperatures for the different steels, were determined with a chromel/alumel thermocouple welded to the ends of the test specimens. These specimens were repolished following welding of the thermocouple to give as close a finish as possible to the

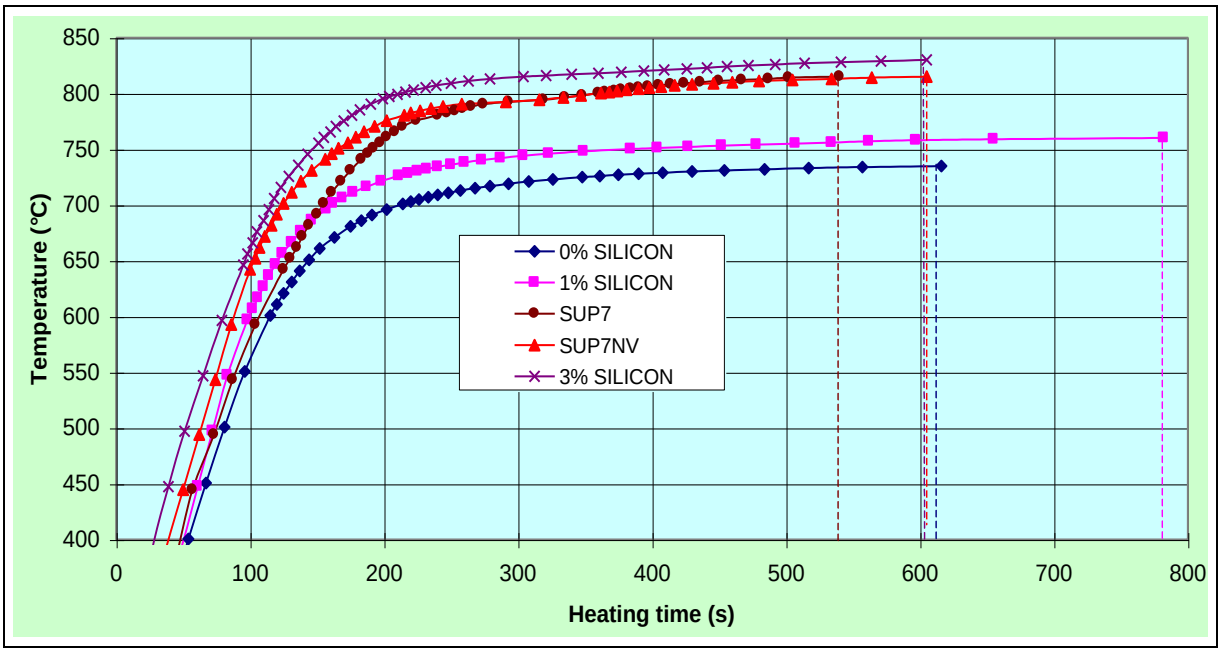

Figure 7.3 Heating profiles for 5mm diameter by 50mm test specimens inserted into the tube furnace hot zone at the respective Ac_3 temperatures for furnace cooled initial structures of the different steels.

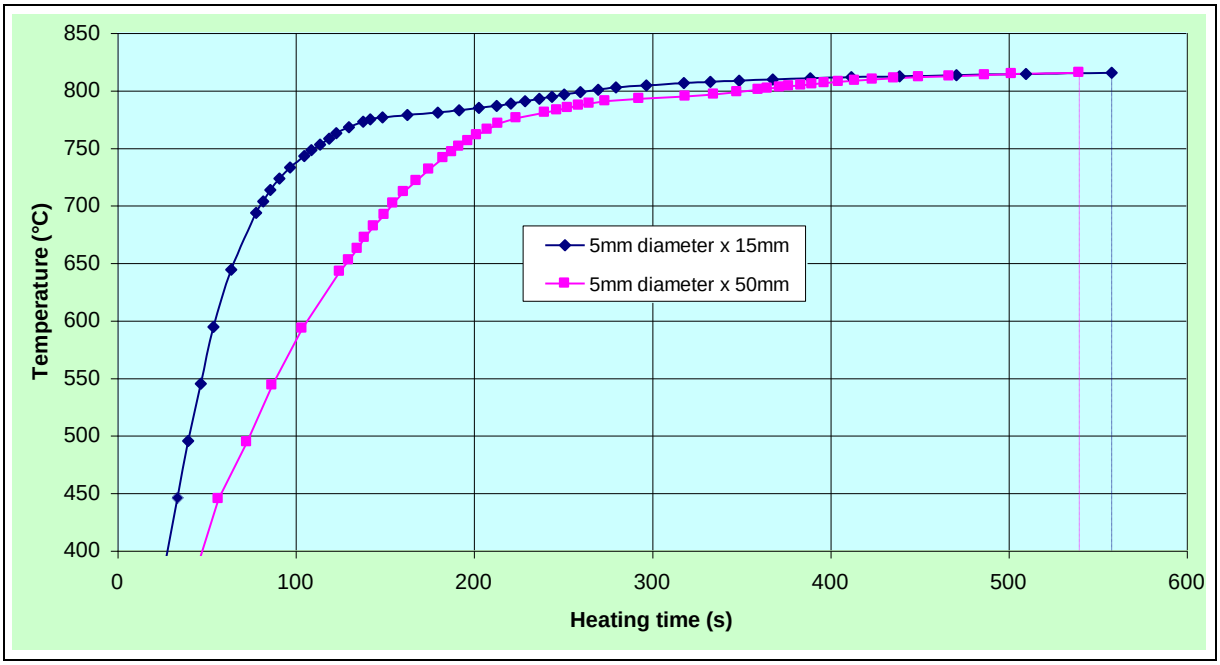

Figure 7.4 Heating profiles for 5mm diameter by 15 and 50mm SUP7 furnace cooled initial specimens inserted into the tube furnace hot zone at 820°C.

original ground surface finish. These heating times are given in Table 7.5. Figure 7.3 illustrates the heating profiles for 5mm diameter by 50mm test specimens of the various steels at the respective Ac_3 temperatures. Figure 7.4 illustrates that the heating profiles for the SUP7 15 and 50mm length test specimens were similar from 800°C upwards. Therefore, the heating times are also applicable for the 5mm diameter by 10mm austenitisation test specimens. It was assumed that the heating times for each steel to their respective Ac_3 temperatures, as listed in Table 7.5, applied to the other austenitisation temperatures used for the steels.

Table 7.5 Heating times to within 5°C of the tube furnace temperature maintained at the respective Ac_3 temperatures for furnace cooled initial structures of the different steels.

DESCRIPTION	Heating time (s)
0% SILICON	616
1% SILICON	782
SUP7	540
SUP7NV	605
3% SILICON	605

The austenitisation heat treatment procedure involved:

- Rinsing the test specimens in acetone, then ethanol, and drying under a hot air stream;
- A 5min flush of the tube furnace with a 2.5L/min inert argon flow;
- Removal of the left hand end cap and insertion of the test specimens into the hot zone. The test specimens were strapped with 0.4mm diameter stainless steel wire into a mesh stainless steel basket;
- Reconnection of the end cap, followed by a 10min argon flush at 2.5L/min;
- Reduction of the argon flow rate to a displacement flow for the remainder of the heat treatment;
- Removal of the left hand end cap;
- Removal of the test specimens, followed by quenching into water maintained at room temperature;
- Tempering of the specimens for 1hr at 250°C in the Gallenkamp furnace.

An inert gas flush of five volumes of the tube furnace is recommended for the replacement of the ambient atmosphere with the inert atmosphere[152]. This corresponds to an argon flush of 8min 30s at 2.5L/min for the stainless steel tube used. For heat treatments involving the same test with specimens having different initial microstructures, the specimens were heat treated simultaneously by inserting the test specimens on the basket together.

7.6 Decarburisation heat treatments

7.6.1 Heat treatments

The tube furnace was slowly heated to temperature and calibrated with the platinum/rhodium thermocouple. The experimental procedure prior to testing involved:

- Filling the first and second water containers to the appropriate water levels;
- Heating the first water bath to the selected temperature by selecting the variac setting for the immersed heating element;
- Heating the second water bath to temperature by selecting the temperature setting on the Thermomix 1419 Stirrer;
- Selecting the variac settings to yield the wall temperatures for the plumbing insulated with silicon heating wire;
- A 5min argon flush at 1,000cm^3/min through the whole system to ensure an inert ambient atmosphere;
- A 5min hydrogen flush at 1,000cm^3/min through the whole system to establish a water/hydrogen atmosphere in the system;
- A 5min argon flush at 2,500cm^3/min through the tube furnace only.

The remainder of the experimental sequence was dependent on which type of decarburisation experiment was undertaken. The two options were:

a) Heating and austenitisation of the test specimens in an inert argon atmosphere prior to the introduction of the decarburisation atmosphere;
b) Introduction of the test specimens into the hot zone once the decarburisation atmosphere was established.

Some of the SUP7 decarburisation experimentation involved heating and austenitising the test specimens in an inert argon atmosphere prior to the introduction of the decarburising atmosphere. This involved either inserting the specimens into the hot zone and flushing with argon, or flushing with argon and then inserting the specimens into the hot zone.

i) Inserting the specimens into the hot zone prior to the argon flush

The experimental sequence for these heat treatments involved:

- Ultrasonic cleaning of the specimens in a Cole-Parmer 8853 12L Ultrasonic Cleaner in acetone, then ethanol, before drying in a hot stream of air. The specimens were mounted in the 316 stainless steel specimen holder, as illustrated in Figure 7.5;
- Removal of the left hand end cap and insertion of the specimen holder into the tube furnace, with the test specimens located in the hot zone;
- Replacement of the left hand end cap followed by the introduction of a 2,500cm^3/min argon flush for 10min, with the argon exhausting the right hand end cap by flowing directly into the water traps.

ii) Flushing with argon prior to inserting the specimens into the hot zone

The experimental sequence for these heat treatments involved:

- Ultrasonic cleaning of the specimens in a Cole-Parmer 8853 12L Ultrasonic Cleaner in acetone, then ethanol, before drying in a hot stream of air. The specimens were mounted in the 316 stainless steel specimen holder of Figure 7.5;
- Removal of the right hand end cap and insertion of the specimen holder into the tube furnace, with the test specimens located in the cold end of the tube;
- Replacement of the right hand end cap followed by the introduction of a 2,500cm^3/min argon flush for 10min, with the argon exhausting the right hand end cap by flowing directly into the water traps;
- Insertion of the specimens into the hot zone using the pusher rod arrangement with continuation of the argon flush for another 5min.

Both methods then followed the remaining procedure, which involved:

- Reduction of the argon flow rate to a displacement flow until the desired austenitisation time elapsed;
- Introduction of the decarburisation atmosphere, either hydrogen, water/hydrogen or water/hydrogen/argon, into the furnace at a flow rate of 500cm^3/min;
- An argon flush of the tube furnace at 500cm^3/min for 5min to conclude the testing;
- Removal of the left hand end cap and quenching of the test specimens into water at room temperature.

The remainder of the decarburisation experimentation involved introduction of the test specimens into the hot zone once the decarburisation atmosphere was firmly established. Consequently, the test specimens were exposed to the decarburisation atmosphere as they heated to the furnace temperature. This testing sequence involved:

- Ultrasonic cleaning of the specimens in a Cole-Parmer 8853 12L Ultrasonic Cleaner in acetone, then ethanol, before drying in a hot stream of air. The specimens were mounted in the 316 stainless steel specimen holder of Figure 7.5;
- Removal of the right hand end cap and insertion of the specimen holder into the tube furnace, with the test specimens located in the cold end of the tube;
- Replacement of the right hand end cap followed by the introduction of a 2,500cm^3/min argon flush for 10min, with the argon exhausting the right hand end cap by flowing directly into the water traps;
- A 10min hydrogen flush of 2,000cm^3/min through the whole system with the gas flow exiting the tube furnace directly into the water traps;
- The hydrogen flush reduced to 500cm^3/min with the appropriate two- and three-way valves switched to allow the gas exiting the tube furnace to flow through the gas analysers;
- Stabilisation of the system at the hydrogen flow rate of 500cm^3/min;
- Introduction of the test specimens into the hot zone with the pusher rod arrangement;
- An argon flush of the tube furnace at 2,500cm^3/min to remove the decarburisation atmosphere as quickly as possible upon conclusion of testing, with the flow path switched immediately prior to the argon flush to allow the gas flow directly into the water traps;

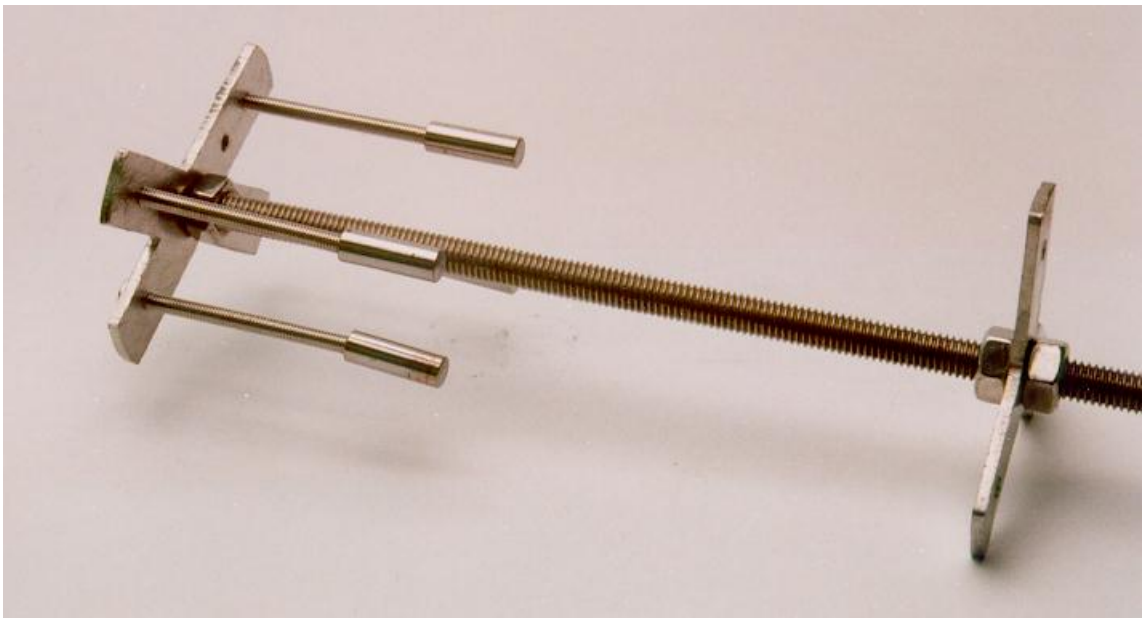

Figure 7.5 Decarburisation test specimen holder with four 5mm diameter by 15mm SUP7 test specimens.

- Removal of the left hand end cap, and quenching of the specimens into a bucket of cold water.

Different initial structures requiring the same decarburisation heat treatment after heating and austenitisation in argon were mounted on the furnace holder and decarburised in the furnace simultaneously. The positioning of the test specimens on the holder, Figure 7.5, allowed a uniform decarburising atmosphere gas flow over the specimens. Each test method requires the appropriate specification of the decarburisation test duration. The definition for the start of the test is taken as when the test specimens were first exposed to the decarburisation atmosphere while positioned in the hot zone. The precise definition of when the tests started for the two methods, these being heating and austenitisation in argon prior to the introduction of the decarburisation atmosphere, and insertion into the established decarburisation atmosphere, are:

a) ***Prior austenitisation*** The test commenced upon introduction of the decarburisation atmosphere into the tube furnace with the test specimens already present in the hot zone;

b) ***No pre-heating*** The test commenced when the test specimens were inserted into the hot zone with the decarburisation atmosphere already established.

Similarly, the overall test duration has to be specified. The test duration is defined as the time difference between when the test specimens were first exposed to the decarburisation atmosphere once they were in the hot zone, and when the final argon flush commenced. The precise definition of the test duration for the two methods is:

a) ***Prior austenitisation*** The test duration was the time difference between introduction of the argon atmosphere to conclude the decarburisation, and when the decarburisation atmosphere was first introduced into the tube furnace. The argon flush gas flow rate was matched to the initial hydrogen gas flow rate;

b) ***No pre-heating*** The test duration was the time difference between introduction of the argon atmosphere to conclude the decarburisation, and when the test specimens were first introduced into the hot zone of the tube furnace.

From these definitions it can be seen that the two test durations differ. The entire test duration was at the furnace temperature for the decarburisation experiments involving prior heating and austenitisation, while the test duration for insertion of the test specimens into the hot zone once the decarburisation atmosphere was established included the heating time of the specimens. The following experimental parameters were monitored throughout the course of the decarburisation experiments:

- Atmospheric pressure;
- Hydrogen flow rate;
- Water bath temperatures;
- Water container and flask temperatures;
- Plumbing wall temperatures at various points in the system;
- Pressure transducer mV readings and associated temperatures.

The MPX200AP tube furnace inlet and exit pressure transducers allowed the pressure in the hot zone to be estimated through addition of the two pressures, and then division by two. This was necessary since the p_{H_2O} / p_{H_2} ratios were calculated assuming atmospheric pressure. Measurement of the hot zone pressures during the decarburisation heat treatments allowed the water partial pressures to be adjusted to maintain the desired p_{H_2O} / p_{H_2} ratios. The transducers were calibrated using a Dead Pan Pressure Testing Rig connected to the 3468A Hewlett Packard Digital Multimeter, as detailed in Appendix H. This yielded the following two equations for transducer pressure as a function of temperature and mV multimeter reading:

$$P_{inlet} = 1.7055 mV_{inlet}\left[1 + (T_{inlet} - 20)(0.0019)\right] - 40.035 \qquad (7.3)$$

$$P_{outlet} = 1.8726 mV_{outlet}\left[1 + (T_{outlet} - 20)(0.0019)\right] - 52.941 \qquad (7.4)$$

where P_{inlet}, P_{outlet} = inlet and outlet transducer pressures in kPa;

mV_{inlet}, mV_{outlet} = inlet and outlet transducer pressures in mV;

T_{inlet}, T_{outlet} = inlet and outlet transducer temperatures in °C.

7.6.2 Infrared gas analysis of decarburisation atmosphere

The monitoring of the reacted decarburisation gas was only undertaken for the heat treatments involving the introduction of the test specimens into the established decarburisation atmosphere. This involved monitoring the reacted decarburisation gas in the hot zone. Continuous monitoring of carbon monoxide was undertaken with the Beckham infrared gas analyser, while carbon dioxide and methane were monitored by the Horiba analysers. All three analysers were connected to the Sekonic three-pen recorder, and required calibration against a purified zero gas, and a range of typical gas concentrations. An argon flow through the Labclear and Oxyclear gas purifiers was used as the zero gas, while the span gas of Table 7.6 was used. Gas sampling was undertaken once the test specimens were inserted into the hot zone.

After a warm-up period of one day, the three analysers were calibrated using the calibration apparatus of Figure 6.10. This is detailed in Appendix J. The gas analysers were calibrated before every series of tests, with the relationship between gas composition and pen recorder height for the CO and CO_2 gas analysers illustrated in Figure 7.6 and given by equations (7.5) to (7.7):

Table 7.6 Composition of the calibration span gas.

DESCRIPTION	Composition		Accuracy	
	(volume %)	(wt.%)	(volume %)	(wt.%)
CO	0.270	2700	0.005	50
CO_2	0.098	980	0.002	20
CH_4	0.0232	232	0.0005	5
Ar	99.609	-	-	-

$$V_{CO}(Range2) = 4.58x10^{-6}\,x_{recorder}^{2} + 1.55x10^{-3}\,x_{recorder}; \quad (7.5)$$

$$V_{CO}(Range3) = 3.86x10^{-4}\,x_{recorder}; \quad (7.6)$$

$$V_{CO_2}(Range3) = -3.37x10^{-7}\,x_{recorder}^{2} + 3.17x10^{-4}\,x_{recorder} + 2.29x10^{-4}. \quad (7.7)$$

where $V_{CO}(Range2)$, $V_{CO}(Range3)$, $V_{CO_2}(Range3)$ = CO and CO_2 concentrations for the respective ranges in vol.%;

$x_{recorder}$ = pen recorder height in mm.

The gas volumes of the plumbing from the hot zone to the carbon monoxide, carbon dioxide, and methane analysers are 28.3, 36.6, and 41.6cm^3 respectively. These correspond to sampling lags of 3.4, 4.4, and 5.0s from the hot zone for a gas flow rate of 500cm^3/min. The gas concentrations were continuously recorded using the Sekonic pen recorder. A chart speed of 600mm/hr was used for the pen recorder during the first 15min of the heat treatments, and 60mm/hr for the remainder. The Range 2 setting on the carbon monoxide analyser was used during the first 15min, and Range 3 for the remainder.

7.7 Specimen preparation for microstructural analysis

7.7.1 Austenitisation specimens

Two types of austenitisation test specimens were heat treated, namely the 12mm diameter by 2mm salt bath specimens, and the 5mm diameter by 10mm tube furnace specimens. The 12mm diameter specimens were rinsed in ethanol immediately after the heat treatment and tempering at 250°C, then compression mounted in Bakelite. The mounted specimens were wet ground with 180, 320, and 600 grit wheels rotating for 30s at 300rpm and 32psi on a semi-automatic Leco VP-160 Variable Speed Grinder/Polisher with an AP-60 Grinder/Polisher attachment. The specimens were polished for 3min at 250rpm and 30psi with 1µm diamond, and 60s at 150rpm and 15psi using 0.05µm alumina. This produced a flat, scratch-free surface.

The 5mm diameter specimens were cross-sectioned through the diameter halfway along their length by a 1/16th inch thick Buehler cutoff wheel, and compression mounted in Bakelite.

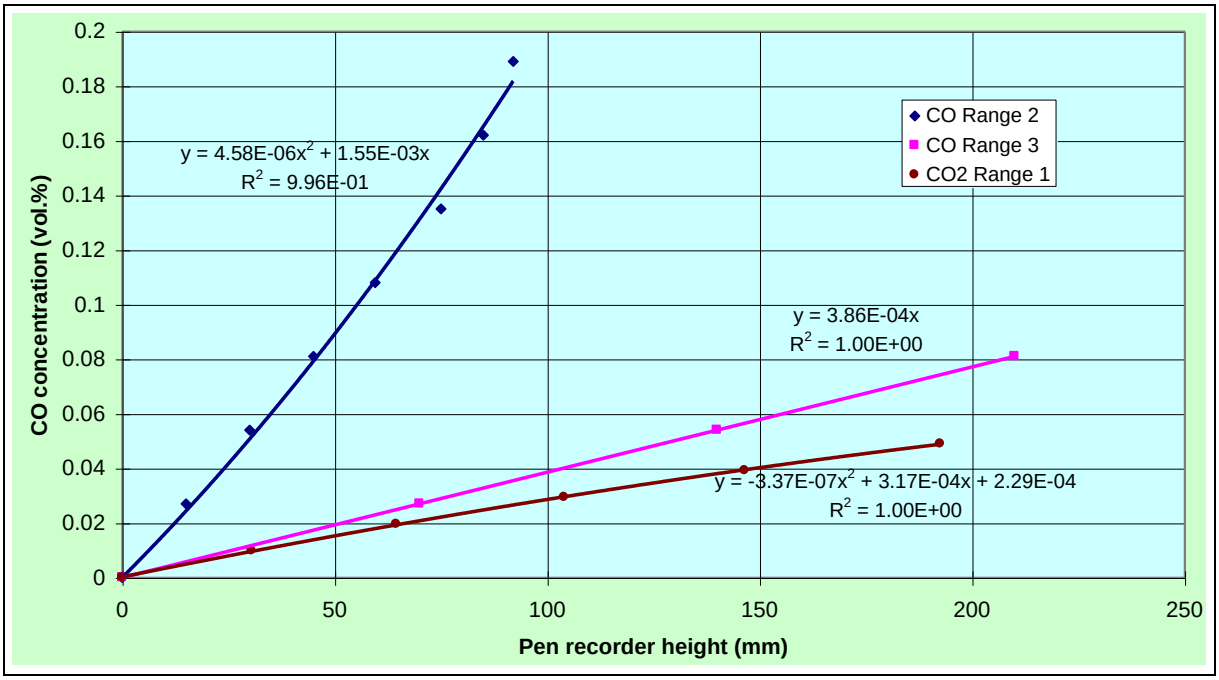

Figure 7.6 Typical calibration curves for the CO and CO_2 infrared gas analysers.

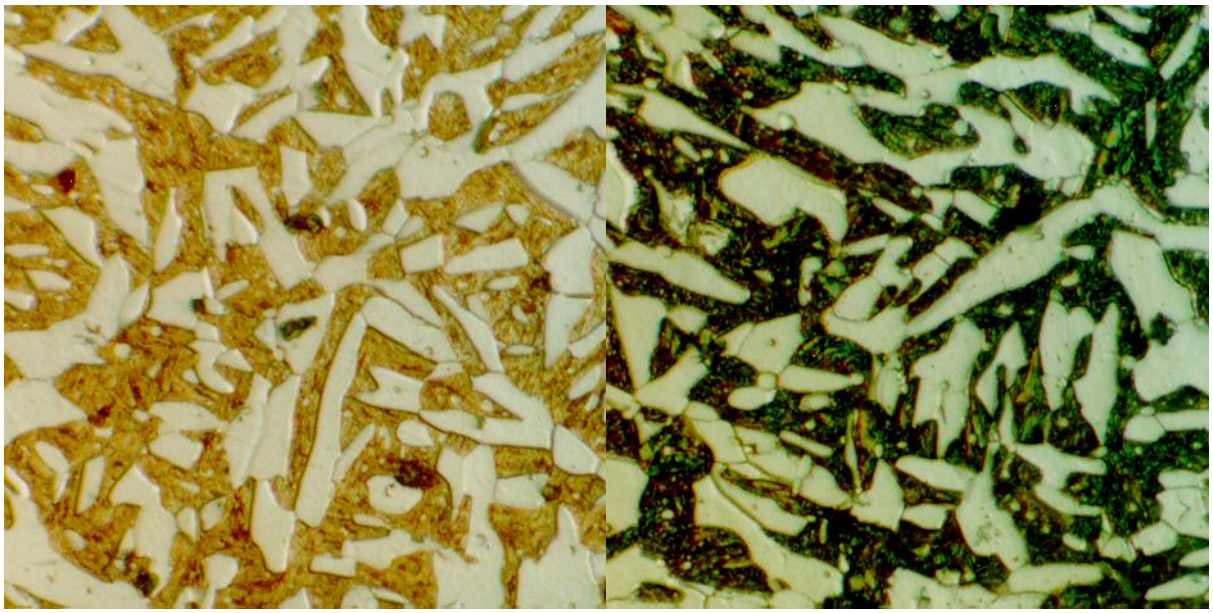

(a) **(b)**

Figure 7.7 Comparison of 2% Nital, (a) and sodium metabisulphite, (b) etchants for a SUP7 initial structure tempered for 96hr at 735°C, Structure D, and austenitised for 24hr at 765°C. 1,150x magnification.

These specimens were then ground and polished by the same method used for the 12mm diameter specimens. The polished specimens were given a light pre-etch in 2% Nital for 5 to 10s, then a 20s etch in sodium metabisulphite to colour the martensite black[33]. Figure 7.7 illustrates the difference between a specimen etched in 2% Nital and sodium metabisulphite. Selected specimens were etched with a Nital/Picral etch for subsequent image analysis of the cementite particles. The chemical specifications of the various etchants used are detailed in Appendix I.

7.7.2 Decarburisation specimens

The decarburised test specimens were carefully rinsed in ethanol and dried under a hot air stream immediately after quenching, before being plated with electroless nickel. The nickel layer was plated to improve edge retention[153] for accurate measurement of the surface decarburisation and oxidation thicknesses. A uniform nickel layer approximately 10µm thick was deposited on the heat treated specimens with the experimental apparatus illustrated in Figure 7.8, and the electroless nickel plating solution of Appendix I, by:

- Deposition of a very thin gold layer on the test specimens with a Polaron SEM E5000 Sputter Coating Unit;
- Assembly of the test specimens as shown in Figure 7.8 with aluminium spacers in intimate contact with the test specimens to allow galvanic initiation, and therefore the beginning of the plating process;
- Heating of the nickel plating solution to between 82 and 88°C using a Chiltern Hot Plate with a magnetic stirrer;
- Insertion of the test specimens into the solution for 1hr;
- Removal of the specimens from the solution, followed by water and ethanol rinses, and drying in a stream of hot air.

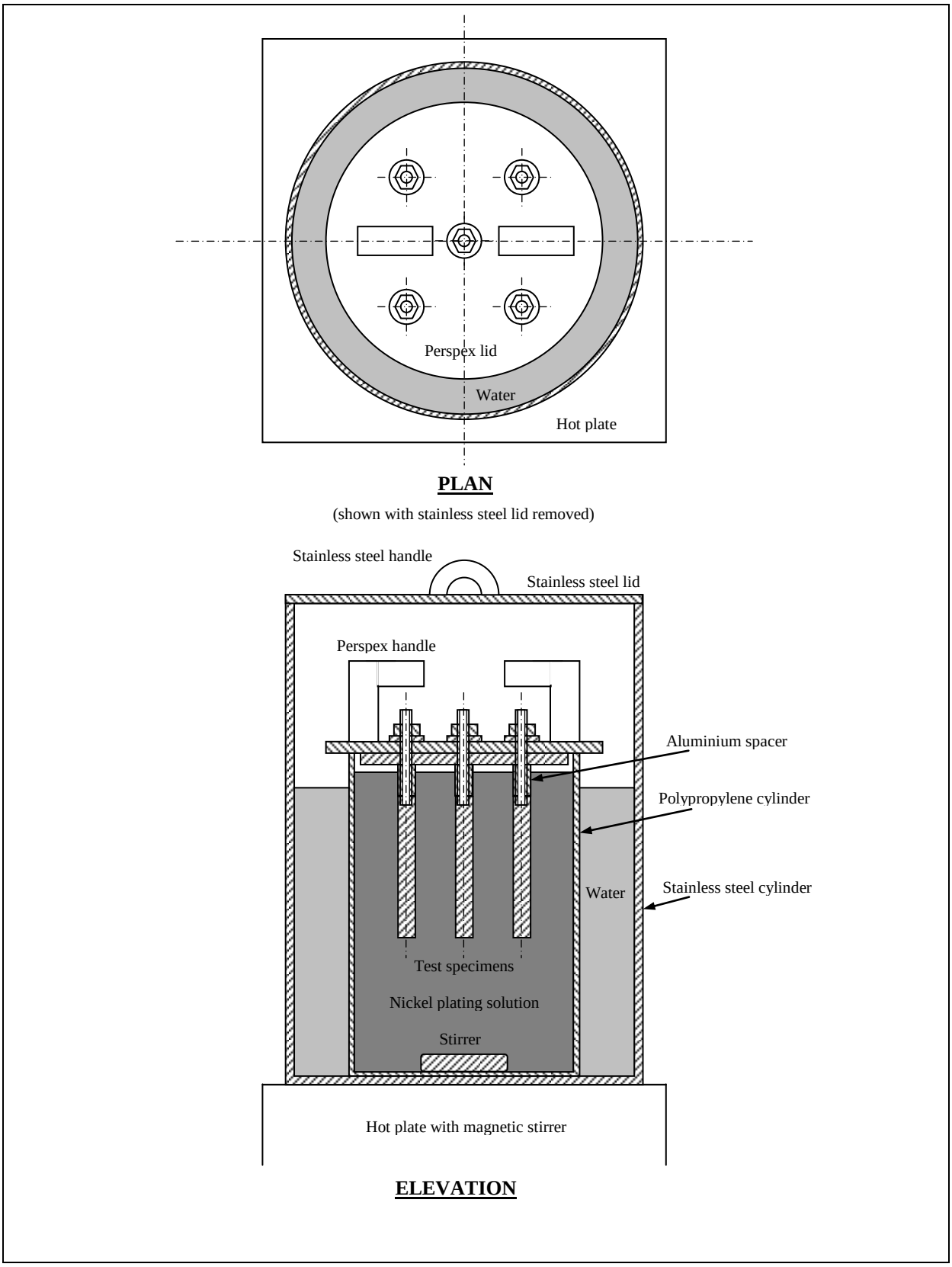

Figure 7.8 Schematic illustration of the electroless nickel plating apparatus.

The 5mm diameter specimens were cold mounted in Epofix to provide a transparent mount with low shrinkage between the mount and the test specimen. 6mm was removed from the specimens by sectioning with the 0.30mm thick diamond wafer wheel of an Isomet Low Speed Saw. The test specimens were ground and polished to either 1µm diamond or 0.05µm alumina finishes using the semi-automatic Leco Grinder/Polisher. This yielded flat, scratch-free surfaces with very little separation between the Epofix mould and the nickel layer, and between the nickel and oxide layers. The specimens were then etched for 10 to 60s in 2% Nital.

The experimental techniques used for this project were described in this chapter. The following chapter details the analytical techniques undertaken to determine the various structural and physical properties of the austenitised and decarburised test specimens.

CHAPTER 8

ANALYTICAL TECHNIQUES

8.1 Introduction

The analysis of the heat treated austenitisation and decarburisation specimens prepared for microstructural analysis required various analytical techniques. These involved the investigation of the microstructures to determine various structural and physical properties, from which the austenitisation and decarburisation could be qualified and quantified. This involved five distinct areas:

a) Quantitative measurements of the austenitised test specimens;
b) Decarburisation exhaust gas analysis;
c) Decarburisation and oxidation layer measurements for the decarburised test specimens;
d) Microhardness testing of the austenitised and decarburised structures;
e) Energy Dispersive X-Ray Spectrum Analysis of the alloying element partitioning between the phases present in the austenitised and decarburised structures;

Quantitative metallography, which is often referred to as stereology, deals with the quantitative relationship between measurements made in the two-dimensional plane of polish, and the magnitudes of the microstructural features in the three-dimensional steel[154]. Stereology is the methodology that permits the statistical estimation of the geometry of the three-dimensional structure from observations made on the two-dimensional image[155]. Various stereological properties of interest can be determined from optical or scanning electron microscopic images, including the:

- Volume fraction;
- Surface area to volume ratio;
- Grain and particle sizes;
- Pearlite true interlamellar spacing;

- Particle equivalent area diameter, size distribution, and shape factor;
- Number of particles per unit area;
- Number of particles per unit volume.

These properties can be obtained from a combination of manual and automatic techniques which predominantly involve simple counting measurements. The relevant decarburisation terminology is given by the following definitions[156]:

Complete decarburisation	Loss of carbon content at the surface of a steel specimen to a level below the solubility limit of carbon in ferrite so that only ferrite is present;
Free ferrite depth	The perpendicular distance from the surface of the specimen to that location where the structure is no longer fully ferritic;
Partial decarburisation	Loss of carbon content at the surface of a steel specimen to a level less than the bulk carbon content of the unaffected interior, but greater than the solubility limit of carbon in ferrite;
Total decarburisation depth	The perpendicular distance from the specimen surface to that location in the interior where the bulk carbon content is reached. This is the sum of the complete and partial decarburisation depths.

The free ferrite depth can be measured microscopically using the contrast upon etching of the ferrite and martensite layers. The partial decarburisation can be measured microscopically, or by image analysis at various distances from the surface until the phase compositions remain constant. The total depth of decarburisation can also be measured by a microindentation hardness method as long as the specimens do not contain two constituents of significantly different hardness[156]. The total depth of decarburisation is that depth where the hardness becomes constant and equal to that of the interior. The carbon removed from the steels at their respective Ac_3 temperatures can be determined from the analysis of the decarburisaion atmosphere exhausting from the hot zone, and subsequently converted to the free ferrite depths.

The alloying elements present in the various phases of the austenitised and decarburised structures can be quantified by the use of a scanning electron microscope using Energy Dispersive X-ray Spectrum Analysis. Mean values can be calculated for the experimental parameters analysed, with the standard deviations and 95% confidence intervals defined by standard statistical techniques. This chapter details the various analytical techniques applied to the austenitised and decarburised test specimens, and the calculations used to specify the various experimental parameters determined.

8.2 Initial microstructures

The different initial structures used for the austenitisation and decarburisation heat treatments can be specified by various stereological properties, and by the alloy content of the respective phases. The austenite grain size prior to the production of the different initial microstructures can be determined. Pearlitic structures are specified by the true cementite interlamellar spacing, and spheroidal cementite structures by the size and distribution of cementite particles, and by the ferrite grain size. The stereological measurements were undertaken with a Video Pro 32 Colour Image Analysis software package loaded into a 486 Pentium Computer with 12MB RAM and a 541MB hard disc drive. The image analysis software is coupled to an Olympus BH2-MA-2 Optical Microscope via a JVC TK-870E video camera. The pearlitic and spheroidal cementite images were obtained from computer printouts of a JEOL JSM-610 SEM loaded via the JVC video camera. X-ray analysis of the various phases allows the distribution of the alloying elements to be quantified, and was undertaken with the LINK QX2000 Energy Dispersive X-ray analyser of the JEOL SEM.

8.2.1 Prior austenite grain size

In order to determine the prior austenite grain size, the different steels were water quenched from 900°C after austenitising for 12hr. Various etchants were used in an attempt to delineate the prior austenite grain boundaries, as described in Appendix I. However, only the boundaries of the 0% Silicon steel could be well defined, as illustrated in Figure 8.1. Therefore, the prior austenite grain size was only determined for the 0% Silicon steel. The grain size measurements were made in accordance with the single circle intercept method of ASTM E112-88[157]. An intercept was tallied each time the test circle intercepted a grain, or

portion thereof, of the phase being measured. The intersection of the test circle with the junction of three grains was tallied as two intercepts. The analysis was undertaken with the image analysis apparatus using the following procedure:

- Binary storage of a 5cm diameter circle videoed at an appropriate magnification to cover approximately two-thirds of the screen;
- Random placement of the optical microscope at 50x magnification over the specimen;
- Selection of the appropriate magnification to give a minimum of 15 grain boundary intercepts, and an optimum of 35 intercepts, with the test circle;
- Freezing of the image on screen;
- Retrieval of the stored binary image and application to the screen image, as in Figure 8.1;
- A manual count of the number of grain boundary intercepts with the test circle;
- Random re-application of the microscope to the test specimen at 50x magnification, and repetition of this method until a minimum of 500 intercepts were tallied.

For each test circle placement[158],

$$N_{Li}(\gamma) = \frac{N_{i\gamma}}{L_{ti}}, \tag{8.1}$$

where $N_{Li}(\gamma)$ = number of austenite grains intercepted per unit length of test circle for the field;i^{th}

$N_{i\gamma}$ number of austenite grains intercepted by the test circle for the field;i^{th}

L_{ti} = true test circle length for the field.i^{th}

The average value, $\bar{N}_L(\gamma)$, can be determined from

$$\bar{N}_L(\gamma) = \sum_{i=1}^{n} \frac{N_{Li}(\gamma)}{n}, \tag{8.2}$$

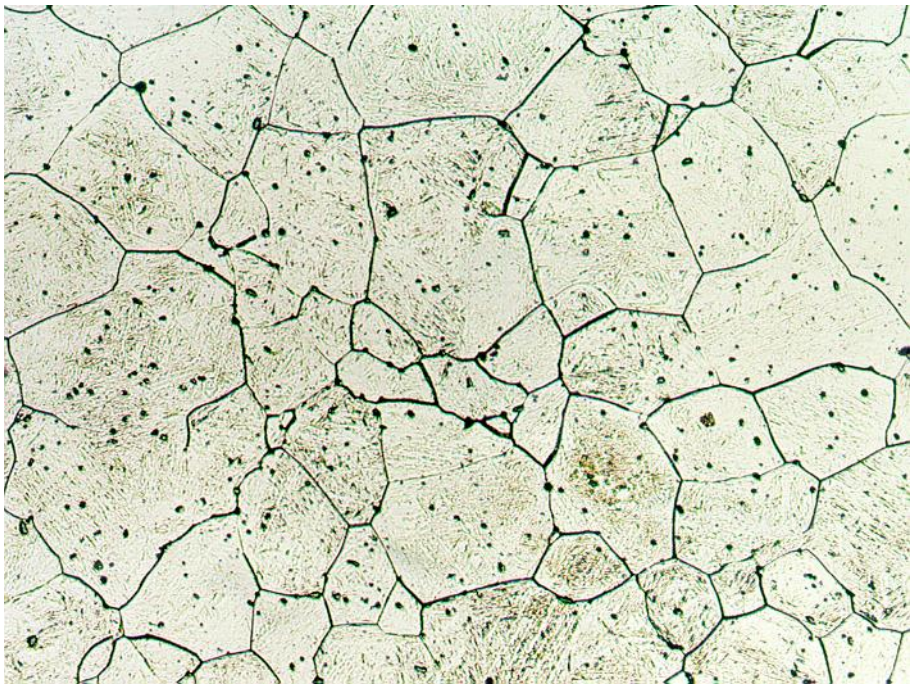

Figure 8.1 Prior austenite grain boundaries for the 0% Silicon steel austenitised for 12hr at 900°C and quenched in water. “Picral/white cat etch”. 115x magnification.

where $\bar{N}_L(\gamma)$ = mean number of austenite grain intercepts per unit length of test circle for n fields measured;

n = number of fields measured.

The mean lineal intercept length of the austenite grains, $\bar{l}_\gamma$, can be determined from

$$\bar{l}_\gamma = \frac{1}{\bar{N}_L}, \tag{8.3}$$

where $\bar{l}_\gamma$ is in μm or mm.

The standard deviation, s, of the individual measurements of $N_{Li}(\gamma)$ can be determined from

$$s = \left[\frac{1}{n-1} \sum_{i=1}^{n} \{N_{Li}(\gamma) - \bar{N}_L(\gamma)\}^2 \right]^{\frac{1}{2}}. \tag{8.4}$$

The mean ASTM austenite grain size, G_γ, can be determined from

$$G_\gamma = [6.643856 Log\, \bar{N}_L(\gamma)] - 3.288 \tag{8.5}$$

with $\bar{N}_L(\gamma)$ in mm^{-1}. This grain size is rounded off to the nearest tenth unit.

The 95% confidence interval, $95\%CI$, can be determined from

$$95\%CI = \pm \frac{t.s}{\sqrt{n}}, \tag{8.6}$$

where t is the 95% confidence interval multiplier.

The percent relative accuracy, $\%RA$, is determined from

$$\%RA = \frac{95\%CI}{\bar{N}_L(\gamma) \text{ or } \bar{l}_\gamma}. \qquad (8.7)$$

This method allows the ASTM grain size to be defined to an accuracy of $1/10^{th}$ of a unit with a 95% confidence interval and a relative accuracy of less than 10%.

8.2.2 Pearlite true interlamellar spacing

As the cementite lamellae of the air cooled and furnace cooled pearlitic structures are too fine to be resolved with optical microscopy, scanning electron microscope images were necessary to determine the mean true interlamellar spacing. Vandervort[158] suggests that the best method to determine the mean true spacing is to first determine the mean random spacing. This was achieved by electronically superimposing a template comprising 15 circles over scanning electron microscopic images, and analysing with an appropriate image analysis program. The following procedure details the preparation of the scanning electron microscope images for image analysis, which involved the:

- Printout of a diffraction grating with a square grid spacing of 0.463 m viewed with a JEOL JSM-6100 Scanning Electron Microscope at 10,000x magnification in accordance with ASTM E766-86[159];
- Random selection of 12 different pearlitic images at 10,000x magnification using the electron microscope, with each image stored electronically as a BITMAP file and printed out with a Hewlett Packard Laser Jet 4SiMX laser printer, with a typical printout illustrated in Figure 8.2. The white lamellae are cementite, while the remainder of the matrix is ferrite. The printouts of the pearlitic images were the same size as the printout of the diffraction grating, so that subsequent calibration of the image analyser with the diffraction grating was applicable to the image analysis of the pearlitic images. The images were obtained with an accelerating voltage of 20kV, and a working distance of 8 for greater structural resolution;
- Videoing in the diffraction grating into the image analysis software using the JVC video camera with electronic storage as a JPEG file;

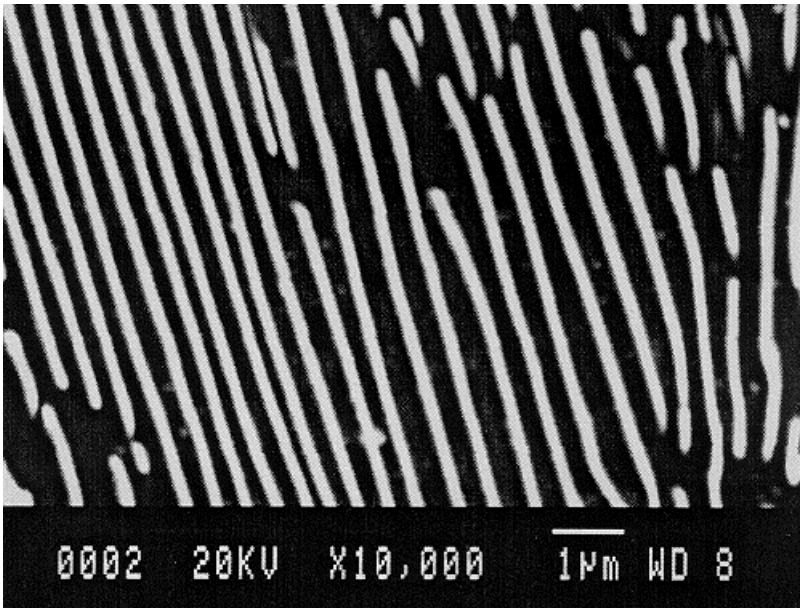

Figure 8.2 SEM laser printout of a SUP7 furnace cooled initial structure. 10,000x magnification. 2% Nital etch.

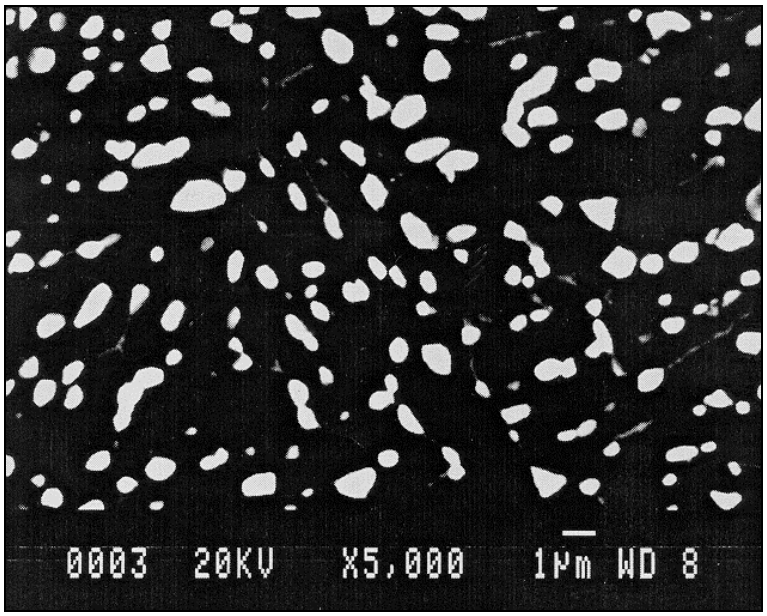

Figure 8.3 Laser printout of a SEM SUP7 12hr tempered martensite initial microstructure. 5,000x magnification. 2% Nital etch.

- Videoing of the scanning electron microscope images using the same camera set up with electronic storage as JPEG files;
- Set up of a 10,000x magnification calibration data file by using the diffraction grating;
- Binary storage of a template comprising five rows by three columns of 1cm diameter circles videoed in at an appropriate magnification to cover approximately 2/3rd of the screen.

Two image analysis programs were written to determine the true mean pearlite interlamellar spacing, with these programs listed in full in Appendix K1. The methodology was based on that used by Fowler[160] to determine the pearlite interlamellar spacing using digital image analysis. PEARST2, Appendix K1-(i), set up the columns to measure the true mean spacing, and then ran the analysis program PEARAN2, Appendix K1-(ii), which proceeded by the:

- Operator appending a data file to allow the measured values to be stored;
- Automatic reading, thresholding, and storage of the circular template image;
- Reading of the operator selected pearlitic image;
- Operator thresholding of the cementite lamellae;
- Automatic BINARY STORE AND command to produce the intersection of the circular template with the cementite lamellae;
- Automatic binary commands ERODE to remove any small spots, DILATE to restore the size, and MEDIAN to smooth the pearlite image.

Depending on the pearlitic structure, and the orientation of the section to be counted, short lamellae segments often appear in the template circles, along with the longer lamellae that extend across the entire diameter of the circles. It has been demonstrated that these short segments tend to produce a count that is higher than the true number of lamellae intersections[161]. These extra counts can be removed by a SIZER edit involving a SHAPE FACTOR, SF, defined as

$$SF = 100 - \left(400\pi \frac{A_P}{P_P^2} \right), \tag{8.8}$$

where A_P = area of cementite lamellae;

P_P = perimeter of lamellae.

This shape factor yields a minimum value of 0 for circular objects, and increases for more elongated objects to a maximum value of 100. As the short lamellae have a higher area to perimeter ratio, their shape factor is closer to zero than that of longer lamellae. Consequently, specification of a minimum shape factor allows removal of the shorter lamellae segments. Several different minimum shape factors were trialed until a value of 40 was selected as the cut-off point for removal of short lamellae. The remainder of PEARAN2 involved:

- Automatic sizer edit to eliminate the short lamellae;
- Automatic counting of the number of cementite lamellae remaining;
- Calculation of the mean random and true pearlite interlamellar spacings by

$$\sigma_r = \frac{15\pi d_{template}}{N_T}, \tag{8.9}$$

where σ_r = random pearlite interlamellar spacing in μm;

$d_{template}$ = diameter of template circles in μm;

N_T = number of lamellae intersections,

and

$$\sigma_t = \frac{\sigma_r}{2}, \tag{8.10}$$

where σ_t = true pearlite interlamellar spacing in μm.

This sequence was repeated for each image. The standard deviation, % confidence interval and percent relative accuracy were calculated by equations 8.4, 8.6, and 8.7.

8.2.3 Cementite particles

An initial attempt was made to whiten the cementite particles with Klemm's I Reagent so that they could be quantitatively analysed with optical microscopy. However, the maximum magnification of 1,000x was insufficient to allow the accurate measurement of the cementite particles. Consequently, 12 randomly selected SEM images at 5,000x magnification with a working distance of 8 were electronically stored for each specimen as BITMAP files and printed out with the Hewlett Packard printer. The selection of a suitable combination of SEM contrast and brightness produced a white cementite particle outline, with the ferrite grain boundaries being almost undetectable, as illustrated in Figure 8.3. The remainder of the matrix is ferrite. Some manual editing of the images was necessary to delete the ferrite grain boundaries and complete the outlines of cementite particles.

The SEM image printouts were videoed and stored electronically as JPEG files, with a 5,000x calibration file established from a 5,000x magnification diffraction grating printout. Two image analysis programs were written to determine the volume fraction, shape factor, equivalent area diameter and cementite size distribution for the cementite particles. These programs are detailed in Appendix K2. CEMSTI, Appendix K2-(i), set up the columns to measure the volume fraction, shape factor, equivalent area diameter and cementite size distribution, and then ran the analysis program CEMANI, Appendix K2-(ii), which proceeded by:

- Appending a data file to allow the measured values to be stored;
- Reading the operator selected image;
- Operator thresholding of the cementite particles, then binary commands ERODE2 to remove any small spots, DILATE2 to restore the size of the cementite particles, and MEDIAN2 to smooth the image.

When an image is viewed on the computer screen, the screen frame intersects certain cementite particles. The counting of these partial cementite particles, in conjunction with the particles within the frame, for the calculation of the cementite particle size, would yield a smaller value than the actual size. A more accurate particle size was obtained by deleting the

particles along one half of the frame, and then using a count of the remainder of the particles to determine the particle size[154]. This was achieved by CEMANI with:

- Operator deletion of the right and bottom frame cementite particles using ERASE and EDIT FILL;
- Automatic storage of this image, and measurement of the cementite particle count and shape factor.

Due to the range of cementite particles sizes in the initial microstructures, it was useful to specify the cementite particle size distribution[115]. The majority of the cementite particles appeared to be approximately spherical, which allowed different cementite particle size intervals to be defined by[154]:

$$A_{cem} = \frac{\pi d^2}{4}, \tag{8.11}$$

where A_{cem} = area of the equivalent diameter spherical cementite particle in μ m^2;

d_{cem} = diameter of the particle in μ m.

Consequently a SIZER edit was performed using an AREA variable to measure only the cementite particles that fell within a certain size interval. 13 size intervals were measured, with 12 of those in 0.25 μ m intervals from 0 to 3 μ m equivalent area diameter, and the other for diameters greater than 3 μ m. CEMANI continued as follows:

- Automatic retrieval of the previous edited image, with a sizer edit using area to specify an equivalent area diameter of 0 to 0.25 μ m;
- An automatic COUNT of the number of particles falling within that size interval;
- The automatic procession through the remainder of the size intervals to count the number of particles falling within each size interval;
- Following measurement of the size intervals, the original image was again automatically thresholded using the earlier threshold settings, with the total area and volume fraction of

all the cementite particles, including those on the left and bottom of the frame, being measured;

- Automatic calculation of the equivalent area diameter by

$$d_{eq} = \sqrt{\frac{4A_{cem}}{\pi N}}, \qquad (8.12)$$

where d_{eq} = equivalent area diameter of the spherical particles in m; μ

$=A_{cem}$ total cementite particle area measured in m^2; μ

N = total number of cementite particles measured after deleting the left and bottom particles;

and automatic calculation of the particle distribution within the various size intervals by

$$\%i^{th} \text{ interval} = \frac{N_{icem}}{N}.100, \qquad (8.13)$$

where $\%i^{th}$ interval = percentage of total cementite particles present falling within the i^{th} size interval;

N_{icem} = number of cementite particles having a size within the i^{th} interval range.

This sequence was repeated for each image. The standard deviation, 95% confidence interval, and percent relative accuracy were calculated for the volume fraction, shape factor, equivalent area diameter and cementite size distribution by a similar approach to equations 8.4, 8.6, and 8.7.

8.2.4 Ferrite grain size

A full description of the initial spheroidal cementite structures involves the mean cementite particle size, the particle size distribution, and the ferrite grain size. The ferrite grain size in the ferrite/cementite structures can be calculated in accordance with the methods of ASTM

E112-88[157] and ASTM E1382-91[161] for effective grain sizes in metals containing two phases. The effective grain size values normally obtained indicate a dimensionally smaller size than that obtained by treating the same material as a single phase, which prevents the interchange of the two types of grain sizes. The first step in determining the effective ferrite grain size was the measurement of the cementite point fraction. The number of ferrite grains intercepted by the test circle were then counted, which allowed the ferrite grain size to be calculated. The ferrite point fraction was determined by the:

- Random placement of the optical microscope at 50x magnification over the specimen;
- Selection of the appropriate magnification for analysis of the cementite particles.

ASTM E562-89[162] recommends a grid spacing of 49 points for an area fraction of 5 to 10%, which corresponds to the cementite fraction present in the initial structures. By electronically superimposing a 7x7 grid over the optical microscope image, the total number of grid points falling within the cementite particles, or on the cementite boundaries, were counted. Each grid point falling within a cementite particle was tallied as one count, while those on the cementite boundaries were tallied as one half of a count. When doubt existed as to whether the point was inside or outside the cementite boundary, it was counted as one half. The cementite point fraction for the field, i^{th} $P_c(i)$, is given by

$$P_c(i) = \frac{P_i}{P_T}, \tag{8.14}$$

where P_i = point count for the field; i^{th}

P_T = total number of test grid points.

The ferrite point fraction in the field, i^{th} $P_\alpha(i)$, is then given by

$$P_\alpha(i) = 1 - P_c(i). \tag{8.15}$$

The ferrite grains were then counted by:

- Selection of the appropriate magnification to give a minimum of 15, and an optimum of 35, grain boundary intercepts with the test circle;
- Electronic superimposition of the test circle over the microscope image;
- A manual count where one intercept was tallied each time the circle intercepted a ferrite grain or portion thereof, and two intercepts for the intersection of three ferrite grains;
- Random re-application of the microscope to the test specimen at 50x magnification, and repetition of the point and ferrite intercept counts until a minimum of 500 ferrite grain boundary intercepts were obtained.

The mean lineal intercept length of the ferrite grains, $\bar{l}_\alpha$, is calculated by

$$\bar{l}_\alpha = \frac{(\bar{P}_\alpha)(L_{ti})}{\bar{N}_\alpha}, \tag{8.16}$$

where $\bar{P}_\alpha$ = the average ferrite point fraction;

$\bar{N}_\alpha$ = the average value of the number of ferrite grains intercepted by the test circle.

The calculation of the lineal intercept length of the ferrite grains for the i^{th} field, $l_{\alpha i}$, is used to determine the standard deviation of $\bar{l}_\alpha$ for n fields, as for equation 8.4. The 95% confidence interval and percent relative accuracy are determined from equations 8.6 and 8.7 respectively. The mean ASTM ferrite grain size, G_α, can be determined from

$$G_\alpha = (-6.643856 Log\, \bar{l}_\alpha) - 3.288, \tag{8.17}$$

with $\bar{l}_\alpha$ in mm.

8.2.5 Energy Dispersive X-Ray Spectrum Analysis of alloying elements

The alloying element distribution in the initial microstructures between the ferrite and cementite phases can be quantitatively analysed with energy dispersive spectroscopy, EDS, by a SEM equipped with an electron probe microanalyser. EDS is suitable for elements that are[163]:

a) Heavier than or equal to sodium in atomic weight;
b) Present in tenths of a percent or greater by weight;
c) Occupying a few cubic micrometers, or more, of the specimen.

EDS will not provide a truly quantitative analysis if the specimen is inhomogeneous at the micrometer level. The minimum size of particles that can be analysed is calculated from equation 8.18, where

$$R = \frac{0.064(E_o^{1.68} - E_c^{1.68})}{\rho}, \qquad (8.18)$$

where R = the minimum particle size for EDS in μm;
E_o = the accelerating voltage in kV;
E_c = the critical excitation potential in keV;
ρ = the density in g/cm^3.

Iron is the element comprising the majority of the steels investigated. Assuming a 100% iron structure with a density[164] of 7.87g/cm^3, an accelerating voltage of 20kV, and a critical excitation potential of 7.1keV, equation 8.18 yields a minimum size of 1 μm. As the cementite lamellae of the pearlitic structures are considerably thinner than 1 μm, this technique cannot be used to analyse the alloying element content of the pearlitic structures. Furthermore, analysis of the spheroidal cementite structures is limited to particles greater than 1 μm diameter. The spheroidal cementite initial structures were analysed by a JEOL JSM-6100 SEM equipped with a LINK QX2000 Energy Dispersive X-Ray Analyser by the following method:

- Setting the SEM to a tilt angle of 0 degrees, a working distance of 39, and an accelerating voltage of 20kV;
- Focussing on a Cobalt standard at 4,000x magnification;
- Selection of the ZAF-4/FLS matrix correction program;
- Recall and selection of the set up file;
- Set up of an analysis file;
- Calibration of the gain;
- Collection of the cobalt calibration spectrum using an X-ray acquisition time of 100s, and a detector dead time of approximately 25%.

Five to ten analyses per calibration were made by:

- Positioning of the electron beam on the phase of interest at a magnification of 1,000 to 12,000x using the microscope cross hairs;
- Collection of the sample spectrum using the spot mode to form a probe to analyse the minimum volume using an X-Ray acquisition time of 100s, and a detector dead time of approximately 25%;
- Repetition of the analysis for that phase by random re-application of the microscope to the specimen and selection of appropriate size particles, until a minimum of five acceptable analyses per phase were obtained.

A fit index of less than two was deemed acceptable, with the results discarded if the fit indices were greater than two. Alloying element totals of approximately 100wt.% were expected for the analysis of the ferrite and martensite phases, and approximately 93wt.% for the analysis of cementite particles, since cementite comprises 6.67wt.%C. An analysis was discarded if the total differed by more than 2wt.% from that expected for the phase sampled, as this suggested that the electron beam had penetrated another phase. If an individual analysis was not consistent with the others for the phase under investigation, it was also discarded. The mean, standard deviation, 95% confidence interval and percent relative accuracy of the alloying element fractions are calculated by equations similar to 8.2, 8.4, 8.6 and 8.7.

8.3 Austenitisation heat treatments

8.3.1 Austenite formation

Etching of the heat treated structures with 2% Nital, followed by sodium metabisulphite resulted in excellent contrast between the dark martensite phase, which is austenite at the heat treatment temperature, and the remainder of the matrix, as illustrated in Figure 8.4. It was assumed that the austenite fraction at the heat treatment temperature corresponded to the fraction at room temperature, ignoring transformation strains.

For well heated and hardened steels with greater than 0.55wt.% carbon, some retained austenite usually persists upon quenching[55]. This is due to lowered martensite start and finish temperatures, with a water quench invariably yielding less retained austenite than an oil quench[55]. Manganese stabilises austenite, and therefore favours the retention of austenite, while silicon has little influence on the amount of austenite retained[55]. A 0.56wt.%C/0.30wt.%Si/0.75wt.%Mn steel has a martensite finish temperature of 100°C, and a maximum diameter of 15mm for full transformation of austenite to martensite with a water quench[164]. A 0.62wt.%C/1.90wt.%Si/0.85wt.%Mn steel has a martensite finish temperature of 80°C, and a maximum diameter for full austenite transformation to ferrite of 50mm[164]. Consequently, a water quench to room temperature should yield little retained austenite for the 0 to 3% silicon steels.

The image of Figure 8.4 is suitable for image analysis, where the martensite phase is thresholded, and then analysed. Two image analysis programs were developed, with one for microstructures exhibiting discrete martensite particles, and the other for structures where the martensite grains had coalesced. For microstructures with discrete martensite particles, the volume fraction, surface area to volume ratio, equivalent area diameter, shape factor, the number of particles per unit area, and the number of particles per unit volume for the martensite particles were determined. 20 fields were electronically stored as JPEG files after randomly positioning the optical microscope at 50x magnification with the placement pattern of Figure 8.5, and then selecting the appropriate magnification for analysis. The image analysis program STARTM3, detailed in Appendix K3-(i), set up the columns to measure the

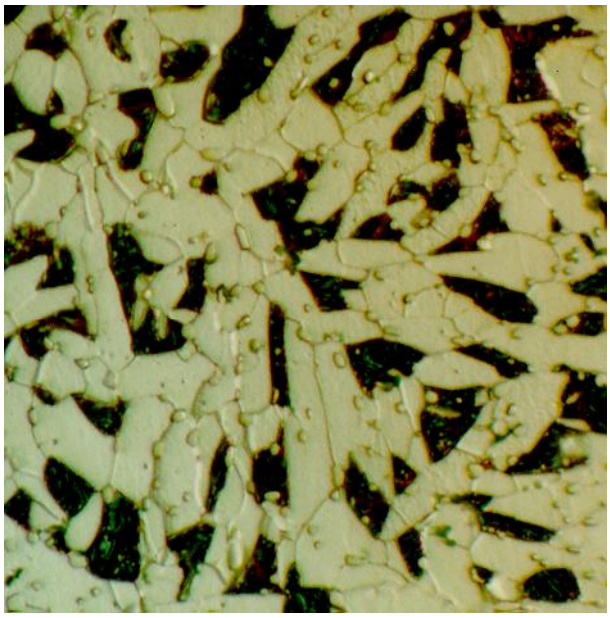

Figure 8.4 Illustration of the microstructure of a SUP7 96hr tempered martensite initial structure austenitised at 755°C for 24hr and etched with 2% Nital followed by sodium metabisulphite to darken the martensite. 1150x magnification.

various parameters, and then ran the analysis program ANALYM3, Appendix K3-(ii). ANALYM3 involves the following sequence of operations:

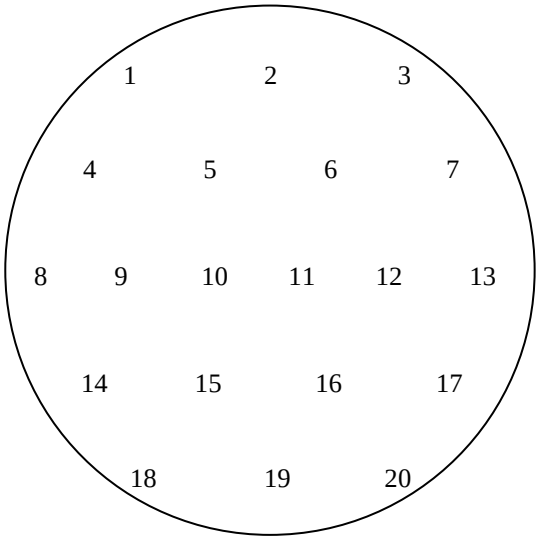

Figure 8.5 Optical microscope placement pattern at 50x magnification for image analysis of the austenitisation structures.

- Operator appending of a data file to allow storage of the measured values;
- Reading of the operator selected image;
- Operator thresholding of the martensite particles;
- Automatic binary commands ERODE to remove any small spots, DILATE to restore the size of the martensite particles, and MEDIAN to smooth the image;
- Operator deletion of the right and bottom frame martensite particles to determine the martensite particle size, as for the cementite particles of section 8.2.3, using EDIT ERASE and EDIT FILL;
- Automatic measurement of the martensite particle count to give the equivalent area diameter, as calculated in equation 8.12;
- Automatic re-thresholding by BINARY, ERODE, DILATE and MEDIAN operations on the image;
- Automatic measurement of the total area, shape factor, and volume fraction of the martensite grains, with the shape factor calculated by equation 8.8;

Another commonly determined stereological property is the grain boundary surface area per unit volume, S_v, given by[155]:

$$S_v = 2\bar{P}_L, \tag{8.19}$$

where $\bar{P}_L$ = mean number of grain boundaries intersected per unit length of test line.

The surface area to volume ratio was determined by overlaying 14 horizontal lines over the image and counting the number of intersections between the lines and the martensite grain boundaries by:

- Drawing an overlay comprising 14 horizontal lines of $5\,\mu m$ spacing at 1,000x magnification using MEASURE GRID HORIZONTAL, HEIGHT and DRAW commands;
- Automatic binary storage of the overlay;
- Automatic thresholding of the martensite particles, then binary commands ERODE to remove any small spots, DILATE to restore the size of the martensite particles, and MEDIAN to smooth the image;
- Automatic detection of the intersections between the horizontal lines and the martensite grains by BINARY STORE AND, and measurement of the intersection count;
- Automatic calculation of the volume fraction, surface area to volume ratio, equivalent area diameter, shape factor, the number of grains per unit area, N_A, and the number of grains per unit volume assuming a spherical particle shape and log-normal size distribution[165], N_V, where:

$$N_V = \frac{3\pi^2}{4} N_A^3 V_V . \tag{8.20}$$

Both N_A and N_V were calculated using the martensite particle count determined from the thresholded image edited to remove the martensite particles intersecting the right and bottom sides of the computer screen. The mean, standard deviation, 95% confidence interval and

percent relative accuracy for the various parameters were calculated similar to equations 8.2, 8.4, 8.6, and 8.7.

For martensite structures where the martensite grains coalesced to the extent that the measurement of the individual particle equivalent area diameters was no longer appropriate, which occurred at approximately 20 to 30% martensite, only the volume fraction and surface area to volume ratio were determined. The same sequence involving the storage of images, operator thresholding and binary commands undertaken for the microstructures with discrete martensite grains, which involved STARTM3 and ANALYM3 programs, was used for structures having significant impingement of the growing austenite. STARTM2, Appendix K4-(i) sets up the columns for the various parameters, and then ran the analysis program ANALYM2, Appendix K4-(ii). Following the binary command operations, and before deletion of the right and bottom particles for ANALYM3, the program proceeded by:

- Automatic measurement of the volume fraction;
- Automatic drawing of 14 horizontal lines, binary storage of the lines, thresholding of the image, and binary commands to clean up the image;
- Automatic detection of the intersections between the horizontal lines and the martensite grain boundaries by BINARY STORE AND, and measurement of the intersection count;
- Automatic calculation of volume fraction and surface area to volume ratio, with the mean, standard deviation, 95% confidence interval and percent relative accuracy determined similar to equations 8.2, 8.4, 8.6 and 8.7.

8.3.2 Cementite dissolution

The dissolution of the cementite particles for the austenitised specimens initially comprising spheroidal cementite structures was determined by measuring the volume fraction, shape factor and equivalent area diameter of the particles. Good contrast between the cementite particles and the remainder of the microstructure was achieved by a Nital/Picral etch, Appendix I. 12 randomly selected cementite images were electronically stored for each specimen at 5,000x magnification, printed out, and manually edited to delete unwanted grain boundaries and to complete the outlines of partially detected cementite particles. This image was then videoed into the image analyser by the same procedure used for the cementite

structures of Section 8.2.3. CMNSEST, Appendix K5-(ii) set up the columns to measure the volume fraction, shape factor and equivalent area diameter, and then ran the analysis program CMNSEAN, Appendix K5-(ii). This read, thresholded and edited the image by the same method of CEMANI for Section 8.2.3, except that the cementite size distribution was not determined. The statistical analysis was undertaken by equations similar to 8.2, 8.4, 8.6 and 8.7.

8.3.3 Ferrite grain size

The ferrite grain size was determined for austenitised specimens obtained from spheroidal cementite initial structures, with either two phase ferrite/cementite or three phase ferrite/cementite/martensite structures present. The martensite phase predominantly comprised discrete martensite particles for a volume fraction of up to 20 to 30%. An effective ferrite grain size was determined for the two phase structures by the method of Section 8.2.4. The method differed slightly for the three phase structures, with the 7x7 grid applied to the martensite grains to determine the martensite point fraction. Equation 8.15 was modified with the ferrite point fraction subsequently determined by

$$P_\alpha(i) = 1 - P_c(i) - P_M(i), \qquad (8.21)$$

where $P_M(i)$ = the martensite point fraction.

The effective grain size was determined by application of the 5cm diameter test circle to count at least 500 grain boundary intercepts in conjunction with the point fraction, where equation 8.16 uses $\bar{P}_\alpha$ calculated from equation 8.21 to determine the ASTM grain size. The 95% confidence interval and percent relative accuracy were determined similar to equations 8.6 and 8.7.

8.3.4 Energy Dispersive X-Ray Spectrum Analysis of alloying elements

The alloy element concentrations of the ferrite, martensite and cementite phases, where present, were measured by the same method involving the JEOL SEM with Energy Dispersive

X-Ray Spectrum Analysis that was used for the spheroidal cementite initial structures of Section 8.2.5.

8.3.5 Microhardness

The microhardness testing of the austenitised specimens was undertaken with a LECO M-400-H1 Hardness Testing Machine. Microhardness testing was only undertaken on specimens austenitised at the Ac_3 temperatures, and comprising close to 100% martensite. Assuming almost complete cementite and/or graphite dissolution, the martensite carbon content approximates that of the bulk steel value of 0.6wt.%. The hardness of steel only increases slightly for carbon contents above approximately 0.55wt.%, unless there is a variation in residual cementite content or retained austenite[156]. Therefore, although it was determined that the martensite carbon contents of intermediate transformation structures were sometimes higher, this could not be confirmed using microhardness testing. Furthermore, the martensite particles for lower martensite fractions were often smaller than the indentations made by the diamond indenter, even at small test loads.

The heat treated specimens were polished to a 0.05µm finish, and etched sufficiently in 2% Nital to delineate the martensite from the remainder of the microstructure. The etch was as light as possible, since etched surfaces can yield microhardness results different from unetched surfaces, depending on the extent of etching[166]. Each test was undertaken with an indenter load of 200g, and a load application time of 10s using a Vickers indenter. Eight indentations were made in different martensite areas for each specimen, with the indentations measured at 400x magnification. The mean hardness of each specimen, and the associated standard deviations, 95% confidence intervals and percent relative accuracies were determined by equations similar to 8.2, 8.4, 8.6 and 8.7 respectively.

8.4 Decarburisation heat treatments

8.4.1 Decarburisation depth measurements

Depending on the steel, the decarburisation atmosphere, and the heat treatment temperature, four distinct decarburised structures were observed, namely:

a) A free ferrite surface layer with a martensite core, Figure 8.6(a);
b) A decarburised surface layer comprising ferrite and martensite, Figure 8.6(b);
c) A free ferrite surface layer with a two phase ferrite/martensite or ferrite/cementite, or three phase ferrite/martensite/cementite core, Figure 8.6(c);
d) A free ferrite surface layer separated from a martensite core by a ferrite/martensite decarburised layer, Figure 8.6(d).

The optical microscopy apparatus used for the measurement of the decarburised structures included:

- The MEASURE LINE function of the Video Pro image analyser for 50 to 1,000x magnification;
- The X- and Y-scale digital verniers of the LECO M-400-H1 Hardness Testing Machine at 100 and 400x magnification.

The decarburisation depths measured by the image analyser were limited to the width of the computer screen for the magnifications used. Consequently, the greater the decarburisation depth, the smaller the magnification at which the decarburised structure can appear on screen, with the maximum screen width being 2mm at 50x magnification. The hardness tester digital verniers have the advantage of allowing measurements to be made up to 25mm along the specimen in the X and Y directions.

Decarburisation measurements were made in accordance with the principles outlined in ASTM B487-85[167], with an absolute measuring accuracy of 0.8µm possible at 1,000x magnification. Measurements were predominantly made using the image analyser. The X and Y scales were calibrated at the various magnifications using a graduated scale with a line spacing of 0.01mm. 12 fields were measured by positioning the optical microscope with the placement pattern of Figure 8.7. Positions 1 to 4 were measured, before the mounted test specimen was removed from the plasticine holder, rotated and re-pressed to allow measurements 5 to 8, and 9 to 12 to be made.

The magnification was chosen where possible to give a field of view 1.5 to 3 times the decarburisation depth. The free ferrite depths can be precisely specified, while the mixed

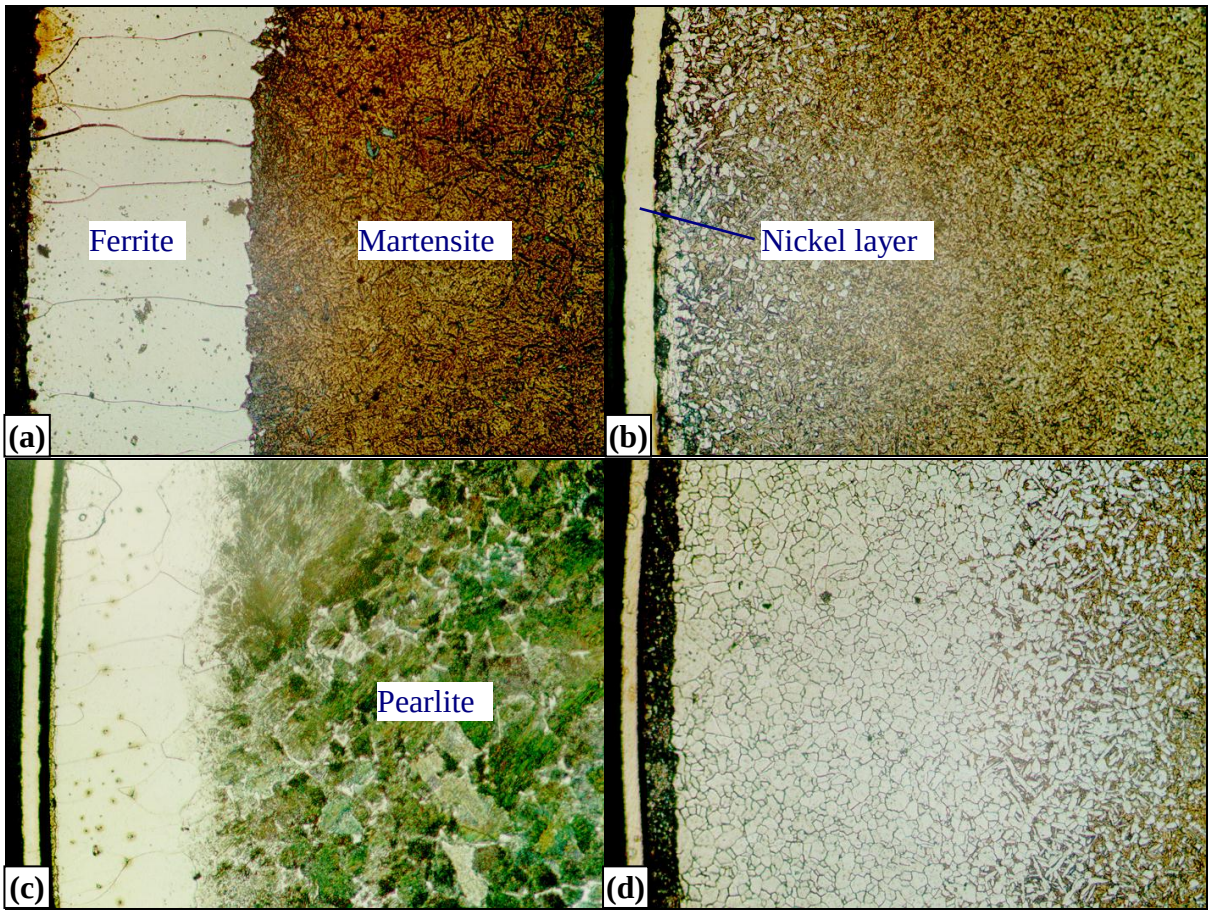

Figure 8.6 Microphotos of decarburised SUP7 furnace cooled initial structures with p_{H_2O} / p_{H_2} =0.05 after (a) 1hr at 820°C, (c) 4hr at 700°C, and a SUP7NV 96hr tempered martensite initial structure austenitised in argon (b) decarburised 12hr at 820°C with p_{H_2O} / p_{H_2} =0.05 and (d) decarburised 12hr at 820°C with p_{H_2O} / p_{H_2} =0.25. 2% Nital etch. 230x magnification.

ferrite/martensite layers are generally less precisely measured due to the subjective operator judgement required to specify where the decarburised layer merged with the core structure. The mean decarburisation depths were calculated, along with the accompanying standard deviation, 95% confidence interval and percent relative accuracy.

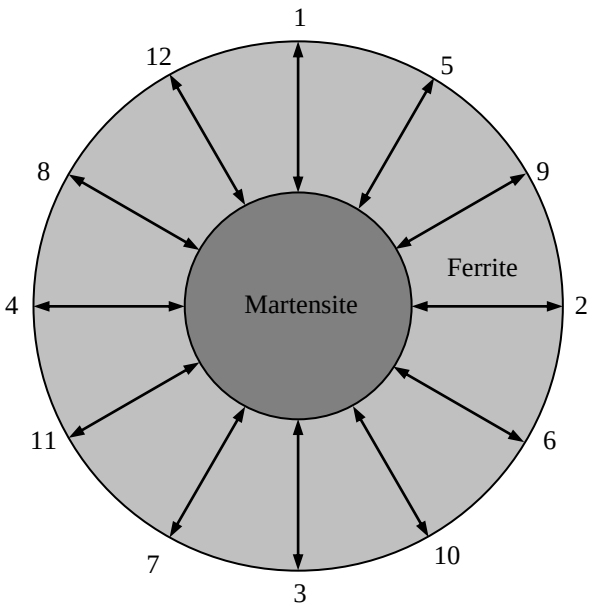

Figure 8.7 Optical microscope placement pattern for decarburisation depth measurements.

8.4.2 Oxidation thickness measurements

Figure 8.8 illustrates the surface oxide structure of a SUP7 specimen decarburised for 24hr at 820°C, with the overplated electroless nickel plated layer also visible. The electroless plating of the nickel layer over the oxide layer(s) forming during decarburisation resulted in sharply defined interfaces between the oxide and nickel layers. 12 measurements were made for each specimen in accordance with ASTM B487-85[167] using the optical microscope pattern of Figure 8.7 at 1,000x magnification, or 2,000x using a 2x enlargement on the optical microscope via the ELVIS program of the image analyser.

8.4.3 Decarburised ferrite grain structures

Two types of grain structures were observed in the free ferrite decarburised region, namely:

a) Columnar ferrite grains;
b) Equiaxed ferrite grains.

The grain size of the columnar structures was measured for the width of the grains[66] by a manual count to determine the number of grain intersections with five horizontal lines parallel to the cross-section surface at 200 to 1,000x magnification. The optical microscope was positioned approximately in the centre of the decarburised columnar microstructure at the appropriate magnification, with the specimen rotated approximately 15 degrees between measurements until more than 500 intersections were counted. Intersections were tallied as recommended by ASTM E112-88[161], with half an intersection counted when the end of the line exactly touched a grain boundary, one for a tangential intersection of the line with the grain boundary, and one and a half intersections for the junction of three grains. For each field measured, the number of ferrite grain boundary intersections per unit length of test lines, $P_{Li}(\alpha)$, was determined from

$$P_{Li}(\alpha) = \frac{P_i(\alpha)}{L_{ti}}, \tag{8.22}$$

where $P_i(\alpha)$ = the number of grain boundaries intersected by the test lines for the i^{th} field;

L_{ti} = the total length of the horizontal test lines for the i^{th} field.

$\bar{P}_L(\alpha)$, the mean number of ferrite grain boundary intersections per unit length of test lines for n fields, was determined from

$$\bar{P}_L(\alpha) = \sum_{i=1}^{n} \frac{P_{Li}(\alpha)}{n}, \tag{8.23}$$

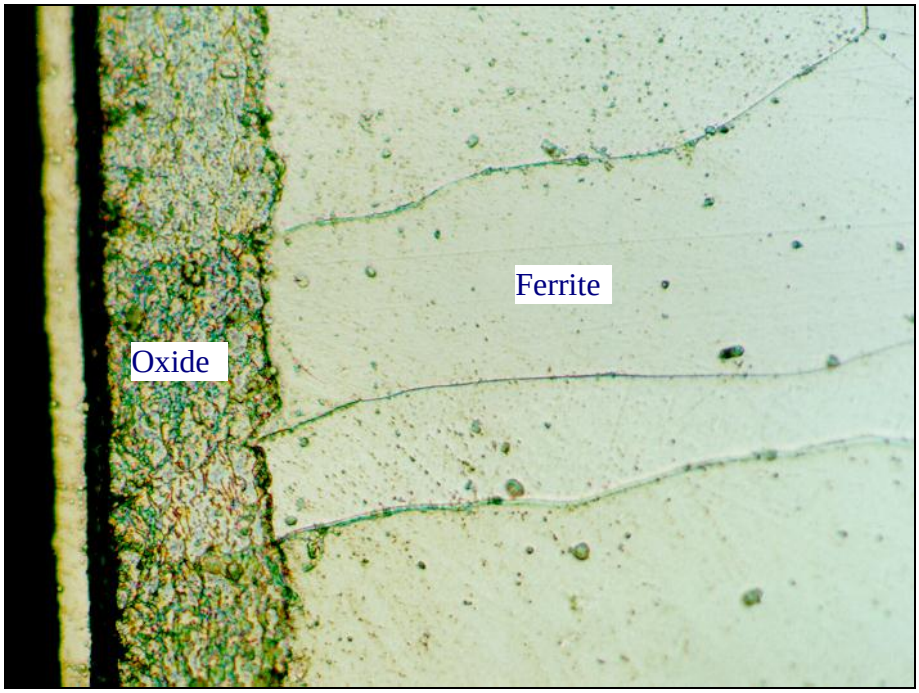

Figure 8.8 Surface oxide structure of a 5mm diameter by 15mm SUP7 furnace cooled specimen decarburised for 24hr at 820°C with prior heating and austenitisation, p_{H_2O} / p_{H_2} =0.25. 2% Nital etch. 575x magnification.

and the mean lineal intercept length of the ferrite grains, $\bar{l}(\alpha)$, from

$$\bar{l}(\alpha) = \frac{1}{\bar{P}_L(\alpha)}. \qquad (8.24)$$

The mean ASTM ferrite columnar grain size, $G_{C\alpha}$, was determined from

$$G_{C\alpha} = [6.643856 Log\, \bar{P}_L(\alpha)] - 3.288, \qquad (8.25)$$

with $\bar{P}_L(\alpha)$ in mm^{-1}. The grain size is rounded off to the nearest tenth unit, with the standard deviation, 95% confidence interval and percent relative accuracy determined from equations 8.4, 8.6 and 8.7.

The equiaxed free ferrite grains of the decarburised structures were measured using a similar method to that for measurement of the prior austenite grain size of Section 8.2.1. A 5cm diameter circle was electronically superimposed over the centre of the decarburised image at the appropriate magnification, the grain boundary intersections with the circle counted, and the specimen rotated 15 degrees until enough fields to tally 500 intersections had been measured. $N_{Li}(\alpha)$, $\bar{N}_L(\alpha)$, $\bar{l}(\alpha)$, s, G_α, $95\%CI$ and $\%RA$ were determined as for the prior austenite grain sizes by equations 8.1 to 8.7.

8.4.4 Energy Dispersive X-Ray Spectrum Analysis of alloying elements

The alloying elements concentrations of the decarburised structures were measured using the JEOL SEM using Energy Dispersive X-Ray Spectrum Analysis by the same method used for the spheroidal cementite structures of Section 8.2.5. The electron beam was positioned on the oxide structures, and at various positions throughout the remainder of the ferrite and martensite phases.

8.4.5 Analysis of infrared gas data

The free ferrite depths measured from the decarburised microstructures obtained during heat treatments at the Ac_3 temperatures for the respective steels can be compared with those calculated from the carbon monoxide, carbon dioxide and methane gas concentrations evolved during decarburisation. Figure 8.9 illustrates the carbon monoxide and carbon dioxide gas concentration data measured as a function of time using the Sekonic three-pen chart recorder. The methane concentrations detected were negligible, although the sensitivity of the methane infrared gas analyser was insufficient for low vppm measurements.

The data of Figure 8.9 can be converted into gas concentration through the use of equations 7.5 to 7.7, with the pen recorder height measured directly off the chart. With a recorder chart speed of 600mm/hr for the first 15min, and 60mm/hr thereafter, the gas concentration at various heat treatment durations can be obtained from the pen recorder chart. The decarburisation gas composition as a function of time for carbon monoxide and carbon dioxide are illustrated in Figure 8.10. Higher order polynomial curves were fitted to the data points of Figure 8.10.

The average concentration for each gaseous constituent over a period of time was calculated by the integration of the respective polynomial curves fitted to the experimental data points. The four-term Gauss Quadrature integration formula is used to give an exact integral for the sixth order polynomial curves[168], with the integration formula for

$$I = \int_A^B f(x)dx \tag{8.26}$$

given by

$$I = (B-A)\{0.1739274226[f(x_1)+f(x_2)]+0.3260725775[f(x_3)+f(x_4)]\}, \tag{8.27}$$

where $x_1 = 0.0694318442B + 0.9305681558A;$

$x_2 = 0.9305681558B + 0.0694318442A;$

$x_3 = 0.3300094782B + 0.6699905218A;$

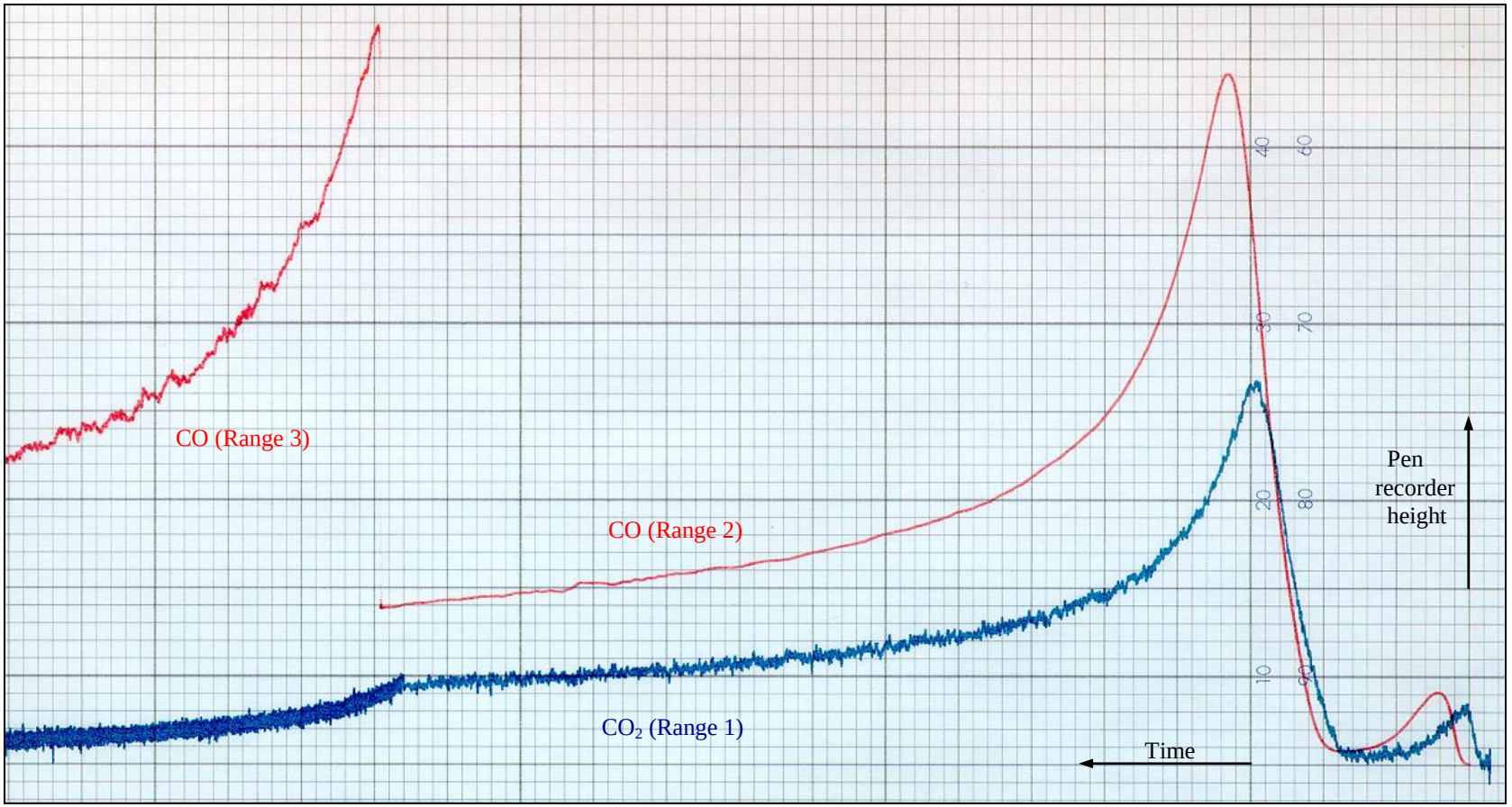

Figure 8.9 Pen recorder data for carbon monoxide and carbon dioxide gases evolved during decarburisation of a 5mm diameter x 50mm SUP7 air cooled specimen at 820°C with p_{H_2O} / p_{H_2} =0.05.

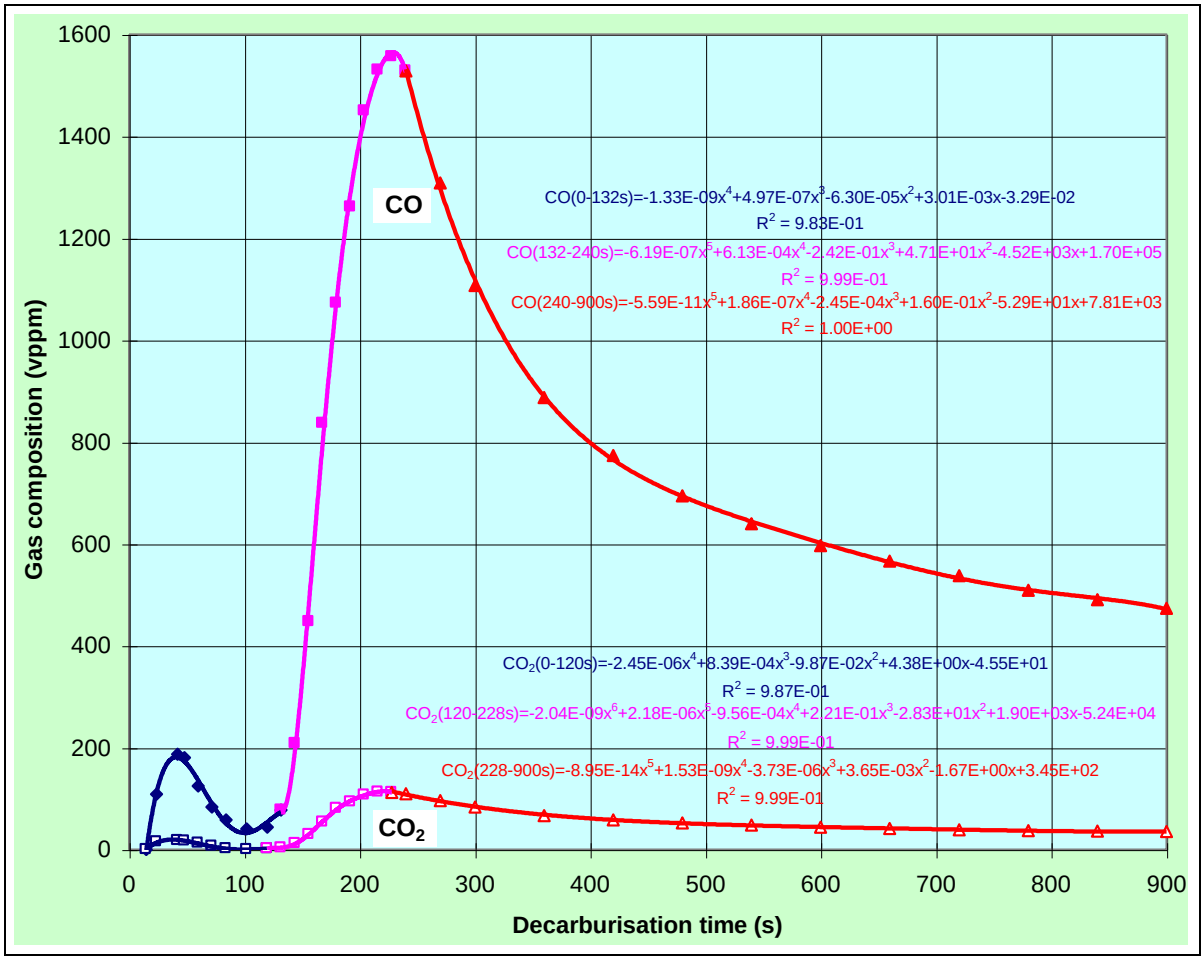

Figure 8.10 Carbon monoxide and carbon dioxide gas compositions during decarburisation of a 5mm diameter x 50mm SUP7 12hr tempered martensite initial structure for the first 15min at 820°C with p_{H_2O} / p_{H_2} =0.05.

$$x_4 = 0.6699905218B + 0.3300094782A.$$

The mean gas composition in volume %, $\bar{C}_{gas}$, is obtained from equation (8.28) by

$$\bar{C}_{gas} = \frac{I}{t_d}, \tag{8.28}$$

where t_d = decarburisation time in s.

The volume of gas evolved over an interval of time, V_{gas}, is given by

$$V_{gas} = \frac{\dot{V} t_d \bar{C}_{gas}}{100}, \tag{8.29}$$

where V_{gas} = volume of gas liberated in cm^3;

$\dot{V}$ = decarburisation atmosphere gas flow rate.

The mass of gas evolved, m_{gas}, is given by

$$m_{gas} = \frac{\rho_{gas} V_{gas}}{1000}, \tag{8.30}$$

where m_{gas} = mass of gas evolved in g;

ρ_{gas} = density of gas - 1.25kg/m^3 for carbon monoxide, 1.98 kg/m^3 for carbon dioxide. 0.72kg/m^3 for methane[169].

Equation 8.31 yields the moles of gas evolved,

$$n_{gas} = \frac{m_{gas}}{Mr_{gas}}, \tag{8.31}$$

where n_{gas} = moles of gas evolved;

Mr_{gas} = molecular mass of gas; 28g/n for carbon monoxide, 44g/n for carbon dioxide and 16g/n for methane.

Decarburisation occurs by the reactions quoted in Chapter 3, where

$$[C] + 2H_2(g) = CH_4(g) \qquad (3.1)$$

$$[C] + H_2O(g) = CO(g) + H_2(g) \qquad (3.3)$$

$$CO(g) + H_2O(g) = CO_2(g) + H_2(g) \qquad (3.4)$$

From equations 3.3 and 3.1, one mole of carbon reacts to form one mole of carbon monoxide or one mole of methane, and for carbon monoxide and methane

$$n_{CO}, n_{CH_4} = n_C, \qquad (8.32)$$

where n_{CO}, n_{CH_4} = the number of moles of carbon monoxide and methane evolved;

n_C = the number of moles of carbon removed during decarburisation.

For carbon dioxide, one mole of carbon monoxide reacts to form one mole of carbon dioxide by equation 3.4. Therefore, some of the carbon monoxide produced by equation 3.3 is consumed by equation 3.4 when forming carbon dioxide, where

$$n_{CO_2} = n_C, \qquad (8.33)$$

where n_{CO_2} = the number of moles of carbon dioxide evolved.

n_{CO}, n_{CO_2} and n_{CH_4} can be calculated from the infrared gas analysis data, such as Figure 8.10, by following the calculations of 8.26 through 8.31. This gives

$$n_C(total) = n_{CO} + n_{CO_2} + n_{CH_4}, \qquad (8.34)$$

where $n_C(total)$ = total number of moles of carbon removed during decarburisation.

The mass of carbon removed in the decarburisation gas, m_C, is given by

$$m_C = n_C(total)\,Mr_C, \tag{8.35}$$

where m_C = mass of carbon removed in g;

Mr_C = molecular mass of carbon, 12g/n.

Carbon removal at the Ac_3 temperature results in the formation of a ferrite layer on the surface of an initially austenitic structure, with a sharp interface between the ferrite and austenite. The carbon concentration profile for this situation is illustrated in Figure 8.11, assuming a linear carbon concentration profile in the ferrite[99]. This differs slightly from the concentration profiles illustrated in Figure 3.2, which are based on diffusion controlled decarburisation. However, since the ferrite saturation carbon concentrations are small in comparison with the Ac_3 austenite carbon concentrations, the ferrite concentration profile can be approximated by a linear relationship. Assuming that the only decarburisation corresponds to that removed to yield ferrite from the initially austenitic microstructure, the volume of steel over which carbon is removed, V_{steel}, is given by

$$V_{steel} = \frac{(m_C)(100)}{(\rho)(\%\text{C removed})}, \tag{8.36}$$

where V_{steel} = volume of steel over which carbon is removed in cm^3;

ρ = density of steel[170], 7.833g/cm^3;

%C removed = austenite carbon concentration – mean ferrite carbon concentration, in wt.%.

Figure 8.11 illustrates that the mean ferrite carbon concentration equals $C_{sat}/2$. The value of C_{sat} is temperature dependent, and so changes as a test specimen heats to temperature following insertion into the furnace hot zone. However, given the low values of C_{sat} compared

to the Ac_3 austenite carbon concentrations, and that the specimen heats to temperature within minutes, a value of C_{sat} corresponding to that for the different silicon steels at their respective Ac_3 temperatures can be assumed.

The core of a test specimen will transform fully to austenite after a certain period of time has elapsed following insertion of the specimen into the furnace hot zone. At this stage the austenite carbon concentration will correspond to the bulk steel content. However, carbon removal at shorter test durations will occur from two or three phase core structures, with austenite carbon concentrations not necessarily corresponding to the bulk steel value. The influence of intermediate transformation structures on the difference between the measured free ferrite depths, and those calculated with an austenite carbon concentration corresponding to the bulk steel content, will depend on the rate of transformation of the initial structure to austenite, and the difference in the intermediate austenite carbon contents relative to the bulk steel value.

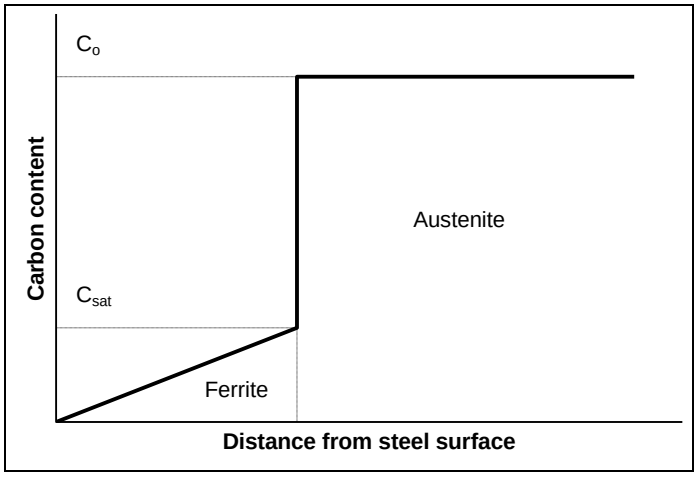

Figure 8.11 Carbon concentration profile in ferrite and austenite for decarburisation at the Ac_3 temperature.

The volume of steel over which carbon is removed is equal to

$$V_{steel} = \pi(R_o^2 - R_i^2)L(\text{C.F.}), \tag{8.37}$$

where R_o = original radius of test specimen in cm;

R_i = radius of austenite core after decarburisation in cm;

L = length of test specimen in cm;

C.F. = correction factor.

Figure 8.12 schematically illustrates carbon removal from along the length and the two ends of a test specimen. The correction factor of equation 8.37 is necessary to account for:

- The finite size of the test specimens, where carbon removal occurs from the ends, as well as from along the length;
- The changing surface area of the austenite core due to the inwards motion of the ferrite/austenite interface with the austenite to ferrite transformation upon carbon removal at the Ac_3 temperature.

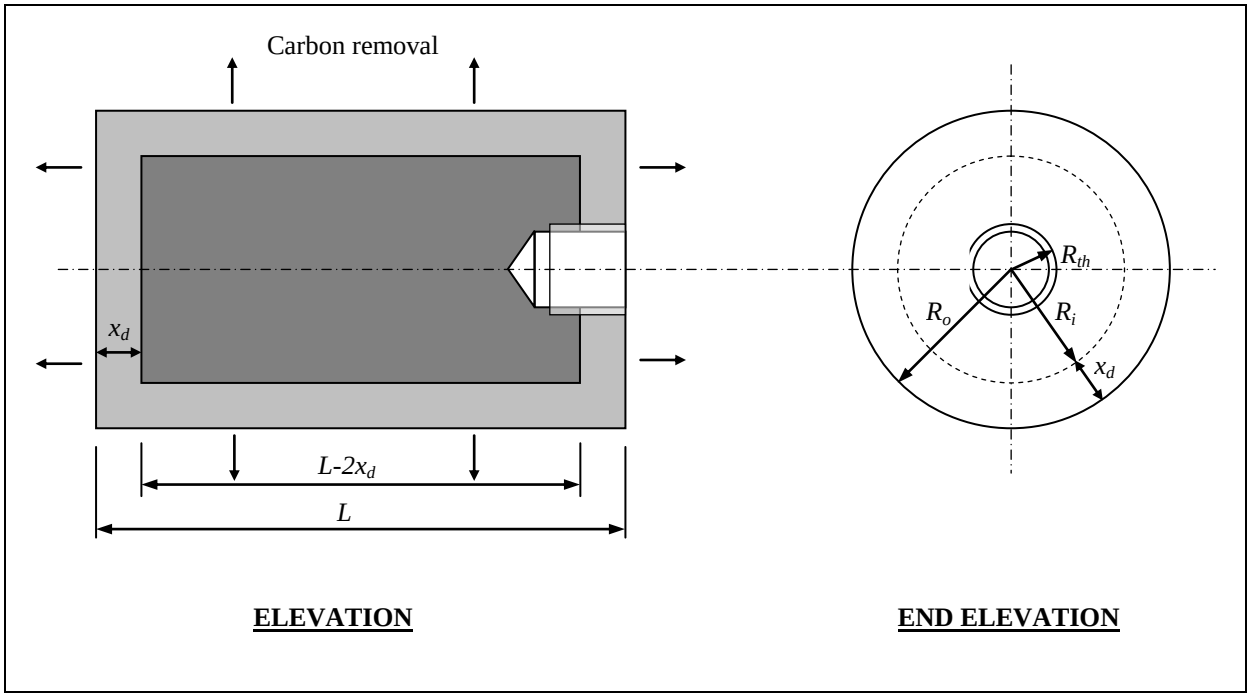

Figure 8.12 Schematic illustration of the cross-section for a test specimen at an intermediate stage of decarburisation at the Ac_3 temperature.

The correction factor can be defined as

$$\text{C.F.} = \frac{\text{Total surface area of the austenitic structure}}{\text{Austenitic surface area along the test specimen length}}. \qquad (8.38)$$

Assuming that the free ferrite layer depth is constant over the whole test specimen, the correction factor can be calculated from

$$\text{C.F.} = \frac{(2R_o - 2x_d)(L - 2x_d) + (R_o - x_d)^2 + (R_o - x_d)^2 - R_{th}^2}{(2R_o - 2x_d)(L - 2x_d)}; \qquad (8.39)$$

where x_d = the decarburisation depth in cm;

R_{th} = the radius of the threaded hole in cm.

Figure 8.13 illustrates the variation of correction factor with decarburisation depth for the different cylindrical test specimens. Rearranging equation 8.37 yields

$$R_i = \sqrt{R_o^2 - \frac{V_{steel}}{(\pi l)(\text{C.F.})}}, \qquad (8.40)$$

with the decarburisation depth, x_d, given by

$$x_d = R_o - R_i. \qquad (8.41)$$

For equation 8.40, a correction factor corresponding to no free ferrite was used as an initial estimate to calculate R_i, and therefore x_d. The correction factor obtained from the calculated value of x_d was then substituted back into equation 8.40 to calculate a more precise value of x_d. This iteration is repeated until

$$\left|\frac{x_d(i) - x_d(i-1)}{x_d(i)}\right|.100 \le 0.01, \qquad (8.42)$$

where $x_d(i)$ = the decarburisation depth for the i^{th} iteration in mm;

$x_d(i-1)$ = the decarburisation depth for the $(i\text{-}1)^{th}$ iteration in mm.

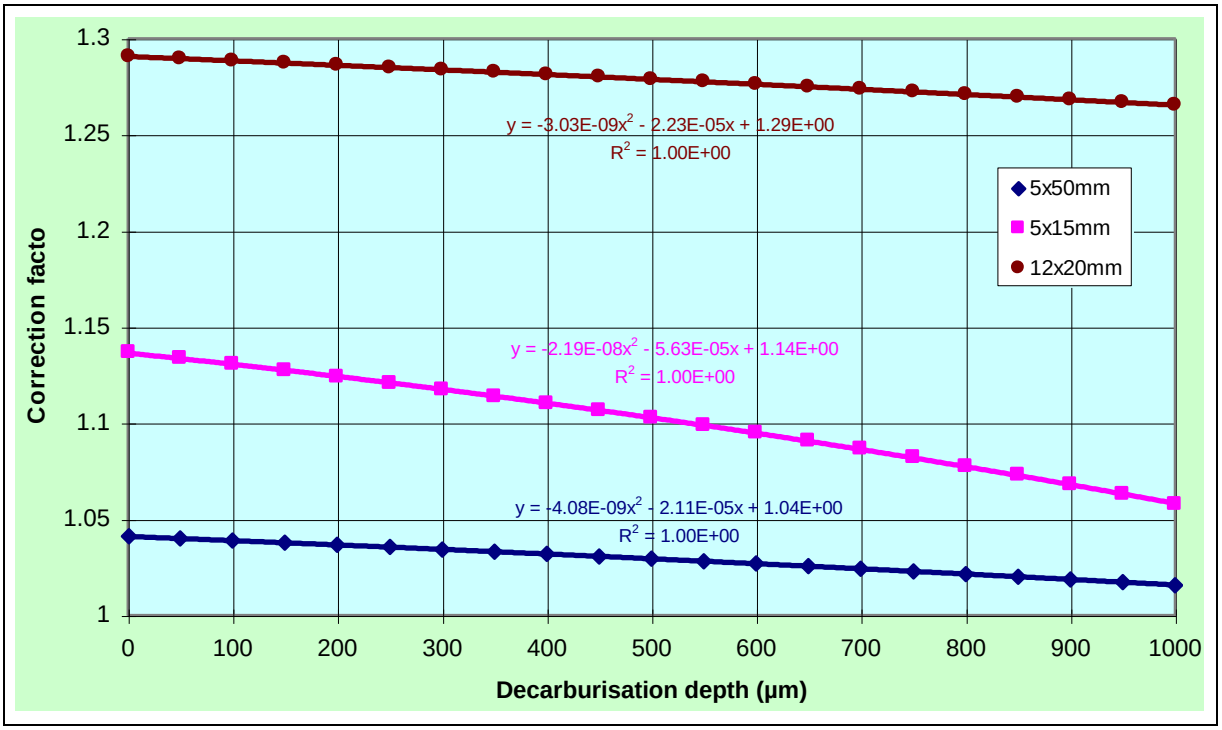

Figure 8.13 Variation of correction factor with decarburisation depth for different cylindrical test specimens.

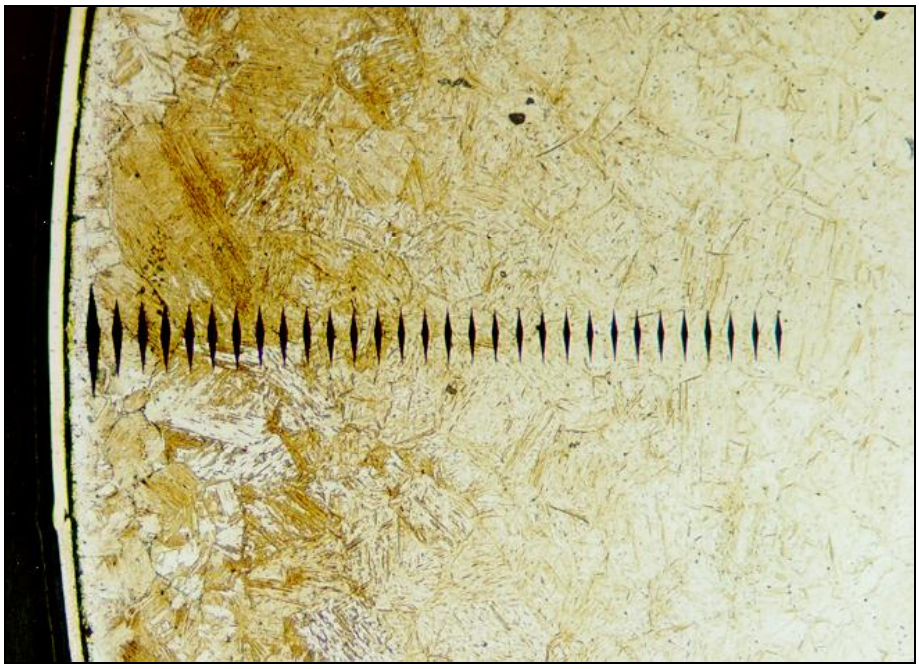

Figure 8.14 Microindentation profile for a 5mm diameter x 50mm 0% Silicon furnace cooled initial structure decarburised for 4hr at 900°C with p_{H_2O} / p_{H_2} =0.05. 115x magnification. 2% Nital etch. Load =200g, *t*=10s.

8.4.6 Microhardness profiles

Microhardness indentation profiles were made across the ferrite and martensite phases of specific decarburised specimens using the LECO Hardness Testing Machine. A Knoop indenter was used, with the indentations positioned at 25µm intervals from the oxide/steel and ferrite/martensite interfaces inwards. 50 and 200g loads were used for the ferrite and martensite phases respectively. At these loads, a 25µm spacing corresponds to at least 2.5 times that of the diagonal length of the indenter perpendicular to the surface, as recommended by ASTM E1077-91[156]. Figure 8.14 illustrates the indentation profile across the martensite for the 0% Silicon steel decarburised at 900°C. The specimens were lightly etched in 2% Nital, with a 10s load application time. Four indentation traverses were made for each specimen at different points around the specimen, with the indentations measured at 400x magnification.

This chapter described the analytical techniques used to determine the structural and physical properties of the austenitised and decarburised test specimens. Chapter 9 details the results of austenitisation investigation, while Chapters 10 and 11 are concerned with the decarburisation results obtained. Chapters 12 and 13 detail the conclusions and recommendations for future research.

CHAPTER 9

AUSTENITISATION HEAT TREATMENTS

9.1 Introduction

Five different steels comprising silicon contents of 0 to 3wt.% were austenitised at various temperatures for test durations ranging from 30s to 192hr. The heat treated specimens were mounted, ground, polished, and etched to reveal the microstructures present. Image analysis, in conjunction with scanning electron microscopy, was used to determine the stereological properties of these microstructures. Energy dispersive analysis was used to determine the microalloy contents within the various phases.

These heat treatments and analytical techniques allowed the mechanisms controlling the nucleation and growth of austenite from a variety of initial structures comprising ferrite and cementite to be investigated. The decarburisation investigation of these steels requires knowledge of the processes through which carbon becomes available for diffusion, with this knowledge obtainable from the austenitisation investigation. The influence of the heat treatment temperature, initial structure, and alloy content on the austenite transformation, and concurrent ferrite and cementite dissolution, are detailed in this chapter.

9.2 Preliminary experimentation

9.2.1 Determination of transformation temperatures

The theoretical Ac_1 and Ac_3 transformation temperatures listed in Table 7.3 were determined from the formulae of Andrews[102]. For SUP7, the Ac_1 and Ac_3 temperatures of 774 and 844°C respectively calculated from these formulas are higher than the experimentally determined values of 743 and 816°C for a SAE 9260* steel[152]. An accurate knowledge of the transformation temperatures is required, where the temperatures calculated from the formulae

* SUP7 and SAE 9260 have similar experimental compositions.

of Andrews[102] can differ by ±25°C[102].

Dilatometry is commonly used[164,171] to determine the Ac_1 and Ac_3 temperatures, with a heating rate of 2°C typical. A Griffin 555-180-185 Dilatometer was used to determine the Ac_1 and Ac_3 temperatures of SUP7, with a heating rate of approximately 2°C/min utilised. Four specimens were used, with a typical dilatometry curve illustrated in Figure 9.1. The Ac_1 and Ac_3 temperatures were determined from the inflections on the curve during heating, and yielded an average Ac_1 temperature of 755 ± 5°C, and an average Ac_3 temperature of 830 ± 5°C.

Ideally the equilibrium values Ae_1 and Ae_3 which correspond to the equilibrium transformation temperatures for the start and finish of ferrite to austenite transformation would be determined. Dilatometric methods which yield the Ac_1 and Ac_3 temperatures during heating tend to yield values higher than the true Ae_1 and Ae_3 equilibrium temperatures[172]. At slower heating rates, the Ac_1 and Ac_3 temperatures more closely approximate the equilibrium temperatures[173]. Grange[173] found that the Ae_3 temperatures for a variety of steels were on average 12°C higher than the predicted equilibrium values for a heating rate of 2°C/min.

An alternative approach to determining the transformation temperatures involves holding specimens at each of a series of constant temperatures for varying periods of time up to several hours, or at least until doubling the holding time results in no appreciable change in the amount of austenite formed. This is followed by a quench to room temperature[173]. The Ac_1 transformation temperature is taken as that temperature at which a "trace amount" of austenite forms in the ferrite matrix, and does not increase perceptibly in amount while the heating time is doubled[173]. The Ac_3 temperature corresponds to the maximum temperature at which a barely detectable amount of ferrite can exist in a hypoeutectoid steel[164].

Consequently, the SUP7 Ac_1 and Ac_3 temperatures were determined by holding the test specimens for 24hr at the dilatometrically determined temperatures, followed by a water quench. Different temperatures were then tried until the transformation temperatures were obtained. Martensitic specimens formed by quenching were used to determine the Ac_1 temperature, as it was observed during preliminary experimentation that austenite formation was faster in martensitic structures than pearlitic structures around the Ac_1 temperature.

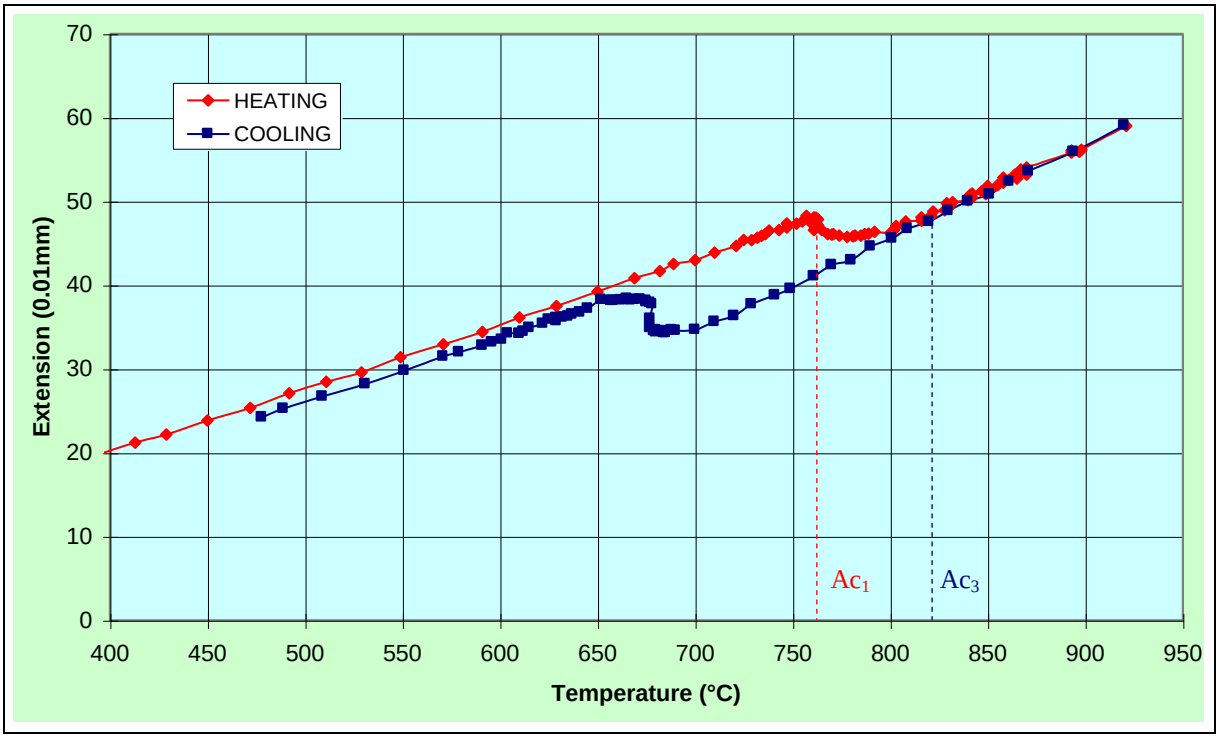

Figure 9.1 Dilatometry curves for heating and cooling of SUP7 at 2°C/min.

However, specimens with a fine pearlitic structure were used to determine the Ac_3 temperatures, as it was also observed during preliminary experimentation that pearlitic structures transformed faster than martensitic structures at temperatures around the Ac_3 value.

Typical examples of microstructures obtained for temperatures close to the Ac_1 and Ac_3 temperatures for SUP7 are illustrated in Figure 9.2. The Ac_1 and Ac_3 temperatures were determined to an accuracy of ± 5°C, and are listed in Table 9.1. The Ac_1 and Ac_3 temperatures determined by the dilatometric method are approximately 10°C higher than that of the microscopically determined values. The temperatures obtained by the microscopic method were taken as closer to true equilibrium than those of the dilatometric method and formulae of Andrews[102], due to the closer agreement between the values determined by this method with the values given for a SAE 9260 steel[152] relative to the other methods. Consequently the Ac_1 and Ac_3 transformation temperatures were determined by the microscopic method for the 0% Silicon, 1% Silicon, SUP7NV and 3% Silicon steels. The initial temperatures used to determine the Ac_1 and Ac_3 temperatures were calculated from the formula of Andrews[102]. Different temperatures were then used until the transformation temperatures were determined. These transformation temperatures are listed in Table 9.1.

Table 9.1 Ac_1 and Ac_3 temperatures determined by the microscopic method.

DESCRIPTION	Ac_1 temperature (°C)	Ac_3 temperature (°C)
0% SILICON	706	740
1% SILICON	728	760
SUP7	745	820
SUP7NV	748	820
3% SILICON	770	835

9.2.2 Initial microstructures

The preliminary experimentation was undertaken with SUP7. A range of six initial SUP7 microstructures were produced by a variety of heat treatments. Two pearlitic structures of different coarseness were produced by air cooling, Structure A, and furnace cooling, Structure B, respectively, with the furnace cooled structure having a coarser lamellar structure than the

air cooled structure. Scanning electron microscope photos of these two microstructures are illustrated in Figures 9.3(a) and (b) respectively. The structures produced by the two tempered martensite heat treatments comprised elongated ferrite structures with the majority of the cementite particles located on the ferrite grain boundaries, Figures 9.3(c) and (d) respectively.

These carbide particles were identified as cementite, since the iron composition of the particles analysed by energy dispersive spectroscopy were consistent with that of cementite. The cementite carbon content was not determined during this quantitative analysis. However, element totals of approximately 7wt.% lower than 100 indicate the presence of a low mass number element, which was thought to be carbon. Variations from the stoichiometric 92.3wt.%Fe:6.7wt.%C composition of cementite arose from the partitioning of other alloying elements to the cementite particles. No other types of carbides were detected for any of the steels at any stage in the heat treatments. However, these carbides could have been present if they were smaller than the minimum analysed particle size of 1μm.

The 96hr tempered martensite microstructure, Structure D, had a coarser grain structure and cementite particle size than the 12hr tempered martensite structure, Structure C. The mean ferrite effective grain size was determined to be 3.8±0.2μm for Structure D. The ferrite grain boundaries of the other SUP7 spheroidal cementite initial structures, and for the other steels, did not etch well enough for the effective ferrite grain size to be determined. Structure D also had a more equiaxed ferrite grain structure than Structure C. A small graphite fraction was present in the 96hr tempered martensite structure.

A further type of spheroidal cementite initial structure, comprising an equiaxed ferrite grain structure with the majority of the cementite particles located within the ferrite grains, was desired. This type of structure is often produced by a high temperature transformation of inhomogeneous austenite[37]. A fundamental difference exists between this structure and that produced by tempering martensite, with the latter having an elongated ferrite grain structure with the cementite particles predominantly located on the ferrite grain boundaries.

Some difficulty arose in trying to produce the desired inhomogeneous austenite structure. Several heat treatments similar to that undertaken by Nehrenberg[37] for a range of steels were attempted. This involved austenitising and water quenching, followed by combinations of heat

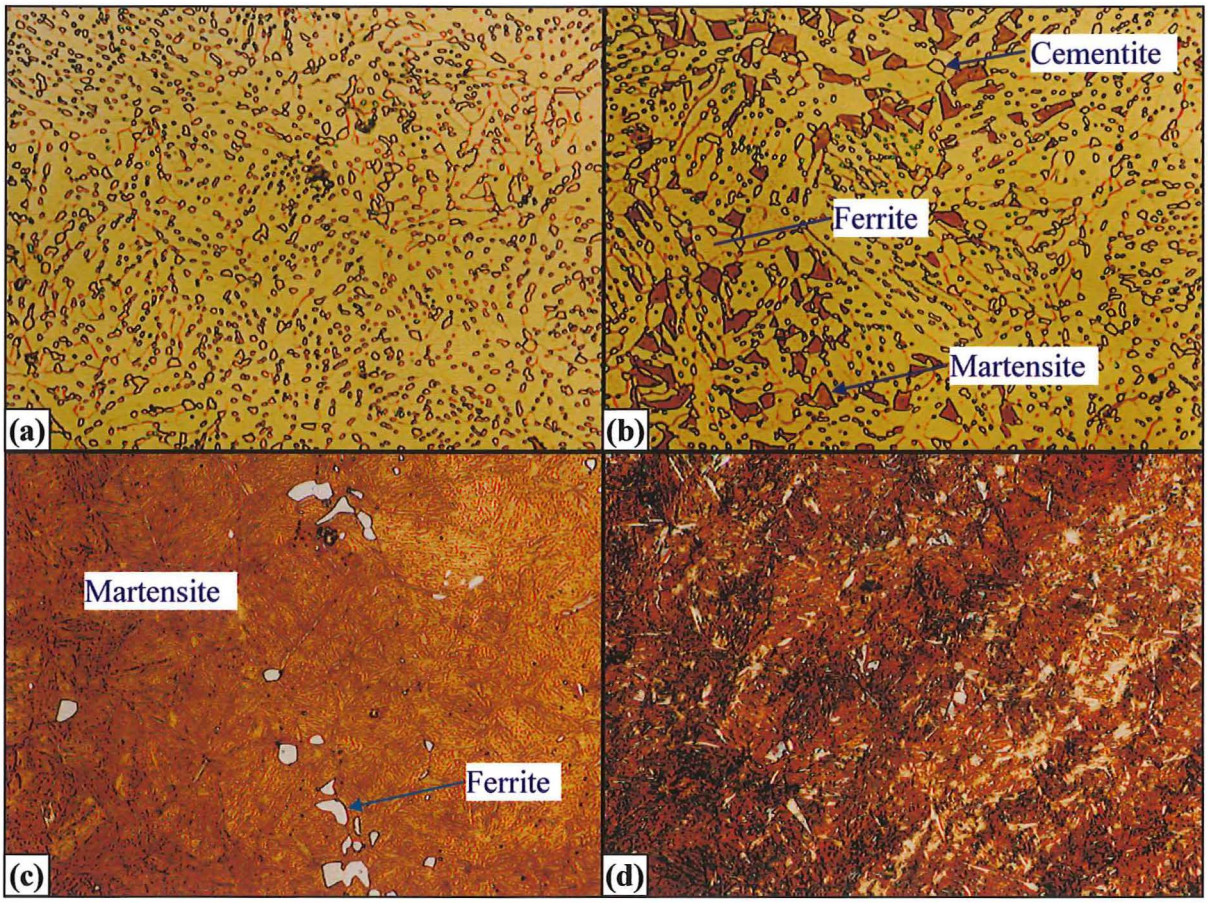

Figure 9.2 Microstructures obtained during determination of the Ac_1 SUP7 temperature of 745°C at (a) 743°C, (b) 748°C, and during the determination of the Ac_3 SUP7 temperature of 820°C at (c) 818°C, (d) 820°C. 1,150x magnification. 2% Nital etch.

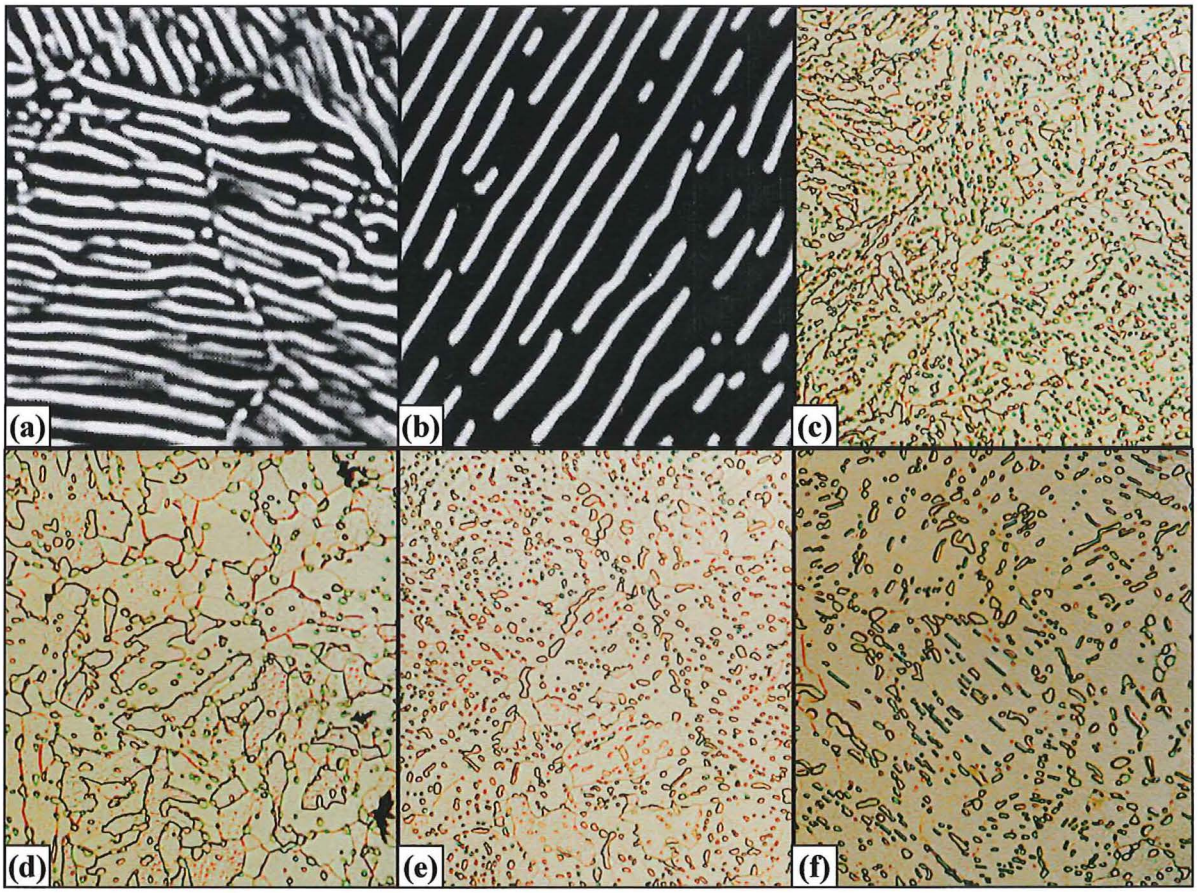

Figure 9.3 The six initial SUP7 microstructures produced by (a) air cooling-Structure A (10,000x), (b) furnace cooling-Structure B (10,000x), (c) tempering martensite for 12hr at 735°C-Structure C (1,150x), (d) tempering martensite for 96hr at 735°C-Structure D (1,150x), (e) via austenite-Structure E (1,150x), and (f) an intercritical heat treatment-Structure F (1,150x). 2% Nital etch.

treating between the Ac_1 and Ac_3 temperatures, cooling and prolonged holding at a temperature below the Ac_1 temperature, a slow furnace cool to about 700°C, and then air cooling. The most successful heat treatment was that used to produce Structure E of Figure 9.3(e), with the heat treatment detailed in Table 7.4. However, the ferrite grains of this microstructure were still elongated, with a considerable fraction of the cementite particles located on the ferrite grain boundaries.

Mehl[174] observed that pearlite tended to nucleate throughout the austenite grains in heterogeneous austenite containing undissolved carbides, and on the austenite grain boundaries for homogeneous austenite. Inhomogeneous austenite can be obtained by austenitising at temperatures close to the Ac_1 value, or for short periods of time, due to the incomplete dissolution of the carbides[13]. Spheroidal carbides are then obtained upon cooling, instead of the lamellar carbides produced from higher austenitisation temperatures.

Payson[175] obtained equiaxed ferritic structures with spheroidal cementite particles located within the ferrite grains by heat treating an initially pearlitic structure. This heat treatment involved a subcritical anneal for 2hr at just below the Ac_1 temperature, an intercritical anneal of 1hr at just above the Ac_1 temperature, and a prolonged subcritical anneal at just below the Ac_1 temperature. The heat treatment was completed by cooling in air. Payson[175] demonstrated that the temperature band above and below the Ac_1 temperature for the intercritical and subsequent prolonged subcritical heat treatments that gave predominantly spheroidal carbides, instead of lamellar carbides, was limited for steels containing 0.3 to 0.7wt.% carbon. The formation of a spheroidal cementite product was aided by a subcritical anneal prior to the intercritical anneal.

Consequently the intercritical heat treatment used to produce Structure F, Table 7.4, with an equiaxed ferrite grain structure and cementite particles located predominantly within the ferrite grains, was achieved by:

a) Austenitising above the Ac_3 temperature, and air cooling to room temperature to produce a pearlitic structure;
b) A subcritical anneal at just below the Ac_1 temperature;
c) An intercritical anneal above the Ac_1 temperature;

d) A prolonged subcritical anneal at just below the Ac_1 temperature;
e) A prolonged furnace cool;
f) Air cooling to room temperature.

An optical microscope photo of Structure F is illustrated in Figure 9.3(f). Some cementite particles were still present on the ferrite grain boundaries, which was indicative of an intercritical heat treatment at a temperature too high above the Ac_1 temperature. Furnace cooled, 96hr tempered martensite and intercritical structures for the 0% Silicon, 1% Silicon, SUP7NV and 3% Silicon steels were produced by the heat treatments detailed in Table 7.4. The 1% Silicon furnace cooled structure was coarser than the 0% Silicon steel, as illustrated in Figures 9.4(a) and (b) respectively. Both SUP7 and SUP7NV exhibited similar furnace cooled structures.

The formation of graphite became significant for the 3% Silicon steel due to the higher silicon content. This is illustrated in Figure 9.4(c), with the graphite having a grey rosette structure. Areas of higher graphite concentrations were associated with very few cementite particles, due to the 100wt.%C content of graphite denuding the areas surrounding the graphite particles of carbon, while areas devoid of graphite had a predominantly pearlitic structure, Figure 9.4(d). It was observed that the graphite particles were located on grain boundary triple points. SEM energy dispersive analysis was undertaken for these graphite particles, with the results presented in Table 9.2. The low alloy totals indicate that the majority of the particles were comprised of a low atomic mass number element, presumably carbon.

Table 9.2 Energy dispersive analysis of graphite particles for the 3% silicon steel furnace cooled initial structure.

Spectrum	Fe (wt.%)	Si (wt.%)	Mn (wt.%)	Cr (wt.%)	TOTAL (wt.%)
1	6.6	0.6	0.8	0	8.2
2	15.0	0.7	0	0	15.8
3	8.7	0.5	0	0	9.3
4	8.2	0.4	0	0	8.7
5	3.4	0.2	0	0	3.7
6	18.5	0.6	0	0	19.2
7	14.5	0.6	0	0	15.2

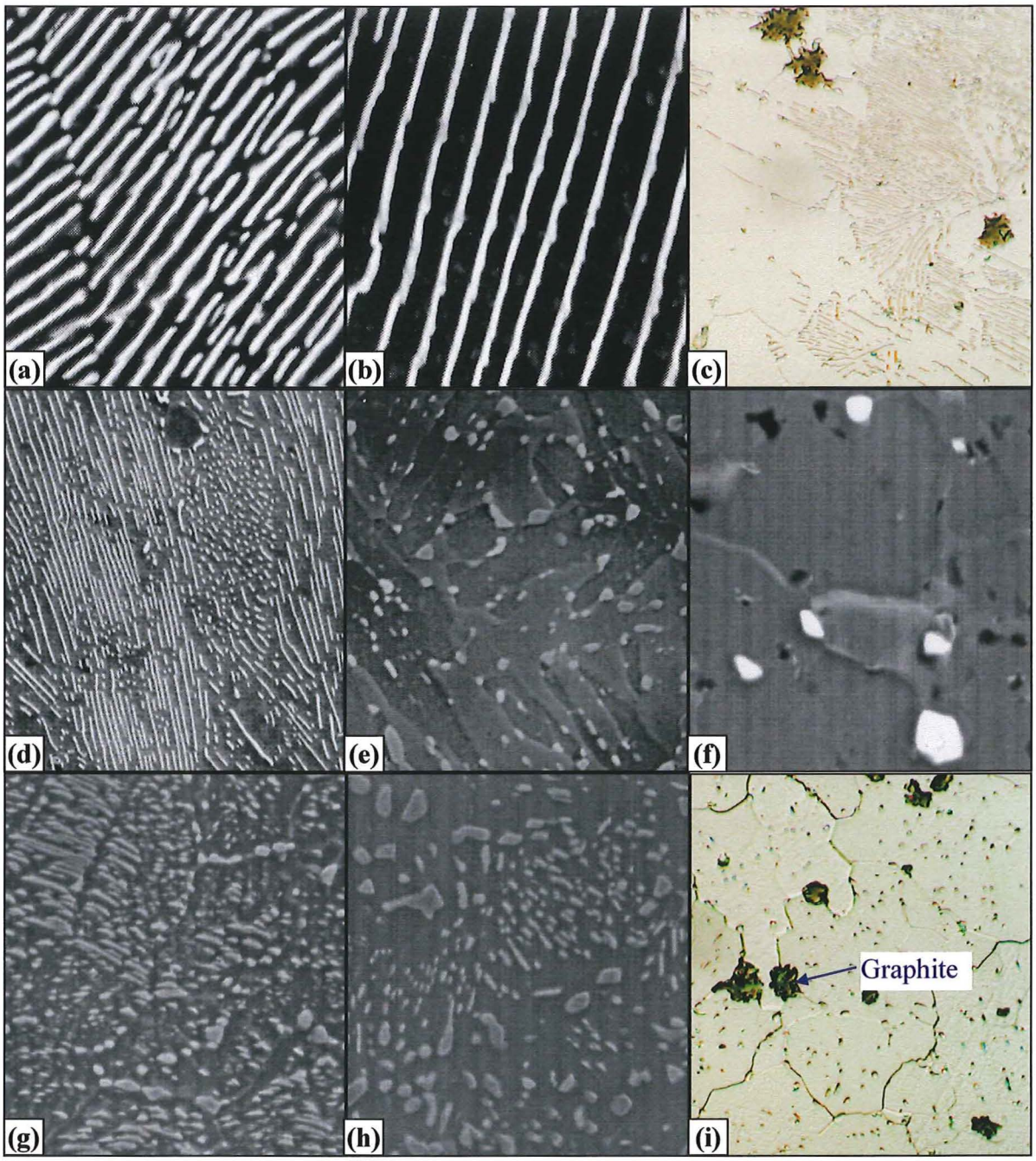

Figure 9.4 Initial austenitisation microstructures produced by furnace cooled (a) 0% Silicon (10,000x), (b) 1% Silicon (10,000x), (c) 3% Silicon (1,150x), (d) 3% Silicon (2,000x), produced by 96hr tempered martensite for (e) 0% Silicon (2,500x), (f) 3% Silicon (5,000x), and by an intercritical heat treatment of (g) 0% Silicon (2,500x), (h) 1% Silicon (2,500x), and (i) 3% Silicon (1,150x). 2% Nital etch.

Olen[176] found that graphite nucleated on small silica particles in a 0.54wt.%C/2.84wt.%Si steel. The graphite nuclei were surrounded by a ferritic volume denuded of cementite, through which carbon diffuses from the cementite particles to facilitate the growth of the graphite particles. Once critically sized graphite nuclei existed, graphitisation continued to completion at temperatures below the Ac_1 temperature[177-181].

The 96hr tempered martensite microstructure of the 0% Silicon steel was also finer than that of the higher silicon steels. This structure comprised elongated ferrite grains with the majority of the cementite particles located on the ferrite grain boundaries, Figure 9.4(e). The 96hr tempered martensite initial microstructures for the 1% Silicon, SUP7 and SUP7NV steels were similar. However, the 3% Silicon steel possessed a low cementite fraction on equiaxed ferrite grain boundaries, Figure 9.4(f). A considerable fraction of graphite particles, which were significantly finer than those of the furnace cooled structure, were also present.

Not all of the cementite particles of the 0% Silicon intercritical initial structure were spheroidal, with a significant fraction of undissolved lamellar cementite present, Figure 9.4(g). However, the majority of the cementite was observed to be present within the ferrite grains. The cementite particles of the intercritical initial structures for the 1% Silicon, SUP7 and SUP7NV steels were coarser and more spheroidal than those of the 0% Silicon steel. Figure 9.4(h) illustrates the 1% Silicon intercritical structure. The 3% Silicon intercritical structure comprised a significant graphite fraction located on the equiaxed ferrite grain boundary triple points, Figure 9.4(i). Predominantly spheroidal cementite particles were also present within the ferrite grains, although the cementite fraction was considerably lower than that of the lower silicon intercritical steel structures. The lower cementite fractions of the tempered martensite and intercritical 3% Silicon structures relative to the lower silicon steels were due to the carbon associated with the graphite.

9.2.3 Quantitative description of the initial microstructures

For initial ferrite/cementite microstructures, the cementite dispersion and the ferrite grain size must be considered. In pearlitic structures, the mean true pearlite interlamellar spacing may be taken as a measure of the cementite dispersion. The size and size distribution of the cementite particles in spheroidised structures quantifies the cementite dispersion. The ferrite grain size

has no precise meaning for pearlitic or spheroidised initial sturctures[43]. Attempts were made to measure the prior austenite grain size of the different silicon steels water quenched from the heat treatment temperature after 12hr at 900°C. However, only the prior austenite grain boundaries of the 0% Silicon steel were sufficiently well defined upon etching for the prior austenite grain size to be determined, which was 50±3μm.

The pearlite mean true interlamellar spacings of the air and furnace cooled pearlitic structures of the different steels, determined by the method of Section 8.2.2, are illustrated in Figure 9.5. The interlamellar spacing increased with increasing silicon content, from 0.18μm for the 0% Silicon steel to 0.52μm for the 3% Silicon steel. For the 3% Silicon steel, only predominantly pearlitic areas were chosen for the determination of the interlamellar spacing. As the 3% Silicon structure comprised a considerable fraction of graphite rich areas, specification of the interlamellar spacing only applies to the pearlitic areas of the structure. The increase in pearlite interlamellar spacing with silicon content was due to the higher Ac_3 temperatures from which the austenite to pearlite transformation commenced, and therefore greater mean diffusion distances for carbon. This temperature increased from 740°C for the 0% Silicon steel to 835°C for the 3% Silicon steel. The interlamellar spacing of the air cooled SUP7 structure was half that of the furnace cooled SUP7 structure.

Figure 9.6 illustrates the cementite volume fractions for the spheroidal cementite structures of the different silicon steels. Despite similar bulk carbon contents, the cementite volume fractions differ between the different steels, and between the different initial structures for each steel. A 0.60wt.% carbon steel with a spheroidal cementite structure would comprise 9vol.% cementite, assuming a ferrite carbon content of 0wt.%. Variations from this value for the different cementite microstructures can be attributed to various sources:

i) Uncertainties in the cementite fraction measurements, with 95% confidence intervals of up to 1vol.%;
ii) Undissolved cementite lamellae from initially pearlitic structures for the intercritical structures, with the associated orientation effects increasing the apparent cementite volume fraction;
iii) A ferrite saturation carbon content which increases with increasing silicon content[182], thus lowering the cementite fraction;

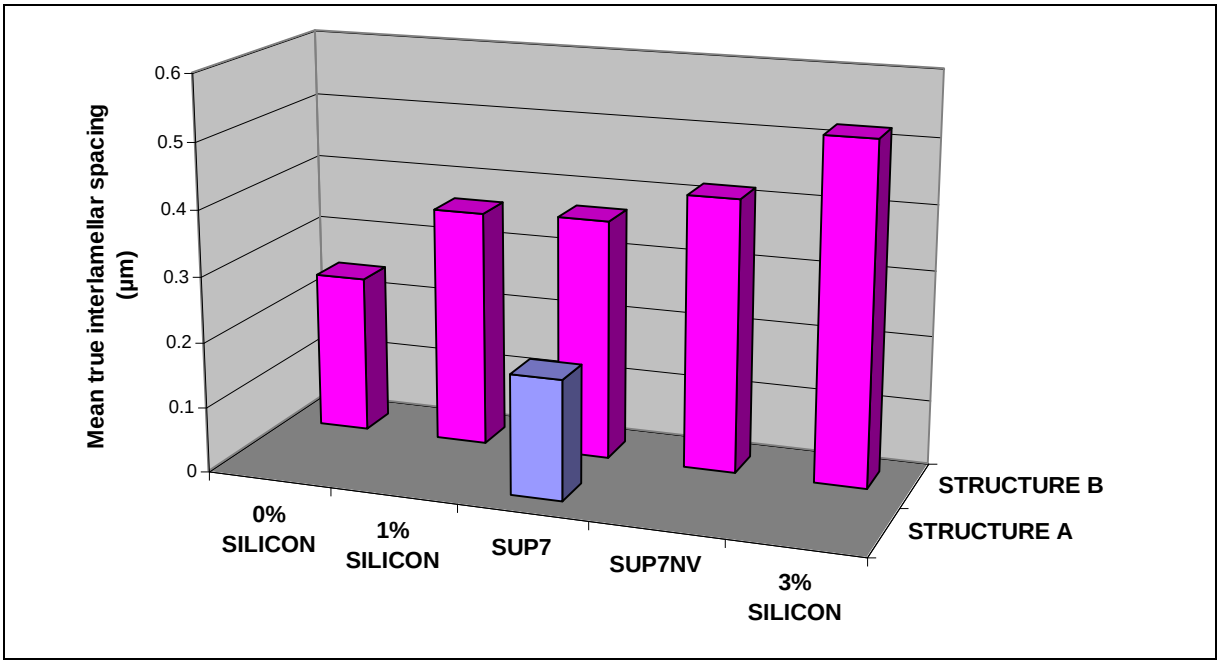

Figure 9.5 Pearlite mean true interlamellar spacings for the pearlitic structures of the different silicon steels.

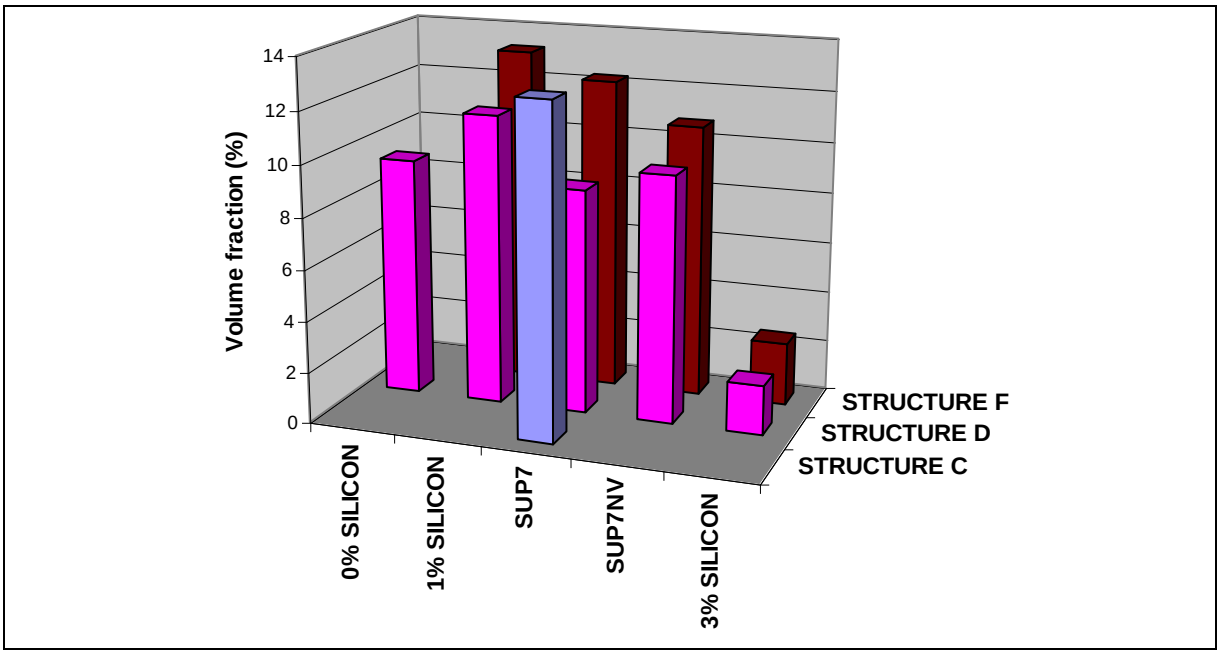

Figure 9.6 Cementite volume fractions for the spheroidal cementite structures of the different silicon steels.

iv) Increasing graphitisation of carbon for the higher silicon contents at the expense of cementite formation.

Consequently, the higher cementite fractions of the intercritical initial structures appear to be due to orientation effects associated with undissolved pearlite. The intercritical cementite fractions decreased with increasing silicon content due to greater cementite spheroidisation, increased ferrite carbon solubility, and greater graphitisation. The increased ferrite carbon solubility and graphitisation with increased silicon content explains the diminishing cementite volume fractions of the 96hr tempered martensite structures as the silicon content increased.

As the silicon content increased from 2.11wt.% for SUP7NV to 3.05wt.% for the 3% Silicon steel, the 96hr tempered martensite and intercritical cementite fractions decreased sharply; from 9.6 and 10.7vol.% cementite to 1.9 and 2.5vol.% respectively for the 3% Silicon steel. This was associated with an increase to 2.0wt.% graphite for the 3% Silicon intercritical structure. It should be noted that the uncertainty associated with the determination of this graphite fraction was large, with a 95% confidence interval of 0.4vol.%.

Assuming graphite to be 100% carbon, the wt.% carbon content associated with the graphite fraction averaged for the whole specimen can be determined from the graphite volume fraction by:

$$wt.\%C_{graphite} = V_{v\,graphite}\frac{\rho_{graphite}}{\rho_{iron}}, \qquad (9.1)$$

where $wt.\%C_{graphite}$ = graphite contribution to the bulk steel carbon content in wt.%;

$V_{vgraphite}$ = graphite volume fraction in %;

$\rho_{graphite}$ = graphite density[169] of 2.24g/cm^3;

ρ_{iron} = iron density[169] of 7.87g/cm^3.

From equation 9.1, approximately 0.5wt.% carbon is associated with the graphite fraction of the intercritical structures. Since the cementite fraction present is associated with a further 0.15wt.% carbon, the total carbon content approximates the bulk steel content of 0.58wt.%.

Therefore, the majority of the carbon associated with the 3% Silicon initial structures was in the form of graphite. Due to the fine graphite particle size and the small volume fraction, the 3% Silicon 96hr tempered martensite initial graphite fraction could not be determined with any degree of accuracy.

The cementite particle size distributions for the 96hr tempered martensite initial structures of the different silicon steels are illustrated in Figure 9.7, while Figure 9.8 illustrates the cementite particle size distribution for different SUP7 spheroidal cementite initial structures. The 0% Silicon steel had the finest size distribution, with 70% of the particles having an equivalent area diameter of 0.25 to 0.75µm. This was due to the lower temperature of 696°C used for the 96hr temper relative to the other steels.

The cementite size distributions of the 1 to 3% Silicon steels were reasonably similar, despite the tempering temperatures varying from 718°C for the 1% Silicon steel to 760°C for the 3% Silicon steel. The cementite particle sizes were spread over a greater range than the 0% Silicon steel, with almost 90% of the particles sized from 0.25 to 1.25µm. The cementite particles were predominantly coarser than the 0% Silicon steel, with approximately 50% of the cementite particles ranging in size from 0.5 to 1.0µm diameter. Of the SUP7 spheroidal cementite structures, Figure 9.8, the 12hr tempered martensite structure had the finest cementite distribution. This was due to the shorter 12hr temper. The 96hr tempered martensite and intercritical structures had coarser and wider cementite size distributions than the 12hr tempered martensite structure.

The 0% Silicon steel had the smallest mean equivalent area diameter for the cementite particles, 0.7µm, of the different silicon steels produced by tempering martensite for 96hr. This is illustrated in Figure 9.9. The mean cementite particle sizes were greater for the higher silicon steels, with the largest mean cementite size of 1.1µm for SUP7. The intercritical structures tended to have slightly smaller mean cementite sizes than the respective 96hr tempered martensite structures. The 12hr SUP7 tempered martensite structure mean size of 0.7µm was smaller than the 96hr tempered martensite structure mean size of 1.1µm. The mean equivalent area diameter of the graphite particles for the furnace cooled initial structure was larger than the intercritical initial structure, being 5.1 versus 3.5µm.

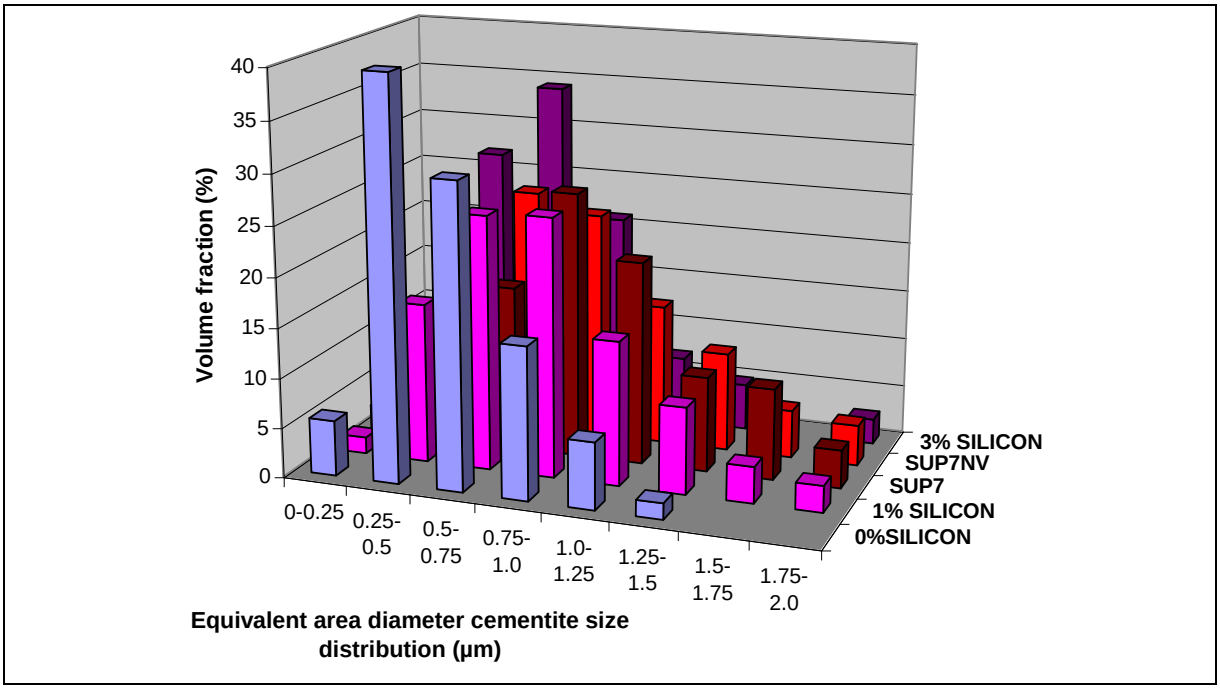

Figure 9.7 Cementite particle size distribution for 96hr tempered martensite initial structures of the different silicon steels.

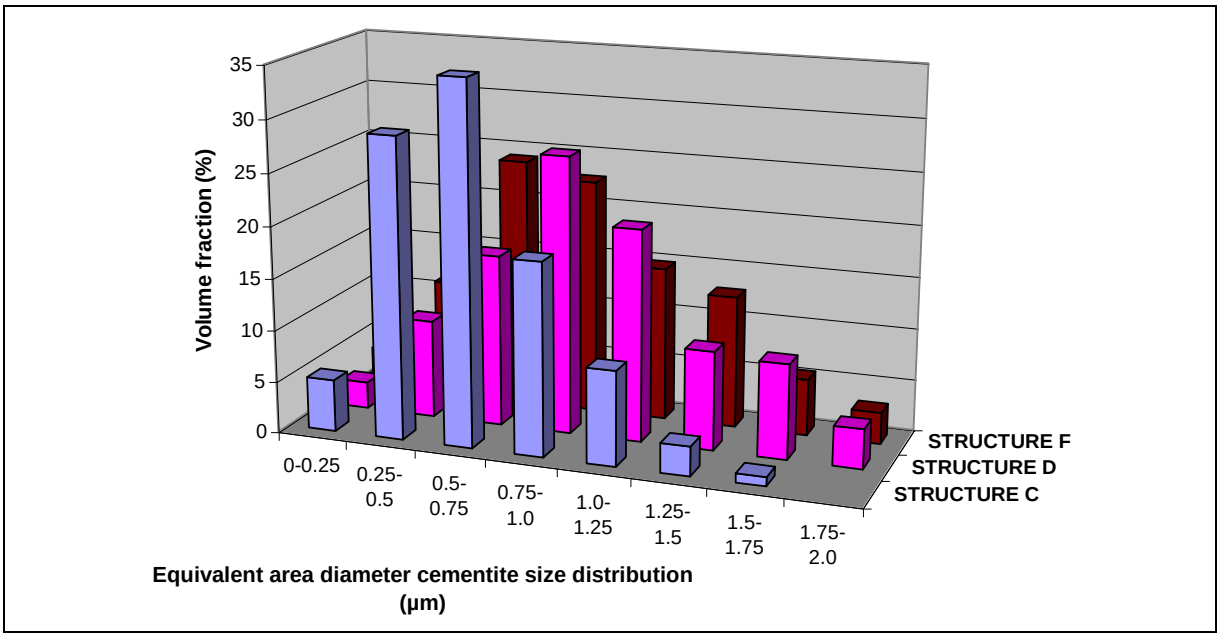

Figure 9.8 Cementite particle size distribution for different initial SUP7 spheroidal cementite structures.

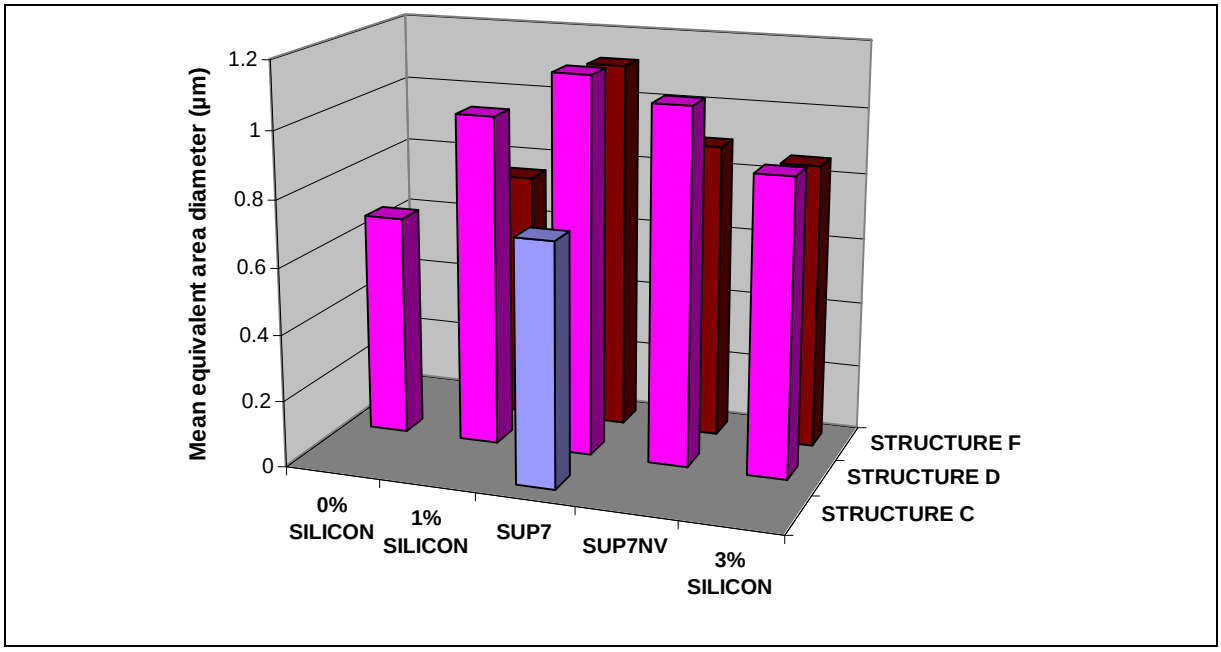

Figure 9.9 Cementite particle mean equivalent area diameters for the spheroidal cementite structures of the different silicon steels.

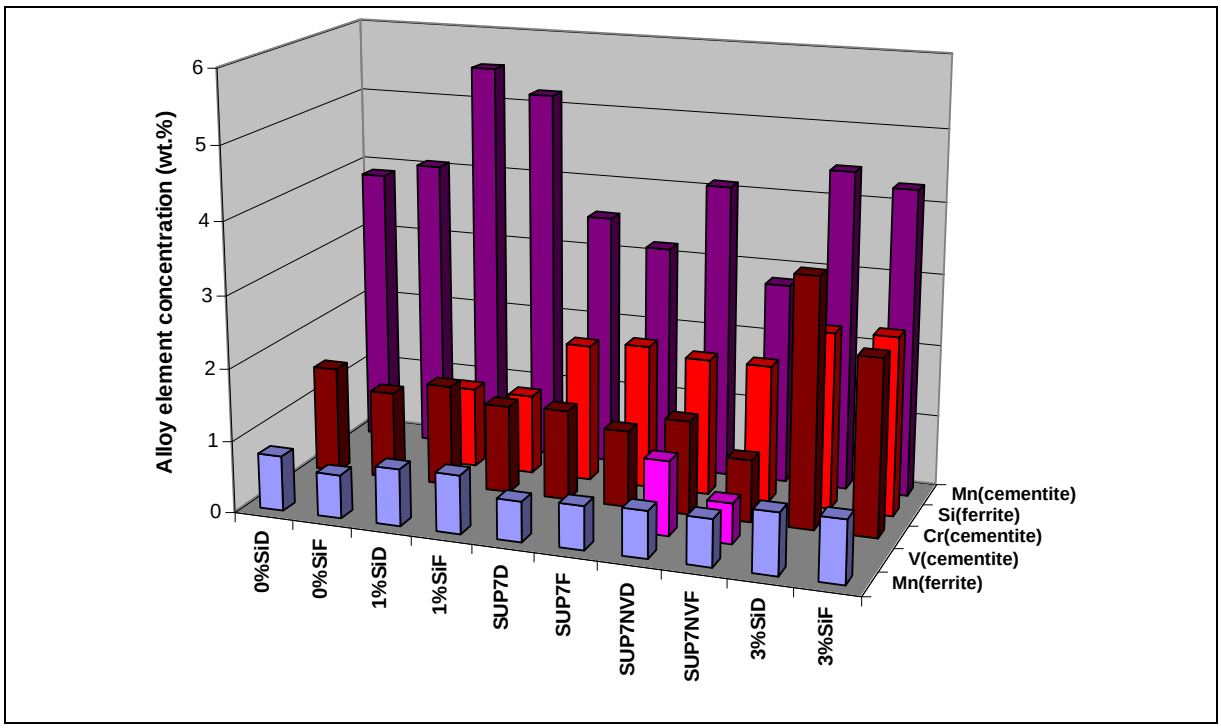

Figure 9.10 Ferrite and cementite alloying element concentrations for 96hr tempered martensite and intercritical structures of the different silicon steels.

The ferrite and cementite alloying element concentrations of the initial 96hr tempered martensite and intercritical structures for the different silicon steels are shown in Figure 9.10. Alloy element concentrations of less than 0.2wt.% are not illustrated, due to the uncertainty associated with such small values given the 0.1wt.% resolution of the energy dispersive analyser. The ferrite chromium and cementite silicon concentrations did not exceed 0.2wt.% for the different silicon steels.

The alloying element concentrations of the cementite particles were determined using particles larger than the 1μm diameter analysed by the electron beam with energy dispersive spectroscopy. These concentrations correspond to values averaged over the 1μm diameter of the electron beam interaction volume, and do not account for any inhomegeneity at the sub-micron level. If the heat treatment duration was long enough for equilibrium conditions to be obtained, the alloying element concentrations will be constant across each cementite particle, with the composition independent of size[183]. However, for intermediate test durations, concentration profiles exist across the cementite particles, with these profiles varying for different size particles[58]. Concentration profiles will also exist in the ferrite close to the ferrite/austenite interfaces[58].

In order to minimise the effect of these concentration profiles, the larger cementite particles were analysed, since the concentration profiles are uniform over larger fractions of the cementite particles relative to smaller particles[58]. The ferrite grains tended to be larger than the cementite particles, with analysis in the centre of the larger ferrite grains ensuring less sub-micron inhomogeneity relative to the cementite particles. A minimum of five analyses per phase for each specimen were undertaken to reduce the effect of particle-to-particle composition variations.

Several generalisations can be made for the alloying element concentrations of 96hr tempered martensite and intercritical initial structures for the different steels:

i) The tempered martensite and intercritical structures had similar ferrite silicon and manganese concentrations;
ii) The tempered martensite structures had higher cementite manganese and chromium concentrations, and in the case of SUP7NV, higher vanadium concentrations, than the

intercritical structures. This was due to the longer heat treatments of the 96hr tempered martensite structures allowing greater manganese and chromium partitioning to the cementite particles;

iii) The higher bulk steel alloy concentrations tended to yield higher phase concentrations.

The exception to the third generalisation arose for the 3% Silicon steel. The cementite manganese concentrations were higher than all but the 1% Silicon steel, while the cementite chromium concentrations were over twice those of the other steels. This was despite the 3% Silicon steel having the lowest bulk manganese concentration of 0.78wt.%, and a similar bulk chromium concentration, of the five steels. This elevated alloying element partitioning relative to the other steels was due to the graphitisation of the 3% Silicon steel at the expense of cementite formation. Considerable manganese and chromium partitioning to cementite occurred with prolonged isothermal heat treatments. The lower spheroidal cementite fractions of the 3% Silicon 96hr tempered martensite and intercritical initial structures relative to the other steels allowed greater manganese and chromium partitioning per cementite particle. This effect was greatest for the chromium partitioning. A similar situation occurred for a Fe-C-2wt.%Si-2wt.%Mn-1wt.%Cr steel where the manganese and chromium concentrations of the cementite particles decreased as the carbon content increased from 0.14 to 0.80wt.%[183], due to the increasing cementite fraction with carbon content.

9.3 Microstructural investigation

9.3.1 Influence of temperature on austenitisation

When a steel is heated to a temperature above the Ac_1 temperature, austenite will eventually be nucleated from an initial structure of ferrite and cementite, as discussed in Chapter 2. The austenite nucleation, and the rate and extent of the subsequent austenite growth, is dependent upon the composition, initial microstructure and the heat treatment temperature. For temperatures just above the Ac_1 value, austenite nucleation and growth is sluggish. This is evident during the intercritical heat treatment of SUP7, with Figures 9.11 (a) and (b) illustrating that only a small fraction of austenite had formed in the different initial structures after heat treating for 4hr at 10°C above the Ac_1 temperature of 745°C. The austenite fractions

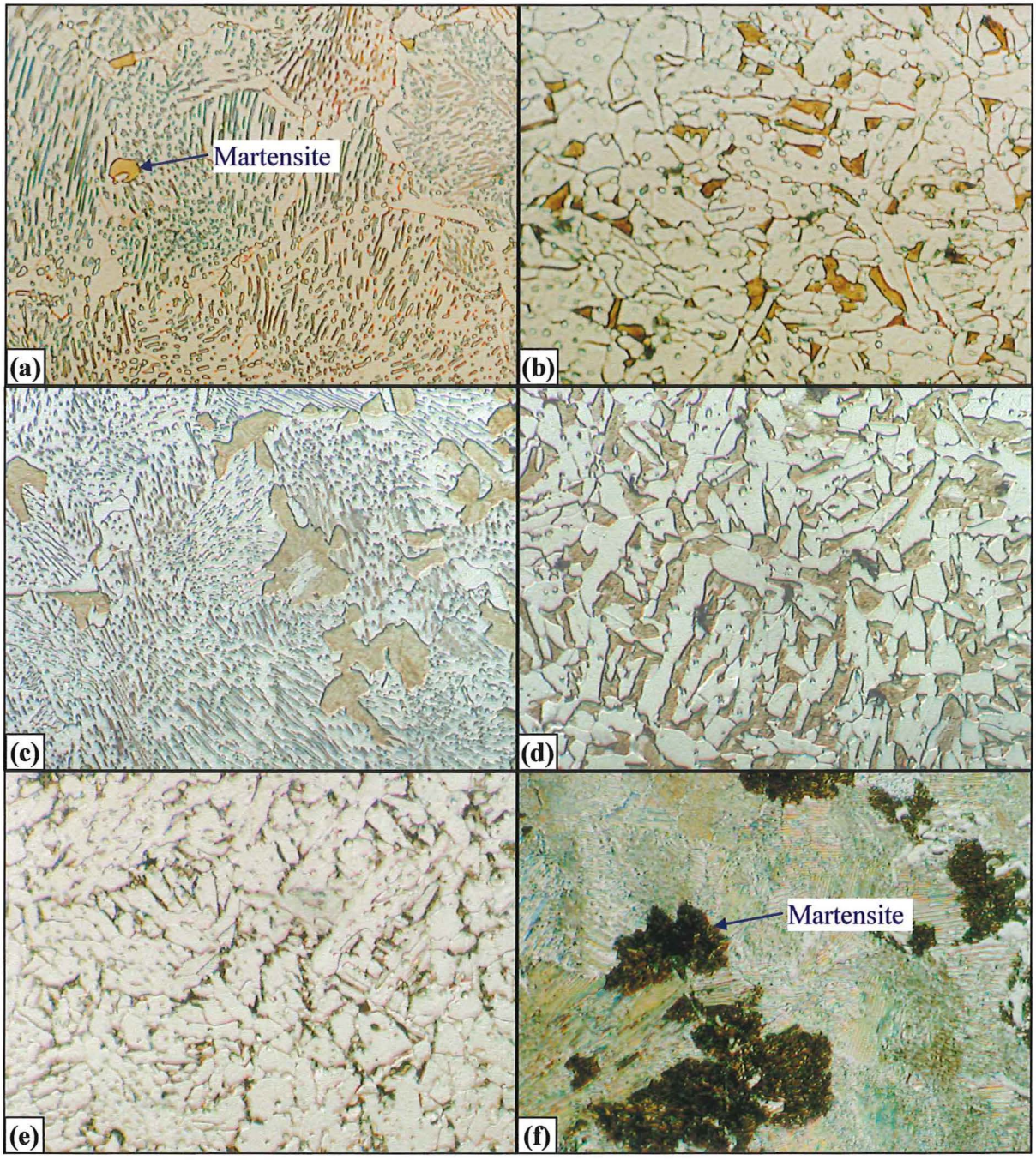

Figure 9.11 Microstructures obtained after austenitisation of SUP7 furnace cooled and 96hr tempered martensite initial structures at 755°C for 4hr (a), (b), at 765°C for 4hr (c), (d), and at 780°C for 2min (e), (f). 1,150x magnification. (a) to (d) 2% Nital etch. (e), (f) sodium metabisulphite etch.

quoted in the following sections refer to the martensite fractions that were measured from the microstructures, where austenite transformed to martensite upon quenching.

An increase of 10°C considerably accelerated the austenite formation, with the martensite fractions measured from the microstructures of the 4hr heat treated specimens with furnace cooled and 96hr tempered martensite initial, Figures 9.11(c) and (d), indicating that 10.1 and 27.4% austenite had formed. This compares with 0.2 and 7.0% for the furnace cooled and tempered martensite initial structures at 755°C. The austenite formation for the tempered martensite structure was greater at both 755 and 765°C. However, the austenite formation at 780°C was faster for the furnace cooled structure. This is illustrated in Figures 9.11(e) and (f), with 12.3% austenite present for the furnace cooled structure after 2min at 780°C, compared with 6.8% austenite for the tempered martensite structure.

Austenitisation optical microscopy photos of different initial SUP7 microstructures heat treated for 30s at the Ac_3 temperature of 820°C are illustrated in Figure 9.12. At this temperature the austenitisation of the furnace cooled structure was very rapid, with 80.9% austenite after only 30s, Figure 9.12(a). Undissolved cementite particles were visible in the austenite. The austenitisation reaction was even faster for the finer air cooled pearlitic structure, which had fully transformed within 30s (not illustrated). The austenitisation kinetics of the pearlitic structures were considerably faster than the spheroidal cementite structures at this temperature. After 30s, 24.0, 13.3 and 7.8% austenite formed for the 12hr tempered martensite, 96hr tempered martensite, and intercritical initial structures respectively, Figures 9.12(b), (c), and (d). The finer tempered martensite structure had a greater austenite fraction than the coarser structure, with both these fractions greater than for the intercritical structure.

9.3.2 Austenite nucleation and growth

The austenitisation investigation commenced with a detailed investigation of SUP7, before being expanded to encompass the 0% Silicon, 1% Silicon, SUP7NV and 3% Silicon steels. Heat treatments were undertaken at a variety of intercritical temperatures for SUP7, as well as at the Ac_3 temperature of 820°C. “Fractional superheats”, as defined in section 5.3.1, of approximately 0.13, 0.25, 0.5 and 0.75 were used, corresponding to 10, 20, 35 and 55°C above the 745°C Ac_1 temperature. The 75°C gap between the Ac_1 and Ac_3 temperatures

allowed this range of fractional superheats to be investigated. However, the percentage change of the low fractional superheats is considerable for temperature changes of a few °C. In order to minimise the temperature fluctuations from one test duration to the next, all the heat treatments were undertaken at the selected furnace temperature before the next heat treatment temperature was selected. So despite the stated temperature uncertainties of ± 5°C, the tube furnace hot zone temperature was observed to remain within ± 2°C of the selected temperature over the duration of each heat treatment temperature.

The intercritical temperature gap between the Ac_1 and Ac_3 temperatures is much smaller for the 0 and 1% Silicon steels than for SUP7, being 34 and 32°C respectively. Therefore, a fractional superheat of 0.13 corresponds to a temperature of only 4°C higher than the Ac_1 values for these two steels. These temperatures were not investigated as any temperature uncertainty would alter the fractional superheat by a large percentage. A 0.25 fractional superheat was investigated for the 0% Silicon steel, which corresponded to 9°C above the Ac_1 temperature. However, the austenitisation kinetics at this temperature were very slow, with 4.3, 5.6 and 0.7vol.% austenite formed after 96hr for the furnace cooled, 96hr tempered martensite and intercritical initial structures respectively. Consequently, the austenitisation heat treatments were undertaken at 0.5 fractional superheats for the 0 and 1% Silicon steels. 0.25 fractional superheats were used for the SUP7NV and 3% Silicon steels as their intercritical temperature ranges of 72 and 65°C are akin to that of SUP7.

i) Intercritical heat treatments

The microstructures obtained by austenitising different 0% Silicon initial structures at 723°C, which corresponds to a 0.5 fractional superheat, are illustrated in Figure 9.13. Austenite grains, which were austenite at the heat treatment temperature, were evident in all three microstructures after 4hr. Austenite nucleated in the pearlitic structure at cementite particles located at the ferrite/pearlite interfaces separating the pearlite colonies, Figure 9.13(a)[36]. The austenite nucleation for the tempered martensite and intercritical structures occurred predominantly at cementite particles located at the edges where three ferrite grains meet[31], Figures 9.13(c) and (e) respectively. The furnace cooled structure had the greatest austenite fraction after 4hr of 7.1%, compared with 4.4 and 0.5% for the tempered martensite and intercritical initial structures respectively. The martensitic grains of the microstructures of

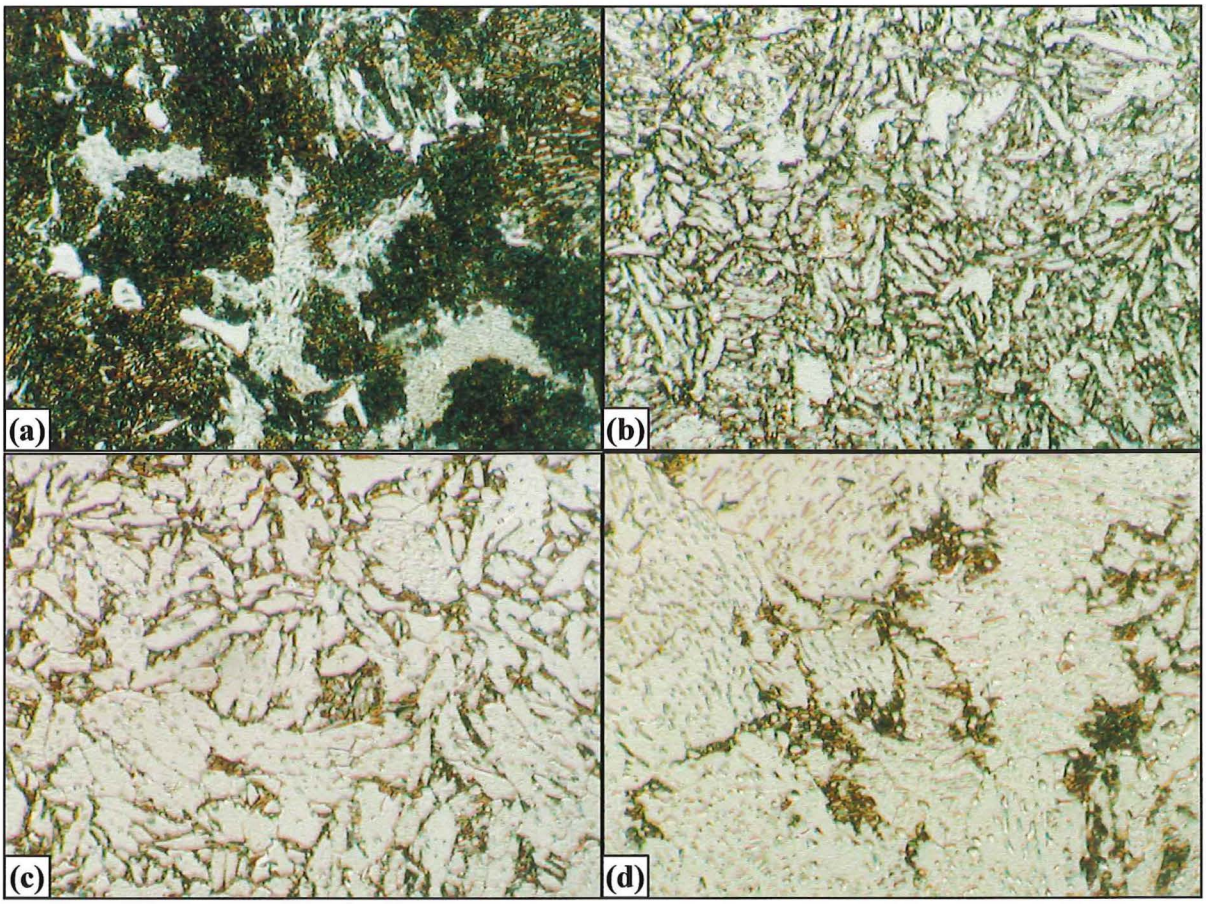

Figure 9.12 Influence of initial structure on SUP7 austenitisation after 30s at 820°C for (a) furnace cooled, (b) 12hr tempered martensite, (c) 96hr tempered martensite, and (d) intercritical structures. 1,150x magnification. Sodium metabisulphite etch.

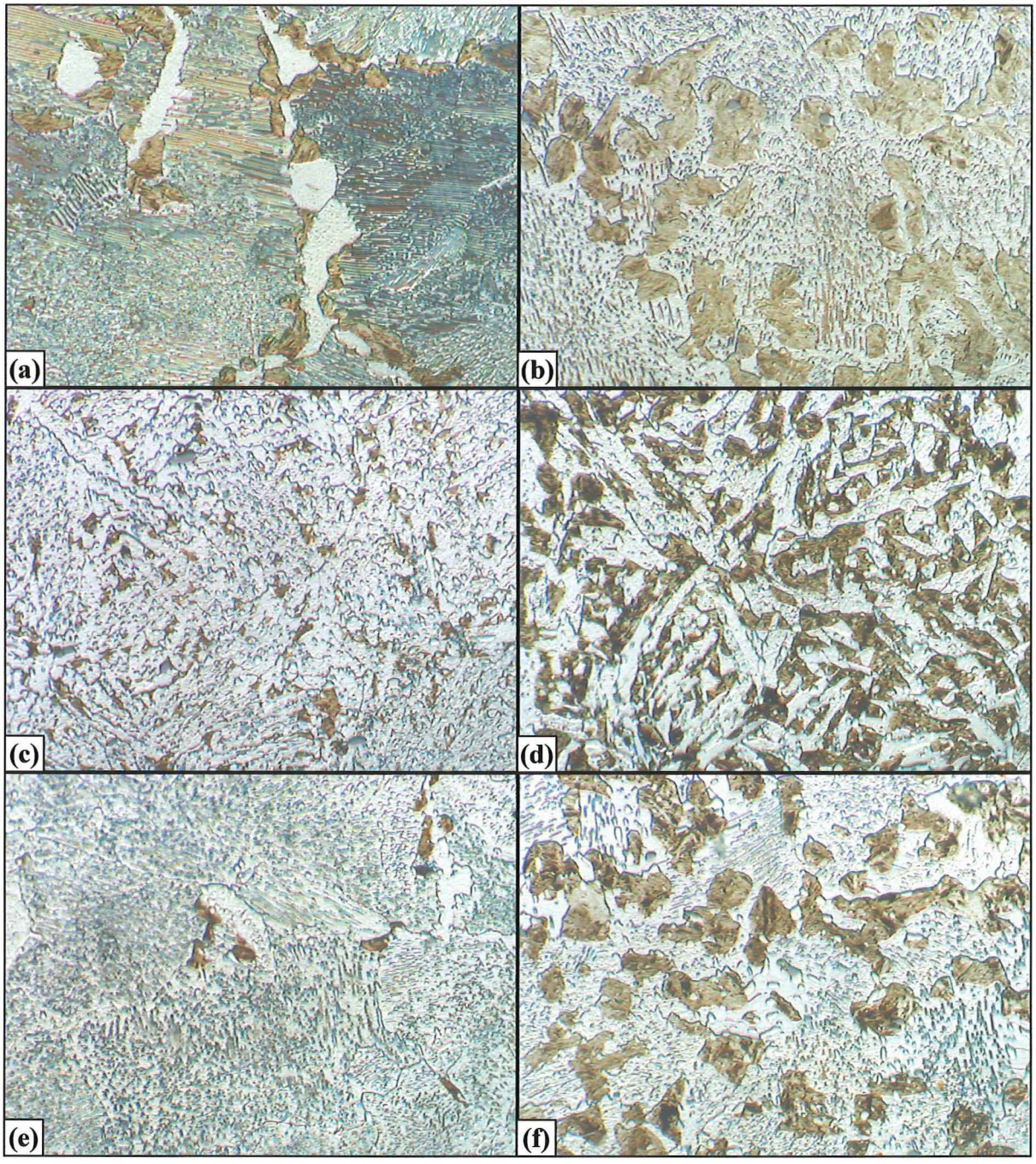

Figure 9.13 Microstructures of 0% Silicon steels heat treated at 723°C with furnace cooled initial structures for (a) 4hr, (b) 96hr, with 96hr tempered martensite initial structures for (c) 4hr, (d) 96hr, and with intercritical structures for (e) 4hr and (f) 96hr. 1,150x magnification. 2% Nital etch.

Figure 9.13 illustrate that coarser austenite grains resulted from the furnace cooled initial structure compared with the tempered martensite initial structure.

After 96hr at 723°C, the 0% Silicon intercritical initial structure transformed to the greatest austenite fraction of 37.0%, compared with the lowest of 31.5% for the furnace cooled structure. The austenite grains, which transformed to martensite upon quenching, were approximately equiaxed for the furnace cooled pearlitic structure[31], Figure 9.13(b). Impingement of the discretely nucleated austenite grains can be seen, which resulted in fewer austenite grains. The approximately equiaxed austenite grain shapes were inherited from the initial pearlitic structure. A considerable fraction of lamellar cementite remained, with undissolved spheroidal cementite particles also present within the austenite.

The austenite grain shapes obtained from the tempered martensite and intercritical initial structures, which were present as martensite in the microstructures at room temperature, were also dependent on the initial ferrite grain shape. Equiaxed austenite grains grew from the intercritical structure, Figure 9.13(f), which possessed equiaxed ferrite grains initially[35,175], while the austenite inherited the elongated grain shape from the ferrite grains of the tempered martensite initial structure, Figure 9.13(d)[35,175]. The austenite grains coarsened with time, where the grain structure was more equiaxed after 96hr than after 4hr. The initial tempered martensite specimen formed a finer austenite structure than the furnace cooled structure, due to the finer initial ferrite grain size. Greater impingement of the austenite grains occurred in the tempered martensite and intercritical structures than in the furnace cooled initial structure.

Undissolved cementite particles were present within the austenite grains obtained from the tempered martensite and intercritical initial structures after 96hr at 723°C. Noticeably fewer undissolved cementite particles remained in the tempered martensite structure compared to the intercritical structure, despite the intercritical structure having a slightly higher austenite fraction. This indicates a higher austenite carbon content for the tempered martensite initial structure. The undissolved cementite fractions for both these initial structures were considerably less than for the furnace cooled initial structure, although this is misleading due to orientation effects of the lamellar cementite of the pearlite structure increasing the apparent cementite fraction.

The microstructures obtained after 4hr austenitisation of SUP7 furnace cooled and 96hr tempered martensite initial structures at 10°C above the Ac_1 temperature of 745°C were illustrated in Figures 9.11(a) and (b). 755°C corresponds to a 0.13 fractional superheat. Unlike the 0% Silicon steel at 723°C, the austenite fraction was greater for the SUP7 tempered martensite initial structure than for the furnace cooled structure, as illustrated in Figures 9.11(c) and (d). Similarly, more austenite had formed after 4hr for the tempered martensite SUP7 initial structure at a 0.25 fractional superheat, 765°C, than for the furnace cooled structure. However, a further 15°C increase to a 0.5 fractional superheat resulted in a greater austenite fraction for the furnace cooled structure after 2min, Figure 9.11(e), than for the SUP7 tempered martensite structure, Figure 9.11(f).

After 192hr austenitisation at 755°C, the SUP7 furnace cooled structure formed less austenite than the tempered martensite initial structure, with 14.6 and 23.3% austenite respectively, Figures 9.14(a) and (b). Impingement of the growing austenite grains along the ferrite grain boundaries for the tempered martensite initial structures had occurred. Undissolved cementite particles remained in both structures, with a significantly higher fraction present in the furnace cooled structure. However, this was at least partly attributable to the smaller austenite fraction of the furnace cooled initial structure. The higher heat treatment temperature of 755°C for SUP7 resulted in greater spheroidisation of the lamellar cementite at the 0.13 fractional superheat than at the 0.5 fractional superheat for the 0% Silicon steel, which corresponded to a temperature of 723°C.

Austenite nucleation and growth for the SUP7 intercritical initial structure at 755°C was initially slower than for the furnace cooled and tempered martensite structures. Figure 9.14(c) shows the microstructure after 24hr austenitisation of the intercritical structure, where just 2.8% austenite had formed. This was less than the 4.0 and 19.7% for the furnace cooled and tempered martensite structures after 24hr. However, by 192hr the austenite fraction of 28.7% exceeded that of the other two structures.

Figure 9.15 illustrates the microstructures after annealing SUP7 96hr tempered martensite initial structures for 96hr at 765°C, Figure 9.15(a), and 780°C, Figure 9.15(b). The austenite fraction increased from 44.9 to 92.2% as the temperature increased from 765 to 780°C. A 10°C increase from 755 to 765°C resulted in 21.6% more austenite after 192hr, while a further

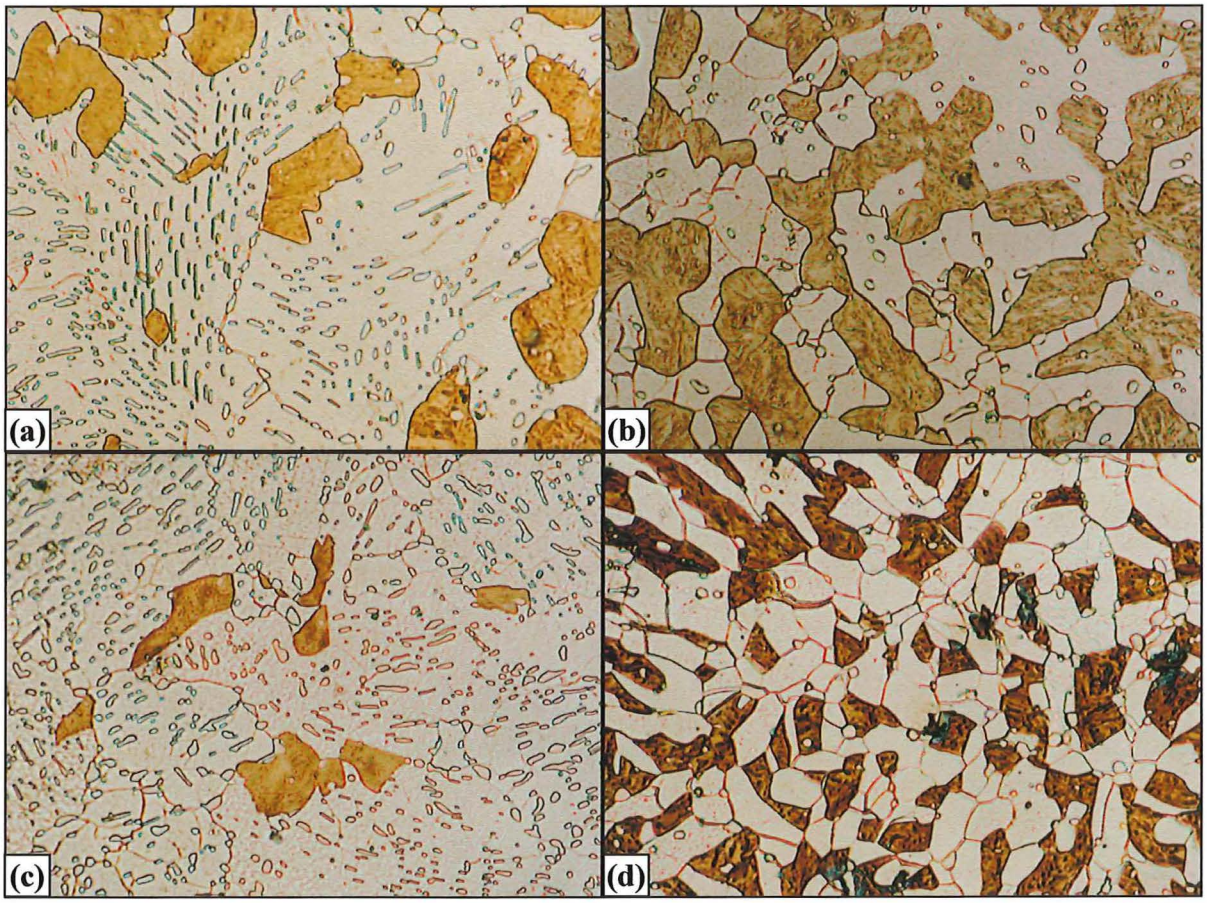

Figure 9.14 SUP7 microstructures obtained upon austenitisation at 755°C for 192hr of (a) furnace cooled, (b) 96hr tempered martensite initial structures, and the intercritical structure for (c) 24hr and (d) 192hr. 1,150x magnification. 2% Nital etch.

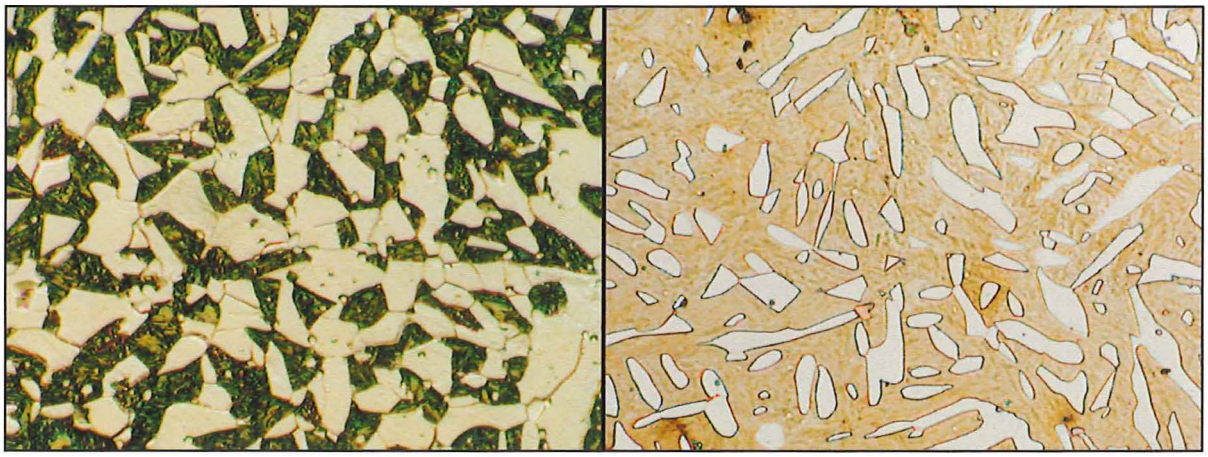

(a) (b)

Figure 9.15 SUP7 96hr tempered martensite initial structures after 96hr at (a) 765°C, and (b) 780°C. 2,500x magnification. Nital/Picral etch.

15°C increase yielded a further increase in the austenite fraction of 47.3vol.%. Such large austenite volume fraction changes with small temperature increases illustrate the necessity of the accurately controlled furnace temperatures achieved with the Nabertherm tube furnace.

The heat treatment of low alloy steels is usually based on the binary iron-cementite phase diagram, where one phase, ferrite or austenite, or two phase, ferrite plus austenite, austenite plus cementite, or ferrite plus cementite, fields exist. However, in some low-alloy steels an eutectoid gap is present instead of the single eutectoid temperature Ac_1, as illustrated in Figure 9.16. This eutectoid gap is limited by two phase boundaries, Ac_1' and Ac_1'', within which the three phases, ferrite, austenite, and cementite, coexist. For many low alloy steels, the temperature difference between Ac_1' and Ac_1'' is small[184].

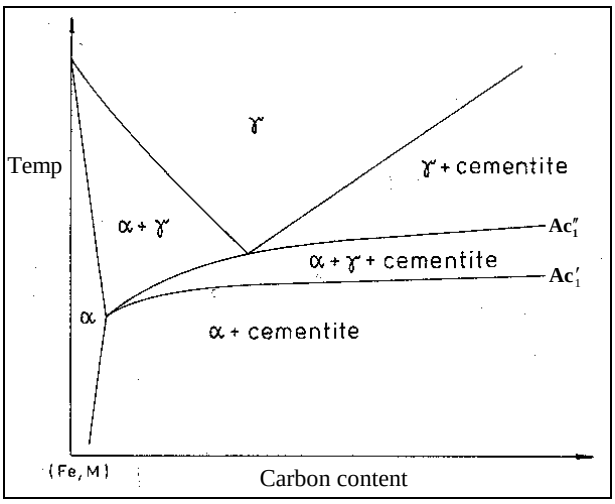

Figure 9.16 Schematic illustration of the eutectoid gap, defined by the phase boundaries Ac_1' and Ac_1'', present in some low alloy steels (from Ref. 54).

However, manganese and silicon enlarge the eutectoid gap, as evident in the Fe-C-Mn[182] and Fe-C-Si[182,185] ternary phase diagrams. Karmazin[54] found that an eutectoid gap of approximately 50°C existed for a 0.80wt.% C/2.06wt.% Mn/2.02wt.% Si/1.05wt.% Cr alloy. Svoboda[183] found that the eutectoid gap remained at approximately 50°C for a Fe-C-2wt.%Si-2wt.%Mn-1wt.%Cr system as the carbon content increased from 0.14 to 0.80wt.%. The presence of an eutectoid gap for SUP7 after austenitising for 192hr at 10°C above the Ac_1

temperature was illustrated in Figure 9.14, which demonstrated the coexistence of ferrite, austenite and cementite at this temperature.

The size of the eutectoid gap was measured by determining the temperature at which undissolved cementite particles were no longer present after austenitising for 192hr. The eutectoid gap may be overestimated by this method as equilibrium may not be reached after 192hr, and the cementite particles observed may dissolve upon longer austenitisation. A few undissolved cementite particles remained after 192hr at 780°C, with no undissolved cementite present after 96hr at 790°C. Therefore, the eutectoid gap for SUP7 was determined to be approximately 35°C.

The considerable graphitisation present in the initial structures of the 3% Silicon steel influenced the austenitisation of this steel. Figure 9.17 illustrates the microstructures obtained after austenitising different initial 3% Silicon structures at 785°C, a 0.25 fractional superheat, for 1hr and 96hr. The tempered martensite initial structure demonstrated the greatest austenite formation of 13.8% after 1hr, compared with 2.7 and 1.2% for the furnace cooled and intercritical structures respectively. However, by 96hr all three initial structures had transformed to approximately 26% austenite.

Austenite nucleation for the 3% Silicon steels occurred at both cementite and graphite particles located on ferrite grain boundary triple points. After 1hr, the majority of the cementite particles present in the initial furnace cooled structure had dissolved, Figure 9.17(a). The absence of cementite particles within the ferrite grains meant that there was no carbon source for austenite growth into the ferrite. This resulted in the formation of elongated austenite grains, despite the initial equiaxed ferrite grains. Only a few cementite particles were present after 96hr austenitisation of the furnace cooled initial structure, Figure 9.17(b). However, the majority of the initial graphite fraction remained, with these graphite particles predominantly located at ferrite/austenite interfaces.

The 96hr tempered martensite initial structure yielded finer austenite structures than those obtained with the comparable heat treatments for the furnace cooled structures, Figures 9.17(c) and (d). Some cementite particles remained after 96hr, as did a considerable fraction of very fine graphite particles. Most of these graphite particles appeared to be present in the

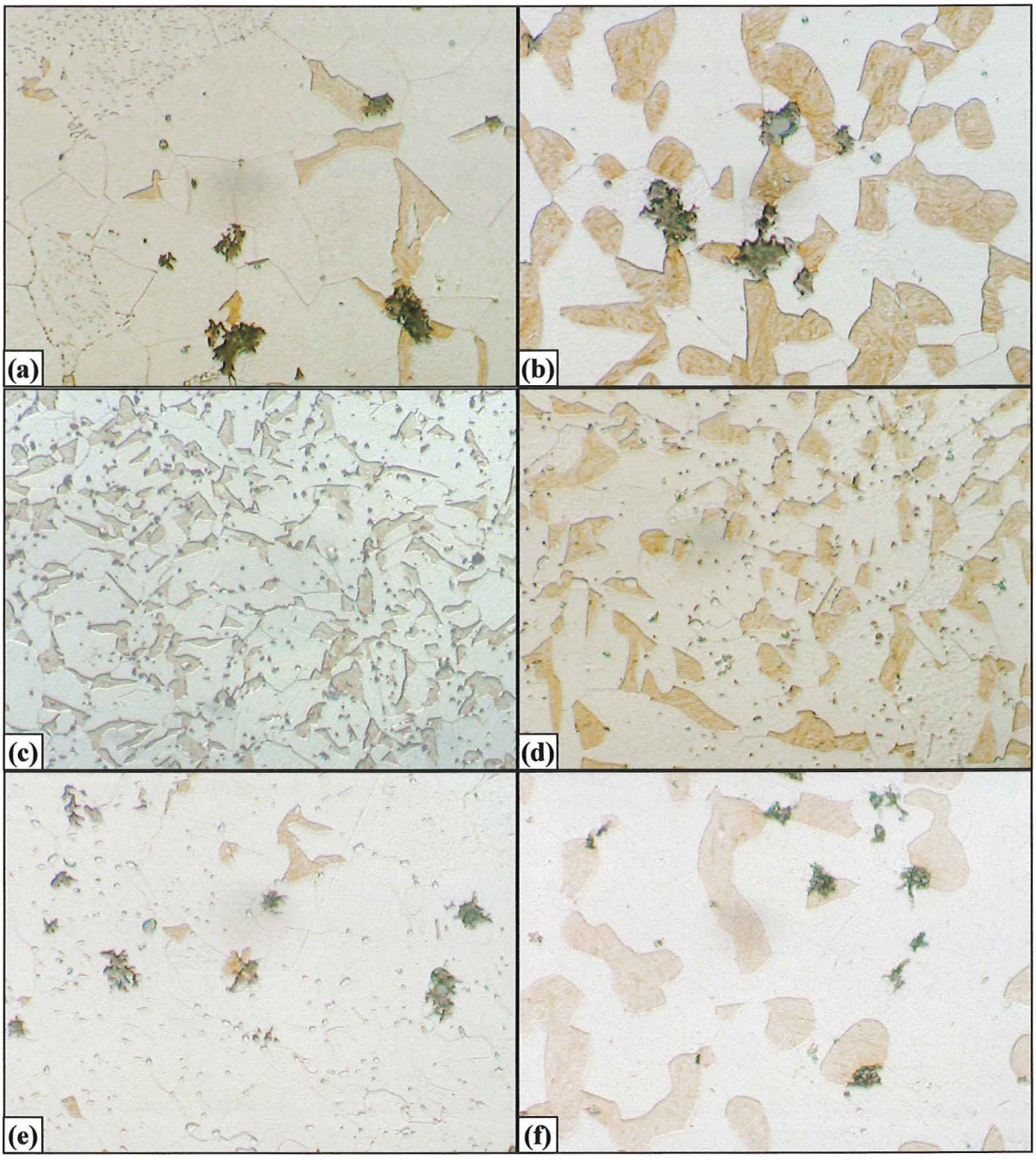

Figure 9.17 Austenitisation microstructures of 3% Silicon steels at 785°C for 1hr and 96hr with initial furnace cooled (a), (b), 96hr tempered martensite (c), (d), and intercritical structures (e) and (f). 1,150x magnification. 2% Nital etch.

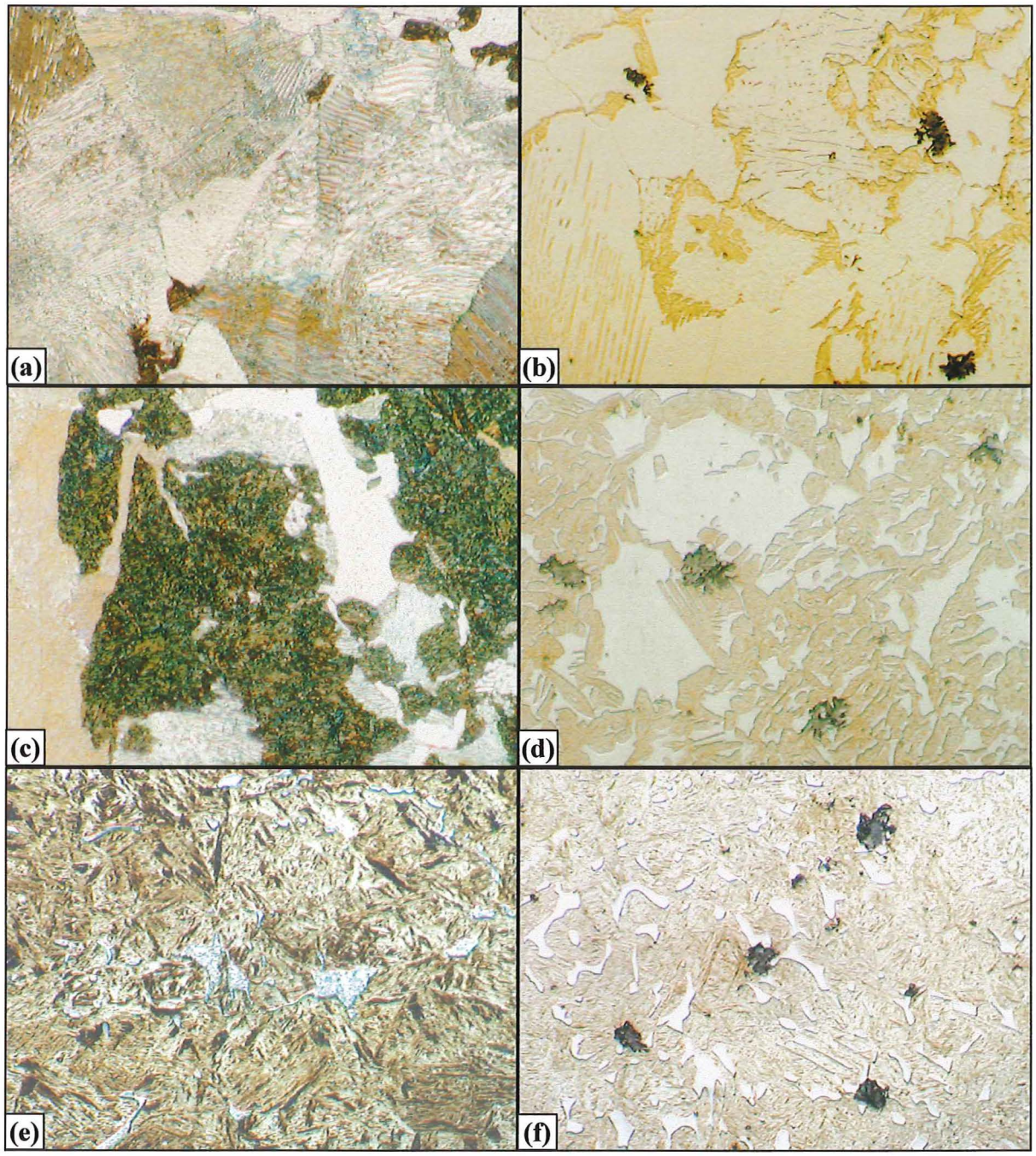

Figure 9.18 Microstructures obtained after Ac_3 temperature austenitisation of the furnace cooled initial structures at 740°C for the 0% Silicon steel for (a) 1min, (c) 2min, (e) 1hr, and 835°C for the 3% Silicon steel for (b) 1min, (d) 2min, and (f) 1hr. 1,150x magnification. (a), (c), sodium metabisulphite etch, (b), (d), (e), (f). 2% Nital etch.

ferrite only. The majority of the austenite nucleation for the intercritical structure after 1hr occurred at cementite particles located on grain boundary triple points, Figure 9.17(e). Limited austenite nucleation occurred at the graphite particles themselves. After 96hr, very few undissolved cementite particles remained. However, the majority of the initial graphite fraction remained, and was predominantly located at the ferrite/austenite interfaces.

ii) Austenitisation at the Ac_3 temperature

Figure 9.18 illustrates the microstructures obtained after austenitising 0 and 3% Silicon furnace cooled initial structures at their respective Ac_3 temperatures of 740 and 835°C. Austenite nucleated at the interface between ferrite grain boundaries and cementite particles in the pearlitic structure for the 0% Silicon steel. An increase of 17°C from a 0.5 fractional superheat to the Ac_3 temperature considerably accelerated the austenitisation kinetics of the 0% Silicon steel, with 0.8% austenite formed after 1min, Figure 9.18(a), and 30.0% present after 2min, Figure 9.18(c). Austenite growth occurred evenly in all directions, with the remainder of the structure predominantly pearlitic. After 1hr, 97.8% austenite had formed, Figure 9.18(e). This compares to the austenitisation at the 0.5 fractional superheat, where austenite had only just formed after 1hr, as illustrated by the small martensite fraction of Figure 9.13(d).

Similar austenite nucleation and growth was observed for the furnace cooled initial structures of the 1% Silicon, SUP7 and SUP7NV steels at their respective Ac_3 temperatures. However, the presence of graphite in the 3% Silicon furnace cooled structure altered the austenitisation. Austenite nucleation occurred predominantly at ferrite/cementite grain boundaries, with the formation of elongated austenite grains, Figure 9.18(b). Some austenite nucleation also occurred at ferrite/graphite grain boundaries.

An increase in silicon content from 0 to 2wt.% for SUP7 accelerated the austenitisation of the initial pearlitic furnace cooled structures, with 80.9% austenite formed after 30s at the Ac_3 temperature of 820°C, Figure 9.12(b). This was due to the increase in Ac_3 temperature at which the heat treatments were undertaken, from 740°C for the 0% Silicon steel to 820°C for SUP7, which accelerated the austenitisation kinetics despite the increased silicon content. However, austenitisation of the furnace cooled 3% Silicon steel initial structure at 835°C was

considerably slower than for SUP7, with only 16.8% austenite formed after 30s. After 1hr at 835°C, the 3% Silicon steel with a furnace cooled initial structure comprised 98.8% austenite, Figure 9.18(f). However, undissolved graphite particles were still present.

Figure 9.19 illustrates the early stages of austenite nucleation and growth at the respective Ac_3 temperatures for the 0% Silicon, SUP7, SUP7NV and 3% Silicon steels with 96hr tempered martensite initial structures. Austenite nucleation occurred at cementite particles located at the edges where three ferrite grains meet for the 0% Silicon steel, Figure 9.19(a). Due to the fine ferrite/cementite structure, the austenite grains nucleated quickly encompassed several undissolved cementite particles, with an equiaxed grain structure. This contrasts with SUP7 and SUP7NV, Figures 9.19(b) and (c). Although austenite nucleation still arose at cementite particles located at the edges where three ferrite grains meet, the grain structure was more elongated. Fewer undissolved cementite particles remained in the austenite of SUP7 and SUP7NV, although they were much larger than for the 0% Silicon steel.

3.0% austenite formed after 2min for the 0% Silicon steel, compared with 13.2 and 8.4% austenite for SUP7 and SUP7NV respectively after 30s. A larger austenite fraction of 29.9% formed after 30s at 835°C for the 3% Silicon steel, Figure 9.19(d). The austenite structure of the 3% Silicon steel was elongated, with few undissolved cementite particles evident in the austenite. Some fine undissolved graphite particles were also present in the ferrite.

Equiaxed austenite grain formation after 4min at 740°C for the 0% Silicon steel was demonstrated by the equiaxed martensite grains of Figure 9.20(a), with fine undissolved cementite particles in the austenite and ferrite. SUP7 had a more elongated structure after 1min at 820°C, Figure 9.20(b), than the 0% Silicon steel heat treated at 740°C for 4min, with larger but fewer undissolved cementite particles in the austenite and ferrite. This was illustrated by the martensitic structures of Figure 9.20(b) and (c), which demonstrated that a coarser austenite structure than the SUP7NV structure formed during austenitisation, despite identical heat treatments. The elevated vanadium and niobium concentrations of SUP7NV resulted in the formation of vanadium and niobium carbides[5,14]. These carbides pin the ferrite grain boundaries more effectively than cementite during the 96hr tempering of the initial structure. Consequently, SUP7NV had a finer ferrite grain size than SUP7 after the initial heat treatment[5,14], which translates to a finer austenitic structure observed during austenitisation.

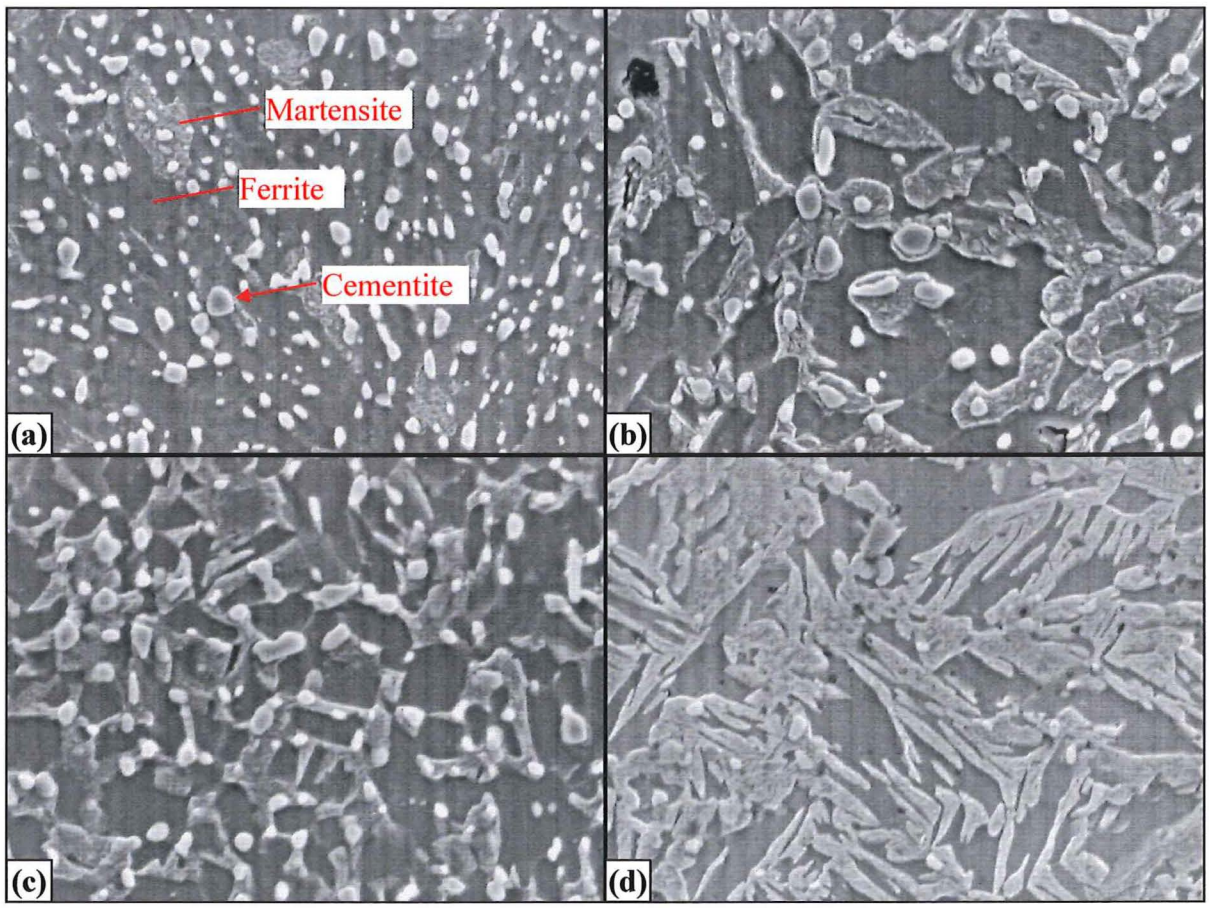

Figure 9.19 Austenitisation microstructures of 96hr tempered martensite initial structures for (a) 0% Silicon after 2min at 740°C, (b) SUP7 after 30s at 820°C, (c) SUP7NV after 30s at 820°C, and (d) 3% Silicon after 30s at 835°C. 2,500x magnification. Nital/Picral etch.

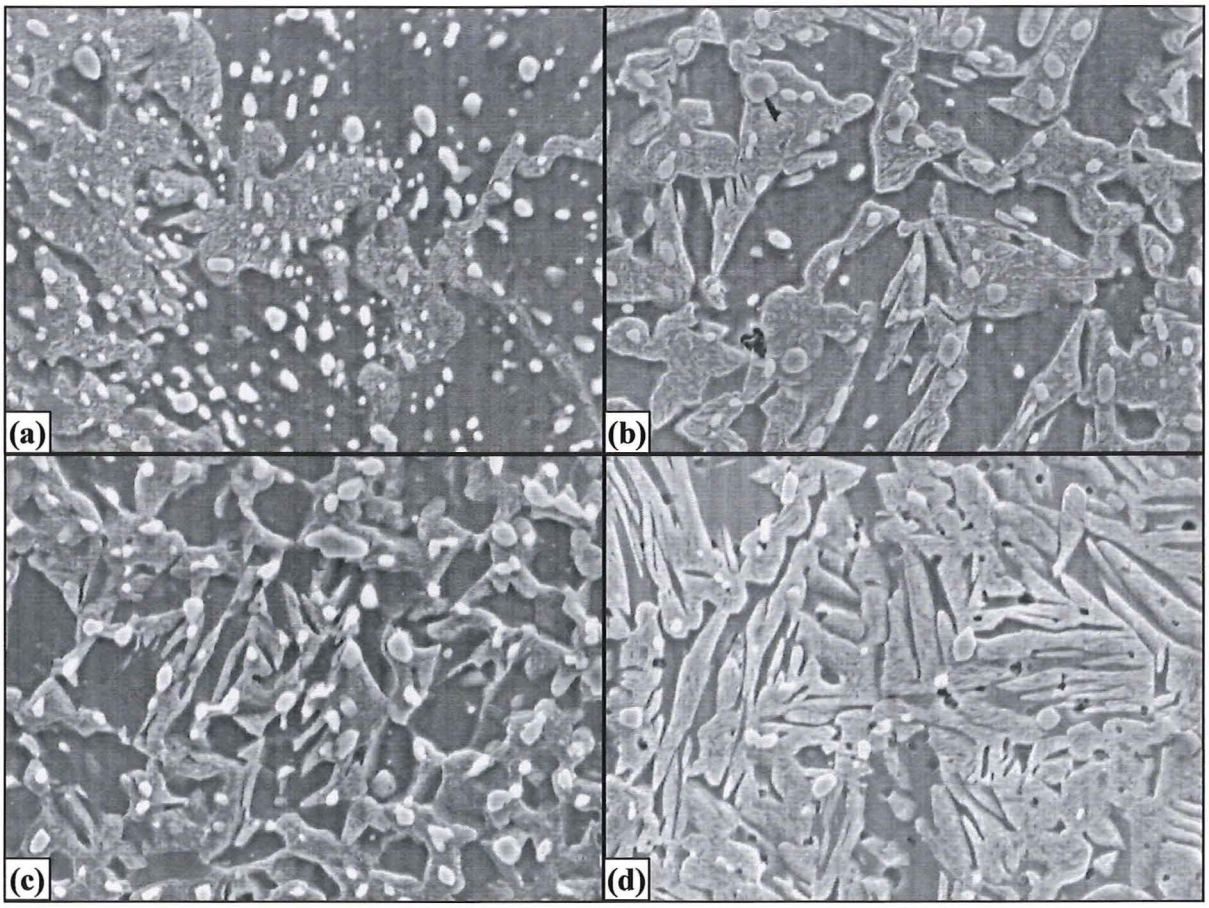

Figure 9.20 Austenitisation microstructures of 96hr tempered martensite initial structures for (a) 0% Silicon after 4min at 740°C, (b) SUP7 after 1min at 820°C, (c) SUP7NV after 1min at 820°C, and (d) 3% Silicon after 1min at 835°C. 2,500x magnification. Nital/Picral etch.

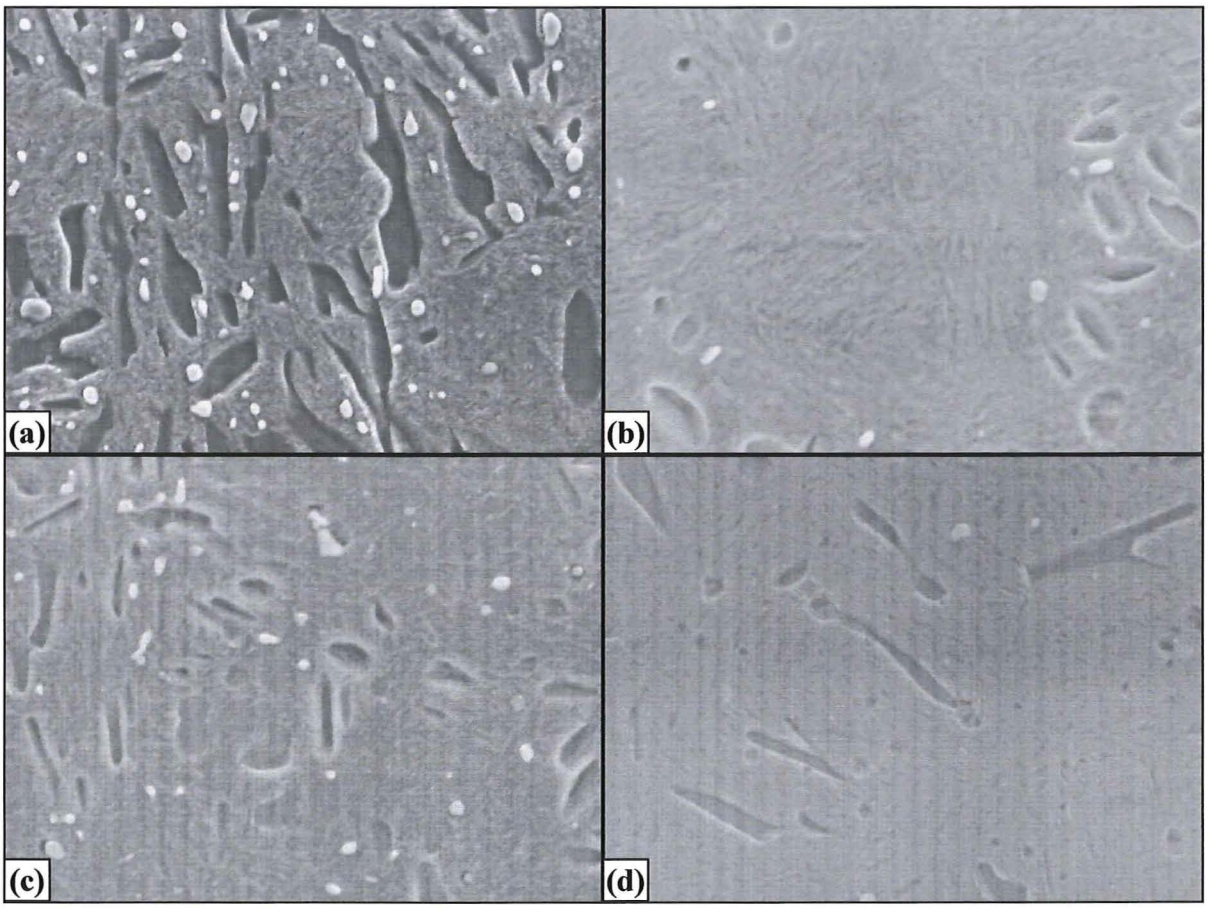

Figure 9.21 Austenitisation microstructures of 96hr tempered martensite initial structures for (a) 0% after 16hr at 740°C, (b) SUP7 after 4hr at 820°C, (c) SUP7NV after 2hr at 820°C, and (d) 3% Silicon after 4hr at 835°C. 2,500x magnification. Nital/Picral etch.

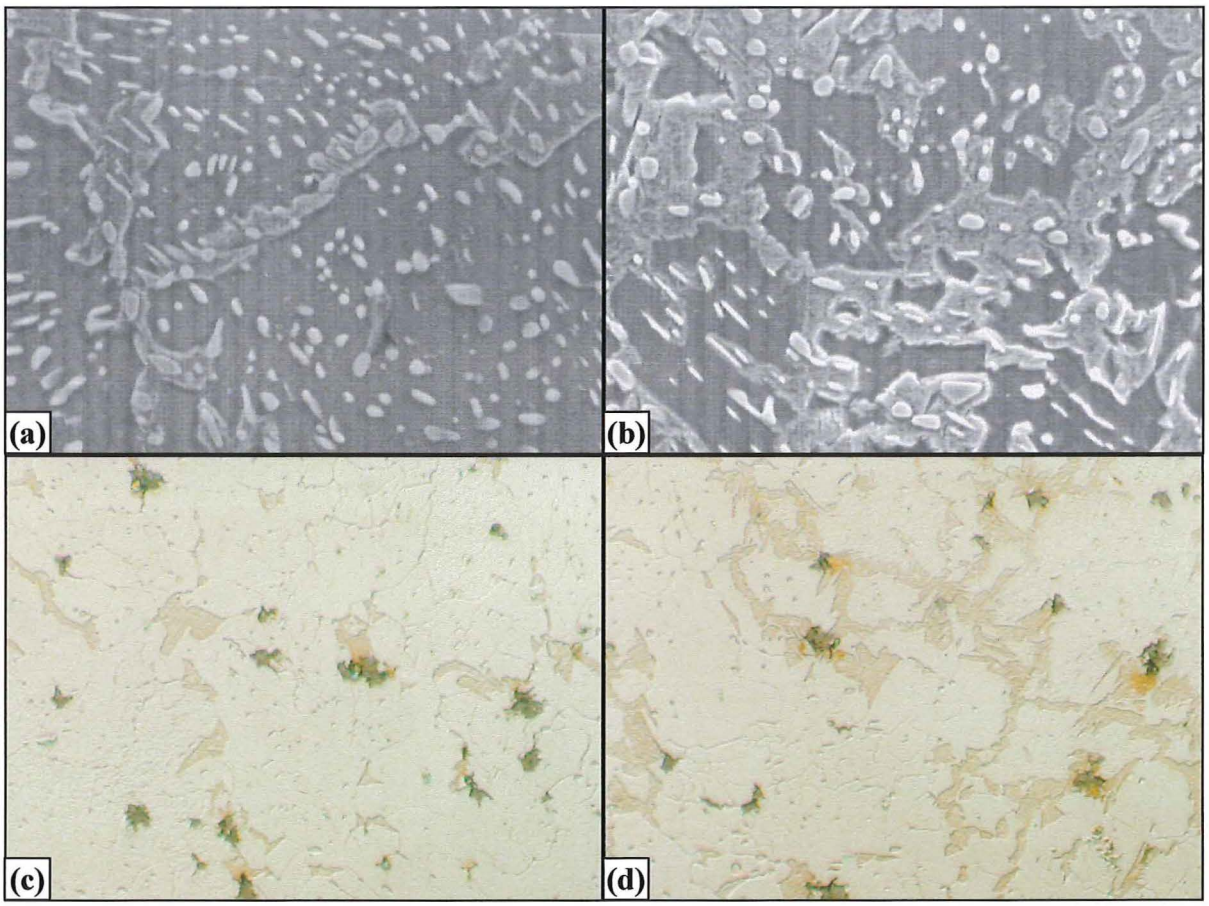

Figure 9.22 Austenitisation microstructures for initial intercritical SUP7 structures at 820°C for (a) 30s, (b) 1min, and for intercritical 3% Silicon structures at 835°C for (c) 30s, and (d) 1min. (a), (b) 2,500x magnification, Nital/Picral etch. (c), (d) 1,150x magnification. 2% Nital etch.

The austenite fraction of 58.8vol.% formed after 1min austenitisation of the 3% Silicon tempered martensite initial structures was approximately three times that of SUP7 and SUP7NV, Figure 9.20(d). Undissolved cementite particles were present in the austenite, with undissolved graphite particles present in the austenite and ferrite.

79.1% austenite formed after 16hr austenitisation at 740°C for the 0% Silicon steel, with the microstructure illustrated in Figure 9.21(a). 1.9vol.% cementite remains undissolved in the austenite. No undissolved cementite was present in the ferrite, since the lower carbon content of the ferrite allowed faster cementite dissolution. Garcia[40] found that the cementite particles of 0.01-0.22wt.%C/1.5wt.%Mn steels that originally resided in the ferrite matrix dissolved during austenitisation. The carbon was thought to have diffused to the growing austenite located at the ferrite grain boundaries.

The austenite transformation was faster for the SUP7 96hr tempered martensite initial structure, resulting in 99.0% austenite and 0.5% undissolved cementite after 4hr at 820°C, Figure 9.21(b). 94.6% austenite formed for SUP7NV after 2hr at 820°C, Figure 9.21(c), compared with 95.4% austenite after 4hr for the 3% Silicon steel at 835°C, Figure 9.21(d). 0.8% undissolved cementite persisted in the SUP7NV austenite, as did a very small cementite fraction in the 3% Silicon steel. The remaining ferrite grains of the four steels were elongated.

The microstructures obtained following austenitisation of SUP7 and 3% Silicon intercritical initial structures at their respective Ac_3 temperatures are shown in Figure 9.22. Austenite nucleated at cementite particles located at the edges where three ferrite grains meet for SUP7, Figure 9.22(a). More equiaxed austenite growth resulted after 1min, Figure 9.22(b), than for the tempered martensite initial structure of Figure 9.20(b). Austenite nucleation in the 3% Silicon steel intercritical structure was predominantly at cementite/ferrite grain boundary triple points, with some nucleation at graphite/ferrite grain boundary triple points, Figure 9.22(c). An elongated austenite grain structure after 1min was demonstrated by the martensite grains present at room temperature, although it was not to the extent of the tempered martensite initial structure for the 3% Silicon steel austenitised 1min at 835°C, Figure 9.20(d). After 1min, the 3% Silicon steel austenite fraction of 20.6% was only a third that of the 96hr tempered martensite initial structure.

9.4 Austenitisation kinetics

9.4.1 Austenitisation kinetics for the different silicon steels

The austenite transformation kinetics for different initial 0 and 1% Silicon steel structures at temperatures corresponding to 0.5 fractional superheats, and their Ac_3 temperatures, are illustrated in Figures 9.23 and 9.24 respectively. Figures 9.25 and 9.26 illustrate the austenitisation kinetics for the SUP7NV and 3% Silicon steels respectively at 0.25 fractional superheats, and at their Ac_3 temperatures. The error bars correspond to 95% confidence intervals, with smoothed lines plotted through the experimental points. The different initial structures are denoted by A, B, C, D or F respectively. These descriptions correspond to the structures formed by the air cooled, furnace cooled, 12hr tempered martensite, 96hr tempered martensite and intercritical heat treatments respectively of Table 7.4. The austenite fractions obtained for the different steels austenitised at intercritical and Ac_3 temperatures are compared in Tables 9.3 and 9.4.

Austenite nucleation occurred after 1hr for the furnace cooled initial 0% Silicon structure at 723°C, Figure 9.23, compared to 2 and 4hr for the tempered martensite and intercritical structures respectively. The furnace cooled structure had the highest austenite fractions of the three initial structures during the early stages of transformation, while the intercritical initial structure had the lowest. However, similar austenite fractions of approximately 31.5% were obtained for the different initial structures after 48hr. The constant austenite fractions for the furnace cooled initial structure from 48hr indicates that the equilibrium austenite fraction had been attained, while the increasing fraction for the intercritical structure indicates that the austenitisation was not complete after 96hr. Both the tempered martensite and intercritical initial structures had greater austenite fractions after 96hr than the furnace cooled structure, Table 9.3, with the intercritical fraction of 37.0% being the greatest.

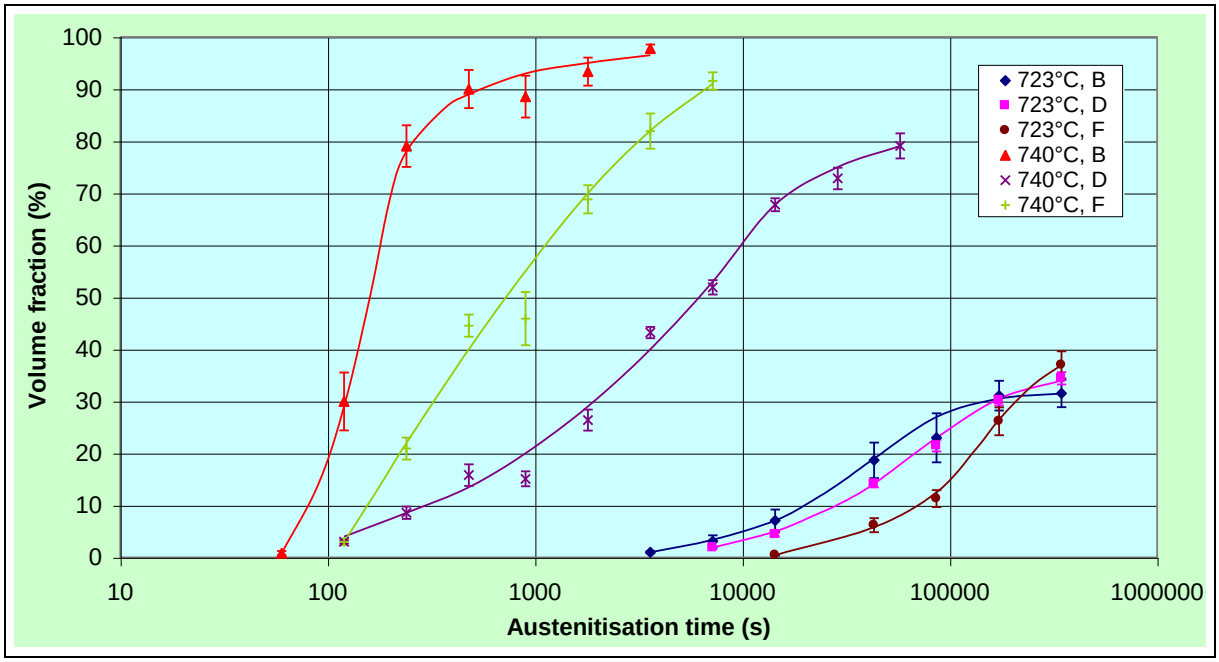

Figure 9.23 Austenitisation kinetics for different initial 0% Silicon structures transformed at 723 and 740°C.

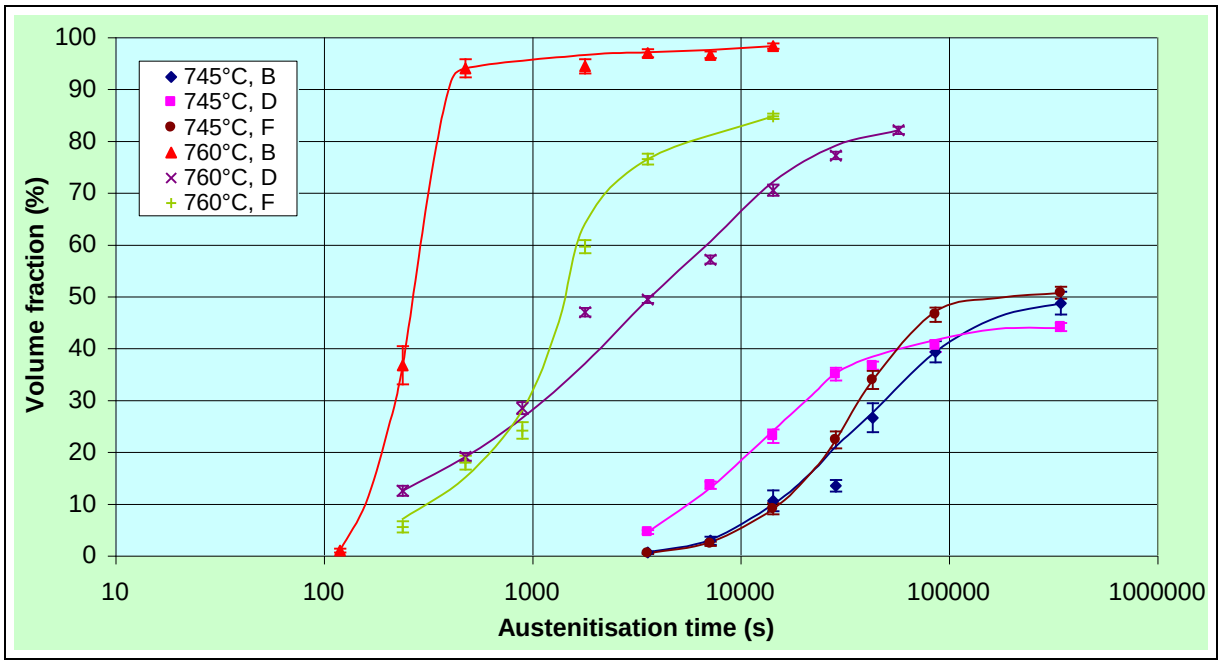

Figure 9.24 Austenitisation kinetics for different initial 1% Silicon structures transformed at 745 and 760°C.

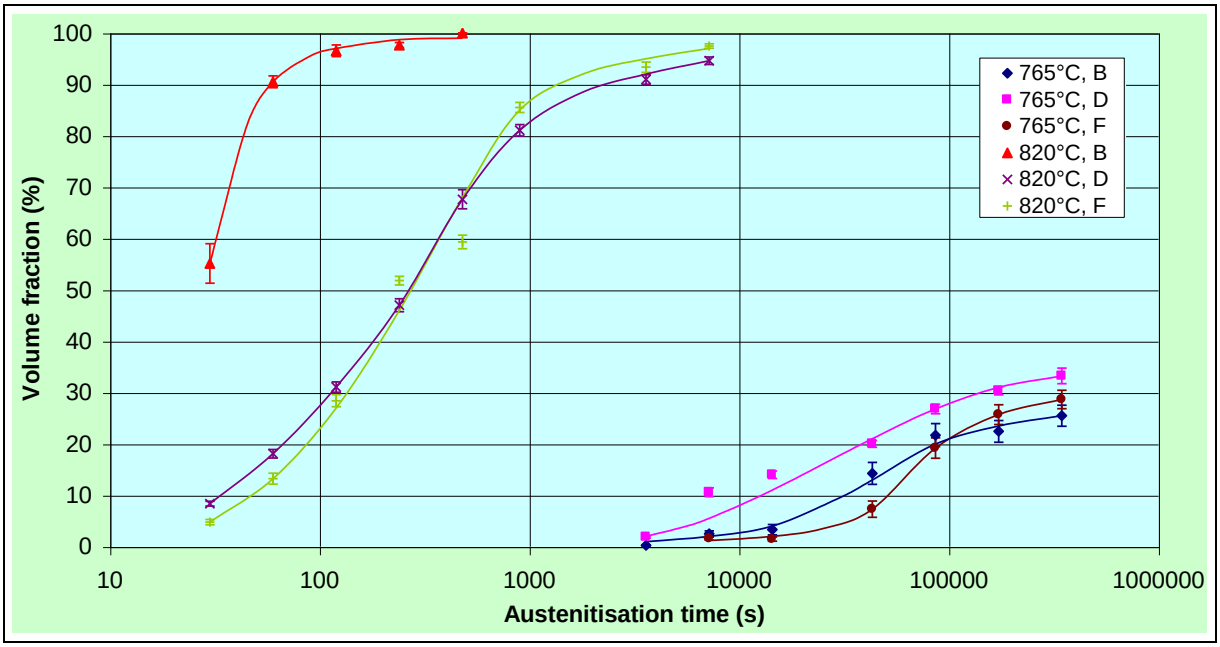

Figure 9.25 Austenitisation kinetics for different initial SUP7NV structures transformed at 765 and 820°C.

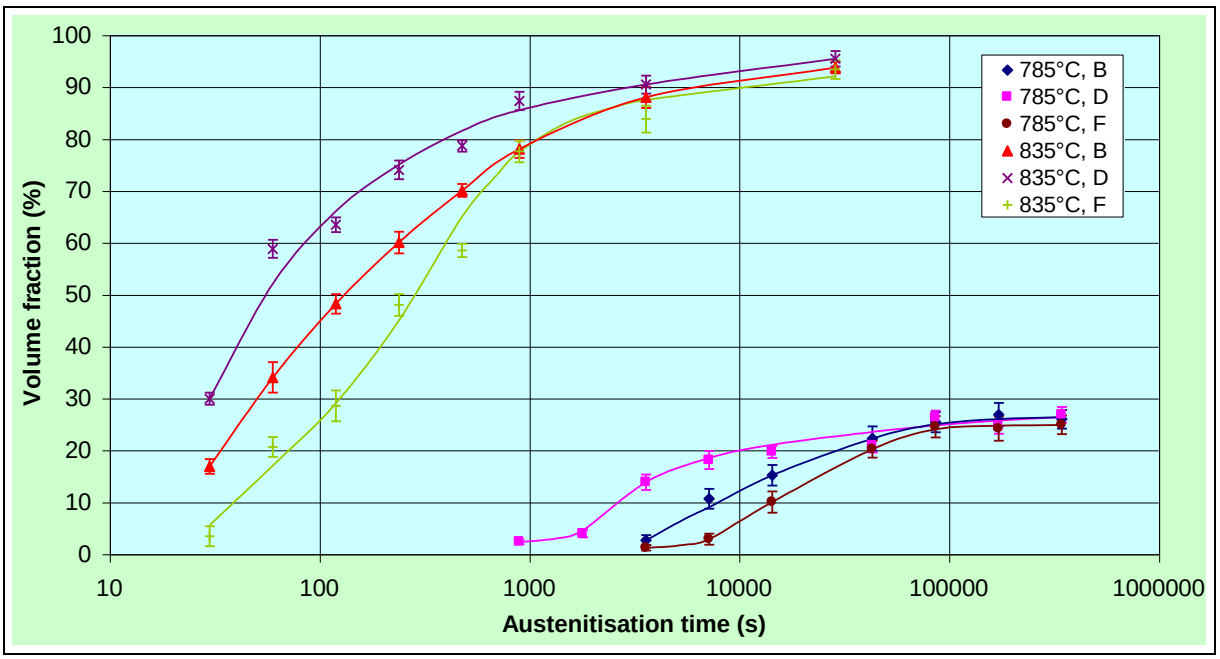

Figure 9.26 Austenitisation kinetics for different initial 3% Silicon structures transformed at 785 and 835°C.

Table 9.3 Austenite fractions obtained for the different silicon steels after intercritical austenitisation.

STEEL	Fractional superheat	Temperature	Structure	AUSTENITE FRACTION (vol.%)			
				1hr	4hr	24hr	96hr
0% Silicon	0.50	723°C	B	1.0	7.1	23.0	31.5
			D	0	4.4	21.5	34.4
			F	0	0.5	11.3	37.0
1% Silicon	0.50	745°C	B	0.5	10.5	39.2	48.6
			D	4.5	23.0	40.4	44.0
			F	0.4	9.0	46.4	50.6
SUP7	0.25	765°C	B	0.6	10.1	28.2	45.8
			D	7.0	27.4	42.6	44.9
			F	0.6	6.2	38.9	48.5
SUP7NV	0.25	765°C	B	0.3	3.3	21.7	25.5
			D	1.8	14.0	26.8	33.3
			F	0	1.5	19.2	28.7
3% Silicon	0.25	785°C	B	2.7	15.2	25.4	26.0
			D	13.8	19.6	26.3	26.8
			F	1.2	10.0	24.5	24.9

Austenite nucleation was observed for all three 1% Silicon steel structures after 1hr at 745°C, as illustrated in Figure 9.24. It can be seen that the tempered martensite structure transformed the fastest during the early heat treatment stages, in comparison with the furnace cooled structure of the 0% Silicon steel at 723°C. 723 and 745°C correspond to the 0.5 fractional superheat temperatures for the 0 and 1% Silicon steels respectively. The constant fraction from 48hr indicates that the austenite transformation was nearing completion after 96hr, with austenite fractions ranging from 44.0% for the tempered martensite initial structure to 50.6% for the intercritical structure. These fractions were higher than those of the 0% Silicon steel with the same fractional superheat, Table 9.3.

Table 9.4 Austenite fractions for the different silicon steels after austenitisation at their respective Ac_3 temperatures.

STEEL	Temperature	Structure	AUSTENITE FRACTION (vol.%)				
			1min	4min	15min	1hr	4hr
0% Silicon	740°C	B	0.8	79.0	88.6	97.8	-
		D	0	8.6	15.1	43.2	67.7
		F	0	20.9	45.9	81.9	-
1% Silicon	760°C	B	0	36.6	93.9	96.8	98.2
		D	0	12.4	28.4	49.3	70.4
		F	0	5.5	24.1	76.4	84.7
SUP7	820°C	B	100	100	100	-	100
		D	24.2	38.8	72.4	-	99.0
		F	18.2	61.0	90.1	-	99.7
SUP7NV	820°C	B	90.6	97.7	100	100	-
		D	18.1	47.0	81.1	91.0	-
		F	13.2	51.8	85.6	93.4	-
3% Silicon	835°C	B	41.4	57.1	75.4	88.8	93.7
		D	58.8	73.9	87.3	90.4	95.4
		F	20.6	48.0	77.5	83.8	93.3

Austenite formation at a 0.25 fractional superheat for SUP7NV, Figure 9.25, and the 3% Silicon steel, Figure 9.26, was also faster for the tempered martensite initial structures. The austenite fractions were still increasing for all three SUP7NV initial structures at 96hr, ranging from 25.5 to 33.3% for the furnace cooled and tempered martensite structures respectively, Table 9.3. However, the transformation kinetics were similar for the three initial 3% Silicon structures after 24hr, with constant austenite fractions of 26.3, 26.8 and 24.9% for the furnace cooled, 96hr tempered martensite and intercritical initial structures respectively.

Figures 9.23 to 9.25 illustrate the faster austenite formation of the furnace cooled 0% Silicon, 1% Silicon and SUP7NV steels at their respective Ac_3 temperatures relative to the tempered martensite and intercritical structures. 79.0% austenite formed after 4min for the furnace cooled 0% Silicon steel initial structure, Table 9.4, compared with 8.6 and 20.9% for the tempered martensite and intercritical structures respectively. However, this austenite growth is

considerably slower than that of a plain carbon Fe-0.96%C steel, which formed 98% austenite in less than 0.1s at the Ac_3 temperature[36]. This compares with 1hr for the 0% Silicon steel to attain 98% austenite. Roosz[186] demonstrated that a 0.78wt.%C/0.35wt.%Si/ 0.55wt.%Mn pearlitic steel required approximately 150s to form 50% austenite, which is consistent with the observed experimental results of the furnace cooled 0% Silicon initial structure.

The shorter diffusion distances for carbon to the growing austenite due to the finer cementite particles of the intercritical structure, which also had a significant lamellar cementite fraction, relative to the tempered martensite initial structure of the 0% Silicon steel at 740°C, resulted in faster austenitisation kinetics. 81.9% austenite formed after 1hr for the intercritical structure, compared with 43.2% for the tempered martensite structure.

Less difference in the austenitisation kinetics were observed for the 1% Silicon intercritical and tempered martensite initial structures at 765°C than for the comparable structures of 0% Silicon steel at 740°C. Smaller austenite fractions were obtained for the intercritical structure up to 15min compared to the tempered martensite structure, Table 9.4, and higher fractions for the longer tests. The transformation kinetics of SUP7NV tempered martensite and intercritical initial structures at the Ac_3 temperature of 820°C, Figure 9.25, were very similar. The tempered martensite initial structure transforms slightly faster for less than 50% austenite, and slower above 70% austenite.

A comparison of Figures 9.23 to 9.26, and the tabulated values of Table 9.4, demonstrate less influence of initial structure on the austenitisation kinetics for the 3% Silicon steel compared to the lower silicon steels at their respective Ac_3 temperatures, which is shown by less difference in the austenite fractions for the different initial structures after comparable test durations.

The austenitisation kinetics were faster for the 96hr tempered martensite 3% Silicon initial structure than for the furnace cooled structure. This differs from the lower silicon steels, where faster austenite formation resulted for the furnace cooled initial structures, and is attributed to the higher graphite and lower cementite fractions of the initial 3% Silicon steel structures relative to the lower silicon steels. Therefore, carbon release from graphite dominated the austenite transformation, with the finer and more numerous graphite particles

of the tempered martensite structure yielding shorter carbon diffusion distances from the dissolving graphite to the growing austenite, and therefore faster austenitisation.

9.4.2 Detailed SUP7 austenitisation kinetics

Given the extensive use of SUP7 in automobile coil springs, the austenitisation kinetics for SUP7 were investigated in more detail than the other steels. The austenitisation kinetics of different initial SUP7 structures at a 0.13 fractional superheat are illustrated in Figure 9.27. A significant incubation time was observed prior to the formation of austenite, being 1hr for the tempered martensite structures, 2hr for the pearlitic structures, and 4hr for the intercritical structure. A higher fraction of austenite formed for the tempered martensite SUP7 initial structures than for the pearlitic structures, with approximately 25 and 15% austenite respectively after 192hr. Despite the longer incubation period for the intercritical initial structure, the austenitisation kinetics of Figure 9.27 illustrate that the rate of austenite growth was faster than the other initial structures once nucleation occurred, with 28% austenite formed after 192hr.

The lower austenite fractions after 192hr for the pearlitic initial structures are thought to be due to banding in the pearlitic initial structures. This results in bands of fine pearlite with high manganese concentrations separated by regions of coarse pearlite with low manganese concentrations[190]. Therefore, segregation in the carbon concentration arises, with higher carbon contents in the banded regions than in the remainder of the matrix. Banding has been observed to be less severe in tempered martensite initial structures[40], with the difference in carbon concentration between the banded and non-banded regions less. Therefore, the average carbon content of the non-banded regions would be higher for the tempered martensite initial structure[40]. This greater uniformity of the initial carbon distribution resulted in the higher austenite fractions for the tempered martensite initial structures after 192hr.

The lower austenite fractions of the pearlitic initial structures demonstrates that the equilibrium austenite fraction has not been obtained. Diffusion of manganese from the high manganese regions will eventually eliminate the local carbon concentration gradients of the pearlitic initial structures arising from the banding, and allow the equilibrium austenite fraction to be obtained. The similarity of the final austenite fractions for the furnace cooled

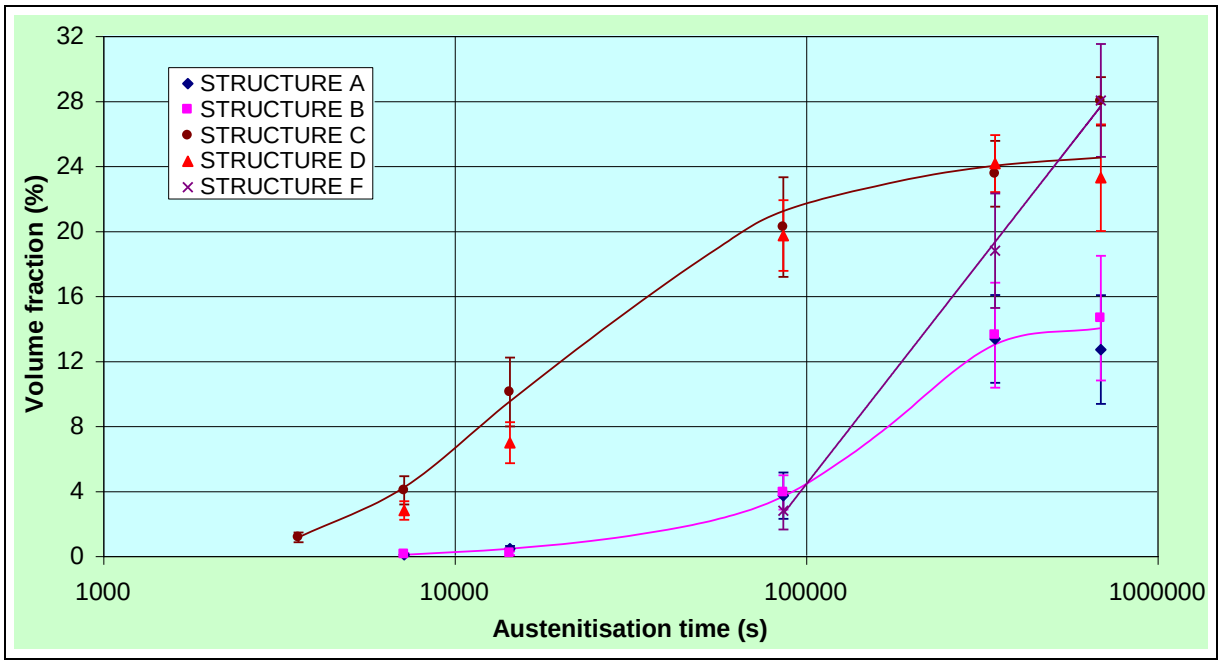

Figure 9.27 Austenitisation kinetics for different initial SUP7 structures at 755°C.

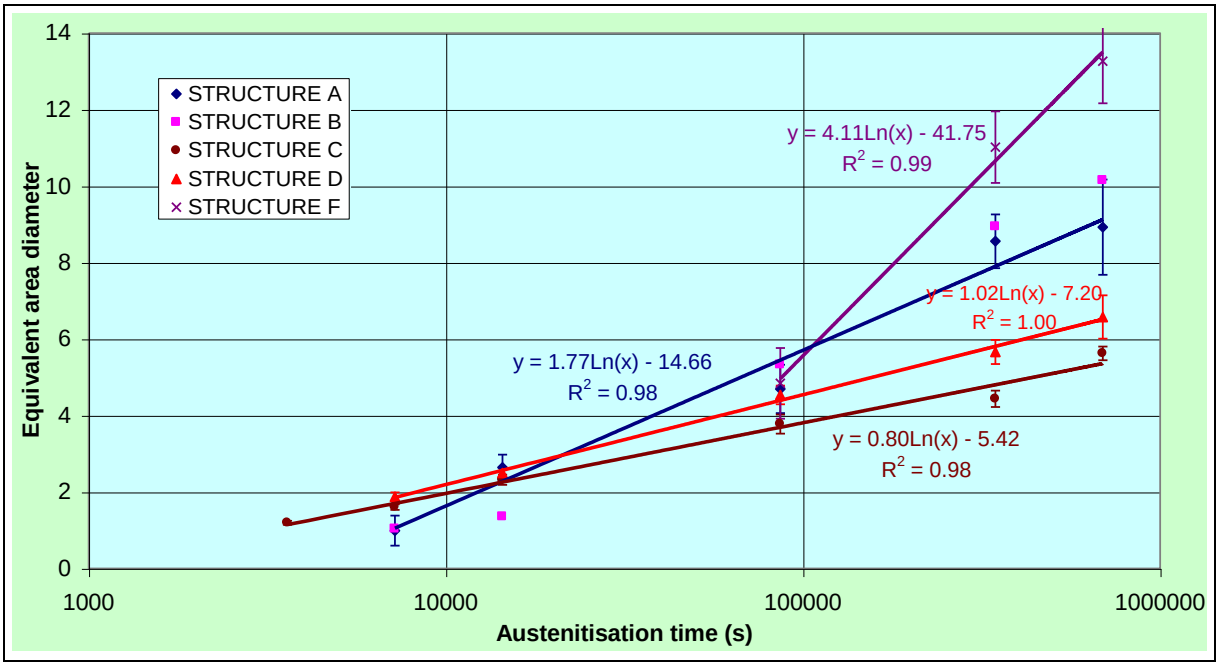

Figure 9.28 Austenite grain growth kinetics for different initial SUP7 structures at 755°C.

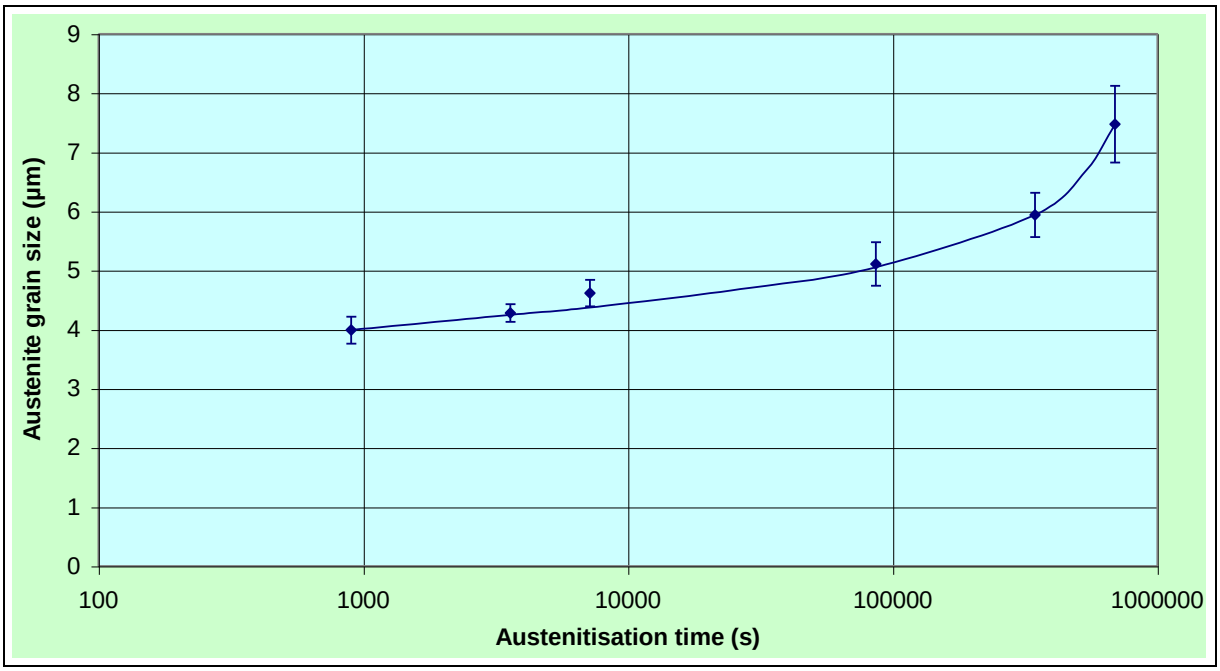

Figure 9.29 Ferrite grain growth kinetics for a 96hr tempered martensite initial SUP7 structure at 755°C.

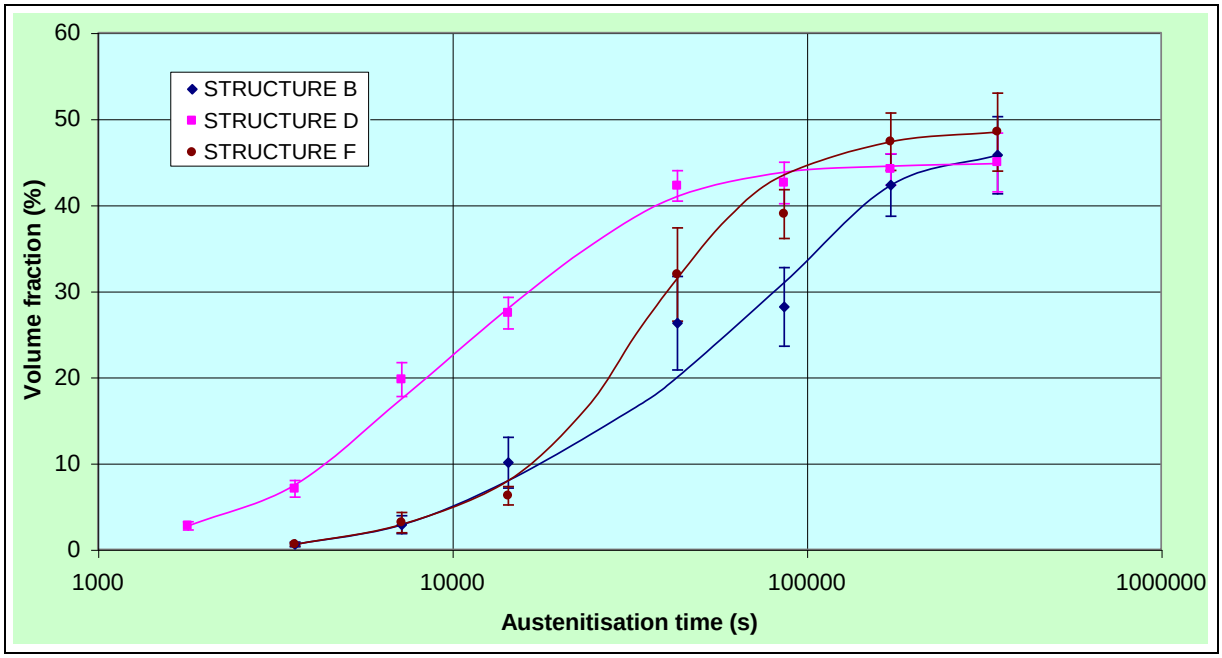

Figure 9.30 Austenitisation kinetics for different initial SUP7 structures at 765°C.

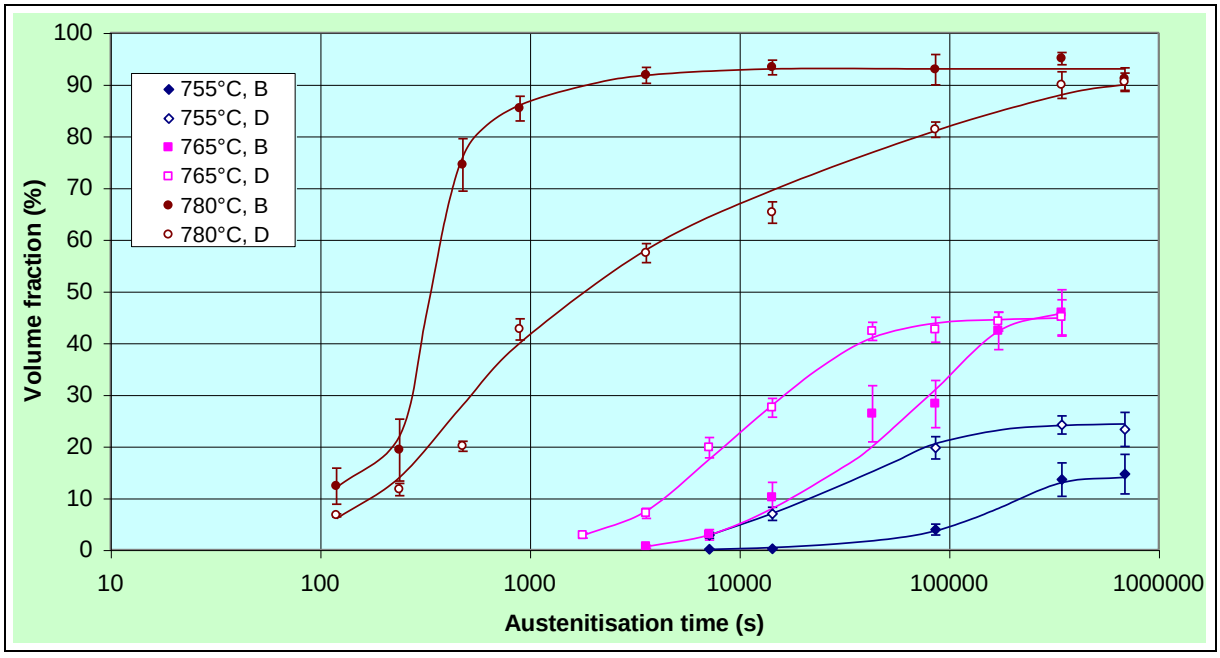

Figure 9.31 Comparison of austenitisation kinetics for SUP7 furnace cooled and 96hr tempered martensite initial structures at different fractional superheats.

and 96hr tempered martensite initial structures, 45.8 and 44.9% respectively, demonstrates the smaller influence of the banded initial structures than at 755°C.

The different coarseness of the two pearlitic structures did not influence the austenitisation kinetics, with both the air and furnace cooled structures exhibiting similar transformation kinetics, Figure 9.27. Similarly, the different ferrite grain sizes and cementite particle size distributions of the 12 and 96hr tempered martensite initial structures did not effect the austenitisation kinetics. The interlamellar spacing of the two pearlitic structures had no influence on the austenite grain size kinetics, as illustrated in Figure 9.28. However, the austenite grain sizes obtained during austenitisation of the 96hr tempered martensite initial structure were coarser than those of the 12hr tempered martensite structure for the comparable heat treatments.

The austenite grain size kinetics for different initial SUP7 structures at 755°C are illustrated in Figure 9.28. The coarser initial ferrite grain size of the 96hr tempered martensite initial structure yielded a coarser austenitic structure than the 12hr tempered martensite structure. The similar kinetics for the pearlitic structures indicates that the pearlite interlamellar spacing did not affect the austenite grain size kinetics of the pearlitic initial structures. The increase in the ferrite grain size of the two or three phase structures, calculated by the method of section 8.2.4, during austenitisation of the 96hr tempered martensite initial structure at 755°C is illustrated in Figure 9.29.

An increase in the heat treatment temperature by 10°C to 765°C for SUP7 accelerated the transformation kinetics, with 27.4% austenite for the 96hr tempered martensite initial structure after 4hr, compared with 7.0% at 755°C. The austenite fractions after 96hr at 765°C were twice those of the 96hr heat treatments at 755°C. The dependence of the austenite fractions on the initial structures for prolonged heat treatments observed at 755°C was not as large at 765°C, varying from 44.9 to 48.5% after 96hr for the tempered martensite and intercritical structures respectively. The austenitisation kinetics for different initial SUP7 structures austenitised at 765°C are illustrated in Figure 9.30.

Figure 9.31 illustrates the influence of heat treatment temperature on the austenitisation kinetics for different initial SUP7 structures. The increasing heat treatment temperature

reduced the incubation time for austenite nucleation, and increased the austenitisation kinetics and the austenite fractions obtained from the longest duration heat treatments. At 0.13 and 0.25 fractional superheats, austenite growth was faster for the tempered martensite structure. However, at a 0.5 fractional superheat, 780°C, the furnace cooled structure transformed considerably faster than the tempered martensite structure.

The mechanisms controlling austenite growth for plain carbon and low alloy steels with pearlitic or spheroidal cementite initial microstructures are subject to some debate. Various authors subscribe to austenite growth being controlled by carbon diffusion in austenite[36,46,189], while others attribute the rate controlling mechanism to an interface reaction at the ferrite/austenite interface[33,186]. It is generally accepted that the growth of austenite from ferrite/pearlite initial structures for 0.06-0.20wt.%C/1.5wt.%Mn steels involves three steps[39]:

1) Very fast austenite growth into pearlite until pearlite dissolution is complete;
2) Slower austenite growth into ferrite at a rate controlled by carbon diffusion in austenite at high temperatures of approximately 850°C, and by manganese diffusion in ferrite or along grain boundaries at lower temperatures of approximately 750°C;
3) Very slow final equilibration of ferrite and austenite at a rate controlled by manganese diffusion in austenite.

The first step involves pearlite dissolution and austenite growth into the pearlite. The growth rate of austenite is controlled by carbon diffusion in the austenite, with the diffusion path lying along the pearlite/austenite interface. The diffusion distance is approximately equal to the pearlite interlamellar spacing[36]. Therefore, the very short diffusion distances results in extremely fast austenite growth. However, at temperatures close to the Ac_1 temperature, the slower diffusion of substitutional elements such as manganese may also be rate controlling, which greatly reduces the austenite growth rate[32,36]. A small temperature increase can cause a transition from substitutional to interstitial diffusion control, and a large increase in the pearlite dissolution rate. Speich[36] demonstrated that the pearlite dissolution rate was three orders of magnitude higher at 780°C than at 730°C.

Two thermodynamic causes contribute to the rate of austenite formation being controlled by manganese diffusion at lower temperatures:

1) The decrease in free energy in the austenite as a function of its manganese content, which is inversely temperature dependent, and so becomes more effective in the lower part of the intercritical temperature range;
2) The decrease in the cementite dissolution rate responsible for supplying carbon to the growing austenite.

Austenite formation in spheroidal cementite initial structures commences with the formation of an austenite particle at suitable ferrite/cementite locations, which forms a shell around the cementite particles as it starts to dissolve. The subsequent growth of the austenite shell requires carbon diffusion from the dissolving cementite particle at the austenite/cementite interface through the austenite to the austenite/ferrite interface, and from ferrite/cementite interfaces through the ferrite to the ferrite/austenite interface.

At the beginning of austenitisation, the austenite shell inherits the alloying element distribution of the initial structure[32]. Consequently, the higher manganese and chromium, and lower silicon concentrations at the cementite/austenite boundary decreases the carbon activity at this interface[35]. At the austenite/ferrite and cementite/ferrite boundaries, lower manganese and chromium, but higher silicon concentrations exist, raising the carbon activity at these interfaces[35]. These local changes in the equilibrium lower the carbon concentration gradient across the growing austenite and across the ferrite from the ferrite/cementite interfaces, which lowers the driving force for carbon diffusion, and therefore reduces the austenite growth rate[35]. The austenitisation is further retarded by the partitioning of silicon to ferrite and manganese to austenite, which increases the stability of the ferrite.

Carbon diffusion across the ferrite from the ferrite/cementite interface to the ferrite/austenite interface is governed by the difference in the carbon activities at these interfaces. If the carbon activity at the cementite/ferrite interface is less than the activity at the ferrite/austenite interface, austenite growth cannot proceed by carbon diffusion through the ferrite. Therefore, austenite growth can only occur by carbon diffusion across the austenite shell from the austenite/cementite interface.

In order to determine whether austenite growth occurred by carbon diffusion through the ferrite or austenite, the carbon activities of the various interfaces have to be determined. The

contribution of carbon diffusion through the ferrite to austenite growth could not be determined because of a lack of information on the carbon activities at the cementite/ferrite interface. However, Hillert[32] concluded that the increase in the austenite growth rate by a factor of 100 for a Fe/0.83wt.%C/0.52wt.%Cr steel, as the temperature increased from 770 to 810°C, was controlled by the carbon concentration gradient across the austenite particles, and that carbon diffusion through the ferrite phase could be neglected.

The driving force for carbon diffusion across the austenite grain depends on the difference between the carbon activities at the austenite/cementite and ferrite/austenite interfaces. It is commonly assumed that the growing austenite inherits the alloy content of the phases into which it grows[32]. Therefore, for austenite nucleation at a cementite particle, the austenite growing into the cementite will inherit the cementite alloy content, while the austenite growing into the ferrite will inherit the ferrite alloy content.

Consider the growth of an austenite particle nucleated at a spheroidal cementite particle for a 96hr tempered martensite SUP7 structure. Assuming that the ferrite and cementite compositions correspond to those of the initial structures, with no partitioning of the alloying elements prior to austenite nucleation, the alloy compositions at the austenite/cementite and ferrite/austenite interfaces can be determined from the quantitative analysis of the initial structure. The quantitative analysis of the initial structures, Section 9.2.3, demonstrates that the austenite in contact with the austenite/cementite interface will inherit an alloy content of 3.5wt.%Mn and 1.3wt.%Cr from the cementite, while the austenite in contact with the ferrite/austenite interface will inherit 1.9wt.%Si and 0.6wt.%Mn from the ferrite. The activity coefficient of carbon in austenite can be determined from the equation of Wada[92] for Fe-Si-Mn-Cr-C alloy, where

$$\log f_c\left[FeMnSiC\right] = \left(\frac{180 + 8.90\%Si}{T}\right)\%C + \left(0.041 + \frac{62.5}{T}\right)\%Si - \left(\frac{21.8}{T}\right)\%Mn - \left(\frac{102}{T} - 0.033\right)\%Cr\,. \qquad (3.12)$$

The carbon contents at the ferrite/austenite and austenite/cementite interfaces correspond to the Ac_3 and A_{cm} values respectively at the heat treatment temperature, and can usually be

determined from the appropriate phase diagram. However, an eutectoid gap exists for SUP7 over 745 to 780°C, with a three phase ferrite/austenite/cementite region, instead of a specific Ac_1 temperature. Therefore, the carbon content at the ferrite/austenite and austenite/cementite interfaces within this temperature range are not defined by the Ac_3 and A_{cm} values.

However, in order to obtain an estimate of the carbon activities at the ferrite/austenite and austenite/cementite interfaces, the eutectoid gap was replaced by an Ac_1 temperature. Therefore, the carbon contents at the ferrite/austenite and austenite/cementite interfaces for temperatures greater than the Ac_1 temperature correspond to the respective Ac_3 and A_{cm} values. The Ac_3 and A_{cm} carbon contents were calculated from the Fe-C-2wt.%Si composition diagram of Bain[55], which is illustrated later in this chapter in Figure 9.49(a). The Ac_1 temperature of this steel differs from that determined for SUP7. However, the manganese and chromium concentrations have a small effect on the phase boundary concentrations, other than to change the Ac_1 temperatures. Therefore, the Ac_3 and A_{cm} carbon contents of the Fe-C-2wt.%Si steel[55] at 10, 20, 35, 55 and 75°C above the Ac_1 temperature were used for the comparable temperature intervals above the Ac_1 temperature of SUP7. These carbon contents are listed in Table 9.5.

The activity coefficients at the ferrite/austenite and austenite/cementite interfaces calculated from equation 3.12 are converted to carbon activities by

$$a_c = f_c.[\%C]. \qquad (3.14)$$

The carbon activities at the austenite/cementite and ferrite/austenite interfaces are listed in Table 9.5. The difference between these two values at 755, 765 and 780°C is negative, which means that austenite growth by carbon diffusion from the austenite/cementite interface cannot occur. However, the austenitisation kinetics of Figures 9.27, 9.30 and 9.31 for these temperatures demonstrate that austenite growth occurred by some other mechanism.

Table 9.5 Calculated carbon activities at ferrite/austenite and austenite/cementite interfaces for a 96hr tempered martensite SUP7 initial structure.

Temperature	Interface carbon content (wt.%)		Interface carbon activity (a_c)		Δa_c^{γ} (γ/cem - α/γ)
	α/γ	γ/cem	α/γ	γ/cem	
755°C	0.56	0.62	1.07*	0.59	-0.48
765°C	0.52	0.64	0.97	0.62	-0.35
780°C	0.47	0.68	0.85	0.67	-0.18
800°C	0.40	0.74	0.70	0.75	0.05
820°C	0.34	0.79	0.58	0.82	0.24

The austenite growth at 755, 765 and 780°C occurred following the diffusion of manganese and chromium from the austenite/cementite interface. This lowered the manganese and chromium contents at this interface, and therefore raised the carbon activity. The absence of initial austenite growth, with low austenite fractions observed for several hours at 755°C, allowed sufficient time for the diffusion of manganese and chromium from the austenite/cementite interface to increase the carbon activity at this interface to higher than the carbon activity at the ferrite/austenite interface. Austenite growth controlled by carbon diffusion through the ferrite could then proceed.

The smaller difference between the austenite/cementite and ferrite/austenite carbon activities as the temperature increased to 780°C required less alloy element diffusion for austenite growth to proceed. This, in conjunction with the increasing diffusivity of the substitutional elements with temperatures, accounts for the austenite growth occurring at shorter times, and at a faster rate. The positive difference between the carbon activities of the austenite/cementite and ferrite interfaces at 800 and 820°C, Table 9.5, meant that alloy diffusion did not have to occur for austenite growth to proceed.

***** A carbon activity greater than one is not theoretically possible. This value of 1.07 is thought to be due to the uncertainties involved in accurately determining the alloy contents present at the ferrite/austenite interface.

Critical temperatures of 795°C and 760°C respectively were determined by Hillert[32] for Fe/0.83wt.%C/0.52wt.%Cr and Fe/0.96wt.%C/0.24wt.%Si/0.20wt.%Mn/0.09wt.%Cr steels with austenite growth controlled by carbon diffusion through the ferrite and austenite without prior alloy element diffusion. The austenite growth observed below these critical temperatures was attributed to alloy element diffusion from the austenite/cementite interface increasing the carbon activity sufficiently for carbon diffusion across the austenite to occur.

Hillert[32] derived equations incorporating the growth rate of austenite by carbon diffusion through ferrite and austenite for spheroidal cementite and pearlitic initial structures. For austenite formation around a spheroidal cementite particle, assuming that the growth rate of the ferrite/austenite interface eventually approaches a constant value, the growth rate is given by[32]:

$$v = \frac{4}{r_o}\left[\frac{u_c^{cem} - u_c^{\alpha}}{\bar{u}_c - u_c^{\alpha}}\right]^{1/3} \cdot \frac{\dfrac{D_c^{\alpha}\Delta u_c^{\alpha}}{u_c^{cem} - u_c^{\alpha}} + \dfrac{D_c^{\gamma}\Delta u_c^{\gamma}}{u_c^{cem} - u_c^{\gamma}}}{1 - \left(1 - \dfrac{u_c^{\gamma/\alpha} - u_c^{\alpha}}{\bar{u}_c - u_c^{\alpha}}\right)^{2/3} \cdot \left(\dfrac{u_c^{cem} - u_c^{\alpha}}{u_c^{cem} - u_c^{\gamma}}\right)^{2/3}}, \qquad (9.2)$$

where v = austenite growth rate;

r_o = initial cementite particle size;

u_c^{cem} = cementite carbon content;

u_c^{α} = ferrite carbon content;

$\bar{u}_c$ = bulk steel carbon content;

D_c^{α} = diffusion coefficient of carbon in ferrite;

$=D_c^{\gamma}$ diffusion coefficient of carbon in austenite;

Δu_c^{α} = $u_c^{cem/\alpha} - u_c^{\alpha/\gamma}$;

= $u_c^{\gamma/cem} - u_c^{\alpha/\gamma}$;

$u_c^{cem/\alpha}$ = carbon content at cementite/ferrite interface;

$u_c^{\alpha/\gamma}$ = carbon content at ferrite/austenite interface;

$u_c^{\gamma/cem}$ = carbon content at austenite/cementite interface.

The austenite growth rate for pearlitic structures is given by[32]

$$v = \frac{D_c^{\alpha}\Delta u_c^{\alpha} + D_c^{\gamma}\Delta u_c^{\gamma}}{\sigma_t\left(u_c^{\alpha/\gamma} - u_c^{\alpha}\right)}, \qquad (9.3)$$

where σ_t = true pearlite interlamellar spacing.

Equations 9.2 and 9.3 demonstrate that the austenite growth rate is influenced by the cementite particle size, the carbon diffusion in ferrite and austenite, and the carbon concentration gradient across the ferrite and the growing austenite. The faster austenitisation kinetics for SUP7 with increasing temperature were due to the increased carbon diffusivity, and the increasing value of Δu_c^{γ} due to the increasing separation between the Ac_3 and A_{cm} lines. The A_{cm} carbon contents correspond to those at the ferrite/cementite interface. The alloying elements have less influence on the austenite growth rate at higher temperatures, due to the increasing separation between the Ac_3 and A_{cm} lines resulting in the magnitude of this separation being proportionally less influenced by the alloy element partitioning.

The contribution of carbon diffusion from dissolving cementite particles through ferrite to the growing austenite could not be determined from the available information. However, the microstructural photos of Figures 9.19 to 9.21 for 96hr tempered martensite initial SUP7 structures after austenitisation at 820°C illustrate that few undissolved cementite particles were present in the ferrite at greater than approximately 20% austenite. Therefore, further austenite growth occurred by carbon diffusion through the austenite from the austenite/cementite interface. However, the presence of undissolved cementite in the ferrite for pearlitic initial structures at high austenite fractions, Figure 9.12, indicates that the possibility of carbon diffusion contributing to the austenite growth cannot be dismissed.

The faster austenitisation kinetics for SUP7 96hr tempered martensite initial structures at 755 and 765°C compared to the furnace cooled initial structures was due to the greater number of austenite particles nucleated. The austenite growth rate at these temperatures was dependent upon the diffusion of carbon and the alloying elements, which in turn was dependent on the cementite particle size and the associated diffusion distances. The greater surface area to

volume ratio of the lamellar cementite relative to the spheroidal cementite of the tempered martensite initial structure, and the shorter diffusion distances, influences the austenite growth in two ways. Faster diffusion of alloying elements can occur from the austenite/cementite interface, while the diffusion distances for carbon through the austenite are shorter. Therefore, a faster austenite growth rate should result for the pearlitic structures.

This is borne out by Figures 9.28 and 9.67,which demonstrate a faster austenite growth rate for the furnace cooled initial structure at 755 and 765°C. The austenite growth rate for the linear portion of Figure 9.67 at 765°C was 40% faster for the furnace cooled initial structure than for the 96hr tempered martensite initial structure. However, the austenitisation kinetics were dependent on the austenite growth rate, and the number of austenite particles. After 4hr at 755°C, the tempered martensite initial structure comprised 13,500 austenite particles per mm^2, as measured from the martensite particles of the microstructure, compared with 400 austenite particles per mm^2 for the furnace cooled structure. Therefore, the larger number of austenite particles for the tempered martensite initial structure more than offset the slower growth rate, resulting in faster austenitisation.

The longer austenite incubation time for the intercritical structure at 755°C relative to the tempered martensite initial structures arises because of the initial location of the majority of the cementite particles within the ferrite grains. As the energy required to nucleate austenite at cementite particles within a ferrite grain is greater than at a ferrite grain boundary[40], very few potential austenite nucleation sites exist for the intercritical structure, and so austenite formation is almost non-existent.

Judd[46] demonstrated that the austenite nucleation incubation period for a 0.1wt.%C/0.45wt.%Mn steel with spheroidised cementite particles located within the ferrite grains was three times that of the same steel with the cementite particles located on the ferrite grain boundaries. This was attributed to the surface energy contribution of the bulk free energy necessary for the formation of stable austenite nuclei. However, after 4hr, considerable recrystallisation of this structure occurred, with the majority of the cementite particles now situated on the ferrite grain boundaries.

The austenite growth for the intercritical initial structure then became faster than that of the tempered martensite structure. This was due to two reasons:

1) Higher cementite manganese and chromium concentrations of the 96hr tempered martensite initial structure relative to the intercritical initial structure;
2) Austenite growth along the ferrite grain boundaries of the tempered martensite initial structure, compared to the equiaxed austenite growth for the intercritical initial structure.

The higher cementite manganese and chromium contents of the tempered martensite structure lower the carbon activity at the austenite/cementite interface relative to the intercritical structure. The considerable cementite particle fraction located within the ferrite grains means that during the movement of the ferrite/austenite interface into the ferrite grains for the intercritical initial structure, the partitioning of the alloying elements on this interface is associated with a volume diffusion of alloying elements in the ferrite and austenite. As the austenite growth occurred predominantly along the ferrite grain boundaries for the 96hr tempered martensite initial structure, greater partitioning of silicon and manganese occurred between the ferrite and austenite relative to the intercritical structure due to the grain boundary diffusion of alloying elements being greater than the volume diffusion. This increased the ferrite stability, while the lower carbon activity at the austenite/cementite interface, and the higher carbon activity at the ferrite/austenite interface lowered the driving force for austenite growth.

The two different pearlitic structures exhibited similar austenitisation kinetics, as did the two tempered martensite initial structures. It could be expected that of the pearlitic and tempered martensite initial structures, the finer structure for each type of heat treatment would have allowed faster manganese and chromium diffusion from the austenite/cementite interface, and therefore faster austenite growth. The greater surface area to volume ratio of the finer structures, and the shorter distances for carbon diffusion should have also contributed to a faster austenite growth rate. Therefore, the reason for the similarity of the austenitisation kinetics observed is not readily apparent.

Table 9.6 compares the influence of temperature on the time required for 50% of the final austenite fraction to form. A 10°C increase from 755 to 765°C decreased this time by a factor of three for the furnace cooled and 96hr tempered martensite initial structures. The time required for 50% of the final austenite fraction to form was 160 times longer at 765°C than at 780°C for the furnace cooled initial structure, and 8 times longer for the tempered martensite initial structure.

Table 9.6 Influence of temperature on the time for 50% of the final austenite fraction to form for SUP7.

Structure	**Time for 50% completion of austenite formation (s)**					**Ratio of higher temperature to lower temperature times for 50% completion of austenite formation**			
						755-765°C	**765-780°C**	**780-800°C**	**800-820°C**
	755°C	**765°C**	**780°C**	**800°C**	**820°C**	$\Delta T = 10°C$	$\Delta T = 15°C$	$\Delta T = 20°C$	$\Delta T = 20°C$
B	150,000	52,000	320	50	<30	3	160	6	-
D	28,000	10,000	1,200	650	340	3	8	2	2

This indicates that a transition had occurred from an austenite growth control mechanism involving diffusion of the substitutional elements to one involving interstitial diffusion as the temperature increased from 765 to 780°C. Consequently, austenite growth did not require diffusion of the alloying elements to increase the carbon activity at the cementite/austenite interface for austenite growth to continue, with the austenite growth instead controlled by the rate of carbon diffusion in the austenite. This transition occurred at a lower temperature than that predicted by Table 9.5. However, this is thought to be due to lower manganese and chromium concentrations at the ferrite/cementite interfaces relative to the centre of the cementite particles[58]. As the quantitative analysis of the initial cementite particles yielded an averaged value for the particles, the alloy concentrations determined will be higher than the actual ferrite/cementite interface concentrations inherited by the growing austenite. Therefore, the carbon activities at the austenite/cementite interfaces calculated in Table 9.5 would have been higher than the actual values, and the temperature at which Δa_c actually became positive would have been lower.

The greater surface area to volume ratio of the lamellar cementite relative to the spheroidal cementite particles, in conjunction with shorter diffusion distances, resulted in the faster austenite formation in the furnace cooled initial structure with 74.4% austenite after 8min at 780°C, compared with 20.0% for the tempered martensite initial structure. The accelerated austenitisation kinetics with increasing temperature were due to the increasing separation of the Ac_3 and Ac_m carbon contents, and the increased carbon diffusivity in austenite.

Figure 9.32 illustrates the influence of initial structure on SUP7 austenitisation at the Ac_3 temperature of 820°C. The two pearlitic structures transformed at different rates, as did the two tempered martensite structures. This differs from the austenitisation kinetics at 755°C, where the two pearlitic initial structures exhibited similar austenitisation kinetics to each other, as did the two tempered martensite structures. The pearlitic initial structures austenitised faster, with 100% austenite (not shown in Figure 9.32) and 80.9% austenite obtained after 30s at 820°C for the air and furnace cooled initial structures respectively. This compares with 24.0, 13.2 and 7.8% austenite for the 12hr tempered martensite, 96hr tempered martensite and intercritical initial structures respectively after 30s at 820°C. The tempered martensite initial structure required 4hr to form 99.0% austenite.

The smaller cementite interlamellar spacing of the air cooled initial structure resulted in faster austenitisation kinetics than for the furnace cooled initial structure. This was due to the greater surface area to volume ratio of the finer cementite lamellae, and the shorter diffusion distances for carbon to the growing austenite. Mehl[174] demonstrated that finer 0.78wt.%C pearlitic structures nucleate and transform faster than coarser structures at temperatures above the Ac_1 value, and that the transformation to austenite was not influenced by the prior austenite grain size. The smaller cementite particle size of the 12hr tempered martensite initial structure also resulted in faster transformation kinetics than observed for the 96hr tempered martensite initial structure.

The higher energy requirements for austenite nucleation at cementite particles within ferrite grains relative to grain boundary particles resulted in the slower austenitisation kinetics observed for the intercritical initial SUP7 structure at 820°C relative to the 96hr tempered martensite initial structure for less than approximately 20% austenite. The greater partitioning of alloy elements during the austenite growth for the tempered martensite initial structure with

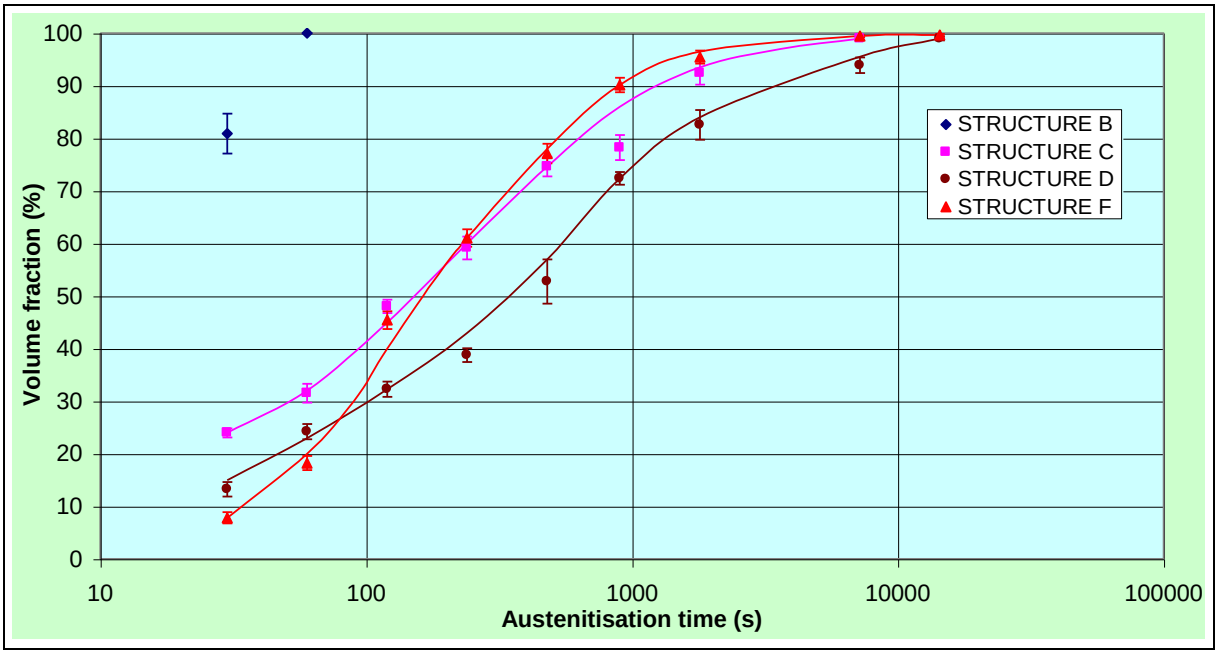

Figure 9.32 Influence of initial structure on the austenitisation kinetics of SUP7 at 820°C.

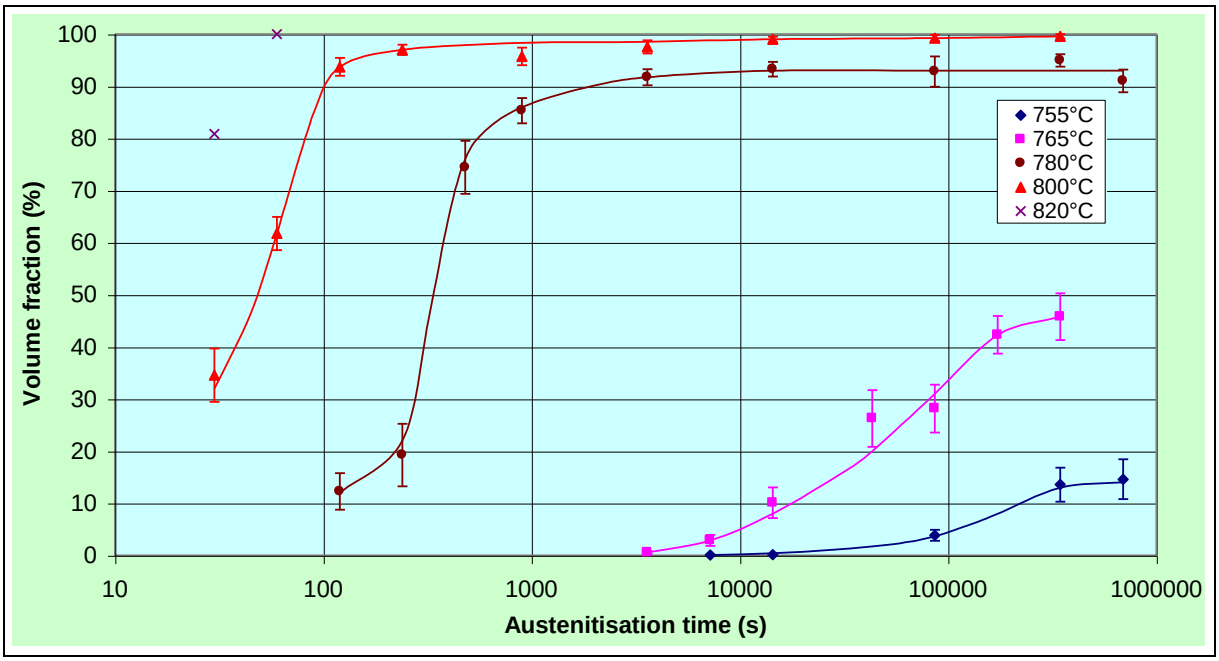

Figure 9.33 Influence of temperature on austenitisation kinetics for SUP7 furnace cooled initial structure.

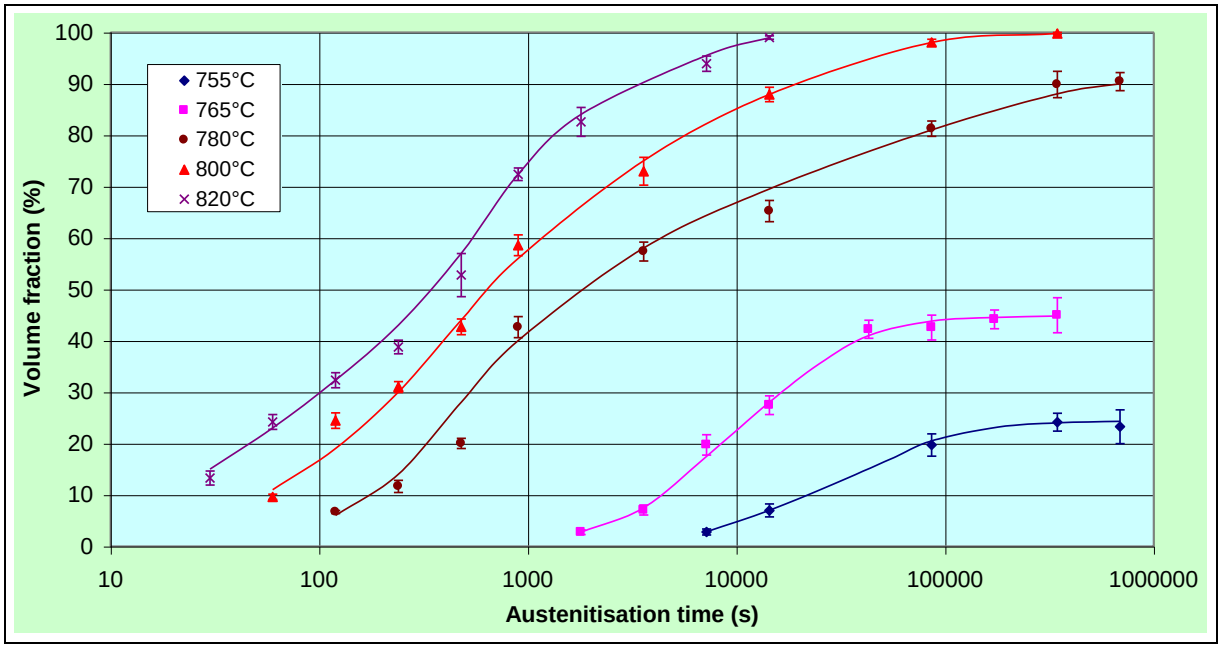

Figure 9.34 Influence of temperature on austenitisation kinetics for a SUP7 96hr tempered martensite initial structure.

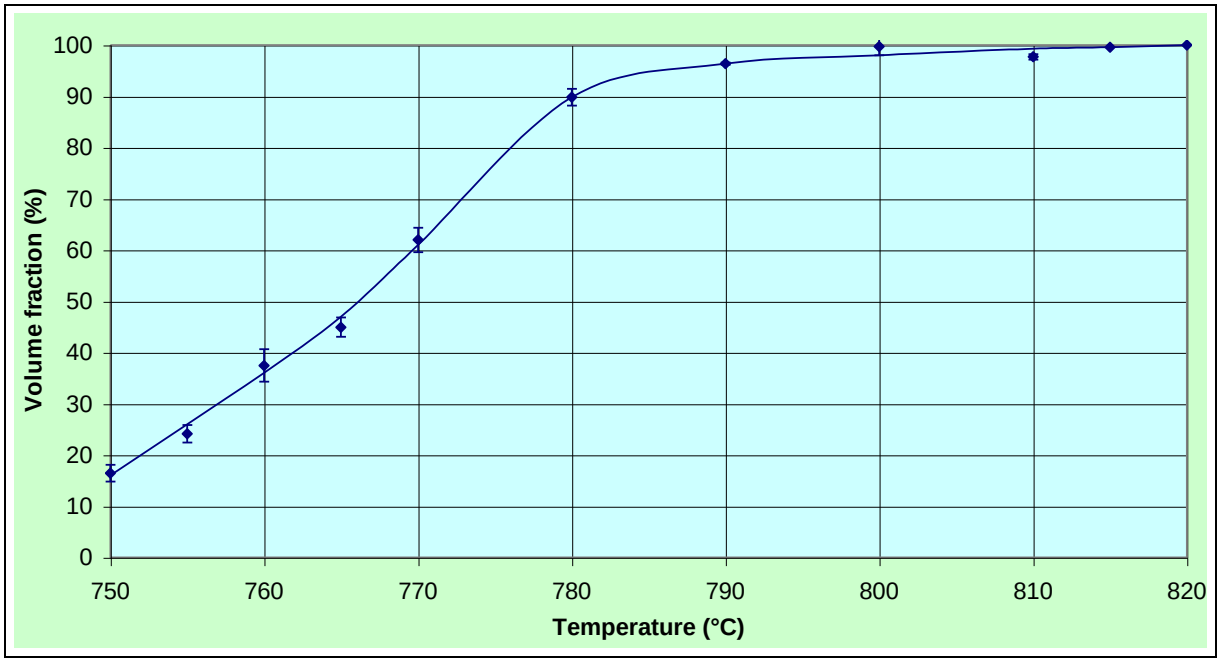

Figure 9.35 Influence of temperature on intercritical austenite fraction for 96hr austenitisation of 96hr tempered martensite SUP7 initial structures.

the associated lowering of the driving force for austenite growth, and the greater ferrite stability, account for the slower austenitisation kinetics relative to the intercritical initial structure for austenite fractions above 60%. The greater similarity of the austenitisation kinetics for the 96hr tempered martensite and intercritical initial structures at 820°C compared to 755°C were due to the increase in the austenite carbon solubility range, defined by the A_{cm}-Ac_3 gap of Figure 9.49, being proportionally less affected[46] by the partitioning of the alloying elements and the subsequent effect on the interfacial carbon activities.

The influence of temperature on the austenitisation kinetics of different furnace cooled and 96hr tempered martensite SUP7 initial structures are illustrated in Figures 9.33 and 9.34. The change in the rate controlling mechanism for austenite growth from substitutional to interstitial diffusional control between 765 and 780°C is illustrated by the large separation of the transformation curves for the furnace cooled initial structures of Figure 9.33 relative to the other temperatures. The greater acceleration of the austenitisation kinetics relative to the tempered martensite initial structure as the temperature increased from 765 to 780°C was due to the shorter diffusion distances for carbon in the pearlitic structures.

The transition to austenite growth controlled by carbon diffusion from the austenite/cementite particles without prior partitioning of the alloy elements resulted in the austenite growth rate being controlled by the carbon diffusivity, rather than by the diffusion of the substitutional elements. The diffusion coefficient of carbon in austenite is approximately four orders of magnitude greater than for manganese in austenite at comparable temperatures[57]. Figure 9.35 illustrates the influence of heat treatment temperature on the austenite fractions obtained after 96hr heat treating of 96hr tempered martensite initial structures.

9.5 Comparison of austenitisation kinetics for the different silicon steels

A comparison of the austenitisation kinetics for the different silicon steels at the same temperatures is of limited significance since the Ac_1 and Ac_3 transformation temperatures vary with silicon content. In order to obtain a more meaningful comparison between the different silicon steels, austenitisation heat treatments were undertaken at specific fractional superheat temperatures, and at their respective Ac_3 temperatures. The austenitisation kinetics of Figures 9.36, 9.38, 9.39 and 9.40 illustrate the austenitisation kinetics for the different silicon steels at

their respective 0.5 fractional superheats and Ac_3 temperatures. Figure 9.37 illustrates the austenitisation kinetics for the SUP7, SUP7NV and 3% Silicon steels at 0.25 fractional superheats.

The austenite growth rate equations for spheroidal cementite and pearlitic initial structures, equations 9.2 and 9.3 respectively, are dependent on a number of variables. Assuming that the austenite growth rate was dependent on the carbon diffusion in the austenite from the austenite/cementite interface, the austenite growth rate is proportional to

$$v \propto \frac{D_c^{\gamma} \Delta u_c^{\gamma}}{r_o} \tag{9.4}$$

Δu_c^{γ} is comparable to the difference in the carbon activities between the austenite/cementite and ferrite/austenite interfaces. Although Δu_c^{γ} differs from Δa_c^{γ}, the relationship between carbon activity and carbon content of equation 3.14 means that Δu_c^{γ} can be replaced by Δa_c^{γ} in equation 9.4 to indicate the relative growth rates of the different silicon steels. Δa_c^{γ} was determined for the 0% Silicon steel by the same approach used for SUP7. Kucera[214] presented equations for the calculation of the diffusion coefficients for carbon in austenite for Fe-Si-Mn-Cr-Ni-C steels. The values of D_c^{γ} were calculated assuming an average austenite carbon content corresponding to the bulk steel content, and average austenite silicon and manganese concentrations based on the quantitative analysis of the austenite particles first nucleated.

Table 9.7 lists the data used to calculate the $D_c^{\gamma} \Delta a_c^{\gamma} / r_o$ values for the 0% Silicon and SUP7 96hr tempered martensite initial structures austenitised at their respective Ac_3 temperatures. These results indicate that the austenite growth rate for SUP7 was approximately twice that of the 0% Silicon steel at the respective Ac_3 temperatures. Although these calculations do not take into account the other factors of equation 9.2, they do indicate that the faster austenitisation kinetics for SUP7 were due to the higher carbon diffusivity in austenite, along with the greater difference between the austenite/cementite and ferrite/austenite carbon activities, and by association the greater austenite carbon concentration gradient. These factors more than offset the larger cementite particle size, and the resultant longer diffusion distances.

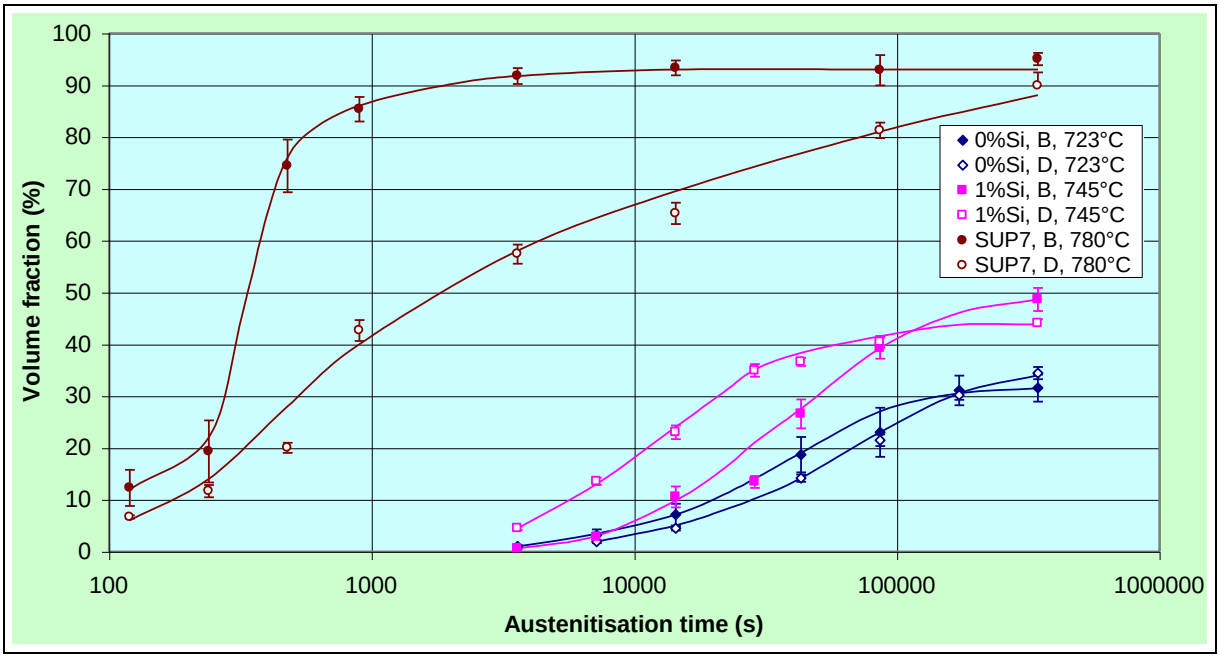

Figure 9.36 Austenitisation kinetics for 0% Silicon, 1% Silicon and SUP7 furnace cooled and 96hr tempered martensite initial structures at 0.5 fractional superheats.

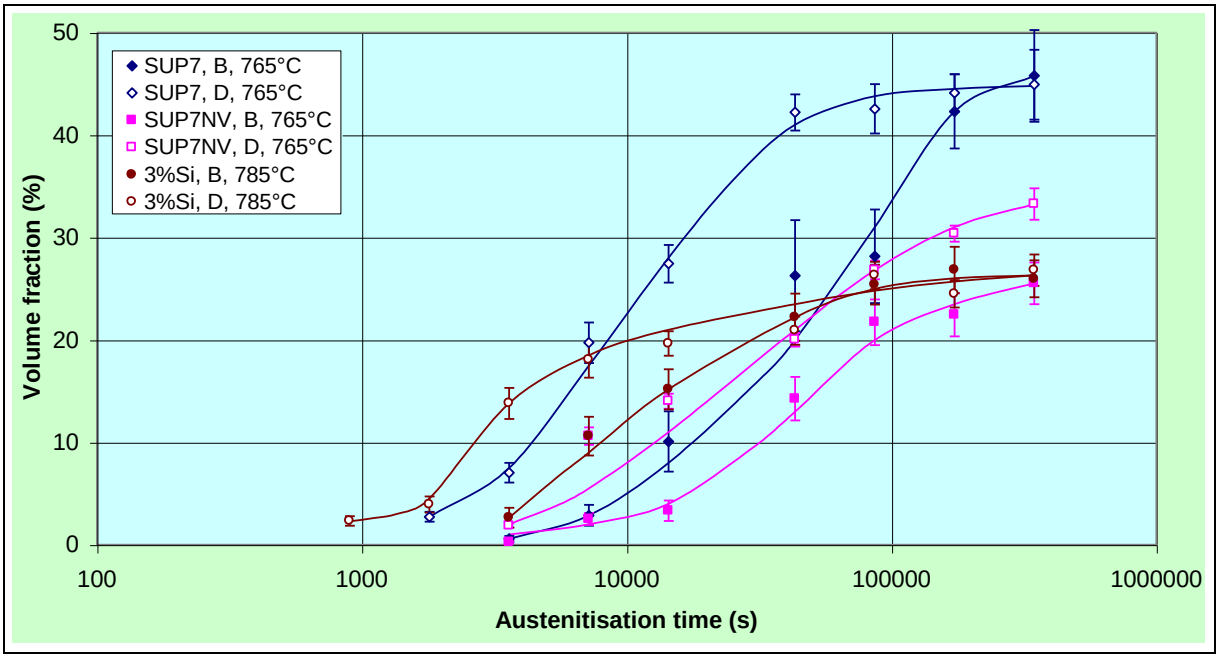

Figure 9.37 Austenitisation kinetics for SUP7, SUP7NV and 3% Silicon furnace cooled and 96hr tempered martensite initial structures at 0.25 fractional superheats.

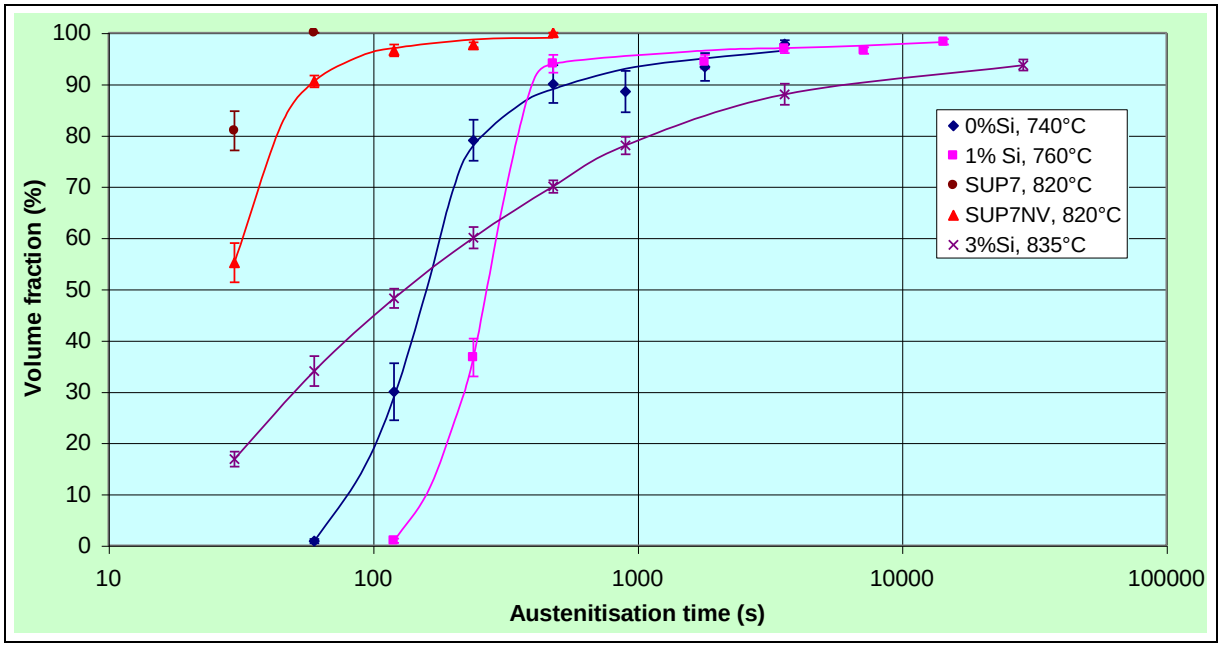

Figure 9.38 Austenitisation kinetics for furnace cooled initial structures of different silicon steels at their Ac_3 temperatures.

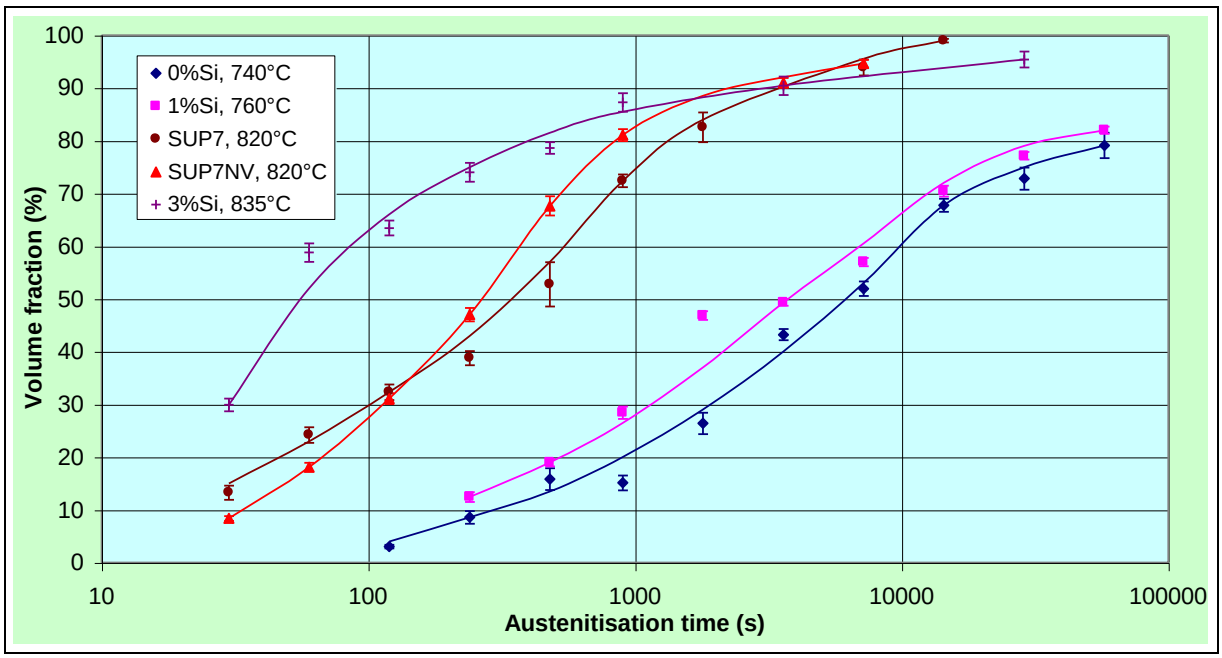

Figure 9.39 Austenitisation kinetics for 96hr tempered martensite initial structures of different silicon steels at their Ac_3 temperatures.

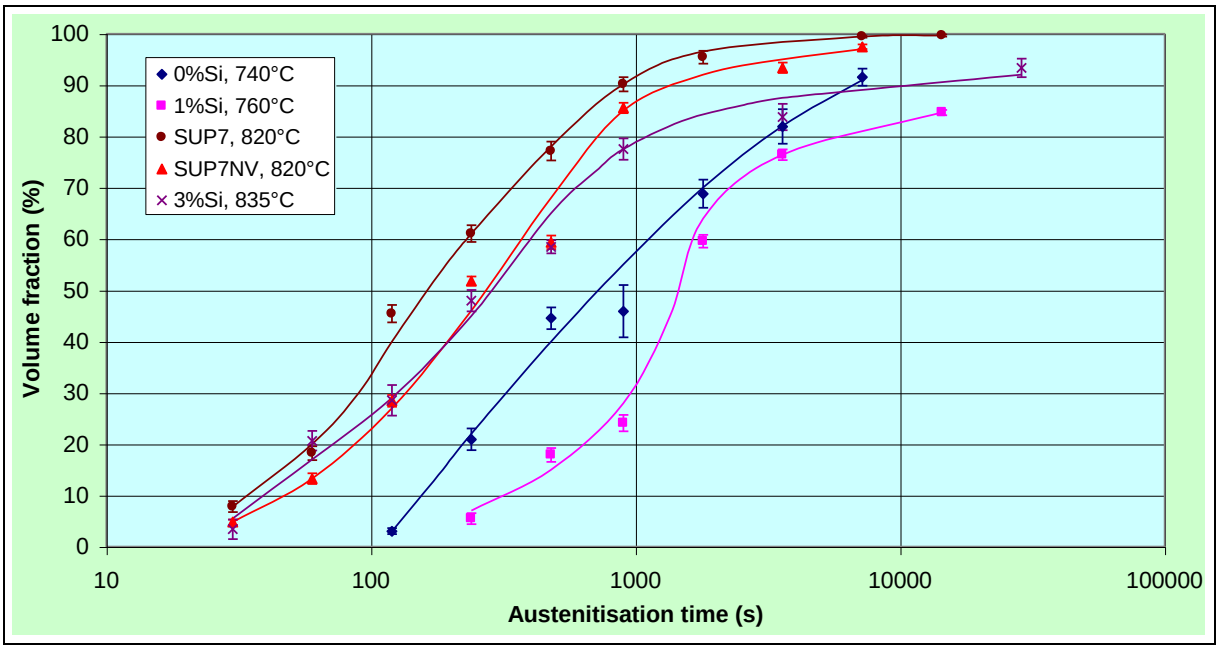

Figure 9.40 Austenitisation kinetics for intercritical initial structures of different silicon steels at their Ac_3 temperatures.

Table 9.7 Calculation of $D_c^{\gamma}\Delta a_c^{\gamma}/r_o$ for 96hr tempered martensite 0% Silicon and SUP7 steels at their respective Ac_3 temperatures.

STEEL	Temperature	D_c^{γ} (cm²/s)	Δa_c^{γ}	r_o	$D_c^{\gamma}\Delta a_c^{\gamma}/r_o$
0% Silicon	740°C	$1.5\text{x}10^{-8}$	0.14	0.7	$2.9\text{x}10^{-9}$
SUP7	820°C	$2.6\text{x}10^{-8}$	0.24	1.1	$5.7\text{x}10^{-9}$

The 0% Silicon, 1% Silicon, SUP7 and SUP7NV steels exhibited faster austenitisation kinetics for the tempered martensite initial structures than for the furnace cooled initial structures at fractional superheats of 0.5 and less. However, the faster austenitisation kinetics for the furnace cooled structures at the respective Ac_3 temperatures, and the large increase in the austenitisation kinetics with temperature, indicate a transition from austenite growth controlled by the partitioning of alloying elements to control by carbon diffusion through the austenite at temperatures below the Ac_3 temperatures. The Δa_c values for the 96hr tempered martensite initial structure of the 0% Silicon steel were –0.10 at 723°C, and 0.14 at 740°C. This indicates that a change in the mechanism controlling the austenite growth occurred between these two temperatures.

Figure 9.38 demonstrates that the austenitisation kinetics were slower for the furnace cooled 1% Silicon initial structure than for the 0% Silicon steel at their respective Ac_3 temperatures for austenite fractions below approximately 85%, despite the 20°C higher heat treatment temperature. This can be explained by reference to the growth rate equation for pearlitic initial structures of equation 9.3. Assuming negligible carbon diffusion in the ferrite, the austenite growth rate is proportional to

$$v \propto \frac{D_c^{\gamma}\Delta u_c^{\gamma}}{\sigma_t}. \qquad (9.5)$$

As the silicon content lowers the carbon diffusivity in austenite[214], the calculated diffusion coefficients were similar[214], being $1.5\text{x}10^{-8}$ and $1.4\text{x}10^{-8}\text{cm}^2/\text{s}$ for the 0 and 1% Silicon steels respectively at their respective Ac_3 temperatures. The higher silicon and manganese concentrations of the 1% Silicon steel would have lowered the austenite/cementite carbon

activity, and raised the ferrite/austenite carbon activity, to a greater extent than the 0% Silicon steel. This would have reduced the driving force for austenite growth controlled by carbon diffusion from the austenite/cementite interface more than for the 0% Silicon steel. Furthermore, the pearlite interlamellar spacing of the 1% Silicon steel was twice that of the 0% Silicon steel, which would have doubled the carbon diffusion distances, and therefore halved the austenite growth rate. These factors account for the faster austenitisation kinetics observed for the furnace cooled initial structure of the 0% Silicon steel. The slower austenitisation kinetics of the SUP7NV furnace cooled initial structures compared to SUP7, despite the same heat treatment temperature, are due to the higher silicon and manganese concentrations of SUP7NV, and the greater pearlite interlamellar spacing.

The greater graphitisation of the furnace cooled 3% Silicon initial structure compared to the lower silicon steels, and the subsequent influence of the graphite on the austenite growth, accounts for the slower austenitisation for greater than approximately 65% austenite. This was despite the 95°C higher Ac_3 temperature of the 3% Silicon steel relative to the 0% Silicon steel. The microstructural photo of Figure 9.18(d) indicates that negligible undissolved cementite remained in the ferrite after 2min. Consequently, further austenite growth occurred by carbon diffusion from the austenite/graphite interface.

The austenitisation kinetics of the respective furnace cooled 3% Silicon and SUP7 steels is influenced by the heat treatment temperature, the size and stability of the cementite and graphite particles, and the partitioning of the alloying elements between the various phases. The slower austenitisation of the 3% Silicon steel relative to SUP7, despite the higher heat treatment temperature of 835°C compared with 820°C, was due to the shorter diffusion distances for carbon to the growing austenite for SUP7 with an initial pearlitic structure, compared to the longer diffusion distances associated with the widely dispersed graphite particles of the 3% Silicon steel. The greater stability of graphite relative to cementite at comparable temperatures would have also contributed to the slower austenitisation of the furnace cooled 3% Silicon steel initial structure.

The austenitisation kinetics of the tempered martensite initial structures of the different silicon steels at their respective Ac_3 temperatures, Figure 9.39, illustrates that the austenite growth was faster for the 3% Silicon steel than the other four steels up to almost 90% austenite. This

was due to the fine graphite particle size distribution offsetting the greater stability for the graphite of the 3% Silicon steel relative to the cementite of the lower silicon steels. The graphite particles of the tempered martensite initial structure were finer than the cementite particles of the SUP7 structure, with the mean equivalent area diameter of the graphite particles estimated to be 0.5μm from the initial microstructures, compared with 1.1μm for the cementite particles. This resulted in shorter diffusion distances for carbon to the growing austenite. The finer graphite particle size of the 96hr tempered martensite 3% Silicon initial structure accounts for the faster austenitisation kinetics of Figure 9.26 relative to the furnace cooled and intercritical initial structures.

9.6 Cementite dissolution kinetics

The kinetics of cementite dissolution for the 0% Silicon, 1% Silicon, SUP7 and SUP7NV steels at their respective Ac_3 temperatures are illustrated in Figure 9.41. The cementite dissolution was faster for SUP7 and SUP7NV than the 0 and 1% Silicon steels, due to the faster austenitisation resulting from the higher heat treatment temperatures. An undissolved cementite fraction remains for all four steels after the longest heat treatments, with 0.5vol.% cementite present in SUP7 after 4hr at 820°C, despite the formation of 99% austenite.

The cementite dissolution kinetics for the 12 and 96hr tempered martensite SUP7 initial structures at 755°C were similar, Figure 9.42. However, the cementite dissolution for the intercritical initial structure was initially slower, due to the slower austenitisation kinetics. Approximately 3% cementite remained after 192hr austenitisation of the three initial structures. The presence of undissolved cementite particles indicates the equilibrium coexistence of a three phase ferrite/austenite/cementite structure, as opposed to the two phase ferrite/austenite structure of plain carbon steels. Figure 9.43 illustrates the austenite growth and the concurrent cementite dissolution for SUP7 96hr tempered martensite initial structures at 755 and 820°C.

Very little cementite remained during the austenitisation of the 3% Silicon steels at 785 and 835°C. Therefore, the graphitisation kinetics were measured instead. The graphite particles could not be measured for the 96hr tempered martensite initial structures as they were too fine to be resolved with optical microscopy, and the contrast between the graphite and the matrix

using the SEM was inadequate for image analysis. However, the larger graphite particles of the furnace cooled and intercritical initial structures allowed the graphite fractions to be determined for these structures using optical microscopy. The 95% confidence intervals were large, due to the uncertainty associated with the measurement of small volume fractions[162].

For both the furnace cooled and intercritical initial structures at 785 and 835°C, Figure 9.44, the graphite fractions initially decreased with time, with the carbon liberated facilitating the austenite growth. However, the graphite fractions reached a minima, before increasing with further austenitisation, despite the concurrent increase in austenite fraction. The final graphite fractions were comparable to the initial fractions. This graphitisation was accompanied by a decrease in the austenite carbon content. For the furnace cooled initial structure after 4hr at 835°C, with an austenite volume fraction of 93.7% and a graphite fraction of 0.8%, equation 9.1 was used to determine the average austenite carbon content of 0.35wt.%. Taking into account the 95% confidence interval of the graphite fraction measurement being ±0.3vol.%, and neglecting the small confidence interval associated with the austenite fraction measurement, the average austenite carbon content was within 0.27 and 0.43wt.%.

Nam[191] measured the hardness of 0.6wt.%C/0.5wt.%Mn/0.5wt.%Cr/0.2wt.%V/1.8wt.%Ni spring steels with different silicon contents. Each steel was austenitised for 30min at 850°C, quenched in oil, and tempered for 30min at 250°C. The hardness increased marginally from 57 to 58HRC as the silicon content increased from 1.02 to 2.44wt.%. SUP7 and SUP7NV steels that were quenched in oil from 900°C and tempered at 250°C had an identical hardness of 60HRC[11]. Microhardness data was obtained for the different silicon steels investigated in this project after the longest duration heat treatments for the furnace cooled initial structures at their respective Ac_3 temperatures. A Vickers indenter with a 200g load was used, with eight measurements made on martensitic areas for each specimen. Table 9.8 lists the average martensite microhardness values for the different steels.

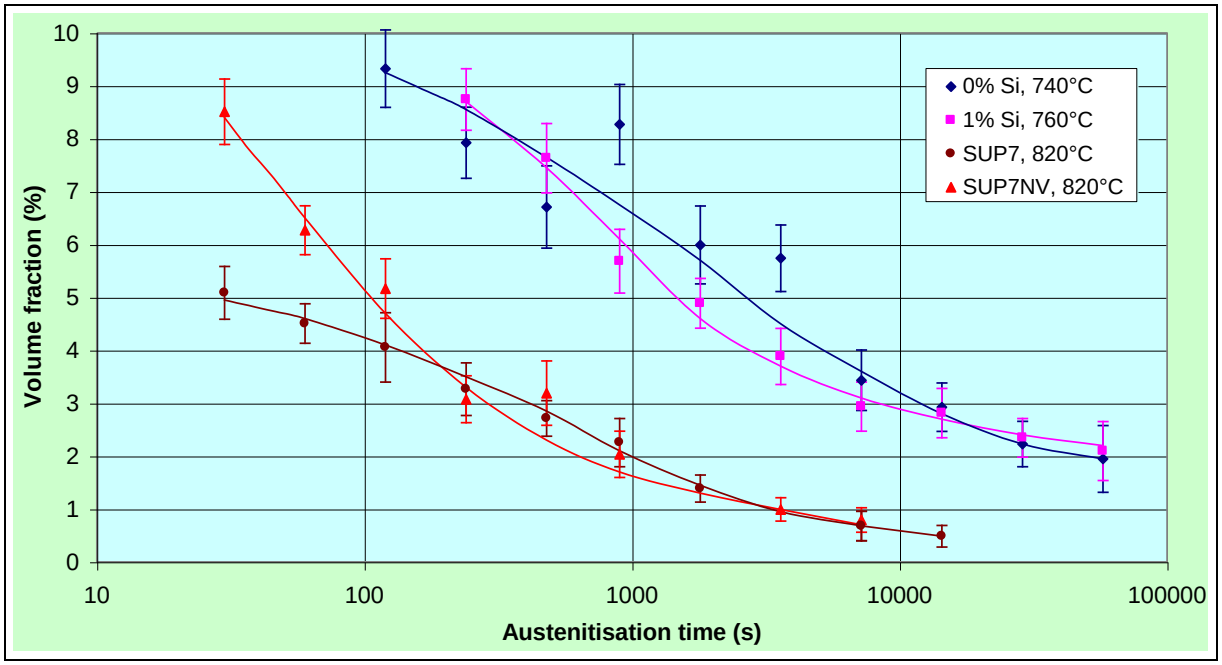

Figure 9.41 Cementite dissolution kinetics for the different silicon steels with 96hr tempered martensite initial structures at their respective Ac_3 temperatures.

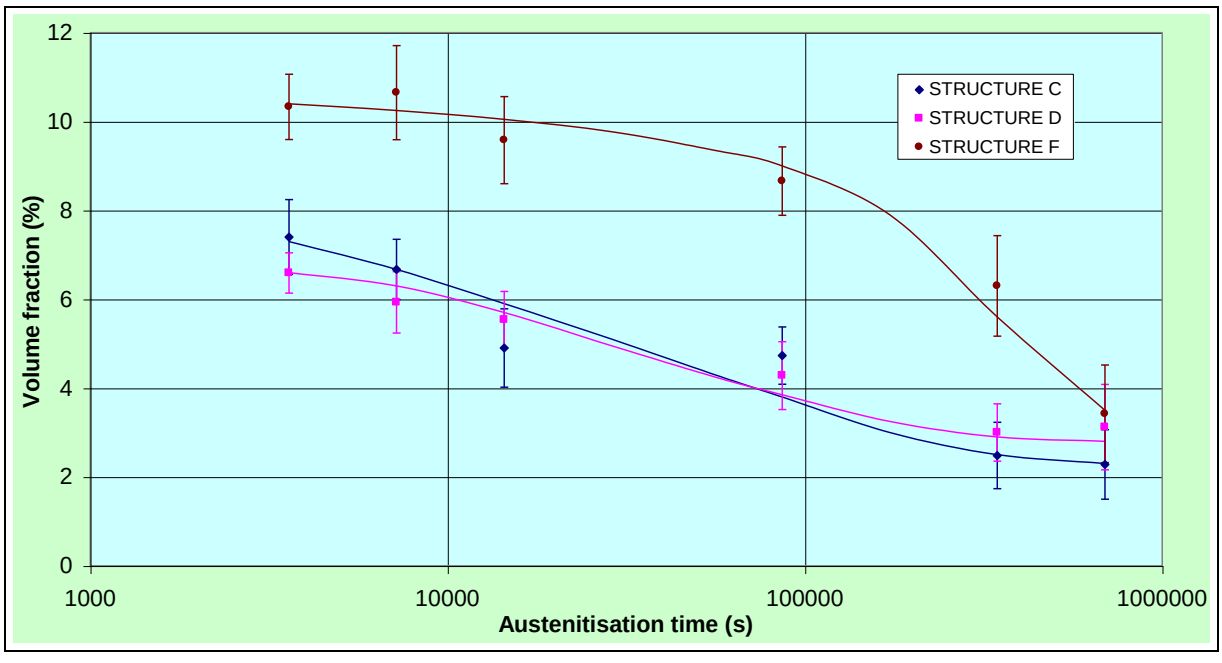

Figure 9.42 Cementite dissolution kinetics for different initial spheroidal cementite SUP7 structures at 755°C.

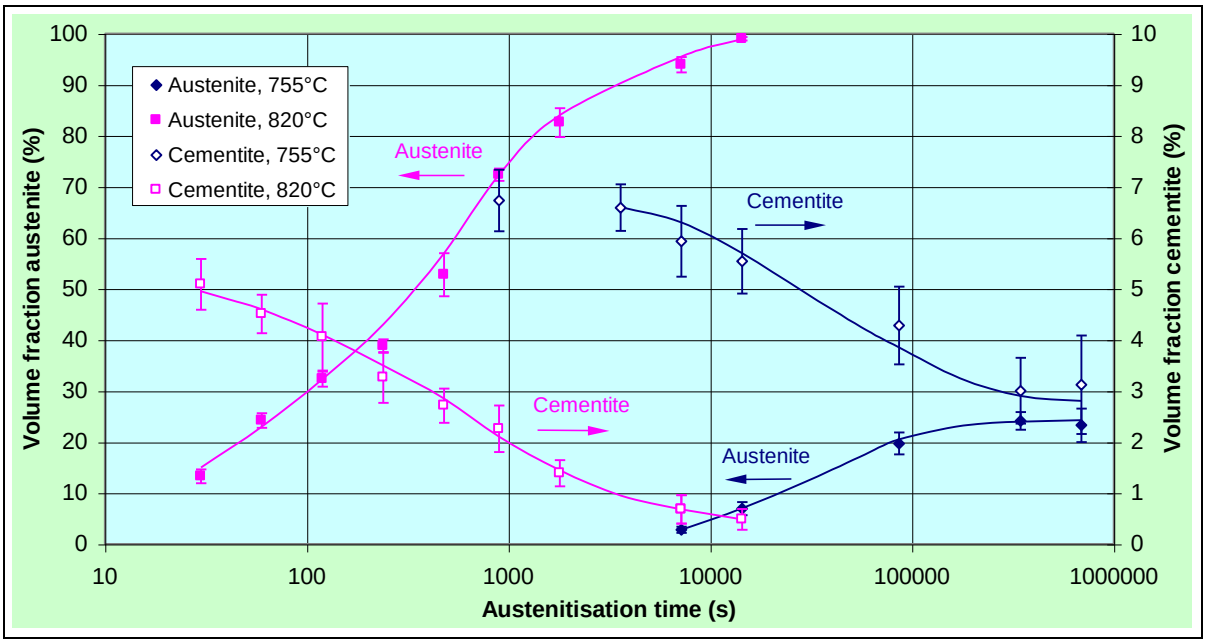

Figure 9.43 Austenite transformation and cementite dissolution kinetics for SUP7 96hr tempered martensite initial structures at 755 and 820°C.

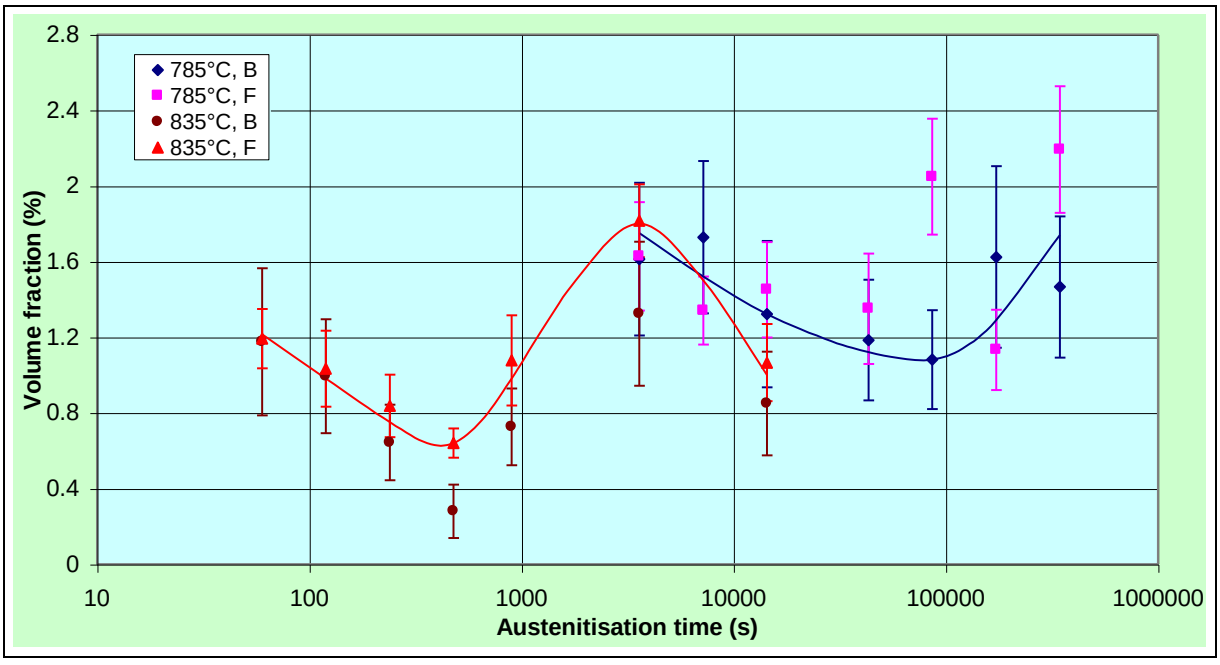

Figure 9.44 Graphitisation kinetics for furnace cooled and intercritical 3% silicon structures austenitised at 785 and 835°C.

Table 9.8 Martensite microhardness data for the different silicon furnace cooled initial structures after austenitisation at their respective Ac_3 temperatures, quenching in water and 1hr at 250°C.

DESCRIPTION	Heat treatment	Austenite (vol.%)	Graphite (vol.%)	Microhardness (HRC)
0% SILICON	1hr at 740°C	97.8	-	59.7
1% SILICON	4hr at 765°C	98.2	-	60.3
SUP7	4hr at 820°C	100	-	61.1
SUP7NV	1hr at 820°C	100	-	60.9
3% SILICON	4hr at 835°C	93.7	1.0	59.7

The martensite hardness for the five steels was similar at approximately 60HRC. This was somewhat surprising for the 3% Silicon steel, which comprised 0.8vol.% graphite after 4hr austenitisation, and therefore a mean austenite carbon content of 0.35wt.%, as opposed to 0.6wt.% for the other steels. Since the hardness of tempered martensite is approximately a linear function of carbon content for any alloy system in the range 0.2 to 0.6wt.%C[192,192], and that an increase in silicon from 1.02 to 2.44wt.% had a limited influence on the hardness of spring steels[191], a lower hardness of 56HRC would be expected for the 3%Silicon steel due to the lower carbon content. The reason why the hardness of the 3% Silicon steel was not lower is not readily apparent. Furthermore, an increased Ac_3 temperature from 740°C for the 0% Silicon steel to 835°C for the 3% Silicon steel had no influence on the martensite hardness.

A gradual decrease in the mean cementite equivalent area diameters occurred during austenitisation of the different silicon steels at their respective Ac_3 temperatures, as illustrated in Figure 9.45. The smaller initial mean cementite size of the 0% Silicon steel resulted in the lowest particle sizes of the four steels. Austenitisation of SUP7 at 755°C yielded coarsening of some of the cementite particle sizes for the different spheroidal cementite initial structures, Figure 9.46, in conjunction with the dissolution of other cementite particles that supplied carbon to the growing austenite. The larger mean cementite particle size of the 96hr tempered martensite initial structure resulted in larger diameter cementite particles than for the 12hr tempered martensite structure. The coarsening of the 96hr tempered martensite and intercritical initial structures was similar, despite the different austenitisation kinetics for the

96hr tempered martensite and intercritical structures. This indicates that the mean cementite particle size was independent of the concurrent austenite formation.

9.7 Determination of austenite carbon contents

Molinder[31] demonstrated that the carbon content of the austenite forming varied with heat treatment temperature and austenite fraction during the austenitisation of a 1.27wt.%C tool steel. In order to determine the austenite carbon concentrations during austenitisation, the ferrite, austenite and cementite volume fractions are necessary. Assuming a cementite carbon content of 6.67wt.%[31], the average austenite carbon content can be estimated if the bulk steel and ferrite carbon contents are known. Assuming that the ferrite is saturated with carbon throughout the austenitisation process due to partial cementite dissolution during the incubation period for austenite nucleation[46], the austenite carbon content, $\%C_\gamma$, can be determined from equation 9.6, where:

$$\%C_\gamma = \frac{\%C_{bulk} - \left[\left(\frac{V_{vcem}.\%C_{cem}}{100}\right) + \left(\frac{V_{v\alpha}.\%C_{\alpha sat}}{100}\right)\right]}{\frac{V_{v\gamma}}{100}}, \qquad (9.6)$$

where $\%C_\gamma$ = average austenite carbon content in wt.%;

$\%C_{bulk}$, $\%C_{cem}$, $\%C_{\alpha sat}$ = bulk, cementite and saturated ferrite carbon contents respectively in wt.%;

V_{vcem}, V_α, V_γ = cementite, ferrite and austenite volume fractions in %.

With the volume fractions of the respective phases determined from the heat treated specimens, the remaining unknown necessary for determination of the average austenite carbon content is the saturated ferrite carbon content. Figure 9.48 illustrates the vertical sections of Fe-C-2wt.%Si and Fe-C-2.5wt.%Mn ternary phase diagrams. The maximum solubility of carbon in ferrite increases with silicon content from 0.022wt.% for a plain carbon steel[187] to 0.035wt.% for a Fe-C-3wt.%Si steel[194] at the respective Ac_1 temperatures. The

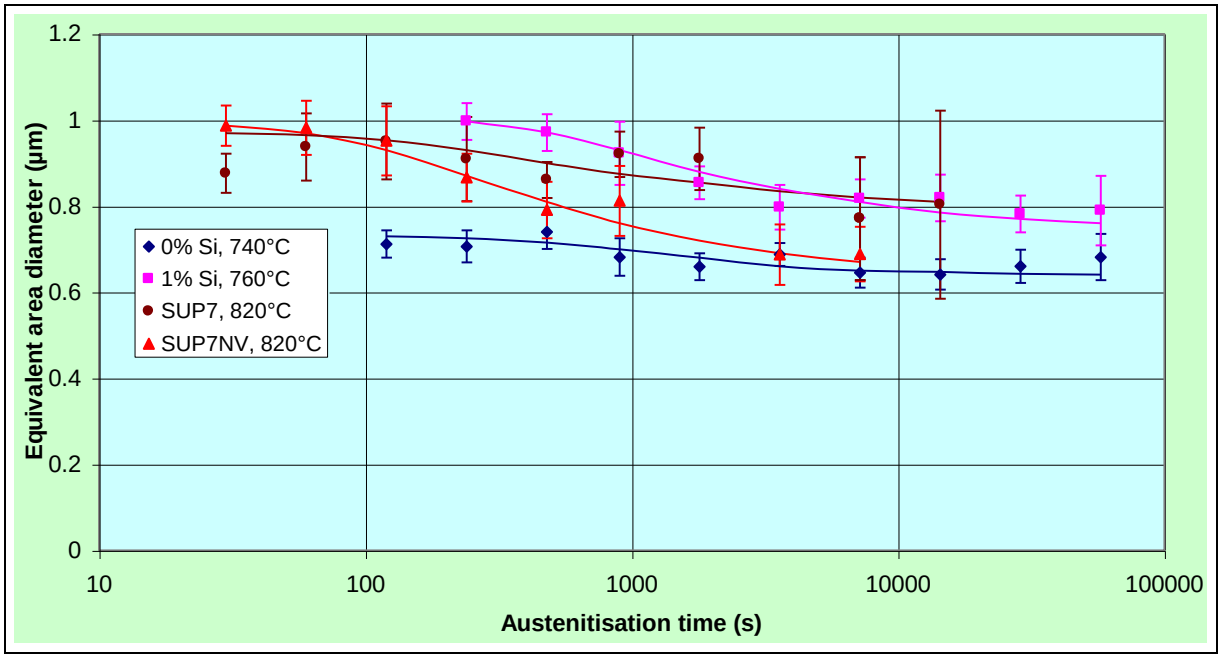

Figure 9.45 Variation in mean cementite equivalent area diameter during austenitisation of 96hr tempered martensite initial structures for different silicon steels at their respective Ac_3 temperatures.

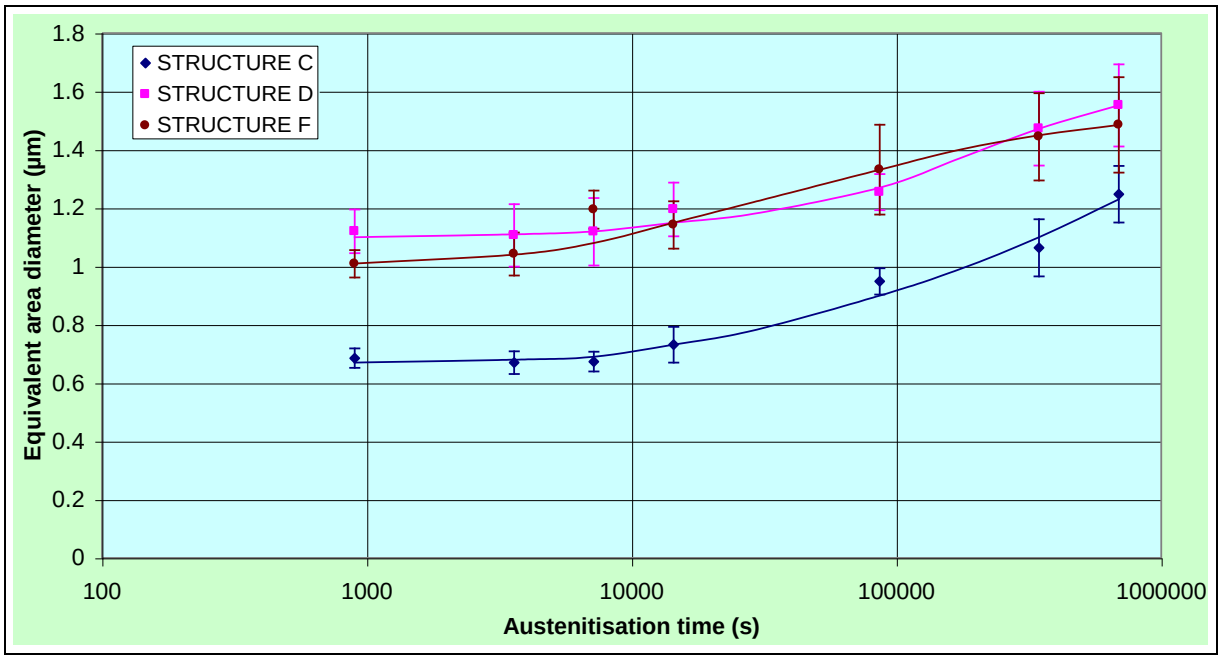

Figure 9.46 Variation in mean cementite equivalent area diameter during austenitisation of different initial spheroidal cementite SUP7 initial structures at 755°C.

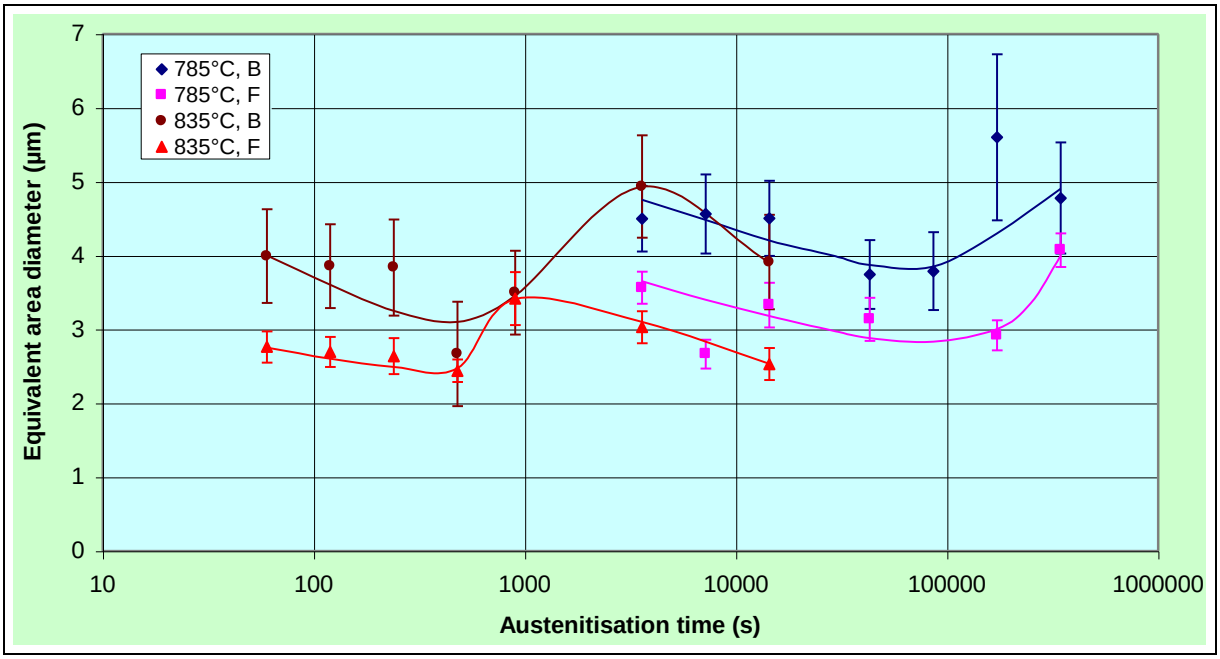

Figure 9.47 Variation in mean graphite equivalent area diameter during austenitisation of furnace cooled and intercritical 3% Silicon initial structures at 785 and 835°C.

manganese content of the different silicon steels has a negligible influence on the ferrite solubility, other than to raise the temperature of the boundary separating the ferrite plus austenite and austenite phases[55,195]. Taking into account this effect of manganese by adjusting the temperatures of the phase boundaries, the saturation ferrite carbon contents of the 0% Silicon steel can be determined from Krauss[187], and from the Fe-C-1wt.%Si and Fe-C-2wt.%Si steel ternary phase diagrams[194] for the 1% Silicon, SUP7 and SUP7NV steels at their respective Ac_3 temperatures. This yields values of 0.018wt.%C for the 0% Silicon steel at 740°C, 0.019wt.%C for the 1% Silicon steel at 760°C, and 0.020wt.%C for SUP7 and SUP7NV at 820°C.

The effect of silicon and manganese on the temperatures and carbon contents of the boundaries separating the ferrite plus austenite and austenite plus cementite phase fields from austenite are illustrated in Figure 9.49. Increasing silicon and manganese concentrations move the eutectoid carbon contents to lower values, with silicon raising, and manganese lowering, the Ac_1 temperature corresponding to the eutectoid carbon content. Assuming that the effects of silicon and manganese on the phase boundaries are additive, the maximum austenite carbon contents of the different silicon steels at their respective Ac_3 temperatures can be estimated. This results in values of 0.88wt.%C for the 0% Silicon steel at 740°C, 0.80wt.%C for the 1%Si steel at 760°C, and 0.79wt.%C for SUP7 and SUP7NV at 820°C.

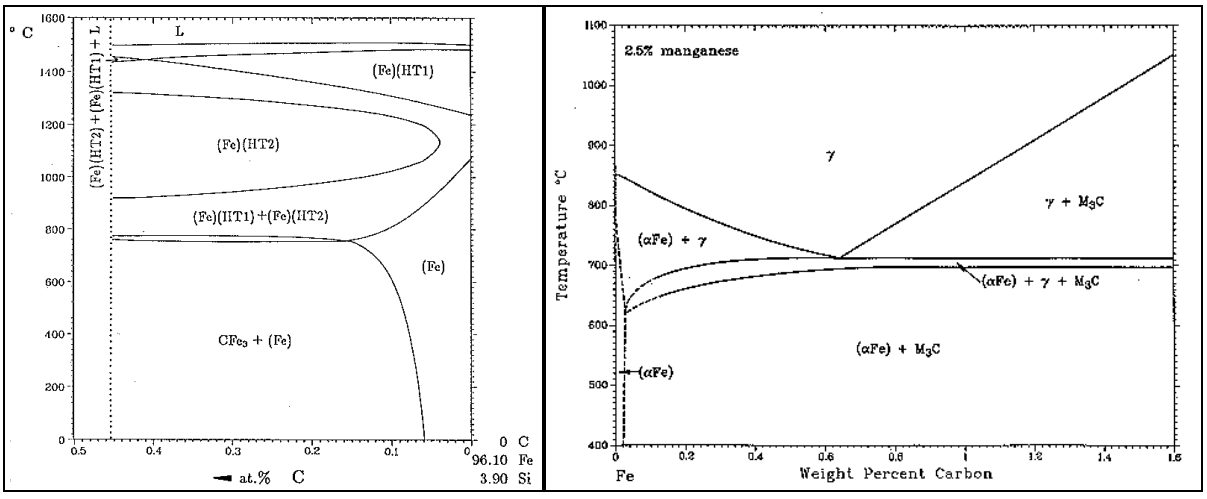

(a) **(b)**

Figure 9.48 Vertical sections of ternary phase diagrams for (a) Fe-C-2wt.%Si (from Ref. 194), and (b) Fe-C-2.5wt.%Mn (from Ref. 182).

Figure 9.50 illustrates the variation in the average austenite carbon contents during austenitisation of the different silicon steels at their respective Ac_3 temperatures calculated from equation 9.2. Austenite carbon contents were not calculated for austenite fractions below approximately 20%, as relatively small inaccuracies in the measured austenite and cementite fractions give large variations in the calculated austenite carbon content. A relative error was introduced to more meaningfully illustrate the uncertainties involved in the austenite carbon content calculations, and is defined in equation 9.7. This was used for the error bars of Figure 9.50.

$$RE = \left[\frac{95\%CI_{cem}}{V_{vcem}} + \frac{95\%CI_{\gamma}}{V_{v\gamma}}\right].\left[\%C_{bulk} - \left(\frac{V_{vcem}.\%C_{cem}}{100} + \frac{V_{v\alpha}.\%C_{\alpha sat}}{100}\right)\right], \qquad (9.7)$$

where RE = relative error in wt.% carbon;

$95\%CI_{cem}$, $95\%CI_{\gamma}$ = cementite and austenite 95% confidence intervals in vol.%.

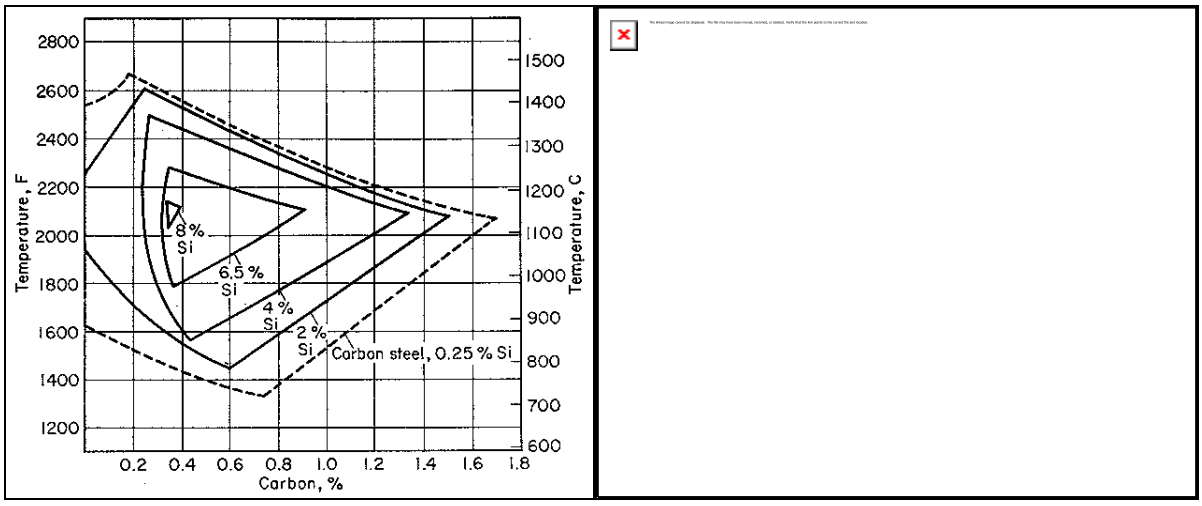

(a) **(b)**

Figure 9.49 Effect of (a) silicon, and (b) manganese contents on the carbon limitations for pure austenite (from Ref. 55).

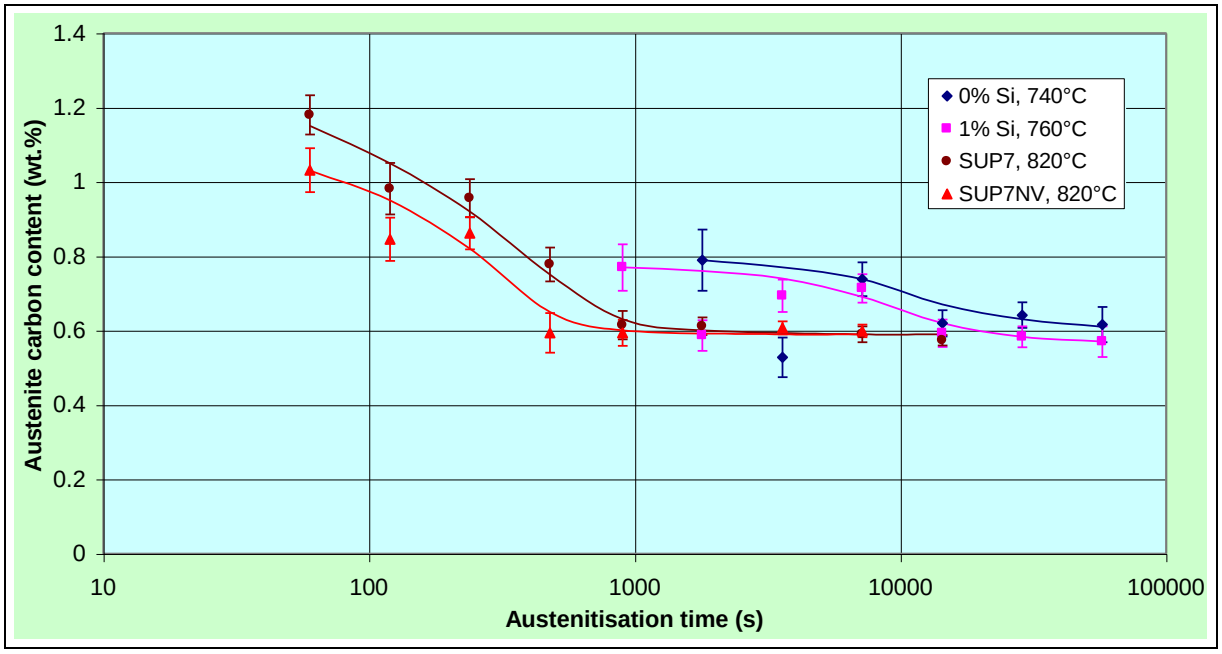

Figure 9.50 Austenite carbon contents during austenitisation of 96hr tempered martensite initial structures for different silicon steels at their respective Ac_3 temperatures.

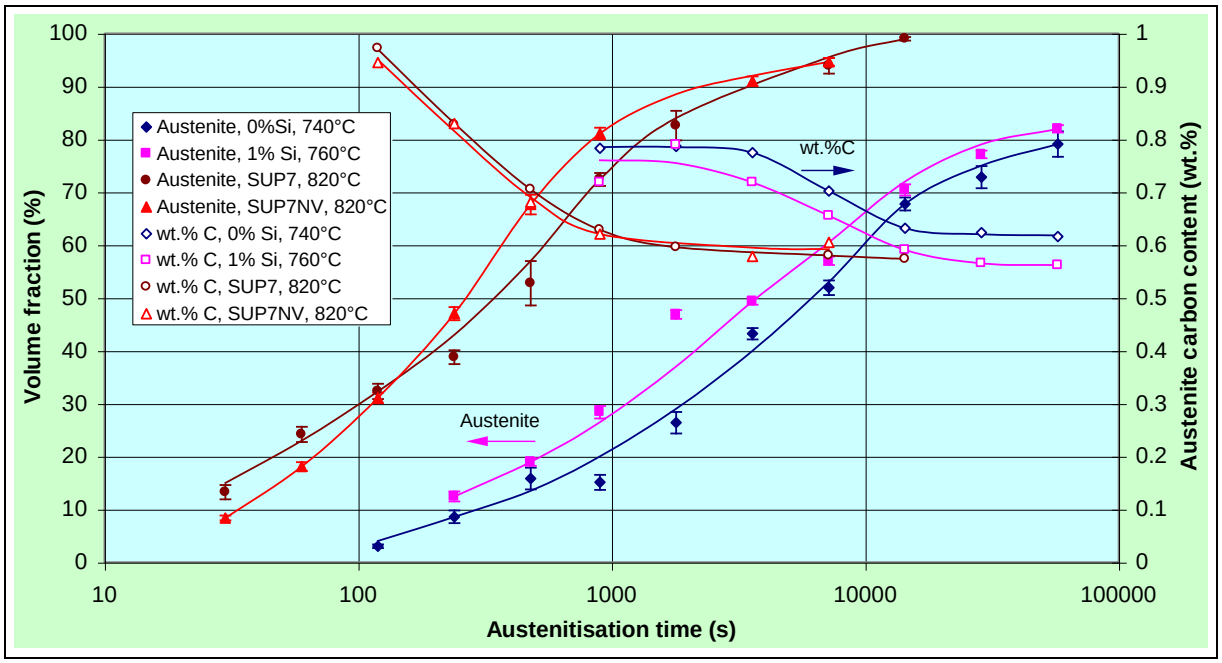

Figure 9.51 Austenitisation kinetics and austenite carbon contents determined from smoothed austenite and cementite kinetic curves for 96hr tempered martensite initial structures of different silicon steels at their respective Ac_3 temperatures.

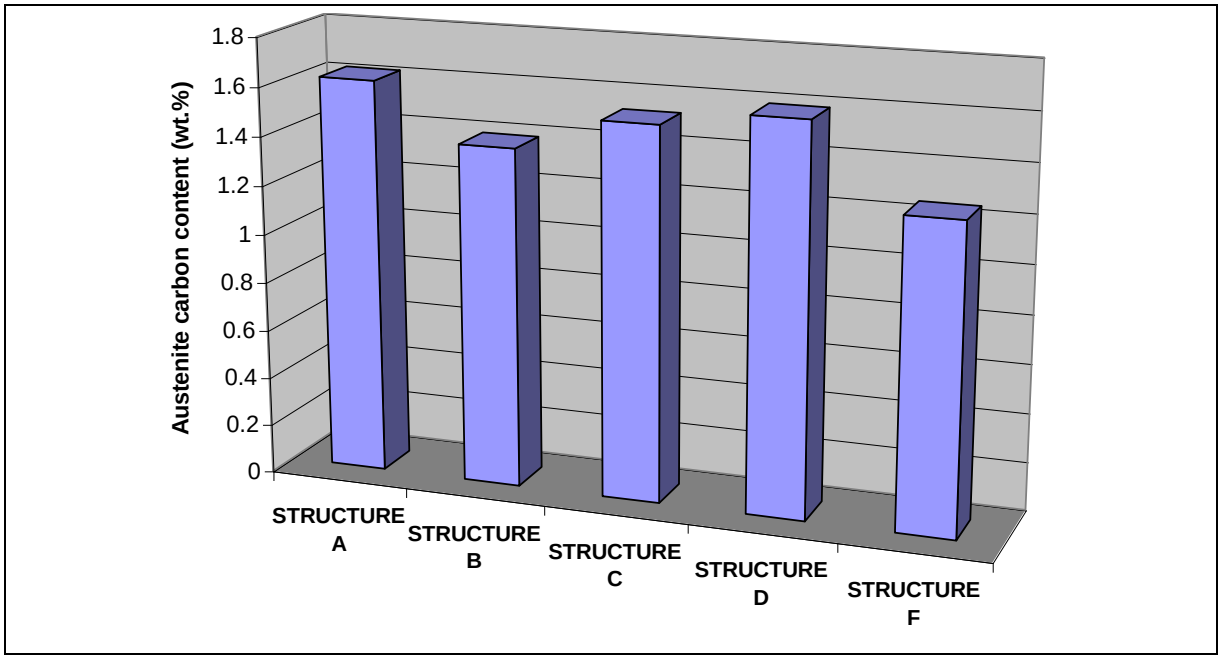

Figure 9.52 Austenite carbon contents for different initial SUP7 structures after 192hr at 755°C.

Figure 9.50 illustrates the decreasing austenite carbon content with increasing austenite formation for the four different steels. The austenite carbon contents corresponded to the bulk values for each steel for greater than approximately 70% austenite. The 0% Silicon and 1% Silicon steels have austenite carbon contents similar to the saturation values at lower austenite fractions, while the SUP7 and SUP7NV values exceed the A_{cm} value of 0.79wt.%C for the lower austenite fractions.

The austenite carbon contents were calculated from smoothed "best fit" curves plotted through the experimental austenitisation and cementite dissolution kinetics for the different silicon steels, and are illustrated in Figure 9.51. The austenite carbon contents of the 0 and 1% Silicon steels decreased from the saturation values at low austenite fractions to the bulk steel contents at higher fractions. However, the austenite carbon contents of SUP7 and SUP7NV for below 50vol.% austenite were greater than the saturation values. The austenite carbon contents for the different SUP7 initial structures after 192hr at 755°C ranged from 1.3 to 1.6wt.%, Figure 9.52.

9.8 Microalloy element partitioning

This section details the partitioning of the alloying elements to the various phases during the austenitisation heat treatments. Element concentration profiles are likely across the dissolving cementite, and growing austenite particles, and to a lesser extent in the ferrite. These concentration profiles arise from the different concentrations of the various phases, which result in concentration profiles across the interfaces of the phases, and the subsequent partitioning of the elements between the phases. The inhomogeneity of the concentration profiles, and the variation with particle size, will be greatest for the shorter duration heat treatments, decreasing for the longer heat treatments where equilibrium conditions are approached. A minimum of five analyses were made per phase on the largest particles present in an attempt to minimise the composition variations of each phase. Table 9.9 lists selected alloy element phase concentrations for the different silicon steels austenitised at their respective Ac_3 temperatures.

The partitioning of the alloy elements between the various phases illustrated in Figures 9.53 to 9.57, and the data of Table 9.9, demonstrates several trends:

- The partitioning of silicon to ferrite, where the ratio of ferrite silicon content to austenite silicon content after the longest duration tests ranged from 1.5 for the 1% Silicon steel to 1.3 for the 3% Silicon steel;
- Higher ferrite and austenite silicon contents for the higher silicon steels, due to the higher bulk silicon contents;
- The partitioning of manganese to austenite, with the ferrite to austenite ratio after the longest duration tests ranging from 0.4 for the 0% Silicon steel to 0.6 for the 3% Silicon steel;
- Constant cementite chromium contents of 1.4wt.% for the 0% Silicon, 1% Silicon, SUP7 and SUP7NV steels;
- A higher cementite chromium content of 3.5wt.% for the 3% Silicon steel, due to the lower cementite fraction which resulted in greater chromium partitioning to the cementite for the same bulk concentration.

The partitioning of the alloy elements between the various phases for the SUP7 96hr tempered martensite and intercritical initial structures at 755 and 820°C, Figures 9.59 to 9.62, demonstrates:

- Similar ferrite and austenite silicon contents for the two initial structures at 755°C, and similar austenite silicon contents at 820°C;
- Greater partitioning of silicon to ferrite for the intercritical initial structure at 820°C, with 2.9wt.%Si after 4hr compared with 2.4wt.% for the tempered martensite initial structure;
- Similar ferrite manganese contents at 755 and 820°C;
- Higher austenite manganese contents for the tempered martensite initial structures at 755°C, but similar contents at 820°C;
- Higher manganese and chromium cementite concentrations at 755 and 820°C for the tempered martensite initial structures.

9.9 Austenite nucleation and growth mechanisms

Austenite formation from ferrite/cementite initial structures can be analysed by the Avrami rate equation[45], where

Table 9.9 Selected alloy element concentrations for the various phases of the different silicon steels with 96hr tempered martensite initial structures austenitised at their respective Ac_3 temperatures.

STEEL	Temperature	Phase	ALLOY CONCENTRATION (wt.%)									
			Shortest test with austenite present				Longest test duration				α/γ ratio (longest test)	
			Time	Si	Mn	Cr	Time	Si	Mn	Cr	Si	Mn
0% Silicon	**740°C**	**Ferrite**	2min	-	0.6	-	16hr	-	0.4	-	-	0.4
		Austenite		-	0.7	-		-	1.0	-		
		Cementite		-	4.9	1.4		-	4.0	1.3		
1% Silicon	**760°C**	**Ferrite**	4min	1.2	0.8	-	16hr	1.5	0.5	-	1.5	0.4
		Austenite		1.0	0.9	-		1.0	1.2	-		
		Cementite		-	5.5	1.4		-	4.9	1.4		
SUP7	**820°C**	**Ferrite**	30s	1.7	0.7	-	4hr (15min for cementite)	2.5	0.5	-	1.5	0.6
		Austenite		1.7	0.7	-		1.7	0.8	-		
		Cementite		-	4.0	1.4		-	3.8	1.4		
SUP7NV	**820°C**	**Ferrite**	30s	1.9	0.7	-	2hr	2.4	0.5	-	1.3	0.6
		Austenite		1.7	0.7	-		1.7	0.9	-		
		Cementite		-	4.0	1.3		-	3.8	1.3		
3% Silicon	**835°C**	**Ferrite**	30s	2.5	0.9	-	4hr (15min for cementite)	3.2	0.5	-	1.3	0.6
		Austenite		2.3	0.8	-		2.3	0.9	-		
		Cementite		-	4.6	3.5		-	4.6	3.5		

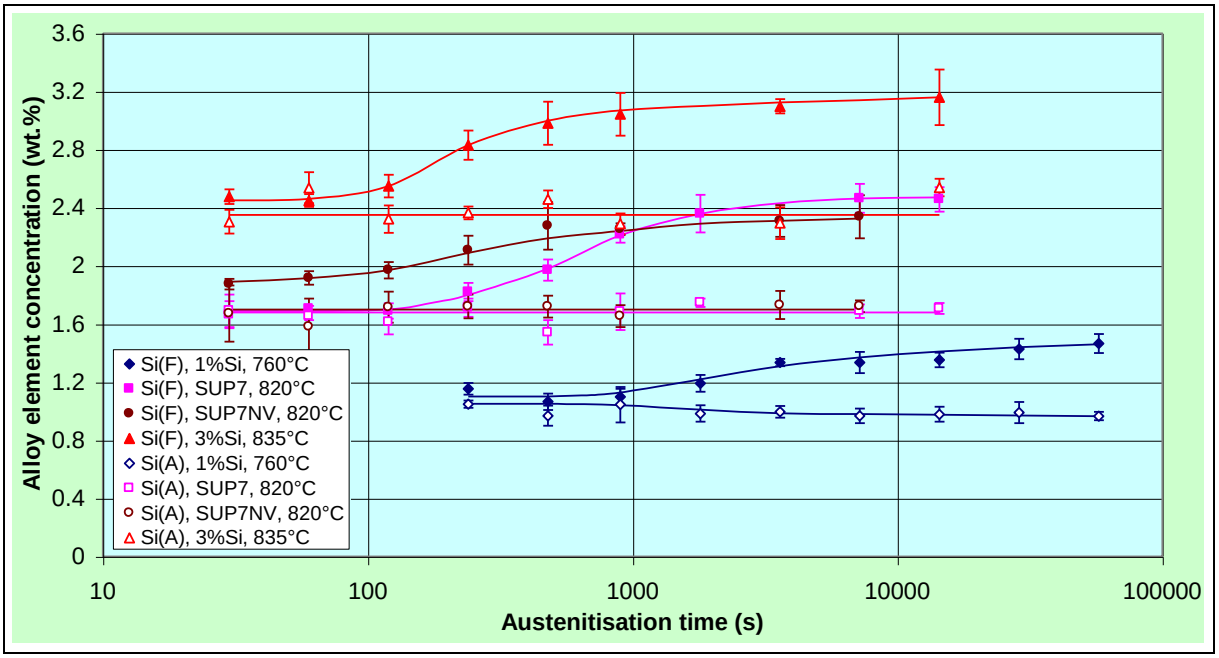

Figure 9.53 Silicon partitioning between ferrite and austenite during austenitisation of 96hr tempered martensite initial structures for different silicon steels at their respective Ac_3 temperatures. F denotes ferrite, A denotes austenite.

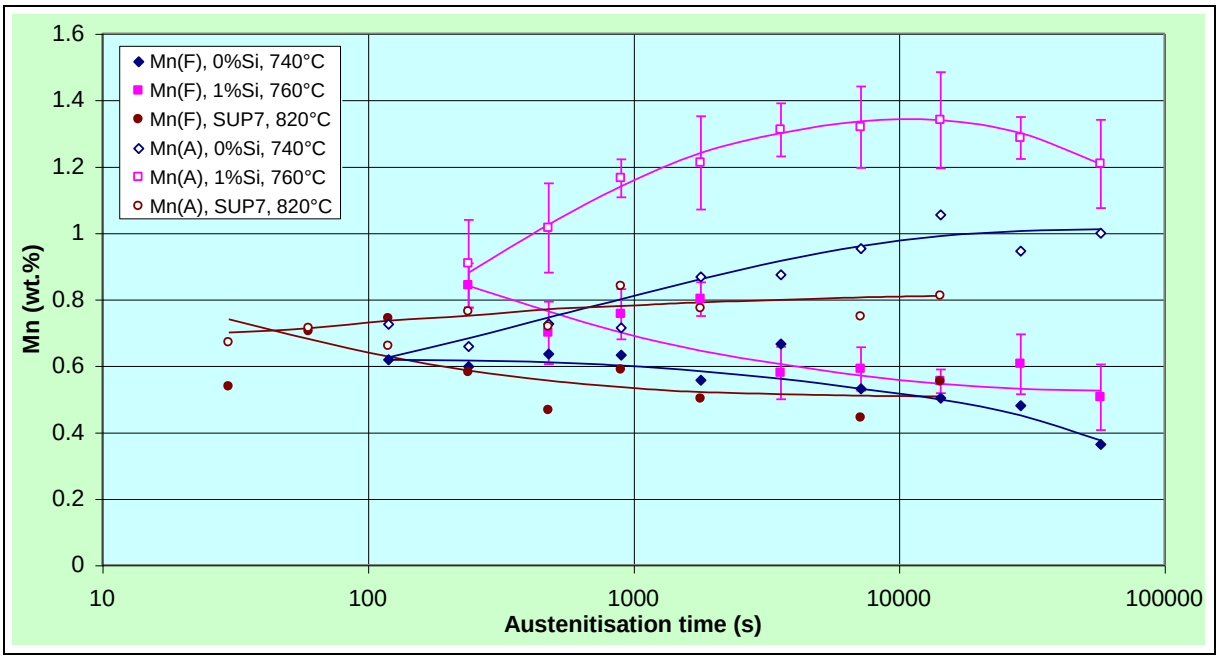

Figure 9.54 Manganese partitioning between ferrite and austenite during austenitisation of 0% Silicon, 1% Silicon and SUP7 96hr tempered martensite initial structures at their respective Ac_3 temperatures. F denotes ferrite, A denotes austenite.

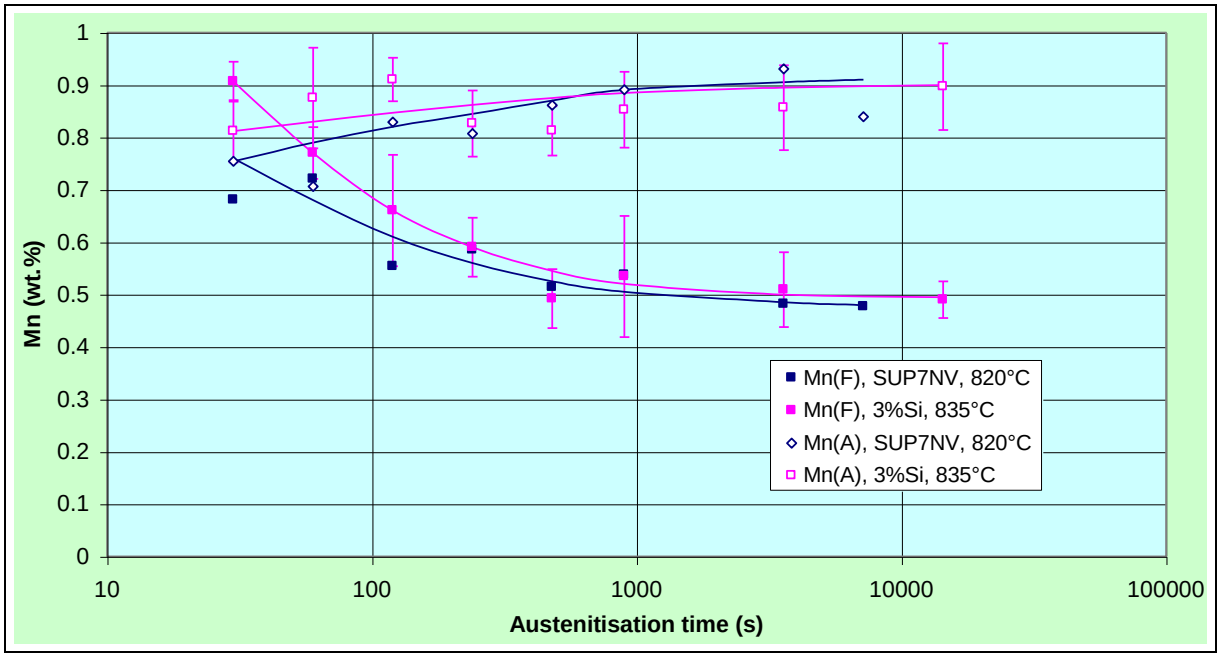

Figure 9.55 Manganese partitioning between ferrite and austenite during austenitisation of SUP7NV and 3% Silicon 96hr tempered martensite initial structures at their respective Ac_3 temperatures. F denotes ferrite, A denotes austenite.

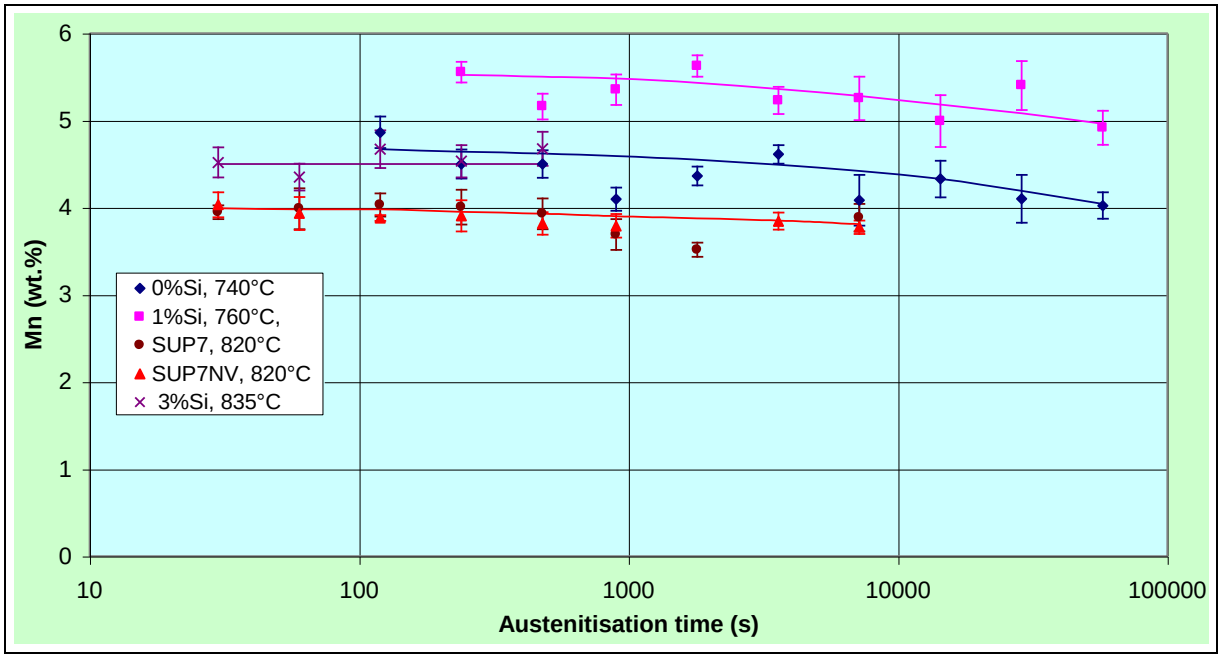

Figure 9.56 Cementite manganese concentrations during austenitisation of different silicon 96hr tempered martensite initial structures at their respective Ac_3 temperatures.

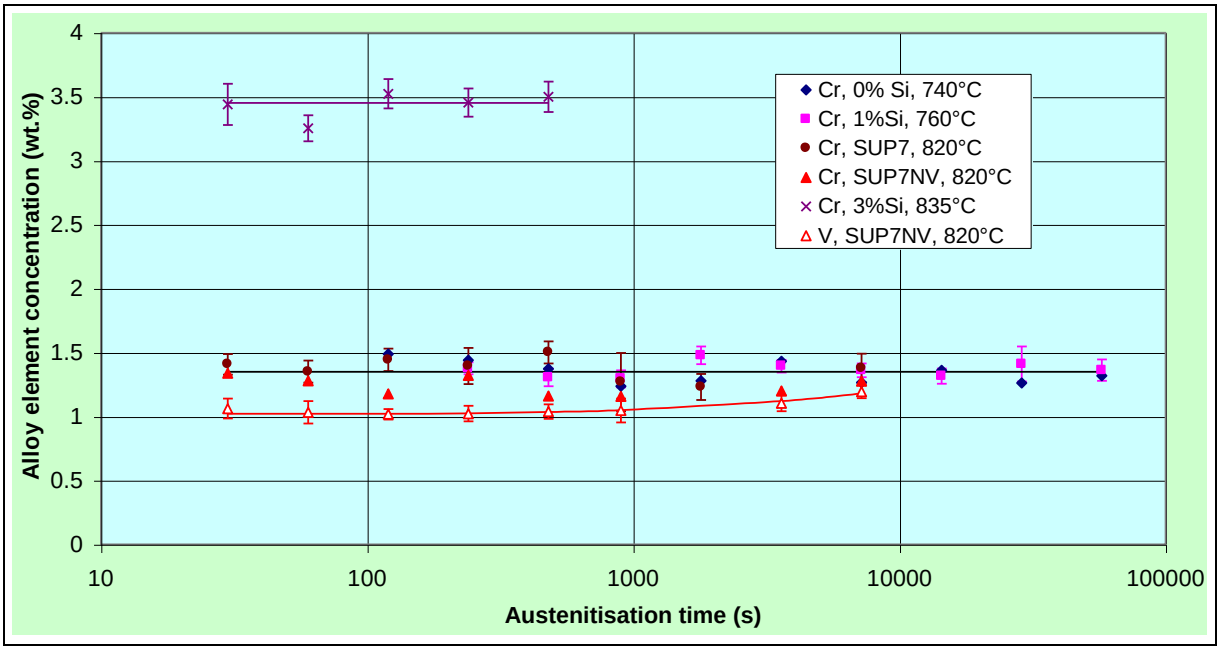

Figure 9.57 Cementite chromium and vanadium concentrations during austenitisation of different silicon 96hr tempered martensite initial structures at their respective Ac_3 temperatures.

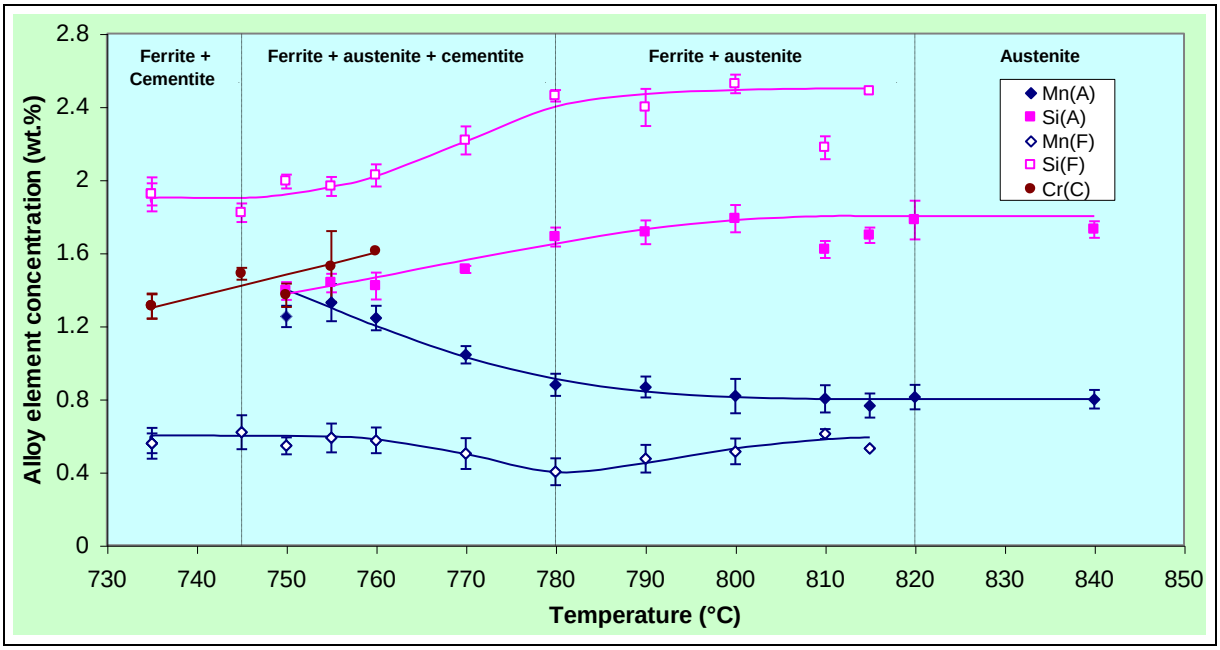

Figure 9.58 Influence of austenitising temperature on alloy element partitioning after 96hr austenitisation of a 96hr tempered martensite SUP7 initial structure. A denotes austenite, F denotes ferrite, C denotes cementite.

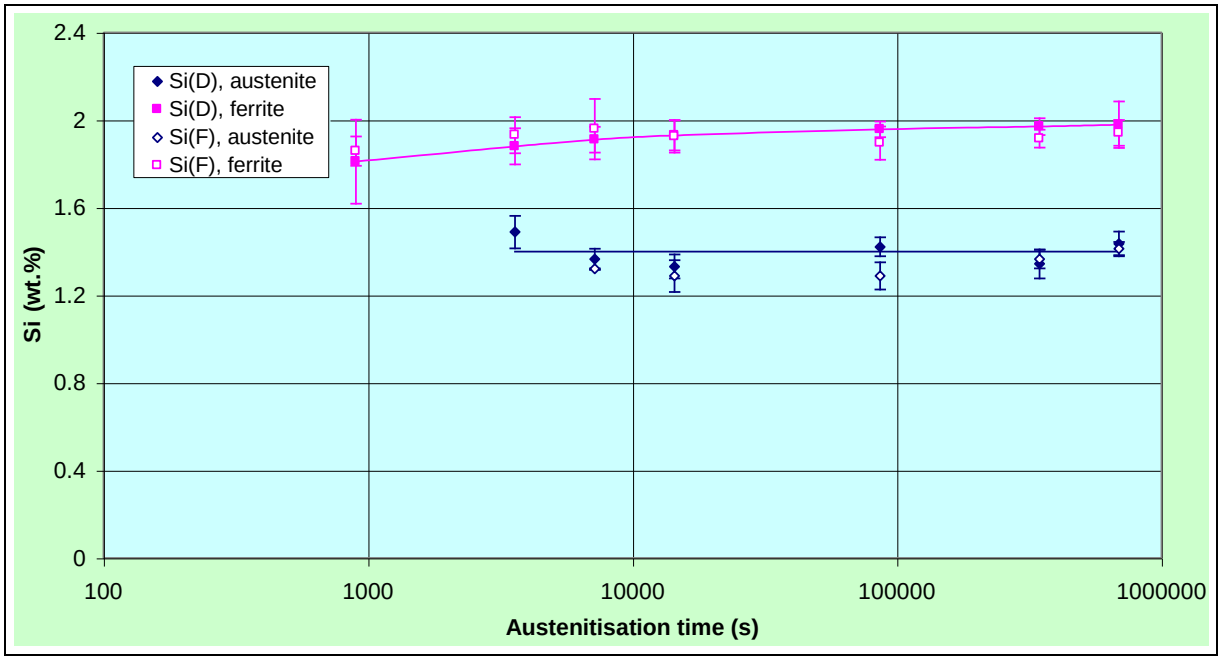

Figure 9.59 Silicon partitioning between austenite and ferrite for SUP7 96hr tempered martensite and intercritical initial structures at 755°C. D denotes a 96hr tempered martensite initial structure, F an intercritical initial structure.

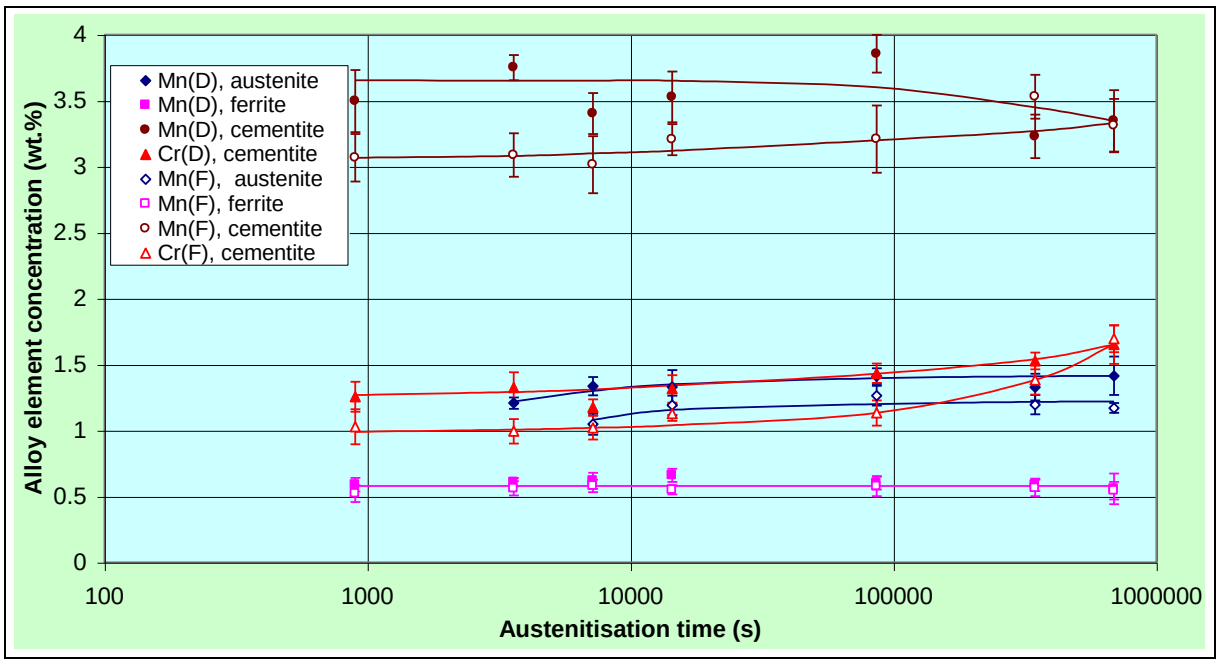

Figure 9.60 Manganese and chromium partitioning for SUP7 96hr tempered martensite and intercritical initial structures at 755°C. D denotes a 96hr tempered martensite initial structure, F an intercritical initial structure.

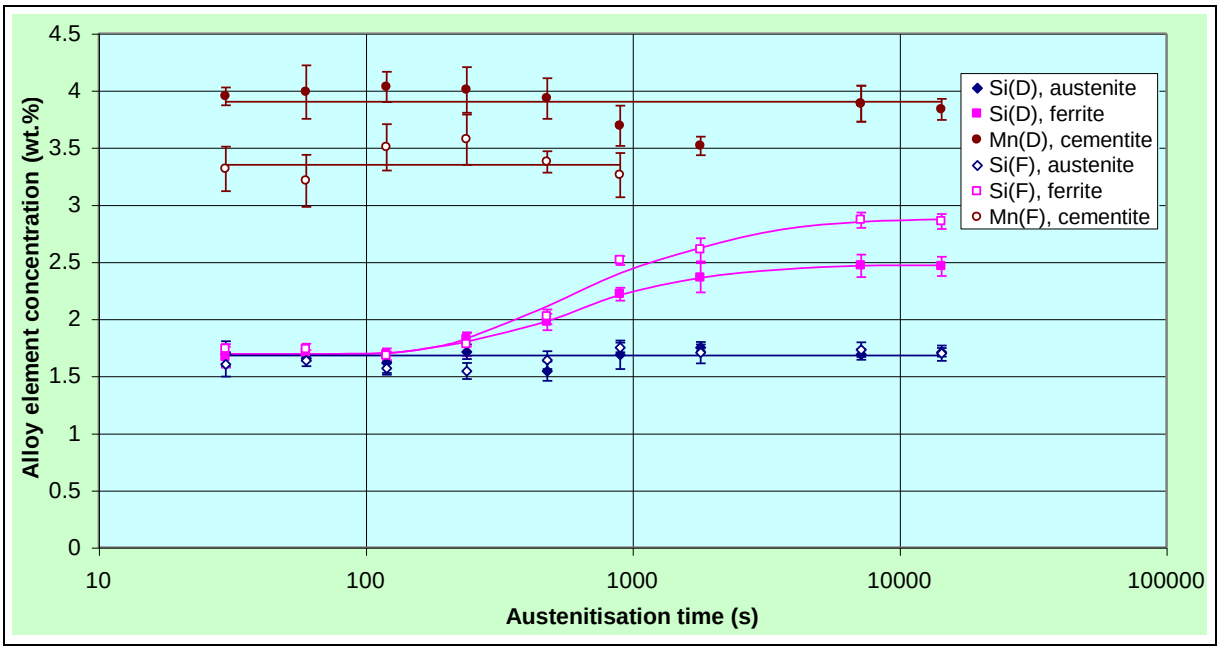

Figure 9.61 Silicon and manganese partitioning for SUP7 96hr tempered martensite and intercritical initial structures at 820°C. D denotes a 96hr tempered martensite initial structure, F an intercritical initial structure.

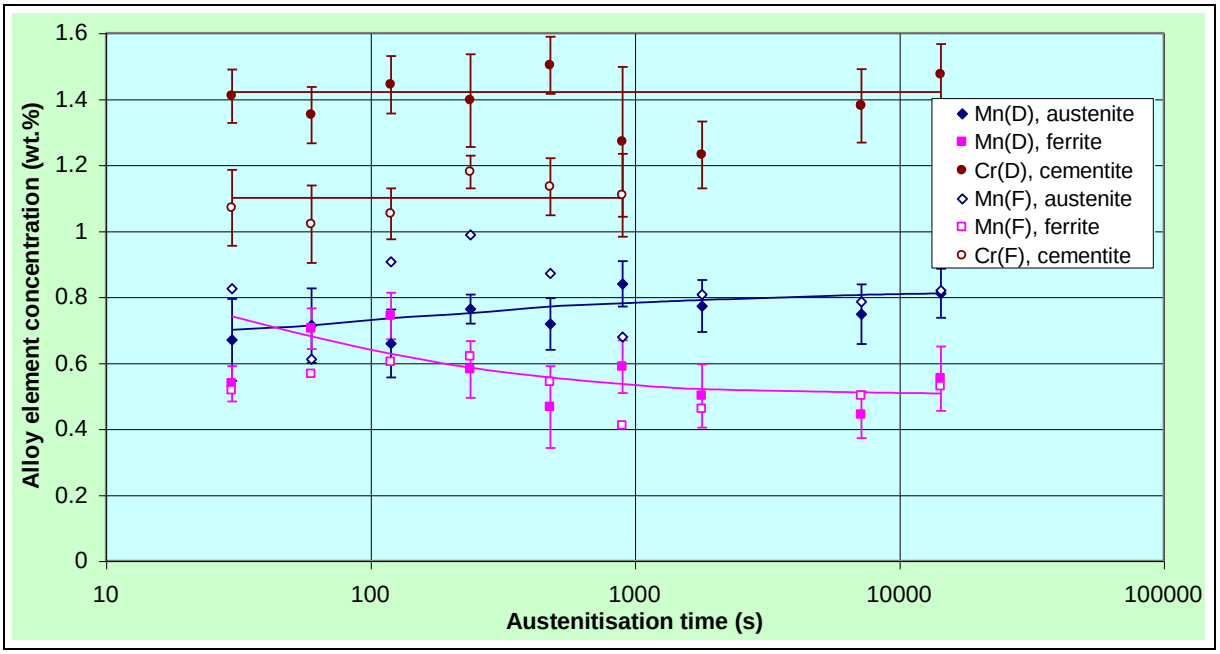

Figure 9.62 Manganese and chromium partitioning for SUP7 96hr tempered martensite and intercritical initial structures at 820°C. D denotes a 96hr tempered martensite initial structure, F an intercritical initial structure.

$$V_v = 1 - \exp(-Kt^n). \quad (2.5)$$

Equation 2.5 can be written in the form

$$\log \ln \left[\frac{1}{1-V_v} \right] = \log K + n \log t. \quad (2.6)$$

The reaction exponent, n, corresponds to the slope of a logln[1/(1-V_v)] versus logt plot. Figures 9.63 to 9.66 illustrate such plots for the 0% Silicon, SUP7 and 3% Silicon steels.

Several generalisations can be made about the reaction exponents of Figures 9.63 to 9.66:

- The curves exhibit either two or three different n values;
- The n_1 values for the different steels and initial structures austenitised at the lower superheat temperatures varied from 1.1 to 2.2, but were often similar;
- A larger variation was observed for the n_1 values of the different silicon steels and initial structures austenitised at their respective Ac_3 temperatures relative to the lower superheat temperatures, with values ranging from 0.6 to 7.2.

The first change in the slope of the logln[1/(1-V_v)] versus logt plots, from n_1 to n_2, is thought to be due to the partitioning of manganese to austenite retarding the movement of the ferrite/austenite interface[33]. This change in slope is less pronounced at higher temperatures, as illustrated by Figure 9.65 for SUP7 tempered martensite initial structures. This arises from the faster austenitisation, with insufficient time for the partitioning of manganese and the subsequent influence on the difference between the n_1 and n_2 values. Greater manganese partitioning at 755°C compared to 820°C is illustrated in Figures 9.60 and 9.62 respectively. The second change in slope, from n_2 to n_3, corresponds to the slow final equilibration of the structures.

Cahn[196] derived kinetic laws for the austenite nucleation sites at cementite particles located on ferrite grain boundary surfaces, at the edges where three ferrite grains meet, and at the corners where four grains meet. Assuming that the ferrite grain boundaries offer no resistance to the

growing austenite, that each newly formed austenite grain grows at a constant radial velocity, G, until it impinges on another grain, and that the nucleation rate, $\dot{N}$, is sufficiently high, then:

$$K_s = 6.7GD^{-1}, \text{(n=1)} \tag{9.8}$$

for grain boundary surface nucleation;

$$K_e = 8.5\pi G^2 D^{-2}, \text{(n=2)} \tag{9.9}$$

for edge nucleation; and

$$K_c = 16\pi G^3 D^{-3}, \text{(n=3)} \tag{9.10}$$

for corner nucleation,

where K_s, K_e, K_c = the reaction coefficients for grain boundary surface, edge and corner nucleation respectively;

D = the mean effective ferrite initial grain diameter.

The radial austenite growth rate was determined by measuring the radius of the largest particles formed in each of twenty fields for the different duration heat treatments, and plotting the averaged values as a function of time. The austenite particle radii were determined by measuring the martensite particle areas from the heat treated microstructure, and then calculating the radius based on the assumption that the particles were spherical. It was assumed that the austenite fraction at the heat treatment temperature corresponded to the martensite fraction at room temperature, as detailed in Section 8.3.1.

Figure 9.67 illustrates the radius of the largest austenite particles as a function of time during the austenitisation of SUP7 furnace cooled and 96hr tempered martensite initial structures at 765°C. The largest austenite particle sizes were only measured for austenite fractions of up to approximately 20vol.%, due to impingement of the growing austenite, and the increased

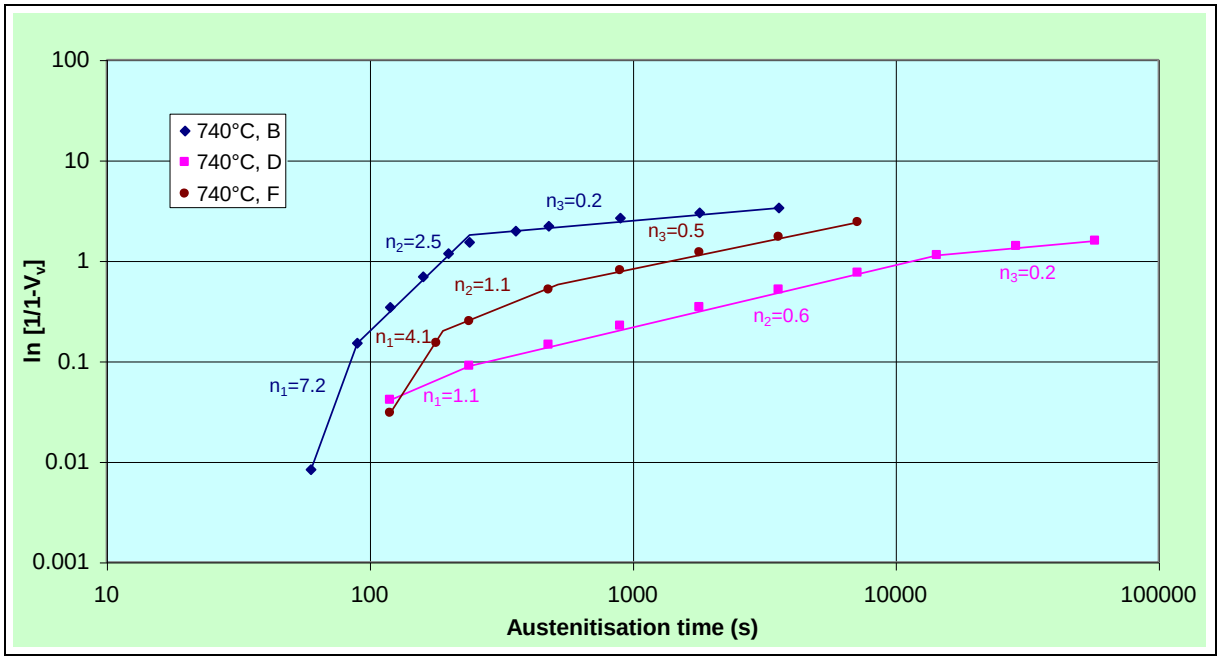

Figure 9.63 Plot of logln[1/(1-V_v)] versus logt for different initial 0% Silicon steel structures at 740°C.

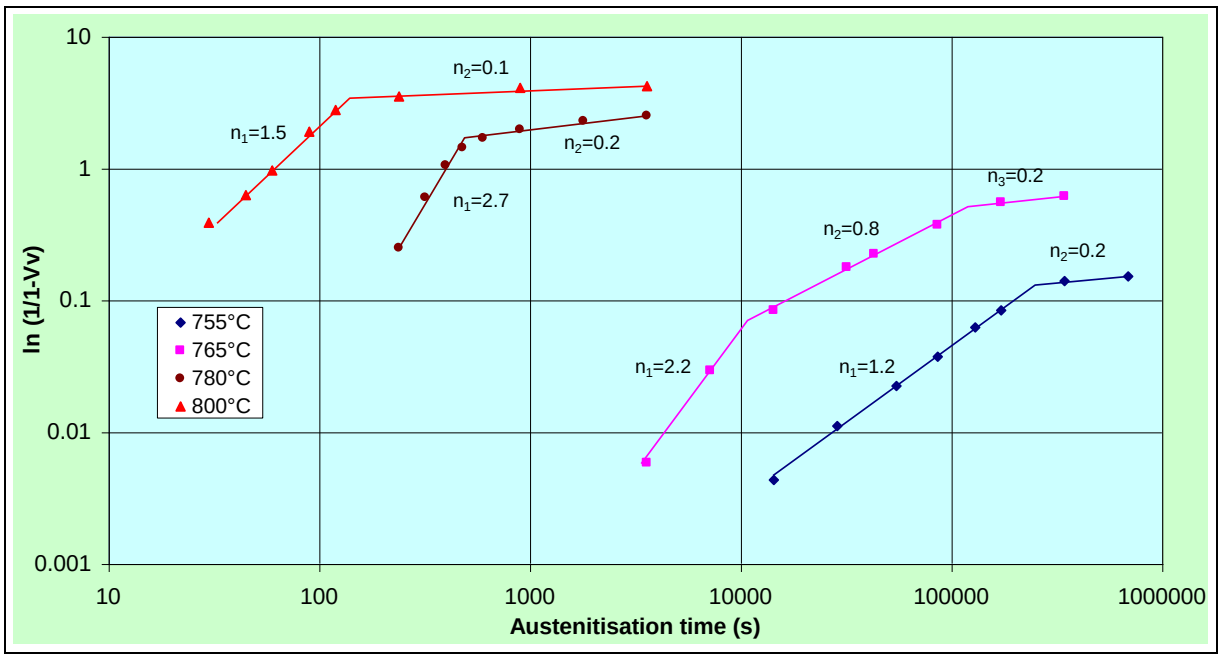

Figure 9.64 Influence of temperature on a plot of logln[1/(1-V_v)] versus logt for furnace cooled initial SUP7 structures.

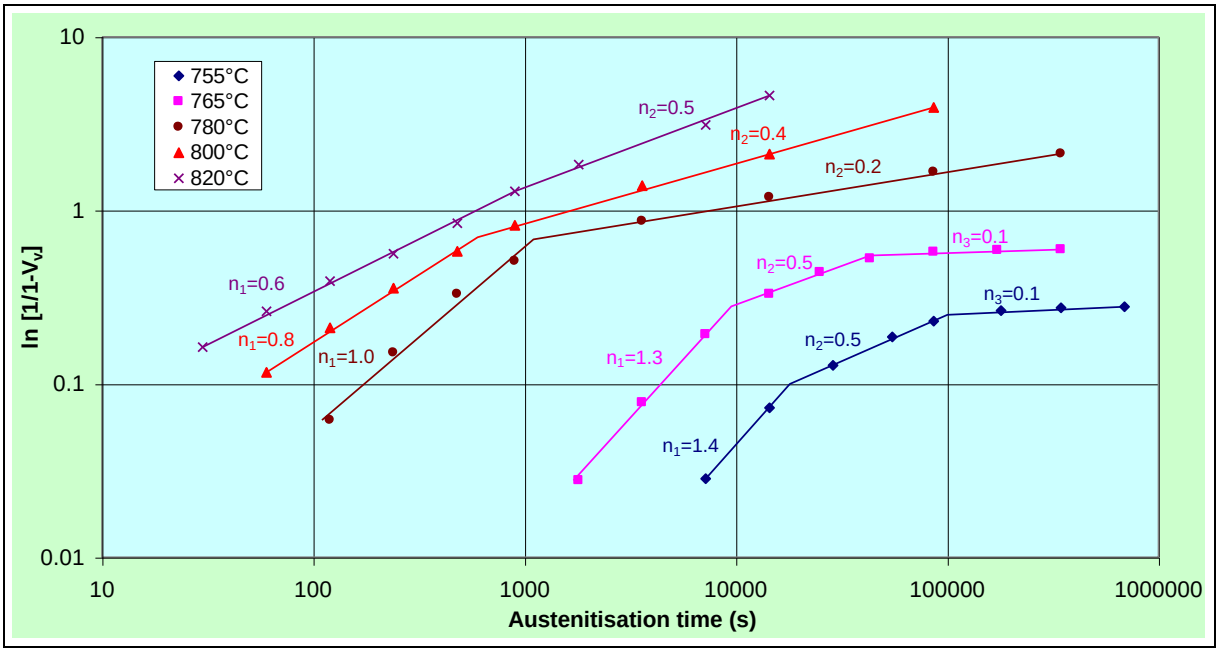

Figure 9.65 Influence of temperature on a plot of logln[1/(1-V_v)] versus logt for 96hr tempered martensite initial SUP7 structures.

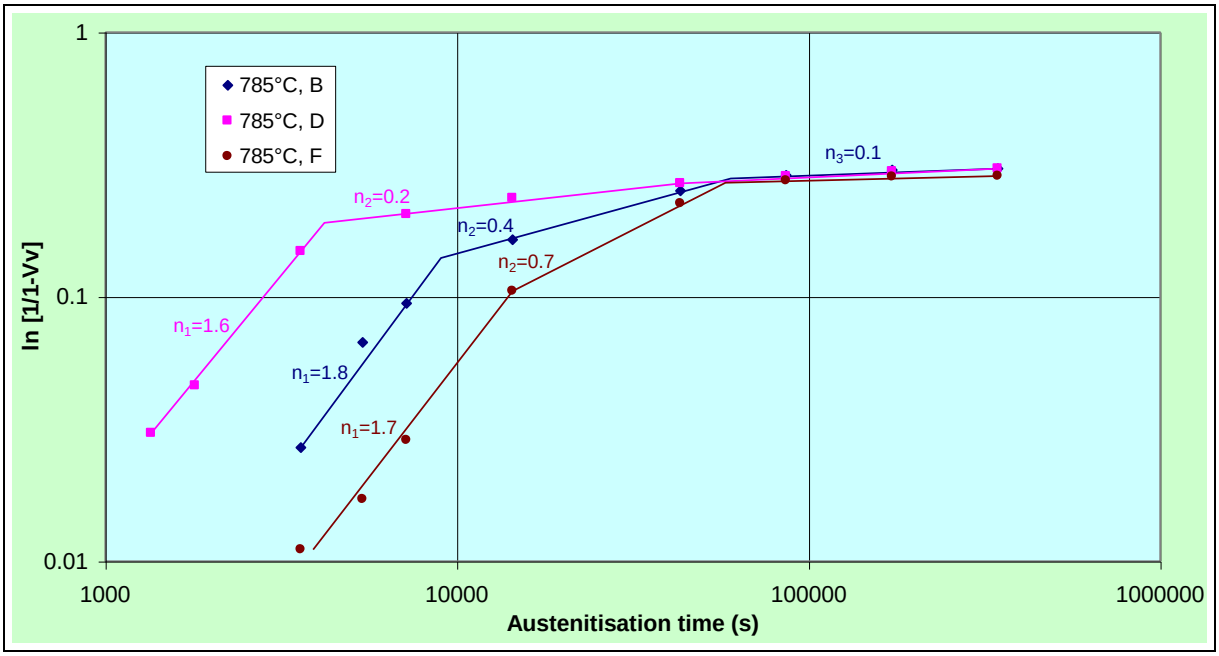

Figure 9.66 Plot of logln[1/(1-V_v)] versus logt for different initial 3% Silicon steel structures at 785°C.

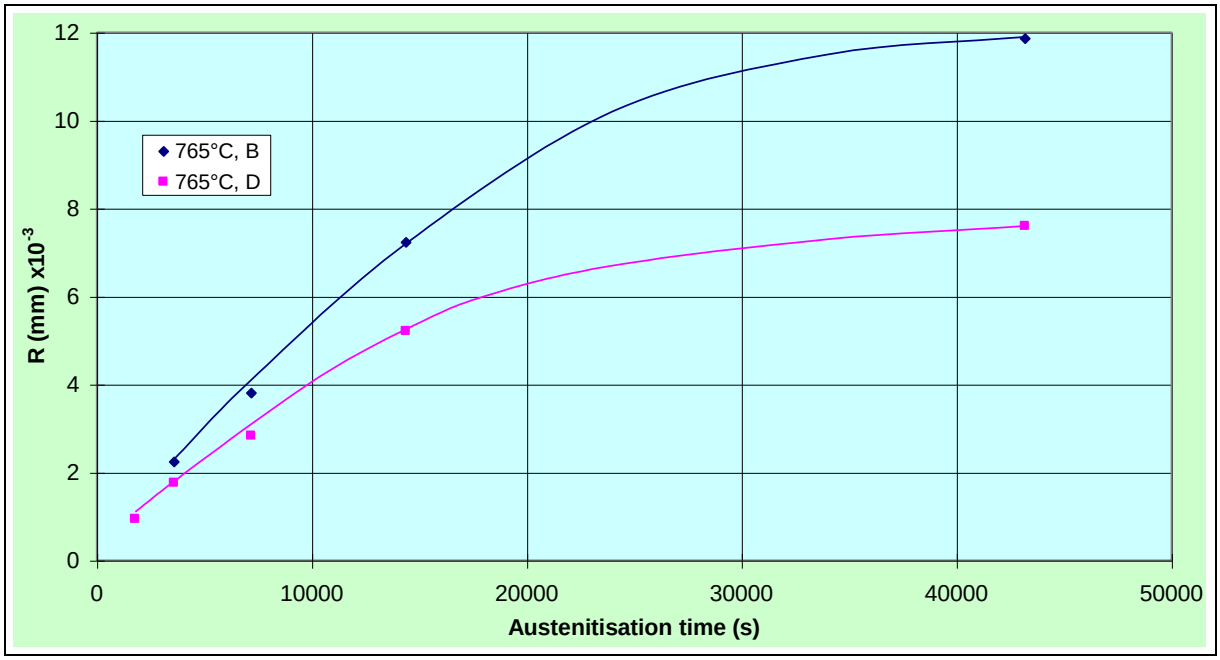

Figure 9.67 Radius of the largest austenite particles versus time for SUP7 furnace cooled and 96hr tempered martensite initial structures at 765°C.

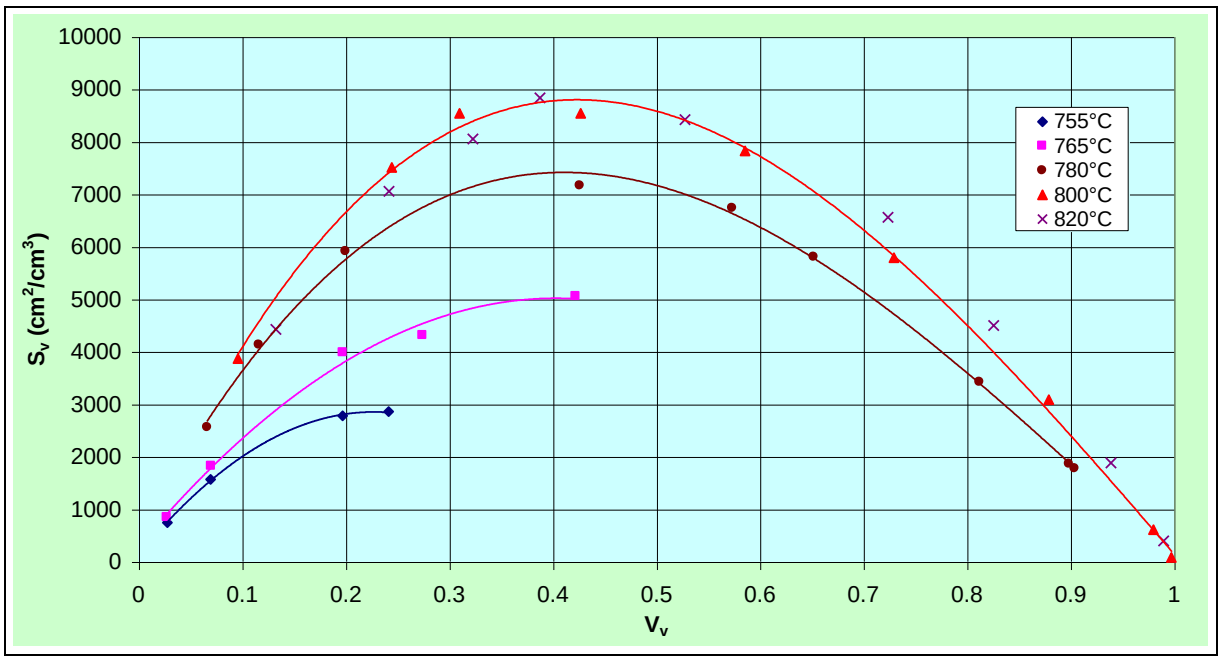

Figure 9.68 Influence of temperature on a plot of S_v versus V_v for 96hr tempered martensite SUP7 initial structures.

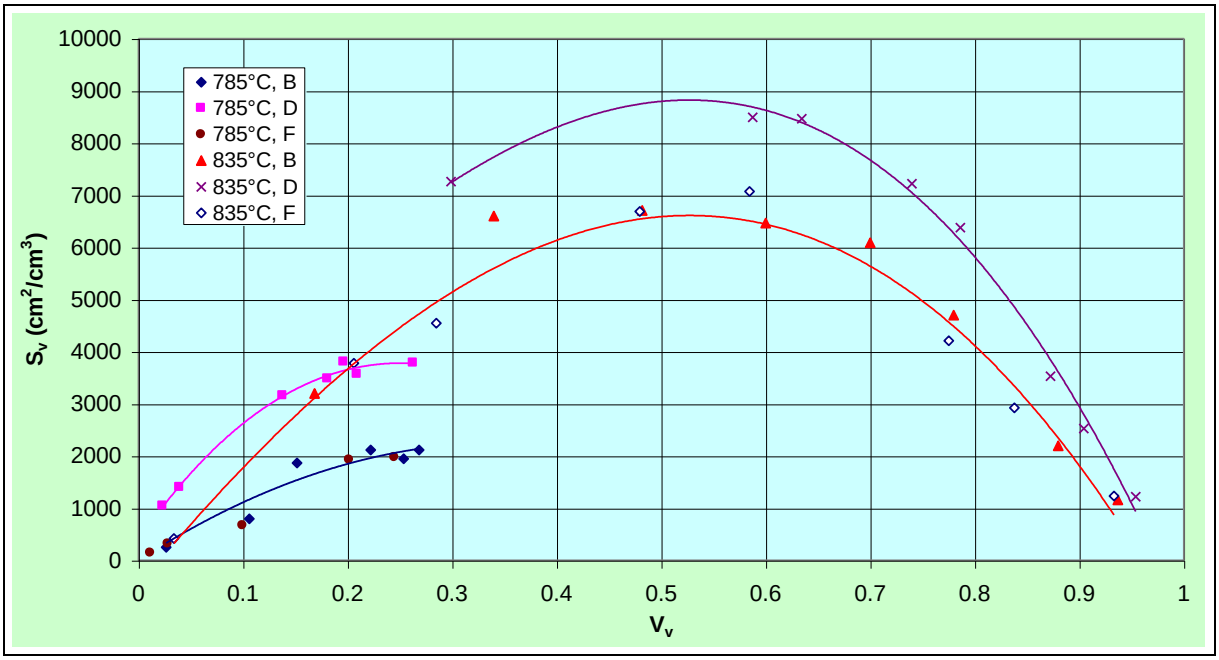

Figure 9.69 A plot of S_v versus V_v for different initial 3% Silicon steel structures at 785 and 835°C.

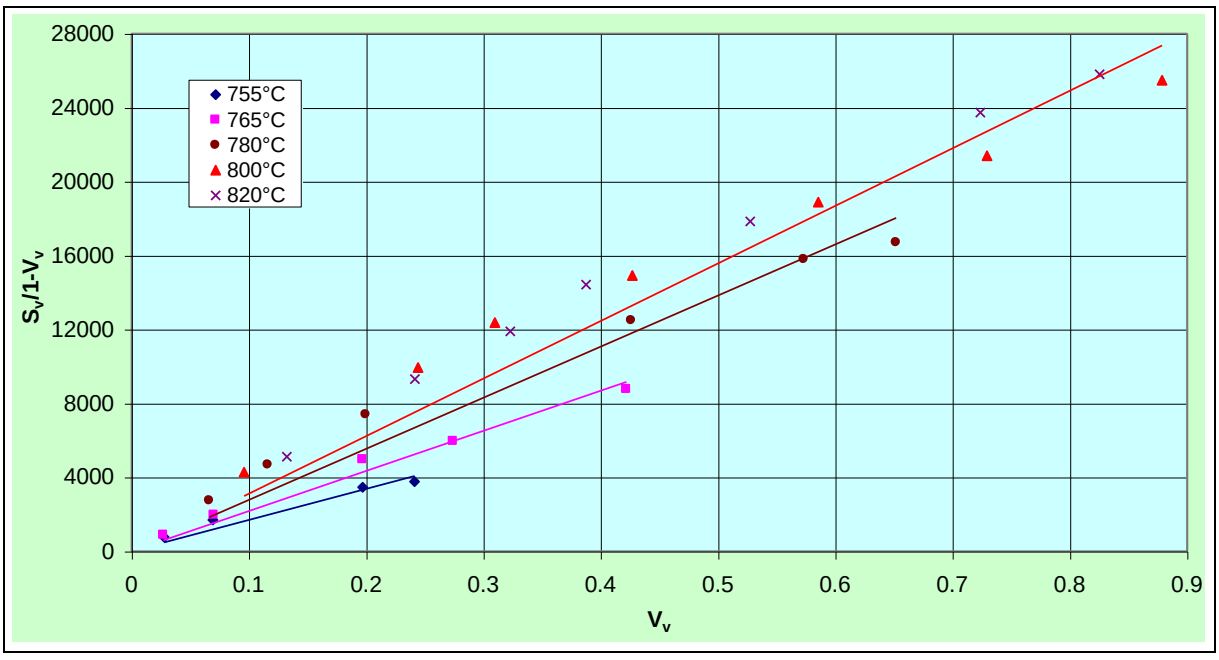

Figure 9.70 Influence of temperature on a plot of $S_v/1-V_v$ versus V_v for 96hr tempered martensite initial SUP7 structures.

overestimation of the resultant austenite growth rate determined from the measured austenite particle sizes. For non-circular austenite particles, the radius of circles equal in area were used instead[33]. The particle sizes were not measured for the higher temperature heat treatments due to the rapid austenitisation. The radius of the austenite particles increased linearly with time for up to approximately 4hr, before levelling off. At this stage, 10.0 and 27.4vol.% austenite formed for the furnace cooled and tempered martensite initial structures respectively.

A microscopic examination confirmed that austenite nucleated at cementite particles located at the edges where three grains meet, as illustrated in Figure 9.11. The radial austenite growth rate was determined from the linear regions of the curves of Figure 9.6, with the growth rate corresponding to the slope of the line. The values of logK_s, logK_e and logK_c were calculated for the growth of austenite in SUP7 96hr tempered martensite initial structures at 755 and 765°C using equations 9.8 to 9.10 respectively. These values are compared to logK_1 in Table 9.10, which were calculated for the slopes of Figures 9.63 to 9.66 corresponding to the n_1 values. The similarities of logK_e with logK_1 at both temperatures support the microscopic observations that the predominant nucleation mechanism for austenite occurred at cementite particles located at the edges where three ferrite grains meet[33]. However, values of n_1 were expected to be closer to two, given the value of n=2 of equation 9.5 for edge nucleation.

Table 9.10 Kinetic data for the formation of austenite in SUP7 96hr tempered martensite initial structures at 755 and 765°C.

Temperature (°C)	D (μm)	G (μm/s)	n_1	logK_1	logK_s	LogK_e	logK_c
755	3.8	1.8×10^{-4}	1.4	-6.8	-3.5	-7.2	-11.3
765	3.8	3.3×10^{-4}	1.3	-7.2	-3.2	-6.7	-10.5

Table 9.11 Kinetic data for site saturation calculations of SUP7 96hr tempered martensite initial structures at 755 and 765°C.

Temperature (°C)	0.1D/G (s)	0.5D/G (s)	$t_{0.5}$ (s)	N_v (no./mm^3)	D/G (s)
755	2100	10500	20100	1.1×10^{7}	21000
765	1150	5750	10000	1.4×10^{7}	11500

For a reaction where austenite nucleation is confined to the grain boundary sites, the criterion for site saturation is[197]:

$$0.1\frac{D}{G} < t_{0.5} < 0.5\frac{D}{G} \qquad (9.11)$$

where $t_{0.5}$ = the time for 50% transformation in s.

Table 9.11 demonstrates that the values of $t_{0.5}$ determined from the austenitisation kinetics of Figure 9.35 fall outside the range for site saturation defined by equation 9.11. Therefore, site saturation did not occur. According to Cahn[33], a condition for site saturation is the formation of at least one austenite nucleus per grain in a time short compared to D/G. The number of ferrite grains per unit volume can be calculated from $2/D^3$, which yields $3.6x10^7$ grains/mm^3 with D=$3.8x10^{-3}$mm for the 96hr tempered martensite initial structure. The maximum values of the number of austenite nodules measured per unit volume, N_v, for 755 and 765°C were $1.1x10^7$ and $1.4x10^7$number/mm^3, and occurred at a time similar to D/G. This further confirms that site saturation did not occur. However, n_1 values of 1.4 and 1.3 were determined for the 96hr tempered martensite initial structures at 755 and 765°C respectively, compared with the value of n=4 usually observed when site saturation does not occur [85,197]. The reason for this is not readily apparent.

Assuming that the geometrical state of a particle can be described by at most three characteristic dimensions, there are three possible growth austenite geometries[199]:

1) *3-Dimensional growth.* All the characteristic dimensions of a particle change with time at comparable rates, and result in equiaxed particles.
2) *2-Dimensional growth.* One characteristic particle dimension does not change with time, such as radial growth of cylindrical particles whose length remains constant.
3) *1-Dimensional growth.* Involves the lengthening of rod-like particles whose cross sectional area does not change with time.

Figures 9.68 and 9.69 illustrate plots of the surface area to volume ratio, S_v, versus V_v, for the 0% Silicon and SUP7 steels respectively. These curves appear to be parabolic, with the

maximum occurring at a volume fraction of approximately 0.5. This suggests a relationship of the form[189]:

$$S_v=KV_v(1-V_v). \qquad (9.12)$$

Figure 9.70 illustrates the linear relationship between (S_v/1-V_v) and V_v for the 96hr tempered martensite SUP7 initial structure. The value of the constant, K, in equation 9.8 can be determined from the slope of this graph. The plots of S_v versus V_v, Figures 9.68 and 9.69, and that of S_v/1-V_v versus V_v of Figure 9.70, demonstrate that K increased with austenitising temperature for the different steels. Figure 9.69 also illustrates that the relationship of S_v with V_v was similar for the furnace cooled and intercritical initial 3% Silicon steel structures at 785 and 835°C. Datta[189] demonstrated that two dimensional austenite growth resulted during the austenitisation of a 0.15wt.%C steel with a pearlitic initial structure that exhibited parabolic relationships similar to Figures 9.68 to 9.70.

The nucleation and growth rates of a pearlitic 0.83wt.%C steel were estimated assuming a random spatial distribution of austenite nuclei[200], with[45,198,201]

$$V_{vex} = \ln\left[\frac{1}{1-V_v}\right], \qquad (9.13)$$

$$S_{vex} = \frac{S_v}{1-V_v}, \qquad (9.14)$$

where V_{vex} = the volume fraction in the extended structure:

S_{vex} = the surface area per unit volume in the extended structure.

The extended structure is defined because of the increasing impingement of the growing austenite grains as the austenite fraction increases. A plot of S_{vex} versus V_{vex} from equations 9.13 and 9.14 for the 0.83wt.%C steel was non-linear, indicating three-dimensional growth[200]. S_{vex} versus V_{vex} plots were made for the 0% Silicon, SUP7 and 3% Silicon steels investigated in this project. These plots were non-linear, which suggests three-dimensional growth. This was in conflict with the two dimensional growth geometry illustrated by Figures 9.68 to 9.70.

Roosz[186] and Speich[36] have demonstrated that austenite nucleation in pearlitic initial structures is not random, because austenite nuclei can only appear on ferrite/cementite interfaces. For non-random austenite nucleation, equations 9.15[202] and 9.16[203] have been suggested.

$$dV_v = (1-V_v)^i dV_{ex}, \tag{9.15}$$

$$S_v = (1-V_v)^i S_{vex}, \tag{9.16}$$

where the exponent *i* is greater than one if the particles are clustered, and less than one if they are ordered. The microstructure photographs of Figures 9.11 to 9.13 illustrated that austenite nucleation occurs at the points of intersection of cementite lamellae with the edges of the pearlite colonies in pearlitic initial structures[186], and at cementite particles located at the edges where three ferrite grains meet for spheroidal cementite initial structures. Therefore, clustered geometrical impingement is likely, with the exponent *i* in equations 9.15 and 9.16 greater than one. Datta[189] determined a value of *i*=2 by trial and error for a pearlitic 0.15wt.C steel. Substituting *i*=2 into equations 9.15 and 9.16 gives

$$V_{vex} = \frac{V_v}{1-V_v}, \tag{9.17}$$

$$S_{vex} = \frac{S_v}{(1-V_v)^2}. \tag{9.18}$$

A plot of S_{vex} versus V_{vex} using equations 9.17 and 9.18 is illustrated in Figure 9.71 for different initial 0% Silicon steel structures at 740°C. The linear relationship between S_{vex} and V_{vex} for the different initial structures indicates two dimensional growth[200], confirming the results obtained from Figures 9.68 to 9.70. Two dimensional austenite growth was also demonstrated for the higher silicon steels by linear S_{vex} versus V_{vex} plots. The nucleation and grain growth rates in a Cu-Be alloy for reaction exponents of less than two were calculated with the following equations[204]:

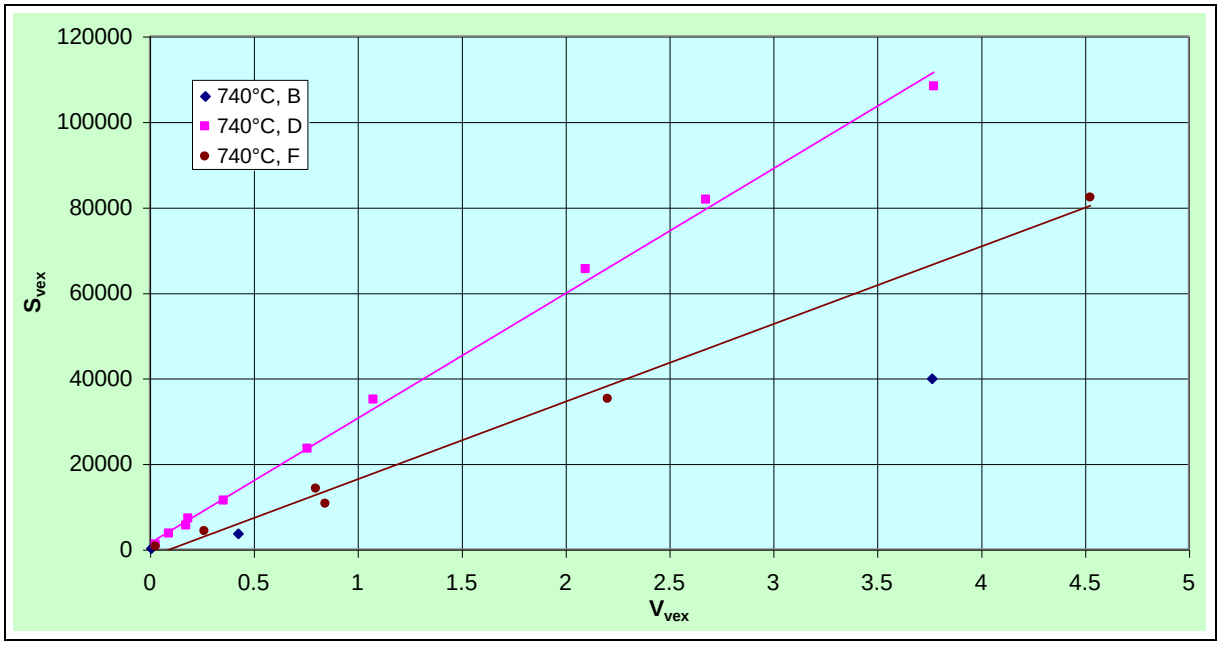

Figure 9.71 A plot of S_{vex} versus V_{vex} with i=2 for different initial 0% Silicon steel structures at 740°C.

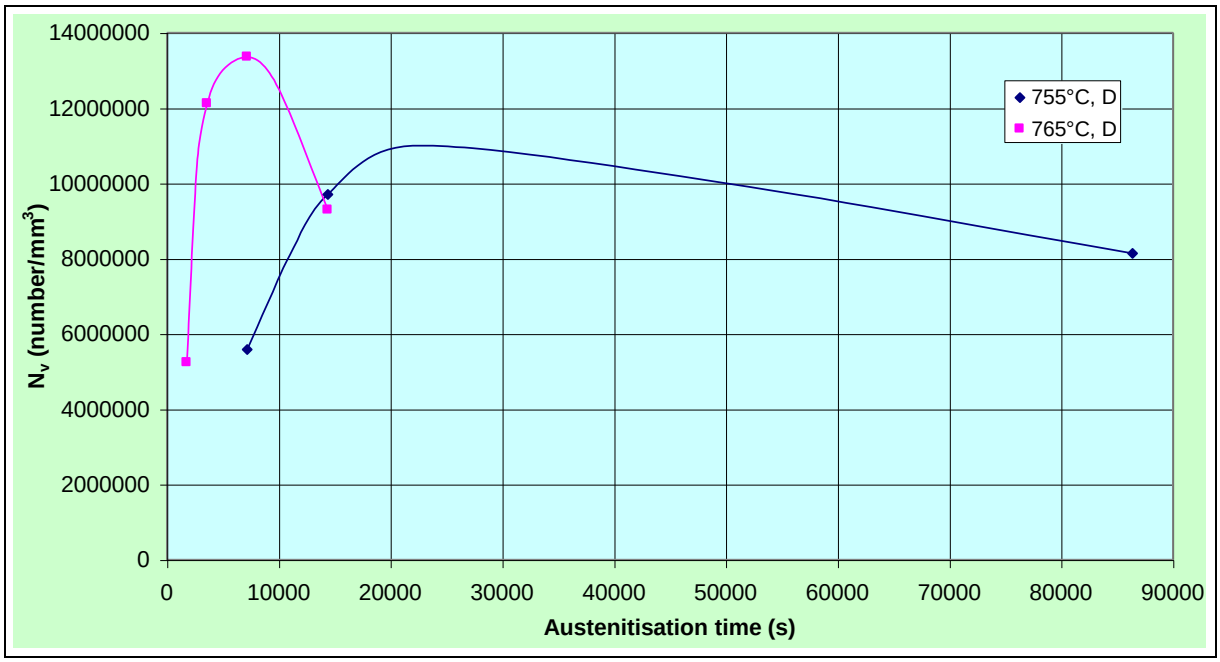

Figure 9.72 A plot of N_v versus time for SUP7 96hr tempered martensite initial structures at 755 and 765°C.

$$\dot{N} = \frac{3S_v^{\ 3}}{54\pi(1-V_v)^3 t\left[\ln\left[\frac{1}{1-V_v}\right]\right]^2}, \tag{9.19}$$

$$G = \frac{n}{S_v t}(1-V_v)\ln\left[\frac{1}{1-V_v}\right]. \tag{9.20}$$

Similar equations were obtained by Roosz[186] for austenite formation in pearlitic initial structures for a 0.78wt.%C steel, with a value of n=4 for equation 9.20. Figure 9.72 illustrates a plot of the number of austenite nodules per unit volume, N_v, versus time for SUP7 96hr tempered martensite initial structures at 755 and 765°C. The number of austenite nodules per unit area, N_A, were counted for heat treatment durations that yielded up to approximately 20vol.% austenite. Given that the austenite particles were not spherical, randomly distributed throughout the microstructure, or of discrete sizes, N_v was calculated from N_A using the Saltikov equation[205]:

$$N_v = 2.38(N_A)^{1.6}. \tag{9.21}$$

Initially, there is a linear relationship between N_v and time, Figure 9.72, before the curve reached a maximum. The slope of the linear portion of the curves corresponds to the nucleation rate[33], $\dot{N}$. The kinetic data for the calculated and measured nucleation rates for SUP7 furnace cooled and 96hr tempered martensite initial structures at 765°C are given in Table 9.12.

Table 9.12 Kinetic data for the calculation of the linear austenite nucleation and radial growth rates for SUP7 furnace cooled and 96hr tempered martensite initial structures at 765°C.

Specimen	S_v **(cm^3/s)**	V_v	t **(s)**	n	$N_{calculated}$ **(no/mm^{3}s)**	$N_{measured}$ **(no/mm^{3}s)**	$G_{calculated}$ **(μm/s)**	$G_{measured}$ **(μm/s)**
Structure B	1160±300	0.10±0.03	10800	2.2	280	70	$1.6\text{x}10^{-4}$	$4.6\text{x}10^{-4}$
Structure D	1820±220	0.07±0.01	2700	1.3	4540	3820	$1.9\text{x}10^{-4}$	$3.3\text{x}10^{-4}$

The measured and calculated austenite nucleation rates for the 96hr tempered martensite initial structure are similar, while the calculated nucleation rate for the furnace cooled initial structure is four times the measured value. When the number of austenite particles were counted, it is probable that some of the particles contained more than one austenite nucleus, particularly for the higher austenite fractions. Therefore, the true nucleation rate will be higher than the measured rate. Furthermore, the calculated nucleation rates are susceptible to errors in the experimentally determined values of S_v and V_v. The larger errors for the furnace cooled initial structure relative to the tempered martensite structure also account for the greater difference between the measured and calculated nucleation rates for the furnace cooled structure, with a minimum nucleation rate of 80number/mm^{3}s calculated from equation 9.19 and the uncertainties of the S_v and V_v measurements of Table 9.11.

The calculated radial austenite growth rates of the SUP7 furnace cooled and 96hr tempered martensite initial structures are approximately half that of the measured rates. This could be due to:

i) Impingement of the growing austenite where one austenite particle measured from the microstructure had two or more nuclei before impingement. This results in faster growth rates than the actual values;
ii) Lengthwise austenite growth along the ferrite grain boundaries at low volume fractions before impingement of the growing austenite grains occurred, in conjunction with the assumed radial austenite growth. The measurement of the area of the austenite nodule, and the subsequent conversion to an equivalent area diameter would yield radial growth rates higher than the actual values.

9.10 Summary of austenitisation investigation

The austenitisation investigation detailed in this chapter involved the following:

i) Production of experimental steels with 0, 1 and 3wt.%Si;
ii) Heat treatments to determine the Ac_1 and Ac_3 transformation temperatures of the different silicon steels;
iii) Heat treatments to produce pearlitic and spheroidal cementite initial microstructures for the different silicon steels;
iv) Quantitative stereological and SEM energy dispersive spectroscopical analysis of the initial microstructures;
v) Austenitisation heat treatments at temperatures corresponding to intercritical and critical temperatures for the different steels;
vi) Quantitative stereological, SEM energy dispersive spectroscopical, and microhardness analysis of the austenitised specimens;
vii) Description of the austenite nucleation and growth, and concurrent cementite dissolution, from a qualitative microstructural investigation;
viii) Comparison of the effect of initial structure on the austenitisation kinetics for the different steels at intercritical and Ac_3 temperatures;
ix) A detailed comparison of the austenitisation kinetics for a range of pearlitic and spheroidal cementite initial SUP7 structures over a range of temperatures;
x) A description of the mechanisms controlling austenite nucleation and growth for SUP7;
xi) Comparison of the austenitisation kinetics for the different silicon steels;
xii) Comparison of the austenite microhardness for the different silicon steels;
xiii) Comparison of the cementite dissolution kinetics for the 0% Silicon to SUP7NV steels with 96hr tempered martensite initial structures;
xiv) Determination of the graphitisation kinetics for the 3% Silicon steel at intercritical and critical temperatures;
xv) Calculation of the austenite carbon contents during the austenitisation of the 0% Silicon to SUP7NV steels with 96hr tempered martensite initial structures;
xvi) Comparison of the alloy element partitioning kinetics for 96hr tempered martensite initial structures for the different silicon steels;

xvii) Comparison of the partitioning kinetics for SUP7 96hr tempered martensite and intercritical initial structures;

xviii) Determination of the austenite nucleation sites in pearlitic and spheroidal cementite initial structures;

xix) Determination of the austenite growth geometry;

xx) Comparison of the experimentally determined austenite nucleation and growth rates for SUP7 with the theoretically determined values.

The following chapter details the decarburisation experimentation undertaken for SUP7.

CHAPTER 10

DECARBURISATION OF SUP7

10.1 Introduction

Preliminary decarburisation heat treatments were undertaken with 5mm diameter by 80mm SUP7 test specimens using a range of hydrogen flow rates to determine the minimum required hydrogen flow rate. Test specimens, 5mm diameter by 15mm with a range of initial structures, were then decarburised for various test durations at different p_{H_2O} / p_{H_2} ratios, and different temperatures. These specimens were heated to temperature in an inert argon atmosphere prior to exposure to the decarburisation atmosphere. Austenitisation heat treatments prior to the introduction of the decarburisation atmosphere were also undertaken. The heat treated specimens were mounted, ground, polished and etched, with the free ferrite and oxide thicknesses, and the free ferrite grain sizes, measured. Energy dispersive spectroscopy was used to determine the microalloy contents of the oxidation structures.

In order to ascertain more detailed information on the decarburisation processes, especially during the early stages of the heat treatment, 5mm diameter by 50mm test specimens were decarburised with continuous monitoring of the carbon monoxide and carbon dioxide evolved. These heat treatments were undertaken at the Ac_3 temperature for p_{H_2O} / p_{H_2} ratios of 0 to 1.0, and at temperatures of 650 to 900°C using a p_{H_2O} / p_{H_2} ratio of 0.05. The gas concentrations measured at the Ac_3 temperature were converted to mass of carbon removed, and subsequently to free ferrite depths. Free ferrite decarburisation depths, oxide thicknesses, oxide element concentration profiles, microhardness profiles and free ferrite columnar grain sizes were all measured from the mounted, ground, polished, and etched microstructures.

This investigation allowed the decarburisation and oxidation kinetics of SUP7 to be quantified as a function of decarburisation atmosphere composition, initial structure, and heat treatment temperature. This chapter details the results obtained for the decarburisation of SUP7, and the subsequent analysis and explanation of these results.

10.2 Dependence of decarburisation on hydrogen flow rate

Decarburisation in water/hydrogen or water/hydrogen/argon atmospheres with low water contents can lower the water content of the atmosphere downstream from the test specimen in the tube furnace relative to that upstream, to the extent that the changing atmosphere alters the decarburisation kinetics along the specimen. This arises from the reaction of the decarburisation atmosphere with the specimen, which consumes the water. In order to prevent significant changes in the decarburisation atmosphere along the length of the test specimens, the hydrogen or hydrogen/argon flow rate has to be high enough for the quantity of water consumed by the decarburisation reaction to be insignificant in comparison with the total volume flowing past the specimen.

5mm diameter by 80mm test specimens with the initial pearlitic structure of the as-supplied bar stock were decarburised in water/hydrogen atmospheres for 2hr at 0.05 and 0.25 p_{H_2O} / p_{H_2} pressure ratios, with gas flow rates of 200 to 1,000 cm^3/min. 80mm long test specimens were used, which allowed greater water consumption than the shorter specimens used for subsequent decarburisation experimentation. The heat treatments were concluded with a water quench. Each heat treated test specimen had a 20mm length cut from the ends of the specimen. These 20mm lengths were mounted, and sectioned longitudinally using the 0.30mm thick diamond wafer wheel of the Isomet Low Speed Saw, before being ground, polished and etched.

The free ferrite decarburisation depths were measured along the length of the sectioned specimens, with a mean decarburisation depth calculated for the ends of each test specimen. It was assumed that the decarburisation depths measured at room temperature corresponded to the decarburisation depths at the heat treatment temperature prior to quenching. The percentage difference between the room temperature and heat treatment temperature free ferrite depths can be calculated from:

$$\frac{\Delta L}{L} = \alpha \Delta T.100, \qquad (10.1)$$

where $\frac{\Delta L}{L}$ = percentage difference between the heat treatment and the room temperature decarburisation depths;

α = coefficient of thermal expansion with units of $10^{-6}K^{-1}$;

ΔT = difference between heat treatment and room temperatures in °K.

For a heat treatment temperature of 800°C, and a room temperature of 20°C, the temperature weighted value of α [206] for pure iron is $13.9x10^{-6}K^{-1}$. This yields $\Delta L/L = 1\%$. Consequently, the difference between the free ferrite depths measured at room temperature and those at the actual heat treatment temperature are small enough to be neglected. This also assumes a negligible influence of the core phase change from austenite to martensite upon quenching. Figure 10.1 illustrates the free ferrite depths for the different hydrogen flow rates at the upstream and downstream ends of the test specimen. If a significant amount of water was consumed by the decarburisation reactions, the water content and therefore the p_{H_2O} / p_{H_2} ratio would decrease along the length of the test specimens. Collin[95] calculated that if 10% of the available water disappeared from the decarburisation atmosphere because of the decarburisation reaction, the reaction rate would be lowered. A sufficient decrease in the water content would presumably result in lower decarburisation depths at the downstream end of the test specimens.

Figure 10.1 illustrates the similarity of the decarburisation depths at the upstream and downstream ends for the two p_{H_2O} / p_{H_2} ratios, indicating that the water consumed by the decarburisation reactions did not lower the decarburisation depths within the 95% confidence intervals of the free ferrite measurements. The volume of steel over which carbon was removed, V_{steel}, is given by equation 8.37, where

$$V_{steel} = \pi(R_o^2 - R_i^2)L(\text{correction factor}). \qquad (8.37)$$

For a test specimen length of 80mm, the surface area of the ends is negligible in comparison with the surface area along the length of the specimen. Therefore, a correction factor of one can be used. The mass of carbon removed by the decarburisation atmosphere can be calculated from rearranging equation 8.36 to give

$$m_C = \frac{V_{steel}\rho_{steel}(\%C_{removed})}{100}, \tag{10.2}$$

The moles of carbon removed by the decarburisation atmosphere, n_C, can be calculated by rearranging equation 8.35 to yield

$$n_C = \frac{m_C}{Mr_C}. \tag{10.3}$$

The predominant decarburisation reaction in wet hydrogen atmospheres is that of equation 3.3[64,69-71,73], even for p_{H_2O} / p_{H_2} ratios of 0.001[95], where

$$[C] + H_2O(g) = CO(g) + H_2(g). \tag{3.3}$$

Therefore, one mole of carbon reacts with one mole of water, with every mole of carbon removed from the steel corresponding to the consumption of a mole of water. The mass of water consumed, $m_{H_2O}(consumed)$, is given by

$$m_{H_2O}(consumed) = n_{H_2O} Mr_{H_2O}, \tag{10.4}$$

where $m_{H_2O}(consumed)$ = mass of water consumed in g;

Mr_{H_2O} = molecular mass of water, 18g/n.

The mass of water transported by a given flow rate for a specific p_{H_2O} / p_{H_2} ratio and test duration, m_{H_2O}, can be calculated from Appendix F. The mean percentage of water consumed, $\%H_2O(consumed)$, is given by

$$\%H_2O(consumed) = \frac{m_{H_2O}(consumed)}{m_{H_2O}} \cdot 100. \tag{10.5}$$

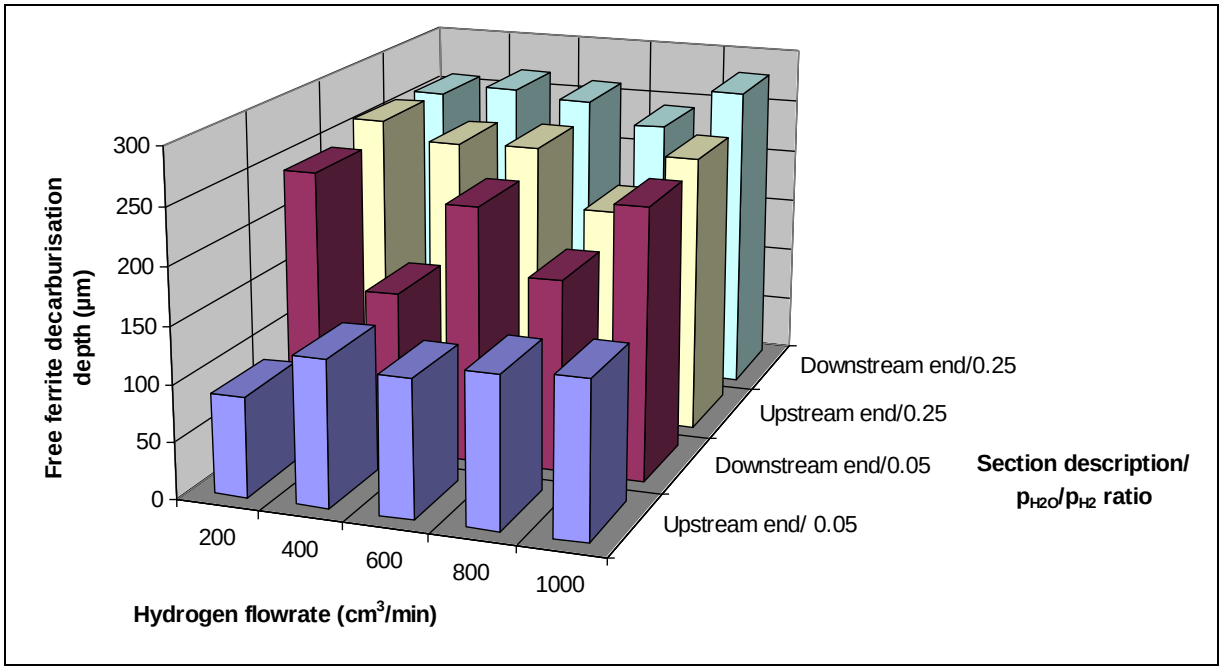

Figure 10.1 Influence of hydrogen flow rate on the free ferrite decarburisation depths of 5mm diameter by 80mm SUP7 specimens decarburised for 2hr at 800°C.

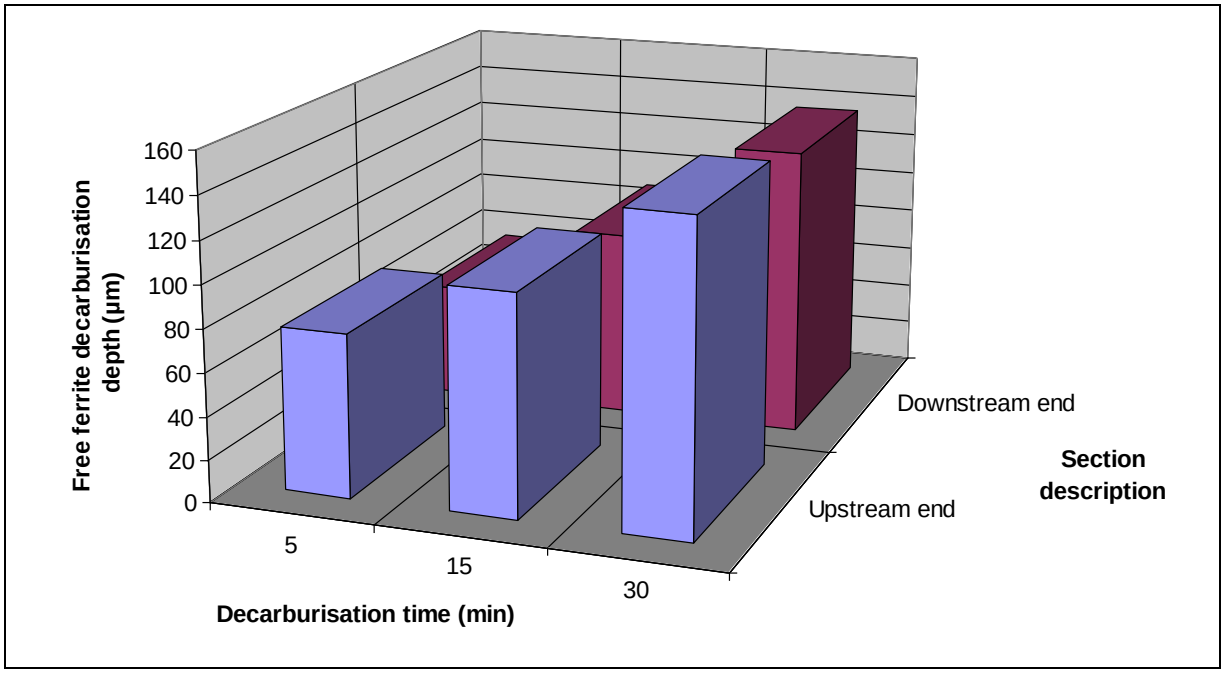

Figure 10.2 Free ferrite depths for 5mm diameter by 80mm SUP7 specimens decarburised at a hydrogen flow rate of 200cm^3/min at 840°C with p_{H_2O} / p_{H_2} =0.025.

Table 10.1 summarises the percentage of water consumed for various flow rates and p_{H_2O} / p_{H_2} ratios. It can be seen from Table 10.1 that the percentage of water consumed is greater at lower hydrogen flow rates and p_{H_2O} / p_{H_2} ratios. As the rate of decarburisation is often greatest during the early stages of decarburisation[67,69,78], the percentage of water consumed will be greatest at low flow rates and p_{H_2O} / p_{H_2} ratios during the early stages of decarburisation. Therefore, the same experimental technique for the decarburisation and measurement of the 80mm test specimens described earlier in this section was undertaken at 840°C for test durations of 5min, 15min and 30min at a p_{H_2O} / p_{H_2} ratio of 0.025. Figure 10.2 illustrates the decarburisation depths obtained for the three test durations, which are smaller at the downstream end of the test specimens for the 5 and 15min heat treatments.

Table 10.1 Mean percentage of water consumed at different flow rates and p_{H_2O} / p_{H_2} ratios for 2hr decarburisation of 5mm diameter by 80mm specimens at 800°C.

			%H₂O(consumed)				
			Flow rate (cm^3/min)				
p_{H_2O} / p_{H_2} **/time**	**Free ferrite depth (μm)**	$m_{H_2O}(consumed)$ **(g)**	**200**	**400**	**600**	**800**	**1000**
0.05/2hr	163	0.0135	1.51	0.76	0.50	0.38	0.30
0.25/2hr	250	0.0203	0.45	0.23	0.15	0.11	0.09

Table 10.1 demonstrates that for a hydrogen flow rate of 200cm^3/min, decarburisation of 5mm diameter by 80mm test specimens for 2hr at 800°C resulted in mean values of only 1.5 and 0.5% water being consumed for p_{H_2O} / p_{H_2} ratios of 0.05 and 0.25 respectively. Both these figures are well below the value of 10% specified by Collin[95] for a lowering of the reaction rate. However, for 5min decarburisation at 840°C for a p_{H_2O} / p_{H_2} of 0.025, 30.6% of the water in a hydrogen flow of 200cm^3/min was consumed. For 15 and 30min decarburisation, this average value drops to 14.4 and 10.4% respectively. This illustrates that the mean percentage consumption of water is greatest for shorter test durations and lower p_{H_2O} / p_{H_2} ratios. For the 5mm diameter by 50mm test specimens decarburised using exhaust gas analysis with a hydrogen flow rate of 500cm^3/min, the mean percentage of water consumed over 5min for a p_{H_2O} / p_{H_2} ratio of 0.025 drops to 7.6%, which is within the 10% limit[95].

10.3 Decarburisation with prior heating to and austenitisation at the Ac_3 temperature

The majority of decarburisation studies undertaken involve insertion of the test specimens into the hot zone of a furnace once the decarburisation atmosphere is fully established[64,67,69,72,73,78,100,207]. For thin steel specimens that heat rapidly to temperature, and transform to austenite within seconds at the heat treatment temperature, carbon removal predominantly occurs from the austenitic structure. However, for larger specimens that take longer to heat to the furnace temperature, more carbon removal will occur during heating of these specimens in the decarburisation atmosphere[67,69,78] than for thinner specimens. Consequently, the decarburisation of the steel will be influenced by the specimen dimensions and heating rate.

Once the specimen attains the uniform heat treatment temperature, decarburisation will initially occur while the core of the specimen transforms to its austenitic structure. It was demonstrated in Chapter 9 that different test durations were required at the different heat treatment temperatures for transformation to the respective austenitic structures. Different initial structures heat treated at the same temperature also austenitised at different rates. Therefore, once the specimens have heated to the heat treatment temperature, different temperatures and initial structures with different austenitisation kinetics may prevent meaningful comparisons between the specimens. In order to allow direct comparisons between different initial structures, and at different temperatures, two types of decarburisation experiments were undertaken for SUP7 at the Ac_3 temperature. These involved:

1) Insertion of the specimens into the furnace hot zone, followed by the establishment of an argon atmosphere. The decarburisation atmosphere was introduced after a time sufficient for the specimens to heat to within 5°C of the furnace temperature;
2) Insertion of the specimens into the hot zone, followed by the establishment of an argon atmosphere. The specimens were annealed in argon for a time equivalent to the heating time to within 5°C plus the time for 95% austenite formation, before the decarburisation atmosphere was introduced.

For both types of heat treatments, the specimens were inserted into the hot zone. The establishment of an argon atmosphere followed this, with the specimens annealed in argon

until they heated to within 5°C of the heat treatment temperature. Assuming that the inert argon atmosphere replaces the initial ambient atmosphere before the specimen heats to a high enough temperature for the specimen to react with the atmosphere, carbon removal will only occur from the specimens at the hot zone temperature upon introduction of the decarburisation atmosphere. No free ferrite was present after a 24hr argon anneal of a SUP7 furnace cooled initial structure, which suggested that the furnace atmosphere did become inert before carbon removal could occur during specimen heating. For the first type of decarburisation experiment, where the decarburisation atmosphere was introduced once the specimens had heated to temperature, the initial structures will have only partially transformed. As the different initial structures transform to the equilibrium structures at different rates, the effects of initial structure and transformation rate on the decarburisation can be quantified.

The second type of decarburisation experiment involved heating and austenitising in argon before the decarburisation atmosphere was introduced. The slowest initial structure to transform to 95% austenite was Structure D, tempered 96hr at 735°C, which requires approximately 2hr. Consequently all the specimens were austenitised for 2hr before the decarburisation atmosphere was introduced with carbon removal therefore occurring from austenitic structures. The different austenitisation kinetics will result in different austenite grain sizes for the initial structures due to the time taken for the structures to form austenite. As carbon diffusion in austenite occurs predominantly by bulk diffusion[108], the different austenite grain sizes of the different initial structures should not influence the decarburisation kinetics.

10.3.1 Microstructural investigation

5mm diameter by 15mm specimens were decarburised at p_{H_2O} / p_{H_2} ratios of 0.05 and 0.25 for test durations ranging from 15min to 24hr. Figure 10.3 illustrates a specimen decarburised for 24hr at a p_{H_2O} / p_{H_2} ratio of 0.25 after heating to temperature in argon. Figure 10.3(a) shows the macrostructure of the decarburised specimen, with the darker coloured ferrite case separated from the lighter coloured martensite core. This martensite core was austenite at the heat treatment temperature. The columnar grain structure of the ferrite grains is visible despite the low magnification. The interface between the free ferrite and the martensite is sharply

defined, Figure 10.3(b), even after 24hr decarburisation. This figure also illustrates the columnar grains, perpendicular to the surface, more distinctly. The surface oxide layer, visible in Figure 10.3(b), is shown at a larger magnification in Figure 10.3(c). The thin dark layer separating the nickel and oxide layers corresponds to separation of the deposited nickel layer from the specimen.

The microstructures of test specimens decarburised for 4hr at a p_{H_2O} / p_{H_2} ratio of 0.05 are shown in Figure 10.4. Figure 10.4(a) illustrates a free ferrite/martensite structure obtained when the specimen was heated in argon before the introduction of the decarburisation atmosphere. In contrast, the microstructure of the specimen austenitised for 2hr prior to the introduction of the decarburisation atmosphere exhibited very little decarburisation for the majority of the test specimen, Figure 10.4(b). However, free ferrite areas were present in places, as illustrated in Figure 10.4(c).

10.3.2 Decarburisation kinetics

This section details the decarburisation kinetics for the different initial SUP7 structures heat treated at 820°C. The free ferrite decarburisation depths were plotted against the logarithm of time, with the experimental data points displayed on the graphs. Error bars, which correspond to the 95% confidence intervals calculated from equation 8.6, give the statistical variation in the measured decarburisation depths. Microsoft Excel was used to generate the graphs and fit the error bars to the data points. Various types of best-fit regression lines can be fitted to the data points using Microsoft Excel, along with the regression line equation and the R^2 value. The R^2 value gives an indication of the goodness of fit of the regression line to the experimental data points, with a R^2 value of one corresponding to a perfect fit. However, this is influenced by the number of experimental data points, where a line fitted between two points will always yield a R^2 value of one. Therefore, on the occasions where only a few data points were obtained, and different types of regression lines yielded similar R^2 values, limited significance can be attached to the mechanisms of decarburisation indicated by these lines.

Both the furnace cooled and 96hr tempered martensite SUP7 initial structures exhibited similar free ferrite depths after heating in argon and decarburisation at 820°C with a

(a) (b) (c)

Figure 10.3 Microstructures formed after heating in argon and 24hr decarburisation of a SUP7 96hr tempered martensite initial structure at 820°C with p_{H_2O} / p_{H_2} =0.25 illustrating (a) the macrostructure, 15x magnification, (b) the free ferrite layer, 58x magnification, and (c) the oxide layer, 575x magnification. 2% Nital etch.

(a) (b) (c)

Figure 10.4 Microstructures formed after 4hr decarburisation of a SUP7 96hr tempered martensite initial structure at 820°C with p_{H_2O} / p_{H_2} =0.05 which was heated in argon with (a) no austenitisation, and (b), (c) 2hr austenitisation. 230x magnification. 2% Nital etch.

p_{H_2O} / p_{H_2} ratio of 0.05, Figure 10.5. No decarburisation was observed for the 15min heat treatments of either structure, with a free ferrite layer only observed at 1hr for the 96hr tempered martensite structure, and 4hr for the furnace cooled structure. The furnace cooled initial structure had a sharp interface that delineated the free ferrite case and the martensite core. However, this interface was less well defined for the tempered martensite structure, with a ferrite/martensite layer separating the ferrite case and the martensite core, Figure 10.4(a). The measurement of the thickness of the ferrite/martensite layer was less exact than that of the free ferrite depths, due to the imprecision associated with determination of where the core became martensitic. The thickness of the ferrite/martensite zone separating the free case and martensite core for 1 to 24hr duration heat treatments was approximately constant at 100µm.

The furnace cooled initial structure transformed to austenite after only 1min, while the 96hr tempered martensite structure required 15min to transform to 72% austenite. Consequently, carbon removal initially occurred from a ferrite/austenite/cementite structure during the decarburisation of a 96hr tempered martensite initial structure once it had heated to temperature in argon and the decarburisation atmosphere was introduced. With ferrite areas adjacent to austenite areas at the surface, carbon removal resulted in the ragged ferrite/martensite interface being maintained at progressively deeper free ferrite decarburisation depths.

The thickness of the partial decarburisation zone remained approximately constant. This was due to the greater diffusivity of carbon in ferrite than in austenite at the same temperature, with the diffusion coefficient of carbon in ferrite for a Fe-C steel at 820°C 150 times that for austenite[99]. In contrast, the transformation of the furnace cooled initial structure to austenite was so rapid that carbon removal occurred from an austenite core, resulting in a well defined interface between the free ferrite core and the austenite case.

Figure 10.6 illustrates the decarburisation kinetics for the five initial SUP7 structures after 2hr austenitisation in argon and decarburisation at a p_{H_2O} / p_{H_2} ratio of 0.05. The free ferrite depths are significantly less than for the comparable test durations involving heating in argon, as illustrated in Figure 10.7. Table 10.2 describes the surface microstructures observed for various heat treatment times. Considerable variability between the different initial structures

was observed, with the 12hr tempered martensite specimen exhibiting no decarburisation until the 24hr heat treatment, while the air cooled, furnace cooled, and 96hr tempered martensite specimens all had some free ferrite patches present after 4hr, with variable decarburisation.

Table 10.2 Description of surface decarburisation structures for different initial SUP7 structures austenitised in argon and decarburised at 820°C with p_{H_2O} / p_{H_2} =0.05.

DESCRIPTION	COMMENTS				
	15min	**1hr**	**4hr**	**12hr**	**24hr**
Structure A	No decarb.*	No decarb.	Patchy decarb.**	Decarb.***	Decarb.
Structure B	No decarb.	No decarb.	Patchy decarb.	Decarb.	Decarb.
Structure C	No decarb.	No decarb.	No decarb.	No decarb.	Decarb.
Structure D	No decarb.	No decarb.	Patchy decarb.	Decarb.	Decarb.
Structure F	No decarb.	No decarb.	No decarb.	Decarb.	Decarb.

No ferrite/martensite decarburisation layers separating a ferrite case and martensite core were observed for the specimens austenitised for 2hr in argon prior to the introduction of the decarburisation atmosphere. This was due to the carbon removal only occurring from an austenitic core, which yielded the sharp ferrite/martensite interfaces observed. Figure 10.7 also illustrates the free ferrite kinetics for the decarburisation of 8mm diameter by 15mm SUP7 air cooled initial structures[208]. These specimens were heated for 15min in argon before the decarburisation atmosphere was introduced. A free ferrite layer was observed after 5min, with greater free ferrite depths than that of the comparable durations for the 5mm diameter specimens. The decarburisation kinetics for five different initial structures austenitised for 2hr prior to decarburisation at a p_{H_2O} / p_{H_2} ratio of 0.25 are illustrated in Figure 10.8. A uniform free ferrite layer was present after 15min for all five initial structures, with the different structures exhibiting similar decarburisation kinetics.

* No decarb. denotes that no decarburisation was present.

** Patchy decarb. denotes that patches of free ferrite were present.

*** Decarb. denotes that a uniform free ferrite surface layer was present.

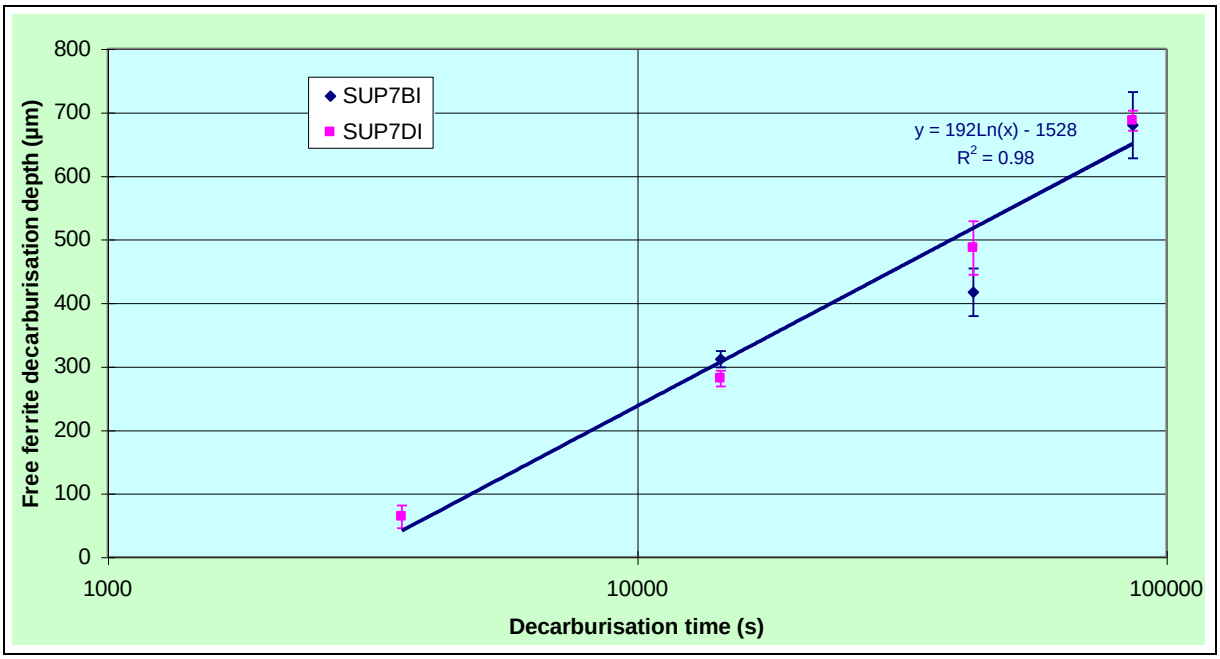

Figure 10.5 Free ferrite decarburisation depths for furnace cooled and 96hr tempered martensite SUP7 initial structures heated in argon and decarburised at 820°C, with p_{H_2O} / p_{H_2} =0.05.

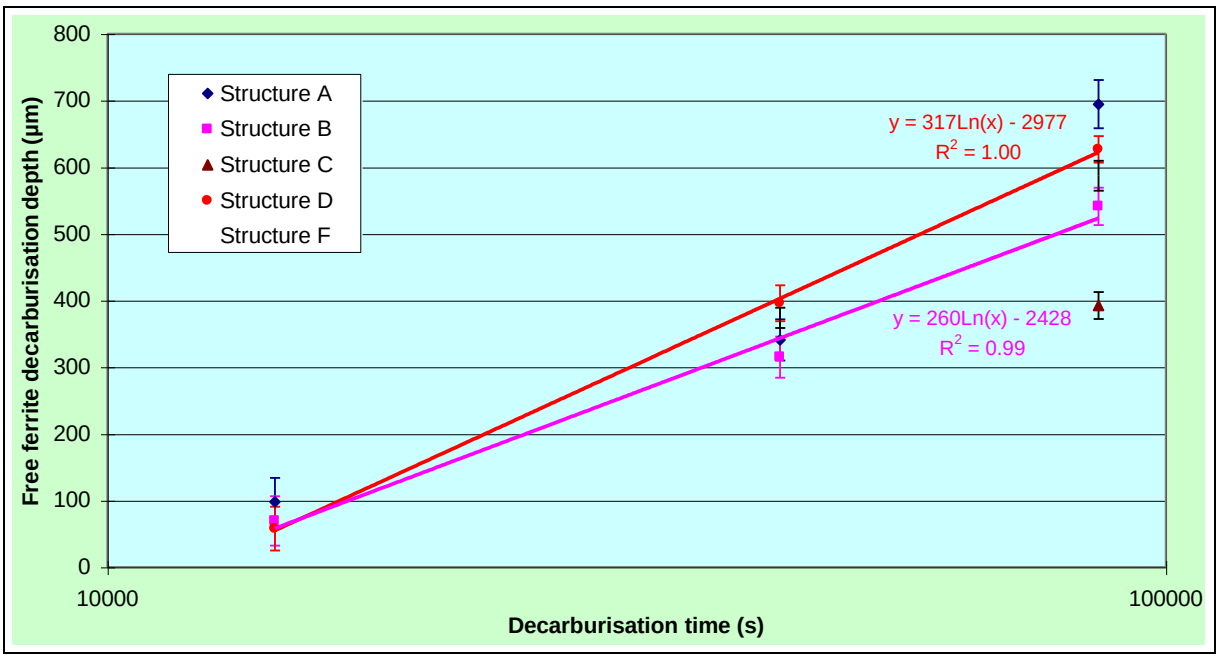

Figure 10.6 Free ferrite decarburisation depths for five different initial SUP7 structures austenitised 2hr in argon and decarburised at 820°C with p_{H_2O} / p_{H_2} =0.05.

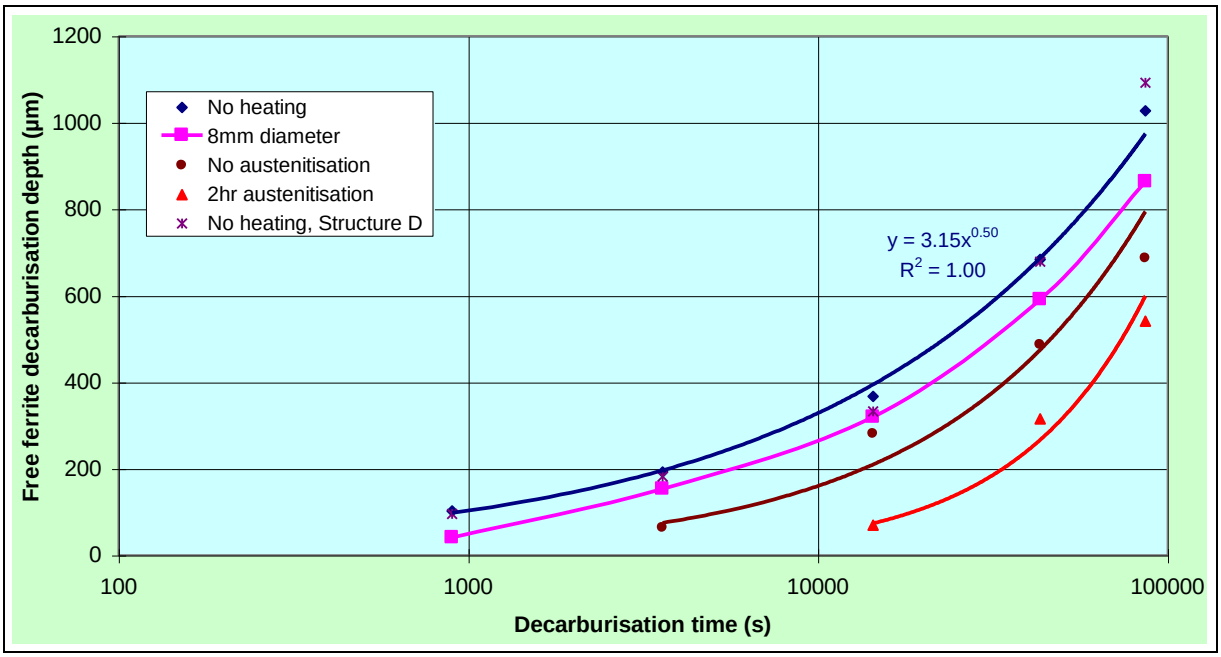

Figure 10.7 Free ferrite depths for SUP7 furnace cooled initial structures decarburised at 820°C with p_{H_2O} / p_{H_2} =0.05 after different heating and austenitisation regimes in argon.

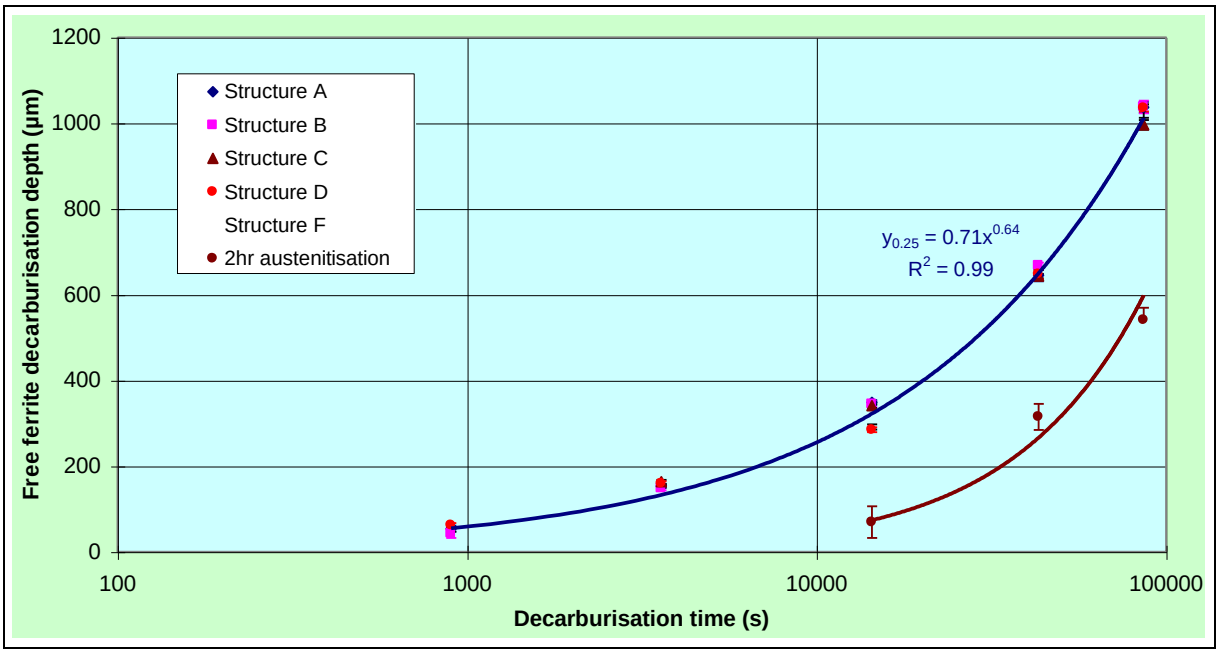

Figure 10.8 Free ferrite decarburisation depths for different initial SUP7 structures austenitised in argon and decarburised at 820°C with p_{H_2O} / p_{H_2} =0.25.

10.3.3 Oxidation kinetics

The oxidation kinetics for the different SUP7 initial structures decarburised at 820°C, Section 10.3.2, were investigated. The oxide thicknesses versus the logarithm of time was plotted, along with error bars and regression lines. The oxide layer thickness corresponds to the surface oxide layer measured, which is delineated by the distance between the deposited nickel layer and the surface of the free ferrite layer. Figure 10.9 demonstrates thicker oxide layers at a p_{H_2O} / p_{H_2} ratio of 0.05 for a furnace cooled specimen with no austenitisation relative to 2hr austenitisation. Comparison of the furnace cooled specimens austenitised for 2hr illustrated that the increased water content of the 0.25 p_{H_2O} / p_{H_2} ratio yielded thicker oxide structures than the 0.05 ratio.

10.3.4 Free ferrite columnar structures

The columnar grain sizes of the different SUP7 initial structures decarburised at 820°C in Section 10.3.2 were determined by measuring the width of the free ferrite grains by the method described in section 8.4.3. The columnar grain size versus the logarithm of time was plotted, along with error bars and regression lines. The columnar grain growth for furnace cooled and 96hr tempered martensite structures heated in argon and decarburised at a p_{H_2O} / p_{H_2} ratio of 0.05 are illustrated in Figure 10.10. The 96hr tempered martensite initial structure had a grain size twice that of the furnace cooled structure after 24hr. The different grain sizes appeared to have no influence on the decarburisation kinetics.

Figure 10.11 demonstrates that the air cooled pearlitic structure exhibited slightly finer columnar grain growth kinetics than the furnace cooled structure when austenitised and then decarburised at a p_{H_2O} / p_{H_2} ratio of 0.25. The 12hr tempered martensite initial structures austenitised for 2hr and then decarburised at a p_{H_2O} / p_{H_2} ratio of 0.25 exhibited larger columnar grain sizes for comparable duration heat treatments of the 96hr tempered martensite and intercritical initial structures, which were similar. However, the decarburisation kinetics were similar despite the different columnar grain sizes.

Marder[66] found that the final columnar grain size of a 0.055wt.% C/0.70wt.%Mn steel specimens decarburised in a 18% hydrogen/82% nitrogen atmosphere with a p_{H_2O} / p_{H_2} ratio of 0.14 increased with larger initial ferrite grain sizes and larger cementite particle sizes. However, despite having larger ferrite grain and cementite particle sizes, the columnar grains of the 96hr tempered martensite structure were smaller, with the 12hr tempered martensite structure grain sizes being approximately 1.5 times larger.

The furnace cooled and 96hr tempered martensite initial structures exhibited similar free ferrite columnar grain growth kinetics for 2hr austenitisation and decarburisation with p_{H_2O} / p_{H_2} ratios of 0.05 and 0.25, as illustrated in Figures 10.12 and 10.13. This was despite the different free ferrite depths obtained with decarburisation at p_{H_2O} / p_{H_2} ratios of 0.05 and 0.25. For a p_{H_2O} / p_{H_2} ratio of 0.05, the columnar grain growth kinetics for heating in argon differed from those for the furnace cooled and 96hr tempered martensite initial structures austenitised prior to introduction of the decarburisation atmosphere.

Power laws were obtained for the kinetics of the free ferrite decarburisation depths, oxide thicknesses and columnar grain growth as a function of time, with the equation having the form $y = Kt_d^n$. A value of 0.5 for the exponent n indicates diffusion controlled kinetics, with this being observed for the free ferrite and oxide kinetics for 2hr austenitisation in argon with decarburisation at a p_{H_2O} / p_{H_2} ratio of 0.25.

10.3.5 SUP7 decarburisation with no heating

The results obtained during the decarburisation of SUP7 structures at a p_{H_2O} / p_{H_2} ratio of 0.05 demonstrated that prior heating and austenitisation in argon influenced the decarburisation kinetics. 5mm diameter specimens, which were heated and then austenitised for 2hr prior to the introduction of the decarburisation atmosphere, decarburised poorly for several hours, with minimal decarburisation observed after 4hr, Table 10.2. Free ferrite layers were observed after 1hr decarburisation of specimens that were heated in argon prior to exposure to the decarburisation atmosphere. The comparable free ferrite depths were greater than those of the specimens austenitised for 2hr, Figure 10.7. 8mm diameter SUP7 specimens

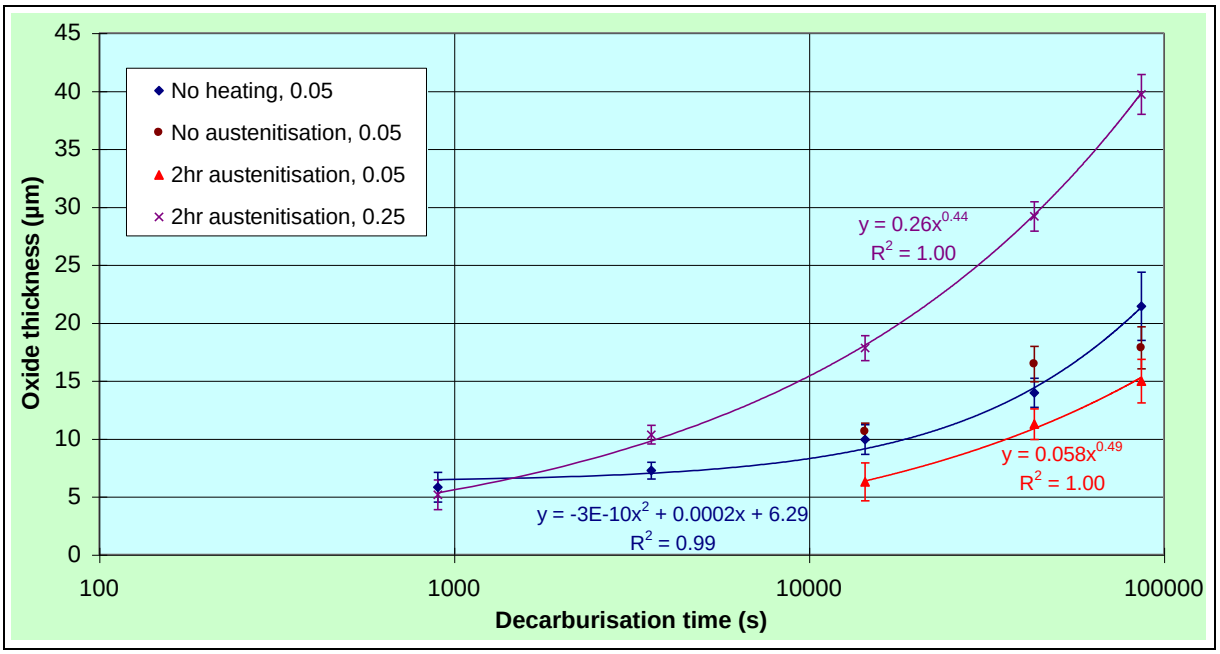

Figure 10.9 Oxidation kinetics for SUP7 furnace cooled initial structures with different heating and austenitisation regimes in argon prior to decarburisation at 820°C with p_{H_2O} / p_{H_2} ratios of 0.05 and 0.25.

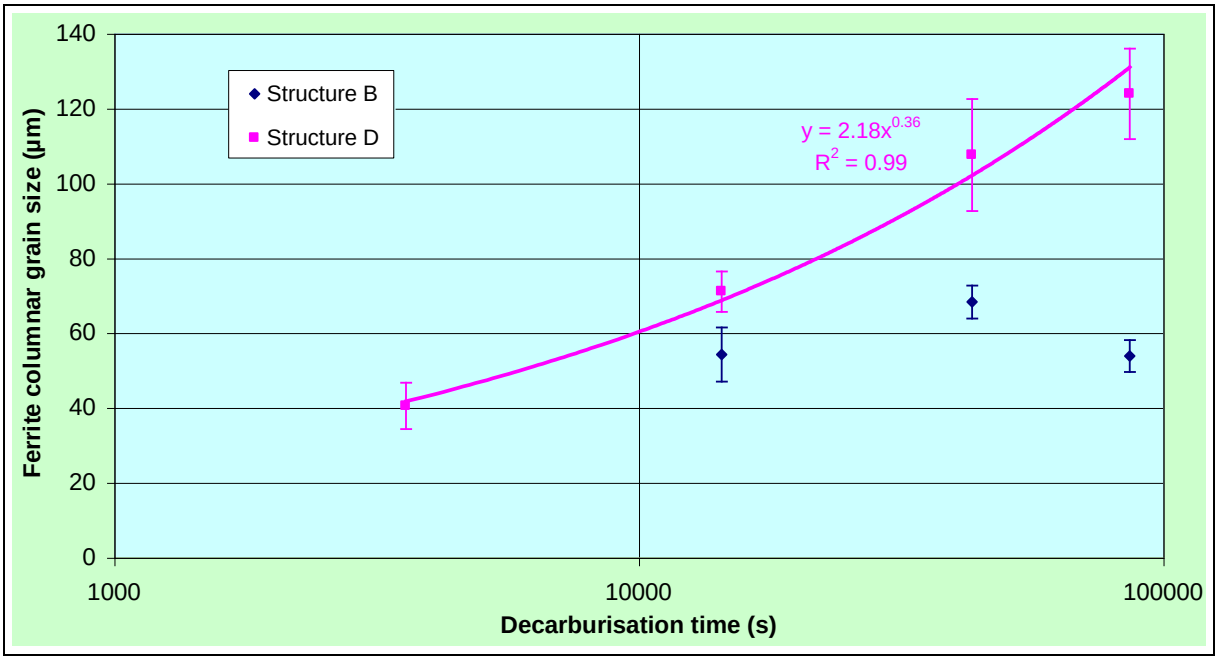

Figure 10.10 Ferrite columnar grain growth kinetics for furnace cooled and 96hr tempered martensite SUP7 initial structures heated in argon and decarburised at 820°C with p_{H_2O} / p_{H_2} =0.05.

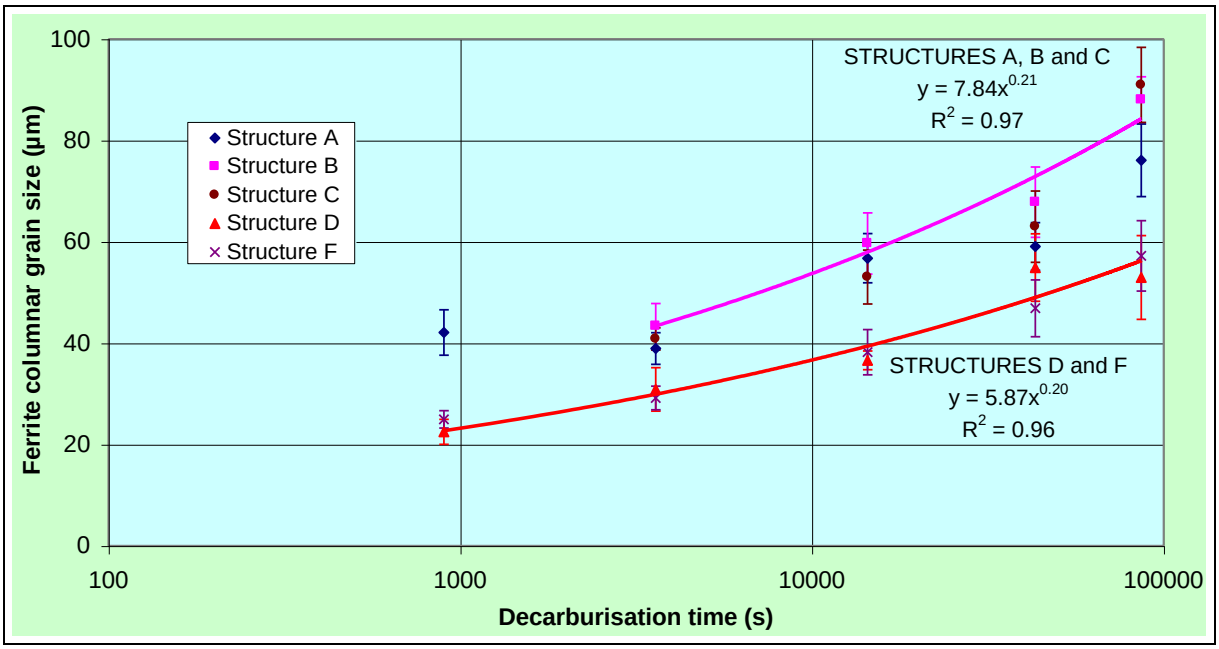

Figure 10.11 Growth of ferrite columnar grains for different SUP7 initial structures austenitised in argon and decarburised at 820°C with p_{H_2O} / p_{H_2} =0.25.

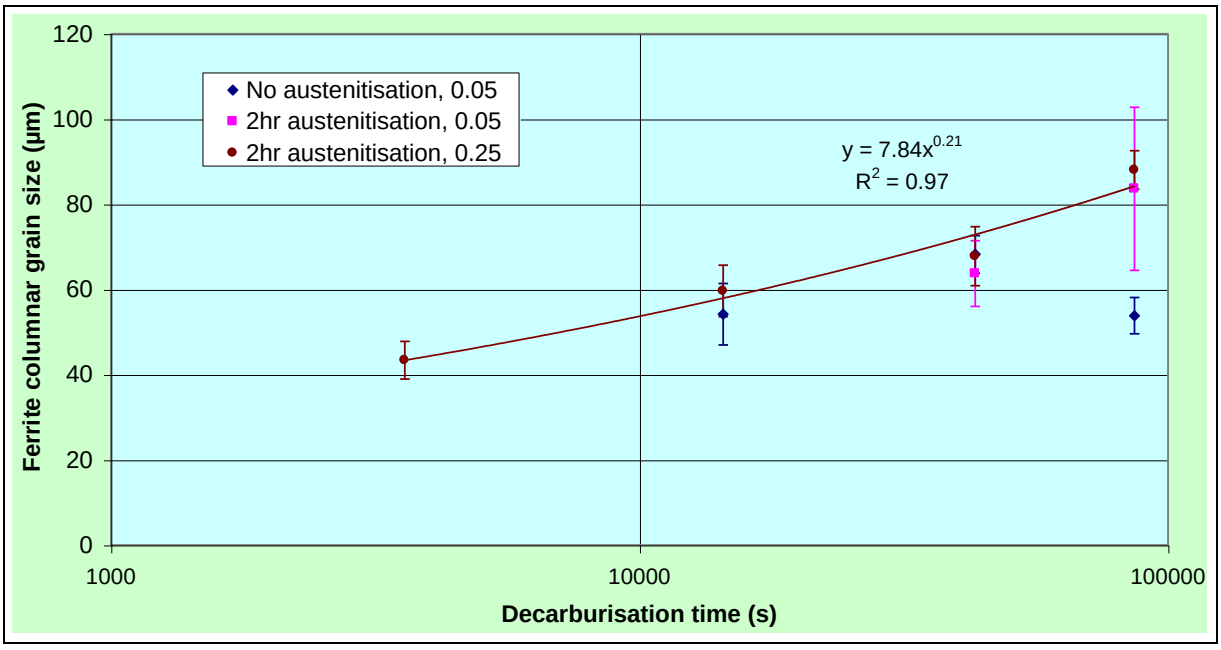

Figure 10.12 Columnar grain growth kinetics for furnace cooled SUP7 initial structures with and without 2hr austenitisation in argon that were decarburised at 820°C with p_{H_2O} / p_{H_2} ratios of 0.05 and 0.25.

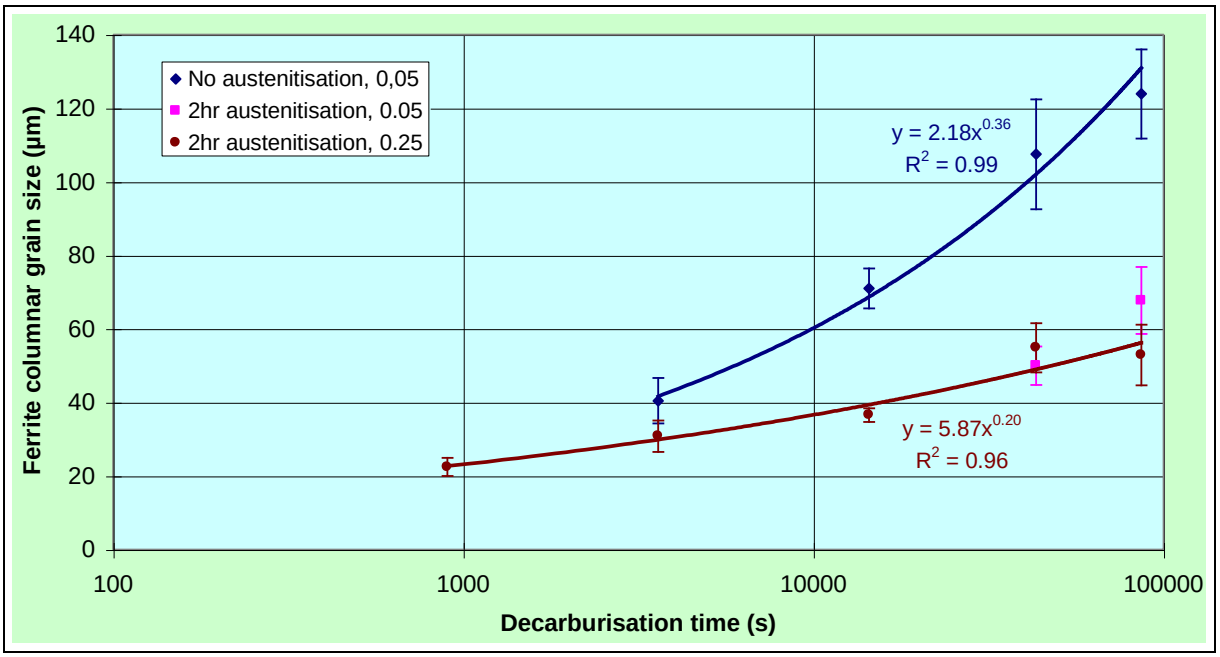

Figure 10.13 Columnar grain growth kinetics for 96hr tempered martensite SUP7 initial structures with and without 2hr austenitisation in argon which were decarburised at 820°C with p_{H_2O} / p_{H_2} ratios of 0.05 and 0.25.

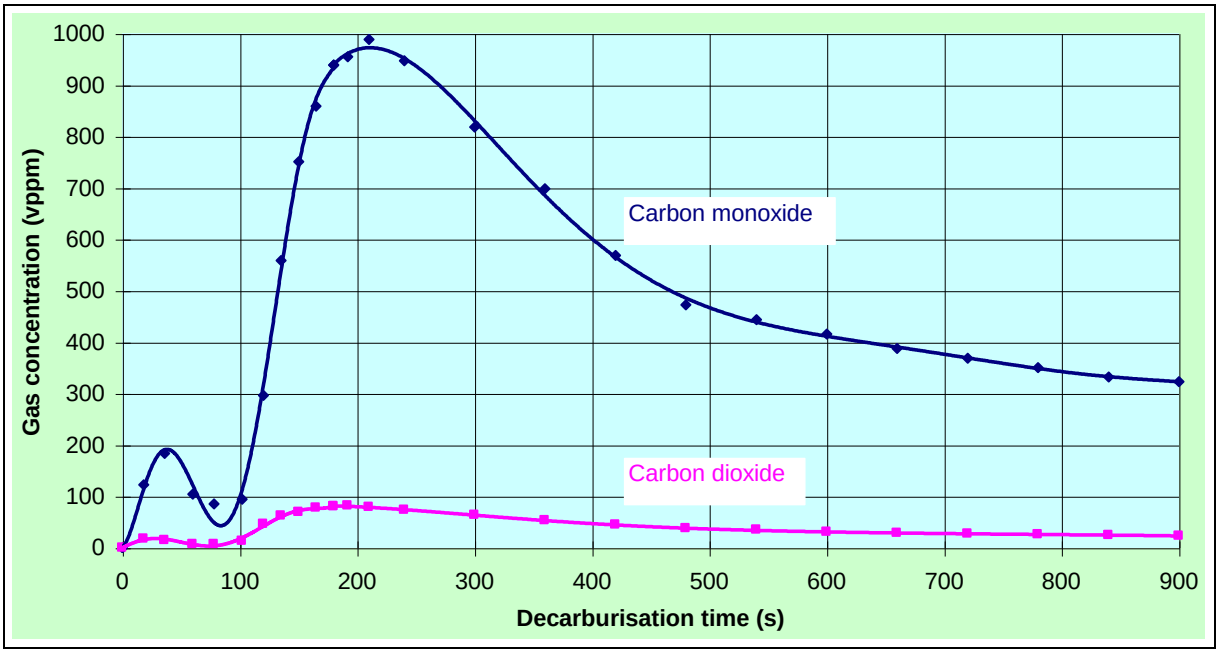

Figure 10.14 Carbon monoxide and carbon dioxide concentration profiles for the decarburisation of furnace cooled and 96hr tempered martensite structures at 820°C and p_{H_2O} / p_{H_2} =0.05, with no heating or austenitisation in argon**.**

heated in argon prior to introduction of the heat treatment atmosphere decarburised more deeply than the comparable tests for the 5mm specimens.

Consequently, a greater understanding of the early stages of the decarburisation processes during specimen heating is necessary. This was facilitated by the use of carbon monoxide and carbon dioxide infra-red gas analysers that allowed the exhaust gas leaving the tube furnace to be continuously monitored. Therefore, the course of carbon removal could be followed from when the specimens were inserted into the hot zone with the established decarburisation atmosphere. 5mm diameter by 15mm SUP7 furnace cooled and 96hr tempered martensite structures were decarburised simultaneously by inserting the specimens from the cold end of the tube furnace into the hot zone once the decarburisation atmosphere was fully established. Consequently, the specimens were exposed to the decarburisation atmosphere as they heated.

Figure 10.7 illustrates that the free ferrite decarburisation depths for the furnace cooled and 96hr tempered martensite structures with no heating or austenitisation were practically identical. A uniform free ferrite layer was evident in the microstructures of the shortest duration heat treatments of 15min. The decarburisation depths were greater than for the other specimens heated with or without austenitisation in argon. Consequently, the temperature at which the steel is exposed to the decarburisation atmosphere influences the degree of decarburisation.

The carbon monoxide and carbon dioxide concentrations measured by the infra-red gas analysers during the first 15min decarburisation of the furnace cooled and 96hr tempered martensite structures decarburised without heating in argon are illustrated in Figure 10.14. Both carbon monoxide and carbon dioxide were detected, with the carbon monoxide content approximately ten times that of the carbon dioxide content throughout the duration of the heat treatment. This confirms that the predominant decarburisation reaction was that of equation 3.3.

Two peaks in carbon monoxide and carbon dioxide content occurred during the early stages of the heat treatments, as detailed in Table 10.7. The first peak occurred after approximately 40s, at a carbon monoxide content of 185vppm. From the heating profiles of the 5mm diameter by 15mm diameter test specimens, Figure 7.4, this corresponds to a temperature of approximately

500°C. The carbon monoxide content then dropped to a minimum of 85vppm after 85s, a temperature of 700°C, before rising to a much higher second peak of 990vppm after 215s. At this time, the specimen has reached a temperature of 785°C. The carbon monoxide and carbon dioxide contents then gradually decreased from this point onwards. After the heating time of 558s, with the specimens at 815°C, the carbon monoxide content had dropped to 430vppm. The carbon monoxide contents were 320, 120, 65 and 30vppm after 15min, 1hr, 4hr and 12hr respectively.

The decarburisation behaviour can be modelled by a diffusion process, with the effective diffusion coefficient of carbon in ferrite given by[99]

$$D_{effective} = \frac{(C_o - \frac{2}{3}C_{sat})}{2} \cdot \frac{x_d^2}{t_d C_{sat}}, \qquad (10.6)$$

where $D_{effective}$ = effective carbon diffusion coefficient in ferrite, cm^2/s;

C_o = initial carbon content of steel in wt.%;

C_{sat} = saturation ferrite carbon content in wt.%;

x_d = free ferrite decarburisation depth in cm;

t_d = decarburisation time in s.

The ferrite carbon concentration profile predicted by Fick's second law can be approximated by a linear carbon concentration profile, since the ferrite saturation carbon contents are small in comparison with the Ac_3 austenite carbon contents[99]. The carbon content across the ferrite layer ranges from zero at the surface to C_{sat} at the ferrite/martensite interface. C_{sat} was determined from section 9.7 to be 0.020wt.% for SUP7 at 820°C, while C_o corresponds to the initial SUP7 carbon content of 0.60wt.%. Figure 10.15 compares the free ferrite depths obtained from the gas analysis data with those calculated for an effective diffusion coefficient of $1.6 \times 10^{-6} cm^2/s$. The experimental values measured from the furnace cooled and 96hr tempered martensite initial structures are also illustrated. Excellent agreement between the experimental and calculated values resulted. The similarity of the free ferrite depths calculated from an effective diffusion coefficient of $1.6 \times 10^{-6} cm^2/s$ with the values calculated from the gas analysis, and with the experimentally measured values for different test durations,

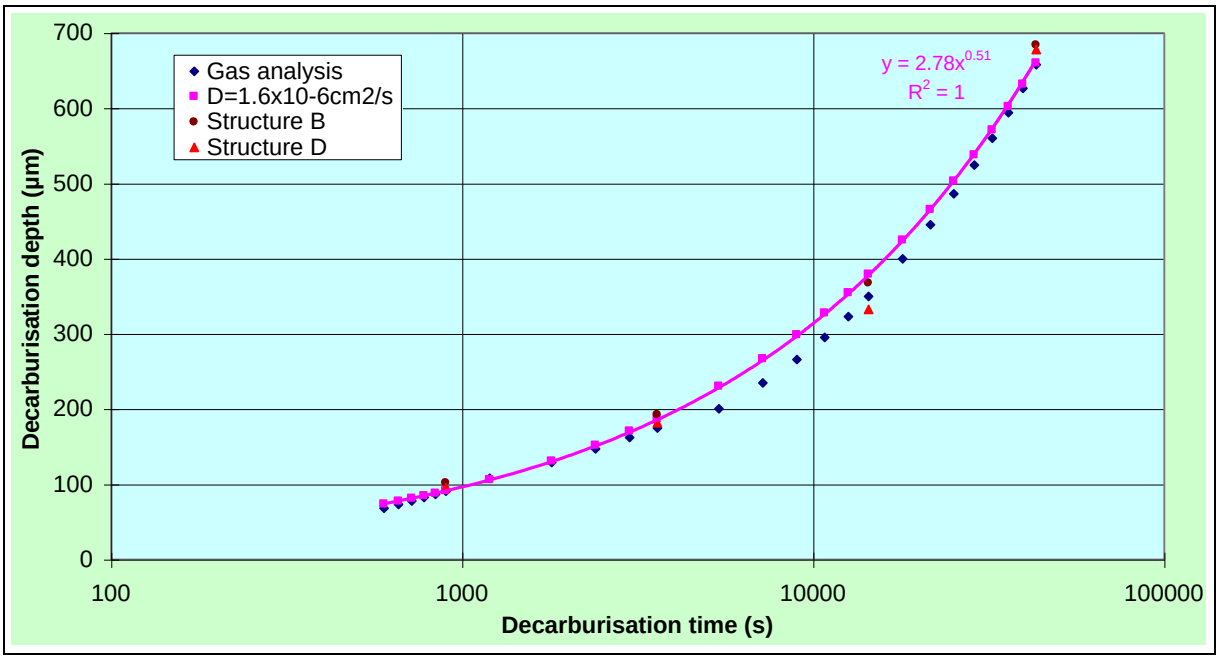

Figure 10.15 Comparison of measured free ferrite depths with those calculated from gas analysis, and $D_{effective}=1.6x10^{-6}cm^2/s$, during the decarburisation of furnace cooled and 96hr tempered martensite SUP7 initial structures at 820°C and p_{H_2O} / p_{H_2} =0.05, with no prior heating or austenitisation in argon.

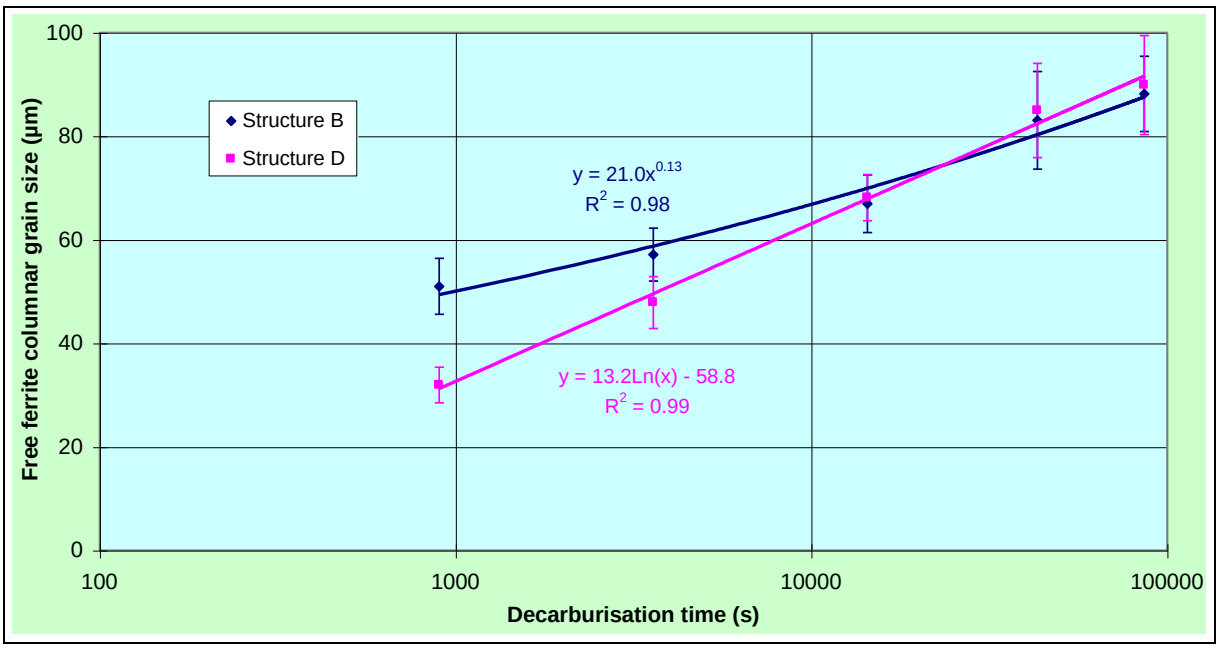

Figure 10.16 Free ferrite columnar grain growth kinetics for the decarburisation of furnace cooled and 96hr tempered martensite SUP7 initial structures at 820°C and p_{H_2O} / p_{H_2} =0.05, with no prior heating or austenitisation in argon.

demonstrates that the carbon removal from the test specimens at the furnace temperature of 820°C occurred at a rate in accordance with a diffusion controlled process.

The effective diffusion coefficient was approximately half the value of $3.6 \times 10^{-6} cm^2/s$ at 820°C for a binary Fe-C steel[99]. Wiesner[73] investigated the decarburisation of 0 to 3wt.% silicon electrical steels at 850°C with different water/hydrogen contents. For silicon contents below 2wt.%, a mean effective diffusion coefficient of approximately an order of magnitude lower than the value for carbon diffusion in pure ferrite, 6×10^{-7} versus $5 \times 10^{-6} cm^2/s$ respectively, was obtained. This decrease was attributed to longer diffusion paths through the oxide, and reduced permeability of the surface for carbon.

The oxidation thicknesses of the furnace cooled and 96hr tempered martensite initial structures decarburised by inserting the test specimens into an established heat treatment atmosphere at 820°C with a p_{H_2O} / p_{H_2} ratio of 0.05 were similar, as illustrated in Figure 10.9. The oxide thicknesses were greater than for the specimens heated and austenitised in argon prior to decarburisation at a p_{H_2O} / p_{H_2} ratio of 0.05 for comparable test durations. The furnace cooled structure exhibited a coarser free ferrite columnar grain structure than the 96hr tempered martensite initial structure until 4hr, when the grain growth kinetics became similar. This is illustrated in Figure 10.16.

During the design of the decarburisation experiments, it was expected that the different initial structures exposed to the heat treatment atmosphere after heating to temperature in argon would exhibit different decarburisation kinetics. The transport of carbon in the steel can occur by diffusion in the bulk, along dislocations and other defects, as well as along grain boundaries. After the heating period, the initial structures possess different pearlite interlamellar spacings, thickness of cementite lamellae, ferrite grain size and shape, cementite particle size, distribution and location. Consequently, the carbon transport through the steel to the surface, with carbon removal from the steel surface, could reasonably be expected to be different for the furnace cooled and 96hr tempered martensite initial structures. However, no significant variation with initial structure was observed in the free ferrite decarburisation kinetics at a p_{H_2O} / p_{H_2} ratio of 0.05 for prior heating in argon, Figure 10.5. This was despite

the finer resultant ferrite columnar grain structures of the furnace cooled initial structure compared with the 96hr tempered martensite structure, as illustrated in Figure 10.10.

The free ferrite depths obtained upon exposure to the decarburisation atmosphere after heating and austenitisation in argon for different initial structures were measured. A range of free ferrite depths were obtained for the different initial structures decarburised at a p_{H_2O} / p_{H_2} ratio of 0.05, Figure 10.6. However, similar free ferrite depths were obtained for the different initial structures decarburised at a p_{H_2O} / p_{H_2} of 0.25, Figure 10.8. There was a considerable variation in ferrite columnar grain sizes between the initial structures, as illustrated in Figures 10.11 to 10.13. Large differences were observed in the free ferrite depths for comparable test durations decarburised after no heating, heating and heating plus 2hr austenitisation in argon prior to introduction of the heat treatment atmosphere. The formation of a surface free ferrite layer took longer when the specimen was heated in argon prior to introduction of the decarburisation atmosphere relative to no heating. This delay was even longer with heating and austenitisation in argon.

The delay in the free ferrite formation upon exposure to the decarburisation atmosphere after annealing in argon was surprising, as it was expected that carbon removal would occur as soon as the test specimens were exposed to the decarburisation atmosphere. The 8mm and 5mm diameter specimens were both heated for similar durations prior to the introduction of the decarburisation atmosphere. However, the greater thermal inertia of the 8mm diameter specimens resulted in deeper decarburisation. The 8mm diameter specimens were therefore exposed to the heat treatment atmosphere at a lower temperature, yielding the deeper decarburisation observed.

Oxidation and decarburisation of SUP7 was possible in an argon anneal with incomplete flushing of the ambient atmosphere from the tube furnace, or if the argon supply contained enough water and oxygen to effect carbon removal. The argon used to flush the ambient atmosphere and then anneal the test specimens was passed through Labclear and Oxyclear gas filters to reduce the water and oxygen impurities to less than 50vppb. The 5mm diameter specimens that were annealed in argon exhibited no decarburisation. No oxide structure was visible with the optical or scanning electron microscopes. This would suggest that the water

and oxygen contents in the argon atmosphere were reduced to a level sufficient to prevent any decarburisation or oxidation of SUP7.

However, it is possible that minute concentrations of water vapour still remained in the argon atmosphere upon completion of the argon flush. Since the argon flush was then reduced to a displacement flow, this water vapour remained in the furnace as the specimens were heated, and during any subsequent decarburisation. At low water concentrations, a thin dense SiO_2 layer can form, which will increase in thickness with time. A 2.96wt.% silicon electrical steel annealed for 1hr at 850°C with a p_{H_2O} / p_{H_2} ratio of $1x10^{-3}$ formed a SiO_2 layer only 0.0225 μm thick[85], which is not observable under the optical microscope. Fast[209] found that a 2.0wt.% silicon electrical steel with an initial carbon content of 0.071wt.% decarburised to a final carbon content of 0.003wt.% at 900°C in pure hydrogen. However, no decarburisation was observed for a p_{H_2O} / p_{H_2} ratio of $3x10^{-5}$. As the p_{H_2O} / p_{H_2} ratio increased to $3x10^{-4}$ and $1x10^{-3}$, the steel decarburised to final carbon contents of 0.033 and 0.010wt.% respectively.

A similar situation appears likely here with the formation of a very thin dense SiO_2 layer during the heating and austenitising of the SUP7 specimens in argon. This layer, which could not be observed with the optical or scanning electron microscopes, would have prevented the reaction of the heat treatment atmosphere with the steel, and hence the decarburisation of SUP7. However, decarburisation did commence at some stage for a p_{H_2O} / p_{H_2} ratio of 0.05, with free ferrite layers observed after 1hr for prior heating in argon, and after 4hr for 2hr prior austenitisation. Once the free ferrite layers formed, the oxide became thick and porous, and the free ferrite depths increased with time. For a free ferrite layer to form, the heat treatment atmosphere had to be able to react with the bulk steel. With a SiO_2 layer in contact with the bulk steel, decarburisation by the solid state reaction of equation 10.7 can occur[69].

$$C_{(\text{in steel})} + SiO_{2(s)} = SiO_{(g)} + CO_{(g)} \qquad (10.7)$$

From reaction 10.7,

$$\log(P_{CO} \cdot P_{SiO}) = \log a_c - \frac{\Delta G_o}{4.574T}, \qquad (10.8)$$

where P_{CO}, P_{SiO} = partial pressures of carbon monoxide and SiO at reaction equilibrium in Pa;

ΔG_o = 158,300+8.44T$\log T$-107.83T in cal.

For SUP7, a_c can be calculated from the equations of Wada[92], equations 3.12 to 3.14, for a quinternary iron/silicon/manganese/chromium/carbon alloy. Assuming a SiO_2/austenite interface exists before any carbon removal has occurred, the value of a_c with graphite as the standard state is 0.90. This gives:

$$P_{CO} \cdot P_{SiO} = 1.4\text{x}10^{-10}.$$

Consequently, P_{CO} is of the order of $1.2\text{x}10^{-5}$, which corresponds to 12vppm carbon monoxide. Equation 10.7 gives a direct contribution to the decarburisation, and also facilitates the reaction between carbon and water, equation 3.3, to form carbon monoxide by diminishing the blocking of the surface with SiO_2[209]. Eventually the SiO_2 layer will become non-blocking, allowing the reaction between the heat treatment atmosphere and the steel, and therefore faster decarburisation. The longer duration for the formation of a free ferrite layer for the specimens heated and austenitised for 2hr compared with those only heated before exposure to the decarburisation atmosphere can be attributed to a thicker SiO_2 layer forming during the 2hr austenitisation. This layer then takes longer to become non-blocking by the solid state reaction of equation 10.7. The earlier free ferrite formation for a p_{H_2O} / p_{H_2} ratio of 0.25 compared to the 0.05 ratio with 2hr austenitisation, 15min versus 4hr, arose from the greater driving force of the higher water content facilitating a more rapid breakdown of the SiO_2 layer to a non-blocking structure.

Once the SiO_2 layer becomes non-blocking, oxygen can diffuse into the steel and react with silicon to precipitate SiO_2 within an iron rich structure[87]. Faster growth of the oxide structure will then occur. The greater oxide thicknesses for heating in argon at a p_{H_2O} / p_{H_2} ratio of 0.05 compared with heating and 2hr austenitisation was due to the earlier breakdown of the impervious SiO_2 layer, and hence the earlier commencement of the growth of this layer. Faster oxidation kinetics were obtained for heating and 2hr austenitisation prior to decarburisation at a p_{H_2O} / p_{H_2} ratio of 0.25 compared to the 0.05 ratio, due to the earlier breakdown of the SiO_2

layer, and the higher water content supplying a greater oxygen flux. The SiO_2 layer, which formed during the decarburisation of specimens heated to temperature in the established decarburisation atmosphere, was non-blocking, with decarburisation initiating at as low as 300°C.

10.4 Influence of water content on decarburisation at the Ac_3 temperature

Decarburisation heat treatments were undertaken in Section 10.3 with 5mm diameter by 15mm SUP7 test specimens with different initial structures at p_{H_2O} / p_{H_2} ratios of 0.05 and 0.25 at 820°C. These heat treatments involved heating or austenitising the specimens in argon prior to introduction of the decarburisation atmosphere. Further heat treatments were undertaken with the test specimens inserted into the furnace hot zone once the decarburisation atmosphere was established, with the carbon monoxide and carbon dioxide concentrations continuously recorded. The remainder of the decarburisation heat treatments were undertaken by the latter method using 5mm diameter by 50mm test specimens. p_{H_2O} / p_{H_2} ratios ranging from zero to 1.0 were investigated for the furnace cooled initial SUP7 structure at the Ac_3 temperature. Heat treatments were undertaken at temperatures ranging from 650 to 900°C for the furnace cooled SUP7 initial structure at a p_{H_2O} / p_{H_2} ratio of 0.05. Five different initial structures were decarburised at the Ac_3 temperature of 820°C with a p_{H_2O} / p_{H_2} ratio of 0.05.

The carbon monoxide and carbon dioxide gas concentrations profiles during the first 15min decarburisation of furnace cooled SUP7 initial structures at 820°C with p_{H_2O} / p_{H_2} ratios ranging from 0.01 to 1.0 are illustrated in Figures 10.17 and 10.18 respectively. An increase in the p_{H_2O} / p_{H_2} ratio from 0.01 to 0.05 was accompanied by a transition in the gas concentration profiles from three to two distinct peaks. At the lower ratio, the maximum carbon monoxide and carbon dioxide concentrations were 625 and 20vppm, and occurred after 420s. The peak carbon monoxide and carbon dioxide concentrations increased sharply for the 0.05 ratio, being 1615 and 120vppm after 230s. The highest peak values were 1815 and 150vppm carbon monoxide and carbon dioxide respectively after 220s for a p_{H_2O} / p_{H_2} ratio of 0.25. Lower peak values of 1270 and 79vppm respectively were obtained after 240s for a p_{H_2O} / p_{H_2} ratio of 0.50.

At the highest p_{H_2O} / p_{H_2} ratio of 1.0, the total hydrogen/argon flow rate was 1,000cm^3/min, which was twice that used for the other ratios. The carbon monoxide and carbon dioxide concentrations measured at the 1.0 ratio were therefore converted to the equivalent concentrations at 500cm^3/min to allow a direct comparison between the gas concentrations for the other p_{H_2O} / p_{H_2} ratios. The carbon monoxide peak of 1520vppm after 240s for the 1.0 p_{H_2O} / p_{H_2} ratio was higher than the 0.50 ratio. However, the carbon dioxide peak of 60vppm is lower than the value of 80vppm for the 0.50 ratio. After 15min, the carbon monoxide concentrations for the different ratios converge, ranging from 350vppm at the 0.50 ratio to 485vppm at the 1.0 ratio. This contrasts with the carbon dioxide concentrations after 15min, which vary from 8vppm at a p_{H_2O} / p_{H_2} ratio of 0.01 to 60vppm at a p_{H_2O} / p_{H_2} ratio of 0.25.

The free ferrite decarburisation depths calculated from the gas concentrations for 15min decarburisation, and the depths measured from the microstructures after 4hr, are illustrated in Figure 10.19. The free ferrite depths calculated for 15min decarburisation varied from 50 μm at a p_{H_2O} / p_{H_2} ratio of 0.01 to 75 μm at the 0.25 ratio. The smallest free ferrite depth of 247 μm after 4hr was obtained at the lowest p_{H_2O} / p_{H_2} ratio of 0.01. The free ferrite depths were then constant for p_{H_2O} / p_{H_2} ratios of 0.05 to 1.0, with 399 μm free ferrite at the 0.25 ratio. Mayer[67] demonstrated that the decarburisation rate almost doubled as the p_{H_2O} / p_{H_2} ratio increases from 0.03 to 0.25 for a 0.04wt.%C/0.68wt.%Si steel, then halved as the p_{H_2O} / p_{H_2} ratio increased from 0.5 to 0.6.

The thinnest oxide structure of 7.5μm after 4hr decarburisation at various p_{H_2O} / p_{H_2} ratios resulted for the lowest ratio of 0.01, Figure 10.20. The oxide thickness increased logarithmically from a value of 11.5 μm at a p_{H_2O} / p_{H_2} ratio of 0.05 to 31 μm at the highest ratio of 1.0. This increasing oxide thickness was presumably due to the increase in oxygen potential at the higher p_{H_2O} / p_{H_2} ratios, resulting in a greater oxygen supply for oxide growth. No influence of p_{H_2O} / p_{H_2} ratio on the measured free ferrite columnar grain size was observed after 4hr decarburisation at 820°C, Figure 10.21. The free ferrite grain size was approximately 60 μm for p_{H_2O} / p_{H_2} ratios of 0.01 to 1.0.

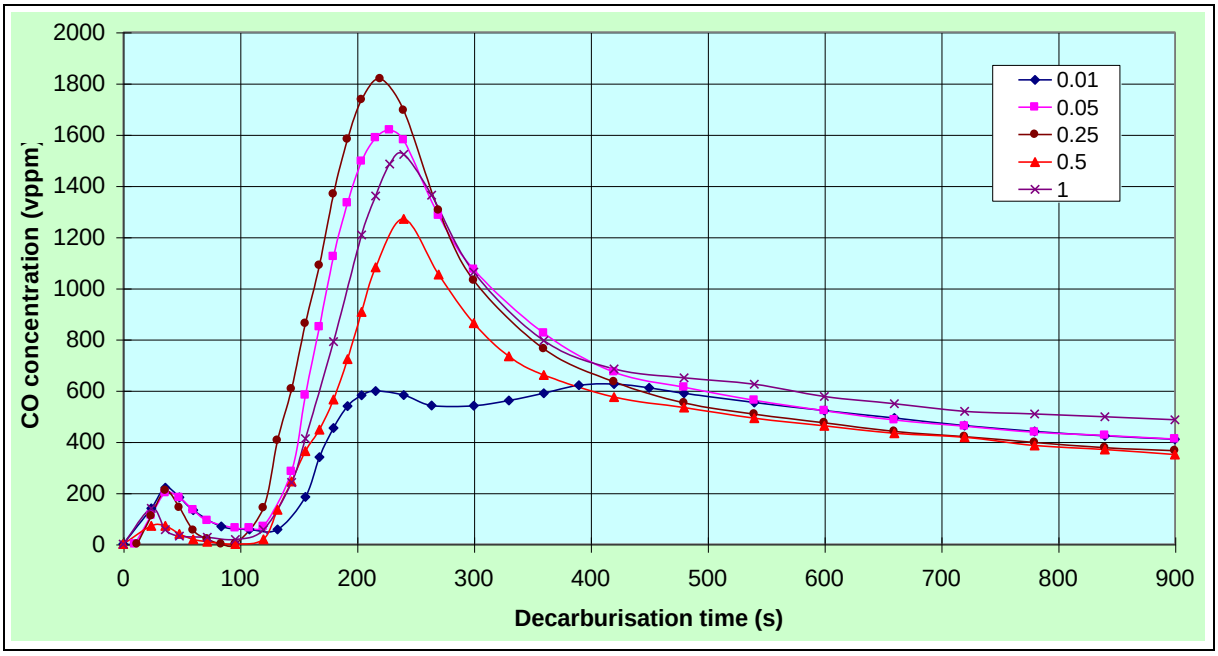

Figure 10.17 Carbon monoxide concentration profiles during the decarburisation of furnace cooled SUP7 initial structures at 820°C with different p_{H_2O} / p_{H_2} ratios.

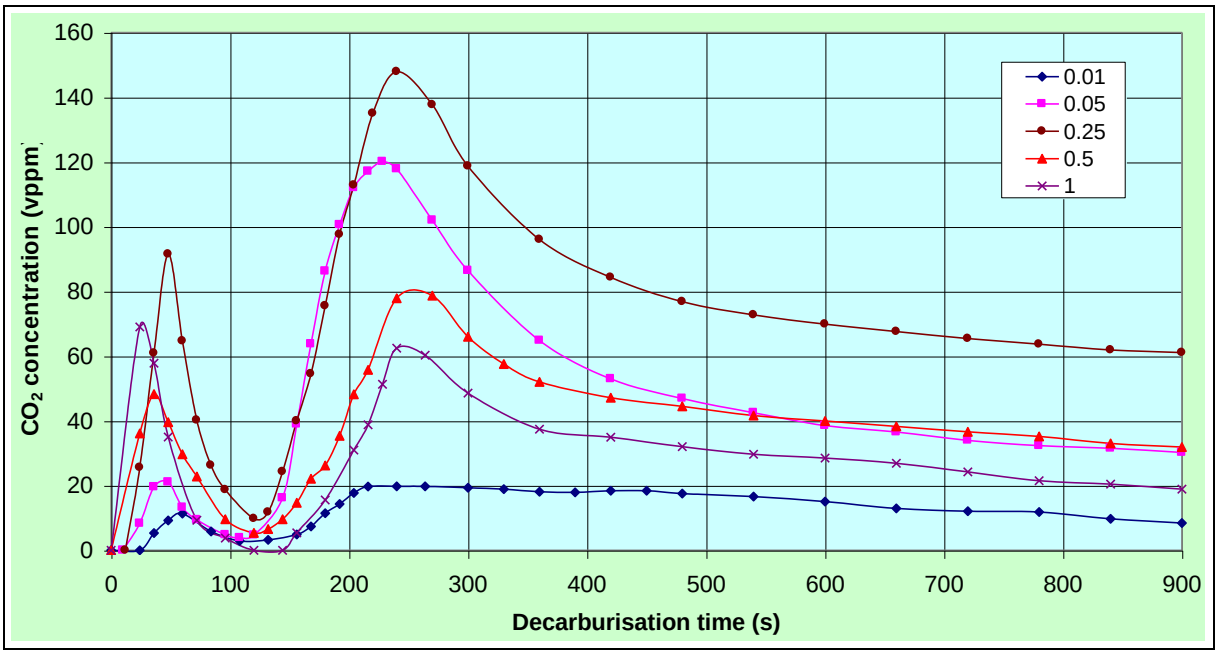

Figure 10.18 Carbon dioxide concentration profiles during the decarburisation of furnace cooled SUP7 initial structures at 820°C with different p_{H_2O} / p_{H_2} ratios.

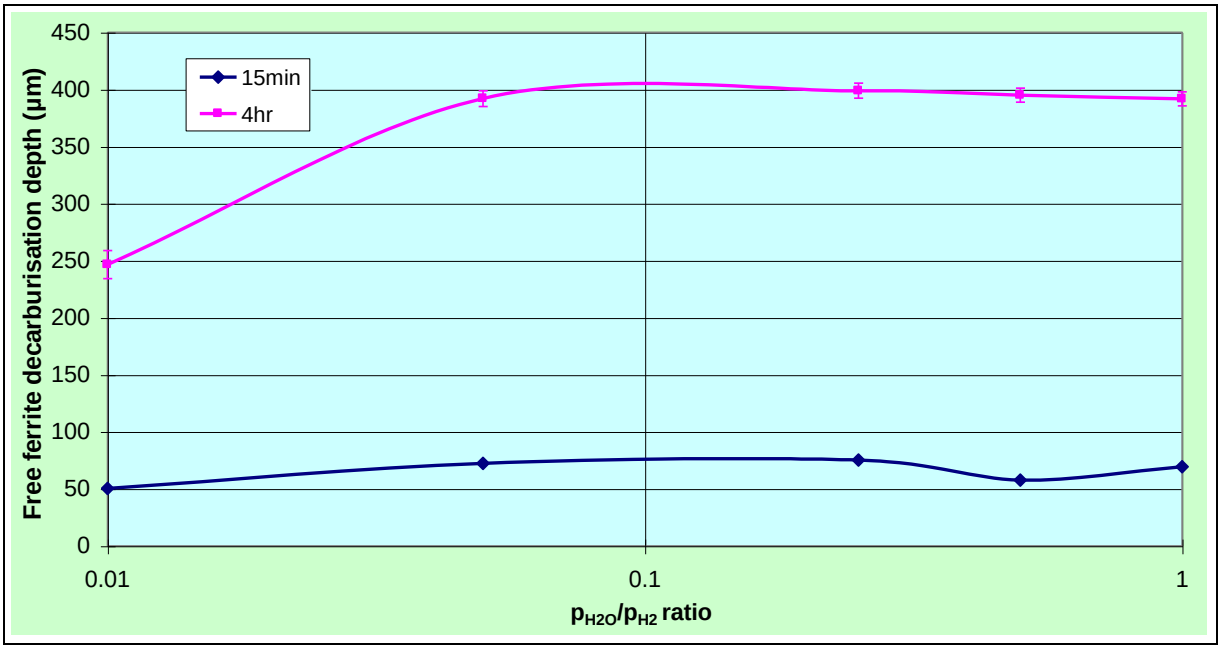

Figure 10.19 Free ferrite decarburisation depths for furnace cooled SUP7 initial structures heat treated at 820°C with different p_{H_2O} / p_{H_2} ratios.

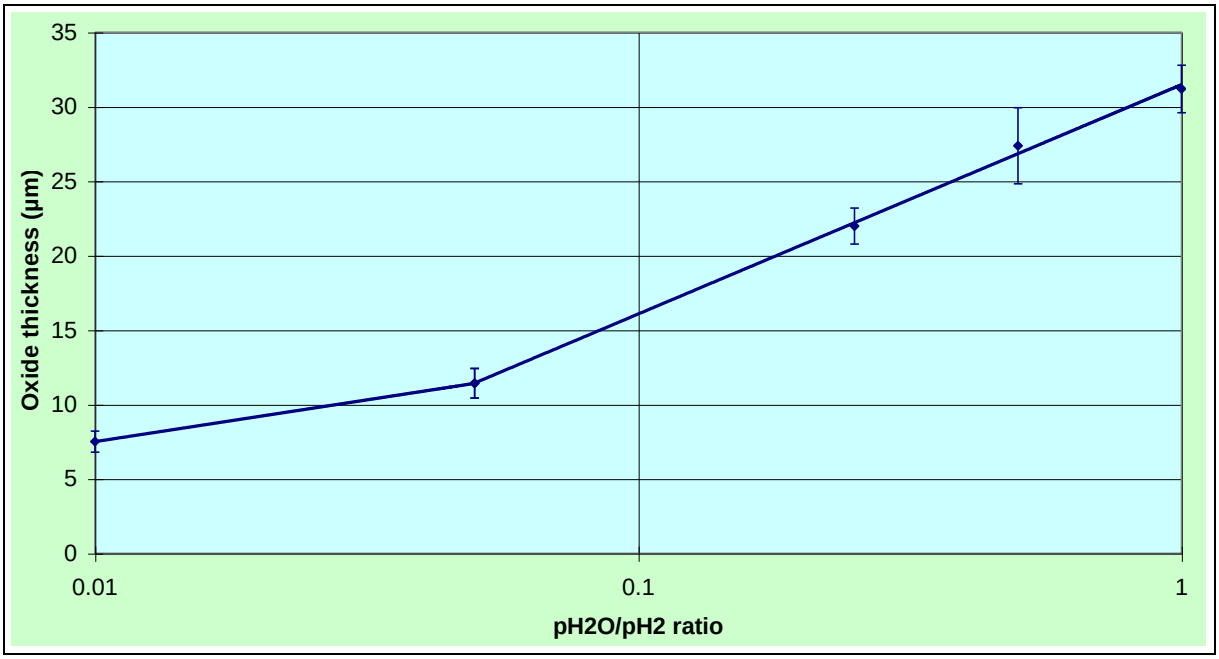

Figure 10.20 Oxide thickness kinetics for the decarburisation of furnace cooled SUP7 initial structures after 4hr at 820°C with different p_{H_2O} / p_{H_2} ratios.

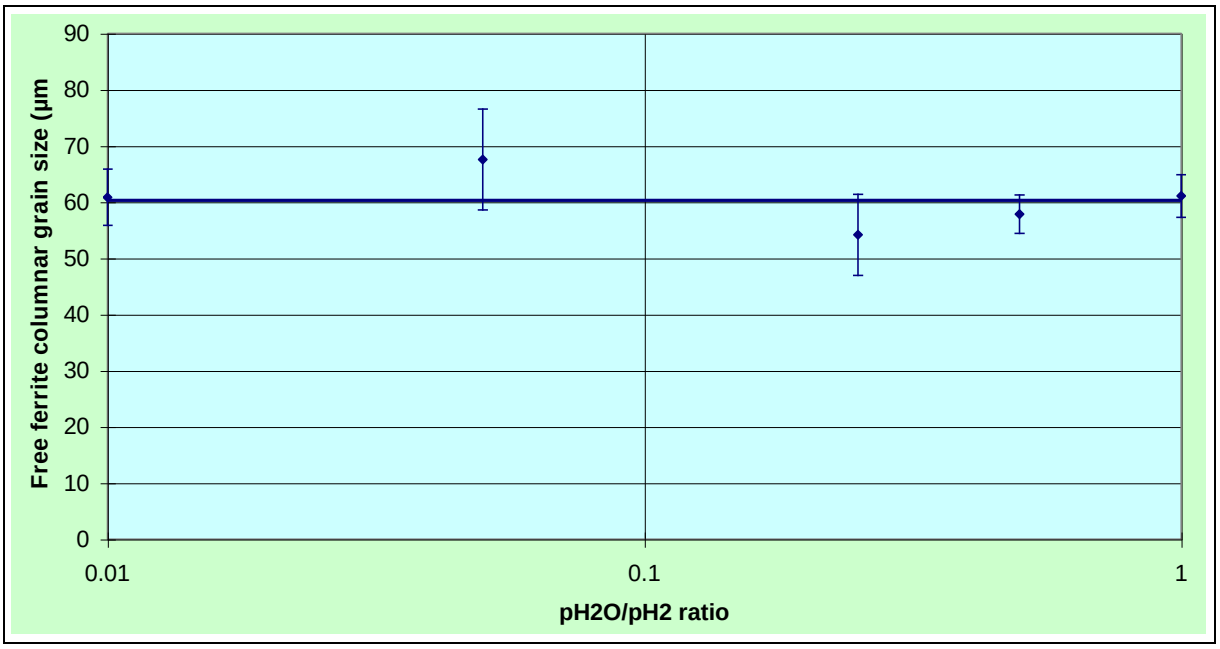

Figure 10.21 Free ferrite columnar grain growth kinetics of furnace cooled SUP7 initial structures after decarburisation at 820°C with different p_{H_2O} / p_{H_2} ratios.

The lower free ferrite decarburisation depth after 4hr at a p_{H_2O} / p_{H_2} ratio of 0.01 occurred despite a similar columnar ferrite grain size to the specimens decarburised at the higher p_{H_2O} / p_{H_2} ratios. This indicates that the ferrite grain boundaries, which provide low energy paths for carbon diffusion from the ferrite/austenite interface through the ferrite relative to the ferrite grains, did not significantly influence the thickness of the free ferrite layer. Furthermore, the decarburisation depths were similar for p_{H_2O} / p_{H_2} ratios of 0.05 to 1.0, despite the oxide layer thicknesses varying from 11.5 to 31μm. This indicates that the increasing thickness of the oxide structure with p_{H_2O} / p_{H_2} ratio did not significantly influence the thickness of the free ferrite layer obtained after 4hr decarburisation, despite the longer diffusion paths for carbon removal from the steel.

10.5 Influence of temperature on decarburisation

10.5.1 Microstructural investigation

Figure 10.22 illustrates the microstructures obtained from furnace cooled pearlitic initial structures decarburised for 4hr at various temperatures. At 700 and 750°C, Figures 10.22(a) and (b) respectively, a free ferrite/pearlite interface exists. This interface is sharper at 700°C. Decarburisation at the Ac_3 temperature of 820°C, Figure 10.22(c), resulted in a sharp free ferrite/martensite interface. This interface was less well defined at 900°C, as illustrated in Figure 10.22(d). Columnar ferrite grain structures were observed for decarburisation at temperatures of 700 to 900°C, which corresponds to temperatures below, within and above the intercritical temperature region for SUP7. These results differ from previous research into an eutectoid plain carbon steel[64] and low carbon steels[65,66], where columnar grain structures were only observed within the intercritical region.

10.5.2 Decarburisation kinetics

The carbon removal from furnace cooled pearlitic structures varies considerably with temperature over a range of 650 to 900°C during the early stages of the heat treatments. Figures 10.23 and 10.24 illustrate the influence of temperature on the carbon monoxide and carbon dioxide concentration profiles during the first 15min of decarburisation at different

temperatures. The carbon monoxide and carbon dioxide concentrations detected at 650°C were small. As the temperature increased to 700°C, two carbon monoxide and carbon dioxide concentration peaks were observed. The second peaks increased in concentration, became narrower, and occurred earlier, as the temperature increased. The carbon monoxide and carbon dioxide peaks increased from 180 and 14vppm at 700°C to 2395 and 155vppm at 900°C. The peak concentrations occurred after 900s at 700°C, and after only 138s at 900°C.

The influence of temperature on the free ferrite depths after 4hr decarburisation are illustrated in Figure 10.25. The free ferrite depths increased from 24 μm at 650°C to 392 μm at 820°C, before decreasing to 357 μm at 850°C and 126 μm at 900°C. The influence of initial structure on the carbon monoxide and carbon dioxide concentrations during decarburisation at 820°C are illustrated in Figures 10.26 and 10.27 respectively. The height and width of the second concentration peaks varied with initial structure. The air cooled pearlitic structure exhibited the highest carbon monoxide and carbon dioxide peaks of 1880 and 160vppm respectively, while the 96hr tempered martensite spheroidal cementite structure had the lowest peak concentrations of 1270 and 100vppm.

Of the two pearlitic structures, and the two tempered martensite spheroidal cementite structures, the finer structures exhibited higher concentration peak values. The concentration profiles with lower peak values then decreased more slowly from the peak values, with the carbon monoxide concentration after the heating time of 540s 0.35 times that of the peak value for the furnace cooled initial structure, compared with a ratio of 0.30 for the air cooled structure. Initial carbon removal during decarburisation occurred directly from the steel surface. The higher peak concentrations of the finer structures appears to be a consequence of the finer structures facilitating faster surface carbon removal. The sharper peak concentration profiles for the pearlitic structures were thought to be due to the greater surface area to volume ratio of the cementite lamellae relative to the spheroidal cementite of the tempered martensite initial structures resulting in the faster cementite dissolution and associated faster carbon supply for decarburisation.

The slower decreasing carbon monoxide and carbon dioxide concentrations from the peak values for the spheroidal cementite initial structures was presumably due to the slower transformation of the core structure to austenite than for pearlitic initial structures. The lower

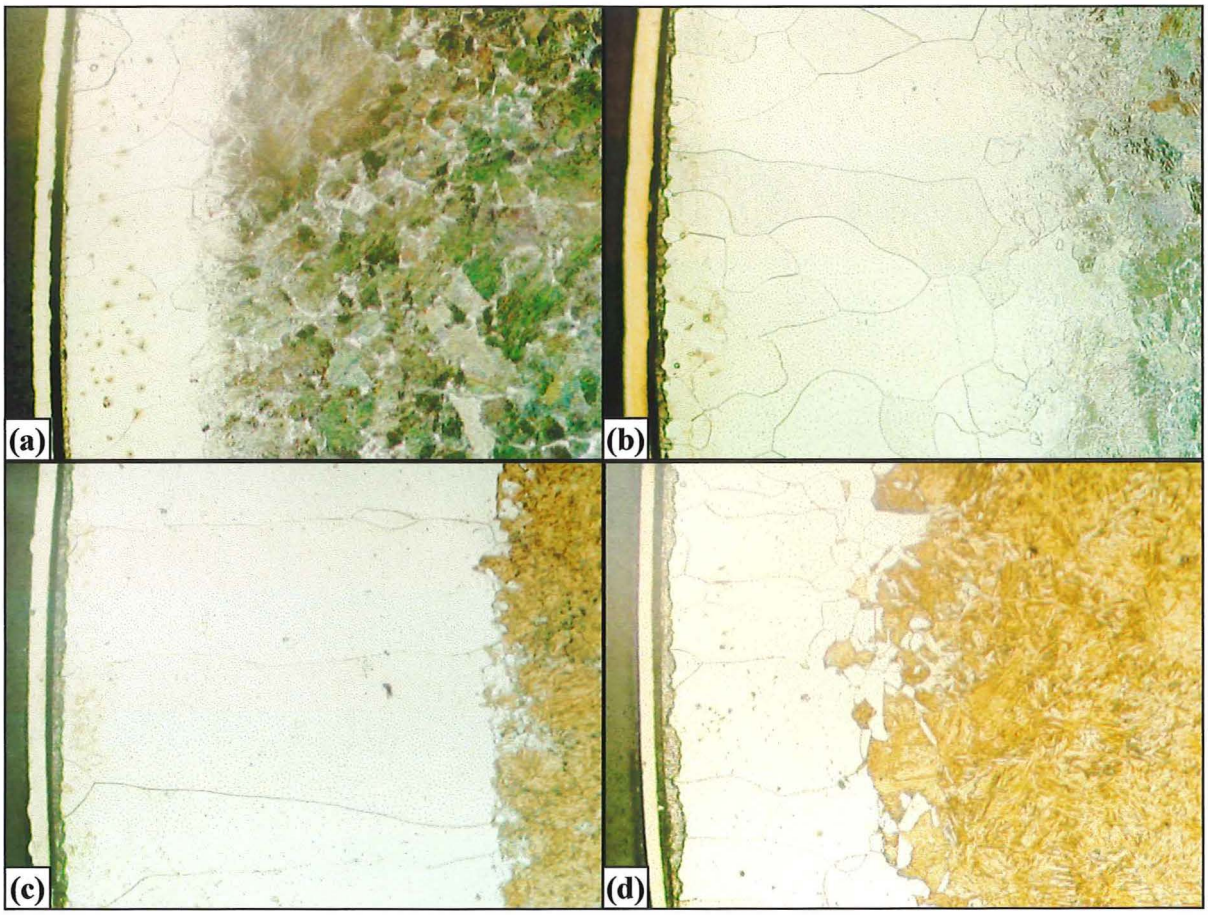

Figure 10.22 Decarburisation microstructures for furnace cooled SUP7 initial structures after 4hr heat treatment with a p_{H_2O} / p_{H_2} ratio of 0.05 at (a) 700°C, (b) 750°C, (c) 820°C, and (d) 900°C. 2% Nital etch. 230x magnification.

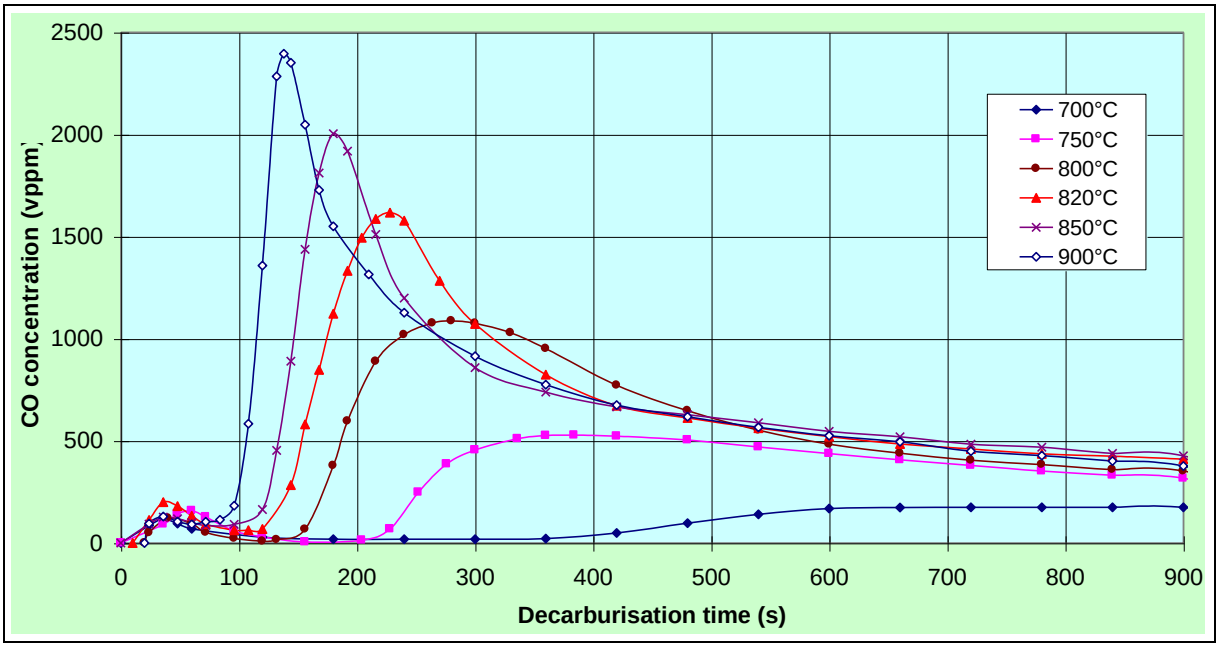

Figure 10.23 Carbon monoxide concentration profiles for decarburisation of furnace cooled SUP7 initial structures at different temperatures with p_{H_2O} / p_{H_2} =0.05.

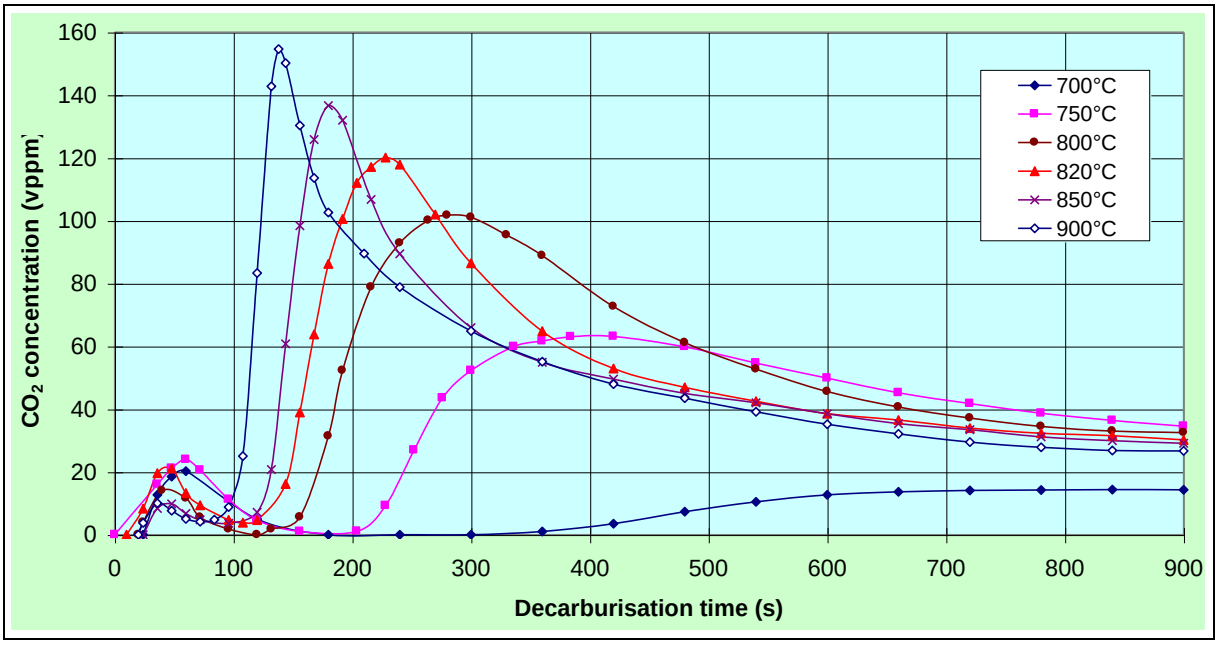

Figure 10.24 Carbon dioxide concentration profiles for decarburisation of furnace cooled SUP7 initial structures at different temperatures with p_{H_2O} / p_{H_2} =0.05.

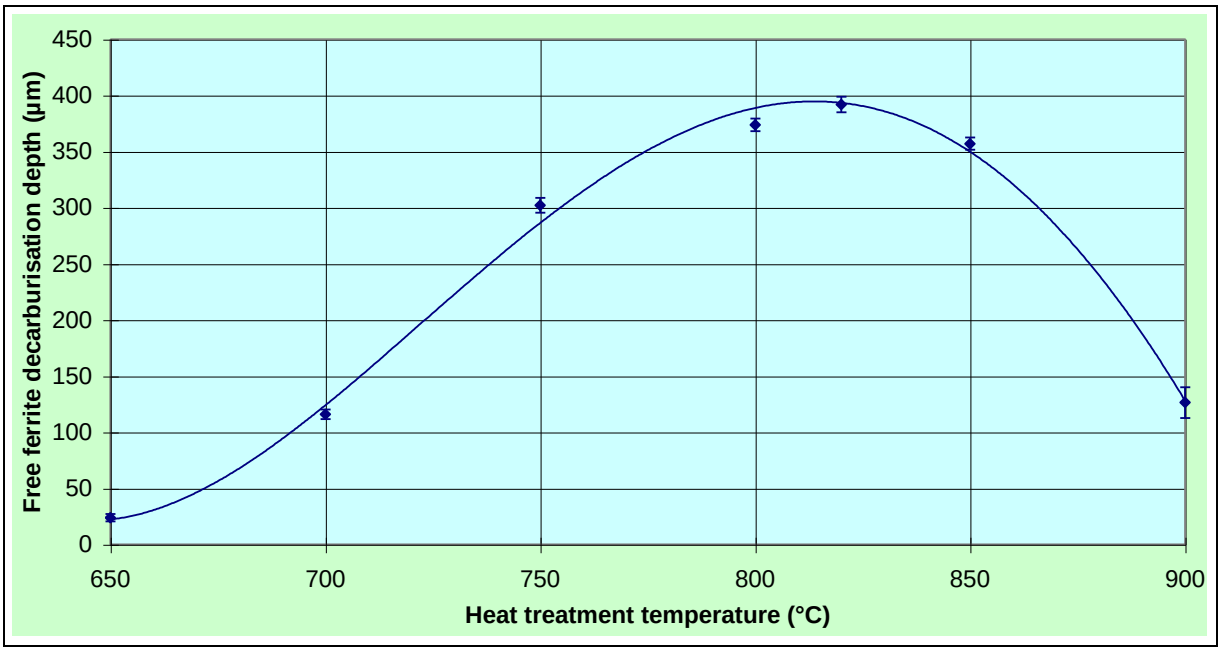

Figure 10.25 Influence of temperature on the free ferrite decarburisation depths for furnace cooled SUP7 initial structures heat treated at p_{H_2O} / p_{H_2} =0.05.

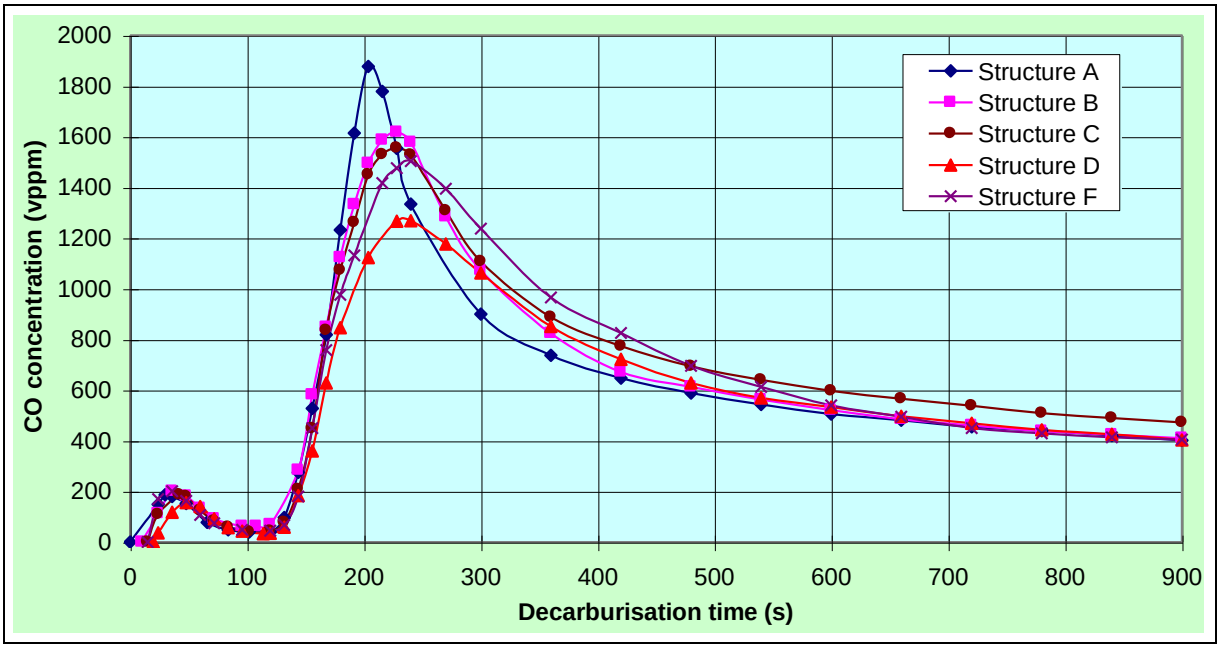

Figure 10.26 Carbon monoxide concentration profiles during the decarburisation of different SUP7 initial structures at 820°C with p_{H_2O} / p_{H_2} =0.05.

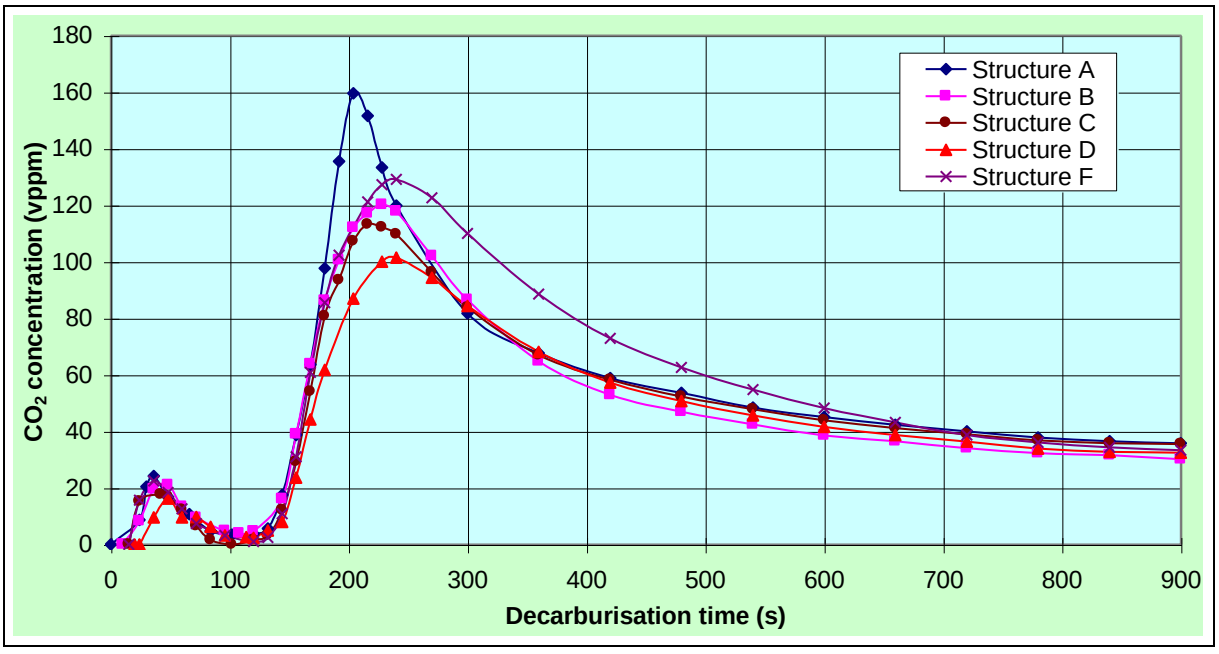

Figure 10.27 Carbon dioxide concentration profiles during the decarburisation of different SUP7 initial structures at 820°C with p_{H_2O} / p_{H_2} =0.05.

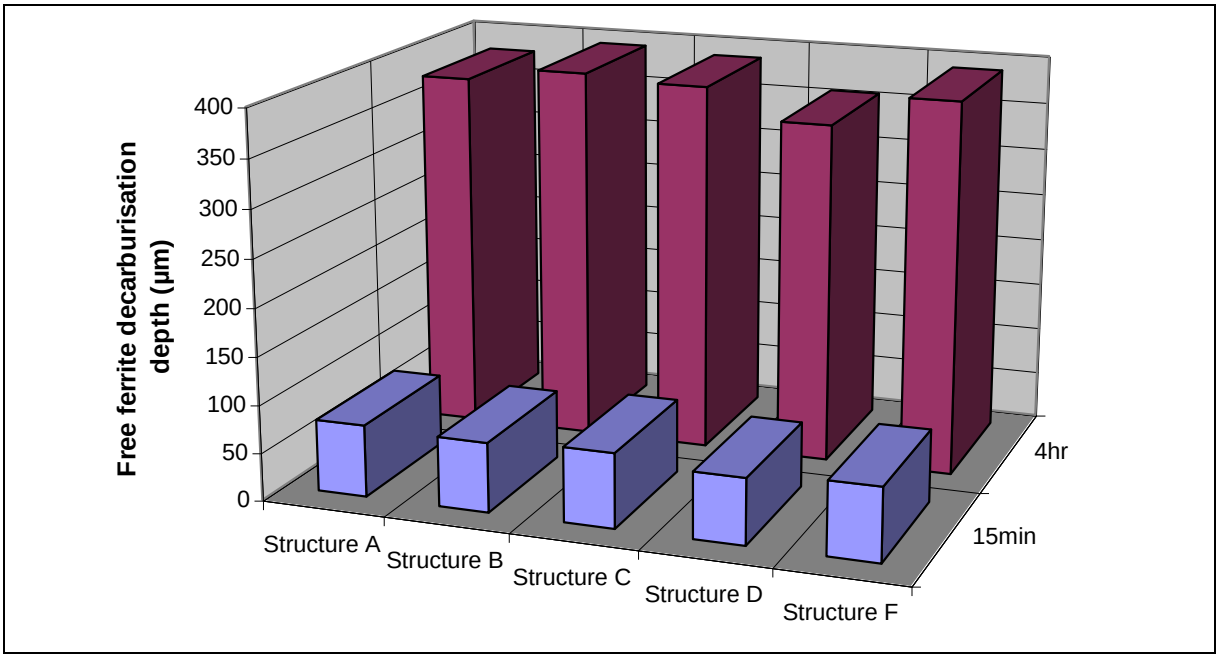

Figure 10.28 Influence of initial structure on the SUP7 free ferrite depths after decarburisation at 820°C with p_{H_2O} / p_{H_2}=0.05.

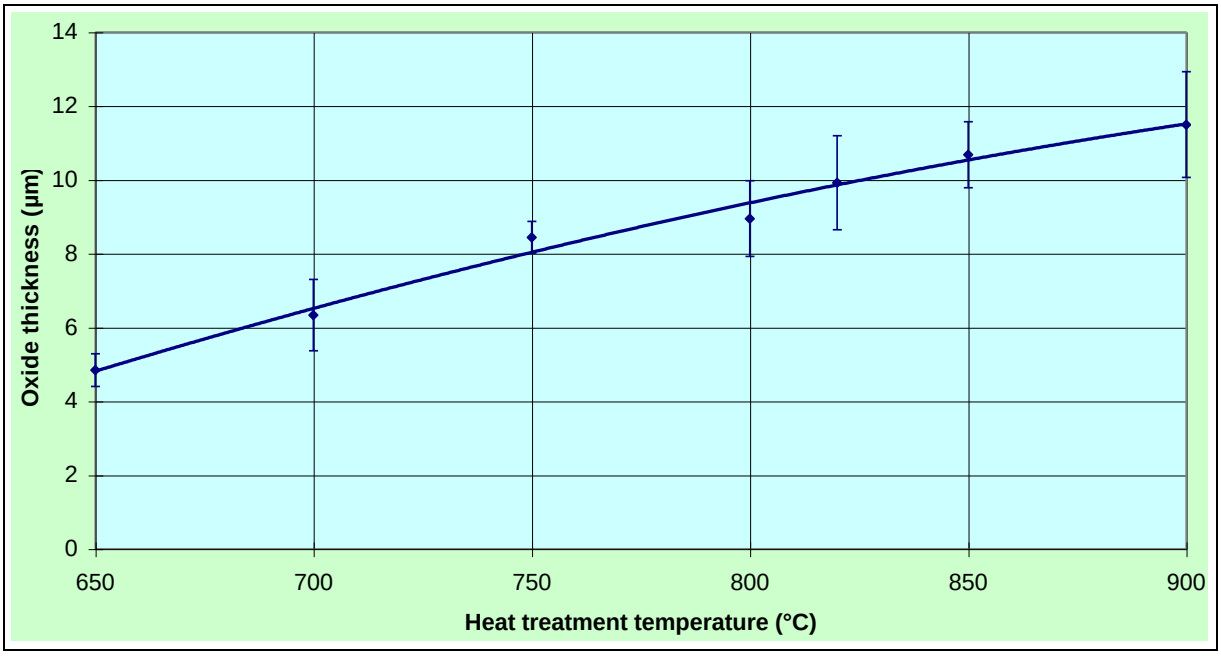

Figure 10.29 Influence of temperature on oxide thickness after 4hr decarburisation of furnace cooled SUP7 initial structures with p_{H_2O} / p_{H_2}=0.05.

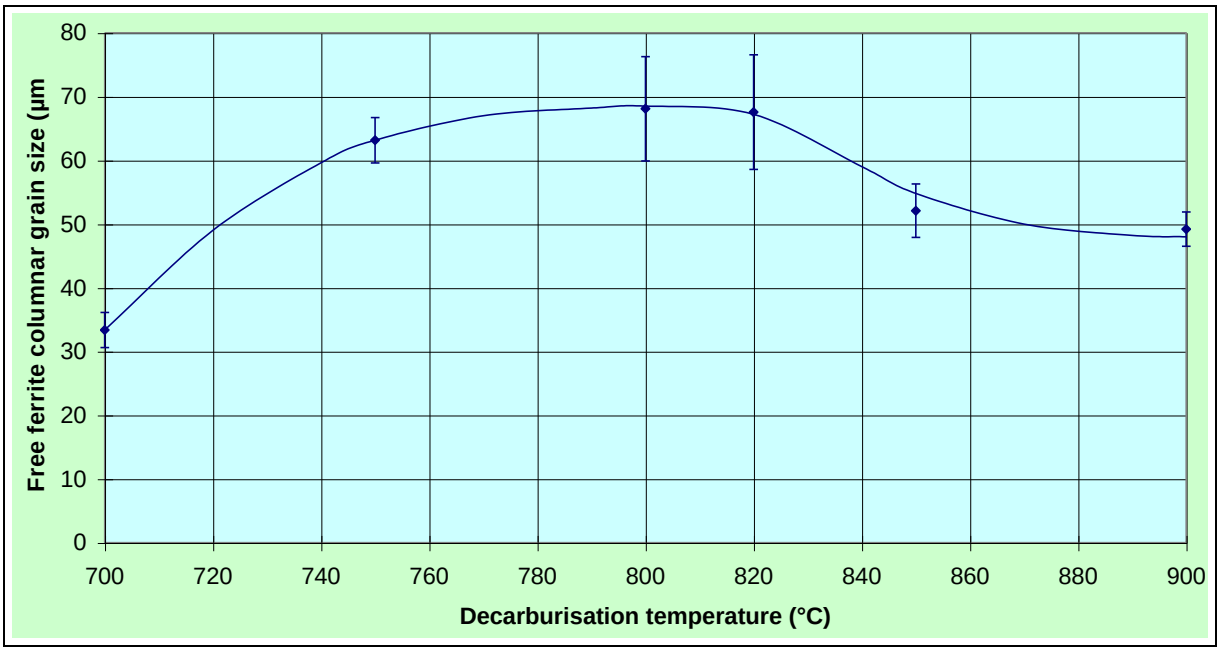

Figure 10.30 Influence of temperature on the free ferrite columnar grain size after 4hr decarburisation of furnace cooled SUP7 initial structures at p_{H_2O} / p_{H_2} =0.05.

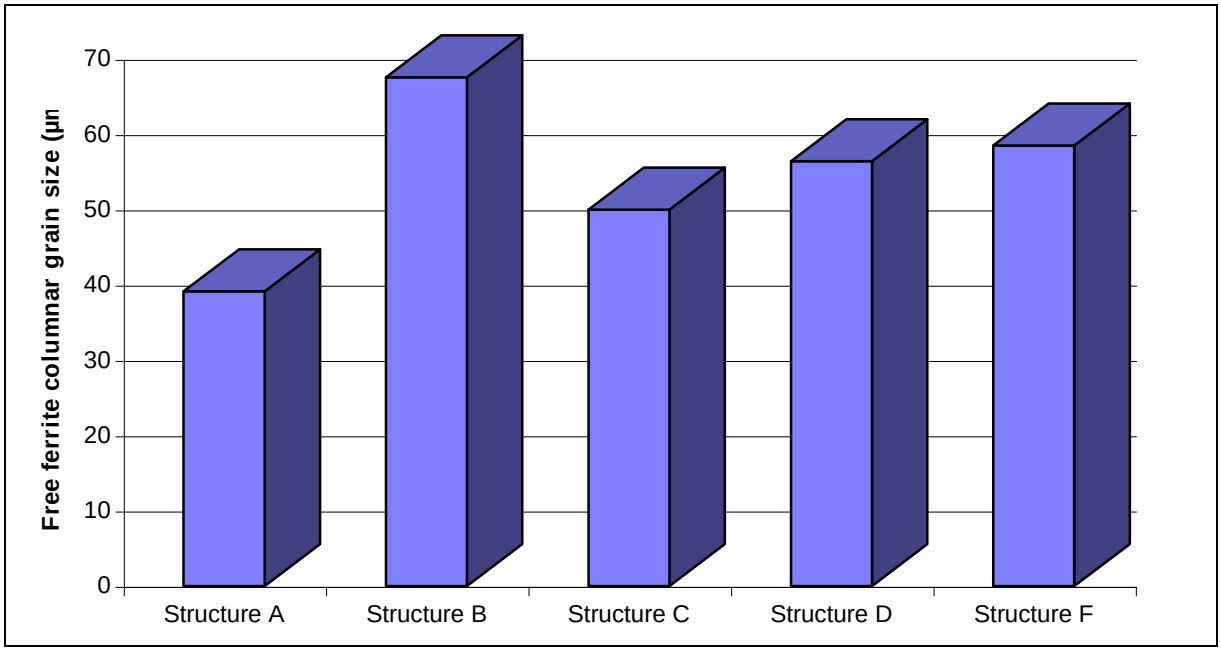

Figure 10.31 Influence of SUP7 initial structure on the free ferrite columnar grain size after 4hr decarburisation at 820°C with p_{H_2O} / p_{H_2} =0.05.

austenite fractions of the spheroidal cementite structures have higher associated carbon contents, increasing the driving force for carbon diffusion through the ferrite. The higher undissolved cementite fraction of the untransformed ferrite will also have increased the rate of supply of carbon across the ferrite due to the higher associated carbon content. The increased surface area of the ferrite/cementite and ferrite/austenite interfaces of the slower transforming spheroidal cementite structures should also yield a greater supply rate of carbon. The slower decrease from the peak values for the intercritical initial structure relative to the tempered martensite initial structures was thought to be due to the slower austenite formation of the core intercritical initial structure during the early stages of transformation.

Figure 10.28 illustrates the free ferrite decarburisation depths calculated from the carbon monoxide and carbon dioxide concentrations after 15min, and those measured after 4hr from the decarburised microstructures. The lowest decarburisation depth of 68 μm after 15min was calculated for the 96hr tempered martensite structure. The other values varied from 72 μm for the furnace cooled structure to 75 μm for the 12hr tempered martensite structure. Measurement of these free ferrite depths after 15min, which would have been similar within the typical 95% confidence intervals, would have indicated that the initial structure had no influence on the decarburisation kinetics. However, the carbon monoxide and carbon dioxide concentration profiles of Figures 10.26 and 10.27 illustrate different decarburisation kinetics for the different initial structures as they heated to temperature.

The calculated values of the free ferrite depths after 15min for the furnace cooled and 96hr tempered martensite initial structures were lower than the respective values of 101 and 95μm for the 5mm diameter by 15mm specimens. The higher measured values were considered to be due to decarburisation occurring after the commencement of the argon flush to remove the decarburisation atmosphere, before the decarburisation atmosphere was sufficiently diluted to end the decarburisation. Following the argon flush, the test specimens were removed from the hot zone and quenched in water.

The smallest mean free ferrite depth of 356μm after 4hr was for the 96hr tempered martensite structure. The other decarburisation depths varied from 377 μm for the air cooled structure to 392 μm for the furnace cooled structure. Given that the 95% confidence intervals were less

than 8 μm, the initial structure had a limited influence on the free ferrite decarburisation depths, except during specimen heating.

10.5.3 Oxidation kinetics

The influence of temperature on the oxide thicknesses after 4hr decarburisation of furnace cooled SUP7 initial structures at a p_{H_2O} / p_{H_2} ratio of 0.05 is illustrated in Figure 10.29. The oxide thickness increases from 4.8 μm at 650°C to 11.5 μm at 900°C. The oxide thickness for different initial structures decarburised 4hr at 820°C with a 0.05 p_{H_2O} / p_{H_2} ratio varied from 9.9 μm for the furnace cooled structure to 11.2 μm for the 12hr tempered martensite structure. However, as the 95% confidence intervals were up to 1.0 μm, these results indicate that the oxidation thicknesses were similar for the different initial structures.

10.5.4 Free ferrite columnar grain growth kinetics

Figure 10.30 illustrates the influence of temperature on the free ferrite columnar grain size after 4hr decarburisation of furnace cooled initial structures at a p_{H_2O} / p_{H_2} ratio of 0.05. The grain size increased from 33 μm at 700°C to approximately 65 μm from 750 to 820°C. The grain size then decreased to 52 and 49 μm at 850 and 900°C respectively. Considerable variation occurred in the columnar grain size after 4hr decarburisation of different initial structures at 820°C, Figure 10.31. The air cooled pearlitic initial structure had the finest grain size of 39 μm, while the furnace cooled structure the coarsest grain size of 68 μm. The finer pearlitic and spheroidal cementite structures yielded smaller columnar grain sizes than the respective coarser structures. The similar free ferrite depths for the different initial structures after 4hr despite the different columnar grain sizes indicate that the range of columnar grain sizes had little influence on the decarburisation kinetics.

10.6 Further decarburisation experiments

10.6.1 Interrupted decarburisation tests

A further heat treatment was undertaken to investigate the microstructural changes that may occur if the heat treatment was completed with a prolonged argon anneal before being water quenched. A furnace cooled specimen was decarburised for 4hr at 820°C with a p_{H_2O} / p_{H_2} ratio of 0.05, followed by the introduction of a 500cm^3/min purified argon flow which was maintained for 4hr. Table 10.3 compares the free ferrite decarburisation depths, oxide thicknesses, and columnar grain sizes for a furnace cooled initial structures decarburised for 4hr with and without a subsequent 4hr argon anneal.

Table 10.3 Comparison of decarburisation parameters for furnace cooled pearlitic structures decarburised for 4hr at 820°C with p_{H_2O} / p_{H_2}=0.05, and decarburised 4hr followed by a 4hr argon anneal.

Specimen	Free ferrite (μm)	Oxide thickness (μm)	Grain size (μm)
4hr decarburisation	392	9.9	68
4hr decarburisation/4hr argon	369	15.5	59

The free ferrite decarburisation depth for the specimen annealed in argon was 23μm less than that for the specimen without the argon anneal. The respective microstructures were similar, although the occasional growth of austenite, which transformed upon quenching to the martensite observed in the microstructures, into the ferrite from the interface was observed along the ferrite grain boundaries. Decarburisation at the Ac_3 temperature of 820°C means that the bulk steel carbon content of 0.60wt.% corresponds to the carbon content of austenite in equilibrium with ferrite. Therefore, similar free ferrite depths were expected with and without the 4hr argon anneal. The replacement of the H_2O/H_2 atmosphere with argon meant that no carbon removal occurred since the inert argon atmosphere did not react with the carbon in the steel to effect decarburisation. The oxide thickness after the 4hr argon anneal was greater, 15.5 versus 9.9μm, while the columnar grain sizes were similar.

10.6.2 Further investigation into austenitisation prior to decarburisation

Decarburisation experiments were undertaken in Section 10.3 with the test specimens either heated in argon before the introduction of the decarburisation atmosphere, or heated and then austenitised for 2hr in argon prior to the introduction of the decarburisation atmosphere. Heating and 2hr austenitisation in argon ensured that the initial structure had transformed to at least 95% austenite before being exposed to the decarburisation environment. Consequently, carbon removal could only occur from a predominantly austenitic structure. However, minute water concentrations present in the argon were considered to have resulted in the formation of a very thin impervious SiO_2 oxide during the austenitisation, which prevented carbon removal from the steel. This retarded decarburisation initiation to the extent that only some free ferrite patches were observed 4hr after the decarburisation atmosphere was introduced for a furnace cooled specimen heat treated at 820°C with a p_{H_2O} / p_{H_2} ratio of 0.05.

Consequently, decarburisation experiments were undertaken where the test specimens were inserted from the cold end of the tube furnace into the fully established decarburisation atmosphere. This allowed the specimens to be exposed to the decarburisation atmosphere as they were heating. A SUP7 furnace cooled initial structure was also decarburised in hydrogen, which resulted in negligible decarburisation, as illustrated in Figure 10.32.

Therefore, the influence of heating and austenitisation prior to introducing the decarburisation atmosphere was undertaken with hydrogen instead of argon used as the non-decarburising austenitising atmosphere. 5mm diameter by 50mm furnace cooled SUP7 specimens were inserted into the hot zone at 820°C once the hydrogen atmosphere was established, heated for 540s to within 5°C of the hot zone temperature, and then austenitised for 2hr. The infra-red gas analysers were zeroed once the hydrogen atmosphere was established, which allowed the carbon monoxide and carbon dioxide gas concentrations to be continuously recorded upon introduction of the decarburisation atmosphere. The decarburisation heat treatments were undertaken for 4hr at p_{H_2O} / p_{H_2} ratios of either 0.05 or 0.25.

Figures 10.33 and 10.34 show the carbon monoxide and carbon dioxide gas concentration profiles for the first 15min after the introduction of the decarburisation atmosphere. At both

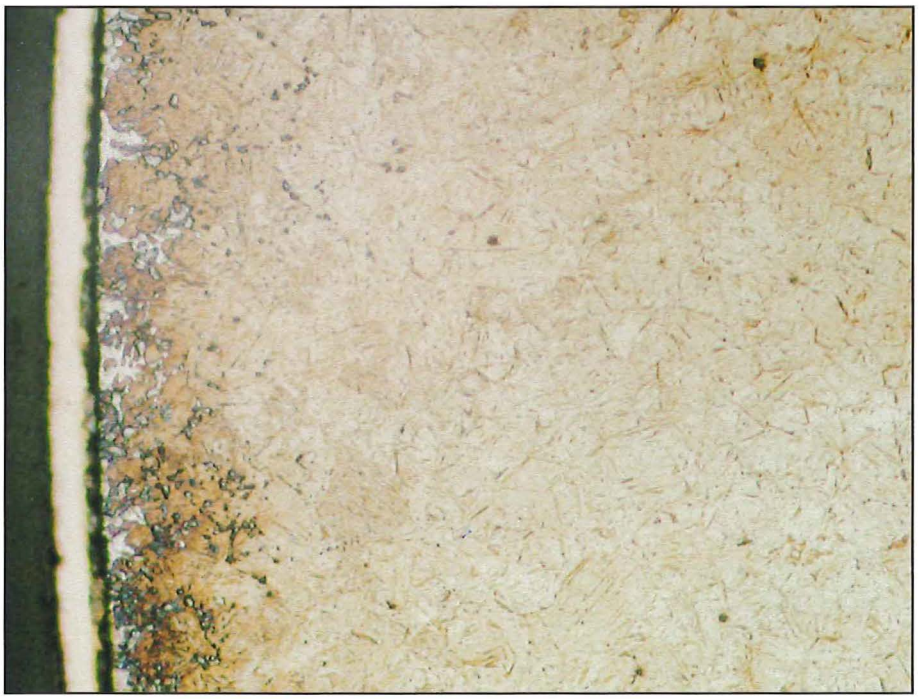

Figure 10.32 Microstructure of a furnace cooled SUP7 initial structure decarburised 2hr in hydrogen. 2% Nital etch. 230x magnification.

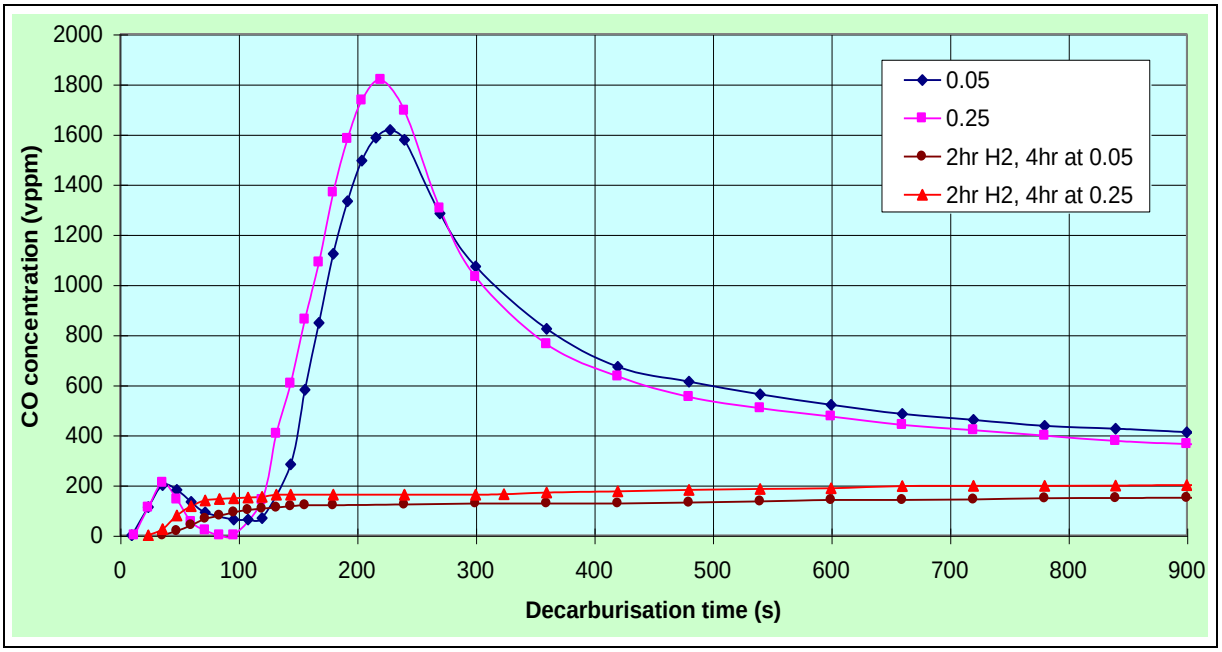

Figure 10.33 Carbon monoxide concentration profiles for the decarburisation of furnace cooled SUP7 initial structures at 820°C for p_{H_2O} / p_{H_2} ratios of 0.05 and 0.25 with, and without, heating and 2hr austenitisation in hydrogen.

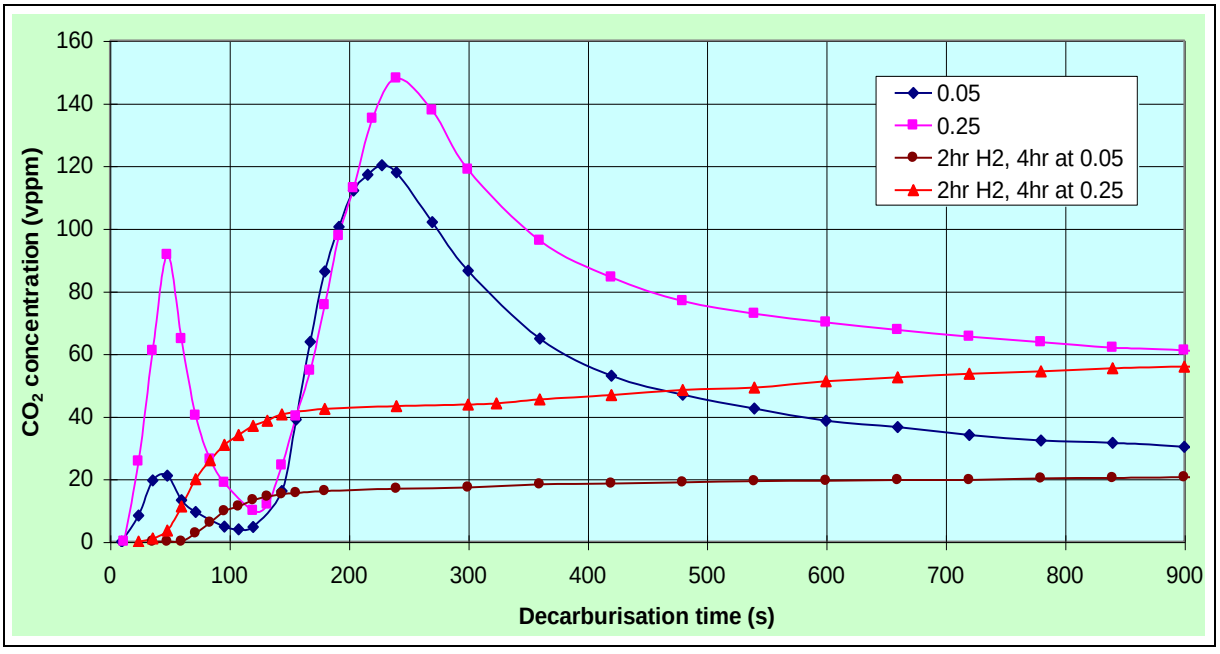

Figure 10.34 Carbon dioxide concentration profiles for the decarburisation of furnace cooled SUP7 initial structures at 820°C for p_{H_2O} / p_{H_2} ratios of 0.05 and 0.25 with, and without, heating and 2hr austenitisation in hydrogen.

p_{H_2O} / p_{H_2} ratios, carbon monoxide and carbon dioxide were detected within 60s of the decarburisation atmosphere being introduced. The gas concentration profiles differed considerably from those obtained by inserting the specimens from the cold end of the tube furnace into the hot zone with the decarburisation atmosphere established. Only one concentration peak was exhibited, with the carbon monoxide and carbon dioxide concentrations for the specimens austenitised in hydrogen increasing gradually from 100 to 900s. The carbon monoxide and carbon dioxide concentrations at test durations equivalent to those of the peak concentrations for the specimens without austenitisation or heating in hydrogen were an order of magnitude lower.

The concentration profiles obtained with and without the 2hr hydrogen anneal were influenced by the former being at the heat treatment temperature when first exposed to the decarburisation atmosphere, while the latter was inserted into the established decarburisation atmosphere from the cold end of the tube furnace. After 2hr austenitisation in hydrogen, the initial ground surface will have been replaced by a darker surface with increased irregularities. Ito[210] investigated the decarburisation of a 0.8wt.% Fe-C steel at 790°C and a p_{H_2O} / p_{H_2} ratio of 0.06 with a polished surface, and a carburised surface with a thin oxide layer comprising Fe_2O_3 and Fe_3O_4. The estimated flux of carbon atoms for the growth of the first 10μm of free ferrite was found to be three to five times greater for the polished surface relative to the carburised surface[210]. At thicker free ferrite depths, the increasing thickness of the free ferrite layer was controlled by carbon diffusion though the ferrite[210]. The rougher surface of the specimen after 2hr austenitisation in hydrogen presumably contributed to the lower initial carbon monoxide and carbon dioxide concentrations. The more similar concentration profiles after 15min indicate that the decarburisation had become diffusion controlled.

The gas concentrations after 1hr were similar for both types of tests, with the respective gas concentrations after 1hr listed in Table 10.4. The carbon dioxide concentrations for the 2hr austenitised specimens exceeded the respective concentrations for the non-austenitised specimens after 1hr, although the sum of the carbon monoxide and carbon dioxide concentrations were similar for all four specimens.

Table 10.4 Selected carbon monoxide and carbon dioxide gas concentrations for the decarburisation of furnace cooled SUP7 initial structures at 820°C with p_{H_2O} / p_{H_2} ratios of 0.05 and 0.25 with, and without, heating and 2hr austenitisation in hydrogen.

DESCRIPTION	Gas concentration (vppm)			
	p_{H_2O} / p_{H_2} =0.05		p_{H_2O} / p_{H_2} =0.25	
	No austenitisation	2hr austenitisation	No austenitisation	2hr austenitisation
Peak CO*	1615	123	1815	162
Peak CO_2*	120	17	148	43
CO at 15min	411	150	365	200
CO_2 at 15min	9	21	61	56
CO at 1hr	185	170	154	153
CO_2 at 1hr	12	23	25	49
Total $CO+CO_2$(1hr)	**197**	**193**	**179**	**202**

The gas concentration profiles for the 0.25 p_{H_2O} / p_{H_2} ratio were significantly higher than for the 0.05 ratio after heating and austenitisation in hydrogen. The carbon monoxide and carbon dioxide concentrations of 200 and 56vppm respectively after 15min decarburisation were greater than the 150 and 21vppm for the 0.05 p_{H_2O} / p_{H_2} ratio. The increase in decarburisation at the higher p_{H_2O} / p_{H_2} ratio is also evident in the free ferrite depths measured after 4hr, Figure 10.35. The free ferrite depth of 275μm for the 0.05 ratio was less than the value of 346μm for the 0.25 ratio. This could have been due to some SiO_2 formation during the austenitisation, with the higher p_{H_2O} / p_{H_2} ratio facilitating more rapid breakdown of the oxide layer, and therefore greater carbon removal.

* The peak carbon monoxide and carbon dioxide values for the specimens austenitised for 2hr prior to introduction of the decarburisation atmosphere correspond to the values obtained at the time when the peak values were observed for the specimens not austenitised in hydrogen.

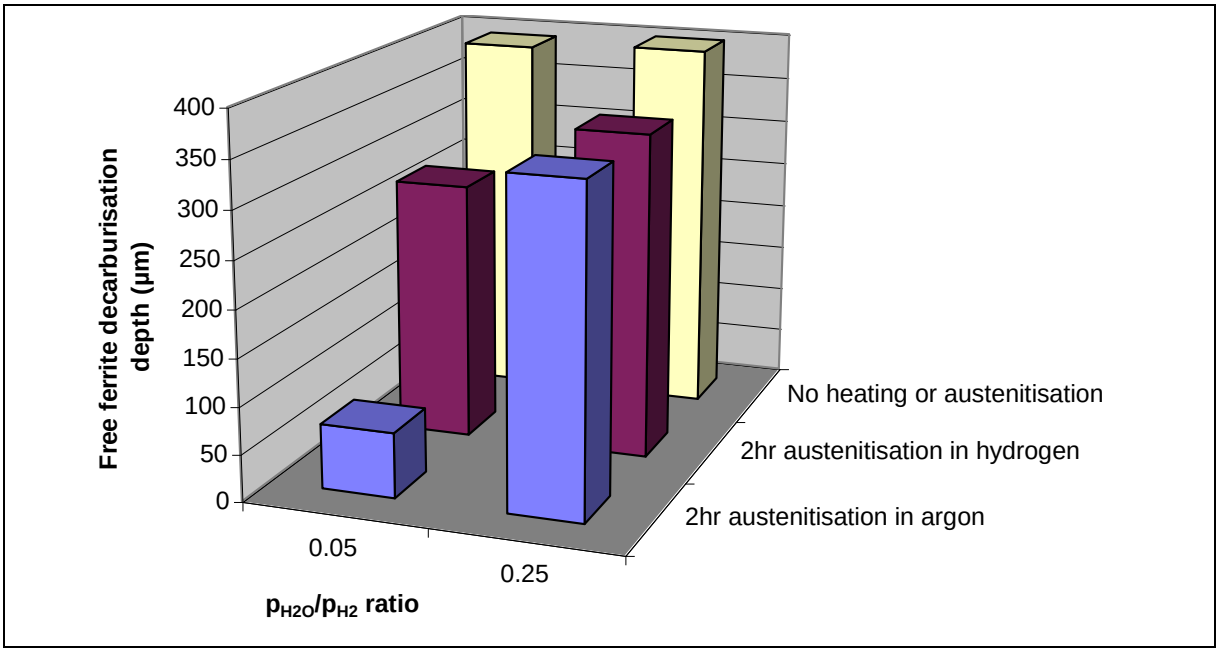

Figure 10.35 Free ferrite decarburisation depths for furnace cooled SUP7 initial structures after 4hr decarburisation at 820°C using p_{H_2O} / p_{H_2} ratios of 0.05 and 0.25 with, and without, heating and 2hr austenitisation in argon and hydrogen.

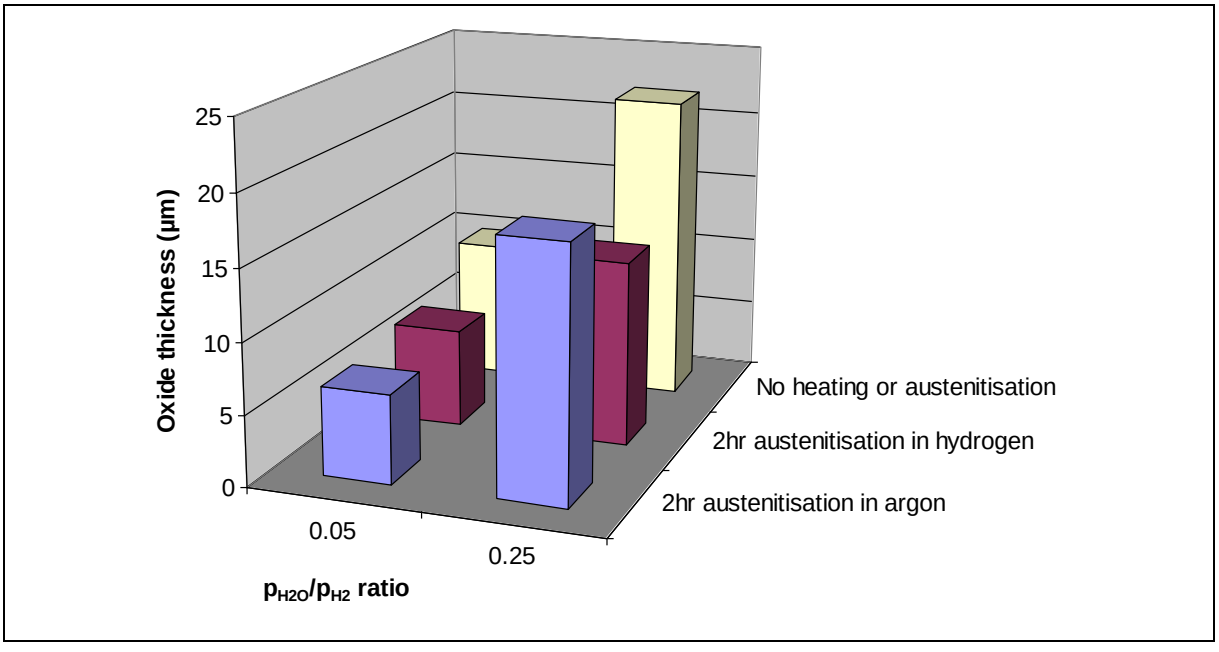

Figure 10.36 Oxide thicknesses for furnace cooled SUP7 initial structures after 4hr decarburisation at 820°C using p_{H_2O} / p_{H_2} ratios of 0.05 and 0.25 with, and without, heating and 2hr austenitisation in argon and hydrogen.

Both values were lower than the 392 and 399μm measured for the p_{H_2O} / p_{H_2} ratios of 0.05 and 0.25 of the specimens decarburised without prior austenitisation. The oxide structures were also thinner than those obtained at the comparable p_{H_2O} / p_{H_2} ratios for the specimens decarburised without prior austenitisation, as illustrated in Figure 10.36. The oxide thicknesses for decarburisation at p_{H_2O} / p_{H_2} ratios of 0.05 and 0.25 after prior austenitisation in argon and hydrogen were similar.

Decarburisation commenced as soon as the decarburisation atmosphere was introduced after austenitising in hydrogen, which differs from the decarburisation with a prior argon anneal. The decarburisation inhibition after austenitisation in argon was more prevalent at the 0.05 p_{H_2O} / p_{H_2} ratio, with a free ferrite depth of only 69μm. This compares to 275μm for austenitisation in hydrogen. However, the free ferrite depths after decarburisation at a p_{H_2O} / p_{H_2} ratio of 0.25 with prior austenitisation in argon and hydrogen were similar.

The greater free ferrite depths at the 0.05 p_{H_2O} / p_{H_2} ratio for prior austenitisation in hydrogen compared with argon are considered to be due to the more complete hydrogen flush undertaken before the specimens were inserted into the hot zone, as opposed to the argon flush which was undertaken while the specimens were heating to temperature. Consequently, the lower resulting water content in the hydrogen during austenitisation relative to the argon anneal while the specimens heated would have resulted in less SiO_2 formation , and therefore less carbon removal inhibition. The larger free ferrite depths obtained without prior austenitisation in hydrogen or argon appear to be mainly due to the rapid decarburisation that occurred when the specimens were exposed to the decarburisation atmosphere as they were heating.

10.6.3 Carbon removal during specimen heating

The decarburisation occurring during the early stages of the heat treatments was dependent upon whether the specimens were inserted from the cold end of the tube furnace into the established decarburisation atmosphere, or were austenitised in hydrogen prior to introduction of the decarburisation atmosphere. The heating profile of a 5mm diameter x 50mm furnace cooled specimen to within 5°C of the Ac_3 temperature of 820°C is illustrated in Figure 10.37,

in conjunction with the associated carbon monoxide and carbon dioxide concentration profiles for decarburisation at a p_{H_2O} / p_{H_2} ratio of 0.25. The time from when the second curve concentration profiles began after 100s, to the peak concentrations, was only 120s. Over this period of time the temperature increased from 590 to 775°C. In order to investigate the early stages of decarburisation, it was necessary to increase the time between these two temperatures.

This was achieved by heat treating 12mm diameter by 20mm specimens. The 5 and 12mm diameter specimens have identical surface areas along their lengths of 754mm^2, although the total surface area of the 12mm diameter specimen, 980mm^2, was higher than the 825mm^2 of the 5mm diameter specimen,. The heating and gas concentration profiles of the 12mm diameter specimens at 820°C with a p_{H_2O} / p_{H_2} ratio of 0.25 are also illustrated in Figure 10.37. The heating of the 12mm diameter specimen to comparable temperatures for the 5mm diameter specimen was slower. The time from the start to the peak of the second curve for the larger diameter specimen almost doubled to 216s, with the second peak starting after 204s.

The peak carbon monoxide and carbon dioxide concentrations for the 5mm diameter specimen of 1815 and 150vppm respectively, differed considerably from the values of 1325 and 480vppm for the 12mm diameter specimen. Given that the surface area of the 12mm diameter specimen was almost 20% greater than the 5mm diameter specimen, and that the early stages of decarburisation were controlled by surface carbon removal before oxidation influenced the decarburisation processes, higher peak gas concentrations were expected for the 12mm diameter specimen. However, the sum of the peak carbon monoxide and carbon dioxide concentrations yielded similar values of 1965 and 1805vppm respectively for the 5 and 12mm diameter specimens. The lower carbon monoxide, and higher carbon dioxide peak concentrations for the 12mm diameter specimen illustrate that a greater fraction of the carbon removed from the steel was present in the exhaust gas as carbon dioxide.

The carbon monoxide and carbon dioxide concentrations of 530 and 200vppm for the 12mm diameter specimen after 15min exceeded the respective concentrations of 365 and 60vppm for the 5mm diameter specimen. The total gas concentrations after 15min of 730vppm for the 12mm diameter specimen was almost twice the value of 425vppm for the 5mm diameter

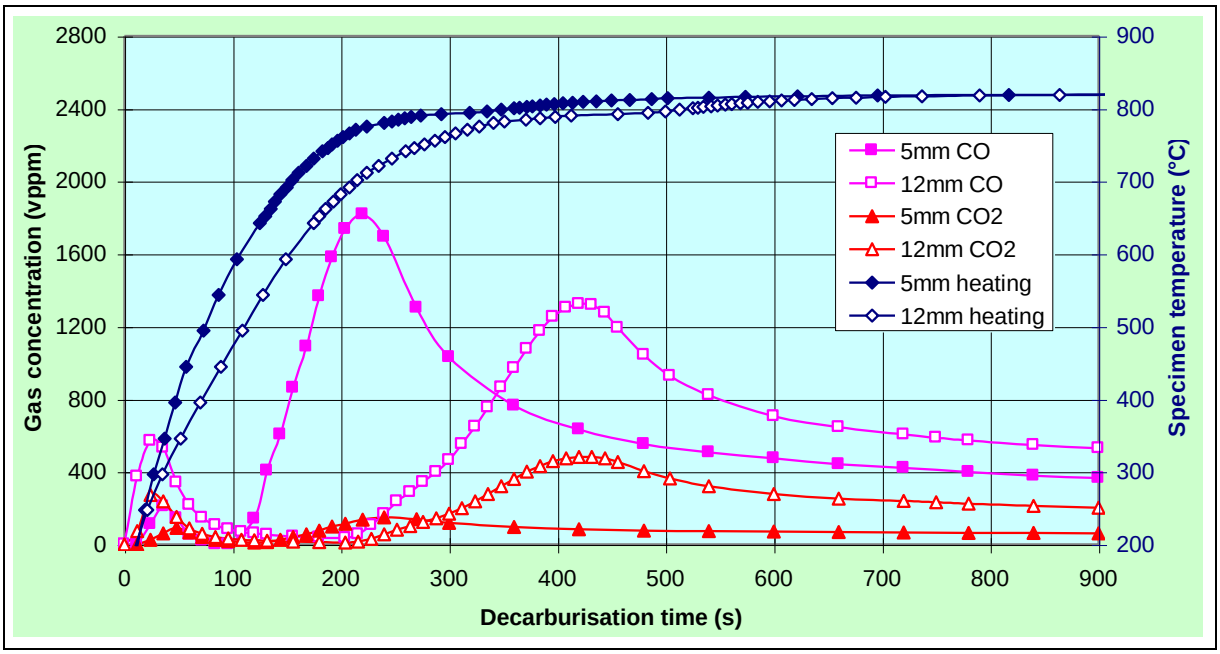

Figure 10.37 Heating and gas concentration profiles for decarburisation of 5mm diameter by 50mm and 12mm diameter by 20mm furnace cooled SUP7 initial structures at 820°C with p_{H_2O} / p_{H_2} =0.25.

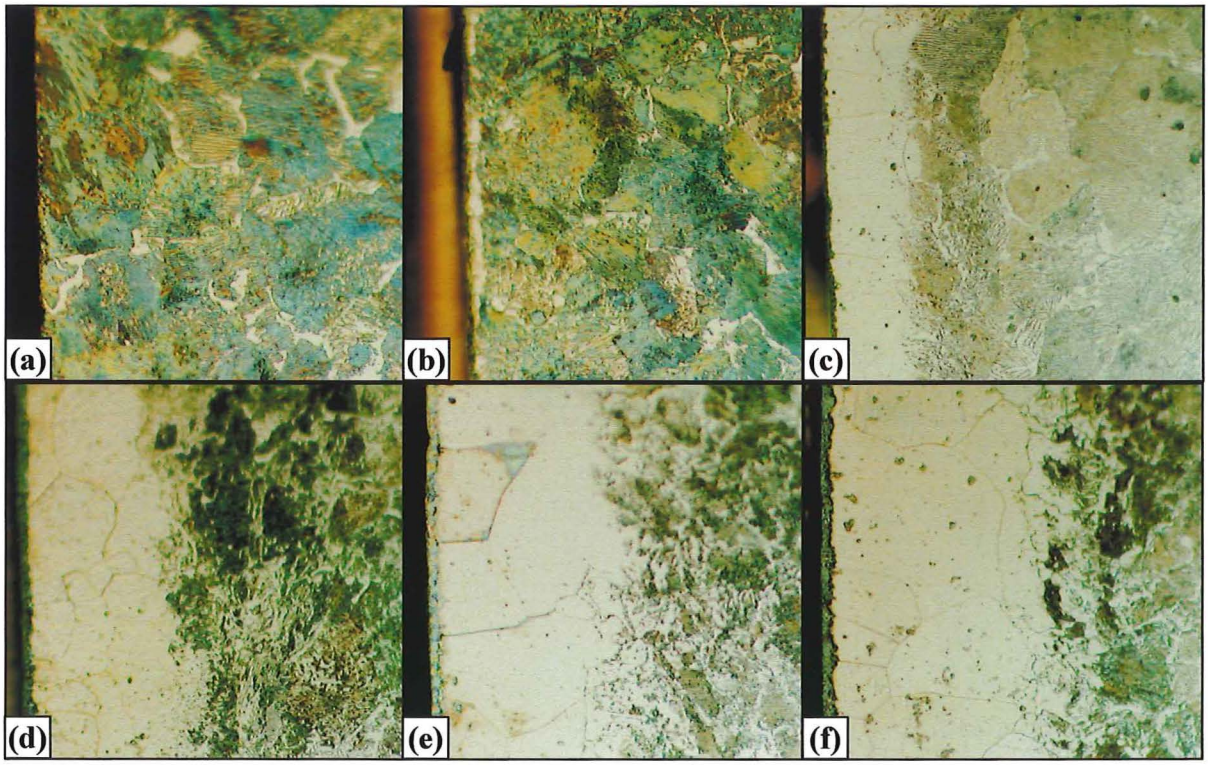

Figure 10.38 Microstructures for 12mm diameter by 20mm furnace cooled SUP7 initial structures decarburised at 820°C with a p_{H_2O} / p_{H_2} ratio of 0.25 for (a) 2.5min, (b) 5min, (c) 7.5min, (d) 10min, (e) 12.5min, and (f) 15min. 2% Nital etch. 575x magnification.

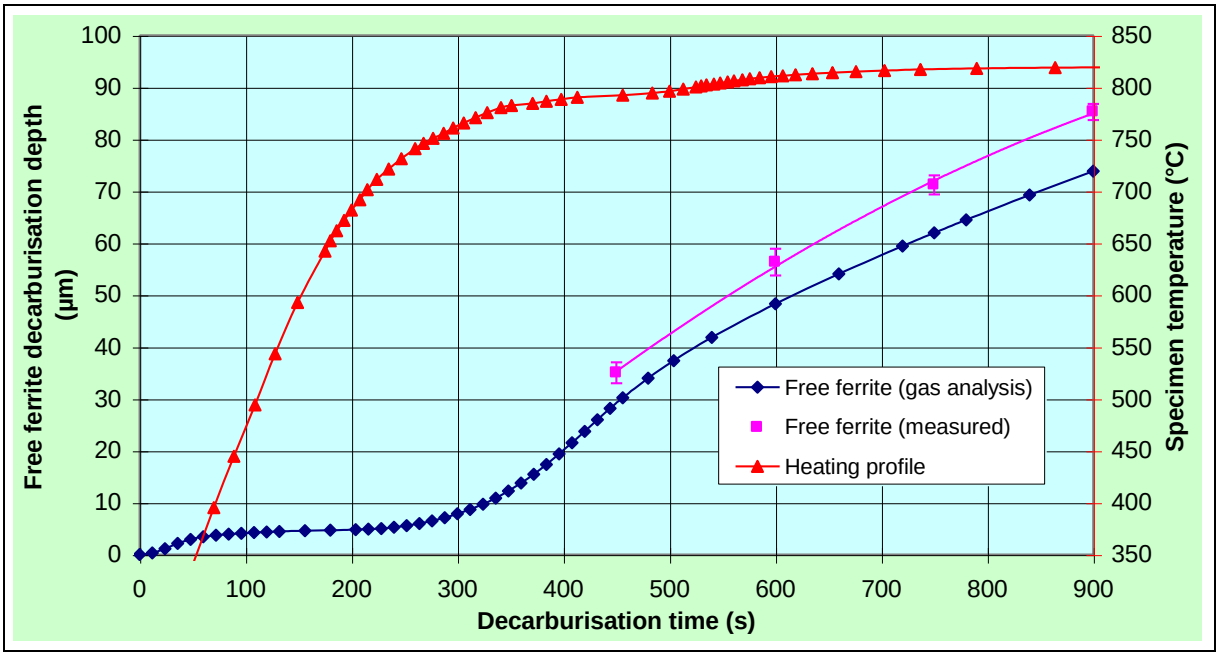

Figure 10.39 Measured and calculated free ferrite depths for the decarburisation of 12mm diameter by 20mm furnace cooled SUP7 initial structures at 820°C with p_{H_2O} / p_{H_2} =0.25.

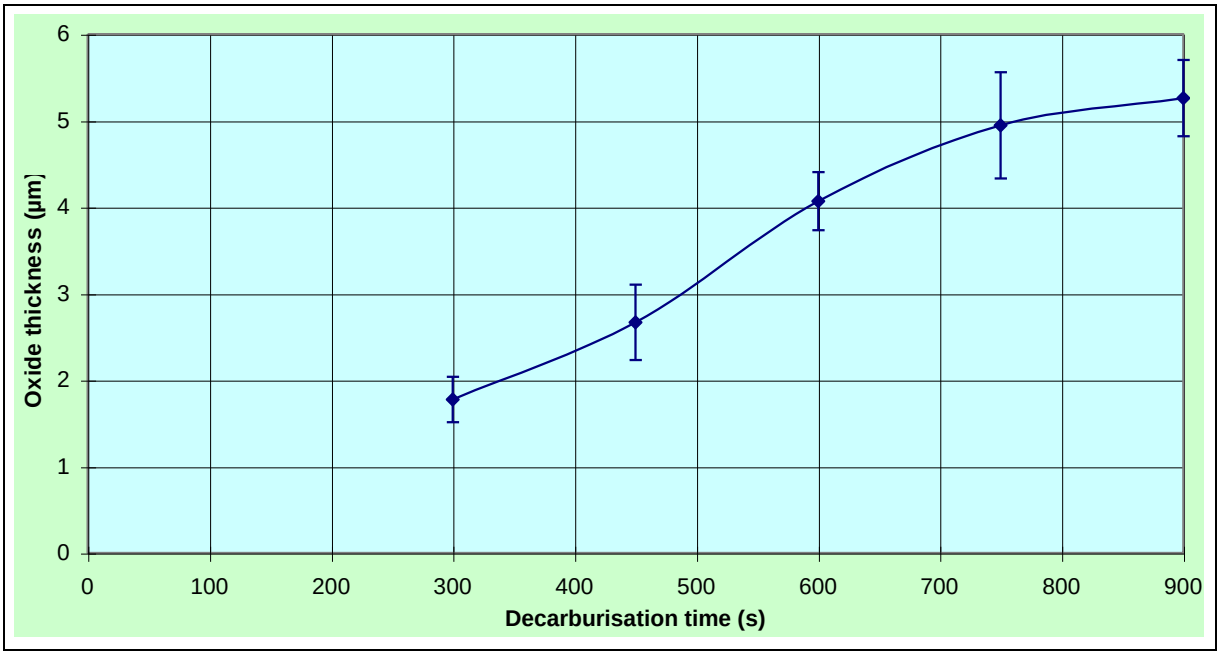

Figure 10.40 Oxidation kinetics for the decarburisation of 12mm diameter by 20mm furnace cooled SUP7 initial structures at 820°C with p_{H_2O} / p_{H_2} =0.25.

specimen. This was considered to be due to the slower heating of the 12mm diameter specimen than the 5mm diameter specimen, which resulted in slower austenitisation kinetics, and the greater surface area of the ferrite/austenite interface at the heat treatment temperature. Consequently, the higher austenite carbon contents, and greater ferrite/cementite and ferrite/austenite interfacial areas of the 12mm diameter specimen at comparable test durations resulted in a greater rate of carbon supply for removal by the decarburisation atmosphere.

The start of the second gas concentration curves for the 5mm diameter specimen occurred at approximately 590°C, which was 100°C lower than for the 12mm diameter specimen. However, the peak gas concentrations occurred at similar temperatures of 775 and 790°C for the 5 and 12mm diameter specimens respectively. The microstructures obtained during the early stages of decarburising 12mm diameter test specimens were investigated for 2.5min time intervals, from 2.5 to 15min. A p_{H_2O} / p_{H_2} ratio of 0.25 was used, as it gave the fastest decarburisation kinetics during the first 15min of the p_{H_2O} / p_{H_2} ratios investigated, as illustrated in Figures 10.17 and 10.18 respectively. This allowed the difference between the 2.5min time intervals to be accentuated by the maximum amount. The higher p_{H_2O} / p_{H_2} ratio also yielded measurable oxide thicknesses. Table 10.5 lists the specimen temperatures at the end of each test duration investigated.

The tests commenced with the specimen being pushed from the right hand end cap end of the tube furnace into the hot zone, once the decarburisation atmosphere was fully established. The test was concluded by pushing the specimen out of the hot zone to the left hand end cap end of the tube furnace, with a 5min argon flush at 2L/min established to ensure that the specimen cooled in an inert atmosphere. Figure 10.38 illustrates the microstructures obtained for the six time intervals. No surface free ferrite or oxide structure was visible after 2.5min, Figure 10.38(a). After 5min, Figure 10.38(b), a very thin surface free ferrite layer had formed around most of the test specimen, with a surface oxide layer visible. The free ferrite depth had increased considerably by 7.5min, Figure 10.38(c), with a columnar grain structure and a uniform ferrite/pearlite interface. The free ferrite depth and oxide thickness increased further with time, as illustrated in Figures 10.38(d) to 10.38(f).

Table 10.5 Temperatures obtained after each test duration for the 12mm diameter by 20mm furnace cooled initial structures.

Time (s)	150	300	450	600	750	900
Temperature (°C)	593	762	792	810	817	819

The free ferrite depths measured from the heat treated microstructures are illustrated in Figure 10.39. Also plotted are the decarburisation depths calculated from the carbon monoxide and carbon dioxide gas concentration data, with the measured free ferrite depths greater than the calculated values. The lower calculated values could have been due to some carbon removal occurring by equation 3.1, resulting in methane formation. The increasing oxide thickness with time is illustrated in Figure 10.40.

10.7 Summary of decarburisation investigation

The decarburisation investigation for SUP7 detailed in this chapter involved the following:

i) Decarburisation of 5mm diameter by 80mm test specimens with different hydrogen flow rates and p_{H_2O} / p_{H_2} ratios to determine the influence of flow rate on the decarburisation;

ii) Decarburisation heat treatments of furnace cooled and 96hr tempered martensite initial structures at the Ac_3 temperature and a p_{H_2O} / p_{H_2} ratio of 0.05 after heating;

iii) Decarburisation heat treatments of different initial structures at the Ac_3 temperature and p_{H_2O} / p_{H_2} ratios of 0.05 and 0.25 after heating and 2hr austenitisation in argon;

iv) Comparison of the free ferrite kinetics for the furnace cooled and 96hr tempered martensite initial structures after heating in argon and decarburisation at the Ac_3 temperature with a p_{H_2O} / p_{H_2} ratio of 0.05;

v) Determination of the influence of the initial structure on the free ferrite kinetics after austenitisation in argon and decarburisation at the Ac_3 temperature with 0.05 and 0.25 p_{H_2O} / p_{H_2} ratios;

vi) Comparison of the oxidation kinetics for the furnace cooled and 96hr tempered martensite initial structures after heating in argon and decarburisation at the Ac_3 temperature with a p_{H_2O} / p_{H_2} ratio of 0.05;

vii) Comparison of the ferrite columnar grain growth kinetics for the furnace cooled and 96hr tempered martensite initial structures after heating in argon and decarburisation at the Ac_3 temperature with a p_{H_2O} / p_{H_2} ratio of 0.05:

viii) Determination of the influence of the initial structure on the columnar grain growth kinetics after austenitisation in argon and decarburisation at the Ac_3 temperature with 0.05 and 0.25 p_{H_2O} / p_{H_2} ratios;

ix) Decarburisation heat treatments of SUP7 furnace cooled and 96hr tempered martensite initial structures inserted into the established decarburisation atmosphere maintained at the Ac_3 temperature with a p_{H_2O} / p_{H_2} ratio of 0.05;

x) Comparison of the free ferrite, oxide thickness and columnar grain growth kinetics for heat treatments involving no heating, heating, and heating plus 2hr austenitisation in argon prior to the introduction of the decarburisation atmosphere at the Ac_3 temperature and a p_{H_2O} / p_{H_2} ratio of 0.05;

xi) Comparison of the free ferrite depths measured with those calculated from the carbon monoxide and carbon dioxide evolved during decarburisation and from an effective diffusion coefficient for carbon in ferrite of $1.6 \times 10^{-6} cm^2/s$ for decarburisation involving the insertion of the specimens into the established decarburisation atmosphere;

xii) Decarburisation heat treatments for furnace cooled initial structures inserted into the established decarburisation atmosphere at the Ac_3 temperature and different p_{H_2O} / p_{H_2} ratios;

xiii) Decarburisation heat treatments of furnace cooled initial structures inserted into the established decarburisation atmosphere at different temperatures with a p_{H_2O} / p_{H_2} ratio of 0.05;

xiv) Decarburisation heat treatments for different initial structures inserted into the established decarburisation atmosphere at the Ac_3 temperature and a p_{H_2O} / p_{H_2} ratio of 0.05;

xv) Determination of the influence of p_{H_2O} / p_{H_2} ratio on the carbon monoxide and carbon dioxide concentration profiles at the Ac_3 temperature;

xvi) Determination of the influence of temperature on the carbon monoxide and carbon dioxide concentration profiles at a p_{H_2O} / p_{H_2} ratio of 0.05;

xvii) Determination of the influence of initial structure on the carbon monoxide and carbon dioxide concentration profiles at the Ac_3 temperature and a p_{H_2O} / p_{H_2} ratio of 0.05;

xviii) A description of the influence of p_{H_2O} / p_{H_2} ratio on the free ferrite depths, oxide thicknesses and ferrite columnar grain sizes after 4hr decarburisation at the Ac_3 temperature;

xix) A description of the influence of temperature and initial structure on the free ferrite depths, oxide thicknesses and ferrite columnar grain sizes after 4hr decarburisation at a p_{H_2O} / p_{H_2} ratio of 0.05;

xx) Influence of a 4hr argon anneal on the free ferrite depths, oxide thicknesses and ferrite columnar grain sizes after 4hr decarburisation at the Ac_3 temperature and a p_{H_2O} / p_{H_2} ratio of 0.05;

xxi) Comparison of the decarburisation behaviour of a furnace cooled initial structure obtained following 2hr austenitisation in hydrogen with that for insertion of the specimen into the established decarburisation atmosphere;

xxii) An investigation into the decarburisation kinetics of a furnace cooled initial structure inserted into the established heat treatment atmosphere while the specimen heated to temperature.

The following chapter details the decarburisation experimentation undertaken for the different silicon steels.

CHAPTER 11

DECARBURISATION OF THE DIFFERENT SILICON STEELS

11.1 Introduction

In order to facilitate a consistent decarburisation investigation between the different steels, 5mm diameter by 50mm specimens with furnace cooled initial structures and ground surface finishes were produced. The decarburisation heat treatments were undertaken by inserting the test specimens into an established decarburisation atmosphere, with no prior heating or austenitisation. The carbon monoxide and carbon dioxide gases evolved during each heat treatment were measured. Decarburisation experiments were undertaken at the respective Ac_3 temperatures for each steel with p_{H_2O} / p_{H_2} ratios of 0 to 1.0, and for temperatures of 650 to 900°C with a p_{H_2O} / p_{H_2} ratio of 0.05.

The free ferrite depths, oxide thicknesses, oxide concentration profiles and microhardness profiles were measured from the decarburised microstructures. This investigation allowed the decarburisation and oxidation kinetics of the different steels to be quantified as a function of the decarburisation atmosphere composition and heat treatment temperature. The influence of silicon and manganese on the decarburisation behaviour was also quantified. This chapter details the results obtained from the decarburisation of the different silicon steels, and the analysis and explanation of these results.

11.2 Microstructural investigation

11.2.1 Influence of p_{H_2O} / p_{H_2} ratio

The microstructures obtained after 4hr decarburisation of the 0% Silicon, 1% Silicon, SUP7 and SUP7NV steels at their respective Ac_3 temperatures and a p_{H_2O} / p_{H_2} ratio of 0.01 are illustrated in Figure 11.1. Some surface free ferrite was evident for the 0% Silicon steel at 740°C, Figure 11.1(a), with a deeper free ferrite layer for the 1% Silicon steel at 760°C,

Figure 11.1(b). However, the ferrite/martensite interface was poorly defined. The ferrite layer was thicker for SUP7 at 820°C, with a columnar ferrite grain structure, and a sharply defined ferrite/martensite interface, as illustrated in Figure 11.1(c). Figure 11.1(d) shows negligible surface decarburisation for SUP7NV at 820°C. This was despite the only difference between the SUP7 and SUP7NV compositions being the elevated niobium and vanadium contents of SUP7NV. No decarburisation was observed for the 3% Silicon steel at 835°C with a p_{H_2O} / p_{H_2} ratio of 0.01.

The decarburised microstructures for the 0% Silicon, 1% Silicon, SUP7 and 3% Silicon steels at the respective Ac_3 temperatures and a p_{H_2O} / p_{H_2} ratio of 0.05 are illustrated in Figure 11.2. The increase in the p_{H_2O} / p_{H_2} ratio from 0.01 resulted in uniform free ferrite layers for the 0 and 1% Silicon steels, Figures 11.2(a) and 11.2(b) respectively. The 0% Silicon steel had a columnar ferrite grain structure, while the ferrite grains of the 1% Silicon steel, which exhibited an increased depth of decarburisation, were equiaxed. The reason for this is not readily apparent. The free ferrite depth of SUP7, Figure 10.22(c), was greater than that of the 0 and 1% Silicon steels, with the ferrite grains being columnar. The 0% Silicon, 1% Silicon and SUP7 steels had uniform ferrite/martensite interfaces, compared to the poorly defined interface for SUP7NV, Figure 11.2(c). The free ferrite depth of SUP7NV was similar to SUP7. However, instead of the columnar grain structure of SUP7, SUP7NV exhibited a predominantly fine equiaxed ferrite grain structure, with some larger equiaxed grains near the surface.

Negligible decarburisation was observed for the 3% Silicon steel at a p_{H_2O} / p_{H_2} ratio of 0.05, Figure 11.2(d). However, decarburisation at a p_{H_2O} / p_{H_2} ratio of 0.25 yielded a free ferrite layer for the 3% Silicon steel, Figure 11.3(a). The ferrite grains were equiaxed, with a poorly defined ferrite/martensite interface. The incomplete transformation to austenite after 4hr was illustrated by the undissolved ferrite in the ferrite/austenite core. Uniformly distributed graphite was also evident in the ferrite and the martensite. No free ferrite was observed for the five steels after 4hr decarburisation in hydrogen at their respective Ac_3 temperatures, as illustrated for SUP7 in Figure 11.3(b).

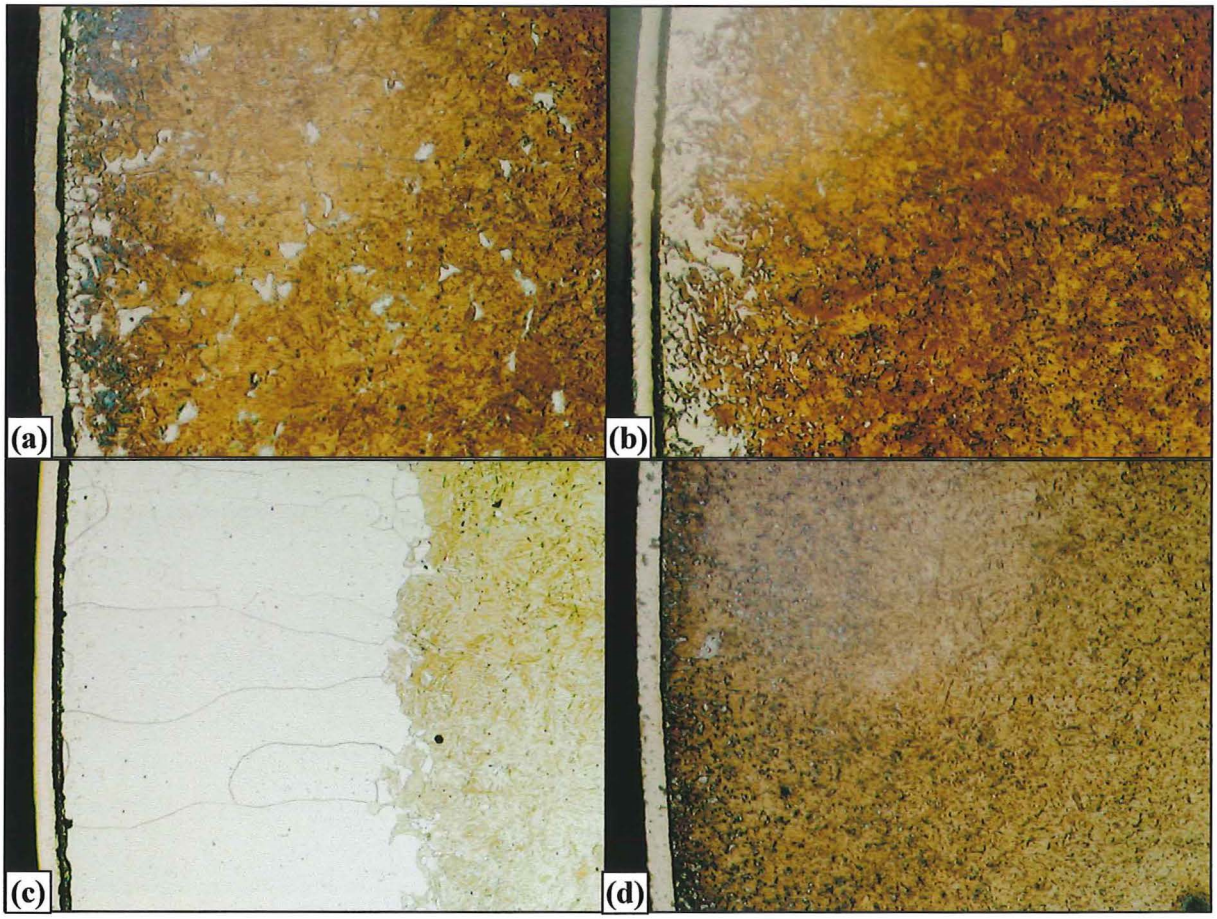

Figure 11.1 Decarburised microstructures for furnace cooled initial structures after 4hr heat treatment at p_{H_2O} / p_{H_2}=0.01 for (a) 0% Silicon at 740°C, (b) 1% Silicon at 760°C, (c) SUP7 at 820°C, and (d) SUP7NV at 820°C. 2% Nital etch. 230x magnification.

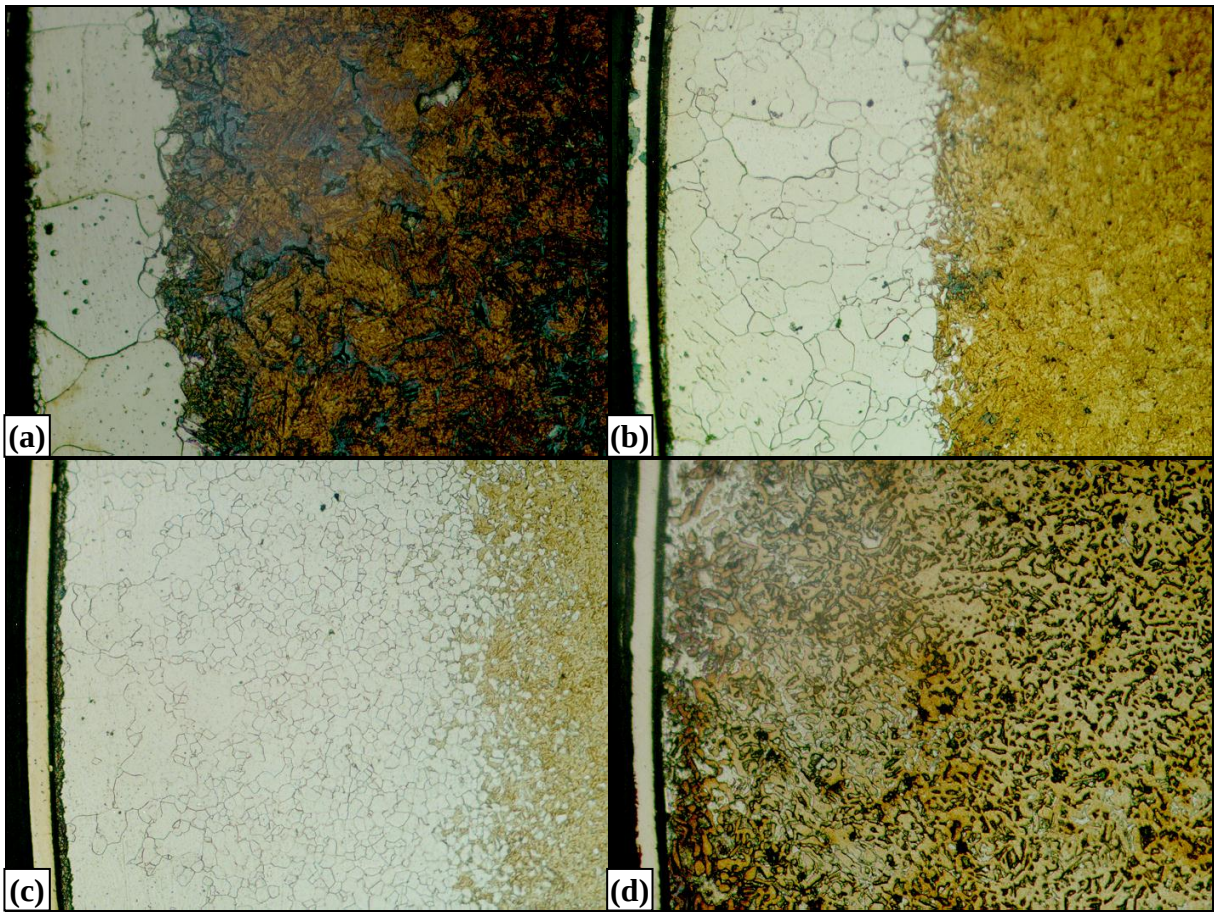

Figure 11.2 Decarburised microstructures for furnace cooled initial structures after 4hr heat treatment at p_{H_2O} / p_{H_2} =0.05 for (a) 0% Silicon at 740°C, (b) 1% Silicon at 760°C, (c) SUP7NV at 820°C, and (d) 3 Silicon at 835°C. 2% Nital etch. 230x magnification.

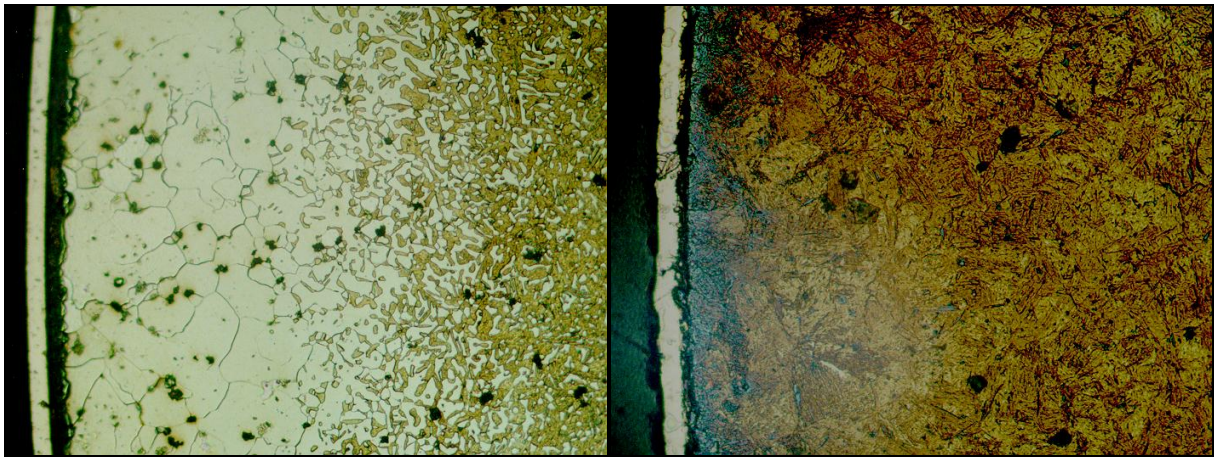

(a) **(b)**

Figure 11.3 Decarburised microstructures for furnace cooled initial structures after 4hr heat treatment of (a) 3% Silicon with a p_{H_2O} / p_{H_2} ratio of 0.25 at 835°C, and (b) SUP7 in hydrogen at 820°C. 2% Nital etch. 230x magnification.

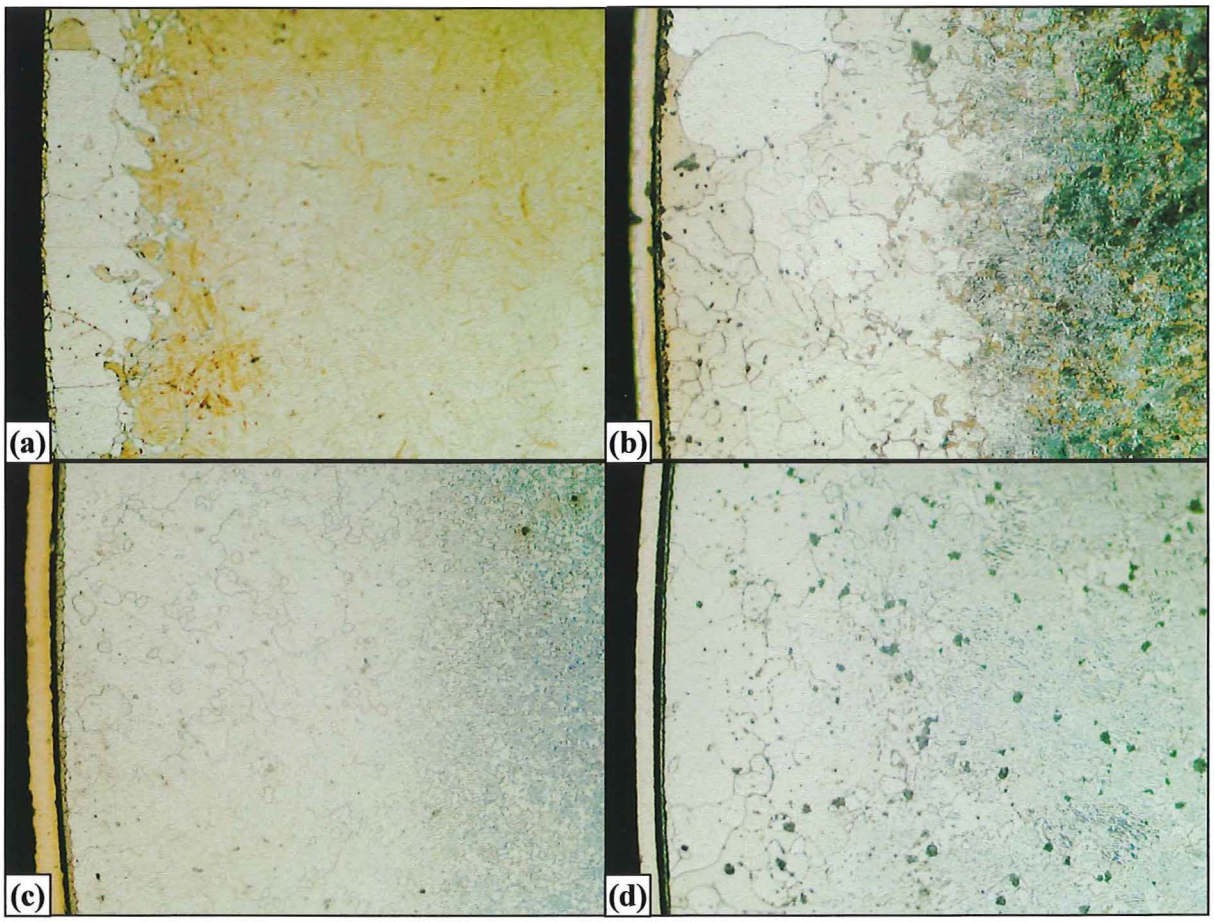

Figure 11.4 Decarburisation microstructures after 4hr heat treatment at 750°C with p_{H_2O} / p_{H_2}=0.05 for furnace cooled initial structures of (a) 0% Silicon, (b) 1% Silicon, (c) SUP7NV, and (d) 3% Silicon steels. 2% Nital etch. 230x magnification.

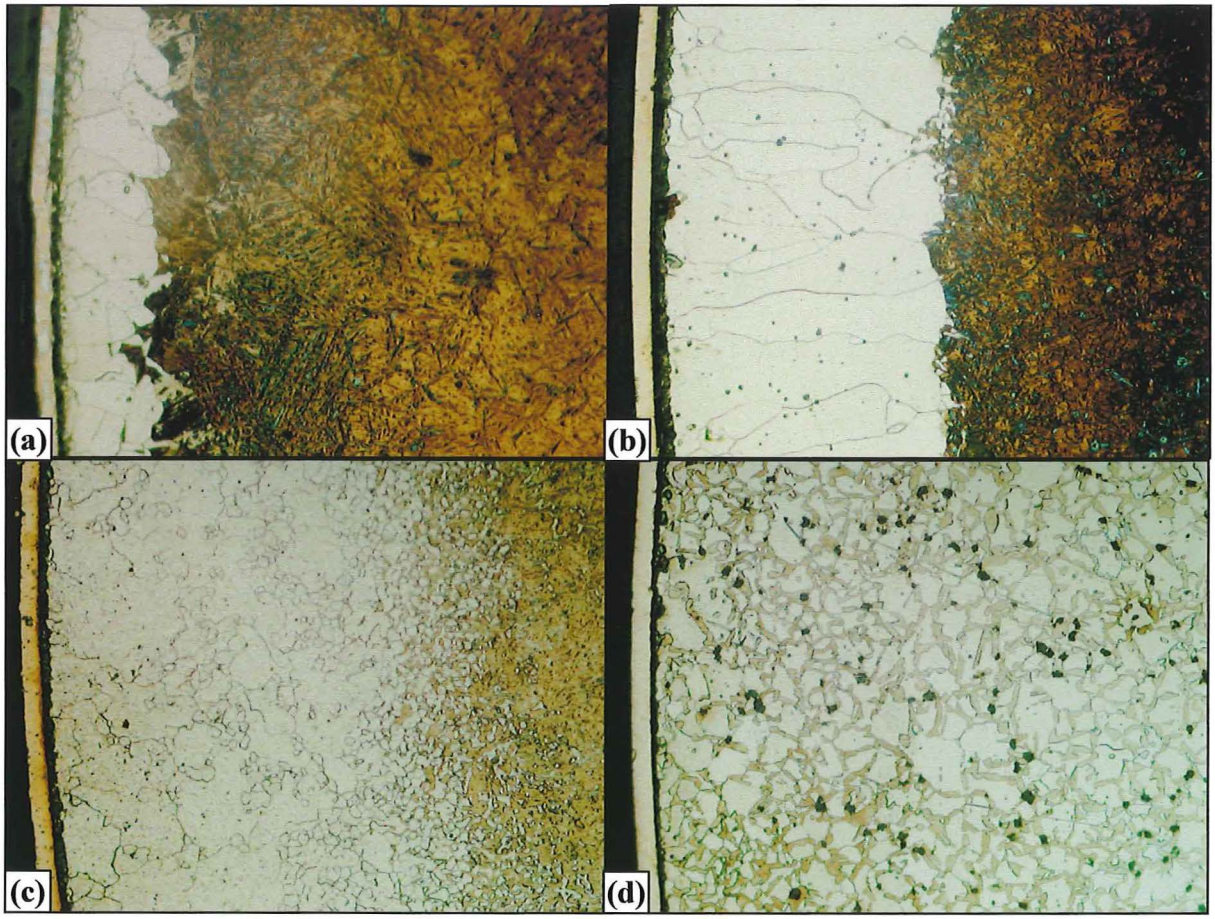

Figure 11.5 Decarburisation microstructures after 4hr heat treatment at 800°C with p_{H_2O} / p_{H_2}=0.05 for furnace cooled initial structures of (a) 0% Silicon, (b) 1% Silicon, (c) SUP7NV, and (d) 3% Silicon steels. 2% Nital etch. 230x magnification.

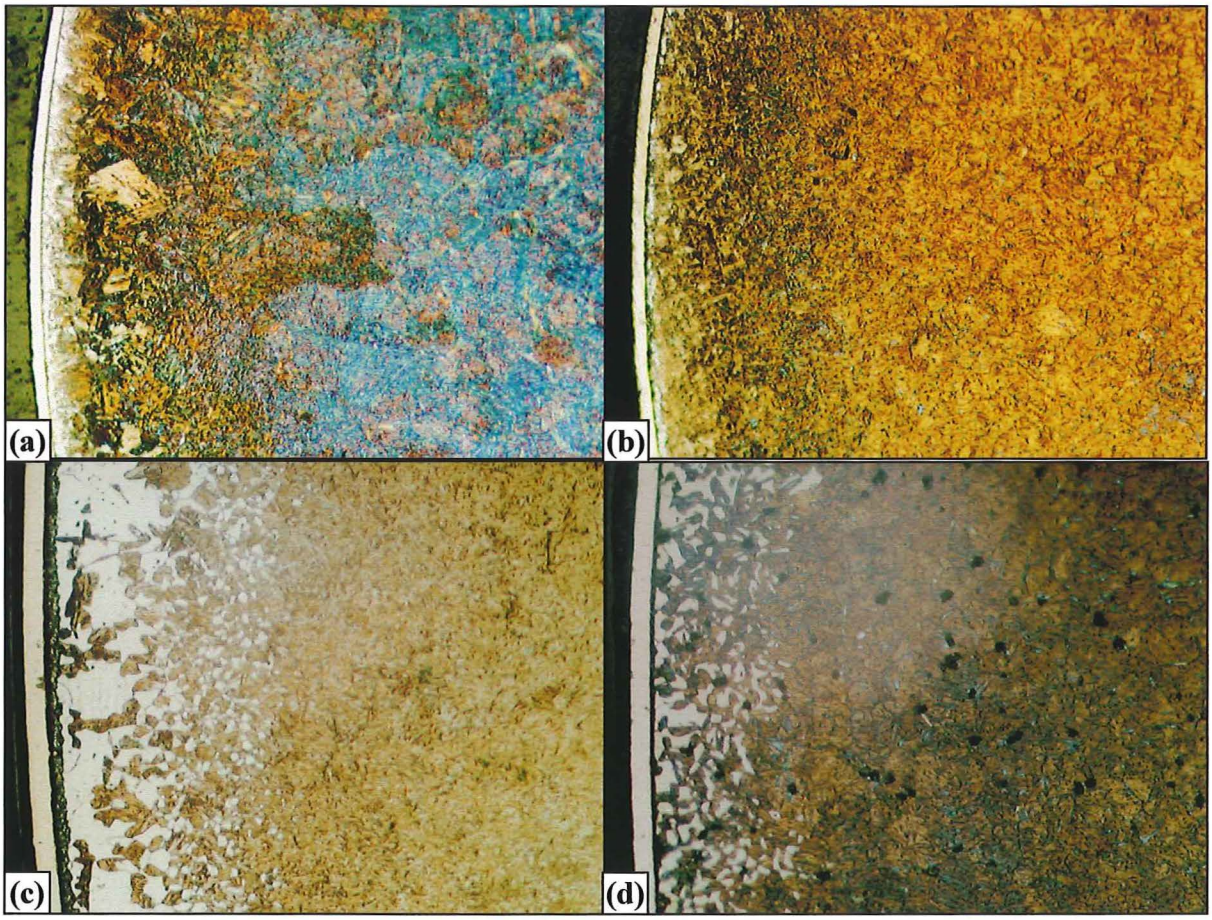

Figure 11.6 Decarburisation microstructures after 4hr heat treatment at 900°C with p_{H_2O} / p_{H_2} =0.05 for furnace cooled initial structures of (a) 0% Silicon, (b) 1% Silicon at 115x magnification, and (c) SUP7NV, and (d) 3% Silicon at 230x magnification. 2% Nital etch.

11.2.2 Influence of temperature

Decarburisation of the different silicon steels at 750°C with a p_{H_2O} / p_{H_2} ratio of 0.05 yielded a columnar free ferrite layer for the 0% Silicon steel separated from a martensite core by a poorly defined ferrite/martensite interface, Figure 11.4(a). A thicker free ferrite surface layer with an equiaxed grain structure was observed for the 1% Silicon steel, Figure 11.4(b). The interface separating the free ferrite and the pearlite/martensite core comprised discrete martensite grains on the ferrite grain boundaries. The thickest free ferrite layer resulted for SUP7, with the columnar free ferrite layer and pearlite core illustrated in Figure 10.22(b). Some fine cementite particles delineated the ferrite/martensite interface.

The free ferrite depth of SUP7NV at 750°C, Figure 11.4(c), was similar to that of SUP7. However, the ferrite grains were equiaxed with a duplex structure comprising small and large grains. A large number of fine carbides were present in the free ferrite. Figure 11.4(d) illustrates the thinner ferrite layer of the 3% Silicon steel relative to SUP7 and SUP7NV. This ferrite was equiaxed, with graphite particles distributed throughout the pearlite core.

A thinner columnar free ferrite layer was observed for the 0% Silicon steel decarburised at 800°C, Figure 11.5(a), than at 750°C. The ferrite/martensite interface was also poorly defined. Figure 11.5(b) shows a deeper free ferrite layer for the 1% Silicon steel than at 750°C. The ferrite/martensite interface was sharply defined, with the equiaxed grain structure of 750°C replaced by a columnar structure. The ferrite/martensite interface for SUP7NV at 800°C was poorly defined, as illustrated in Figure 11.5(c). A duplex free ferrite equiaxed grain structure was again evident, with fine undissolved carbides present in the ferrite. No decarburisation was observed at 800°C for the 3% Silicon steel, Figure 11.5(d). The microstructure comprised martensite grains dispersed on the ferrite grain boundaries, with uniformly dispersed graphite particles in the martensite grains.

The decarburisation microstructures at 900°C differ considerably from these at 800°C. Figure 11.6(a) and (b) shows that no free ferrite surface layers were present for the 0 and 1% Silicon steels. There was a noticeable change in the colour of the martensite from the surface inwards, which suggests a carbon concentration gradient. This was confirmed by the microhardness profiles of Section 11.7.2. SUP7 exhibited a thinner free ferrite layer at 900°C, Figure 10.22,

than at 820°C, with a poorly defined ferrite/martensite interface. Figure 11.6(c) illustrates that SUP7NV also had a thinner free ferrite layer at 900°C than at 800°C, with martensite grains in contact with the surface in some areas. No undissolved carbides were present in the ferrite. Some free ferrite was observed for the 3% Silicon steel at 900°C, with graphite particles dispersed throughout the microstructure.

11.3 Infra-red gas analysis data

This section details the carbon monoxide and carbon dioxide gas concentration profiles for the decarburisation of the 0% Silicon, 1% Silicon, SUP7NV and 3% Silicon steels with different p_{H_2O} / p_{H_2} ratios at their respective Ac_3 temperatures, and at different temperatures with a p_{H_2O} / p_{H_2} ratio of 0.05. Tables 11.1 and 11.2 list the peak carbon monoxide concentrations, the concentrations at 15min, and the mass of carbon removed after 15min as a function of p_{H_2O} / p_{H_2} ratio and temperature. The results of this section indicate that the decarburisation kinetics were dependent on the temperature, p_{H_2O} / p_{H_2} ratio and the alloy content of the steels. The following sections detail the free ferrite decarburisation depths, the oxide thicknesses, and the analysis of the oxidation structures of the different silicon steels. These results allowed the mechanisms controlling the decarburisation of these steels to be established, as described in Section 11.7.5.

11.3.1 Decarburisation of the 0% Silicon steel

The carbon monoxide and carbon dioxide concentration profiles during the first 15min decarburisation of the 0% Silicon steel at the Ac_3 temperature of 740°C for p_{H_2O} / p_{H_2} ratios of 0.01 to 0.50 are illustrated in Figures 11.7 and 11.8 respectively. The concentration profiles for the 1.0 ratio were not recorded as the carbon monoxide gas analyser malfunctioned at this ratio. The peak* carbon monoxide concentrations increased from 50vppm to 210 and 220vppm as the p_{H_2O} / p_{H_2} ratio increased from 0.01 to 0.05 and 0.25, Table 11.1, before decreasing to 115vppm at the 0.50 ratio. However, the peak carbon dioxide concentration almost tripled to 60vppm as the p_{H_2O} / p_{H_2} ratio increased to 0.25.

*Peak taken as the highest value of the second or third peak.

Table 11.1 Influence of p_{H_2O} / p_{H_2} ratio on the gas concentrations and carbon removal during the decarburisation of the different silicon steels with furnace cooled initial structures at their respective Ac_3 temperatures.

STEEL	Temperature	Gas concentration/ Carbon removed	p_{H_2O} / p_{H_2} RATIO									
			0.01		0.05		0.25		0.5		1.0	
			CO	CO_2	CO	CO_2	CO	CO_2	CO	CO_2	CO	CO_2
0% Silicon	740°C	$vppm_{PEAK}$	50	0	210	25	220	60	115	20	-	-
		$vppm_{15min}$	35	0	165	15	170	45	105	20	-	-
		$\mu g\ C_{15min}$	0.17		0.73		0.81		0.36		-	
1% Silicon	760°C	$vppm_{PEAK}$	65	0	315	30	465	130	345	80	260	40
		$vppm_{15min}$	60	0	280	25	335	100	315	70	240	40
		$\mu g\ C_{15min}$	0.24		1.04		1.65		1.09		0.66	
SUP7	820°C	$vppm_{PEAK}$	600	20	1615	130	1815	150	1270	80	1520	60
		$vppm_{15min}$	410	8	410	30	365	60	350	30	485	20
		$\mu g\ C_{15min}$	1.83		2.63		2.74		2.11		2.52	
SUP7NV	820°C	$vppm_{PEAK}$	195	9	995	130	1130	400	770	265	1190	320
		$vppm_{15min}$	125	4	400	45	315	110	235	80	400	100
		$\mu g\ C_{15min}$	0.66		2.45		2.71		1.73		2.49	
3% Silicon	835°C	$vppm_{PEAK}$	45	0	750	85	1215	405	805	275	1060	345
		$vppm_{15min}$	30	0	60	7	295	95	225	90	180	120
		$\mu g\ C_{15min}$	0.16		0.85		2.57		1.47		2.24	

Table 11.2 Influence of temperature on the gas concentrations and the carbon removal during the decarburisation of the different silicon steels with furnace cooled initial structures at a p_{H_2O} / p_{H_2} ratio of 0.05.

STEEL	Gas concentration/ Carbon removed	TEMPERATURE (°C)									
		700		750		800		850		900	
		CO	CO_2	CO	CO_2	CO	CO_2	CO	CO_2	CO	CO_2
0% Silicon	$vppm_{PEAK}$	30	0	195	15	240	20	415	35	720	55
	$vppm_{15min}$	25	0	140	10	135	10	200	15	310	20
	$\mu g\ C_{15min}$	0.13		0.61		0.75		1.12		1.80	
1% Silicon	$vppm_{PEAK}$	45	0	175	10	430	40	515	50	685	65
	$vppm_{15min}$	35	0	175	10	220	20	235	20	265	20
	$\mu g\ C_{15min}$	0.18		0.54		1.16		1.40		1.73	
SUP7	$vppm_{PEAK}$	180	15	530	65	1085	100	2005	135	2395	155
	$vppm_{15min}$	180	150	315	35	350	30	425	30	375	25
	$\mu g\ C_{15min}$	0.36		1.31		2.15		2.63		2.81	
SUP7NV	$vppm_{PEAK}$	65	11	295	55	795	80	1315	110	1795	260
	$vppm_{15min}$	65	11	260	50	340	35	290	20	370	65
	$\mu g\ C_{15min}$	0.20		0.99		2.02		2.10		2.89	
3% Silicon	$vppm_{PEAK}$	50	9	200	30	460	60	660	80	1470	135
	$vppm_{15min}$	50	9	150	20	415	6	110	15	185	15
	$\mu g\ C_{15min}$	0.14		0.61		0.84		0.99		1.36	

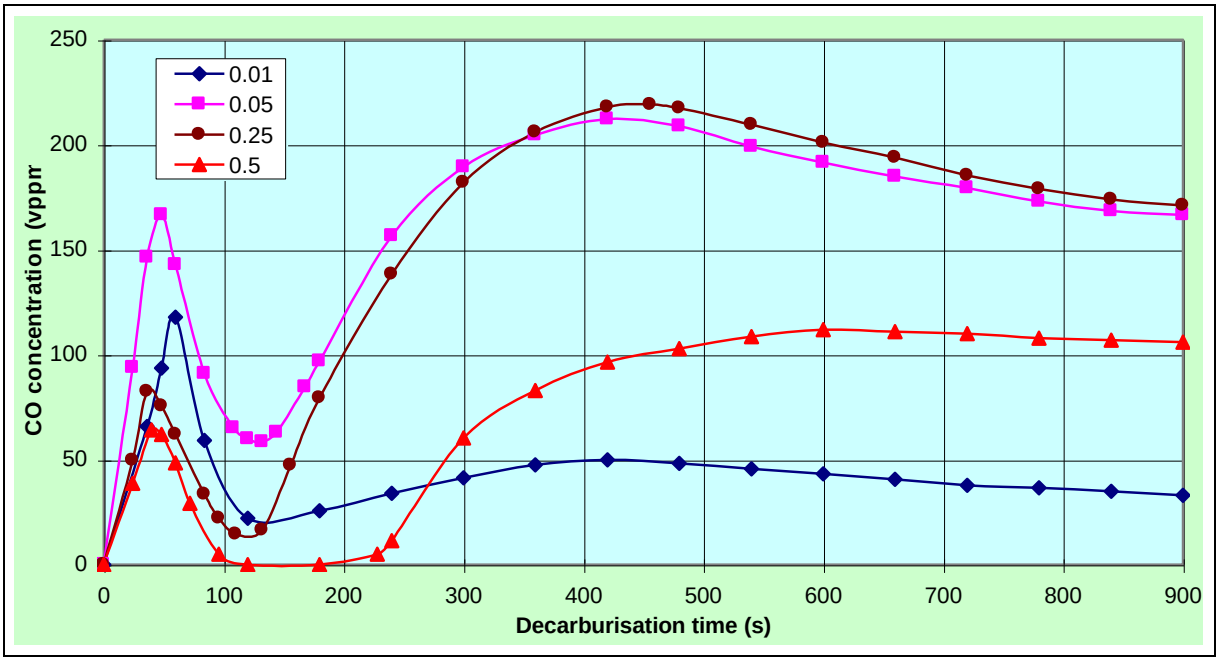

Figure 11.7 Carbon monoxide concentration profiles for the decarburisation of 0% Silicon furnace cooled initial structures at 740°C with different p_{H_2O} / p_{H_2} ratios.

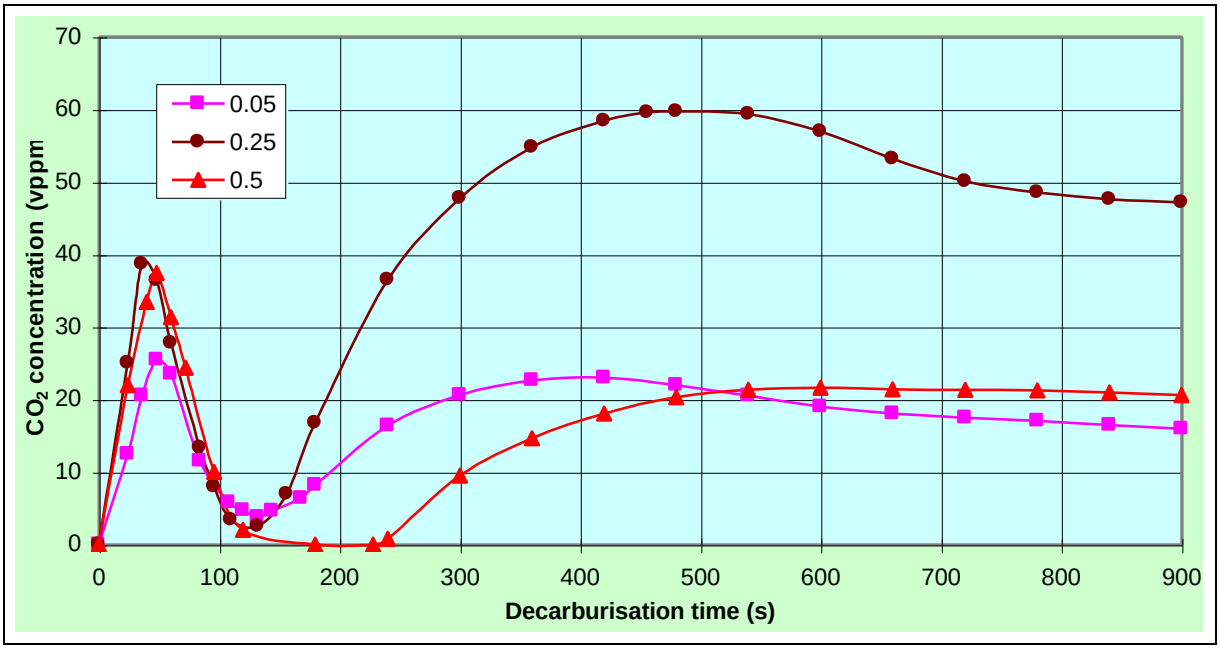

Figure 11.8 Carbon dioxide concentration profiles for the decarburisation of 0% Silicon furnace cooled initial structures at 740°C with different p_{H_2O} / p_{H_2} ratios.

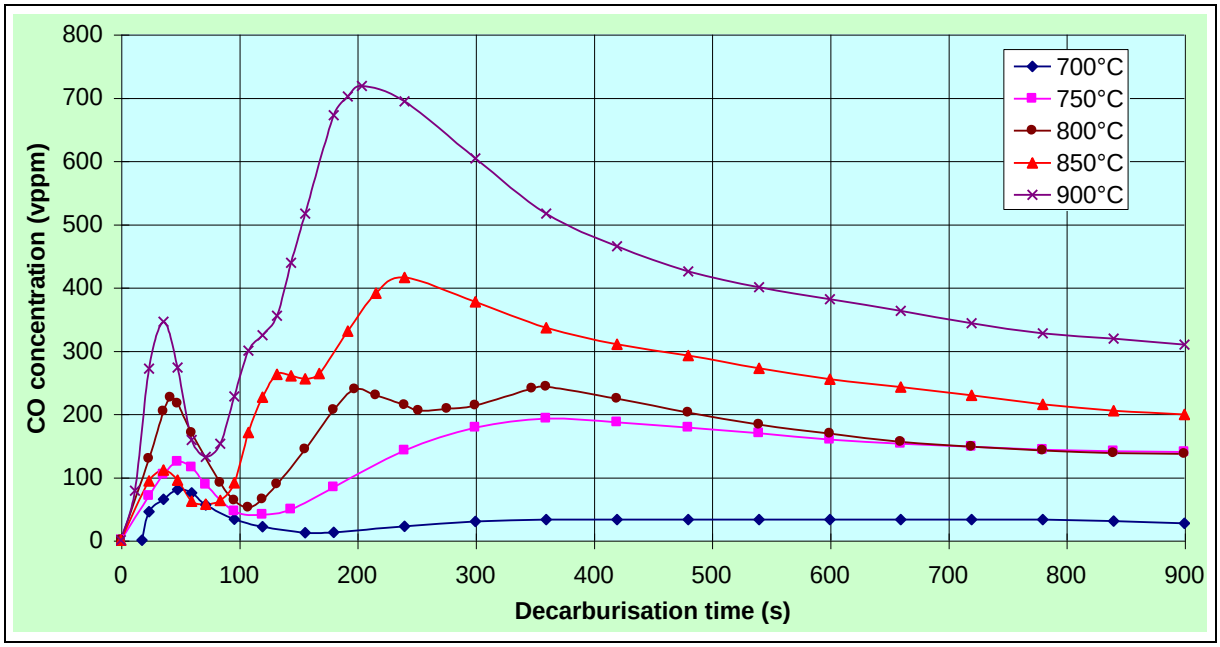

Figure 11.9 Carbon monoxide concentration profiles for the decarburisation of furnace cooled 0% Silicon initial structures at different temperatures with p_{H_2O} / p_{H_2} =0.05.

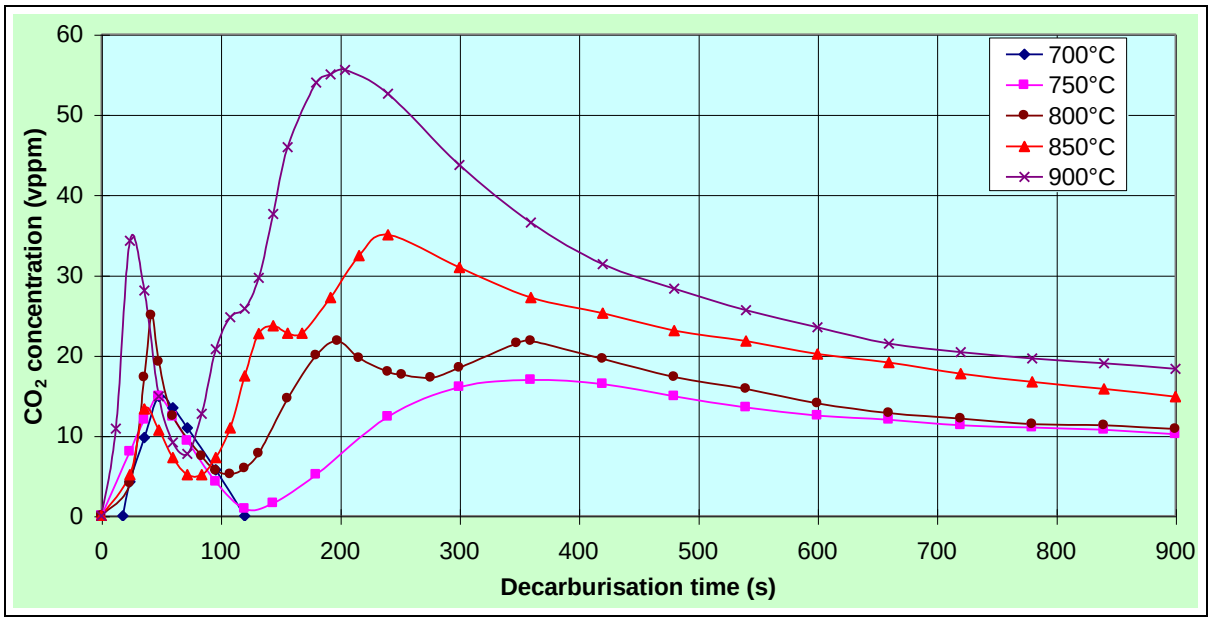

Figure 11.10 Carbon dioxide concentration profiles for the decarburisation of furnace cooled 0% Silicon initial structures at different temperatures with p_{H_2O} / p_{H_2} =0.05.

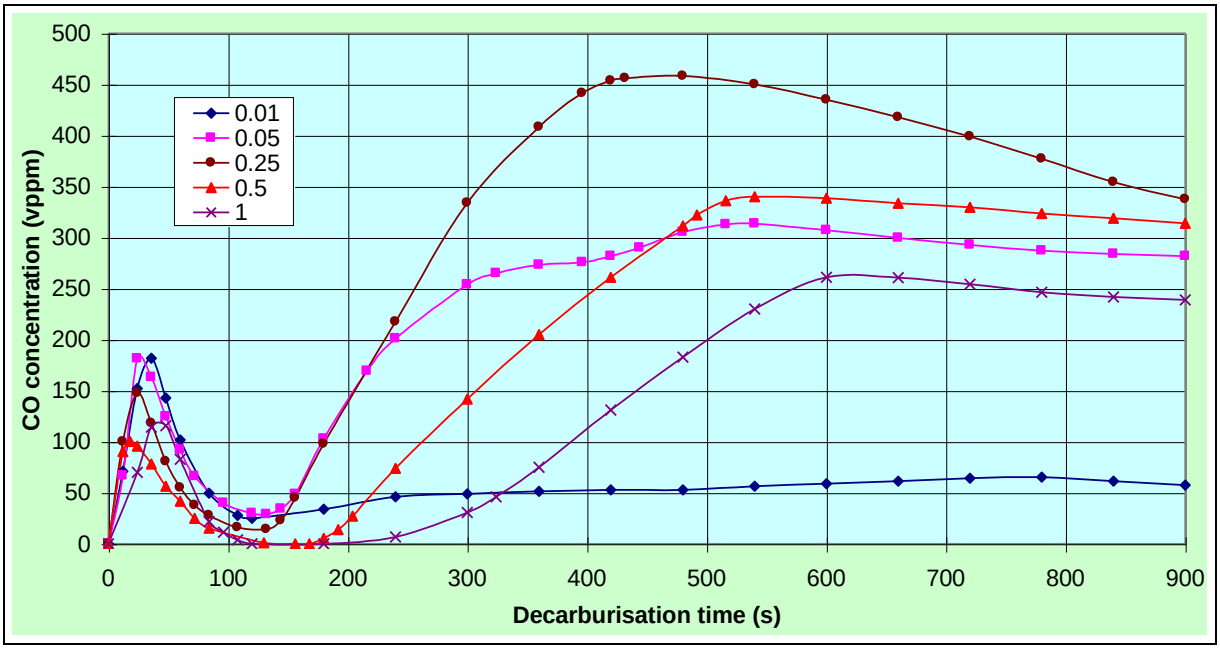

Figure 11.11 Carbon monoxide concentration profiles for the decarburisation of furnace cooled 1% Silicon initial structures at 760°C with different p_{H_2O} / p_{H_2} ratios.

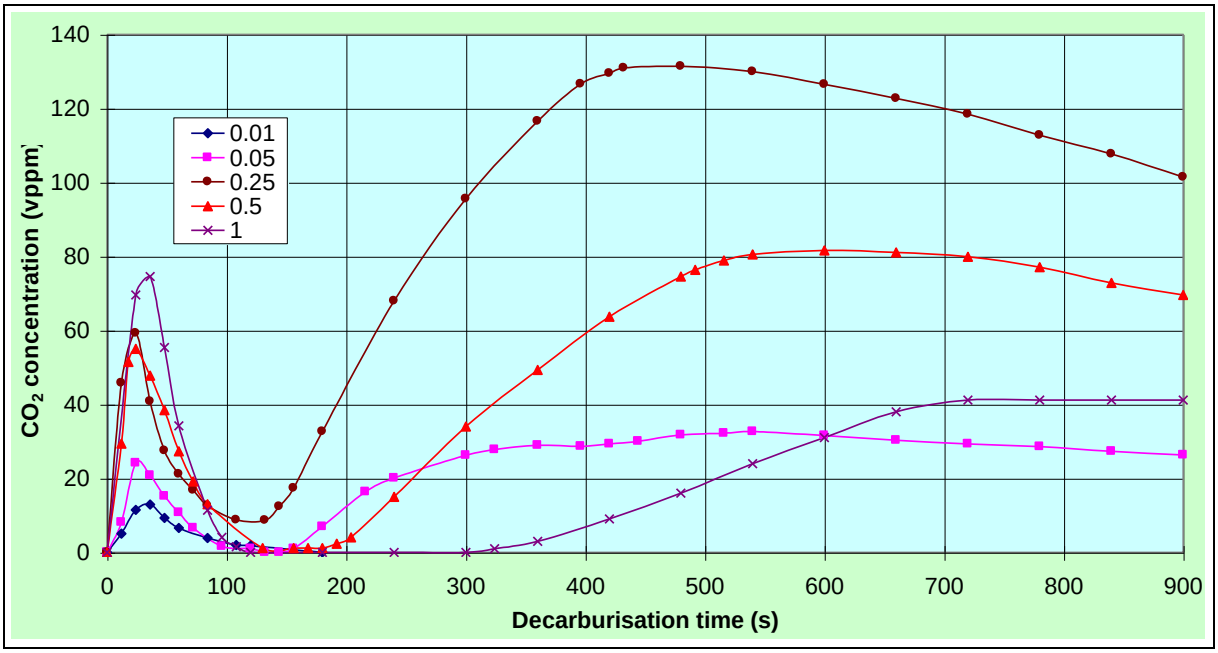

Figure 11.12 Carbon dioxide concentration profiles for the decarburisation of furnace cooled 1% Silicon initial structures at 760°C with different p_{H_2O} / p_{H_2} ratios.

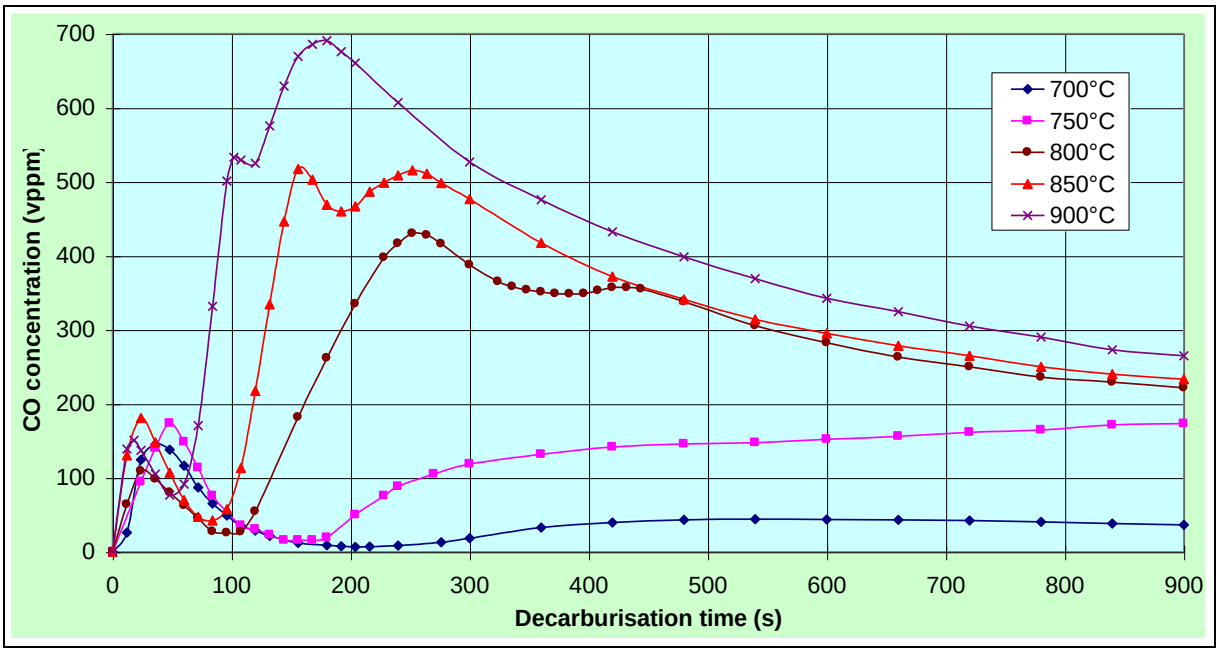

Figure 11.13 Carbon monoxide concentration profiles for the decarburisation of furnace cooled 1% Silicon initial structures at different temperatures with p_{H_2O} / p_{H_2} =0.05.

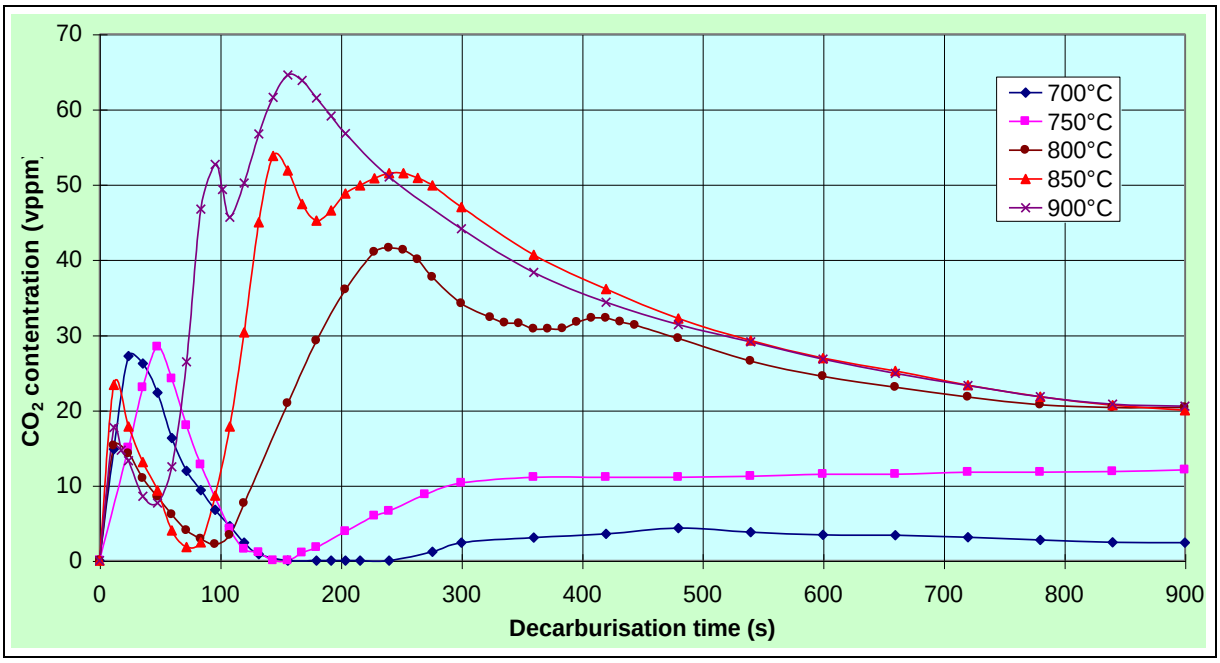

Figure 11.14 Carbon dioxide concentration profiles for the decarburisation of furnace cooled 1% Silicon initial structures at different temperatures with p_{H_2O} / p_{H_2} =0.05.

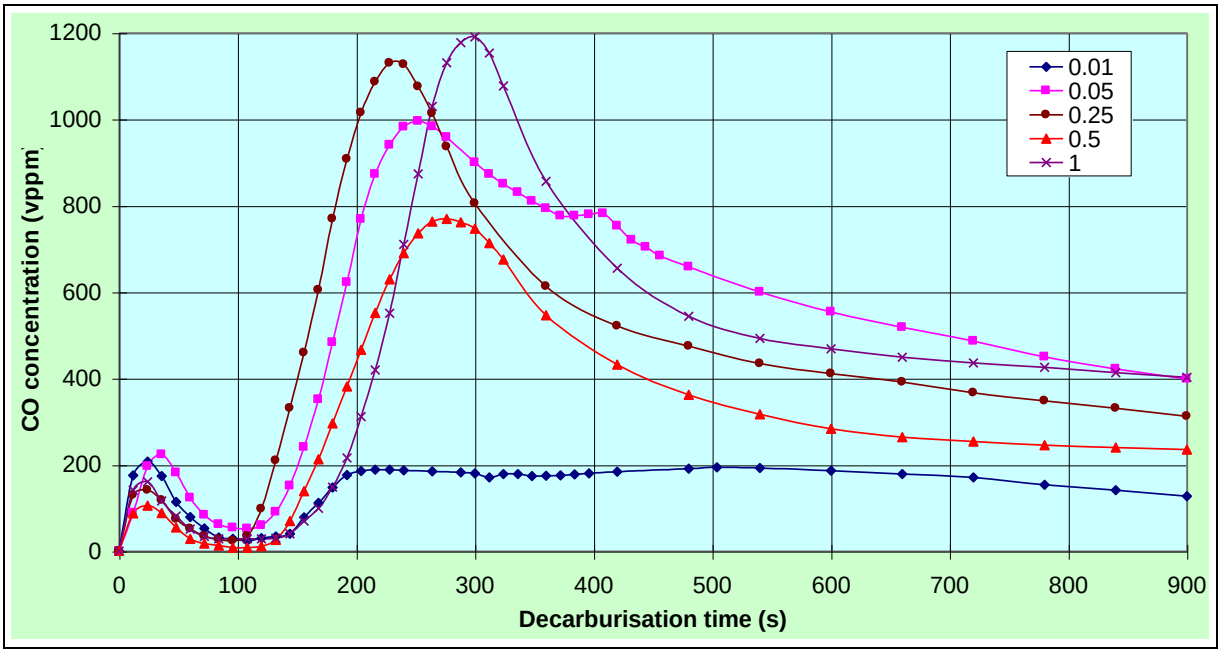

Figure 11.15 Carbon monoxide concentration profiles for the decarburisation of furnace cooled SUP7NV initial structures at 820°C with different p_{H_2O} / p_{H_2} ratios.

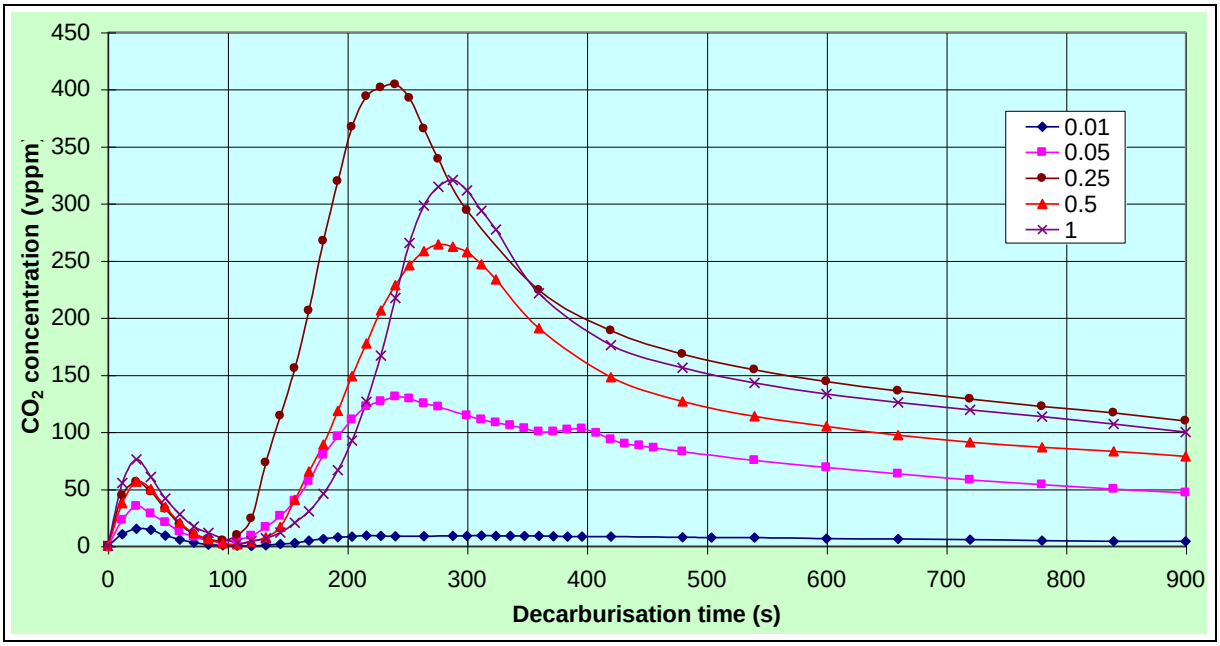

Figure 11.16 Carbon dioxide concentration profiles for the decarburisation of furnace cooled SUP7NV initial structures at 820°C with different p_{H_2O} / p_{H_2} ratios.

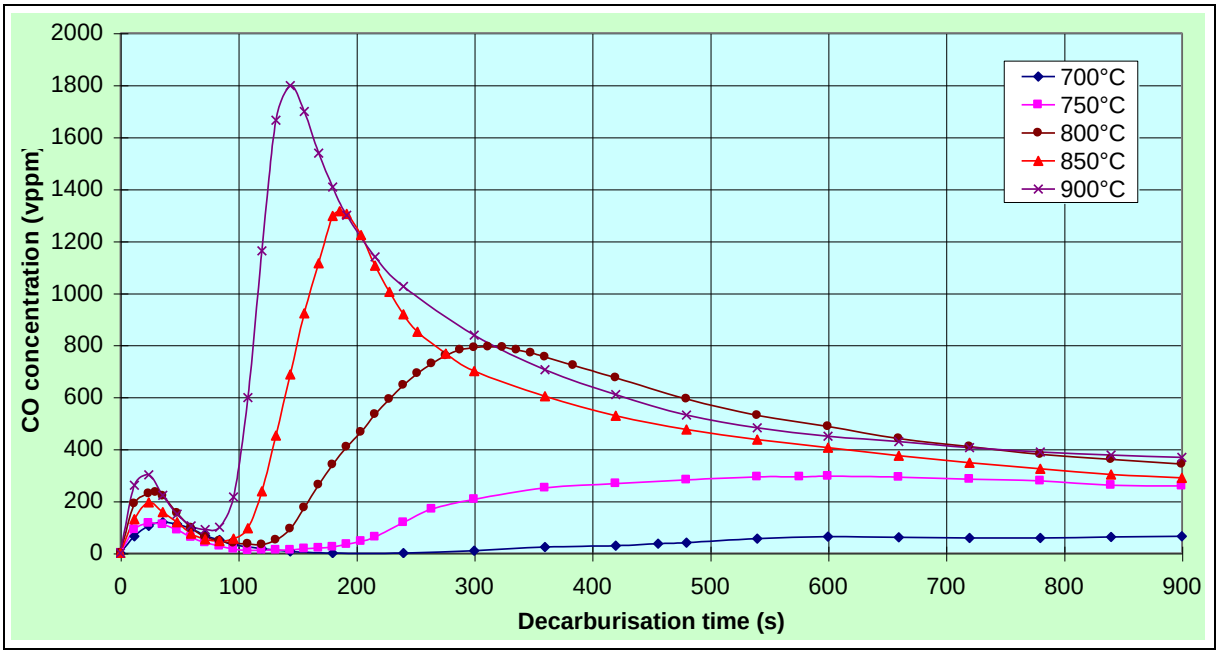

Figure 11.17 Carbon monoxide concentration profiles for the decarburisation of furnace cooled SUP7NV initial structures at different temperatures with p_{H_2O} / p_{H_2} =0.05.

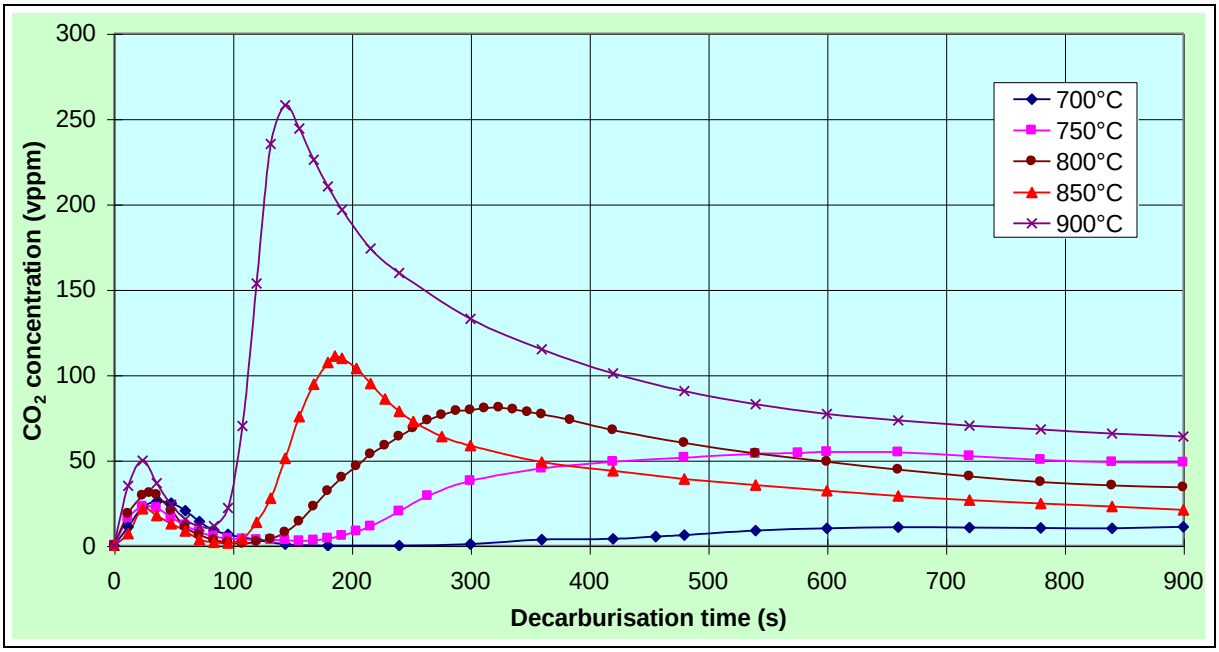

Figure 11.18 Carbon dioxide concentration profiles for the decarburisation of furnace cooled SUP7NV initial structures at different temperatures with p_{H_2O} / p_{H_2} =0.05.

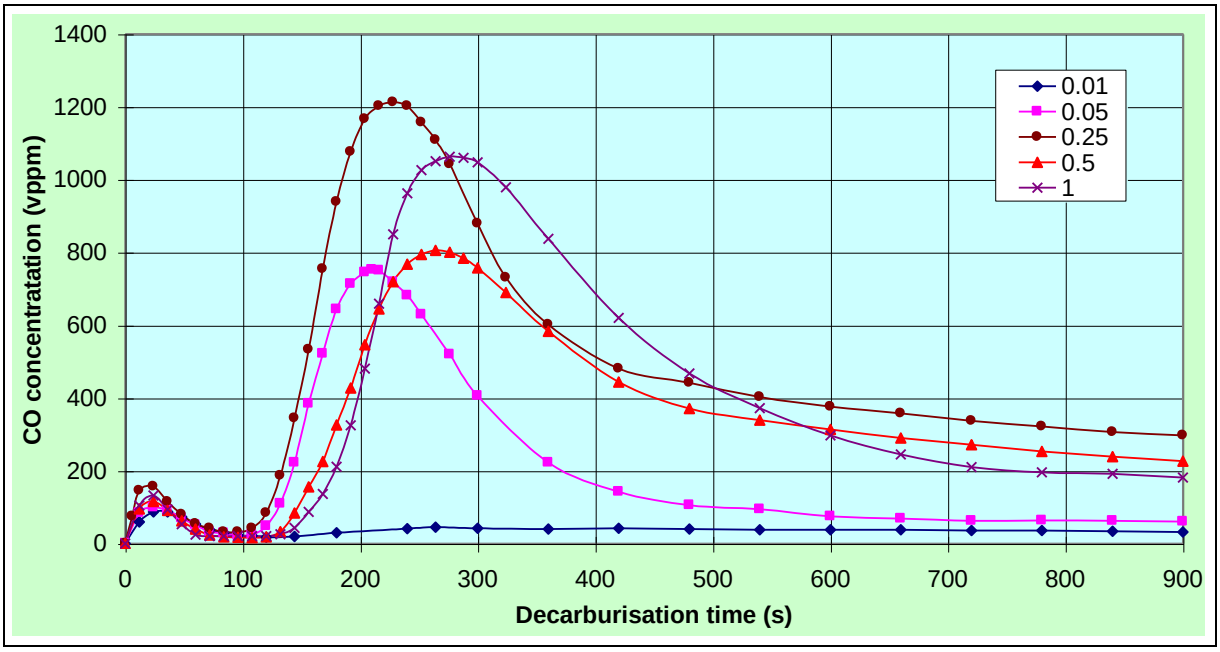

Figure 11.19 Carbon monoxide concentration profiles for the decarburisation of furnace cooled 3% Silicon initial structures at 835°C with different p_{H_2O} / p_{H_2} ratios.

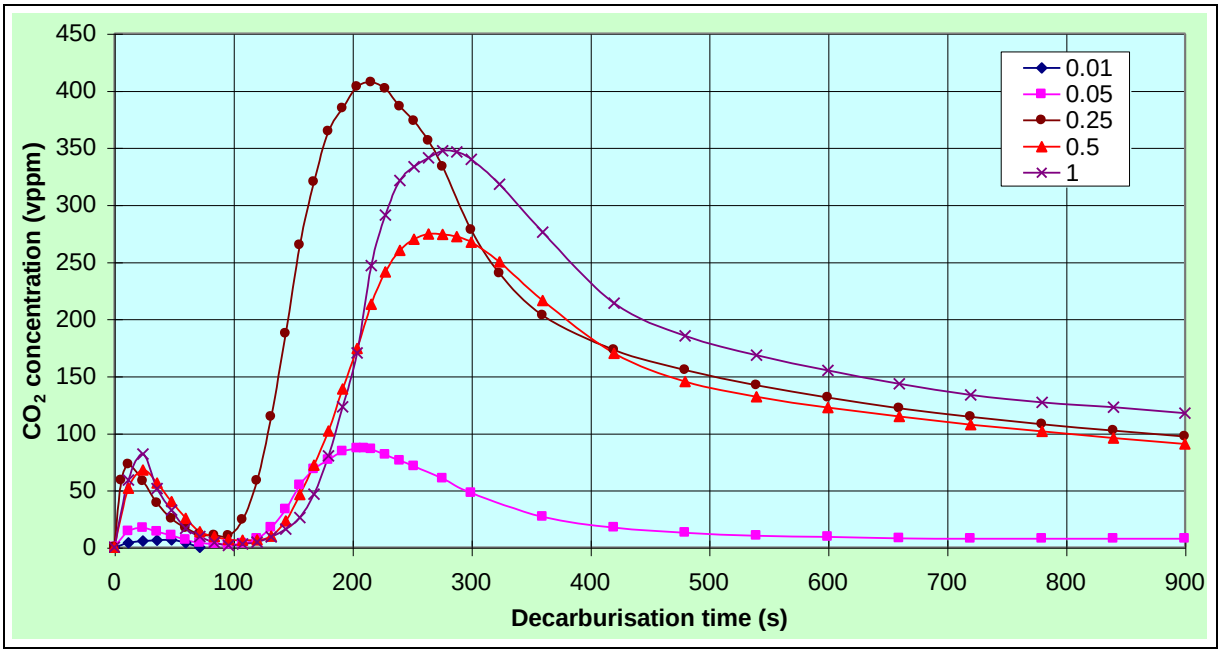

Figure 11.20 Carbon dioxide concentration profiles for the decarburisation of furnace cooled 3% Silicon initial structures at 835°C with different p_{H_2O} / p_{H_2} ratios.

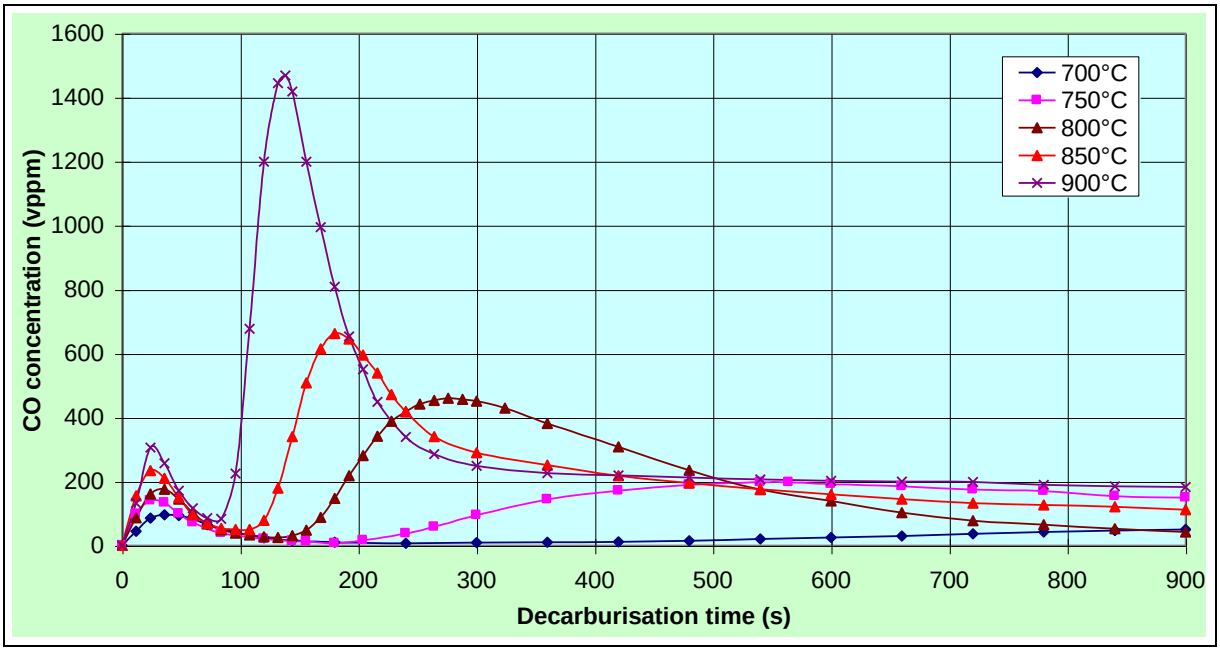

Figure 11.21 Carbon monoxide concentration profiles for the decarburisation of furnace cooled 3% Silicon initial structures at different temperatures with p_{H_2O} / p_{H_2} =0.05.

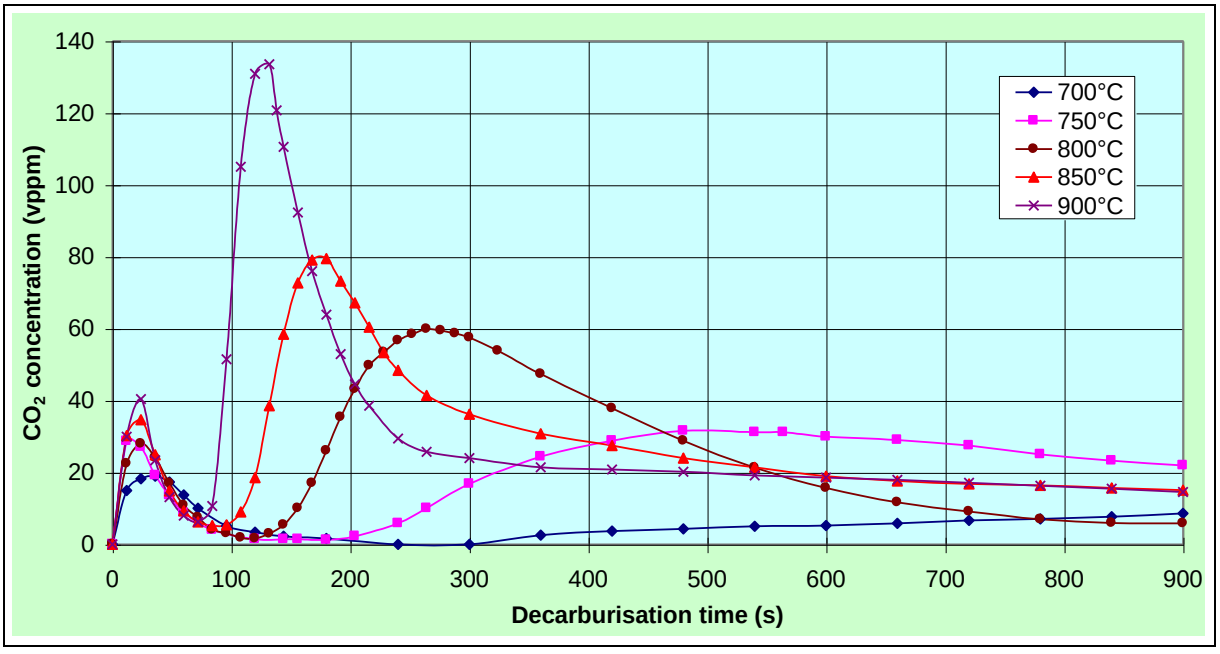

Figure 11.22 Carbon dioxide concentration profiles for the decarburisation of furnace cooled 3% Silicon initial structures at different temperatures with p_{H_2O} / p_{H_2} =0.05.

The effect of temperature on the carbon monoxide and carbon dioxide concentration profiles during the decarburisation of the 0% Silicon steel at a p_{H_2O} / p_{H_2} ratio of 0.05 are illustrated in Figures 11.9 and 11.10 respectively. The peak carbon monoxide concentration increased from 30vppm at 700°C to 720vppm at 900°C, Table 11.2. The concentration peaks become sharper and occurred earlier with increasing temperature. The carbon monoxide concentrations after 900s increased from 25vppm at 700°C to 310vppm at 900°C.

11.3.2 Decarburisation of the 1% Silicon steel

The peak carbon monoxide concentration for the decarburisation of the 1% Silicon steel at 760°C of 465vppm occurred at a p_{H_2O} / p_{H_2} ratio of 0.25, Table 11.1, and was higher than the peak values of 345 and 315vppm for the 0.50 and 0.05 ratios respectively. A similar trend was observed for the carbon dioxide gas concentrations. The peak carbon monoxide and carbon dioxide concentrations at the 0.25 ratio were more than twice those of the 0% Silicon steel. A gradual decrease from the peak gas concentrations occurred similar to that for the 0% Silicon steel, with the gas concentrations of the 1% Silicon steel after 900s approximately twice those of the 0% Silicon steel at the comparable p_{H_2O} / p_{H_2} ratios. The carbon monoxide and carbon dioxide gas concentration profiles for decarburisation of the 1% Silicon steel at p_{H_2O} / p_{H_2} ratios of 0.01 to 1.0 are illustrated in Figures 11.11 and 11.12 respectively.

The peak carbon monoxide and carbon dioxide concentrations of Figures 11.13 and 11.14 increased from 45 and 4vppm at 700°C to 690 and 65vppm respectively at 900°C, Table 11.2. Similar trends were evident with respect to the shape of the concentration profiles for the 0% and 1% Silicon steels, with three concentration peaks for temperatures of 800°C upwards.

11.3.3 Decarburisation of SUP7NV

An increase in the silicon content from 1.24wt.% for the 1% Silicon steel to 1.94wt.% for SUP7 resulted in higher peak gas concentrations for comparable p_{H_2O} / p_{H_2} ratios. The peak carbon monoxide concentrations for SUP7 were approximately four times that of the 1% Silicon steel, Table 11.1. However, the peak carbon dioxide concentrations for p_{H_2O} / p_{H_2}

ratios of 0.25 to 1.0 were similar. The carbon monoxide and carbon dioxide concentration profiles for SUP7 at different p_{H_2O} / p_{H_2} ratios were illustrated in Figures 10.17 and 10.18.

The SUP7 carbon monoxide concentrations after 900s for p_{H_2O} / p_{H_2} ratios of 0.01 to 1.0 were similar, unlike the 0 and 1% Silicon steels. The mass of carbon removed from the steel after 15min was determined from the carbon monoxide and carbon dioxide profiles by the method detailed in Section 8.4.5. The values of Table 11.1 demonstrate that the mass of carbon removed increased from the 0% Silicon steel to that of SUP7, with the maximum carbon removal occurring at the 0.25 p_{H_2O} / p_{H_2} ratio. 1.83μgC was removed from SUP7 at a p_{H_2O} / p_{H_2} ratio of 0.01, which was eight times that of the 0 and 1% Silicon steels. 2.74μgC removal at the 0.25 ratio was higher than the values of 0.81 and 1.65μgC for the 0 and 1% Silicon steels respectively at this ratio.

The carbon monoxide and carbon dioxide concentration profiles for SUP7NV decarburised at 820°C with p_{H_2O} / p_{H_2} ratios of 0.01 to 1.0 are illustrated in Figures 11.15 and 11.16.

At the lowest p_{H_2O} / p_{H_2} ratio of 0.01, the peak SUP7NV carbon monoxide concentration of 195vppm was only one third that of SUP7, despite the same heat treatment temperature and similar silicon content. At the higher p_{H_2O} / p_{H_2} ratios, the peak carbon monoxide values of SUP7NV were closer, being two-thirds that of SUP7. Unlike for SUP7, convergence of the carbon monoxide concentrations did not occur after 900s, with values ranging from 125 to 400vppm. However, the peak carbon monoxide concentrations for SUP7NV were greater than those of SUP7 for p_{H_2O} / p_{H_2} ratios of 0.25 to 1.0, with the peak SUP7NV carbon dioxide concentration of 320vppm at the 1.0 ratio was six times that for SUP7. The mass of carbon removed after 15min was similar for SUP7 and SUP7NV at comparable p_{H_2O} / p_{H_2} ratios of 0.05 to 1.0, Table 11.1. However, three times more carbon was removed for SUP7 at a p_{H_2O} / p_{H_2} ratio of 0.01.

The carbon monoxide and carbon dioxide gas concentration profiles for the decarburisation of SUP7NV at temperatures of 700 to 900°C with a p_{H_2O} / p_{H_2} ratio of 0.05 are illustrated in

Figures 11.17 and 11.18. The peak SUP7NV carbon monoxide and carbon dioxide concentrations increased from 65 and 11vppm at 700°C to 1795 and 260vppm at 900°C.

11.3.4 Decarburisation of the 3% Silicon steel

Figures 11.19 and 11.20 demonstrate the decarburisation concentration profiles for the 3% Silicon steel at 835°C with p_{H_2O} / p_{H_2} ratios of 0.01 to 1.0. The silicon content of 3.05wt.% altered the decarburisation behaviour relative to the lower silicon steels. At the lowest ratio of 0.01, the peak carbon monoxide concentration was only 30vppm, compared with 600vppm for SUP7.

An increase in the p_{H_2O} / p_{H_2} ratio to 0.05 sharply increased the peak carbon monoxide and carbon dioxide concentrations to 750 and 85vppm, Table 11.1. However, these values were considerably less than the peak concentrations of 1615 and 130vppm for SUP7 at the same p_{H_2O} / p_{H_2} ratio. The carbon monoxide and carbon dioxide concentrations for the 3% Silicon steel then decreased sharply, with values of 60 and 8vppm respectively after 900s almost an order of magnitude lower than for SUP7 after 900s. This resulted in lower masses of carbon removed for the 3% Silicon steel, as listed in Table 11.1.

The peak, and carbon monoxide concentrations after 900s for the 3% Silicon steel were only two thirds that of the SUP7 concentrations at p_{H_2O} / p_{H_2} ratios of 0.25 to 1.0. However, the carbon dioxide concentrations exceeded those of SUP7, with the peak carbon dioxide concentration of 345vppm six times that of SUP7 at a p_{H_2O} / p_{H_2} ratio of 1.0. The influence of temperature on the carbon monoxide and carbon dioxide concentration profiles for the 3% Silicon steel are illustrated in Figures 11.21 and 11.22. The peak carbon monoxide and carbon dioxide concentrations increase from 50 and 9vppm at 700°C, Table 11.2, to 1470 and 135vppm respectively at 900°C.

11.3.5 Observations on decarburising different silicon steels at their Ac_3 temperatures

SUP7 exhibited the highest carbon monoxide concentrations of the five silicon steels at comparable p_{H_2O} / p_{H_2} ratios. However, the carbon dioxide concentrations for the SUP7NV

and 3% Silicon steels were greater than those of SUP7 at p_{H_2O} / p_{H_2} ratios of 0.25 to 1.0. The reason for the increasing fractions of carbon present in the exhaust gas as carbon dioxide for the SUP7NV and 3% Silicon steels was not readily apparent. The decarburisation concentration profiles exhibited either two or three peaks. The temperatures at which the concentration profiles began increasing to the second peaks were determined from the heating profiles of the different steels, Figure 7.3, and the concentration profiles, and are illustrated in Figure 11.23.

The second concentration curves began to increase at the lowest temperatures for SUP7, with the lowest value of 590°C at a p_{H_2O} / p_{H_2} ratio of 0.25. The lower temperatures for SUP7 were thought to be due to SUP7 having the fastest decarburisation kinetics of the five steels. This was also indicated by the highest peak gas concentrations observed for SUP7 at the p_{H_2O} / p_{H_2} ratio of 0.25 corresponding to the lowest temperature at which the second concentration curves commenced. A similar trend was observed for the other steels, with these temperatures being higher than for SUP7.

The peak gas concentration temperatures for the different steels are illustrated in Figure 11.24. These temperatures increased with silicon content, and appeared to be independent of the p_{H_2O} / p_{H_2} ratio for each steel. The peak concentrations occurred at temperatures lower than the Ac_3 values for the respective steels, and were dependent on:

a) The longer diffusion distances for carbon removal due to the increasing ferrite depths outweighing the effect of the increasing temperature on the carbon diffusivity;
b) Oxide formation impeding the carbon removal sufficiently to decrease the peak concentrations, despite the increasing carbon diffusivity with temperature.

11.3.6 Temperature dependence of decarburisation for the different silicon steels

The different Ac_3 temperatures of the steels prevents direct comparisons between the steels as a function of the p_{H_2O} / p_{H_2} ratio. They can be compared by decarburisation at the same temperatures and p_{H_2O} / p_{H_2} ratios, although this does not account for the different equilibrium core structures at the same temperatures. A comparison of the decarburisation gas

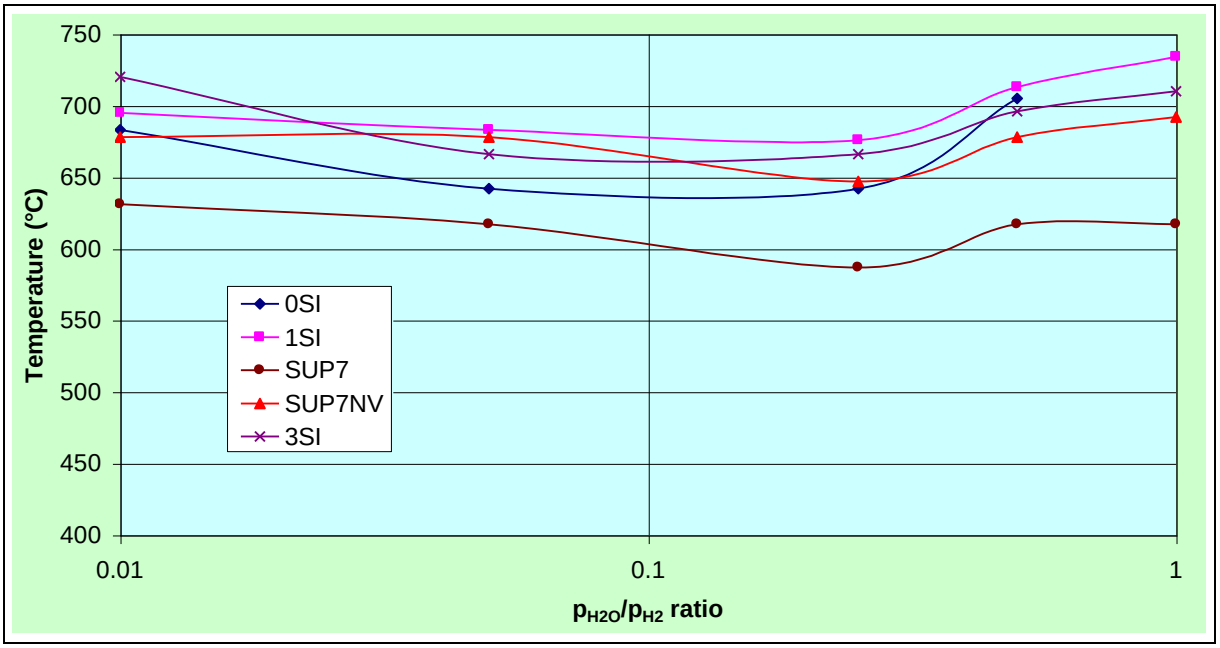

Figure 11.23 Temperatures at which the second carbon monoxide concentration curves commenced for the different silicon steels with furnace cooled initial structures decarburised at their Ac_3 temperatures and different p_{H_2O} / p_{H_2} ratios.

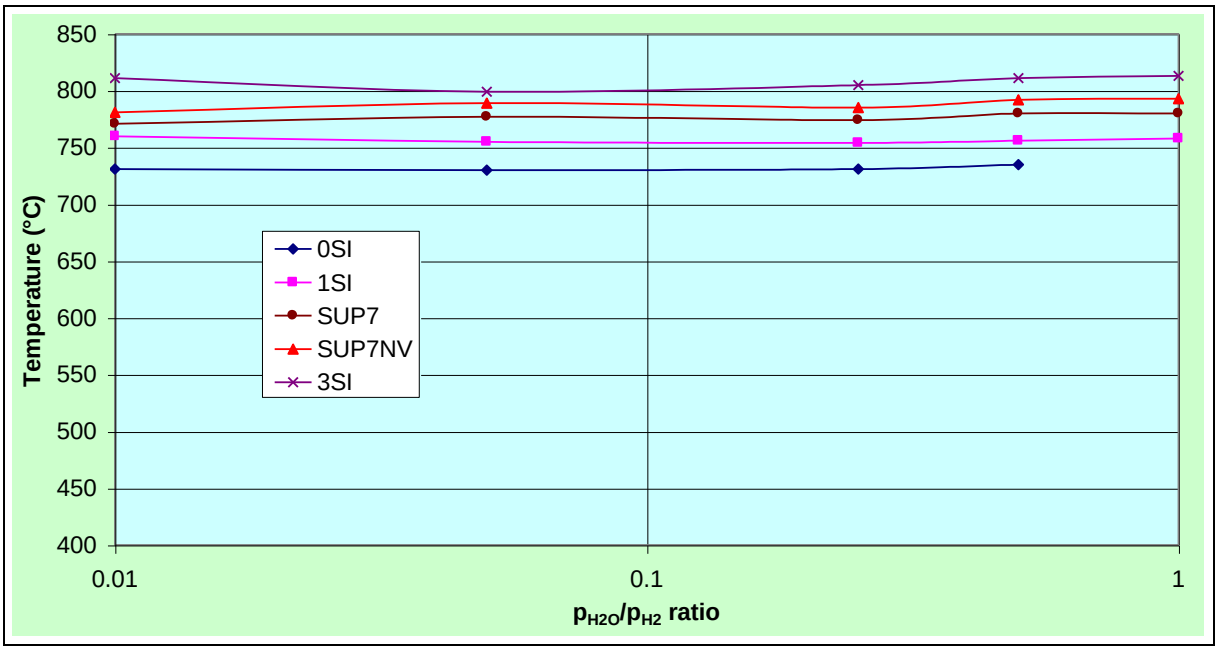

Figure 11.24 Temperatures of peak carbon monoxide concentrations for different silicon steels with furnace cooled initial structures decarburised at their respective Ac_3 temperatures with different p_{H_2O} / p_{H_2} ratios.

concentrations and the carbon removed for the different silicon steels decarburised at 700 to 900°C, Tables 11.1 and 11.2, demonstrates several trends:

- The increasing peak carbon monoxide and carbon dioxide concentrations, and the mass of carbon removed after 15min, with temperature;
- The height of the gas concentration profiles for the different silicon steels can be arranged in order from the highest to the concentrations at each temperature, which this order being

SUP7 > SUP7NV > 3% Silicon > 1% Silicon > 0% Silicon;

- The greatest carbon removal at each temperature occurred for SUP7, then for SUP7NV;
- Similar carbon removal after 15min for the 0, 1 and 3% Silicon steels at 700 and 750°C, with greater carbon removal for the 1% Silicon steel at higher temperatures.

During the decarburisation of the different silicon steels, the carbon monoxide and carbon dioxide concentrations increased from zero to peak concentrations during the first 50s from when the specimens were inserted into the hot zone with the established decarburisation atmosphere. The gas concentrations then decreased as the specimens heated to temperature, before increasing to higher second peak values. At the lower temperatures, the concentrations decreased from the first peaks to almost zero. This decrease was less at the higher temperatures, with the two peaks occurring after shorter durations, due to the higher temperatures obtained after comparable times.

Marini[78] attributed peak concentrations during the heating of a Fe-3wt.%Si steel to temperature to the formation of an oxide layer, which then inhibited carbon removal. As the specimen heated further, the oxide structure became less dense, which allowed carbon removal to recommence. The carbon monoxide and carbon dioxide concentrations then increased until second peaks were reached. The first peak gas concentrations for the different silicon steels were also thought to be due to the formation of an oxide layer inhibiting carbon removal. Carbon removal then recommenced at higher temperatures when the oxide layer became less dense.

The increasing concentration profiles to the second peaks arose from the increasing temperatures allowing faster carbon removal from the surface of the steel. Eventually a stage was reached where the increasing diffusion coefficient of carbon in ferrite with increasing temperature was more than offset by a combination of the longer diffusion distances for carbon to the surface due to the thicker ferrite layers, and the inhibiting effect of the oxide structures. This resulted in lower carbon monoxide and carbon dioxide concentrations. The second carbon monoxide and carbon dioxide peak concentrations occurred earlier for the 3% Silicon steel than for SUP7 at 800 to 900°C, due to the higher silicon content of the 3% Silicon steel resulting in oxide layers that inhibited carbon removal to a greater extent.

11.3.7 Multiple linear regression analysis

The concentration profiles of the different silicon steels detailed in sections 11.3.1 to 11.3.6 demonstrate that the decarburisation was influenced by the alloy content, the heat treatment temperature, and the p_{H_2O} / p_{H_2} ratio. In order to establish relationships between these variables, multiple linear regression analysis, MLR, was undertaken using the regression data analysis function of Microsoft Excel. MLR analysis involves simultaneously "fitting" linear relationships to several selected variables by a complex form of least-squares fit so as to minimise the errors in the prediction of the dependent variable[211].

Three possibilities were considered for the dependent variable, namely the:

1) Sum of the peak carbon monoxide and carbon dioxide concentrations;
2) Sum of the carbon monoxide and carbon dioxide concentrations at 15min;
3) Mass of carbon removed during the first 15min of decarburisation.

The most applicable of these is the mass of carbon removed from the steel. MLR regression analysis was therefore undertaken to determine if a relationship existed between the mass of carbon removed during the first 15min decarburisation of the steels and the alloy content, temperature and p_{H_2O} / p_{H_2} ratio. This resulted in 49 data points, comprising 0.06 to 3.05wt.%Si, 0.77 to 1.09wt.%Mn, temperatures of 700 to 900°C, and p_{H_2O} / p_{H_2} ratios of 0.01 to 1.0. The silicon content, manganese content, temperature in °C, and p_{H_2O} / p_{H_2} ratio were selected as the independent variables. A MLR analysis of the data yielded the following

relationship between the mass of carbon removed after 15min, m_C(15min), and these variables:

$$m_C(15\text{min}) = -0.0729\%Si - 1.8614\%Mn + 0.0096T + 0.7522\ p_{H_2O} / p_{H_2}. \quad (11.1)$$

Table 11.3 lists the statistics for the MLR analysis. The R^2 value of 0.52 indicates that this equation explains 52% of the variation in the mass of carbon removed, while the F-critical value lower than the F-statistics indicates that this equation is statistically useful for the prediction of m_C(15min). The higher magnitude of the t-statistic relative to the t-critical value for the manganese content, temperature and p_{H_2O} / p_{H_2} ratio indicate that these variables are useful for the prediction of m_C(15min). However, the lower magnitude of the t-statistic for the silicon content indicates that this variable is not useful for the prediction of m_C(15min).

Table 11.3 MLR analysis results for the mass of carbon removed during the first 15min decarburisation of the different silicon steels at 700 to 900°C.

Description	n	R^2	S.E.	F	$F_{critical}$	$t_{statistic}$				
						%Si	%Mn	T	p_{H_2O} / p_{H_2}	$t_{critical}$
0-3wt.%Si p_{H_2O} / p_{H_2} **=0.01-1.0**	49	0.52	0.61	13.80	2.58	-0.62	-1.92	5.93	2.40	1.68
0%Si-SUP7NV p_{H_2O} / p_{H_2} **=0.01-0.25**	32	0.84	0.37	40.96	2.73	3.19	-2.85	9.11	4.41	1.70
0%Si-SUP7 p_{H_2O} / p_{H_2} **=0.01-0.25**	24	0.89	0.29	48.13	2.90	4.45	-3.80	9.38	4.24	1.73

The data of Tables 11.1 and 11.2 demonstrate that the mass of carbon removed increased with up to 2.11wt.%Si, with temperature, and with p_{H_2O} / p_{H_2} ratios up to 0.25. However, the m_C(15min) values for the 3% Silicon steel, and for p_{H_2O} / p_{H_2} ratios higher than 0.25, indicate a complex relationship between the variables as the range of silicon contents and p_{H_2O} / p_{H_2} ratios is extended, which cannot be fully explained by the MLR analysis. This is indicated by the low R^2 and high standard error values. If the analysis is restricted to the 0% Silicon to

SUP7NV steels, and for p_{H_2O} / p_{H_2} ratios of 0.01 to 0.25, the regression equation for m_C(15min) becomes

$$m_c(15\text{min}) = 0.2976\%Si - 1.7932\%Mn + 0.0101T + 4.1418\ p_{H_2O} / p_{H_2}. \quad (11.2)$$

The R^2 value of 0.84, Table 11.3, explains a higher proportion of the variation in the m_C(15min) value than equation 11.1, with a lower standard error of 0.37µgC. The lower t-statistic relative to the critical value for the independent variables indicates that all four variables are useful in predicting the value of m_C(15min). If the analysis is further restricted to the 0% Silicon, 1% Silicon and SUP7 steels, since SUP7NV has elevated niobium and vanadium contents, an even higher proportion of the variation in the m_C(15min) results are explained, with an R^2 value of 0.89 and a standard error of 0.29µgC. The resultant MLR equation is

$$m_C(15\text{min}) = 0.3701\%Si - 1.8666\%Mn + 0.0092T + 3.5938\ p_{H_2O} / p_{H_2}. \quad (11.3)$$

Equations 11.2 and 11.3 indicate a statistically good relationship between the silicon, manganese, temperature and p_{H_2O} / p_{H_2} variables for 0.06 to 2.11wt.%Si, 0.77 to 1.09wt.%Mn, 700 to 900°C, and p_{H_2O} / p_{H_2} ratios of 0.01 to 0.25. The individual coefficients of these equations demonstrate that the total mass of carbon removed increased with silicon content, temperature and p_{H_2O} / p_{H_2} ratio, but was decreased by manganese. The retarding effect of manganese on the mass of carbon removed is five times greater than the accelerating effect of silicon for the same change in composition.

11.4 Free ferrite decarburisation depths for the different silicon steels

The free ferrite depths for the different silicon steels after 4hr decarburisation at their respective Ac_3 temperatures with p_{H_2O} / p_{H_2} ratios of 0.01 to 1.0 are illustrated in Figure 11.25. Only SUP7 exhibited a uniform free ferrite layer after decarburisation at a p_{H_2O} / p_{H_2} ratio of 0.01, with a free ferrite depth of 247µm. The free ferrite depths for the 1% Silicon steel at p_{H_2O} / p_{H_2} ratios of 0.05 to 1.0 were greater than the 0% Silicon steel, with the maximum values of 256 and 163µm for the 1 and 0% Silicon steels obtained by decarburising

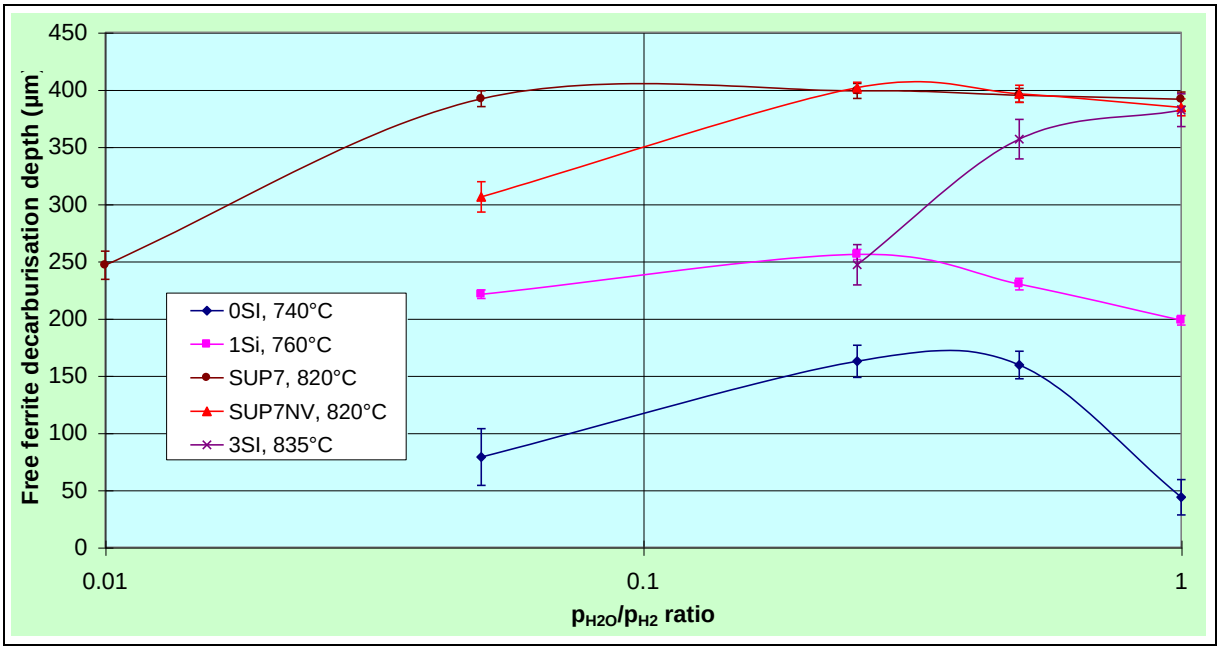

Figure 11.25 Free ferrite depths for the different silicon steels with furnace cooled initial structures decarburised at their respective Ac_3 temperatures with different p_{H_2O} / p_{H_2} ratios.

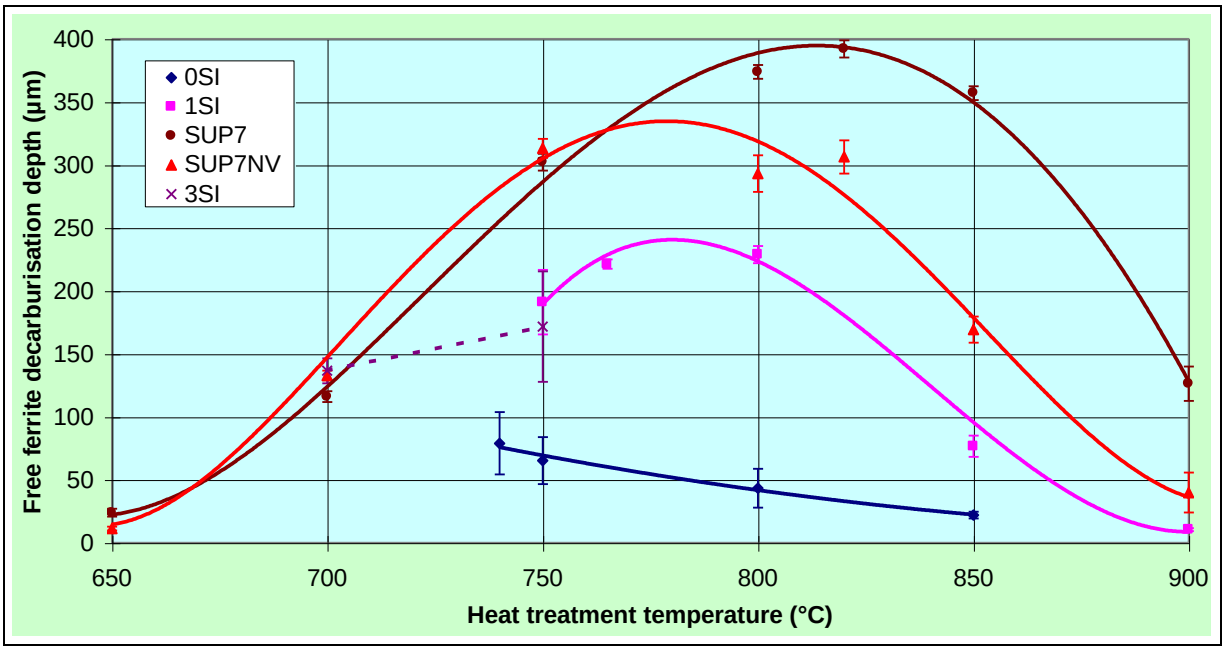

Figure 11.26 Influence of temperature on the free ferrite depths for the different silicon steels with furnace cooled initial structures decarburised at p_{H_2O} / p_{H_2} =0.05.

at a p_{H_2O} / p_{H_2} ratio of 0.25. The free ferrite depths decreased at the higher p_{H_2O} / p_{H_2} ratios, with the decrease greater for the 0% Silicon steel at a 1.0 ratio.

The free ferrite depths were greater for SUP7 than the 1% Silicon steel at the comparable p_{H_2O} / p_{H_2} ratios. The free ferrite depth of 306μm for SUP7NV was also less than the 392μm for SUP7 at the 0.05 ratio. However, the free ferrite depths of SUP7 and SUP7NV were similar at p_{H_2O} / p_{H_2} ratios of 0.25 to 1.0. No free ferrite was present for the 3% Silicon steel upon decarburisation at p_{H_2O} / p_{H_2} ratios of 0.01 and 0.05. However, free ferrite was present at the higher p_{H_2O} / p_{H_2} ratios, and increased sharply in thickness with increasing p_{H_2O} / p_{H_2} ratios. The value of 382μm at a ratio of 1.0 was similar to that of SUP7 and SUP7NV.

As the silicon content increased from 0.06wt.% for the 0% Silicon steel to 1.94wt.% for SUP7, the free ferrite depth at the 0.05 p_{H_2O} / p_{H_2} ratio became closer to that of the 0.25 ratio. However, as the silicon content increased to 2.11 and 3.05wt.% for the SUP7NV and 3% Silicon steels respectively, the highest free ferrite depths were obtained at increasing p_{H_2O} / p_{H_2} ratios; 0.25 for SUP7NV and 1.0 for the 3% Silicon steel.

A comparison of the free ferrite depths measured at the respective Ac_3 temperatures for the different silicon steels is misleading, since the effect of the different Ac_3 temperatures can not be quantified. A comparison of the free ferrite depths measured at the same temperatures and p_{H_2O} / p_{H_2} ratio for the different steels is more meaningful. However, such a comparison is not strictly accurate at temperatures in excess of the Ac_3 values for the respective steels. This is due to some carbon removal being associated with a carbon concentration gradient across the austenite from the ferrite/austenite interface inwards. Figure 11.26 illustrates the influence of temperature on the free ferrite depths measured for the different silicon steels at a p_{H_2O} / p_{H_2} ratio of 0.05.

No free ferrite was observed for the decarburisation of the 0% Silicon steel at 650 or 700°C. The maximum free ferrite depth of 79μm occurred at the Ac_3 temperature of 740°C, and decreased to 22μm at 850°C. No free ferrite was observed at 900°C, as carbon removal at this temperature only yields a single phase austenite region. The range of temperatures over which free ferrite formed, and the free ferrite thicknesses, were greater for SUP7 than for the lower

silicon steels. A thin free ferrite surface layer of 24μm resulted upon decarburisation of SUP7 at 650°C, with the greatest value of 392μm obtained at the Ac_3 temperature of 820°C.

The free ferrite depths for SUP7NV were similar to those of SUP7 at temperatures of 650 to 750°C, but less at the higher temperatures. The shape of the ferrite versus temperature profiles were similar for the 1% Silicon, SUP7 and SUP7NV steels, with the greatest free ferrite depths measured at the respective Ac_3 temperatures. The free ferrite depths then decreased at the higher temperatures. Free ferrite was observed for the 3% Silicon steel at 700 and 750°C. However, negligible free formation resulted for the 3% Silicon steel decarburised at temperatures of 800°C and greater. This was due to the transition from internal to external SiO_2 oxidation at a p_{H_2O} / p_{H_2} ratio of 0.05 as the temperature increased from 750 to 800°C.

Block[86] observed that the p_{H_2O} / p_{H_2} ratio at which the transition from external to internal SiO_2 oxidation occurred for a 0.023wt.%C/3.17wt.%Si/0.58wt.%Mn steel increased from 0.05 at 750°C to 0.09 at 800°C. For internal oxidation, the base metal matrix is available for the diffusion of carbon to the surface to react with the decarburisation atmosphere. However, an external oxide layer is less porous, and therefore inhibits carbon removal to a greater extent than internal oxidation. The transition from internal to external oxidation[86] as the temperature increased from 750 to 800°C for the 3% Silicon steel resulted in the greater inhibition of carbon removal. This accounts for a ferrite layer 172μm thick being observed at 750°C, but no free ferrite formation at 800°C. The higher peak carbon monoxide and carbon dioxide concentration profiles at 800°C compared with 750°C, Figures 11.21 and 11.22, were due to carbon removal during heating before external oxidation was sufficient to inhibit the carbon removal. The lower carbon monoxide and carbon dioxide concentrations at 800°C from 500s onwards relative to 750°C demonstrates that sufficient external oxidation had occurred to strongly inhibit the carbon removal.

11.5 Oxide layer thicknesses for the different silicon steels

Figure 11.27 illustrates the oxide thicknesses for the 1% Silicon, SUP7, SUP7NV and 3% Silicon steels after 4hr decarburisation at their respective Ac_3 temperatures for p_{H_2O} / p_{H_2} ratios of 0.01 to 1.0. The oxide structures of the 0% Silicon steel were too thin to be measured by optical microscopy. The oxide thickness increased with p_{H_2O} / p_{H_2} ratio for the different

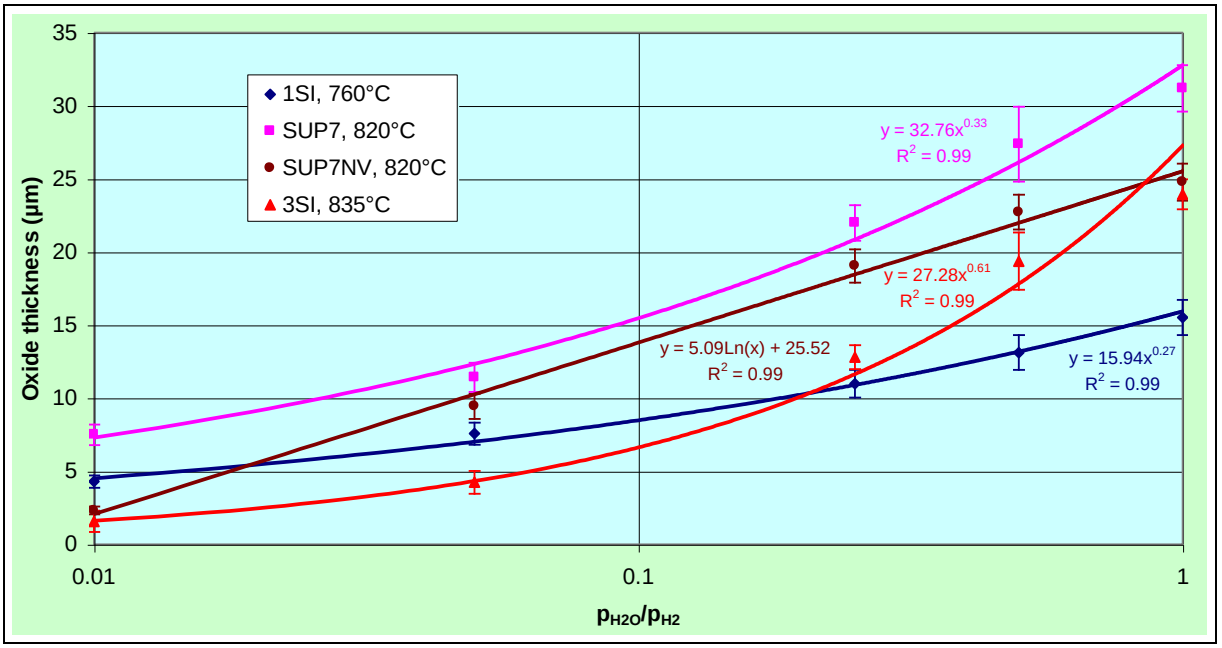

Figure 11.27 Oxide thickness kinetics for the decarburisation of different silicon steels with furnace cooled initial structures after 4hr at their respective Ac_3 temperatures with different p_{H_2O} / p_{H_2} ratios.

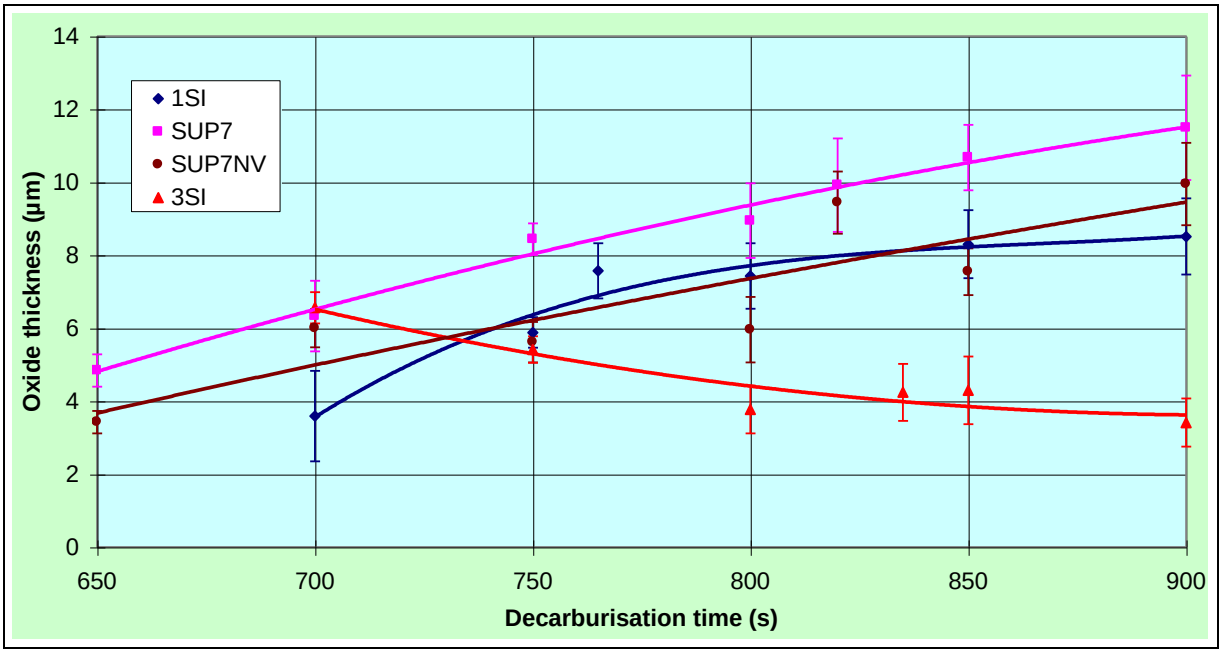

Figure 11.28 Influence of temperature on the oxide thickness after 4hr decarburisation of the different silicon steels with furnace cooled initial structures at p_{H_2O} / p_{H_2} =0.05.

silicon steels, and was described by a power law for the 1% Silicon, SUP7 and 3% Silicon steels, and by a logarithmic relationship for SUP7NV. The thickest oxide structures, at the comparable p_{H_2O} / p_{H_2} ratios, resulted from decarburisation of SUP7.

The thicker SUP7 oxide structures compared to the 1% Silicon steel were thought to be due to the faster diffusivity of the substitutional elements from the bulk of the steel to steel/oxide interface resulting from the higher heat treatment temperature, and the higher bulk silicon content. SUP7NV exhibited thinner oxide layers than SUP7 for comparable p_{H_2O} / p_{H_2} ratios, despite the same decarburisation temperature and similar silicon contents. The factors contributing to this include:

- The higher silicon and manganese content of SUP7NV, with thinner oxides observed for the same heat treatments:
- The fine equiaxed grain structure of SUP7NV relative to the larger columnar grains of SUP7, resulting in longer diffusion paths for the substitutional elements along the ferrite grain boundaries to the growing oxide;
- Lower bulk diffusion coefficients of the substitutional elements due to the higher niobium and vanadium contents of SUP7NV.

The thinnest oxide structures were exhibited by the 3% Silicon steel at p_{H_2O} / p_{H_2} ratios of 0.01 and 0.05, despite the highest decarburisation temperature and bulk silicon content. This was due to the formation of an external SiO_2 oxide layer[86] preventing the reaction of the decarburisation atmosphere with the silicon in the steel, and therefore the growth of the oxide layer. The oxide thickness of the 3% Silicon steel was similar to that of SUP7NV at a p_{H_2O} / p_{H_2} ratio of 1.0, where the less dense oxide structure resulting from the transition to internal oxidation at the higher p_{H_2O} / p_{H_2} ratios allowed the decarburisation atmosphere to react with the silicon in the steel.

The oxide thicknesses of the 1% Silicon, SUP7 and SUP7NV steels for decarburisation at a p_{H_2O} / p_{H_2} ratio of 0.05 increased with temperature, Figure 11.28, with the thicknesses at 900°C double the values at 700°C. The oxide thicknesses for SUP7 were approximately 30 to 40% greater than the 1% Silicon steel at the comparable temperatures, indicating an increasing

oxide thickness due to the higher silicon content. The lower manganese content of SUP7 may also have influenced the oxide thickness. At 700°C the oxide thickness of the 3% Silicon steel was similar to that of SUP7. However, the oxide thickness then decreased with increasing temperature, with the oxide thickness at 900°C only half that at 700°C.

11.6 Oxidation structures of the different silicon steels

11.6.1 Microstructural investigation

The oxidation microstructures resulting from the decarburisation of the different silicon steels at their respective Ac_3 temperatures with furnace cooled initial structures are illustrated in Figures 11.29 to 11.32. The thinnest oxide structures arose from decarburisation of the 0% Silicon steel, with oxide layers not observed at p_{H_2O} / p_{H_2} ratios of 0.01 and 0.05. Figures 11.29(a), (b) and (c) illustrate the oxide layers for p_{H_2O} / p_{H_2} ratios of 0.25, 0.50 and 1.0. A thin compact oxide layer approximately 3µm thick was obtained at a p_{H_2O} / p_{H_2} ratio of 0.25. The oxide thickness was twice this value at the highest p_{H_2O} / p_{H_2} ratio, with the structure appearing to be less dense than at the 0.25 ratio.

Oxides layer were observed for the 1% Silicon steel at p_{H_2O} / p_{H_2} ratios of 0.01 to 1.0, with Figures 11.30(a), (b) and (c) illustrating the oxide layers for p_{H_2O} / p_{H_2} ratios of 0.05, 0.25 and 1.0 respectively. These structures have a similar appearance, despite the increasing thickness with p_{H_2O} / p_{H_2} ratio.

Figures 11.31(a), (b) and (c) illustrate that the oxidation structures for SUP7 decarburised at p_{H_2O} / p_{H_2} ratios of 0.01, 0.25 and 1.0 were similar. The oxide layers were thicker and had a less dense appearance than for the 0 and 1% Silicon steels at comparable p_{H_2O} / p_{H_2} ratios. The presence of any oxide layer was hard to determine for the 3% Silicon steel at a p_{H_2O} / p_{H_2} ratio of 0.01, Figure 11.32(a), with any oxide layer no more than 1µm thick. Distinct oxide layers became apparent at higher p_{H_2O} / p_{H_2} ratios, with Figures 11.32(b) and (c) illustrating the oxide layers of 0.25 and 1.0 ratios. Oxide structures similar in appearance to those of SUP7 were observed for the 3% Silicon steel at p_{H_2O} / p_{H_2} ratios of 0.25 to 1.0.

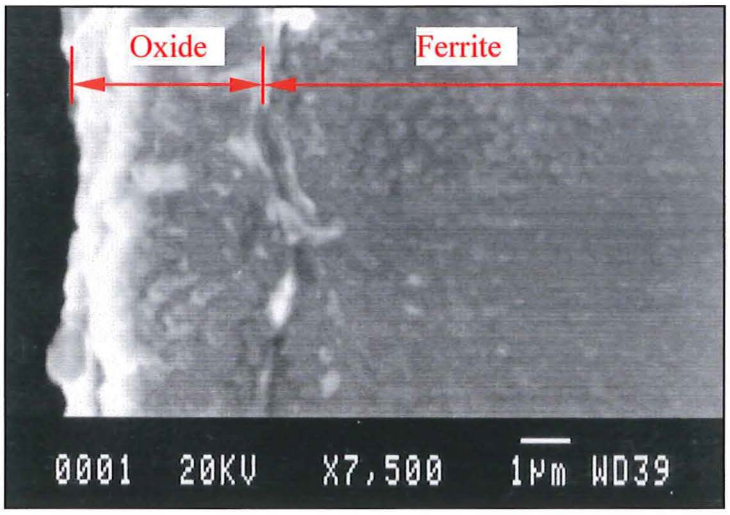

Figure 11.29(a) 0% Silicon decarburised 4hr at 740°C with p_{H_2O} / p_{H_2}=0.25.

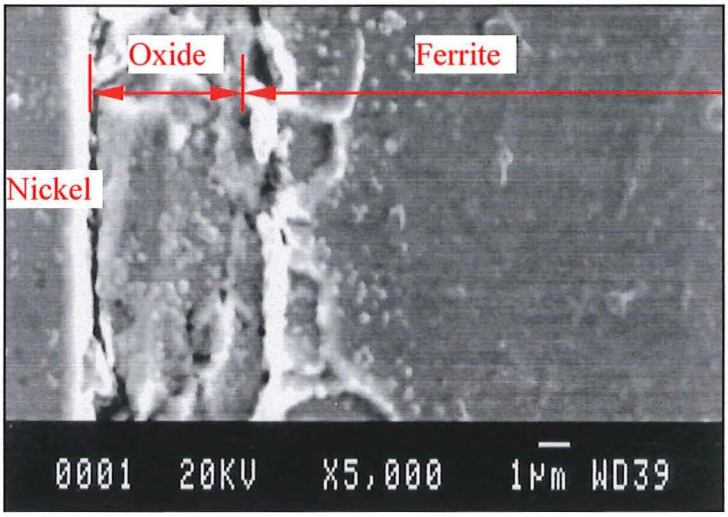

Figure 11.29(b) 0% Silicon decarburised 4hr at 740°C with p_{H_2O} / p_{H_2}=0.50.

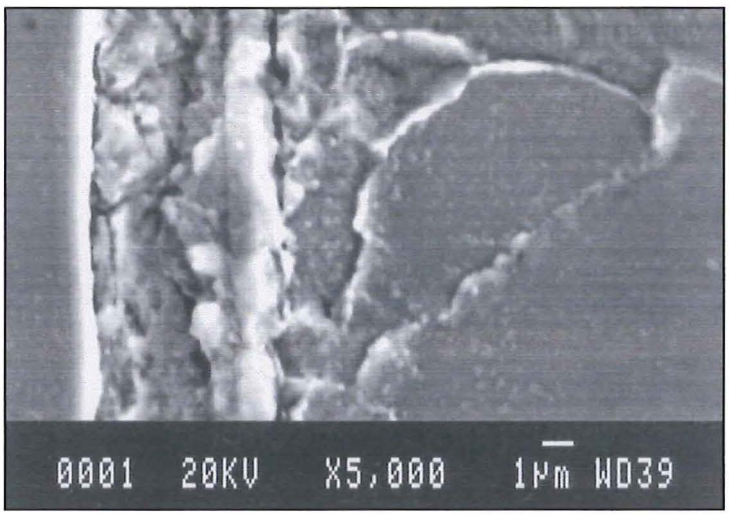

Figure 11.29(c) 0% Silicon decarburised 4hr at 740°C with p_{H_2O} / p_{H_2}=1.0.

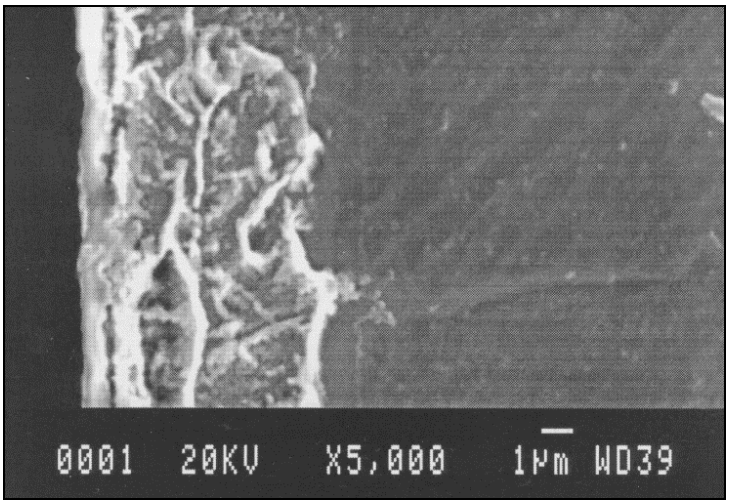

Figure 11.30(a) 1% Silicon decarburised 4hr at 760°C with p_{H_2O} / p_{H_2} =0.05.

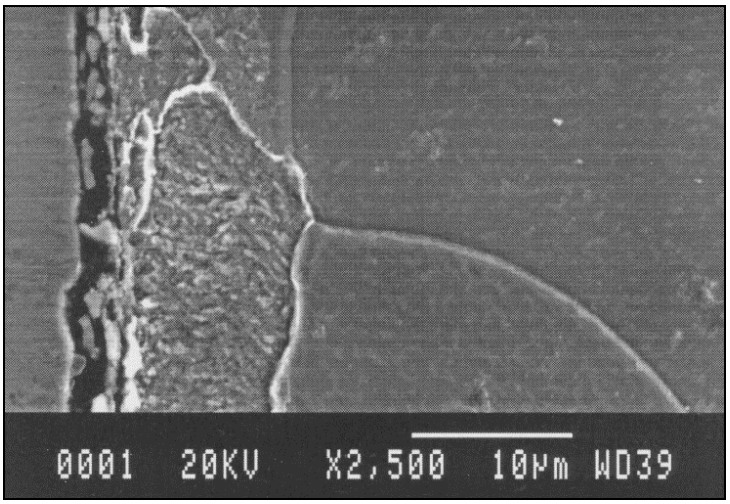

Figure 11.30(b) 1% Silicon decarburised 4hr at 760°C with p_{H_2O} / p_{H_2} =0.25.

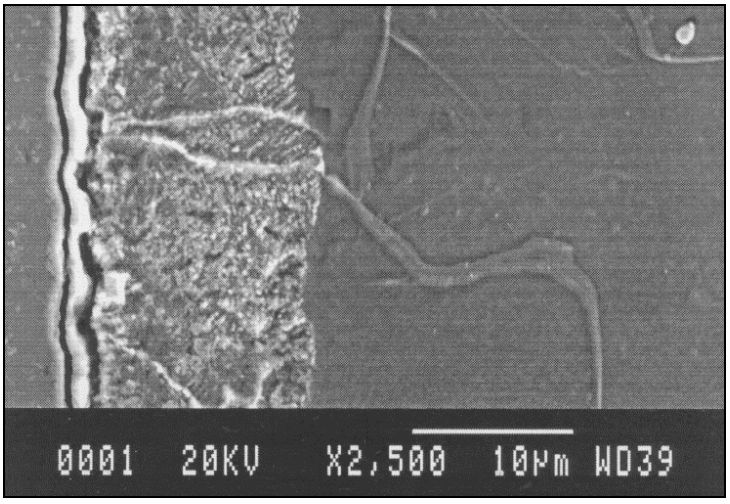

Figure 11.30(c) 1% Silicon decarburised 4hr at 760°C with p_{H_2O} / p_{H_2} =1.0.

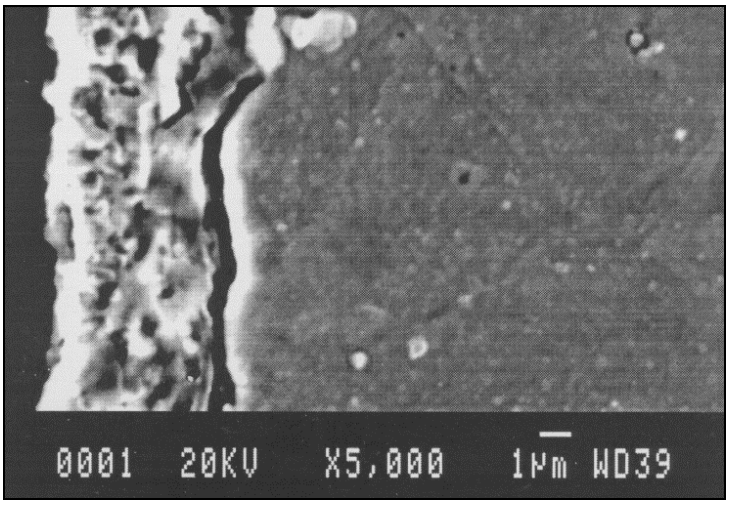

Figure 11.31(a) SUP7 decarburised 4hr at 820°C with p_{H_2O} / p_{H_2} =0.01.

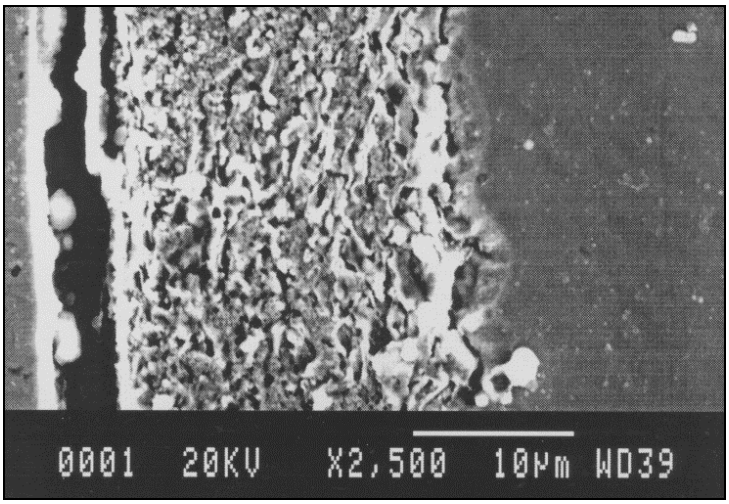

Figure 11.31(b) SUP7 decarburised 4hr at 820°C with p_{H_2O} / p_{H_2} =0.25.

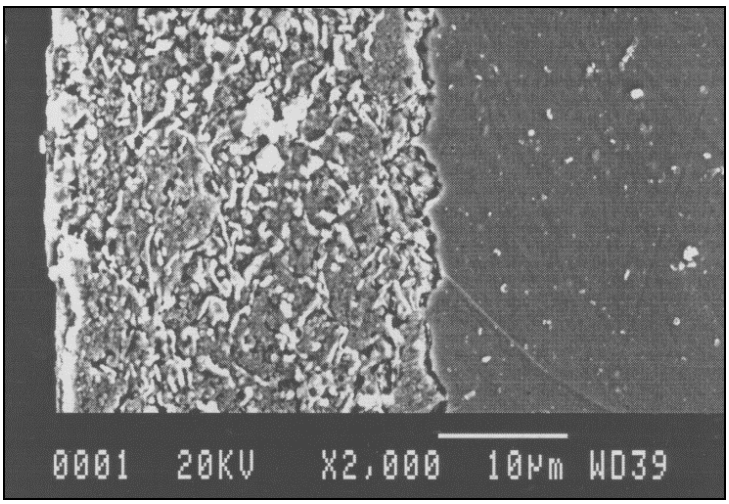

Figure 11.31(c) SUP7 decarburised 4hr at 820°C with p_{H_2O} / p_{H_2} =1.0.

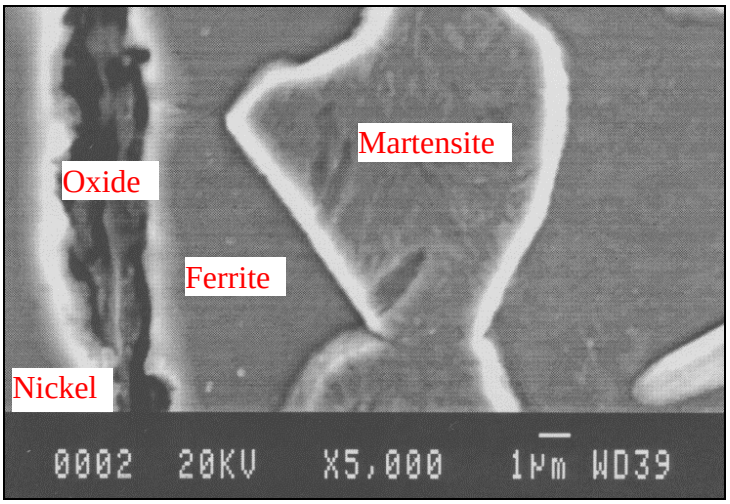

Figure 11.32(a) 3% Silicon decarburised 4hr at 835°C with p_{H_2O} / p_{H_2} =0.01.

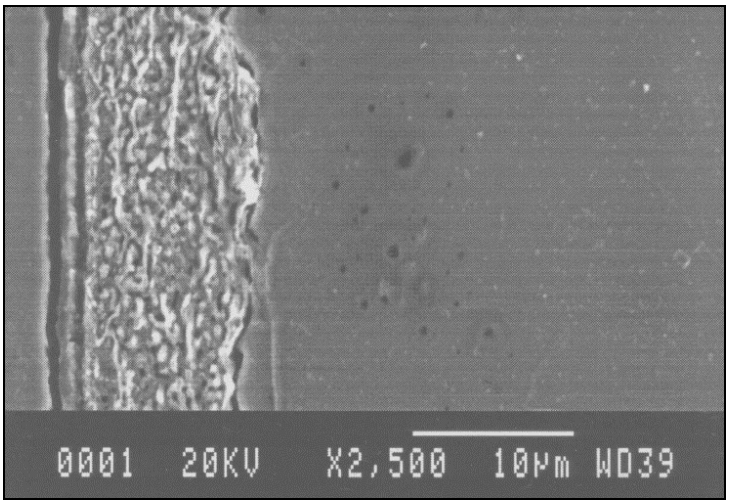

Figure 11.32(b) 3% Silicon decarburised 4hr at 835°C with p_{H_2O} / p_{H_2} =0.25.

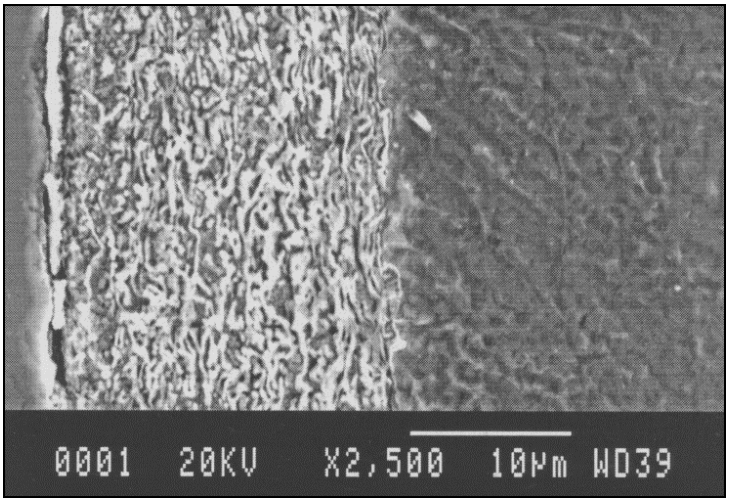

Figure 11.32(c) 3% Silicon decarburised 4hr at 835°C with p_{H_2O} / p_{H_2} =1.0.

11.6.2 Quantitative determination

One alloy element concentration profile was measured across the oxide structures for each of the different silicon steel specimens decarburised at their respective Ac_3 temperatures using the spot mode of the LINK QX2000 Energy Dispersive X-Ray analyser. The energy dispersive analysis was also extended into the ferrite until the bulk ferrite element concentrations were obtained. Figure 11.33 illustrates the oxide structure for SUP7 decarburised 4hr at 820°C with a p_{H_2O} / p_{H_2} ratio of 0.50, and the associated element concentration profiles. The white line through the centre of the photos corresponds to the line along which the analysis was made. The compositional variation of the oxide structures at the micrometre level prevented a truly quantitative analysis by energy dispersive spectroscopy[163]. However, the profiles obtained by energy dispersive spectroscopy illustrate the compositional variation across the oxide structures. Table 11.4 lists the peak silicon, manganese, chromium and aluminium concentrations. The oxide concentration profiles for the 0% Silicon, 1% Silicon, SUP7 and 3% Silicon steels at different p_{H_2O} / p_{H_2} ratios are illustrated in Figures 11.34 to 11.37.

The element concentration profiles across the oxide layers, and into the ferrite adjacent to the oxide/ferrite interface for the 0% Silicon steel at 740°C for p_{H_2O} / p_{H_2} ratios of 0.25, 0.5 and 1.0 are illustrated in Figures 11.34(a), (b) and (c) respectively. Peak silicon contents of less than 0.5wt.% were measured for the three ratios, Table 11.4. The manganese content peaked at 2.0wt.% for the 0.25 ratio, and at 5.6wt.% for the higher ratios. These peak concentrations were greater than the bulk silicon and manganese contents of 0.06 and 0.94wt.% respectively.

The manganese concentration profiles across the oxide layers showed less variation at higher p_{H_2O} / p_{H_2} ratios, with larger average values. This was due to the increasing thickness of the oxide layer with higher p_{H_2O} / p_{H_2} ratios outweighed the diffusion of silicon and manganese into the oxide, subsequently resulting in lower mean oxide concentrations. Figure 11.35 illustrates that the peak silicon concentrations for the 1% Silicon steel ranged from 5.7wt.% at a p_{H_2O} / p_{H_2} ratio of 0.50 to 3.6wt.% at the 1.0 ratio. The peak manganese concentrations were lower than those of the 0% Silicon steel, despite the higher bulk manganese content, and ranged from 4.9wt.% at the 0.01 ratio to 2.2wt.% at the 1.0 ratio, Table 11.4.

Table 11.4 Peak oxide alloy element concentrations obtained from the decarburisation of the different silicon steels decarburised for 4hr at their respective Ac_3 temperatures with different p_{H_2O} / p_{H_2} ratios.

STEEL	p_{H_2O} / p_{H_2} ratio	Element concentration (wt.%)			
		Si	Mn	Cr	Al
0% SILICON	0.25	0.4	2.0	1.1	-
	0.50	0.3	5.5	1.0	-
	1.0	0.5	5.6	0.8	-
1% SILICON	0.01	5.0	4.8	0.8	-
	0.05	4.4	2.7	-	-
	0.25	4.0	4.3	0.5	-
	0.50	5.7	3.6	1.0	-
	1.0	3.6	2.2	0.8	-
SUP7	0.01	11.7	0.3	-	5.2
	0.05	7.9	8.8	0.6	4.5
	0.25	5.5	5.6	1.3	2.6
	0.50	6.3	2.8	0.4	0.5
	1.0	7.2	4.0	0.4	-
3% SILICON	0.05	5.2	10.0	0.5	-
	0.25	9.8	4.3	0.9	-
	0.50	8.8	2.8	0.6	-
	1.0	8.0	2.3	0.4	-

Higher peak silicon contents were measured for SUP7 due to the higher bulk silicon content of 1.94wt.% versus 1.24wt.% for the 1% Silicon steel, and therefore the greater concentration of silicon available for the diffusion from the ferrite to the oxide. A peak value of 11.7wt.%Si was measured for SUP7 at a p_{H_2O} / p_{H_2} ratio of 0.01, with lower peak concentrations at the higher ratios, Table 11.4. The peak oxide manganese concentration was 8.7wt.% at a p_{H_2O} / p_{H_2} ratio of 0.05, decreasing to half this value at the highest p_{H_2O} / p_{H_2} ratios. The mean silicon and manganese concentrations across the oxide layers decreased with increasing p_{H_2O} / p_{H_2} ratio, Figure 11.36. The higher decarburisation temperature of 820°C versus 760°C for the 1% Silicon steel resulted in the greater diffusivity of manganese, and therefore the

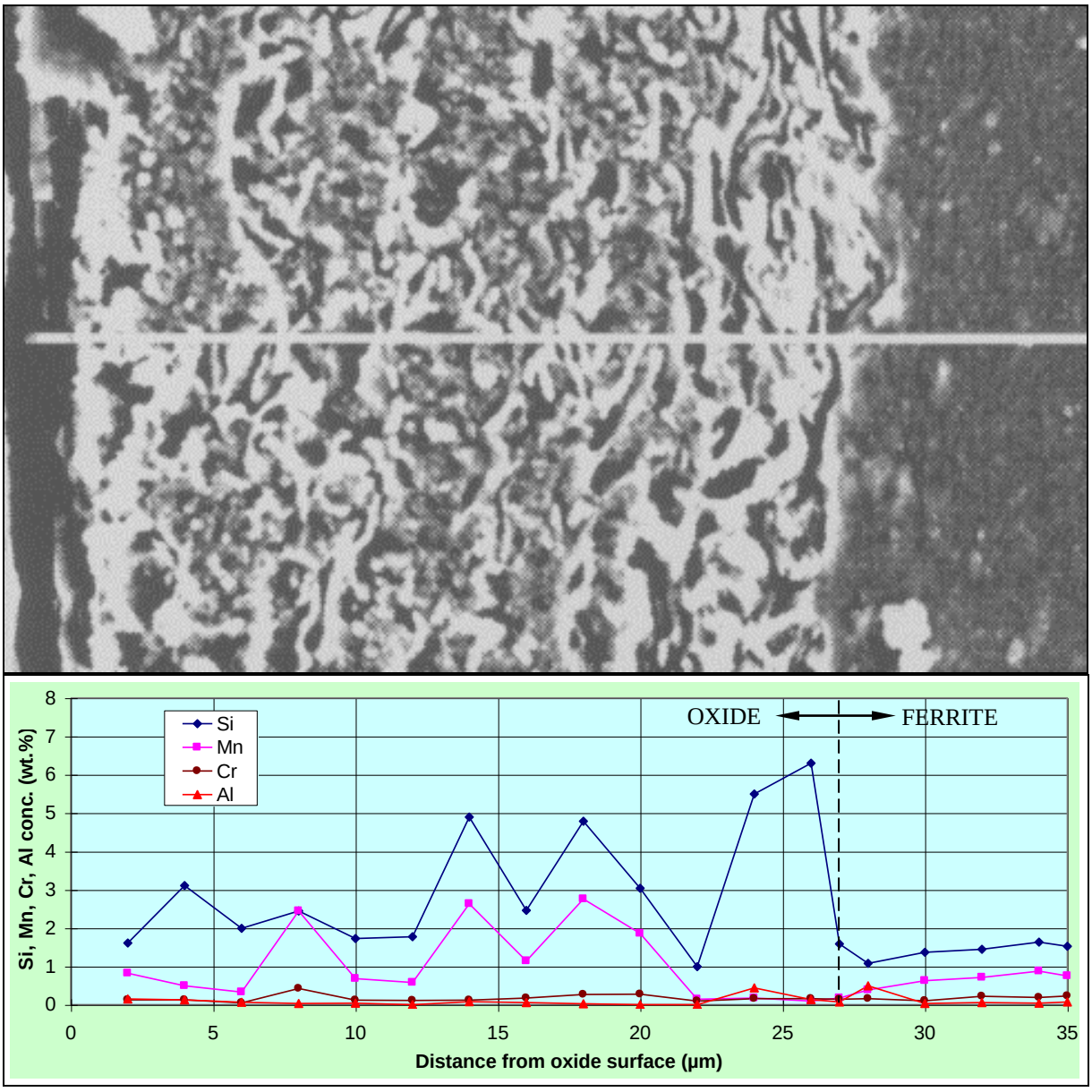

Figure 11.33 Element concentration profiles across the oxide structure obtained by decarburising a SUP7 furnace cooled initial structure at 820°C with p_{H_2O} / p_{H_2}=0.50.

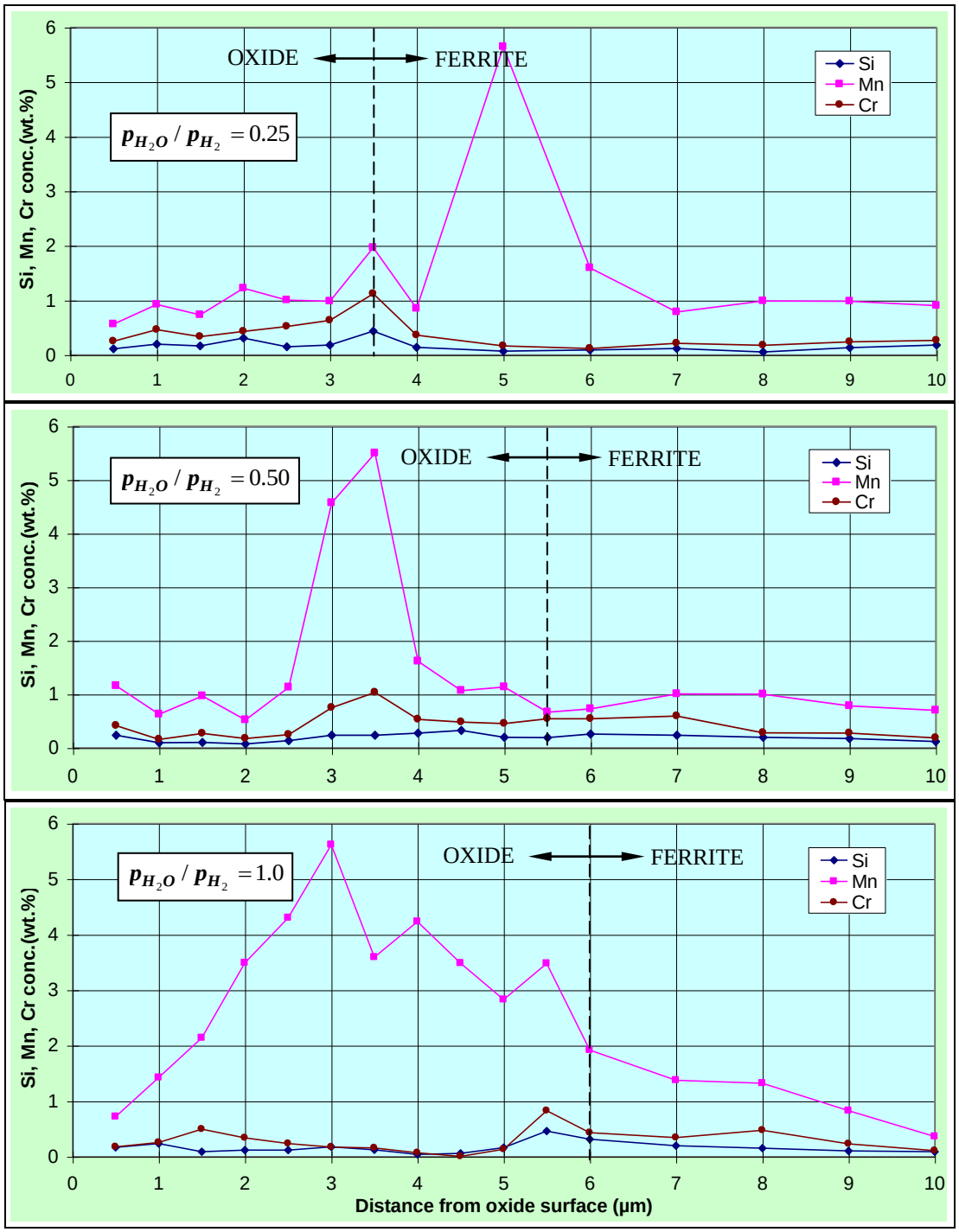

Figure 11.34 Element concentration profiles across the oxide structures of furnace cooled 0% Silicon initial structures after 4hr at 740°C with different p_{H_2O} / p_{H_2} ratios.

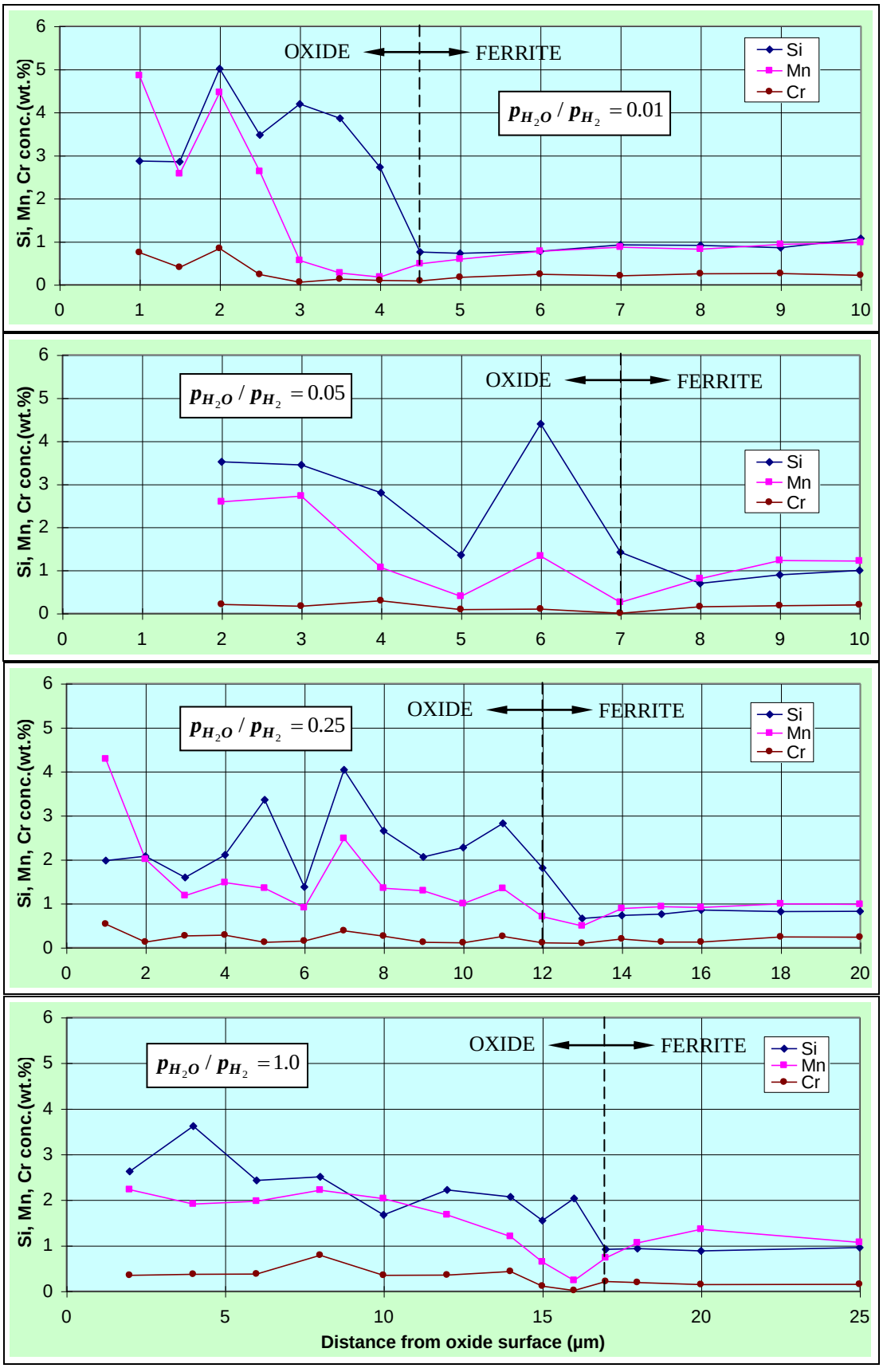

Figure 11.35 Element concentration profiles across the oxide structures of furnace cooled 1% Silicon initial structures after 4hr at 760°C with different p_{H_2O} / p_{H_2} ratios.

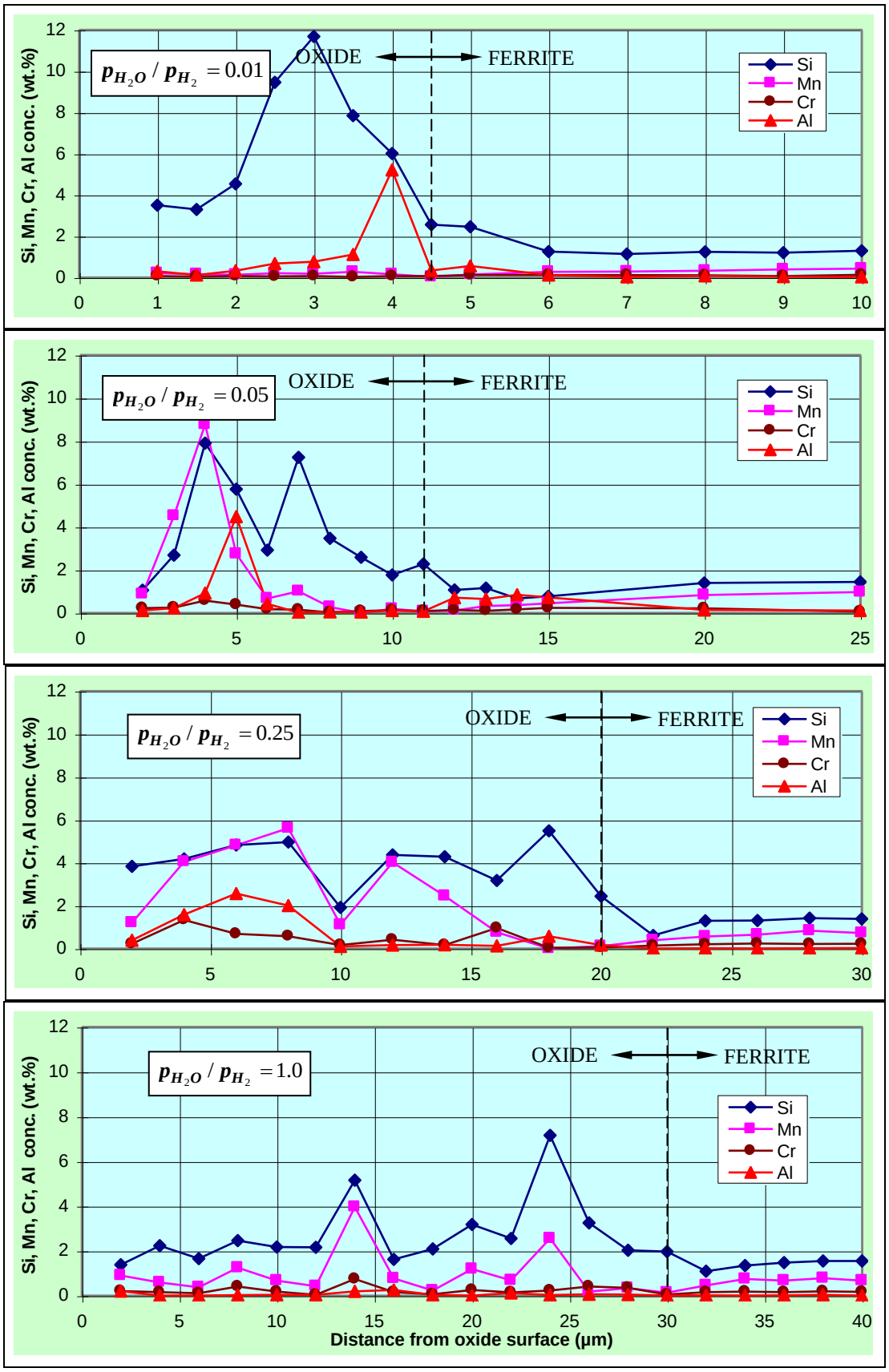

Figure 11.36 Element concentration profiles across the oxide structures of furnace cooled SUP7 initial structures after 4hr at 820°C with different p_{H_2O} / p_{H_2} ratios.

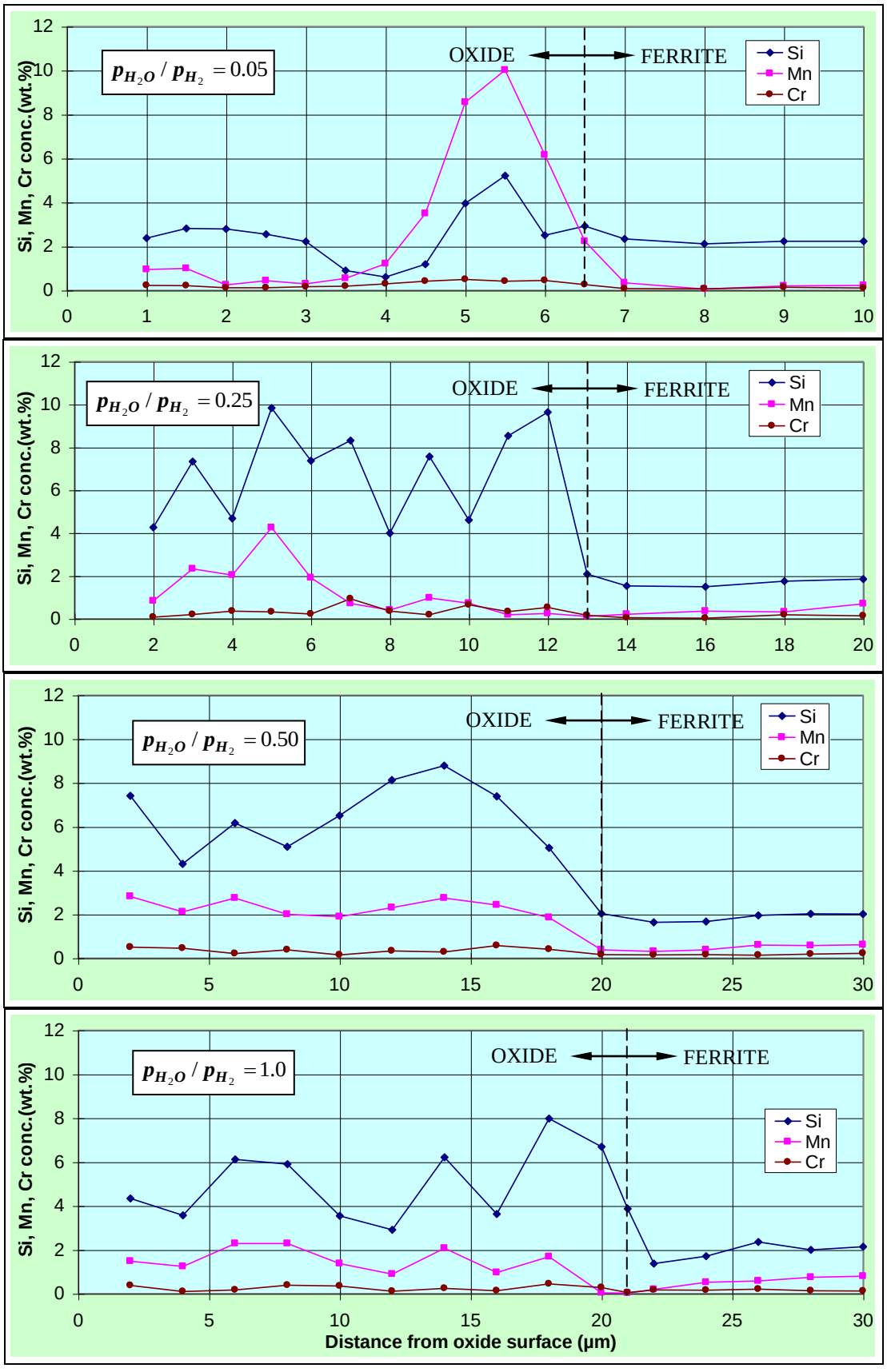

Figure 11.37 Element concentration profiles across the oxide structures of furnace cooled 3% Silicon initial structures after 4hr at 835°C with different p_{H_2O} / p_{H_2} ratios.

higher peak manganese concentrations for SUP7 at p_{H_2O} / p_{H_2} ratios of 0.05 and above. This was despite the lower bulk manganese content of 0.77wt.%, and the thicker oxide structures.

A peak aluminium concentration of 5.2wt.%, more than two orders of magnitude greater than the bulk steel content, was detected for SUP7 decarburised at a p_{H_2O} / p_{H_2} ratio of 0.01. The peak values decreased with increasing p_{H_2O} / p_{H_2} ratios to less than 0.3wt.% at the highest ratio. The oxide layer after decarburisation of the 3% Silicon steel at a p_{H_2O} / p_{H_2} ratio of 0.01 was too thin to be analysed quantitatively with energy dispersive spectroscopy. The peak oxide silicon concentrations decreased from 9.8wt.% at the 0.25 ratio to 8.0wt.% at the 1.0 ratio, Table 11.4. These values were higher than for SUP7 at the comparable p_{H_2O} / p_{H_2} ratios.

The element concentration profiles across the oxide structure for the 3% Silicon steel decarburised at a p_{H_2O} / p_{H_2} ratio of 0.05 requires further explanation. The oxide structure analysed was 6.5μm thick, with silicon and manganese concentrations similar to, or lower than, the bulk steel values over the first 4μm from the oxide surface. The silicon and manganese concentrations then increased, with the peak values of 5.2 and 10.0wt.% respectively 1μm on the oxide side from the oxide/ferrite interface. The similarity of the element concentrations with the bulk steel values over the 4μm from the oxide surface indicates that this corresponds to the steel matrix, and not an oxide layer.

Peak chromium concentrations of up to 1.3wt.% were also observed in the oxide structures, as listed in Table 11.4. The oxide manganese concentrations were almost zero on either side of the oxide/ferrite interfaces for the 1% Silicon, SUP7 and 3% Silicon steels, before increasing to the bulk steel concentration further into the ferrite[84]. Silicon concentrations lower than the bulk steel value were observed in the ferrite immediately adjacent to the oxide/ferrite interface. The silicon concentration then increased to the bulk concentration further into the ferrite. The higher oxide silicon concentrations tended to be associated with the higher manganese and chromium concentrations for the different silicon steels.

11.6.3 Identification of oxide structures

The oxide formation is dependent on the alloy content of the steel, the temperature, and the composition of the atmosphere. The stability of the various oxide phases possible given the steel alloy contents, the decarburisation temperatures and p_{H_2O} / p_{H_2} ratios can be determined thermodynamically. Oxidation of the steels can occur by equations 3.5 to 3.7[69].

$$Si + 2H_2O = SiO_2 + 2H_2 \quad (3.5)$$

$$Fe + H_2O = FeO + H_2 \quad (3.6)$$

$$2Fe + SiO_2 + 2H_2 = Fe_2SiO_4 + 2H_2 \quad (3.7)$$

For equation 11.1, the equilibrium constant $K_{11.1}$ is given by

$$K_{11.1} = \left[\frac{p_{H_2}}{p_{H_2O}}\right]^2 . \frac{a_{SiO_2}}{a_{Si}}, \quad (11.4)$$

where $K_{11.1}$ = equilibrium constant for equation 11.1;

p_{H_2}, p_{H_2O} = hydrogen and water partial pressures at equilibrium in Pa;

a_{SiO_2}, a_{Si} = chemical activity of SiO_2 and Si.

As the activity of a pure phase[212] is 1, a_{SiO_2}=1. Therefore

$$\Delta G^o_{11.1} = -4.574T \log\left(\left[\frac{p_{H_2}}{p_{H_2O}}\right]^2 . \frac{1}{a_{Si}}\right), \quad (11.5)$$

where $\Delta G^o_{11.1}$=Gibbs standard free energy for equation 10.5.

a_{Si} is given by[211]

$$\log a_{Si} = \log(Si \text{ in wt.\%}) + \log f^{Fe}_{Si}, \quad (11.6)$$

where $\log f_{Si}^{Fe}$ is given by[211]

$$\log f_{Si}^{Fe} = -\frac{4540}{T} - 0.549. \tag{11.7}$$

$$\Delta G_{11.1}^{o} = -90{,}300 + 15.5T. \tag{11.8}$$

It was assumed that the presence of approximately 0.6wt.% carbon, 0.8wt.% manganese, and 0.2wt.% chromium have a negligible influence on the activity of silicon in the steels, although this may not be strictly accurate. This gives

$$\log\left[\frac{p_{H_2O}}{p_{H_2}}\right]_{11.1} = -\frac{7601}{T} + K. \tag{11.9}$$

K varies from 2.695 for 0.06wt.%Si to 1.842 for 3.05wt.%Si. A similar approach can be undertaken for reactions 10.6 and 10.7 to give

$$\log\left[\frac{p_{H_2O}}{p_{H_2}}\right]_{11.2} = -\frac{670}{T} + 0.34^{69}; \tag{11.10}$$

$$\log\left[\frac{p_{H_2O}}{p_{H_2}}\right]_{11.3} = -\frac{1891}{T} + 0.84^{69}. \tag{11.11}$$

The elevated manganese, chromium and aluminium concentrations detected in the oxide layers were thought to be present as oxide structures. The mostly likely oxides involving manganese, chromium and aluminium for these steels with p_{H_2O} / p_{H_2} ratios of 0.01 to 1.0 are[212] MnO, Cr_2O_3 and Al_2O_3. A knowledge of the activity of manganese, chromium and aluminium for the element concentrations of these steels was necessary to determine the thermodynamic conditions under which these oxide structures can exist. However, the activity data could not be obtained. Oxidation of iron to Fe_3O_4 and Fe_2O_3 and manganese to Mn_3O_4 can occur, but requires much higher p_{H_2O} / p_{H_2} ratios than those investigated during the

course of the decarburisation experimentation[212]. The stability of the oxidation structures as a function of temperature and p_{H_2O} / p_{H_2} ratio are illustrated in Figure 11.38.

Elevated silicon, manganese, chromium, aluminium and iron concentrations across the oxide structures are in conjunction with lower total alloy concentrations obtained from the ZAF-4 analysis using the Energy Dispersive X-Ray analyser than in the ferrite. Assuming that the lower totals were not a consequence of the somewhat porous oxide structures, it is reasonable to assume that the lower totals were due to the presence of oxygen in oxides. The atomic number of oxygen is too low to be detected with the configuration used for the energy dispersive spectroscopy.

However, if it is assumed that the elevated silicon, manganese, chromium, and aluminium concentrations present in the oxide structures were fully incorporated as oxides, then the oxygen fraction can be calculated from the stoichiometry of the oxides. A similar approach was used by Oh[76] for the oxidation of Fe-Mn-Ni-Si alloys. The alloy element concentrations can then be multiplied by the gravimetric factor for the associated oxide. An adjusted total alloy element concentrations including oxygen can then be calculated by replacing the alloying element concentrations with the value obtained by multiplying the element concentration with the appropriate gravimetric factors.

Figure 11.38 illustrates that SiO_2 formation was thermodynamically possible for p_{H_2O} / p_{H_2} ratios of 0.01 and greater, while Fe_2SiO_4 could form at ratios of 0.25 and greater. FeO formation was thermodynamically possible for p_{H_2O} / p_{H_2} ratios of 0.5 and 1.0 for the 0 and 1% Silicon steels, and at the 1.0 ratio for the SUP7, SUP7NV and 3% Silicon steels. Without the precise knowledge of the oxides present, the calculation of the adjusted totals including oxygen were only estimates. However, they do indicate the likelihood of these elements forming oxides.

The manganese, chromium and aluminium concentrations can be multiplied by gravimetric factors of 1.29, 1.46 and 1.89 to account for the mass of oxygen present as MnO, Cr_2O_3 and Al_2O_3 respectively. Table 11.5 lists the silicon, manganese, chromium and aluminium concentrations in the oxide structures for the quantitative analysis that gave the maximum sum of these elements for the different silicon steels at each p_{H_2O} / p_{H_2} ratio decarburised at their

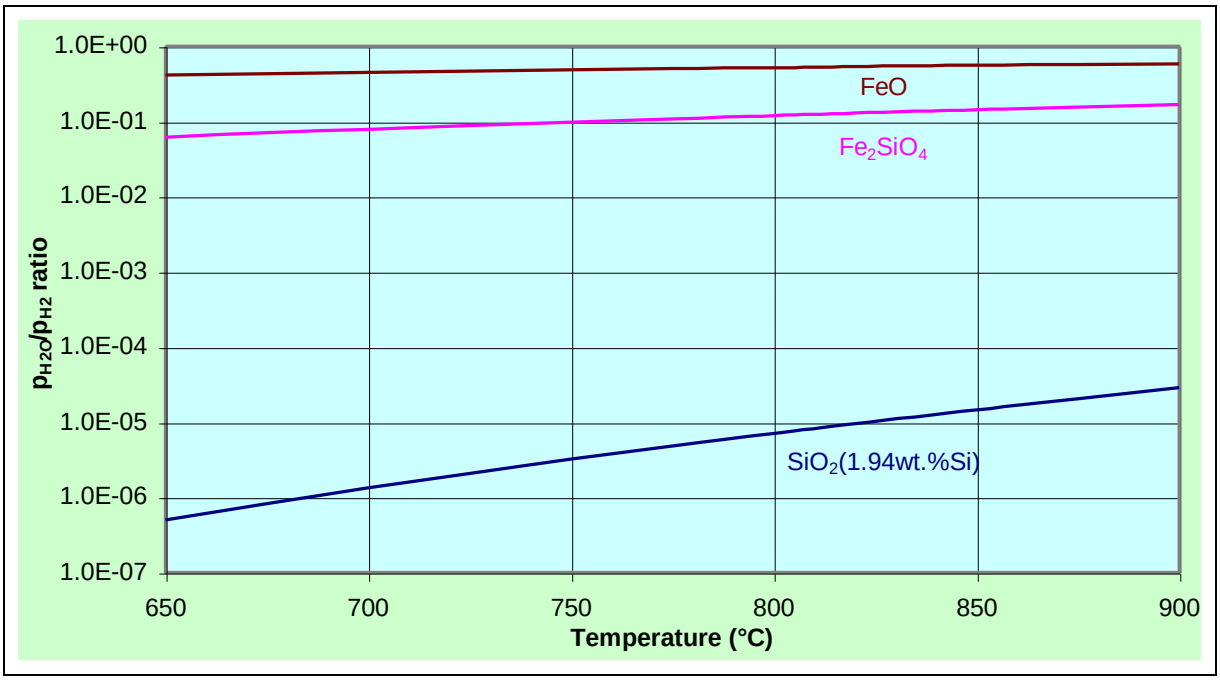

Figure 11.38 Thermodynamics of the possible oxidation structures as a function of temperature and p_{H_2O} / p_{H_2} ratio.

Table 11.5 Calculation of the sum of the total element concentrations, including oxygen, from the assumed oxide structures resulting from the decarburisation of the different silicon steels for 4hr at their respective Ac_3 temperatures with different p_{H_2O} / p_{H_2} ratios.

STEEL	p_{H_2O} / p_{H_2}	Element concs. for max. sum of Si+Mn+Cr+Al (wt.%)					Detected total (wt.%)	Assumed oxides	Adjusted total (wt.%)	Peak ferrite total (wt.%)
		Si	Mn	Cr	Al	Fe				
0% SILICON	**0.25**	-	5.6	-	-	85.4	91.0	MnO	92.6	95.1
	0.50	-	5.5	1.0	-	82.3	88.8	MnO/Cr_2O_3	90.9	96.9
	1.0	-	5.6	-	-	68.9	71.9	MnO/FeO	96.1	96.6
1% SILICON	**0.01**	5.0	4.5	0.8	-	75.1	85.4	$SiO_2/MnO/Cr_2O_3$	92.8	94.9
	0.05	3.4	2.7	-	-	85.1	91.2	SiO_2/MnO	95.9	100.2
	0.25	4.0	2.5	0.4	-	74.1	81.0	$SiO_2/Fe_2SiO_4/MnO/Cr_2O_3$	86.4/91.0*	96.6
	0.50	5.7	2.2	0.5	-	75.0	83.4	$SiO_2/Fe_2SiO_4/MnO/Cr_2O_3$	90.8/97.3	97.6
	1.0	3.6	1.9	0.4	-	86.0	91.9	$SiO_2/Fe_2SiO_4/MnO/Cr_2O_3$	96.7/100.7	94.2
SUP7	**0.01**	11.7	-	-	0.8	72.7	85.2	SiO_2/Al_2O_3	99.3	92.8
	0.05	7.9	8.8	0.6	0.9	63.2	81.2	$SiO_2/MnO/Cr_2O_3/Al_2O_3$	94.0	101.1
	0.25	5.0	5.6	0.6	2.0	66.5	79.7	$SiO_2/Fe_2SiO_4/MnO/Cr_2O_3$	89.0/94.8	92.0
	0.50	4.8	2.8	-	-	84.7	92.3	$SiO_2/Fe_2SiO_4/MnO$	98.5/104.7	99.8
	1.0	5.2	4.0	0.7	-	73.0	88.6	$SiO_2/Fe_2SiO_4/MnO/Cr_2O_3$	90.3/96.0	96.2
3% SILICON	**0.05**	5.2	10.0	0.4	-	58.5	72.9	$SiO_2/MnO/Cr_2O_3$	83.1	99.2
	0.25	9.8	4.3	0.3	-	60.4	72.2	$SiO_2/Fe_2SiO_4/MnO/Cr_2O_3$	87.4/98.5	96.0
	0.50	8.8	2.7	0.3	-	67.4	79.2	$SiO_2/Fe_2SiO_4/MnO/Cr_2O_3$	90.2/100.2	95.9
	1.0	8.0	1.7	0.5	-	73.7	83.9	$SiO_2/Fe_2SiO_4/MnO/Cr_2O_3$	93.7/102.5	97.9

* For SiO_2/Fe_2SiO_4 formation.

respective Ac_3 temperatures. The highest combined totals of silicon, manganese, chromium and aluminium were used to minimise the errors associated with the measurement of the element concentrations by energy dispersive spectroscopy. These concentrations were multiplied by the gravimetric factors of the assumed oxide structures.

The last two columns of Table 11.5 compare the sum of the total element concentrations incorporating oxygen from oxide formation, with the element concentrations measured in the ferrite corresponding to the bulk ferrite concentration. The ferrite total was used due to the low carbon and oxygen concentrations, which theoretically results in a total of 100. Some variation in the ferrite totals from 100 was observed, although similar totals to the ferrite phases obtained during the intercritical annealing of a SUP7 specimen indicated that this was due to the Energy Dispersive X-Ray analyser, rather than the presence of oxygen in the ferrite. Therefore, the difference in the ferrite and the detected totals should correspond to the oxygen content of the oxide.

The presence of oxygen as SiO_2, MnO, Cr_2O_3 and Al_2O_3 is suggested by the similarity of the adjusted and ferrite totals for the 1% Silicon, SUP7 and 3% Silicon steels at p_{H_2O} / p_{H_2} ratios of 0.01 and 0.05. For p_{H_2O} / p_{H_2} ratios of 0.25, 0.5 and 1.0, silicon can be oxidised to SiO_2 or Fe_2SiO_4. Therefore, two adjusted total element concentrations are listed for these p_{H_2O} / p_{H_2} ratios. The first value corresponds to the oxide silicon content yielding SiO_2 formation, while the second value is for Fe_2SiO_4 formation. A comparison of these adjusted totals with those of ferrite at 0.25 and 0.5 p_{H_2O} / p_{H_2} ratios for the 1% Silicon, SUP7 and 3% Silicon steels suggest that silicon was predominantly oxidised to Fe_2SiO_4. This was also predicted from the thermodynamic analysis.

Complete oxidation of the iron to FeO for the 0% Silicon steel decarburised at a p_{H_2O} / p_{H_2} ratio of 1.0 is indicated by the similar totals of the last two columns of Table 11.5. Complete oxidation of the iron to FeO for the higher silicon steels decarburised at a p_{H_2O} / p_{H_2} ratio of 1.0 appears unlikely, as the total element concentrations calculated from the iron content would considerably exceed 100wt.%. The two totals quoted for the 1% Silicon, SUP7 and 3% Silicon steels at this p_{H_2O} / p_{H_2} ratio correspond to complete silicon oxidation to SiO_2 and

Fe_2SiO_4 respectively. These totals suggest that iron is predominantly present in an elemental form at a p_{H_2O} / p_{H_2} ratio of 1.0, rather than as FeO predicted by the thermodynamic analysis.

Mayer[67] demonstrated that the rate of carbon removal increased with increasing p_{H_2O} / p_{H_2} ratios below that for FeO formation for a 0.04wt.%C/0.68wt.%Si/0.31wt.%Mn steel at 850°C. However, the decarburisation rate decreased sharply with increasing p_{H_2O} / p_{H_2} ratio above that at which FeO formed[67]. The decreasing free ferrite for the 0% Silicon steel as the p_{H_2O} / p_{H_2} ratio increased from 0.5 to 1.0 was due to the formation of FeO, with the subsequent inhibition of carbon removal.

The adjusted total element concentrations listed in Table 11.5 indicate that the majority of the iron present in the oxide layer was present in its elemental form, rather than as FeO. This would account for the constant free ferrite decarburisation depths for the 1% Silicon, SUP7 and SUP7NV steels for p_{H_2O} / p_{H_2} ratios of 0.25 to 1.0. The increasing free ferrite depths as the p_{H_2O} / p_{H_2} ratio increased from 0.25 to 1.0 for the 3% Silicon steel are thought to be due to the oxide structure becoming less dense, and therefore allowing faster carbon removal.

11.7 Decarburisation discussion for the different silicon steels

11.7.1 Calculation of effective diffusion coefficients

For decarburisation at temperatures at or below the Ac_3 temperature, carbon removal can result in the formation of a free ferrite layer. Equation 10.6 can then be used to calculate the effective diffusion coefficient of carbon in ferrite. The effective diffusion coefficients for the different silicon steels at their respective Ac_3 cannot be compared directly, due to the temperature dependence of the diffusion coefficients. However, they can be compared to a binary Fe-C steel at the same temperature by the ratio of $D_{effective}/D_\alpha$, where D_α is the diffusion coefficient of carbon in ferrite for a binary Fe-C steel. $D_{effective}$ was calculated from the largest free ferrite depths for each of the different silicon steels decarburised 4hr at their respective Ac_3 temperatures.

Table 11.6 Comparison of the maximum values of $D_{effective}/D_{\alpha}$ for the different silicon steels decarburised at their respective Ac_3 temperatures.

STEEL	Ac_3 temp. (°C)	C_{sat} (wt.%)	C_i (wt.%)	$D_{effective}$ (cm^2/s)	D_{α} (cm^2/s)	$D_{effective}/D_{\alpha}$
0% Silicon	740	0.018	0.62	$3.1x10^{-7}$	$1.4x10^{-6}$	0.22
1% Silicon	760	0.019	0.61	$7.2x10^{-7}$	$1.9x10^{-6}$	0.38
SUP7	820	0.020	0.60	$1.6x10^{-6}$	$3.6x10^{-6}$	0.45
SUP7NV	820	0.020	0.62	$1.7x10^{-6}$	$3.6x10^{-6}$	0.47
3% Silicon	835	0.025	0.58	$1.2x10^{-6}$	$4.2x10^{-6}$	0.28

Table 11.7 Comparison of $D_{effective}/D_{\alpha}$ for the different silicon steels decarburised at 750°C with =0.05. p_{H_2O} / p_{H_2}

STEEL	C_{sat} (wt.%)	C_i (wt.%)	$D_{effective}$ (cm^2/s)	D_{α} (cm^2/s)	$D_{effective}/D_{\alpha}$
0% Silicon*	0.018	0.62	$7.3x10^{-8}$	$1.4x10^{-6}$	0.05
1% Silicon	0.020	0.61	$3.9x10^{-7}$	$1.6x10^{-6}$	0.25
SUP7	0.030	0.60	$6.1x10^{-7}$	$1.6x10^{-6}$	0.38
SUP7NV	0.030	0.62	$6.8x10^{-7}$	$1.6x10^{-6}$	0.43
3% Silicon	0.030	0.58	$1.9x10^{-7}$	$1.6x10^{-6}$	0.12

Table 11.8 Influence of temperature on $D_{effective}/D_{\alpha}$ for SUP7 decarburised with =0.05. p_{H_2O} / p_{H_2}

Temperature (°C)	C_{sat} (wt.%)	C_i (wt.%)	$D_{effective}$ (cm^2/s)	D_{α} (cm^2/s)	$D_{effective}/D_{\alpha}$
650	0.022	0.60	$5.3x10^{-9}$	$4.5x10^{-7}$	0.01
700	0.025	0.60	$1.1x10^{-7}$	$8.7x10^{-6}$	0.13
750	0.030	0.60	$6.1x10^{-7}$	$1.6x10^{-6}$	0.38
800	0.025	0.60	$1.1x10^{-6}$	$2.8x10^{-6}$	0.40
820	0.020	0.60	$1.6x10^{-6}$	$3.6x10^{-6}$	0.44

* The values quoted are for decarburisation of the 0% Silicon steel at the Ac_3 temperature of 740°C, since decarburisation at 750°C results in a carbon concentration gradient in the austenite, in conjunction with the formation of a free ferrite layer. However, the value at 740°C provides a comparison, where D_{α} increases by a factor of 1.1 as the temperature increases from 740 to 750°C.

C_{sat} values for the 0% Silicon steel were calculated from the equilibrium of Krauss[187], and from ternary Fe-C-Si diagrams for 1, 2 and 3wt.% silicon steels for the higher silicon steels[194]. The manganese concentrations of these steels have a negligible influence on the C_{sat} values[182], other than to raise the temperature of the ferrite plus austenite/austenite phase boundary[55]. Therefore, the C_{sat} values of the 0% Silicon steel were determined at a temperature that corresponded to the same temperatures above the Ac_1 line relative to a Fe-C steel. The values of D_α for a Fe-C steel were obtained from Smith[99].

The values of $D_{effective}/D_\alpha$ for the different silicon steels decarburised at their respective Ac_3 temperatures are presented in Table 11.6. $D_{effective}/D_\alpha$ increased from 0.22 for the 0% Silicon steel to 0.47 for SUP7NV, before decreasing to 0.28 for the 3% Silicon steel. The increasing value of $D_{effective}/D_\alpha$ illustrates that the fastest decarburisation occurred for SUP7NV. However, the value of $D_{effective}$ for SUP7NV at 820°C was still only half the value for uninhibited carbon diffusion in ferrite for a Fe-C steel.

Values of $D_{effective}/D_\alpha$ less than one for the higher silicon steels can be attributed to the oxidation of silicon, with this oxidation impeding carbon removal. However, oxidation of silicon in the 0% Silicon steel was not possible, due to the low silicon content. The highest value of $D_{effective}$ for the 0% Silicon steel at 740°C, for decarburisation at a p_{H_2O} / p_{H_2} ratio of 0.25, was only $1/5^{th}$ that of the value for the Fe-C steel. For $D_{effective}/D_\alpha$=1, a free ferrite depth of 345μm would result, compared with 163μm for the 0% Silicon steel with a p_{H_2O} / p_{H_2} ratio of 0.25.

Decarburisation at p_{H_2O} / p_{H_2} ratios of 0.01 to 0.25 are less than that determined from the thermodynamics of Figure 11.38 for the formation of FeO. However, the dense oxide structure of Figure 11.29, and the elevated oxide manganese concentrations of Figure 11.34, indicates that the inhibition of carbon removal for the 0% Silicon steel arose from the oxidation of manganese to form MnO.

Table 11.7 lists the values of $D_{effective}/D_\alpha$ for the different silicon steels decarburised at 750°C with p_{H_2O} / p_{H_2}=0.05. The value of $D_{effective}/D_\alpha$ increased by almost an order of magnitude as the silicon content increased from 0.06wt.% for the 0% Silicon steel to 2.11wt.% for

SUP7NV. However, the ratio of $D_{effective}/D_{\alpha}$ for the 3% Silicon steel was only half that of SUP7NV. The influence of temperature on $D_{effective}/D_{\alpha}$ at temperatures up to the Ac_3 value for SUP7 at a p_{H_2O} / p_{H_2} ratio of 0.05 is detailed in Table 11.8. $D_{effective}/D_{\alpha}$ increased 40 times from 0.01 at 650°C to 0.44 at 820°C.

Hudson[100] found that a Fe/0.11wt.%C/0.56wt.%Mn steel approached the maximum rate of decarburisation controlled by carbon diffusion in ferrite for wet hydrogen atmospheres with p_{H_2O} / p_{H_2} ratios greater than 0.025 at a temperature of 705°C. However, $D_{effective}/D_{\alpha}$ was less than 0.5 during the decarburisation of the different silicon steels. The lower values of $D_{effective}$ relative to a Fe-C steel could be influenced by:

- Uncertainties in the determination of the value of C_{sat} for the Fe-Si-C steels relative to the steels decarburised, where halving the value of C_{sat} for high bulk carbon contents approximately doubles the value of $D_{effective}$ calculated from equation 10.6;
- The lower diffusion coefficient of carbon in ferrite due to the higher silicon, manganese and chromium concentrations;
- Formation of oxide structures which impede carbon removal from the steel;
- The free ferrite grain structure and its influence on carbon diffusion through the ferrite.

11.7.2 Microhardness profiles

The microhardness profile across the ferrite and martensite phases for a furnace cooled initial SUP7 structure decarburised 4hr at 820°C with a p_{H_2O} / p_{H_2} ratio of 0.25 is illustrated in Figure 11.39. The increasing free ferrite carbon content from the surface to the ferrite/martensite interface is demonstrated by the increasing hardness across the ferrite layer, while the microhardness gradient across the martensite from the ferrite/martensite interface illustrates a carbon concentration gradient in the austenite near the ferrite/austenite interface during decarburisation.

It was assumed in sections 10.3.5 and 11.7.1 that decarburisation at the Ac_3 temperature resulted in the formation of a free ferrite layer separated from a ferrite/austenite core, where the ferrite carbon concentration profile increased linearly from zero at the surface to C_{sat} at the ferrite/austenite interface, with a constant austenite carbon content in the core. While the

ferrite microhardness profile of Figure 11.39 approximates a straight line, and therefore a linear carbon concentration profile, the martensite hardness profile indicates that Fick's second law is applicable to this phase. This martensite concentration gradient could have been due to the decarburisation temperature being slightly above the Ac_3 temperature.

The minimum carbon content to which austenite can be decarburised before an austenite to ferrite transformation results decreases with increasing temperature above the Ac_3 temperature. This is evident in Figure 11.40, which illustrates the influence of temperature on the martensite microhardness profiles for the 0% Silicon steel. The increasing temperature resulted in lower martensite microhardness values at the ferrite/austenite interface due to the lower carbon contents, with the hardness profile extending further into the specimen before the core hardness was obtained.

Figure 11.41 illustrates the influence of test duration on the martensite microhardness profiles for SUP7 furnace cooled initial structures decarburised at 900°C. After 15min, the martensite Knoop microhardness 25μm from the ferrite/martensite interface was 640, with the core hardness of 860 obtained within 200μm of the ferrite/martensite interface. From 4hr onwards, the martensite Knoop hardness 25μm from the ferrite/martensite interface was approximately 500. For the 24hr test, the Knoop hardness of 815 at 1350μm from the ferrite/martensite interface was lower than the core value.

The increasing Ac_3 temperatures with silicon content resulted in higher minimum austenite carbon contents at 900°C. This is illustrated in Figure 11.42 by the martensite microhardness profiles for the different silicon steels decarburised 4hr at a 0.05 p_{H_2O} / p_{H_2} ratio. The distance from the ferrite/martensite interface into the martensite at which the core hardness was obtained decreased with increasing silicon content.

11.7.3 Calculation of carbon removed during decarburisation

The total mass of carbon removed from a specimen decarburised at temperatures at or below the Ac_3 temperature with a free ferrite layer separated from the high carbon core by a sharply defined interface can be calculated from the thickness of the free ferrite layer. However, at temperatures greater than the Ac_3 temperature, the carbon concentration profile across the

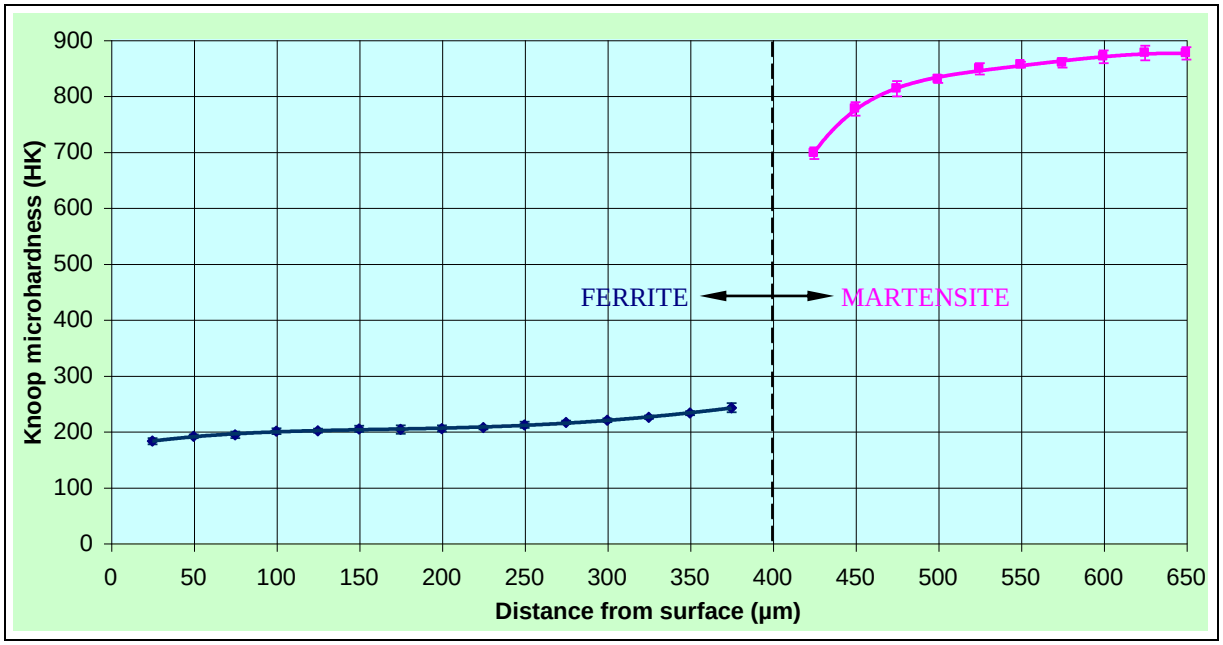

Figure 11.39 Knoop microhardness profile for a SUP7 furnace cooled initial structure decarburised 4hr at p_{H_2O} / p_{H_2}=0.25.

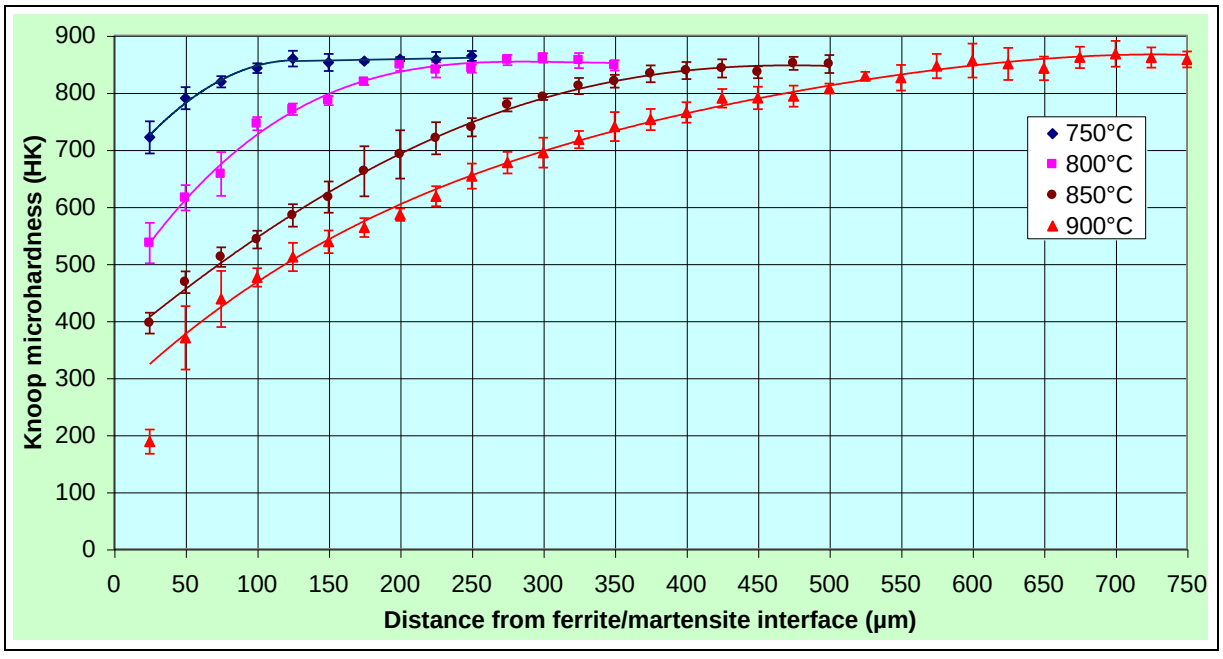

Figure 11.40 Influence of temperature on Knoop martensite microhardness profiles for the 0% Silicon furnace cooled initial structure decarburised 4hr with p_{H_2O} / p_{H_2}=0.05.

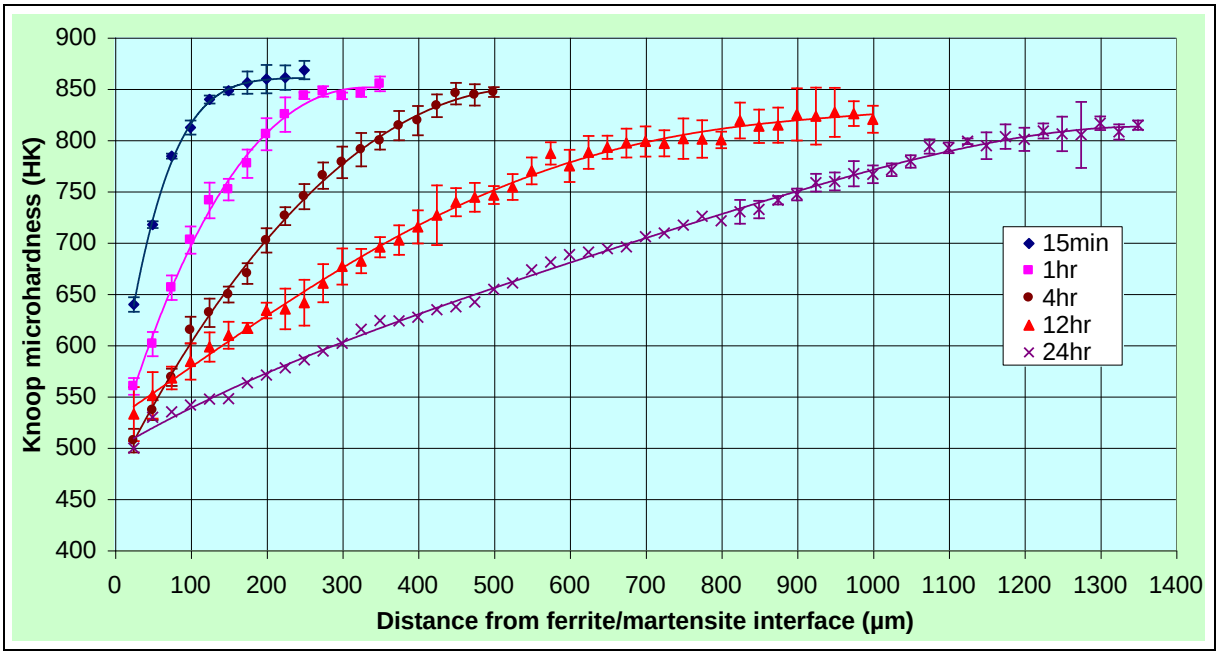

Figure 11.41 Knoop martensite microhardness profiles for SUP7 furnace cooled initial structures decarburised at 900°C with p_{H_2O} / p_{H_2}=0.05.

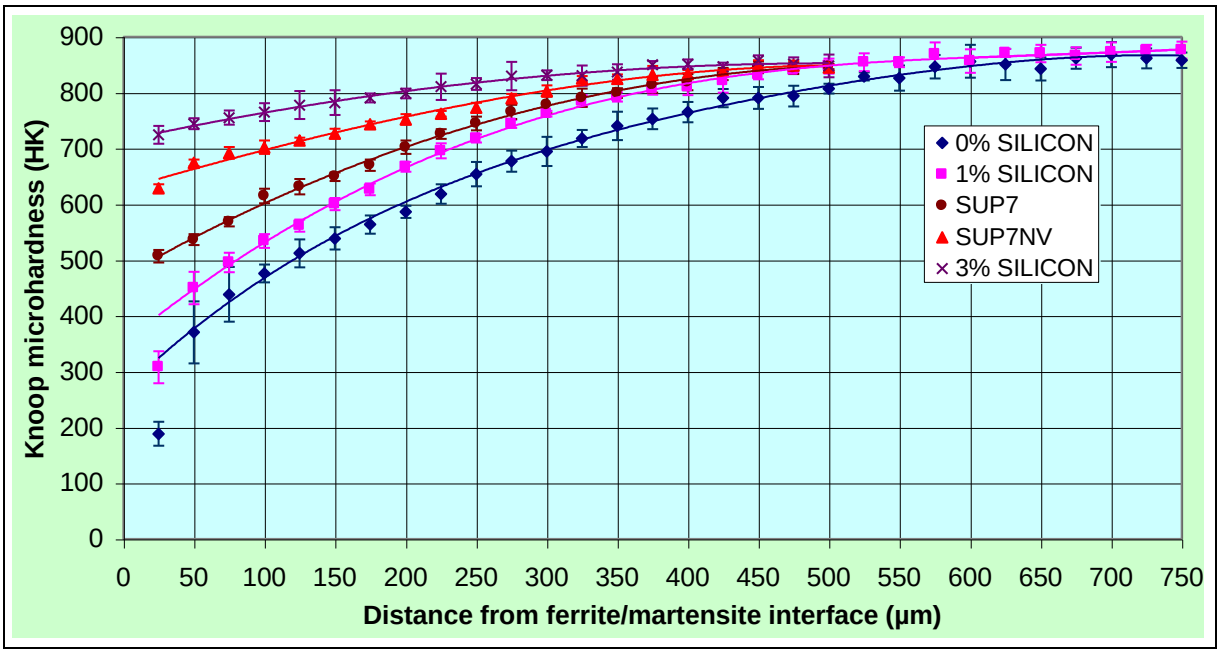

Figure 11.42 Knoop martensite microhardness profiles for different silicon steels with furnace cooled initial structures decarburised 4hr with p_{H_2O} / p_{H_2}=0.05 at their respective Ac_3 temperatures.

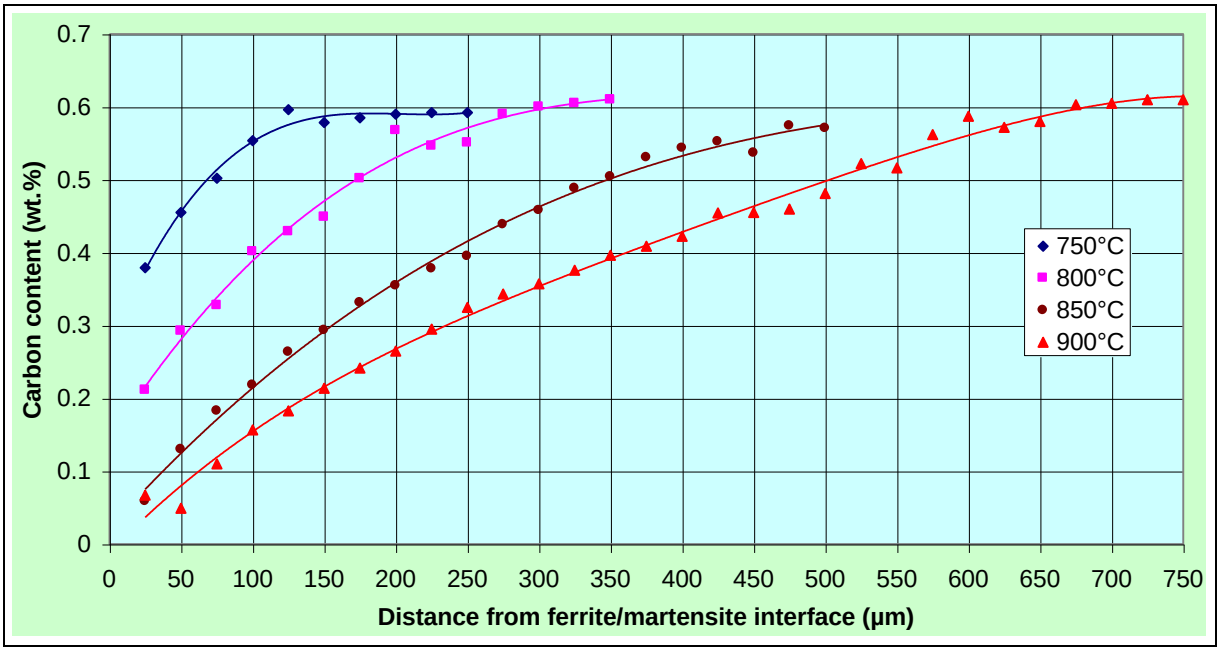

Figure 11.43 Influence of temperature on the calculated carbon concentration profiles for furnace cooled 0% Silicon initial structures decarburised 4hr with p_{H_2O} / p_{H_2}=0.05.

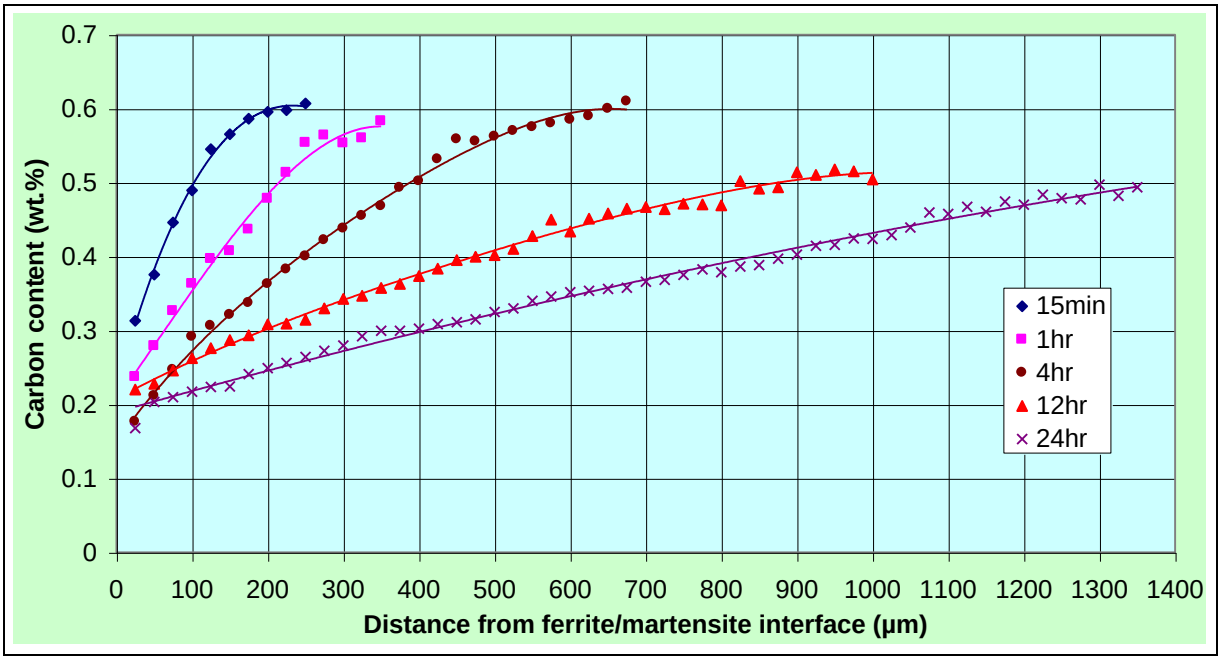

Figure 11.44 Calculated carbon concentration profiles for SUP7 furnace cooled initial structures decarburised at 900°C with p_{H_2O} / p_{H_2}=0.05.

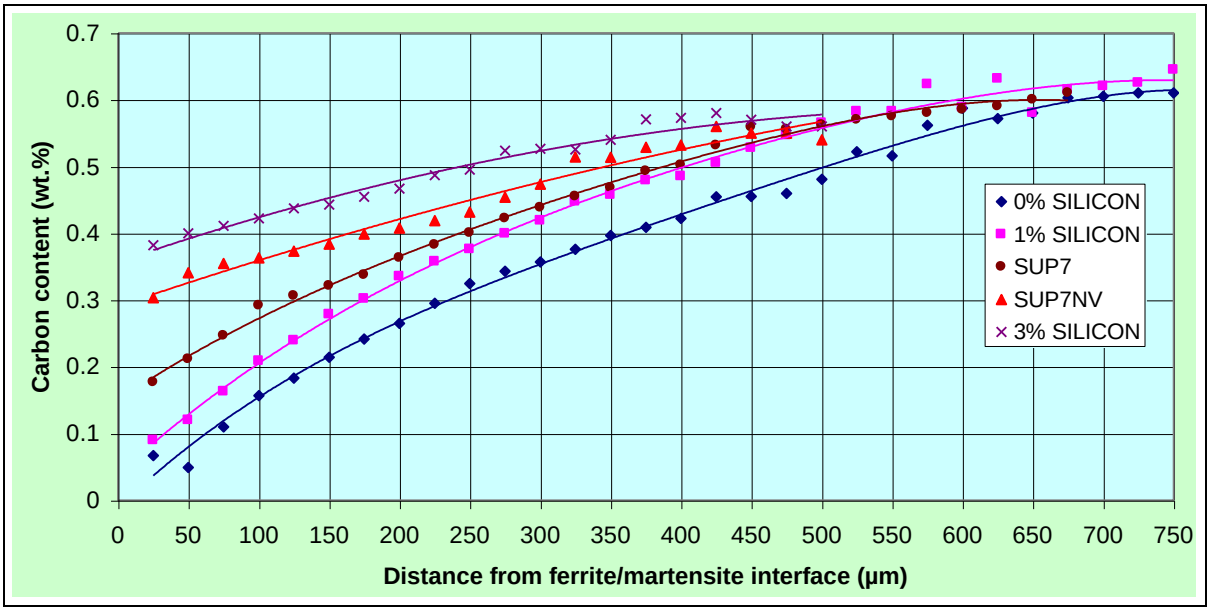

Figure 11.45 Calculated carbon concentration profiles for different silicon steels with furnace cooled initial structures decarburised 4hr with p_{H_2O} / p_{H_2} =0.05 at their respective Ac_3 temperatures.

austenite also has to be determined. The total mass of carbon removed then corresponds to that required to form the free ferrite layer, and the austenite carbon concentration profile. Grange[193] demonstrated that the hardness of as-quenched martensite for a particular carbon content, which was austenite at the heat treatment temperature, did not change significantly with the addition of silicon and manganese[193]. The core martensite microhardness of approximately 860 Knoop for the different silicon steels also corresponded to that for an as-quenched 0.6wt.% carbon steel[193].

Assuming that the effects of silicon and manganese on the temperatures of the boundary separating the ferrite plus austenite and austenite phase fields are additive, the minimum carbon contents to which austenite can decarburise at 900°C before ferrite forms were approximately 0.10, 0.22 and 0.38wt.% for the 1% Silicon, SUP7 and 3% Silicon steels respectively[55]. Free ferrite formation cannot occur during decarburisation of the 0% Silicon steel at 900°C. Assuming that these minimum carbon contents exist in the austenite at the ferrite/austenite interface after 4hr decarburisation, the respective Knoop microhardness values of the as-quenched martensitic structures can be compared to the data of Grange[193]. As the microhardness values of these carbon contents were similar to the values of Grange[193] for the same carbon contents, the data of Grange[193] for hardness versus carbon content was used to convert the microhardness profiles of Figures 11.40 to 11.42 to the carbon concentration profiles of Figures 11.43 to 11.45.

The carbon concentration profile where decarburisation results in the formation of a free ferrite layer and an austenite carbon concentration gradient from the ferrite/austenite interface into the austenite is illustrated schematically in Figure 11.46. The total carbon removed from the steel corresponds to the carbon removed to form the free ferrite layer, and the carbon removed to form the austenite carbon concentration profile.

The average carbon content in wt.% over each interval defined by x_{i+1}-x_i for i=0,1,2,…n, $C_{interval}$, is approximated by

$$C_{interval} = \frac{C_{i+1} + C_i}{2}. \qquad (11.12)$$

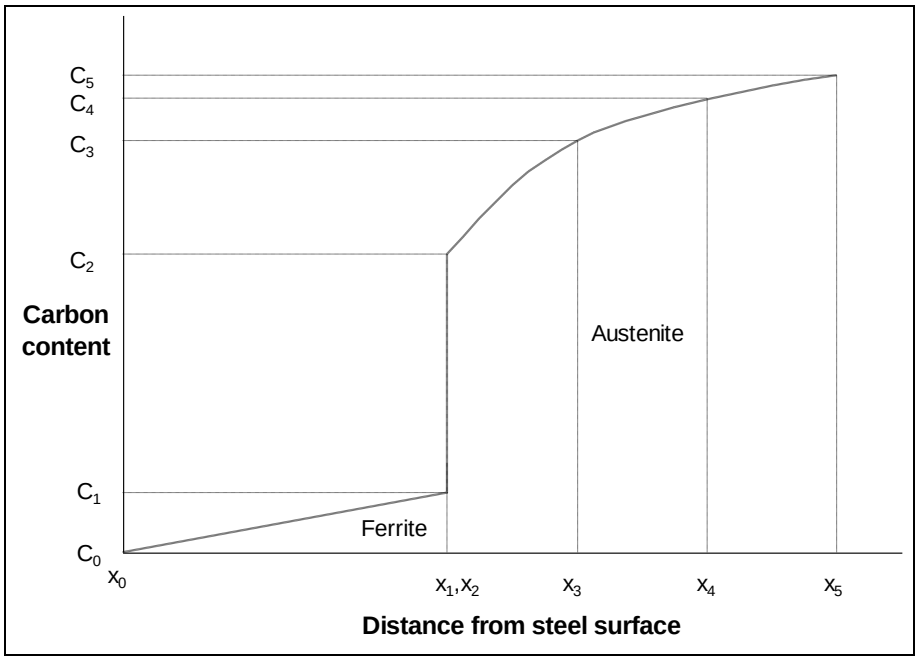

Figure 11.46 Schematic illustration of carbon removal above the Ac_3 temperature with free ferrite formation and an austenite carbon concentration profile.

The 25µm spacing of the microhardness readings resulted in the carbon contents of the linear approximation of equation 11.4 closely following the carbon contents obtained from microhardness profiles. The average carbon content removed over each interval in wt.%, $C_{removed}$, is given by

$$C_{removed} = C_o - C_{interval}. \tag{11.13}$$

The volume of steel over which carbon is removed for each interval in cm^3, $V_{interval}$, corresponds to

$$V_{interval} = \pi(R_i^2 - R_{i+1}^2)L(C.F.). \tag{11.14}$$

The mass of carbon removed over each interval in g, $m_{interval}$, equals

$$m_{interval} = \rho.V_{interval}.\frac{C_{removed}}{100}. \tag{11.15}$$

The mass of carbon removed over each interval can then be summed to determine the total mass of carbon removed during decarburisation. Figure 11.47 demonstrates that the total mass of carbon removed upon decarburising the 0% Silicon steel for 4hr with a p_{H_2O} / p_{H_2} ratio of 0.05 increased linearly with temperature from 3.0μg at 740°C to 10.2μg at 900°C. A greater mass of carbon was removed for comparable test durations during decarburisation of SUP7 at the Ac_3 temperature of 820°C than at 900°C, as illustrated in Figure 11.48. However, the difference between the values for the 12hr and 24hr test will have been less than those illustrated, as carbon removal further into the specimen than that measured occurred, as illustrated by the increasing carbon concentration profiles of Figure 11.44.

The carbon removed for the different silicon steels decarburised at their respective Ac_3 temperatures with a p_{H_2O} / p_{H_2} ratio of 0.05 was higher for SUP7 and SUP7NV than at 900°C, as illustrated in Figure 11.49. The maximum free ferrite depths at the respective Ac_3 temperatures, resulted in greater carbon removal than at 900°C with a 0.05 p_{H_2O} / p_{H_2} ratio for all but the 0% Silicon steel.

11.7.4 Decarburisation in air

Decarburisation heat treatments were undertaken for the different silicon steels at their respective Ac_3 temperatures in air by inserting the specimens into the tube furnace hot zone, with the furnace open to the ambient atmosphere at both ends. This allowed the decarburisation occurring during spring manufacture in an air furnace to be simulated. Figure 11.50 illustrates the free ferrite depths for decarburisation of the respective furnace cooled initial structures after 4hr in air.

The free ferrite depth of 340μm for SUP7 at 820°C was almost twice the values obtained for the other steels, with 186μm free ferrite for SUP7NV at the same temperature. The SUP7 decarburisation was 60μm less than that obtained at 820°C with p_{H_2O} / p_{H_2} ratios of 0.05 to 1.0, while the free ferrite depth for SUP7NV in air was approximately half that over the same p_{H_2O} / p_{H_2} range. No free ferrite resulted for the 0% Silicon steel, while the free ferrite depth for the 1% Silicon steel was less than at the 0.05 to 1.0 p_{H_2O} / p_{H_2} ratios. The 91μm ferrite

depth for the 3% Silicon steel decarburised in air was less than one-quarter the value at the 1.0 p_{H_2O} / p_{H_2} ratio.

The lower free ferrite depths of the different silicon steels relative to decarburisation in the wet hydrogen atmospheres result from the faster oxidation of carbon by water vapour than by air[82]. A considerable fraction of the oxide detached from the specimens during the water quench after decarburising in air, which prevented measurement of the oxide layer thickness, and the quantitative determination of the oxide alloy element composition.

11.7.5 Decarburisation of SUP7 and SUP7NV

The microstructures obtained during the decarburisation of SUP7 and SUP7NV furnace cooled initial structures at 900°C with a p_{H_2O} / p_{H_2} ratio of 0.05, Figure 11.51, demonstrate that the thickest free ferrite layers were observed after 4hr. The free ferrite depth after 24hr was less than at 4hr, with a poorly defined ferrite/martensite interface. Figure 11.52 illustrates the variation in free ferrite depths during the decarburisation of SUP7 and SUP7NV at 900°C. The maximum free ferrite depths were observed after 4hr for both steels, with the maximum value for SUP7 three times that of SUP7NV. The large 95% confidence intervals indicate the variable thickness of the free ferrite layers. The increasing thickness of the oxide layers formed during the decarburisation of SUP7 and SUP7NV at 900°C for longer test durations are illustrated in Figure 11.53. The oxide thickness increased faster with time for SUP7 than for SUP7NV.

Figure 11.48 demonstrated that the total mass of carbon removed from SUP7 and SUP7NV decarburised at 900°C increased with time, despite the decreasing free ferrite depths after 4hr. The thickness of the free ferrite layer increased when carbon from the ferrite/austenite interface diffused through the ferrite layer at a greater rate than that of the carbon supply from the austenite to the ferrite. However, it appears that between 4hr and 12hr, carbon diffusion through the ferrite became slower than the rate of carbon supply from the austenite to the ferrite. This is thought to be due to the oxide structure inhibiting carbon removal from the steel to a greater extent for the longer heat treatment times, with longer diffusion distances for carbon through the thicker oxide, and with the oxide structure possibly becoming less porous with time.

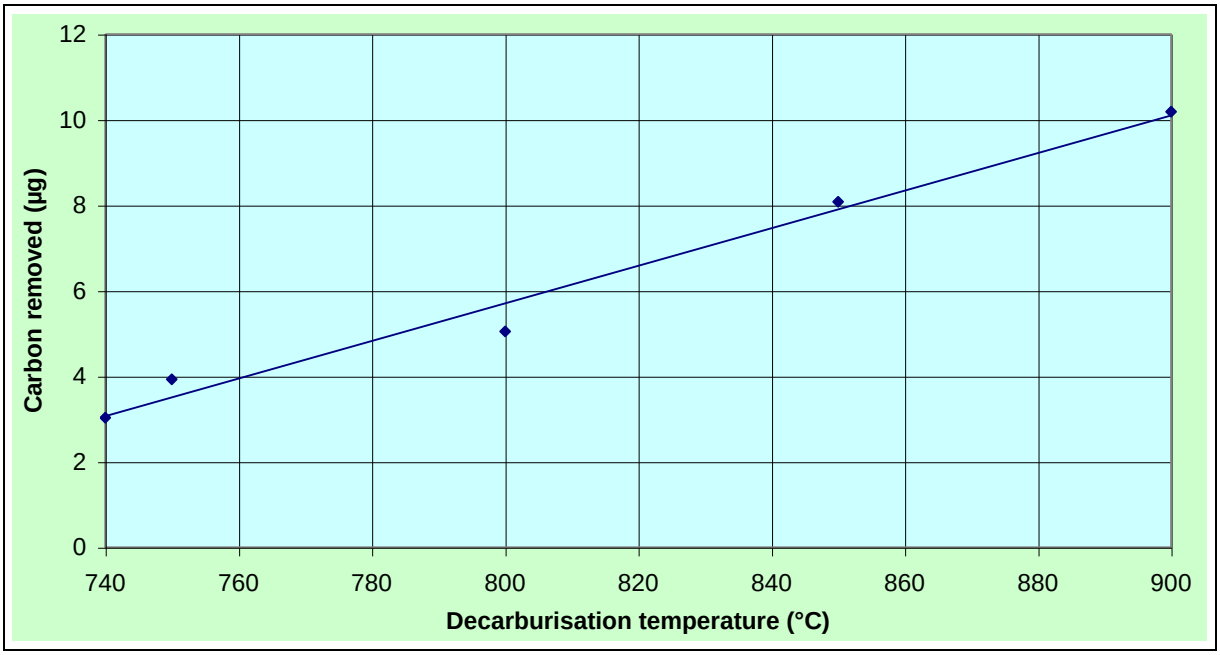

Figure 11.47 Influence of temperature on the total mass of carbon removed for 0% Silicon furnace cooled initial structures decarburised 4hr with p_{H_2O} / p_{H_2} =0.05.

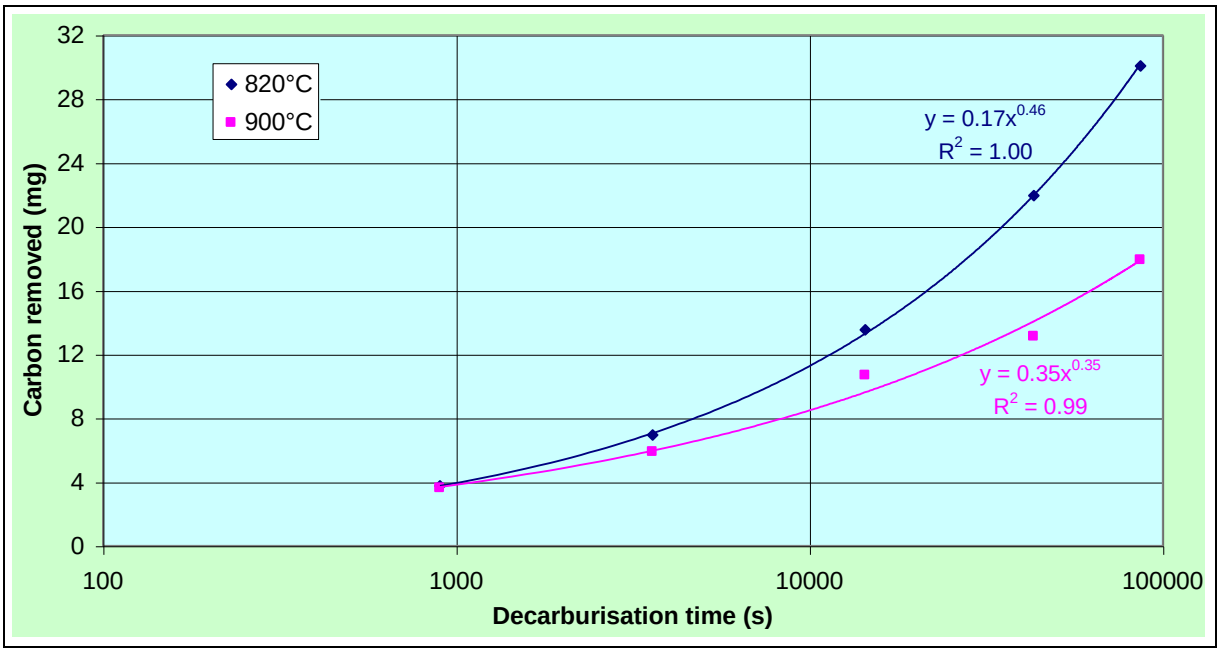

Figure 11.48 Comparison of the total mass of carbon removed for SUP7 furnace cooled initial structures decarburised at 820 and 900°C with p_{H_2O} / p_{H_2} =0.05.

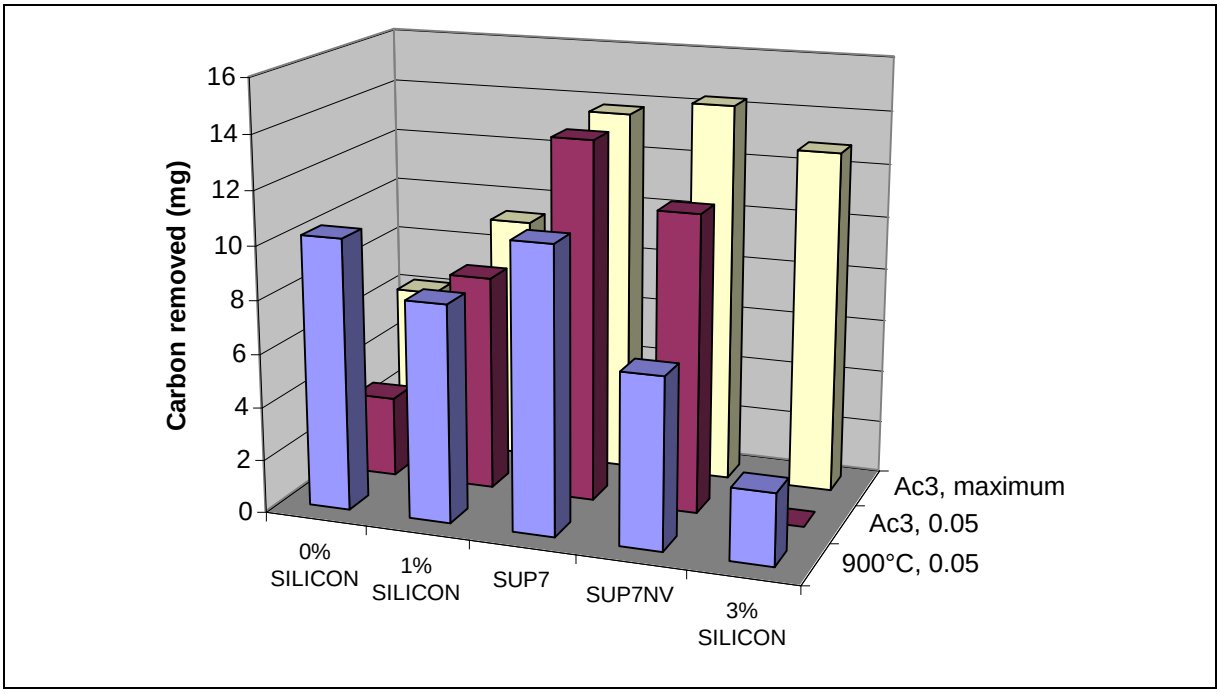

Figure 11.49 Comparison of the total mass of carbon removed for the different silicon steels after 4hr decarburisation of furnace cooled initial structures at their respective Ac_3 temperatures with that at 900°C.

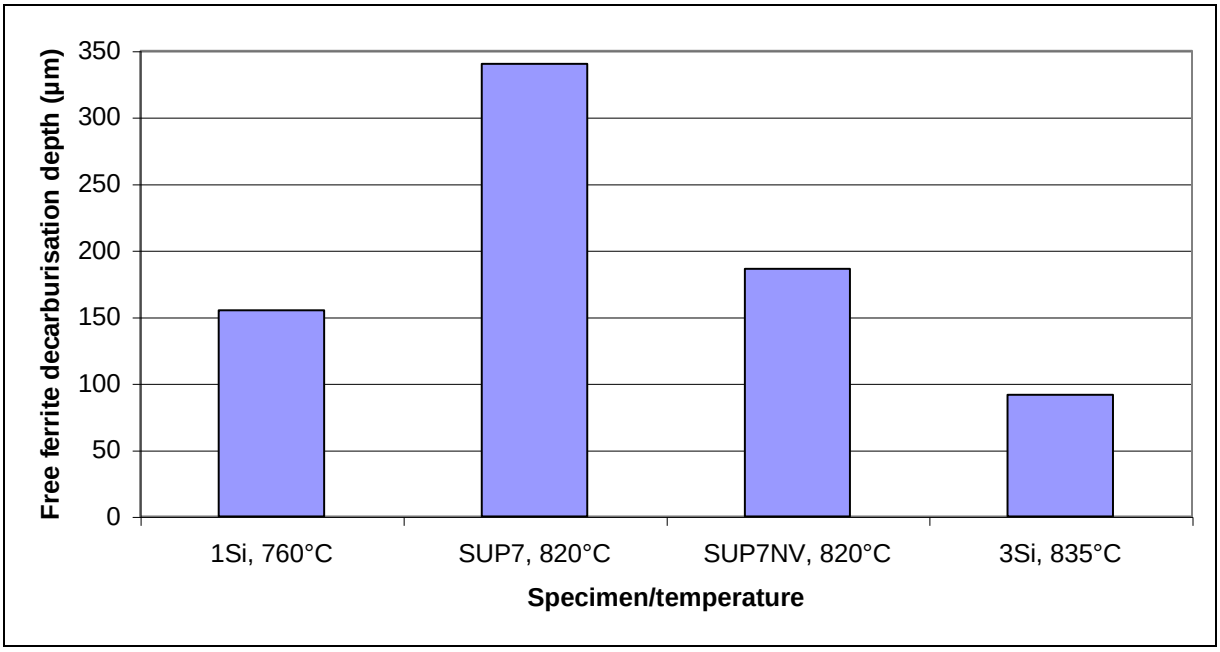

Figure 11.50 Free ferrite depths for the different silicon steels with furnace cooled initial structures decarburised 4hr in air at their respective Ac_3 temperatures.

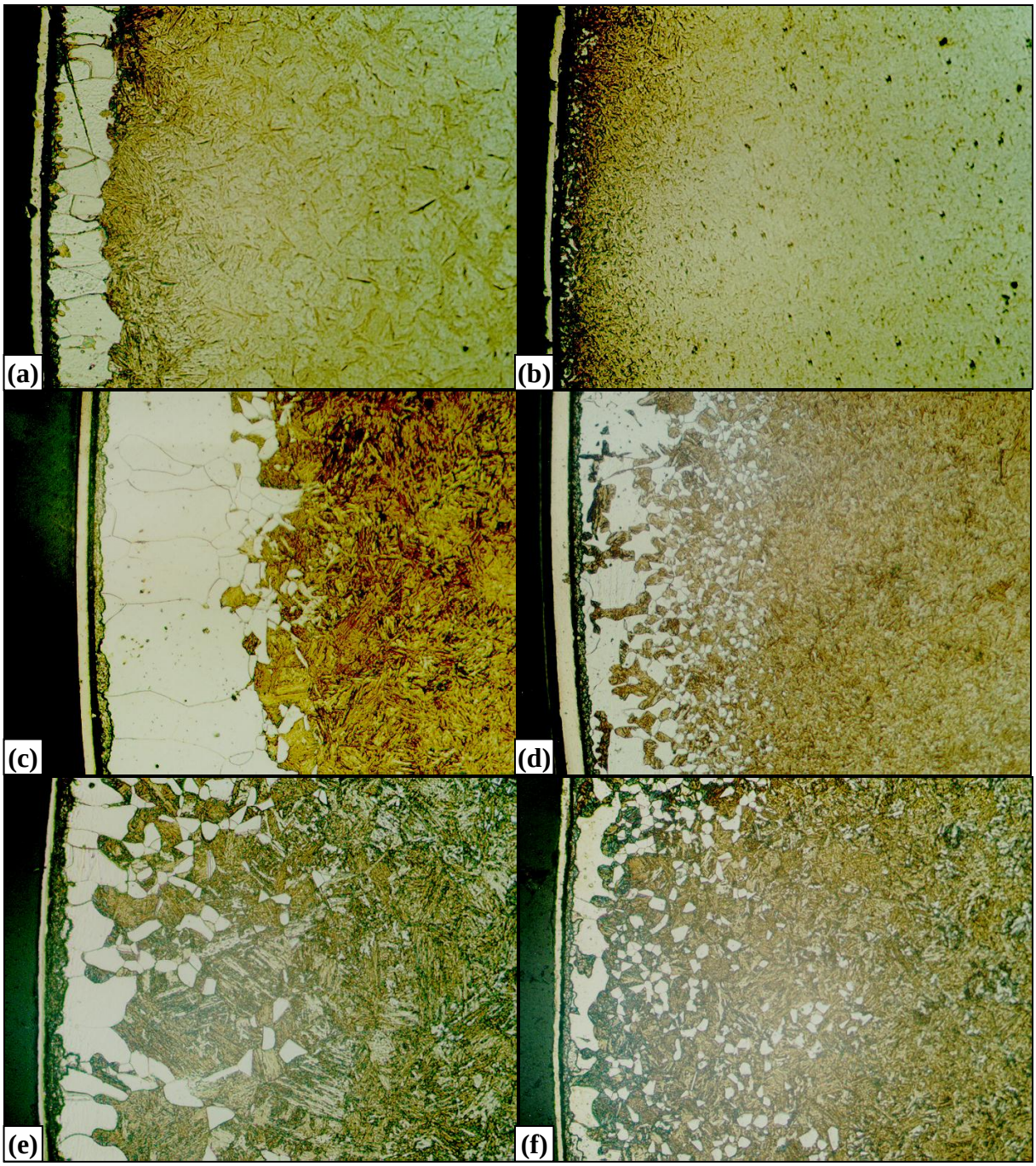

Figure 11.51 Microstructures obtained after decarburising furnace cooled initial structures at 900°C with p_{H_2O} / p_{H_2} =0.05 for SUP7 for (a) 15min, (c) 4hr, (e) 24hr, and for SUP7NV for (b) 15min, (d) 4hr, and (f) 24hr. 230x magnification. 2% Nital etch.

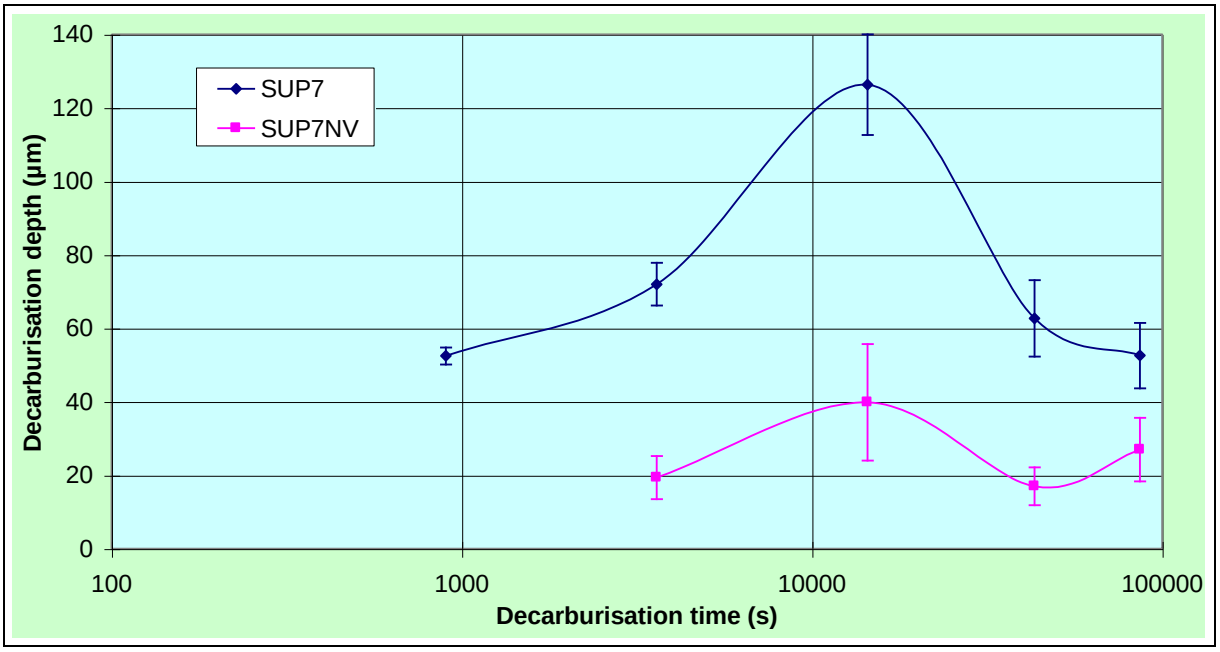

Figure 11.52 Free ferrite depths for SUP7 and SUP7NV furnace cooled initial structures decarburised at 900°C with p_{H_2O} / p_{H_2}=0.05.

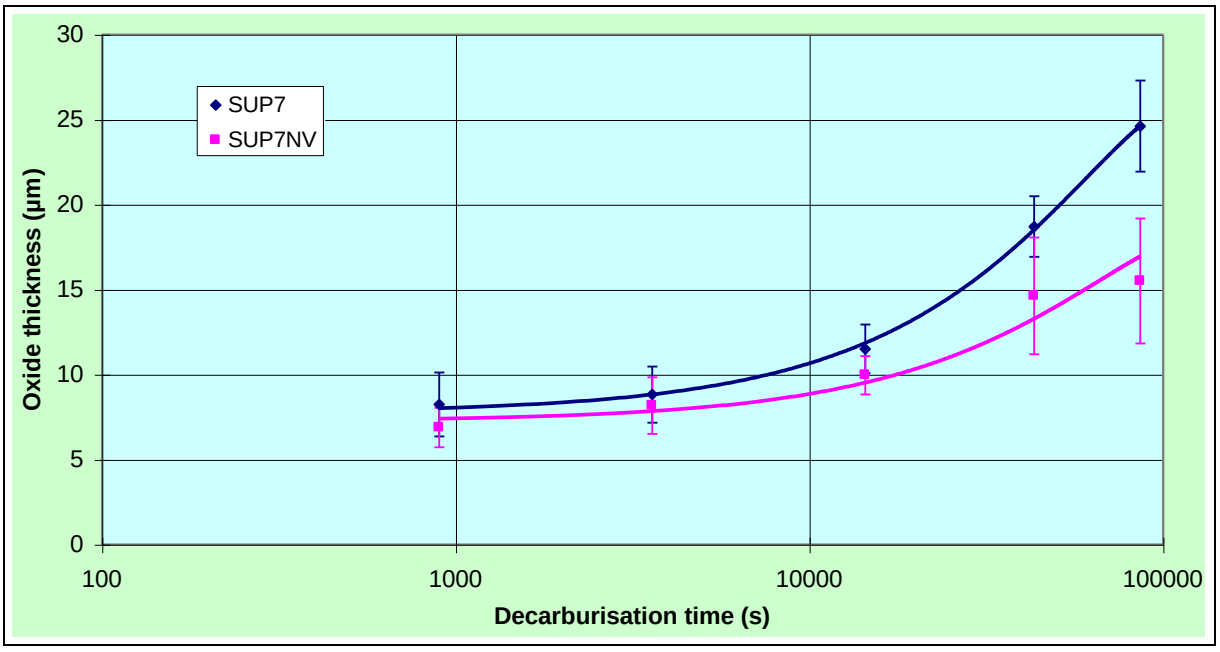

Figure 11.53 Oxide thickness kinetics for the decarburisation of SUP7 and SUP7NV furnace cooled initial structures at 900°C with p_{H_2O} / p_{H_2}=0.05.

The lower rate of carbon removal from the ferrite than that supplied to the ferrite from the austenite resulted in the ferrite carbon content at the ferrite/austenite interface becoming sufficiently high for the transformation of ferrite to austenite. This transformation then occurred further into the free ferrite layer, and was greatest along the ferrite grain boundaries, due to the faster grain boundary diffusion of carbon in ferrite than by bulk diffusion[108], as illustrated in Figures 11.51(e) and (f). This ferrite to austenite transformation can occur more readily at 900°C than at lower temperatures above the Ac_3 value, due to the decreasing mass transfer rate of carbon across the ferrite, as specified by $D_{effective}.C_{sat}$, at temperatures between 820 and 900°C, and the lower carbon content required for austenite formation.

11.7.6 Description of the factors contributing to decarburisation

The austenitisation and decarburisation of spring steels with 0 to 3wt.% silicon has been investigated in this research. This section describes the variables that can contribute to the decarburisation of these steels, and their actual influence on the decarburisation. The carbon removal following insertion of the test specimens into the hot zone of the tube furnace can be followed by considering the decarburisation of a SUP7 furnace cooled initial structure at the Ac_3 temperature of 820°C with a p_{H_2O} / p_{H_2} ratio of 0.05. The test specimen temperatures during decarburisation can be determined from the heating profile of the specimen in conjunction with the carbon monoxide and carbon dioxide concentration profiles.

The carbon content to which a steel can be decarburised depends on the carbon activity of the decarburisation atmosphere. The carbon activity of a moist hydrogen atmosphere where carbon removal is effected by the reaction of equation 3.3 is given by

$$a_C = p_{CO} \frac{p_{H_2}}{p_{H_2O}} \cdot \frac{1}{K}. \qquad (11.16)$$

The highest gas activity occurs at the highest values of p_{CO} and p_{H_2} / p_{H_2O}. Decarburisation of SUP7 at a p_{H_2O} / p_{H_2} ratio of 0.01 resulted in a peak carbon monoxide concentration of 600vppm, which corresponds to p_{CO}=6x10^{-4}atm. With K=9.17 for equation 3.3[213], the carbon activity of 6.5x10^{-3} demonstrates that the carbon activity of the decarburisation atmosphere is

almost zero. Therefore, decarburisation in a moist hydrogen atmosphere will allow the steel carbon content to be lowered to almost zero.

The carbon monoxide and carbon dioxide concentrations increased from zero at a specimen temperature of approximately 300°C, indicating that carbon removal had commenced. These concentrations peaked at a temperature of approximately 450°C, before decreasing upon further heating. This was attributed to the formation of a surface oxide layer that inhibited carbon removal. The gas concentrations then began to increase at 620°C, due to the oxide structures becoming less dense, which permitted faster carbon removal. Second peak concentrations, with magnitudes greater than the first peaks, were reached at a specimen temperature of 770°C. The rate of surface carbon removal increased with p_{H_2O} / p_{H_2} ratios from 0.01 to 0.25, as demonstrated by the increasing peak carbon monoxide and carbon dioxide concentrations for the different silicon steels. The rate of carbon removal from iron has also been demonstrated to increase for p_{H_2O} / p_{H_2} ratios of 0.01 to 0.25[88]. Eventually the increasing free ferrite depth and extent of oxidation lowered the rate of carbon removal from the steel, which resulted in lower carbon monoxide and carbon dioxide concentrations.

Once the specimen had heated to 820°C, the thickness of the ferrite layer increased with time in accordance with a diffusion controlled process. The calculation of an effective diffusion coefficient for carbon in ferrite yielded a value 0.45 times that of a Fe-C steel. The thickness of the free ferrite layer increased with carbon removal due to the faster carbon diffusion in the ferrite than in austenite, resulting in the motion of the ferrite/austenite interface away from the surface.

The initial carbon removal as the specimen heated occurs directly at the surface from cementite particles. This carbon removal lowers the surface carbon content sufficiently for a free ferrite layer to form, where the carbon diffusion across the free surface is faster than along the grain boundaries and in the bulk structure. As the temperature increased, cementite dissolution occurs, with the carbon diffusion through the ferrite to the surface supplied from cementite in contact with the ferrite/ferrite plus cementite interface due to the lower surface carbon activity relative to that of the ferrite/cementite interface.

Once the specimen temperature exceeds the Ac_1 temperature, austenite formation can commence. When austenite does form, the carbon supply for diffusion through the ferrite layer comes from cementite and austenite phases at the ferrite/core interface. As the temperature increases, the cementite dissolution and concurrent austenitisation becomes faster. The core eventually transforms to a fully austenitic structure at the Ac_3 temperature, with decarburisation then involving carbon transport across the ferrite/austenite interface, and diffusion through the ferrite.

Numerous variables contribute to the decarburisation before complete austenitisation of the core. The carbon supply from the ferrite/core interface for growth of the free ferrite layer is dependent upon the interfacial area of the cementite and austenite, the surface area to volume ratio of these phases, and the local carbon concentration at the interface between the dissolving phases and the free ferrite layer. This in turn is influenced by the carbon content of the phases and the alloying element distribution between the particles and the matrix.

Carbon transport through the free ferrite layer can occur by volume diffusion in the ferrite, along the ferrite grain boundaries, and along dislocations and other defects. The relative contributions of these diffusion mechanisms depends on the ferrite grain size and type, the bulk carbon diffusion coefficient in ferrite, the maximum solubility of carbon in ferrite, and the dislocation and vacancy concentrations. The relative contributions of volume and grain boundary diffusion are dependent on whether columnar or equiaxed grains form, and on their grain size. The transport of carbon through the ferrite is dependent on the diffusion coefficient, and the carbon concentration gradient across the ferrite, with both influenced by the alloy content.

Carbon removal from the surface of the steel is dependent upon the surface morphology, where oxide formation can inhibit the reaction of the atmosphere with carbon in the steel, and therefore the decarburisation. The degree of inhibition is dependent on the oxide structure, the surface coverage of the oxide, and the oxide thickness. Porous oxide structures that allow the passage of carbon inhibit the carbon removal to a lesser extent than denser structures.

The list of variables potentially contributing to the decarburisation is a long one, and includes the:

- Carbon activity of the decarburisation atmosphere;
- Ferrite, cementite and graphite size, shape and distributions of the initial microstructures;
- Size of ferrite, cementite, graphite and austenite particles;
- Rate of cementite dissolution;
- Rate of graphite formation or dissolution;
- Rate of austenitisation;
- Rate of surface carbon removal;
- Austenite carbon content;
- Test specimen size;
- Initial alloy content of the steel;
- Partitioning of the alloy elements between the phases;
- Solubility of carbon in ferrite;
- Austenite carbon concentration gradient;
- Diffusivity of carbon in ferrite and austenite;
- Diffusivity of silicon, manganese and chromium in ferrite and austenite;
- Formation of columnar versus equiaxed free ferrite grains;
- Oxide structure, and thickness;
- Thickness of the free ferrite layer;
- Heat treatment temperature;
- p_{H_2O} / p_{H_2} ratio of the decarburisation atmosphere.

It is necessary to determine the variables responsible for the decarburisation kinetics obtained from the decarburisation of the different silicon steels in this research. The ferrite grain size, pearlite interlamellar spacing and cementite particle sizes and distribution of the initial microstructure influenced the carbon release kinetics as the specimens heated. The faster cementite dissolution of the finer ferrite/cementite structures resulted in a greater rate of supply of carbon to the surface, and therefore the higher peak carbon monoxide and carbon dioxide concentrations. The test specimen size influences the rate at which the specimen heats to temperature, and therefore the carbon removal occurring during specimen heating. The elevated manganese and silicon contents of these steels relative to a Fe-C steel increase the

stability of the cementite particles, which retards the cementite dissolution. Therefore, higher peak carbon monoxide and carbon dioxide concentrations should result from a Fe-C steel relative to these steels under comparable experimental conditions.

The microstructural influence is restricted to where the rate of carbon diffusion through the ferrite layer exceeds the rate of carbon supplied to the ferrite from the ferrite/core interface. When the ferrite layer becomes sufficiently thick for the decarburisation to become controlled by the rate of carbon diffusion through the ferrite, different cementite and austenite distributions should not influence the carbon removal rate. This was demonstrated by the similar free ferrite depths after 4hr decarburisation of the different initial SUP7 structures, despite the considerably different austenitisation kinetics. The depth of the free ferrite layers were not influenced by grain boundary diffusion, as shown by the similar free ferrite depths of the different initial structures despite the different columnar grain sizes after 4hr.

Columnar free ferrite grain structures resulted from the decarburisation of the 0% Silicon and SUP7 steels, compared with equiaxed ferrite grains for the 1% Silicon, SUP7NV and 3% Silicon steels. The ferrite/martensite interface for the decarburisation of SUP7 at 820°C was sharply defined, compared with the less well defined interface for SUP7NV, despite the similar carbon, silicon, manganese and chromium contents, heat treatment conditions and free ferrite depths. The equiaxed SUP7NV ferrite grain structure was thought to be due to the presence of niobium and vanadium carbides, resulting from the elevated SUP7NV niobium and vanadium contents. These carbides pinned the ferrite grain boundaries, therefore preventing the directional growth of the ferrite grains from the surface inwards when carbon removal caused an austenite to ferrite transformation.

The much finer SUP7NV free ferrite grain structures may have caused the less well defined ferrite/martensite interface, due to accelerated carbon diffusion along the ferrite grain boundaries relative to the bulk of the structure. The coarser SUP7 grain structure had a lower ferrite grain boundary density and therefore a more uniform ferrite/martensite interface. The reason why the 0% Silicon steel forms columnar free ferrite upon decarburisation, compared with predominantly equiaxed ferrite for the 1% and 3% Silicon steels is not obvious, and requires further investigation.

Multiple linear regression analysis demonstrated that the mass of carbon removed after 15min decarburisation of the 0% Silicon, 1% Silicon, SUP7 and SUP7NV steels increased with silicon content, temperature and p_{H_2O} / p_{H_2} ratio, but decreased with manganese content. However, this analysis does not establish the mechanisms by which these variables influenced the decarburisation. The decarburisation was initially controlled by the rate of carbon removal from the surface, which increased with temperature and p_{H_2O} / p_{H_2} ratios of 0.01 to 0.25. Eventually the increasing decarburisation resulted in the carbon removal either being controlled by the carbon diffusivity in the ferrite and the austenite, or by the rate of carbon diffusion through the oxide.

The free ferrite depths of the different silicon steels allow direct comparisons of the carbon removal kinetics at temperatures below the lowest Ac_3 temperature when decarburisation is controlled by carbon diffusion in the ferrite. 750°C was lower than the Ac_3 temperatures of all the steels, apart from the 0% Silicon steel. However, the free ferrite depth of the 0% Silicon steel at the Ac_3 temperature of 740°C can be used for comparison purposes, as the value of D_α for a Fe-C steel only increases by 10% from 740 to 750°C. The increasing free ferrite depths from 79μm for the 0% Silicon steel after 4hr at 750°C to 310μm for SUP7 and SUP7NV demonstrates faster decarburisation of the higher silicon steels. A further increase in the silicon content to 3.05wt.% then lowered the rate of carbon removal, with a free ferrite depth of 172μm after 4hr. The lower free ferrite depths than that of 350μm for a Fe-0.6wt.%C steel[99] demonstrates that the higher silicon and manganese contents of the five steels decarburised lowered the rate of carbon removal.

The ferrite and austenite carbon diffusivities are influenced by the maximum carbon solubility, which depends upon the alloy content and heat treatment temperature. The oxidation is also influenced by the concentration and diffusivity of silicon, manganese and chromium in ferrite and austenite, which in turn is influenced by the temperature and p_{H_2O} / p_{H_2} ratio. Kucera[213] determined that the diffusivity of carbon in austenite for Fe-Si-Mn-Cr-Ni-C steels increased with carbon content, while silicon, manganese and chromium decreased it. However, the 0% Silicon steel manganese and chromium contents have a negligible influence on the austenite carbon diffusivity[213]. The silicon contents of the 1% Silicon, SUP7 and 3% Silicon steels lower the austenite carbon diffusion coefficients at their respective Ac_3 temperatures to 60, 50 and 35% that of a Fe-C steel at comparable

temperatures[213]. No quantitative information could be obtained for the diffusion of carbon in ferrite for Fe-Si-Mn-Cr-C systems. If silicon has a similar influence on the diffusivity of carbon in ferrite, slower decarburisation with increasing silicon could be expected.

However, this was not borne out by the experimental results, where increasing silicon contents of up to 2wt.% accelerated the decarburisation kinetics. The ratio of the effective diffusion coefficient of carbon in ferrite to that for a Fe-C steel at the respective Ac_3 temperatures doubled as the silicon content increased from 0 to 2wt.%. The decarburisation kinetics then decreased as the silicon content increased to 3wt.%. Therefore, the rate of decarburisation of the different silicon steels is not determined by the respective diffusion coefficients for carbon in ferrite, but by the oxidation behaviour of the different silicon steels.

Hudson[100] demonstrated that the maximum rate of carbon removal from a Fe/0.1wt.%C steel was obtained at p_{H_2O} / p_{H_2} ratios of 0.05 and greater. Therefore, the increasing free ferrite depth of the 0% Silicon steel as the p_{H_2O} / p_{H_2} ratio increased from 0.05 to 0.25 was thought to be due to the oxide structure becoming less dense, with less inhibition of carbon removal. The high manganese content of this oxide indicates that this oxide layer was MnO. The decreasing free ferrite depth as the p_{H_2O} / p_{H_2} ratio increased from 0.5 to 1.0 was due to the formation of FeO, which inhibited the carbon removal to a greater extent than the oxide structures formed at the lower p_{H_2O} / p_{H_2} ratios.

The free ferrite depths for SUP7 increased as the p_{H_2O} / p_{H_2} ratio increased from 0.01 to 0.05, with similar depths for p_{H_2O} / p_{H_2} ratios of 0.05 to 1.0. The oxide structures were observed to be thicker, but less dense, than those of the lower silicon steels. This resulted in less inhibition of carbon removal from the steel, and therefore faster decarburisation kinetics. A consideration of the thermodynamics and the oxide alloy contents indicated that the predominant oxide structures for p_{H_2O} / p_{H_2} ratios of 0.01 and 0.05 were SiO_2 and MnO, with Fe_2SiO_4 present at the higher p_{H_2O} / p_{H_2} ratios. Despite the thermodynamic prediction of FeO formation at a p_{H_2O} / p_{H_2} ratio of 1.0, the quantitative analysis of the oxide alloy contents indicated negligible FeO formation. The absence of FeO formation was also demonstrated by a similar free ferrite depth relative to the lower p_{H_2O} / p_{H_2} ratios, instead of the smaller depths normally associated with FeO formation[67].

Negligible free ferrite was observed for the 3% Silicon steel decarburised at temperatures of 800°C and above with p_{H_2O} / p_{H_2} ratios of 0.05 and less, due to the formation of an external SiO_2 layer. This oxide structure inhibited the carbon removal to a greater extent than the oxide structures of the lower silicon steels at comparable temperatures and p_{H_2O} / p_{H_2} ratios. The transition from external to internal SiO_2 formation occurred for the 3% Silicon steel when decarburised at higher p_{H_2O} / p_{H_2} ratios. This oxide had a less dense structure, which permitted faster carbon removal, and therefore the increasing free ferrite depths with p_{H_2O} / p_{H_2} ratio. The elevated oxide manganese contents indicated a MnO structure, with Fe_2SiO_4 formation also demonstrated at p_{H_2O} / p_{H_2} ratios of 0.25 and greater.

No quantitative information could be obtained for the influence of alloy elements on the carbon diffusivity in ferrite. However, if the effect of silicon on the diffusion coefficients of carbon in ferrite, D_α, is similar to that for austenite, the values of the effective diffusion coefficients of carbon in ferrite for the different silicon steels, $D_{effective}$, can be compared to those for carbon diffusion in ferrite for the different silicon steels. Multiplication of D_α by the ratio of the diffusion coefficient of carbon in austenite for the different silicon steels to that of a Fe-C steel yields $D_{effective}/D_\alpha$ equal to 0.5 for SUP7 and SUP7NV, and 0.35 for the 3% Silicon steel. These values are similar to the maximum values observed for the decarburisation of SUP7 and SUP7NV at 820°C with a p_{H_2O} / p_{H_2} ratio of 0.25, and the 3% Silicon steel at 835°C with a p_{H_2O} / p_{H_2} ratio of 1.0. Therefore, these oxide structures would have had a negligible influence on the carbon removal, with the decarburisation kinetics controlled by the carbon diffusivity in the ferrite. However, this cannot be confirmed without knowing the diffusion coefficients of carbon in ferrite for the different silicon steels.

11.8 Summary of decarburisation investigation

The decarburisation investigation for the different silicon steels involved the following:

i) Decarburisation heat treatments for the different silicon steels with furnace cooled initial structures at their respective Ac_3 temperatures and different p_{H_2O} / p_{H_2} ratios;

ii) Decarburisation heat treatments for the different silicon steels with furnace cooled initial structures at different temperatures with a 0.05 p_{H_2O} / p_{H_2} ratio;

iii) A qualitative description of the influence of silicon content, p_{H_2O} / p_{H_2} ratio and temperature on the decarburisation from a microstructural investigation;

iv) Determination of the effect of p_{H_2O} / p_{H_2} ratio on the carbon monoxide and carbon dioxide concentration profiles for the different silicon steels decarburised at their respective Ac_3 temperatures;

v) Determination of the influence of temperature on the carbon monoxide and carbon dioxide concentration profiles for the different silicon steels decarburised at a p_{H_2O} / p_{H_2} ratio of 0.05;

vi) A comparison of the influence of silicon content on the carbon monoxide and carbon dioxide concentration profiles for the different silicon steels decarburised at comparable temperatures and a p_{H_2O} / p_{H_2} ratio of 0.05;

vii) Multiple linear regression analysis to quantify the contribution of alloy content, temperature and p_{H_2O} / p_{H_2} ratio to the mass of carbon removed after 15min;

viii) A comparison of the free ferrite decarburisation depths for the different silicon steels decarburised at different p_{H_2O} / p_{H_2} ratios at their respective Ac_3 temperatures;

ix) A comparison of the influence of silicon content on the free ferrite depths for the different silicon steels decarburised at comparable temperatures with a p_{H_2O} / p_{H_2} ratio of 0.05;

x) A comparison of the oxide thicknesses for the different silicon steels decarburised at different p_{H_2O} / p_{H_2} ratios at their respective Ac_3 temperatures;

xi) A comparison of the oxide thicknesses for the different silicon steels decarburised at comparable temperatures with a p_{H_2O} / p_{H_2} ratio of 0.05;

xii) A microstructural investigation of the oxide structures for the different silicon steels decarburised at their respective Ac_3 temperatures with different p_{H_2O} / p_{H_2} ratios;

xiii) Quantitative SEM energy dispersive spectroscopical analysis of the oxide element concentration profiles for the different silicon steels decarburised at their respective Ac_3 temperatures with different p_{H_2O} / p_{H_2} ratios;

xiv) Calculation of the effective carbon diffusion coefficients in ferrite for the decarburisation of the different silicon steels at their respective Ac_3 temperatures;

xv) Measurement of selected ferrite and martensite microhardness profiles for the different silicon steels decarburised above their respective Ac_3 temperatures with a p_{H_2O} / p_{H_2} ratio of 0.05;

xvi) Conversion of the martensite microhardness profiles to carbon concentration profiles;

xvii) Determination of the influence of temperature on the carbon removed from the 0% Silicon steel after decarburisation with a p_{H_2O} / p_{H_2} ratio of 0.05;

xviii) Comparison of the carbon removed from the different silicon steels at their respective Ac_3 temperatures with that at 900°C;

xix) Comparison of the decarburisation of SUP7 and SUP7NV at 900°C with a p_{H_2O} / p_{H_2} ratio of 0.05;

xx) A description of the mechanisms controlling the decarburisation of the different silicon steels.

Table 11.1 Influence of p_{H_2O} / p_{H_2} ratio on the gas concentrations and carbon removal during the decarburisation of the different silicon steels with furnace cooled initial structures at their respective Ac_3 temperatures.

STEEL	Temperature	Gas concentration/ Carbon removed	p_{H_2O} / p_{H_2} RATIO									
			0.01		0.05		0.25		0.5		1.0	
			CO	CO_2	CO	CO_2	CO	CO_2	CO	CO_2	CO	CO_2
0% Silicon	740°C	$vppm_{PEAK}$	50	0	210	25	220	60	115	20	-	-
		$vppm_{15min}$	35	0	165	15	170	45	105	20	-	-
		$\mu g\ C_{15min}$	0.17		0.73		0.81		0.36		-	
1% Silicon	760°C	$vppm_{PEAK}$	65	0	315	30	465	130	345	80	260	40
		$vppm_{15min}$	60	0	280	25	335	100	315	70	240	40
		$\mu g\ C_{15min}$	0.24		1.04		1.65		1.09		0.66	
SUP7	820°C	$vppm_{PEAK}$	600	20	1615	130	1815	150	1270	80	1520	60
		$vppm_{15min}$	410	8	410	30	365	60	350	30	485	20
		$\mu g\ C_{15min}$	1.83		2.63		2.74		2.11		2.52	
SUP7NV	820°C	$vppm_{PEAK}$	195	9	995	130	1130	400	770	265	1190	320
		$vppm_{15min}$	125	4	400	45	315	110	235	80	400	100
		$\mu g\ C_{15min}$	0.66		2.45		2.71		1.73		2.49	
3% Silicon	835°C	$vppm_{PEAK}$	45	0	750	85	1215	405	805	275	1060	345
		$vppm_{15min}$	30	0	60	7	295	95	225	90	180	120
		$\mu g\ C_{15min}$	0.16		0.85		2.57		1.47		2.24	

Table 11.2 Influence of temperature on the gas concentrations and the carbon removal during the decarburisation of the different silicon steels with furnace cooled initial structures at a p_{H_2O} / p_{H_2} ratio of 0.05.

STEEL	Gas concentration/ Carbon removed	TEMPERATURE (°C)									
		700		750		800		850		900	
		CO	CO_2	CO	CO_2	CO	CO_2	CO	CO_2	CO	CO_2
0% Silicon	$vppm_{PEAK}$	30	0	195	15	240	20	415	35	720	55
	$vppm_{15min}$	25	0	140	10	135	10	200	15	310	20
	$\mu g\ C_{15min}$	0.13		0.61		0.75		1.12		1.80	
1% Silicon	$vppm_{PEAK}$	45	0	175	10	430	40	515	50	685	65
	$vppm_{15min}$	35	0	175	10	220	20	235	20	265	20
	$\mu g\ C_{15min}$	0.18		0.54		1.16		1.40		1.73	
SUP7	$vppm_{PEAK}$	180	15	530	65	1085	100	2005	135	2395	155
	$vppm_{15min}$	180	150	315	35	350	30	425	30	375	25
	$\mu g\ C_{15min}$	0.36		1.31		2.15		2.63		2.81	
SUP7NV	$vppm_{PEAK}$	65	11	295	55	795	80	1315	110	1795	260
	$vppm_{15min}$	65	11	260	50	340	35	290	20	370	65
	$\mu g\ C_{15min}$	0.20		0.99		2.02		2.10		2.89	
3% Silicon	$vppm_{PEAK}$	50	9	200	30	460	60	660	80	1470	135
	$vppm_{15min}$	50	9	150	20	415	6	110	15	185	15
	$\mu g\ C_{15min}$	0.14		0.61		0.84		0.99		1.36	

Table 11.5 Calculation of the sum of the total element concentrations, including oxygen, from the assumed oxide structures resulting from the decarburisation of the different silicon steels for 4hr at their respective Ac_3 temperatures with different p_{H_2O} / p_{H_2} ratios.

STEEL	p_{H_2O} / p_{H_2}	Element concs. for max. sum of Si+Mn+Cr+Al (wt.%)					Detected total (wt.%)	Assumed oxides	Adjusted total (wt.%)	Peak ferrite total (wt.%)
		Si	Mn	Cr	Al	Fe				
0% SILICON	**0.25**	-	5.6	-	-	85.4	91.0	MnO	92.6	95.1
	0.50	-	5.5	1.0	-	82.3	88.8	MnO/Cr_2O_3	90.9	96.9
	1.0	-	5.6	-	-	68.9	71.9	MnO/FeO	96.1	96.6
1% SILICON	**0.01**	5.0	4.5	0.8	-	75.1	85.4	$SiO_2/MnO/Cr_2O_3$	92.8	94.9
	0.05	3.4	2.7	-	-	85.1	91.2	SiO_2/MnO	95.9	100.2
	0.25	4.0	2.5	0.4	-	74.1	81.0	$SiO_2/Fe_2SiO_4/MnO/Cr_2O_3$	86.4/91.0*	96.6
	0.50	5.7	2.2	0.5	-	75.0	83.4	$SiO_2/Fe_2SiO_4/MnO/Cr_2O_3$	90.8/97.3	97.6
	1.0	3.6	1.9	0.4	-	86.0	91.9	$SiO_2/Fe_2SiO_4/MnO/Cr_2O_3$	96.7/100.7	94.2
SUP7	**0.01**	11.7	-	-	0.8	72.7	85.2	SiO_2/Al_2O_3	99.3	92.8
	0.05	7.9	8.8	0.6	0.9	63.2	81.2	$SiO_2/MnO/Cr_2O_3/Al_2O_3$	94.0	101.1
	0.25	5.0	5.6	0.6	2.0	66.5	79.7	$SiO_2/Fe_2SiO_4/MnO/Cr_2O_3$	89.0/94.8	92.0
	0.50	4.8	2.8	-	-	84.7	92.3	$SiO_2/Fe_2SiO_4/MnO$	98.5/104.7	99.8
	1.0	5.2	4.0	0.7	-	73.0	88.6	$SiO_2/Fe_2SiO_4/MnO/Cr_2O_3$	90.3/96.0	96.2
3% SILICON	**0.05**	5.2	10.0	0.4	-	58.5	72.9	$SiO_2/MnO/Cr_2O_3$	83.1	99.2
	0.25	9.8	4.3	0.3	-	60.4	72.2	$SiO_2/Fe_2SiO_4/MnO/Cr_2O_3$	87.4/98.5	96.0
	0.50	8.8	2.7	0.3	-	67.4	79.2	$SiO_2/Fe_2SiO_4/MnO/Cr_2O_3$	90.2/100.2	95.9
	1.0	8.0	1.7	0.5	-	73.7	83.9	$SiO_2/Fe_2SiO_4/MnO/Cr_2O_3$	93.7/102.5	97.9

* For SiO_2/Fe_2SiO_4 formation.

CHAPTER 12

CONCLUSIONS

One commercially available steel commonly used for the manufacture of automobile coil suspension springs is SUP7. The reduced sag resistance and fatigue strength arising from the decarburisation of SUP7 during spring manufacture, and the methods employed to minimise its effects, are well documented. However, limited research has been undertaken into the austenitisation and decarburisation of spring steels. Five different steels comprising 0 to 3wt.% silicon were therefore investigated in this research. These steels included the commercially available SUP7 and SUP7NV steels, which comprise 2wt.% silicon. Three experimental steels were also produced, with silicon contents of 0, 1 and 3wt.% respectively, and otherwise similar alloying element concentrations to SUP7 and SUP7NV. The five steels were heat treated to give a range of initial microstructures, then machined into test specimens for the austenitisation and decarburisation investigation of these steels.

Austenitisation heat treatments of 30s to 8min were undertaken in a salt bath, while longer tests were undertaken in the hot zone of a tube furnace with an inert argon atmosphere. A range of initial microstructures and temperatures were used for the different steels, with the influence of temperature, initial microstructure and silicon content on the austenitisation quantified from the microscopic measurements of the stereological and physical properties of the heat treated specimens. Decarburisation heat treatments were then undertaken for the five steels in a decarburisation heat treatment rig. The influence of heat treatment atmosphere, temperature, initial microstructure and silicon content on the decarburisation were quantified from the microscopic measurements of the free ferrite depths, microhardness profiles, oxide thicknesses and oxide element concentration profiles of the heat treated specimens. More detailed experimentation was undertaken for SUP7 relative to the other steels due to its widespread use for automobile coil suspension springs.

The most significant experimental results derived from the austenitisation investigation were:

- Austenite nucleated at the interfaces between ferrite grain boundaries and cementite particles of the pearlitic initial microstructures, and at cementite particles located at the edges where three ferrite grains meet for the spheroidal cementite initial microstructures. The resultant austenite grain shapes were inherited from the ferrite grains of the initial structures, with equiaxed austenite grains from pearlitic and intercritical initial structures, and elongated grains from the tempered martensite initial structures. The austenite growth was two-dimensional, where the austenite grew radially once impingement of the growing austenite grains had occurred along the ferrite grain boundaries.

- Increasing heat treatment temperatures accelerated the austenitisation kinetics for the different silicon steels, and became faster as the silicon content increased from 0.06wt.% to 2.11wt.% for comparable fractional superheats and types of initial structures. The austenitisation kinetics were faster for the tempered martensite initial SUP7, SUP7NV and the 3% Silicon steel structures than for the furnace cooled structures at intercritical temperatures corresponding to 0.25 fractional superheats. However, the austenitisation kinetics were faster for the furnace cooled SUP7 and SUP7NV initial structures than for the tempered martensite structures at the respective Ac_3 temperatures of these steels.

- The faster austenitisation of the tempered martensite initial 0% Silicon, 1% Silicon, SUP7 and SUP7NV steel structures at low fractional superheats was due to the higher density of austenite particles compared to the furnace cooled structure. The austenite growth rate was controlled by the substitutional alloy element partitioning at the austenite/cementite interface. At higher intercritical temperatures, a transition from substitutional to interstitial diffusion controlled growth occurred, with the austenite growth rate controlled by the diffusion of carbon in the austenite. The higher surface area to volume ratio of the lamellar cementite, and the shorter diffusion distances of carbon to the growing austenite, then resulted in the faster austenitisation kinetics of the furnace cooled initial structures. The transition from substitutional to interstitial diffusion controlled austenite growth occurred between 765 and 780°C for SUP7, with 50% of the final austenite fraction formed 160 times faster at 780°C. The finer pearlitic and tempered martensite SUP7 initial structures austenitised faster at the Ac_3 temperature than the respective coarser structures.

- Austenite nucleated earlier in the 96hr tempered martensite initial structures than in the intercritical structures, due to the higher austenite nucleation energy at cementite particles located within the ferrite grains, relative to that at the ferrite grain boundary cementite particles of the tempered martensite structures. This was followed by the faster austenitisation kinetics of the intercritical structures, where the greater redistribution of the alloying elements for the tempered martensite structures lowered the carbon concentration gradient across the austenite, and therefore the driving force for austenite growth.

- Only half the austenite fraction was obtained after 192hr at a 0.13 fractional superheat for the furnace cooled initial structure relative to the spheroidal cementite initial structures for SUP7. This was attributed to greater banding present in the pearlitic initial structures, and the associated variation of the manganese and chromium contents within the microstructure. However, similar austenite fractions were observed after the longest duration heat treatments for the different initial structures at higher temperatures.

- The presence of eutectoid gaps with ferrite/austenite/cementite structures were observed for the 0% Silicon, 1% Silicon, SUP7 and SUP7NV steels after prolonged austenitisation at low intercritical temperatures.

- Austenite formation was faster for the tempered martensite 3% Silicon structure at the Ac_3 temperature than for the pearlitic structure. This was due to the greater surface area to volume ratio of the finer graphite size of the tempered martensite initial structure, and the associated shorter carbon diffusion distances in the growing austenite.

- The hardness of the martensite was similar for the different silicon steels at their respective Ac_3 temperatures after the longest heat treatments.

The most significant experimental results derived from the decarburisation investigation were:

- Continuous monitoring of the carbon monoxide and carbon dioxide evolved allowed the carbon release from the steels to be investigated when the specimens were heated in the

hot zone with the established decarburisation atmosphere. Peak carbon monoxide and carbon dioxide concentrations were observed within 50s for the different steels at a range of p_{H_2O}/p_{H_2} ratios, with impervious oxide formation then thought to inhibit the decarburisation. Gas concentrations higher than the first peak values then resulted as the specimens heated to higher temperatures. Second peaks were reached, with the gas concentrations then decreasing due to longer carbon diffusion distances. Higher carbon monoxide concentrations relative to carbon dioxide indicate that decarburisation predominantly occurred by water vapour reacting with carbon to form carbon monoxide and hydrogen.

- Decarburisation of the different silicon steels at their respective Ac_3 temperatures in hydrogen did not yield free ferrite. Free ferrite formation resulted for SUP7 at p_{H_2O}/p_{H_2} ratios of 0.01 and greater. However, free ferrite layers were not obtained until the p_{H_2O}/p_{H_2} ratio increased to 0.05 for the 0% Silicon, 1% Silicon and SUP7NV steels, and to 0.25 for the 3% Silicon steel. Columnar free ferrite grain structures resulted for the 0% Silicon and SUP7 steels, compared with equiaxed ferrite grains for the 1% Silicon, SUP7NV and 3% Silicon steels.

- Greater decarburisation occurred with increasing p_{H_2O}/p_{H_2} ratios up to 0.25 for the 0% Silicon steel at the Ac_3 temperature, before decreasing sharply from the 0.50 to 1.0 ratio due to FeO formation. The maximum free ferrite depths were obtained over a wider range of p_{H_2O}/p_{H_2} ratios as the silicon content increased to that of SUP7, with the negligible decrease in decarburisation at the 1.0 p_{H_2O}/p_{H_2} ratio due to limited FeO formation. The decarburisation increased for the 3% Silicon steel at the 0.50 and 1.0 ratios. An increase from zero to 2.11wt.% Silicon doubled the ratio of the effective diffusion coefficients for carbon diffusion in ferrite at the respective Ac_3 temperatures to that for a Fe-C steel. However, the effective diffusion coefficient decreased for the 3% Silicon steel. The effective diffusion coefficients never exceeded half that of the Fe-C steel.

- Multiple linear regression analysis demonstrated that the total mass of carbon removed after 15min was a function of silicon content, manganese content, temperature and p_{H_2O}/p_{H_2} ratio for 0 to 2.11wt.% Silicon, and p_{H_2O}/p_{H_2} ratios of 0.01 to 0.25. An R^2

value of 0.84 was obtained, with increasing silicon content, temperature and p_{H_2O}/p_{H_2} ratio increasing the mass of carbon removed. Manganese was found to decrease the mass of carbon removed by a factor five times greater than silicon increased the carbon removal for the same compositional change.

- The peak free ferrite depths were obtained by decarburising the different steels at their respective Ac_3 temperatures. The free ferrite depths at comparable temperatures with a p_{H_2O}/p_{H_2} ratio of 0.05 increased with increasing silicon content to that of SUP7. SUP7 and SUP7NV had similar ferrite depths up to 750°C, with deeper free ferrite for SUP7 at the higher temperatures. No free ferrite resulted for the 3% Silicon steel at temperatures greater than 750°C, due to the transition from internal to external SiO_2 oxidation causing stronger carbon removal inhibition. The effective diffusion coefficients of carbon in ferrite at 750°C increased with the silicon content up to that of SUP7NV, then decreased for the 3% Silicon steel. The ratio of the effective diffusion coefficient to that for a Fe-C steel increased 40 times for SUP7 as the temperature increased from 650 to 820°C. The effective diffusion coefficients for SUP7NV at 750°C, and SUP7 at 820°C, were approximately half the Fe-C values. The total mass of carbon removed from the 0% Silicon steel increased with temperature, with comparable masses of carbon removed from the 1% Silicon steel at the Ac_3 temperature and 900°C. Greater carbon removal occurred from the SUP7, SUP7NV and 3% Silicon steels at their respective Ac_3 temperatures than at 900°C.

- The oxide thicknesses increased with increasing p_{H_2O}/p_{H_2} ratio, and with increasing temperature, for all the steels apart from the 3% Silicon steel, where the oxide thicknesses decreased with increasing temperature due to the transition from internal to external oxidation. The thickest oxide structures at the comparable p_{H_2O}/p_{H_2} ratios and temperatures were observed for SUP7. The oxide structures of the different silicon steels had elevated silicon, manganese, chromium and aluminium concentrations, and lower iron concentrations, relative to the bulk steel compositions. The silicon oxide concentrations at comparable p_{H_2O}/p_{H_2} ratios increased with increasing bulk steel silicon content. Multiplication of the alloy element concentrations by the gravimetric factors for the

assumed oxide structures yielded alloy element totals comparable to that of the ferrite. This suggested that these elements were present as various oxides.

- No free ferrite resulted after 4hr decarburisation of the 0% Silicon steel in air at the Ac_3 temperature, while the free ferrite depths were considerably less than the 1% Silicon, SUP7NV and 3% Silicon steels at higher p_{H_2O} / p_{H_2} ratios. However, the SUP7 free ferrite layer after decarburisation in air was closer to the SUP7 values at the higher p_{H_2O} / p_{H_2} ratios.

- Austenitisation of SUP7 in argon at the Ac_3 temperature before the decarburisation atmosphere was introduced prevented free ferrite formation for up to several hours. This was attributed to the formation of an impervious SiO_2 oxide layer resulting from minute concentrations of water vapour present in the argon, which had to break down before decarburisation could commence. Decarburisation at a higher p_{H_2O} / p_{H_2} ratio accelerated this breakdown, resulting in faster decarburisation. Prior austenitisation in hydrogen rather than argon resulted in deeper free ferrite depths at the lower p_{H_2O} / p_{H_2} ratio, but similar depths at a higher ratio. However, greater decarburisation resulted when the test specimens were heated in the established decarburisation atmosphere.

- Different initial SUP7 structures influenced the carbon release kinetics during decarburisation as the specimens heated to temperature. The lamellar cementite of the pearlitic structures yielded higher peak carbon monoxide and carbon dioxide concentrations than the spheroidal cementite of the tempered martensite and intercritical structures, due to the finer lamellar cementite structures facilitating faster surface carbon removal. The finer lamellar and spheroidal cementite structures yielded higher peak concentrations than their respective coarser structures. The slower decrease from the peak concentrations for the spheroidal cementite structures was attributed to the slower austenitisation of the core structures. The effect of the different initial structures for longer decarburisation durations was small, with similar free ferrite depths for the different structures after 4hr, despite a 75% variation in the ferrite columnar grain sizes, which indicated a limited influence of the ferrite grain boundaries on the decarburisation.

- Decarburisation of SUP7 and SUP7NV at 900°C yielded increasing free ferrite depths up to 4hr. Longer heat treatments then resulted in decreasing free ferrite depths due to the transformation of ferrite to austenite at the ferrite/austenite interface, where the carbon removal from the steel was slower than that supplied from the ferrite to the austenite.

In summary, this research contributes the detailed experimental data and controlling mechanisms absent in the literature for the austenitisation and decarburisation of spring steels. It was demonstrated that the austenitisation kinetics of 0 to 3wt.% silicon steels with similar carbon, manganese and chromium contents were dependent on the alloy content, the heat treatment temperature and the initial structure. The decarburisation of these steels was found to be dependent on the silicon and manganese contents, the heat treatment temperature and the p_{H_2O}/p_{H_2} ratio. Increasing silicon contents from 0 to 2wt.% were found to accelerate the decarburisation kinetics, due to less inhibition of carbon removal by the oxide structures. However, it was shown that the decarburisation kinetics were slower for the 3wt.% silicon steel, particularly at higher temperatures and lower p_{H_2O}/p_{H_2} ratios, where the dense oxide structures strongly inhibited carbon removal.

CHAPTER 13

RECOMMENDATIONS FOR FUTURE RESEARCH

13.1 Implications of results to spring manufacture

The results obtained from this research have implications for the manufacture of automobile coil suspension springs that justify further investigation. These include:

- The lower silicon steels decarburised less than SUP7, with the lower Ac_1 and Ac_3 transformation temperatures also requiring lower austenitising temperatures, and therefore smaller heat treatment costs. The as-quenched hardness at 740°C was comparable to SUP7 at 820°C. Therefore, the possibility exists for the manufacture of a suitable combination of alloying additions to obtain the desired tempered hardness, with lower heat treatment temperatures required than for SUP7, and less decarburisation.

- The 3% Silicon steel decarburised less than SUP7, especially at low p_{H_2O} / p_{H_2} ratios and in air. Therefore, the silicon content of SUP7 could be increased to lower the decarburisation.

- The addition of alloy elements to SUP7 to form denser oxide layers, and therefore lower the decarburisation. One possible addition is aluminium, which increases the oxidation resistance more effectively than similar silicon contents[82]. The effect of such alloy elements on the sag resistance, fatigue strength and the spring manufacture heat treatments would also have to be investigated.

- Use of a rapid heating approach such as induction heating to minimise the time taken to attain the austenitisation temperature. This would lower the decarburisation occurring during heating, and take advantage of the lower decarburisation observed for SUP7 following austenitisation prior to the introduction of the decarburisation atmosphere.

13.2 Future research

The proposed areas for future research include:

- A more detailed investigation into the transition from austenite growth controlled by the substitutional alloy element partitioning at the austenite/cementite interface, to that involving carbon diffusion in the austenite. This requires a greater range of short duration heat treatments at the higher temperatures than undertaken in this research, with a faster heating media such as a molten metal. The austenite growth rates could then be measured from the maximum martensite particle sizes of the microstructures. These growth rates would allow the austenite carbon concentration gradients to be determined from equations 9.2 and 9.3. A quantitative measurement of the alloy element concentration profiles across the austenite particles would allow the ferrite/austenite and austenite/cementite carbon activities to be determined more accurately, and therefore the transition temperatures for the austenite growth mechanisms. The contribution of carbon diffusion through the ferrite to the growing austenite at the higher austenitisation temperatures also needs to be determined, which requires a knowledge of the cementite/ferrite carbon activities and the diffusion coefficient of carbon in ferrite.

- Determining whether the peak carbon monoxide and carbon dioxide concentrations were due to the formation of oxide structures impeding the decarburisation, or due to the increasing free ferrite depth with the carbon transport being limited by the ferrite carbon diffusivity. This requires knowledge of the influence of alloy content and temperature on the carbon diffusion coefficient in ferrite. A comparison of the instantaneous carbon removal from the gas with the carbon diffusion through the ferrite would then allow the mechanism limiting the peak gas concentrations to be determined.

- The multiple linear regression analysis demonstrated the relationship between the mass of carbon removed after 15min, and the silicon content, manganese content, temperature and p_{H_2O} / p_{H_2} ratio for the decarburisation of the 0% Silicon to SUP7NV steels with p_{H_2O} / p_{H_2} ratios of 0.01 to 0.25. The production and decarburisation of steels with different carbon, manganese and chromium contents, and the subsequent multiple linear regression analysis, would indicate whether the carbon removal could be predicted for

steels comprising a range of carbon, silicon, manganese and chromium contents decarburised at various temperatures and p_{H_2O} / p_{H_2} ratios.

- Production and decarburisation of a 2.5wt.%Si steel. An increase in the silicon content from 2.11 to 3.05wt.% resulted in less decarburisation, particularly at the lower p_{H_2O} / p_{H_2} ratios. The manufacture and decarburisation of a 2.5wt.%Si steel would allow the influence of silicon content on the decarburisation to be further quantified. This would also give a better indication of the optimal silicon content for the fastest decarburisation.

- Production and decarburisation of a 2wt.%Si steel with elevated aluminium concentrations to see if the oxidation resistance can be supplemented to reduce the decarburisation.

The most desirable outcome would involve the manufacture of a steel with the appropriated combination of alloying elements for comparable or improved sag and fatigue performance to SUP7, without decarburisation during the rolling of the bar stock and the austenitisation heat treatment. This would allow the peeling operation to be eliminated, and the austenitisation would not have to be undertaken in an inert atmosphere. If the alloying element combination also lowered the Ac_3 temperature relative to SUP7, lower heat treatment temperatures would lower the heating costs.

REFERENCES

(1) Prabhudev, K.H., *"Handbook of heat treatment of steels"*, McGraw-Hill Publishing Company, New Delhi, 1988.

(2) Mallick, P.K., *"Static mechanical performance of composite elliptical springs"*, Transactions of the American Society of Mechanical Engineers, Volume 109, January 1987, pp 22-26.

(3) Shigley, J.E., *"Mechanical engineering design"*, McGraw-Hill Book Company, New York, First Metric Edition, 1986.

(4) Mallick, P.K., *"Design and development of composite elliptic springs for automotive suspensions"*, 40th Annual Conference, Reinforced Plastics/Composites Institute, Session 14C, 1985, pp 1-5.

(5) Kawakami, H., et al, *"Effect of chemical composition on sag resistance of suspension spring"*, Report 820128, Society of Automotive Engineers, pp 1-7.

(6) Lee, C.S., *"Microstructural influence on fatigue properties of a high strength steel"*, Materials Science and Engineering A, Volume 241, 1998, pp 30-37.

(7) Brownrigg, A. and Sritharan, T., *"Spring steel hysteresis"*, Materials Forum, Volume 10, Number 1, 1987, pp 58-63.

(8) Koyasu, Y. et al, *"Development of high fatigue strength spring steel"*, Wire Journal International, Volume 29, May 1996, pp 88-91.

(9) Assefpour-Dezfuly, M., *"Parameters affecting sag resistance in spring steels"*, Metallurgical Transactions A, Volume 20A, October 1989, pp 1951-1959.

(10) Tata, H.J., Driscoll, E.R. and Kary, J.J., Steels, *"Steels for automotive coil springs with improved resistance to relaxation"*, Report 800480, Society of Automotive Engineers.

(11) Yamamoto, T. et al, *"Precipitation strengthened spring steel for automotive suspensions"*, Journal of Heat Treating, Volume 3, Number 3, June 1984, pp 220-227.

(12) *"Steel springs"*, Metals Handbook, Volume 1, 10th Edition, Properties and Selection: Iron, Steels and High Performance Alloys, American Society for Metals, Metals Park, Ohio, 1990, pp 302-326.

(13) Metals Handbook, Volume 1, 9th Edition, Properties and Selection:Iron and Steels, 1978.

(14) Ozone, T., et al, *"Precipitation strengthened spring steel for automotive suspensions"*, Report 820129, Society of Automotive Engineers, pp 1-13.

(15) Wylie, P., *"Plastic coil springs set to oust steel"*, The Engineer, London, England, Volume 262, February 20, 1986.

(16) Bain, E.C., *"Functions of alloying elements in steel"*, American Society for Metals, Cleveland, Ohio, 1939.

(17) Gildersleeve, M.J., *"Relationship between decarburisation and fatigue strength of through hardened and carburising steels"*, Materials Science and Technology, Volume 7, April 1991, pp 307-310.

(18) Sato, S., Inoue, K. and Ohno, A., *"The effect of shot-peening to decarburised spring steel plate"*, Proceedings 1st International Conference on Shot Peening, Paris, September 1981, pp 303-312.

(19) Kunio, T., Shimizu, M. and Yamada, K., *"Microstructural aspects of the fatigue behaviour of rapid heat treated steel"*, Proceedings of the 2nd International Conference on Fracture, 1969, pp 630-642.

(20) Cooper, C.V. and Fine, M.E., *"Fatigue microcrack initiation in polycrystalline alpha-iron with polished and oxidised surfaces"*, Metallurgical Transactions, 1985, Volume 16A, April, 1985, pp 641-649.

(21) Nisitani, H., *"Current research on fatigue cracks:current Japanese Materials Research"*, Volume 1, 1987, pp 1-26.

(22) Semenov, V.M., Serebrin, S.M. and Rakhshtadt, A.G., *"Stress relaxation in spring steel with a decarburised layer"*, translated from Metallovedenia I Termicheskaya Obrabotka Metallov, Number 4, April 1974, pp 72-73.

(23) Usami, S., *"Current research on fatigue cracks:current Japanese Materials Research"*, Volume 1, 1987, pp 119-147.

(24) ASTM A125-81, *"Standard specification for steel springs, helical, heat treated"*, American Society for Testing and Materials.

(25) Honma, T. and Takeuchi, *"The influence of shot-peening on the fatigue strength of metals"*, Nippon Kinzoku Gakkai-Si, 1958, pp 14-18.

(26) Ohno, A. and Miyagawa, N., Zairyo-Shiken, 1956, pp 476.

(27) Larsson, M. et al, *"Effects of shot peening on bending fatigue strength of spring steel SS 2090"*, Materials Science and Technology, Volume 7, November 1991, pp 998-1004.

(28) *"Sunday Star Times"*, New Zealand, September 20, 1998, pp 1-6.

(29) Gavard, L. et al, *"Bayesian neural network model for austenite formation in steels"*, Materials Science and Technology, Volume 12, June 1996, pp 453-463.

(30) Brooks, C.R., *"Principles of the heat treatment of plain carbon and low alloy steels"*, American Society for Metals, Metals Park, Ohio, 1996.

(31) Molinder, G., *"A quantitative study of the formation of austenite and the solution of cementite at different austenitising temperatures for a 1.27% carbon steel"*, Acta. Metallurgica, Volume 4, November 1956, pp 565-571.

(32) Hillert, M., Nilsson, K. and Torndahl, L.E., *"Effect of alloying elements on the formation of austenite and dissolution of cementite"*, Journal of the Iron and Steel Institute, January 1971, pp 49-66.

(33) Dirnfeld, S.F., Korevaar, B.M. and Van't Spijker, F., *"The transformation to austenite in a fine grained tool steel"*, Metallurgical Transactions, Volume 5, June 1974, pp 1437-1444.

(34) Hultgren, A., *"The Ac_1 range of carbon steel and related phenomena"*, Transactions American Society for Steel Treating, Volume 16, Number 2, August 1929, pp 227-256.

(35) Karmazin, L., *"Experimental study of the austenitisation process of hypereutectoid steel alloyed with small amounts of silicon, manganese and chromium, and with an initial structure of globular cementite in a ferrite matrix"*, Materials Science and Engineering, 1991, pp 71-77.

(36) Speich, G.R. and Szirmae, A., *"Formation of austenite from ferrite and ferrite-carbide aggregates"*, Transactions of the Metallurgical Society of AIME, Volume 245, May 1969, pp 1063-1074.

(37) Nehrenberg, A.E., *"The growth of austenite as related to prior structure"*, Transactions AIME, Journal of Metals, Volume 188, January 1950, pp 162-174.

(38) Roosz, A., Gasci, Z. and Fuchs, E.G., *"Isothermal formation of austenite in eutectoid plain carbon steel"*, Acta Metallurgica, Volume 31, Number 4, 1983, pp 509-517.

(39) Speich, G.R., Demarest, V.A. and Miller, R.L., *"Formation of austenite during intercritical annealing of dual-phase steels"*, Metallurgical Transactions A, Volume 12A, August 1981, pp 1419-1428.

(40) Garcia, C.I. and Deardo, A.J., *"Formation of austenite in 1.5pct Mn steels"*, Metallurgical Transactions A, Volume 12A, March 1981, pp 521-530.

(41) Thompson, S.W., Fan, G.S. and Howell, P.R., *"Phase transformations in ferrous alloys"*, The Metallurgical Society of the American Institute of Mechanical Engineers, pp 43-47.

(42) Navara, E., Bengtsson, B. and Easterling, K.E., *"Austenite formation in manganese partitioning dual phase steel"*, Materials Science and Technology, Volume 2, December 1986, pp 1196-1201.

(43) Roberts, G.A. and Mehl, R.F., *"The mechanism and the rate of formation of austenite from ferrite-cementite aggregates"*, Transactions of the American Society for Metals, Volume 31, 1943, pp 613-650.

(44) Nemoto, M., *"The formation of austenite from mixtures of ferrite and cementite as observed by HVEM"*, Metallurgical Transactions A, Volume 8A, March 1977, pp 431-437.

(45) Avrami, M., *"Kinetics of phase change"*, Journal of Chemical Physics, Volume 7, December 1939, pp 1103-1112.

(46) Judd, R.R. and Paxton, H.W., *"Kinetics of austenite formation from a spheroidised ferrite-carbide aggregate"*, Transactions of the Metallurgical Society of AIME, Volume 242, February 1968, pp 206-214.

(47) Albut, K.J. and Garber S., *"Effect of heating rate on elevation of critical temperatures of low-carbon mild steel"*, Journal of the Iron and Steel Institute, Volume 204, 1966, pp 1217-1222.

(48) Rose, A. and Straussburg, N., Stahl Eisen, Volume 76, 1956, pp 976.

(49) Rose, A., Harterei Technische Mitteilungen, Volume 13, Number 1, 1958, pp 46-73.

(50) Hultgren, A., Transactions ASA, Volume 39, 1947, pp 915.

(51) Hultgren, A., Jerkont. Ann., 1951, pp 734.

(52) Hultgren, A., KVA Handlingar, Number 3, 1953.

(53) Svoboda, M., Karmazin, L. and Kroupa, A., *"The composition of phases present in hypereutectoid low alloy steel at temperatures within and around the eutectoid zone"*, Materials Science and Engineering, 1989, pp L21-L23.

(54) Karmazin, L., *"Phase transformations of low-alloy steel at temperatures inside the eutectoid gap"*, Materials Science and Engineering", 1988, pp 201-206.

(55) Bain, E.C. and Paxton, H.W., *"Alloying elements in steel"*, American Society for Metals, Metals Park, Ohio, 1961.

(56) Souza, M.M., Guimaraes, J.R.C. and Chawla, K.K., *"Intercritical annealing of two Fe-Mn-C steels"*, Metallurgical Transactions A, Volume 13A, April 1982, pp 575-579.

(57) Pussegoda, N., et al, *"Segregation of manganese during intercritical annealing of dual phase steels"*, Metallurgical Transactions A, Volume 5A, July 1984, pp 1499-1502.

(58) Cai, X-L., Garrett-Reid, A.J. and Owen, W.S., *"The development of some dual-phase steel structures from different starting microstructures"*, Metallurgical Transactions A, Volume 16A, April 1985, pp 543-557.

(59) Erasmus, L.E., *"The diffusion of carbon in a duplex phase steel"*, The Metallurgist and Materials Technologist, September 1975, pp 465-467.

(60) Dunn, W.W. and McLellan, R.B., *"The thermodynamic properties of carbon in body centred cubic iron"*, Materials Transactions, Volume 2, April 1971, pp 1079-1085.

(61) Smith, R.P., *"Equilibrium of iron-carbon alloys with mixtures of CO-CO_2 and CH_4-H_2"*, Journal of the American Chemical Society, Volume 68, Number 1, July 1946, pp 1163-1175.

(62) Askeland, D.R., *"The science and engineering of materials"*, Van Nostrand Reinhold International, Hong Kong, 1988.

(63) Jost, W., *"Diffusion in solids, liquids, gases"*, Academic Press Incorporated, New York, 1960.

(64) Pennington, W.A., *"A mechanism of the surface decarburisation of steel"*, Transactions of the American Society for Metals, Volume 37, 1946, pp 48-109.

(65) Adzema, P.J. and Knight, D.J., *"Columnar grain growth in low carbon steel"*, Transactions of the American Society for Metals, Volume 56, Number 3, 1963, pp 576-582.

(66) Marder, A.R., *"Factors affecting the final grain size of decarburised lamination steels"*, Metallurgical Transactions A, Volume 17A, August 1986, pp 1277-1285.

(67) Mayer, A., *"The decarburisation of cold-rolled silicon steel sheet"*, Stahl u. Eisen, Volume 83, Number 19, September 1963, pp 1169-1176.

(68) Birks, N., *"Mechanisms of decarburisation"*, Conference on Decarburisation, Sheffield, The Iron and Steel Institute, London, 1969, pp 1-12.

(69) Yamazaki, T., *"On the decarburisation of silicon steel sheet"*, Nippon Tekko Kyokai Transactions, Volume 9, 1969, pp 66-75.

(70) Emel'yanenka, L.P., et al, *"The decarburising of steel without oxidation and with the formation of scale"*, translated from Termicheskaya Obrabotka Metallov, Number 3, March 1971, pp 77-79.

(71) Hudson, R.M., Abel, A.W. and Stragand, G.L., *"Equilibrium studies for the reaction C(in steel)+H_2O=CO+H_2"*, Transactions of the Metallurgical Society of AIME, Volume 233, May 1965, pp 879-883.

(72) Pennington, W.A., *"Thermodynamics in the decarburisation of steel with mill scale", Transactions of the American Society for Metals"*, Volume 41, 1949, pp 213-258.

(73) Wiesner, U., *"About oxidation and decarburisation behaviour of Fe-Si alloys"*, Neue Hutte, July 1986, pp 250-253.

(74) Tomida, T. and Tanaka, T., *"Development of (100) texture in silicon steel sheets by removal of manganese and decarburisation"*, Journal of the Iron and Steel Institute, Volume 35, Number 5, 1995, pp 548-556.

(75) Tomida, T., *"A new process to develop (100) texture in silicon steel sheets"*, Journal of Materials Engineering and Performance, Volume 5, June 1996, pp 316-322.

(76) Oh, J.M. and McNallan, M.J., *"Microstructural development in the surface region during oxidation of iron-manganese-nickel-silicon alloys"*, Journal of the Electrochemical Society, Volume 133, Number 5, May 1986, pp 1042-1048.

(77) Oh, J.M. and McNallan, M.J., *"Kinetics of oxidation induced transformations in iron-manganese-nickel-silicon alloys"*, Journal of the Electrochemical Society, Volume 134, Number 4, April 1987, pp 1010-1015.

(78) Marini, P. and Abbruzzese, G., *"Decarburisation rate related to surface oxidation of grain oriented silicon steel"*, Journal of Magnetism and Magnetic Materials, Volume 26, 1982, pp 15-21.

(79) Datta, A., et al, *"Oxidation of 3%Si-Fe during decarburisation"*, Proceedings of the 3rd International Conference on Soft Magnetic Materials, Brotislava, 1977, pp 492-502.

(80) Guy, A.G. and Hren, J.J., *"Elements of physical metallurgy"*, Addison-Wesley Publishing Company, Reading Massachusetts, Third Edition, 1974.

(81) Evans, U.R., *"An introduction to metallic corrosion"*, British Library Cataloguing in Publication Data, 1981.

(82) Tuck, C.W., *"Non-protective and protective scaling of a commercial 13/4% silicon-iron alloy in the range 800°C-1000°C"*, Corrosion Science, Volume 5, 1965, pp 631-643.

(83) Seybolt, A.U. and Alessandrini, E.I., *"Further studies on the metallurgy of silicon iron-some observations on selective oxidation"*, Transactions of the Metallurgical Society of AIME, August 1958, pp 507-509.

(84) Logani, R.C. and Smeltzer, W.W., *"The development of wustite-fayalite nodules on a iron-1.5wt% silicon alloy at 1000°C"*, Oxidation of Metals, Volume 3, Number 1, 1971, pp 15-32.

(85) Ichido, T. and Morrito, N., *"Transition from external to internal oxidation in iron-silicon alloy as a function of oxygen potential of the ambient atmosphere"*, Scripta Metallurgica, Volume 10, 1976, pp 619-622.

(86) Block, W.F. and Jayaraman, N., *"Reactions during decarburisation annealing of electrical steel"*, Materials Science and Technology, Volume 2, January 1986, pp 22-27.

(87) Geiger, A.L., *"Surface oxidation of non-oriented silicon-aluminium electrical steels during annealing"*, Journal of Applied Physics, Volume 49, Number 3, March 1978, pp 2040-2042.

(88) Grabke, H.J., *"Kinetics and mechanisms of the surface reactions occurring during carburisation and decarburisation and also nitrogenation and denitrogenation of iron in gases"*, Arch. Eisenhuttenwesen, Volume 46, Number 2, February 1975, pp 75-81.

(89) Geiger, G.H. and Poirer, D.R., *"Transport phenomena in metallurgy"*, Addison-Wesley Publishing Company, Reading Massachusetts, 1973.

(90) Ure, C.R., *"Computer prediction of the Fe-C phase diagram:the ferrite/austenite equilibrium and the solubilities of graphite in the ferrite and austenite"*, Ph.D. Thesis, University of Canterbury, 1987.

(91) Brooks, C.R., *"Principles of the surface treatment of steels"*, Technomic Publishing Company Incorporated, Pennsylvania, 1992.

(92) Wada, T., et al, *"Thermodynamics of the FCC Fe-Mn-C and Fe-Si-C alloys"*, Metallurgical Transactions, Volume 3, June 1972, pp 1657-1662.

(93) Eckert, E.R.G. and Drake, R.M., *"Heat and mass transfer"*, New York, 1959.

(94) Bird, R.B., Stewart, W.E. and Lightfoot, E.N., *"Transport phenomena"*, NewYork, 1960.

(95) Collin, R., Gunnarson, S. and Thulin, D., *"Influence of reaction rate on gas carburising of steel in a CO-H_2-CO_2-H_2O-CH_4-N_2 atmosphere"*, Journal of the Iron and Steel Institute, October 1972, pp 777-784.

(96) Collin, R., Gunnarson, S. and Thulin, D., *"A mathematical model for predicting carbon concentration profiles of gas carburised steel"*, Journal of the Iron and Steel Institute, October 1972, pp 785-789.

(97) Darken, L.S. and Gurry, R.W., *"Physical chemistry of metals"*, McGraw-Hill Book Company, New York, 1953.

(98) Fast, J.D., *"Interaction of metals and gases. Volume 2. Kinetics and Mechanisms"*, London, 1971.

(99) Smith, R.P. *"The diffusivity and solubility of carbon in alpha-iron"*, Transactions of the Metallurgical Society of AIME, Volume 224, February 1962, pp 105-111.

(100) Hudson, R.M., *"Decarburisation of low-carbon steel sheets in wet atmospheres containing hydrogen"*, Transactions of the Metallurgical Society of AIME, Volume 227, June 1963, 695-699.

(101) Lucke, K., Arch. Eisenhuttenwesen, Volume 25, 1954, pp 181-185.

(102) Andrews, K.W., *"Empirical formula for the calculation of some transformation temperatures"*, Journal of the Iron and Steel Institute, July 1965, pp 721-727.

(103) Kaspersma, J.H. and Shay, R.H., *"A model for carbon transfer in gas-phase carburising of steel"*, Journal of Heat Treating, Volume 1, Number 4, pp 21-28.

(104) Gurry, R.W., *"Weight change as criterion of extent of decarburisation or carburisation"*, Transactions of the American Institute of Mechanical Engineers, Volume 150, 1942, pp 172-183.

(105) Bugakov, V.Z., *"Diffusion in metals and alloys"*, Gostekhteoretizdat, 1949.

(106) Le Claire, A.D. *"Progress in metal physics"*, Volume 1, Butterworths, London, 1949.

(107) Gertsriken, S.D. and Dekhtyar, I.Y., ZhTF, Volume 17, Number 8, 1947, 871.

(108) Krishtal, M.A., *"Diffusion processes in iron alloys"*, Israel Program for Scientific Translations, Jerusalem, 1970.

(109) Gruzin, P.L., Problemy Metallovedeniya I Fiziki Metallov, Issue 4, 1955, 475.

(110) Frenkel, J., *"Kinetic theory of liquids"*, Dover Publishing Incorporated, 1955.

(111) Frenkel, Y.I., *"Introduction to the theory of metals"*, Gostekhizdat., 1948.

(112) Groh, I. And Hevesy, G., Ann. Physics, Volume 65, 1920, 216.

(113) Mirkin, I.L., *"The problem of the diffusion mechanism. Report to the conference on diffusion."*, AN UkrSSR, 1955.

(114) Zener, C., Acta Cryst., Volume 3, Number 5, 1950, 346.

(115) Mirkin, I.L. and Khristal, M.A., *"Diffusion in metals and alloys"*, NTO, Mashprom, Mashgiz., 1959.

(116) Paschke, M. and Hauttmann, A., *"Experiments on diffusion of carbon, silicon and manganese in solid and molten iron"*, Arch. Eisenhuttenwesenen, Volume 9, Number 6, December 1935, pp 305-309.

(117) Wells, C. and Mehl, R.F., *"Rate of diffusion of carbon in austenite in plain carbon in nickel and in manganese steels"*, Transactions of the American Institute of Mining and Metallurgical Engineers, Volume 140, pp 279-306.

(118) Blanter, M.E., ZhTF, Volume, Number 11, 1947, 1331.

(119) Stanley, J.K., Journal of Metals, Volume 185, 752.

(120) Bokshtein, S.Z., *"Coagulation, phase transformations, and mechanical properties of alloy steels during tempering"*, Thesis Summary, 1950.

(121) Wert, C.A., Physical Review, Volume 79, Number 4, 1950, 601.

(122) Gruzin, P.L., et al, Problemy Metallovedeniya I Fiziki Metallov, Issue 5, 1956, 327.

(123) Gruzin, P.L., *"Some regularities of diffusion and distribution of elements in alloys"*, Metallovedenie I Termicheskaya Obrabotka Metallov, Number 10, October 1960, pp 5-13.

(124) Gruzin, P.L., Report to the conference on diffusion, AN UkrSSR, 1955.

(125) Zhukov, A.A., Izvestiya Vuzov. Mashinostroenie, Number 10, 1961.

(126) Blanter, M.E., *"Diffusion in austenite and hardenability of alloy steels"*, Thesis Summary, MIS, 1949.

(127) Yurkov, V.A. and Khristal, M.A., DAN SSSR, Volume 92, Number 6, 1953, 1171.

(128) Bokshtein, S.Z., Kishkin, S.T. and Moroz, L.M., Metallovedenie I Obrabotka Metallov, Number 2, 1957, 2.

(129) Fischer, I.C., Journal of Applied Physics, Volume 22, Number 1, 1951.

(130) Lyubov, B.Y., Report to the Conference on Diffusion, AN Ukr SSR, 1955.

(131) Gertsriken, S.D. and Dekhtyar, I.Y., *"Diffusion in solid solutions of metals and alloys"*, Fizmatgiz., 1960.

(132) Gruzin, P.L., Kuznetsov, E.V. and Kurdyumov, G.V., Problemy Metallovedeniya I Fiziki Metallov, Issue 4, 1955, 494.

(133) Gruzin, P.L. and Kuznetsov, E.V., Problemy Metallovedeniya I Fiziki Metallov, Issue 4, 1955, 498.

(134) Gruzin, P.L. and Noskov, B.M., Problemy Metallovedeniya I Fiziki Metallov, Issue 4, 1955, 509.

(135) Gjostein, N.A., *"Diffusion"*, American Society for Metals, Metals Park Ohio, 1973, pp 241-274.

(136) Martin, G. and Perraillon, B., Journal de Physique, Volume 36, 1975, pp 165-190.

(137) Martin, G. and Perraillon, B., Grain Boundary Structure and Kinetics, American Society for Metals, Metals Park Ohio, 1980, pp 239-295.

(138) Peterson, N.L., Grain Boundary Structure and Kinetics, American Society for Metals, Metals Park Ohio, 1980, pp 209-223.

(139) Peterson, N.L., *"Grain boundary diffusion in metals"*, International Metals Reviews, Volume 28, Number 2, 1983, pp 65-91.

(140) Burton, B., *"Diffusional creep of polycrystalline materials"*, Technical Publication, Bay Village, Ohio, 1977.

(141) Ashby, M.F., *"A first report on deformation mechanism maps"*, Acta Metallurgica, Volume 20, 1972, pp 887-897.

(142) Balluffi, R.W., Grain Boundary Structure and Kinetics, American Society for Metals, Metals Park Ohio, 1980, pp 297-327.

(143) Balluffi, R.W., *"Grain boundary diffusion mechanisms in metals"*, Metallurgical Transactions B, Volume 13B, December 1982, pp 527-553.

(144) Balluffi, R.W. and Cahn, J.W., *"Mechanism for diffusion induced grain boundary migration"*, Acta Metallurgica, Volume 29, pp 493-500.

(145) Bott, C., unpublished research, University of Canterbury, Christchurch.

(146) Payson, P., *"Does silicon accelerate decarburisation?"*, Metal Progress, Volume 78, December 1960, pp 78-81.

(147) Laird, W.J., *"Salt bath equipment"*, Metals Handbook, Volume 4 Heat Treating, Ninth Edition, 1978, pp 293-298.

(148) Globar Silicon Carbide Electric Heating Elements, Resistant Materials Bulletin Number 22, Carborundum.

(149) Personal Communication, BOC Industrial Gases, Christchurch.

(150) Mardon, C.A., *"Decarburisation understanding for improved automobile suspension spring performance"*, Proceedings IPENZ Annual Conference 1994, Volume 2, pp 311-316.

(151) Martin, J.W. and Doherty, R.D., *"Stability of microstructure in metallic system"*, Cambridge University Press, Cambridge, 1976.

(152) *"Gas carburising"*, Metals Handbook, Volume 4 Heat Treating, Ninth Edition, American Society for Metals, Metals Park Ohio, 1978, pp 135-175.

(153) Vander Voort, G.F., *"Metallography principles and practice"*, McGraw-Hill Book Company, New York, 1984.

(154) Underwood, E.E., *"Quantitative metallography"*, American Society for Metals Handbook, Volume 9, Metallography and Microstructures, American Society for Metals, Metals Park Ohio, 1992, pp 123-134.

(155) DeHoff, R.T., *"Stereology and metallurgy"*, Metals Forum, Volume 5, Number 1, 1982, pp 4-12.

(156) ASTM E112-88, *"Standard test methods for determining average grain size"*, American Society for Testing and Materials.

(157) ASTM E1382-91, *"Standard test methods for determining average grain size using semiautomatic and automatic image analysis"*, American Society for Testing and Materials.

(158) Vander Voort, G.F. and Roosz, A., *"Measurement of the interlamellar spacing of pearlite"* Metallography, Volume 17, February 1984, pp 1-17.

(159) ASTM E766-86, *"Standard practice for calibrating the magnification of SEM using NBS-SRM-484"*, American Society for Testing and Materials.

(160) Fowler, D.B., *"A method of determining the interlamellar spacing of pearlite using digital image analysis"*, Microstructural Science, Volume 17, Image Analysis and Metallography, American Society for Metals International, 1989, pp 81-90.

(161) ASTM E1077-91, *"Standard test methods for estimating the depth of decarburisation of steel specimens"*, American Society for Testing and Materials.

(162) ASTM E562-89, *"Standard test method for determining volume fraction by systematic manual point count"*, American Society for Testing and Materials.

(163) ASTM E1508-93a, *"Standard guide for quantitative analysis by energy-dispersive spectroscopy"*, American Society for Testing and Materials.

(164) Atkins, M., *"Atlas of continuous cooling transformation diagrams for engineering steels"*, British Steel Corporation, 1977.

(165) DeHoff, R.T., *"Estimation of particle-size distributions from simple counting measurements made on random plane sections"*, Transactions of the Metallurgical Society of AIME, Volume 233, 1965, pp 25-29.

(166) ASTM E384-89, *"Standard test method for microhardness of materials"*, American Society for Testing and Materials.

(167) ASTM B487-85, *"Standard test method for measurement of metal and oxide coating thickness by microscopical examination of a cross-section"*, American Society for Testing and Materials.

(168) Al-Khafaji, A.W. and Toolet, J.R., *"Numerical methods in engineering practice"*, CBS Publishing Japan Limited, New York, 1986.

(169) *"Bosch automotive handbook"*, Robert Bosch GmbH, Stuttgart, 2nd Edition, 1986.

(170) Brandes, E.A. and Brook, G.B., *"Smithells metals reference book"*, Butterworth-Heinemann Limited, Oxford, 7th Edition, 1992.

(171) Sinha, A.K., "Ferrous physical metallurgy", Butterworths, Boston, 1989.

(172) Kirkaldy, J.S. and Baganis, E.A., *"Thermodynamic prediction of the Ae_3 temperature of steels with additions of Mn, Si, Ni, Cr, Mo, Cu"*, Metallurgical Transactions A, Volume 9A, April 1978, pp 495-501.

(173) Grange, R.A., *"Estimating critical ranges in heat treatment of steels"*, Metal Progress, April 1961, pp 73-75.

(174) Mehl, R.F., *"The structure and rate of formation of pearlite"*, Transactions of the American Society for Metals, Volume 29, 1941, pp 813-862.

(175) Payson, P., Hodapp, W.L. and Leader, J., *"The spheroidising of steel by isothermal transformation"*, Transactions of the American Society for Metals, Volume 28, 1940, pp 306-332.

(176) Olen, K.R. and Birks, N., *"Effect of internal oxidation on graphite nucleation in an iron-3% silicon-0.5% carbon alloy"*, Journal of the Iron and Steel Institute, Volume 208, January 1970, pp 75-80.

(177) Rosen, A. and Taub, A., *"The kinetics of graphitisation in steel at subcritical temperatures"*, Acta Metallurgica, Volume 10, May1962, pp 501-512.

(178) Whiteman, J.A., Ph.D. Thesis, University of Sheffield, 1962.

(179) Harris, J.E., Whiteman, J.A. and Quarrell, A.G., *"Decomposition of cementite in steels at subcritical temperatures"*, Transactions of the American Institute of Mechanical Engineers, Volume 233, Number 1, 1965, pp168-179.

(180) Gibbs, G.B., CEGB Report Number RD/B/N. 313.

(181) Hillert, M., *"Role of interfacial energy during solid state phase transformations"*, Jerkont. Ann., Volume 141, Number 11, 1957, pp 757-789.

(182) *"Alloy phase diagrams"*, American Society for Metals Handbook Volume 3, American Society for Metals International, Materials Park, Ohio, 1990.

(183) Svoboda, M., Kroupa, A. and Karmazin, L., *"Vertical section of Fe-C-2Si-2Mn-1Cr system for carbon contents up to 0.8wt.% and associated phase compositions"*, Materials Science and Engineering, Volume 10, August 1994, pp 691-695.

(184) Schroder, A. and Rose, A., *"De Ferri Metallographia"*, Verlag Stahleisen, Dusseldorf, 1966.

(185) Walton, R.F., *"Iron castings handbook"*, Iron Castings Society, Incorporated, Des Plaines, Illinois, 1981.

(186) Roosz, A., Gasci, Z. and Fuchs, E.G., *"Isothermal formation of austenite in eutectoid plain carbon steel"*, Acta Metallurgica, Volume 31, Number 4, 1983, pp 509-517.

(187) Krauss, G., *"Steel: Heat treatment and processing principles"*, Materials Park, Ohio, 1990.

(188) Clem, P.J. and Fischer, *"The influence of grain boundaries on the nucleation of secondary phases"*, Acta Metallurgia, Volume 3, January 1955, pp 70-73.

(189) Datta, D.P. and Gokhale, A.M., *"Austenitisation kinetics of pearlite and ferrite aggregates in a low carbon steel containing 0.5wt pctC"*, Metallurgical Transactions A, Volume 12A, March 1981, pp 443-450.

(190) Grange, R.A., *"Effect of microstructural banding in steel"*, Metallurgical Transactions, Volume 2, February 1971, pp 417-426.

(191) Nam, W.J. and Choi, H.C., *"Effects of silicon, nickel, and vanadium on impact toughness in spring steels"*, Materials Science and Technology, Volume 13, July 1997, pp 568-574.

(192) Burrier, H., *"Hardenability of carbon and low-alloy steels"*, Metals Handbook, Volume 1, 10th Edition, American Society for Metals International, 1990, pp 464-484.

(193) Grange, R.A., Hribal, C.R. and Porter, L.F., *"Hardness of tempered martensite in carbon and low-alloy steels"*, Metallurgical Transactions A, Volume 8, 1977, pp 1175-1185.

(194) Villars, P., Prince, A. and Okamoto, H., *"Handbook of ternary alloy phase diagrams"*, Volume 5, American Society for Metals International, 1995.

(195) Kroupa, A. and Karmazin, L., *"The metastable quasi-binary phase diagram of low-alloy steels having an increased manganese and silicon content"*, Materials Science and Engineering, 1988, pp L7-L9.

(196) Cahn, J.W., *"The kinetics of grain boundary nucleated reactions"*, Acta Metallurgica, Volume 4, September 1956, pp 449-459.

(197) Cahn, J.W., *"On kinetics of pearlite reaction"*, Journal of Metals, Volume 9, Number 1, 1957, pp 140-144.

(198) Johnson, W.A. and Mehl, R.F., *"Reaction kinetics in processes of nucleation and growth"*, Transactions of the American Institute of Mining and Metallurgical Engineers, Volume 135, 1939, pp 416-442.

(199) Gokhale, A.M., Iswaran, C.V. and DeHoff, R.T., *"Use of the stereological counting measurements in testing theories of growth rates"*, Metallurgical Transactions A, Volume 10A, September 1979, pp 1239-1245.

(200) Gokhale, A.M. and DeHoff, R.T., *"Estimation of nucleation rate and growth rate from time dependence of global microstructural properties during phase transformations"*, Metallurgical Transactions A, Volume 16A, April 1985, pp 559-564.

(201) Kolmogorov, A.N., Bull. Acad. Sci. USSR, Number 3, 1937, 57.

(202) Hillert, M., *"The kinetics of the first stage of tempering"*, Acta Metallurgica, Volume 7, October 1959, pp 653-658.

(203) Gokhale, A.M., Ph.D Thesis, University of Florida, Gainesville, 1977.

(204) Borchers, H. and Schulz, H., *"Quantitative discontinuous precipitation and its effect in cold rolled copper-1.5%Be"*, Acta Metallurgica, Volume 24, July 1976, pp 639-650.

(205) Saltykov, S., Stereometrizeskaya Metallografia. Tech. Izd., 1958, pp 250-252.

(206) Brandes, E.A. and Brooks, G.B., *"Smithells metals reference book"*, Butterworth-Heinemann Limited, Oxford, 1992.

(207) Swisher, J.H., *"Optimum temperature for decarburising low-carbon steels in wet hydrogen"*, Transactions of the Metallurgical Society of the American Institute of Mechanical Engineers, Volume 242, April 1968, pp 763-765.

(208) Mardon, C., Smaill, J. and Sell, L., *"Decarburisation behaviour of high silicon spring steels"*, Proceedings IPENZ Annual Conference 1997, Volume 2, pp 269-271.

(209) Fast, J.D. and Brunning, H.A.C.M., *"Decarburising and denitriding of ferrite-silicon steel"*, Z. Elektrochemie, Volume 63, Number 7, 1959, pp 765-772.

(210) Ito, K., *"Textures in carburised and decarburised steels"*, Transactions of the Iron and Steel Institute of Japan, Volume 11, 1971, pp 86-94.

(211) Leslie, W.C., *"Nitrogen in ferritic steels"*, Volume 25, American Institute of Mechanical Engineers, New York, 1959.

(212) Shilvock, W.D., *"The effect of alloy and impurity variation on the treatment, casting and physical properties of aluminium-silicon eutectic alloys"*, Ph.D. Thesis, University of Canterbury, 1995.

(213) Muan, A., *"Phase equilibria among oxides in steelmaking"*, Addison-Wesley Publishing Company Incorporated, Reading, Massachusetts, 1965.

(214) Kucera, J., Stransky, K. and Dojiva, J., *"Diffusion interaction coefficients β_C^i and thermodynamic interaction coefficients ε_C^i of carbon in alloyed austenitic steels"*, Materials Science and Engineering, Volume A125, Number 1, 1990, pp 75-82.

(215) Karlekar, B.V., *"Thermodynamics for engineers"*, Prentice-Hall Incorporated, Englewood Cliffs, 1983.

(216) Holman, J.P., *"Heat transfer"*, Seventh Edition, McGraw-Hill Book Company, London, 1992.

Appendix A

Salt bath furnace design calculations

Addition of the test specimens into the molten salt of the salt bath will decrease the salt temperature. It is necessary to have a suitable salt volume to minimise this temperature drop. The temperature drop on addition of the test specimens can be calculated from a heat balance by

$[\text{Heat capacity after}]_{\text{salt}}$ = $[\text{Heat capacity before}]_{\text{salt}}$ - [Heat capacity of specimens at molten salt temperature]. (A1)

Assuming that the test specimens heat instantly to the lower salt temperature resulting from their addition into the salt, equation A1 can be written as

$$[m_{salt} C_{p_{salt}} T_{saltafter}] = [m_{salt} C_{p_{salt}} T_{saltbefore}] - [m_{steel} C_{p_{steel}} (T_{after} - T_i)], \quad \text{(A2)}$$

where m_{salt}, m_{steel} = mass of salt and test specimens added in kg;

$C_{p_{salt}}$, $C_{p_{steel}}$ = molar heat capacity of salt and steel in $JK^{-1}mol^{-1}$;

$T_{saltafter}$ = salt temperature after addition of test specimens in °K;

$T_{saltbefore}$ = salt temperature before addition of test specimens in °K;

T_i = initial temperature of test specimens in °K.

Assuming that six test specimens 12mm diameter by 2mm thickness, which are attached to a 3mm diameter by 120mm long threaded stainless steel rod, are inserted into the molten salt, m_{steel} can be calculated from

$$m_{steel} = \rho_{steel} V_{steel}, \quad \text{(A3)}$$

where $V_{steel} = 6\pi(R^2_{specimen} - R^2_{rod})t_{specimen} + \pi R^2_{rod} l_{rod}$, (A4)

with $R_{specimen}$, R_{rod} = radius of specimen and threaded rod in m;

$t_{specimen}$ = thickness of specimen in m;

l_{rod} = length of rod in m.

Thus,

$$V_{steel} = 2.21\text{x}10^{-6}\text{m}^3.$$

With ρ_{steel} [206] = 7833kg/m^3,

$$m_{steel} = 0.01727\text{kg}.$$

The salt mixture in the solid state comprises 55% $BaCl_2$, 25% NaCl and 20% KCl. The room temperature densities[206] are 3856, 2170 and 1980kg/m^3 respectively. By a simple mass proportion calculated from multiplying volume fraction by densities, mass percentages for $BaCl_2$, NaCl and KCl in the solid salt mixture are 69.3, 17.7, and 12.9% respectively. No information could be obtained for this ternary salt mixture in the molten state. However, information for a binary mixture of $BaCl_2$ and NaCl was obtained[206]. The ratio of $BaCl_2$ to $BaCl_2$ plus NaCl for this ternary salt is 79.7%. At 800°C, a mixture of 80.1% $BaCl_2$ and 19.9% NaCl has a density[206] of 2616kg/m^3, while that of molten KCl is 1510kg/m^3. Therefore, the density of the ternary salt mixture can be estimated from a simple proportion, yielding 2470kg/m^3. At 800°C, the molar heat capacities of $BaCl_2$, NaCl and KCl are 456, 1037 and 899J/kgK respectively[206]. Assuming that an approximate molar heat capacity for the molten salt mixture can be calculated from the mass fractions and molar heat capacities of the three constituent salts, then

$$C_{p_{salt}} = 615\text{J/kgK}.$$

For initial salt bath and test specimen temperatures of 800 and 20°C respectively, and a maximum temperature drop of 5°C, $T_{saltbefore}$ = 1073K, $T_{saltafter}$ = 1068K and T_i = 293K. For a 0.49wt.% C, 0.90wt.%Mn, 1.98wt.% Si, 0.64wt.% Cu steel[182], a weighted value of the molar

heat capacities for temperatures between 50 and 800°C can be estimated. This yields $C_{p_{steel}}$ = 710J/kgK. Substituting these values in equation A2 and solving for m_{salt} yields

m_{salt} = 3.09kg.

Consequently, the volume of salt required, V_{salt}, is given by

$$V_{salt} = \frac{m_{salt}}{\rho_{salt}} = 1250\text{cm}^3 \qquad \text{(A5)}$$

Therefore, the volume of molten salt, and hence the volume of the salt pot, should be greater than 1250cm^3 to limit the maximum temperature drop in the salt pot at any stage to 5°C. A 1kW salt pot containing 1200cm^3 of molten salt was found to require approximately 30s to heat the test specimens to within 5°C of the salt temperature. During this heating time, heat inputs from the heating elements and electrodes will return the molten salt to the operational temperature. The heat input required to recover the 5°C drop can be calculated from

$$\text{Heat input} = m_{salt} C_{p_{salt}} (T_{saltbefore} - T_{saltafter}) = 10.97\text{kJ}. \qquad \text{(A6)}$$

Over a 30s heating interval, the power input required is given by

$$\text{Power input} = \frac{\text{heat input}}{\text{heating time}} = 366\text{W}. \qquad \text{(A7)}$$

Therefore, a power input of 366W is required to return the furnace to its operational temperature after the 30s specimen heating time. As this power input is occurring while the specimens are heating, the temperature drop will be lower than 5°C. The values calculated for the molten salt volume, and the power input to return the salt to the operational temperature do not take into account the thermal inertia of the salt pot. This thermal inertia will also result in a smaller decrease in the molten salt temperature upon insertion of the test specimens, and raise the power input required for each °C to return the salt bath to its operational temperature.

Appendix B

Specification of silicon carbide electric heating elements

The recommended power loading on the Globar heating elements[148] is 3.1 to 7W/cm^2. The maximum power required for each element using a rectangular arrangement of four elements with two on either side of the salt pot, where the elements are wired to a single phase supply with a maximum power loading of approximately 2.3kW, is 575W. For a salt pot depth of 160mm, an effective element heating length of 175mm was chosen. Available element diameters are 12.7, 15.9, and 19.1mm. The power loading in W/cm^2 can be calculated from equation B1, with

$$\text{Power loading} = \frac{Power}{\pi \phi_{heatingelement} l_{effective}}, \qquad \text{(B1)}$$

where $\phi_{heatingelement}$ = diameter of heating element in mm;

$l_{effective}$ = element effective heating length in mm.

Table B1 Power loadings and outputs for different diameter elements with 175mm effective heating lengths.

Element diameter (mm)	Power loading at (575W/cm^2)	Minimum power for four elements at 3.1W/cm^2 (W)	Maximum power (W) (limited by either 2.3kW or 7W/cm^2)
12.7	8.24	866	1955
15.9	6.58	1084	2300
19.1	5.48	1302	2300

The power loadings of the different diameter elements to yield 575W are detailed in Table B1, along with the minimum and maximum recommended power outputs. It can be seen that the 15.9mm diameter element gives the widest recommended power range while still achieving the maximum power. Figure B1 allows the element surface temperature to be calculated for various power loadings to obtain the desired salt pot wall temperature, and hence the molten

salt temperature at equilibrium. From Table B2 it can be seen that the maximum element temperature will be 1096°C for a salt pot wall temperature of 900°C. As the maximum operating temperature is 1650°C[148], element overload should not be a problem.

Table B2 Heating element temperatures for various loadings and salt pot wall temperatures.

Power loadings		Element temperatures for specified wall temperatures (°C)							
(kW)	**(W/cm^2)**	**650**	**700**	**750**	**800**	**850**	**900**	**950**	**1000**
1.1	3.15	784	823	863	902	941	980	1020	1059
1.4	4.00	822	861	900	939	978	1017	1056	1095
1.7	4.86	852	889	926	963	1001	1038	1075	1112
2.0	5.72	893	928	964	999	1035	1070	1106	1141
2.3	6.58	922	957	991	1026	1061	1096	1130	1165

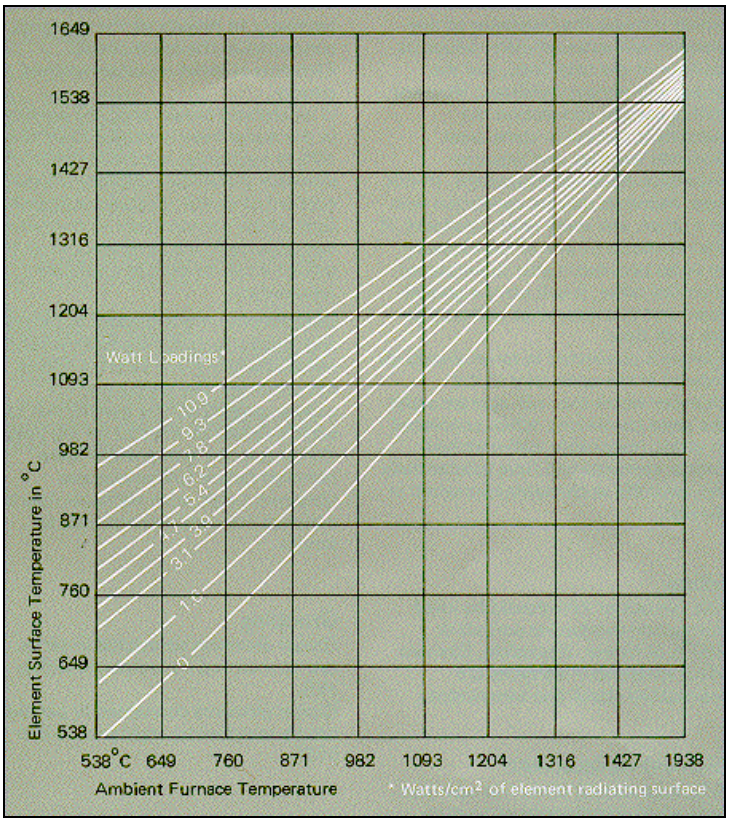

Figure B1 Element surface temperature versus salt pot wall temperature for various power loadings[148].

Appendix C

Nominal composition of heat treatment gases

This appendix details the composition of the gases used for the austenitisation and decarburisation heat treatments.

1)	Argon	Industrial grade

Ar	:	99.99%
H_2O	:	Less than 30vppm
O_2	:	Less than 10vppm
N_2	:	Less than 50vppm
CO_2	:	Less than 10vppm
H_2	:	Less than 10vppm

2)	Hydrogen	Industrial grade

H_2	:	99.8%
H_2O	:	Less than 14vppm
O_2	:	Less than 10vppm
N_2	:	Less than 1000vppm
CO_2	:	Less than 100vppm
CO	:	Less than 5vppm
HC’s	:	Less than 10vppm

3)	Hydrogen	Zero grade

H_2	:	Greater than 99.995%
H_2O	:	Less than 5vppm
O_2	:	Less than 5vppm

CO_2	:	Less than 1vppm
CO	:	Less than 0.5vppm
HC’s	:	Less than 0.5vppm

4) Span gas

Ar	:	99.609%
CO_2	:	980 ± 20vppm
CO	:	2700 ± 50vppm
CH_4	:	232 ± 55vppm

Appendix D

Variation of p_{H_2O} / p_{H_2} ratio with water temperature

Assuming that the pressure in the tube furnace is atmospheric, and that the hydrogen gas flow rate is saturated with water vapour at the water temperature, the p_{H_2O} / p_{H_2} ratio can be calculated from

$$\frac{P_{H_2O}}{P_{H_2}} = \frac{P_{H_2O}}{P_{atmospheric} - P_{H_2O}}, \qquad \text{(D1)}$$

where P_{H_2O} = water vapour saturation pressure at the water temperature of interest in kPa;

P_{H_2} = hydrogen pressure in kPa;

$P_{atmospheric}$ = atmospheric pressure at STP of 101.3kPa and 20°C.

Table D1 gives p_{H_2O} / p_{H_2} ratios as a function of water temperature. The temperature controller of the second water bath can vary the temperature from 20 to 70°C. This limits the p_{H_2O} / p_{H_2} ratio for a hydrogen flow to between 0.024 and 0.445. However, by introducing argon into the H_2O/H_2 gas flow, the maximum p_{H_2O} / p_{H_2} ratio can be raised since

$$P_{atmospheric} = P_{H_2O} + P_{H_2} + P_{Ar}, \qquad \text{(D2)}$$

where P_{Ar} = argon pressure in kPa.

As P_{H_2O} is determined by the water temperature and $P_{atmospheric}$ is fixed at 101.3kPa, the addition of an argon flow lowers the hydrogen pressure, and therefore increases the p_{H_2O} / p_{H_2} ratio of equation D1. Assuming that pressure is proportional to volume flow rate[214] at low

pressures, the p_{H_2O} / p_{H_2} ratio for a hydrogen flow rate of 250cm^3/min with different water temperatures and argon flow rates is given in Table D2.

Table D1 Relationship between water temperature and p_{H_2O} / p_{H_2} ratio.

Temperature (°C)	**Saturation pressure (kPa)**	p_{H_2O} / p_{H_2}	**Temperature (°C)**	**Saturation pressure (kPa)**	p_{H_2O} / p_{H_2}
-40	0.0129	$1.3x10^{-4}$	**30**	4.246	0.0437
-36	0.0201	$2.0x10^{-4}$	**40**	7.384	0.0786
-32	0.0309	$3.1x10^{-4}$	**50**	12.349	0.1388
-28	0.0469	4.6x10-^{4}	**55**	15.758	0.1842
-24	0.0701	$6.9x10^{-4}$	**60**	19.94	0.2451
-20	0.1035	0.00102	**65**	25.03	0.3282
-16	0.1510	0.00149	**70**	31.19	0.4449
-12	0.2176	0.00215	**75**	38.58	0.6151
-8	0.3102	0.00307	**80**	47.39	0.8791
-4	0.4375	0.00434	**85**	57.83	1.3303
0	0.6108	0.00607	**90**	70.14	2.2510
10	1.2276	0.0123	**95**	84.55	5.0478
20	2.339	0.0236	**100**	101.35	∞

Table D2 Relationship between water temperature, argon flow rate and p_{H_2O} / p_{H_2} ratios for a hydrogen flow rate of 250cm^3/min within the range of water temperatures available.

Temperature (°C)	**Saturation pressure (kPa)**	p_{H_2O} / p_{H_2} **ratio** **Argon flow rate (cm^3/min)**			
		0	**250**	**500**	**750**
20	2.339	0.0236	0.0473	0.0709	0.0945
30	4.246	0.0436	0.0872	0.1308	0.1744
40	7.384	0.0786	0.1572	0.2358	0.3144
50	12.349	0.1358	0.2776	0.4164	0.5552
60	19.94	0.2451	0.4902	0.7353	0.9804
70	31.19	0.4449	0.8898	1.3347	1.7796

Appendix E

Maximum allowable hydrogen flow rates

The decarburisation gas flow rate is limited to the volume that can be saturated by the first and second water containers. In a situation where the water diffuses from the bottom of the conical flask into a dry hydrogen atmosphere, with no bubbling of the hydrogen through the water, the amount of water diffusing is given by[215]

$$\dot{m}_{H_2O} = \frac{D_{H_2O} P M_{H_2O} A}{R_o T (x_2 - x_1)} \ln\left[\frac{p_{A_2}}{p_{A_1}}\right], \qquad \text{(E1)}$$

where $\dot{m}_{H_2O}$ = mass flow rate of diffusing water in kg/s;

D_{H_2O} = diffusion coefficient of water in hydrogen in m^2/s;

P = atmospheric pressure in Pa;

M_{H_2O} = molecular weight of water, 18g/n;

A = surface area of flask in m^2;

R_o = universal gas constant of 8315J/kgmolK;

T = system temperature in K;

$(x_2 - x_1)$ = water level in m;

p_{A_2} = P in Pa;

p_{A_1} = $P - p_{H_2O}$, with p_{H_2O} = water saturation pressure in Pa.

Equation E1 assumes that :

- The system is isothermal;
- The total pressure remains constant;
- The system is already at steady state, requiring hydrogen movement to remove water vapour already diffused to that point;

- The hydrogen movement does not create turbulence or otherwise alter the concentration profiles in the second water container;
- Both hydrogen and water behave as ideal gases.

$$D_{H_2O} = \frac{0.001T^{1.75}\sqrt{(1/M_1)+(1/M_2)}}{P\left[(\sum v_1)^{1/3}+(\sum v_2)^{1/3}\right]^2}, \qquad \text{(E2)}$$

where M_1 = molecular weight of water, 18g/n;

M_2 = molecular weight of hydrogen, 2g/n;

P = absolute pressure in atmospheres;

v = atomic diffusion volumes, with $\sum v_1$ = 12.7, $\sum v_2$ = 7.07.

Equation E2 applies for simple systems at low pressures over moderate temperature ranges[215]. For internal dimensions of 205 by 125 by 40mm deep for the water in the water flask, A = 0.0256m^2 and $(x_2 - x_1)$ = 0.04m. p_{A_2}, p_{A_1}, and T all depend on the water temperature, while D_{H_2O} can be calculated from equation E2. Substitution of these values into equation E1 gives $\dot{m}_{H_2O}$. These values are given in Table E1 for various water temperatures.

Table E1 Maximum hydrogen flow rates for water saturation in the water flask.

Water temperature (°C)	p_{H_2O} / p_{H_2}	D_{H_2O} **(m^2/s) x10^{-4}**	p_{A_1} **(Pa) x10^{-3}**	p_{A_2} **(Pa) x10^{-3}**	$\dot{m}_{H_2O}$ **(kg/s) x10^{-6}**	$\dot{V}_{H_2}$ **(cm^3/s)**
20	0.0236	0.845	98.96	101.3	0.944	3202
30	0.0437	0.896	97.06	101.3	1.774	3252
40	0.0786	0.948	93.93	101.3	3.214	3277
50	0.1388	1.002	88.90	101.3	5.648	3264
60	0.2451	1.057	81.38	101.3	9.749	3190
70	0.4449	1.113	70.14	101.3	16.73	3017

The maximum hydrogen flow rate corresponds to when $\dot{m}_{H_2O}$ equals the mass flow rate of water transported by the hydrogen flow. The ideal gas law can be used to determine the mass of water and hydrogen associated with $1m^3$ of the water/hydrogen mixture from

$$m = \frac{pV}{RT}, \tag{E3}$$

where p, V, and T correspond to the respective water and hydrogen pressures, volumes and temperatures at standard temperature and pressure. The ideal gas constant, R, is 461 and 4124J/kgK[214] for water and hydrogen respectively. Therefore,

$$m_{H_2O} = \dot{m}_{H_2O}\, t, \tag{E4}$$

where t = time (s).

The mass of hydrogen, in kg, associated with m_{H_2O} can be calculated from

$$\left(\frac{m_{H_2O}}{m_{H_2}}\right)_{1m^3} = \frac{m_{H_2O}}{m_{H_2}}. \tag{E5}$$

Consequently $\dot{m}_{H_2}$ can be calculated from

$$\dot{m}_{H_2} = \frac{m_{H_2}}{t}, \tag{E6}$$

where $\dot{m}_{H_2}$ = hydrogen mass flow rate in kg/s.

$\dot{V}_{H_{2\max}}$ at standard temperature and pressure can be calculated from

$$\dot{V}_{H_2 \max} = \frac{\dot{m}_{H_2} RT}{p}, \qquad \text{(E7)}$$

where $\dot{V}_{H_2 \max}$ = maximum hydrogen flow rate in m^3/s;

T = 293K,

p = 1.013×10^5Pa.

$\dot{V}_{H_2 \max}$ can be converted to cm^3/min by multiplying by 6×10^7, with these values given in Table E1. Due to the saturation occurring in the first water container, and the further saturation achieved by bubbling the gas into the water, the maximum gas flow rates will be substantially larger than the calculated values. However these calculations demonstrate that the gas flow rates used will be fully saturated at the operational temperature, allowing accurate control over the p_{H_2O} / p_{H_2} ratios.

Appendix F

Calculation of water transported by hydrogen flow

The mass of water transported by the hydrogen or hydrogen/argon flows is dependent on the water vapour partial pressure, and on the gas flow rate. Assuming ideal gas behaviour, the mass of water and hydrogen in a water/hydrogen flow can be calculated from the ideal gas law, where

$$m = \frac{pV}{RT}\,. \qquad \text{(E3)}$$

By a simple proportion, the mass of water that would be transported for a certain hydrogen flow rate, water temperature, and test duration, can be determined from

$$m_{H_2O_{(t,\dot{V}_{H_2})}} = m_{H_2O}\left(\frac{m_{H_{2(t,\dot{V}_{H_2})}}}{m_{H_2}}\right), \qquad \text{(F1)}$$

where $m_{H_2O_{(t,\dot{V}_{H_2})}}$, $m_{H_{2(t,\dot{V}_{H_2})}}$ are the respective water and hydrogen masses, in kg, transported for specific hydrogen flow rates, water temperatures, and test durations;

m_{H_2O}, m_{H_2} are the water and hydrogen masses in kgm^{-3} for specific saturation conditions.

The hydrogen mass flow rate can be determined from

$$\dot{m}_{H_2} = \frac{p\dot{V}_{H_2}}{RT}, \qquad \text{(F2)}$$

where $\dot{m}_{H_2}$ = hydrogen mass flow rate in kg/s;

$\dot{V}_{H_2}$ = hydrogen volume flow rate in m^3/s.

Therefore,

$$m_{H_2(t,\dot{V}_{H_2})} = \dot{m}_{H_2} t\,, \qquad \text{(F3)}$$

where t = test duration in s.

m_{H_2O} and m_{H_2} can be calculated from equation E3. Substituting these values, and that for $m_{H_2(t,\dot{V}_{H_2})}$ into equation F1, gives the mass of water transported in the hydrogen flow. The same approach can also be used to determine the mass of water transported in a water/hydrogen/argon mixture. The water transported for different decarburisation atmospheres is given in Table F1.

Table F1 Mass of water transported by the hydrogen or hydrogen/argon atmospheres for a hydrogen flow rate of 500cm^3/min.

p_{H_2O} / p_{H_2} **ratio**	**Mass of water transported (g)**					
	T **(°C)**	**5min**	**15min**	**1hr**	**4hr**	**24hr**
0.01	6.0	0.02	0.05	0.21	0.85	5.08
0.05	32.2	0.09	0.28	1.12	4.49	26.91
0.25	60.3	0.47	1.40	5.61	22.44	134.63
0.50*	60.3	0.47	1.40	5.61	22.44	134.63
1.0**	60.3	1.88	5.63	22.53	90.11	540.65

* This atmosphere comprised water/hydrogen/argon with hydrogen and argon gas flow rates of 250cm^3/min.

** This atmosphere comprised water/hydrogen/argon with a hydrogen gas flow rate of 250cm^3/min and argon gas flow rate of 750cm^3/min.

Appendix G

Calculation of alloy additions for experimental steel production

Alloy element additions were calculated for experimental steels comprising 0.6wt.% carbon, 0.8wt.% manganese, 0.2wt.% chromium, and 0, 1, or 3% silicon, based on an approximate melt size of 14kg. The desired compositions can be achieved by the appropriate combination of alloying additions, with the compositions of the alloying additions used detailed in Table G1.

Table G1 Composition of alloy additions.

ADDITION	Composition (wt.%)				
	C	Si	Mn	Cr	Fe
Reinforcing bar	0.16	0.14	0.48	0.06	99.16
Graphite	100	0	0	0	0
Low C Fe-Cr	0.03	0	0	69	30.97
Fe-Mn	0.9	0.43	85.7	0	12.97
Fe-Si	0.2	76.5	0	0	23.3

The initial calculations were based on the alloy additions being added into the molten steel just before pouring, and yielding 90% recovery of silicon, manganese, and chromium in the cast steel relative to the initial addition. Carbon was added as graphite at the start of the melt, with the graphite addition calculated for 75% recovery. A base addition of 13.5kg of reinforcing bar was used. The other alloy additions required were then calculated from equation G1, with graphite used for the carbon addition, low C Fe-Cr for the chromium addition, Fe-Mn for the manganese addition, and Fe-Si for the silicon addition.

$$\text{Addition(kg)} = \frac{\left[\text{Required composition contribution(wt.\%)}\right]\left[\text{Total steel mass(kg)}\right]}{\left[\text{Alloy addition composition(wt.\%)}\right]\left[\text{Recovery factor}\right]} \quad \text{(G1)}$$

where Required composition contribution = desired composition-existing composition from other sources (G2)

The calculations were first undertaken for the low C Fe-Cr addition, followed by Fe-Mn, Fe-Si, and graphite. The total steel mass added for equation G1 was initially estimated, with the calculations then repeated using the total mass calculated from the sum of the alloy additions. The alloy addition requirements calculated are listed in Table G2. This yielded steels with the compositions listed in Table G3. The carbon and manganese concentrations listed in Table G3 were too low. Therefore, the steel calculations were repeated based on lower recoveries of 50% for carbon and 75% for manganese. This required the additions listed in Table G4, with the steel compositions obtained detailed in Table G5.

Table G2 Alloy addition requirements for production of experimental steels.

DESCRIPTION	ADDITION (kg) Reinforcing bar*	Graphite	Low C Fe-Cr*	Fe-Mn*	Fe-Si
0% SILICON	13.5	0.0875	0.0324	0.0665	-
1% SILICON	13.5	0.0886	0.0331	0.0687	0.1769
3% SILICON	13.5	0.0906	0.0342	0.0722	0.5959

Table G3 Experimental steel compositions obtained based on 90% recovery for silicon, manganese and chromium, and 75% recovery for carbon.

DESCRIPTION	C (wt.%)	Si (wt.%)	Mn (wt.%)	Cr (wt.%)
0% SILICON	0.48	0.03	0.57	0.29
1% SILICON	0.44	0.98	0.56	0.27
3% SILICON	0.43	3.58	0.76	0.28

Table G4 Alloy addition requirements for production of experimental steels.

DESCRIPTION	ADDITION (kg) Reinforcing bar*	Graphite	Low C Fe-Cr*	Fe-Mn*	Fe-Si
0% SILICON	13.5	0.1428	0.0199	0.1264	-
1% SILICON	13.5	0.1449	0.0201	0.1298	0.1769
3% SILICON	13.5	0.1500	0.0207	0.1023	0.5044

Table G5 Experimental steel compositions obtained based on 75% recovery for manganese and 50% recovery for carbon.

DESCRIPTION	C (wt.%)	Si (wt.%)	Mn (wt.%)	Cr (wt.%)
0% SILICON	0.62	0.06	0.94	0.23
1% SILICON	0.61	1.24	1.09	0.21
3% SILICON	0.58	3.05	0.78	0.18

Appendix H

Calibration of decarburisation test rig pressure transducers

The MPX200AP Motorola pressure transducers used to estimate the average pressure in the stainless steel lining tube of the decarburisation test rig tube furnace were calibrated using the departmental Dead Pan Pressure Testing Rig. Each transducer was calibrated for pressures of 10, 30, 50, 70, and 90kPa. Two millivoltage readings were made for each pressure setting with a 3468A Hewlett Packard Digital Multimeter, with the average value used. The air temperature and atmospheric pressure were recorded for both transducers. The pressure transducer readings are listed in Table H1 for the inlet transducer, and Table H2 for the outlet transducer.

These transducers are not temperature compensated, with the typical temperature dependence over the full-scale temperature span of 0 to 85°C being $0.19 \pm 0.03\%/°C$ of the full-scale reading. This yields the mV readings corrected to 20°C for the two pressure transducers. Figure H1 illustrates the relationship between transducer pressure and mV for the two transducers, from which the following two equations for the calculation of transducer pressures were obtained:

$$P_{inlet} = 1.7055 mV_{inlet}[1 + (T_{inlet} - 20)(0.0019)] - 40.035 \qquad \text{(H1)}$$

$$P_{outlet} + 1.8726 mV_{outlet}[1 + (T_{outlet} - 20)(0.0019)] - 52.941 \qquad \text{(H2)}$$

where P_{inlet}, P_{outlet} = inlet and outlet transducer pressures in kPa;

mV_{inlet}, mV_{outlet} = inlet and outlet transducer pressures in mV;

T_{inlet}, T_{outlet} = inlet and outlet transducer temperatures in °C.

Table H1 Pressure readings for inlet pressure transducer.

Pressure (kPa)	Atmospheric pressure (kPa)	Total pressure (kPa)	Temperature (°C)	Multimeter reading (mV)	
				At 17.5°C	Corrected for 20°C
0	102.17	102.17	17.5	82.93	82.54
10	102.17	112.17	17.5	90.08	89.65
30	102.17	132.17	17.5	101.84	101.36
50	102.17	152.17	17.5	113.64	113.10
70	102.17	172.17	17.5	125.39	124.79
90	102.17	192.17	17.5	137.09	136.44

Table H2 Pressure readings for outlet pressure transducer.

Pressure (kPa)	Atmospheric pressure (kPa)	Total pressure (kPa)	Temperature (°C)	Multimeter reading (mV)	
				At 17.5°C	Corrected for 20°C
0	101.11	101.11	16.5	82.66	82.11
10	101.11	111.11	16.5	88.32	87.73
30	101.11	131.11	16.5	99.05	98.39
50	101.11	151.11	16.5	109.68	108.95
70	101.11	171.11	16.5	120.36	119.56
90	101.11	191.11	16.5	131.23	130.35

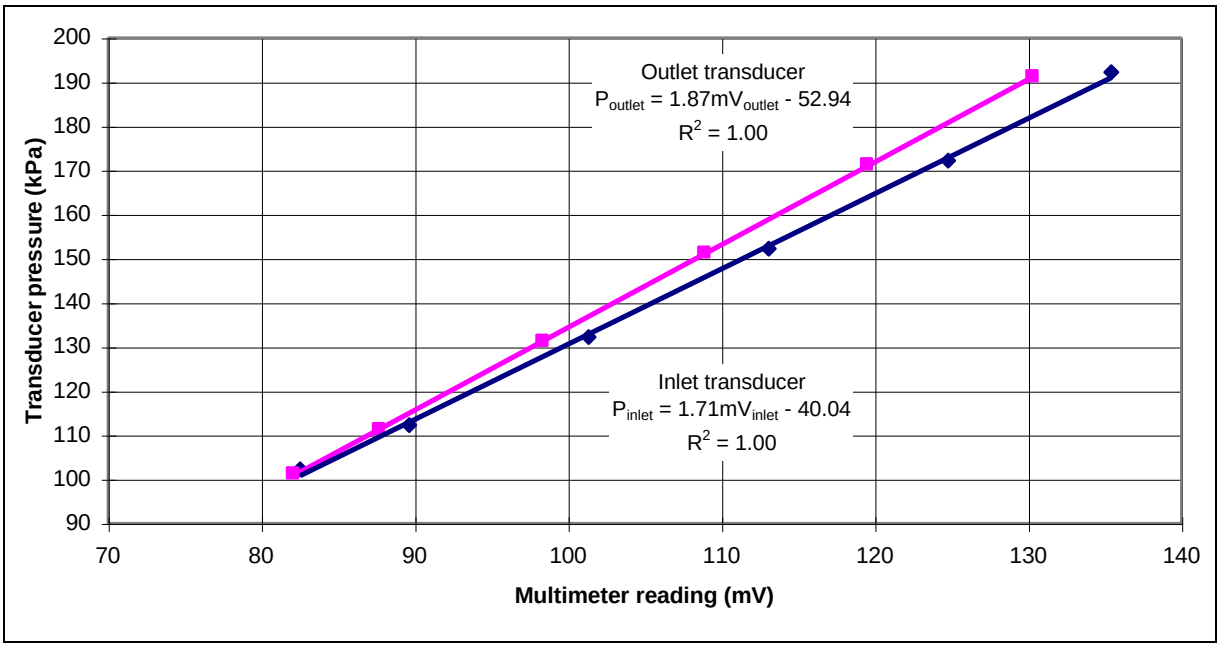

Figure H1 Transducer pressure versus mV at 20°C for the two pressure transducers.

Appendix I

Etchants and chemical solutions

Etchants

The following etchants were evaluated during the course of this research. The majority of these etchants were sourced from Vandervoort[153].

1)	2% Nital	2mL	HNO_3	} Immersed for 10s-1min
		98mL	Ethanol	} at room temperature.

2% Nital was used effectively as a general purpose etchant to reveal the ferrite, martensite, and cementite phases in the austenitised and decarburised microstructures. Martensite etched brown, while the ferrite and cementite remained white.

2)	Sodium Metabisulphite	21g	$Na_2S_2O_5$	} Immersed for 10-20s
		100mL	distilled H_2O	} at room temperature

This etchant was used for austenitised specimens following tempering for 1hr at 250°C, and a light 5-10s 2% Nital pre-etch. It proved effective in colouring martensite black, yielding excellent contrast between the martensite and the remainder of the microstructure for subsequent image analysis.

3)	Ammonium Persulphate	10g	$(NH_4)S_2O_8$	} Immersed for 2min
		100mL	distilled H_2O	} at room temperature

Limited success was obtained with this etchant, which is designed to darken the matrix of the austenitised microstructure and reveal the carbides.

4)	Klemm's I Reagent	50mL	sat. $Na_2S_2O_3$	} Immersed for 2-5min
		1g	$K_2S_2O_2$	} at room temperature

This tint etchant was used after a light 5-10s 2% Nital pre-etch to colour the carbides of the austenitised microstructures white, with the ferrite coloured blue and the martensite brown. This etchant was more effective than Ammonium Persulphate in giving the required contrast for image analysis between the carbides and the remainder of the microstructure. However, a significant fraction of the carbides did not whiten sufficiently for image analysis.

5)	Picral	4g	picric acid	} Immersed for 90s
		100mL	Ethanol	} at room temperature

Allowed reasonable contrast to be obtained between the carbides and the matrix of the austenitised microstructures using the SEM for subsequent image analysis.

6)	Nital/Picral	2g	picric acid	} Immersed for 90s
		0.5mL	HNO_3	} at room temperature

Allowed good contrast to be obtained between the carbides and the matrix of the austenitised microstructures using the SEM for subsequent image analysis.

7)	Bechet and Beaujard's Etch	2g	picric acid	} Immersed for 2-6min
		100mL	distilled H_2O	} in ultrasonic bath, light
		1g	Na tri. sulphonate	} back polish to remove
		0.5g	$CuCl_2$	} surface smut

No success was obtained in resolving the prior austenite grain boundaries for austenitised martensitic microstructures using this prior austenite grain size etchant.

8)	Villela's Reagent	1g	picric acid	} Immersed for a few s
		5mL	HCl	} to 15min at room
		100mL	ethanol	} temperature

Greater resolution of the prior austenite grain boundaries was obtained than by Bechet and Beaujard's Etch, especially after tempering for 1hr at 250°C. However, the prior austenite grain boundaries were still not adequately resolved for grain size determination.

9)	Picral/"White cat"	9g	picric acid	} Picric/H_2O heated to 60°C, then
		80mL	H_2O	} white cat added. Immersed for
		25mL	"white cat"	} 2min at 60°C.

This etch provided good definition of the 0% Silicon steel prior austenite grain boundaries for the grain size determination from martensitic microstructures. However, the prior austenite grain boundaries were poorly resolved for the higher silicon steels.

10)	Oxide scale etchant	240mL	ethanol	} Immersed for 1hr at
		52.5mL	distilled H_2O	} room temperature
		4.5mL	bromo. dye	}

This dye adsorption technique was used to indicate the presence of iron oxides in the decarburised oxide microstructures. FeO is stained blue, Fe_3O_4 beige, and Fe_2O_3 white.

Chemical solutions

The ability of the following chemical solutions to obtain a shiny scale-free metallic surface prior to decarburisation heat treatments of wire-cut tapered needle test specimens were investigated.

11)	Bright Dip Formula	25g	oxalic acid	} Immersed for about
		10mL	H_2O_2	} 30min at room
		1 drop	H_2SO_4	} temperature
		1000mL	distilled H_2O	}

An attempt was made to remove the thin scale forming on wire-cut needle test specimens and leave a bright, smooth surface finish with this bright dip formula. A small amount of material

was removed, but the desired finish was not obtained even after raising the temperature to 40°C and providing agitation.

12)	Pickling formula	250mL	HCl solution with inhibitor	} Immersed about 30min at room temperature
		750mL	distilled H_2O	}

This pickling solution was used in an attempt to remove the oxide layer of the wire-cut needle specimens. Only a small amount of oxide removal occurred.

Plating solutions

13)	Electroless Nickel Plating	37.3g	Ni sulphate	} Used with mild
		26.4g	NaH_2PO_2	} agitation at 82-88°C
		15.9g	CH_3COONa	} for 1hr. Plating rate
		5-6 drops	H_2SO_4	} approx. 0.01mm/hr
		1000mL	distilled H_2O	}

When freshly mixed this solution successfully nickel plated heat treated decarburised test specimens, with good adherence between the oxide and nickel layers. A pre-treatment was required which involved the deposition of a very thin gold layer on the specimens by a Polaron Scanning Electron Microscope E5000 Sputter Coating Unit. Galvanic initiation was required for plating to commence, which involved an aluminium contact with the test specimens as they were immersed into the plating solution.

14) Electroless Copper Plating

Solution A		*Solution B*	
170g	$KNaC_4O_6.4H_2O$	37wt.% formaldehyde	} Mixed 5parts solution A
50g	NaOH		} with 1part solution B at
35g	$CuSO_4.5H_2O$		} 20-40°C, and immersed
1000mL	distilled H_2O		} in solution for 15min.
			} Plating at 0.0001mm/hr

An attempt was made to copper plate scale-free machined specimens, and oxidised specimens, to prevent decarburisation during subsequent heat treatments. However, a satisfactorily adherent copper layer was not obtained.

15)	Electrolytic Copper Plating	200g/L	$CuCl_2$	} Dipped into solution for
		50g/L	H_2SO_4	} 15s for electroless layer,
		Rest	distilled H_2O	} rinsed in H_2O and dried.
				} Electrolytically coated
				} for 30s.

This method allowed the plating of oxidised specimens to prevent decarburisation during subsequent heat treatments.

Appendix J

Calibration of infrared gas analysers

The Beckman carbon monoxide and Horiba carbon dioxide infrared gas analysers were calibrated by the following method:

- Selection of a setting of 50% on the STEC SGD-710 gas divider;
- Introduction of the argon zero gas and calibrated span gas into the gas divider at a flow rate sufficient to give 30kPa pressure on the zero and span gas pressure gauges. This corresponded to a gas flow rate of approximately 500cm^3/min, with the composition of the span gas detailed in Table J1.

Table J1 Span gas composition.

DESCRIPTION	Composition		Accuracy	
	(Volume %)	(vppm)	(Volume %)	(vppm)
CO	0.270	2700	0.005	50
CO_2	0.098	980	0.002	20
CH_4	0.0232	232	0.0005	5
Ar	99.609	-	-	-

- Zeroing of the analysers with the zero knob by selection of a setting of 0% on the gas divider to give the zero gas flow, and a 0mV reading on the Hewlett Packard multimeter for the three analyser ranges;
- Selection of the appropriate gas divider setting to give the required upscale gas concentration, and adjustment of the gain control to give a multimeter reading of approximately 5V. This gives the following range settings of:

  0 - 1000vppm for carbon monoxide RANGE 3

  0 - 5000vppm for carbon monoxide RANGE 2

for the carbon monoxide gas analyser, and

0 - 750vppm for carbon dioxide RANGE 1

for the carbon dioxide analyser.

- Selection of a setting of 0% on the gas divider, and holding for two minutes to establish a zero gas flow;
- Zeroing of the three pens on the Sekonic three-pen chart recorder, and selection of a chart speed of 300mm/hr;
- Selection of the next gas divider setting, namely 10%, and allowing to stabilise for two minutes before recording the carbon monoxide, carbon dioxide, and methane instrument readings, mV readings, and upon completion of the calibration, the pen recorder chart heights;
- Repetition of the previous step for gas divider settings of 20 to 100%;
- Establishment of the desired decarburisation water/hydrogen/argon atmosphere and flow rate, and allowing to stabilise for five minutes;
- Zeroing of the three pens on the pen recorder.

The gas concentrations versus instrument, mV and pen recorder readings for the two gas analysers are given in Tables J2 and J3. Figure J1 illustrates the calibration curves for the three gas analysers.

Ideally, each gas analyser should be calibrated using a span gas containing only the constituent to be measured, as the presence of other constituents will affect the results. Interference checks should then be obtained with other gases comprising the maximum expected concentration of an interfering component. However, financial constraints prevented this rigorous calibration approach. Table J4 details the factory supplied interference data for the gas analysers, in conjunction with the values determined from the experimentation in this project. Hydrogen has a significant effect on the carbon monoxide concentration measured. Consequently, prior to decarburisation when the water/hydrogen or water/hydrogen/argon decarburisation atmospheres were established, the gas analysers were zeroed. The assumption was then made that hydrogen offset the zero value only, and that upon zeroing, the carbon

monoxide, carbon dioxide, and methane concentrations measured were accurate over the ranges of the analysers.

Table J2 Instrument and pen recorder outputs versus carbon monoxide gas concentration for the Beckman carbon monoxide gas analyser.

Gas divider setting (%)	Gas concentration (volume %)	Instrument		Recorder (mm)		Multimeter (mV)	
		Range 2	Range 3	Range 2	Range 3	Range 2	Range 3
0 (zero gas)	0	0	0	0	0	0	0
10	0.027	28	6	15	70	0.31	1.43
20	0.054	56	12	30	140	0.62	2.86
30	0.081	84	18	45	210	0.93	4.29
40	0.108	-	24	60	-	1.24	-
50	0.135	-	30	76.5	-	1.57	-
60	0.162	-	34	82.5	-	1.74	-
70	0.189	-	35.5	89.5	-	1.84	-
80	0.216	-	39.5	98.5	-	2.04	-
90	0.243	-	42.5	108.5	-	2.23	-

Table J3 Instrument and pen recorder outputs versus carbon dioxide gas concentration for Horiba carbon dioxide gas analyser.

Gas divider setting (%)	Gas concentration (volume %)	Instrument	Recorder (mm)	Multimeter (mV)
		Range 1	Range 1	Range 1
0 (zero gas)	0	0	0	0
10	0.0098	11	30.5	0.54
20	0.0196	22.5	64.5	1.16
30	0.0294	36	104	1.85
40	0.0392	50.5	146.5	2.60
50	0.0490	67.5	192.5	3.42

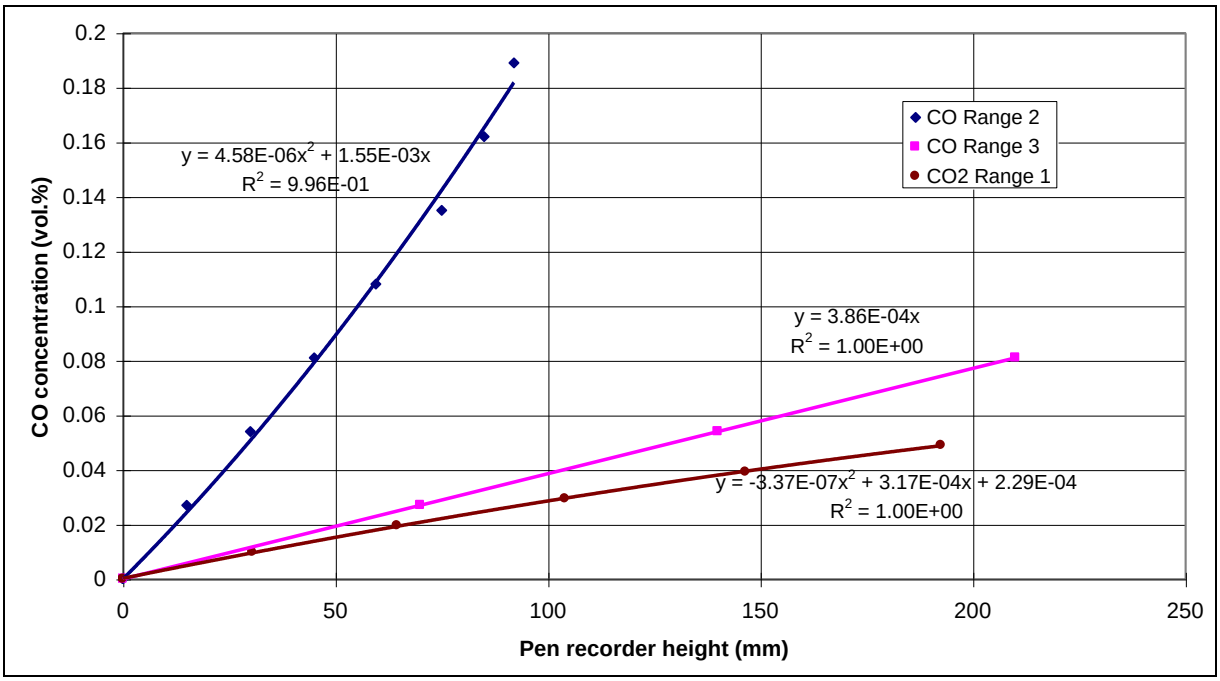

Figure J1 Calibration curves for the three infrared gas analysers.

Table J4 Interference data for the infrared gas analysers.

Interference gas		**Gas analysers (interference value)**			
		CO (0-1000vppm)		**CO_2 (0-5%)**	
DESCRIPTION	**Conc. (vol.%)**	**(% F.S.)**	**(vppm)**	**(% F.S.)**	**(vppm)**
H_2	25-100	- 11	- 110	- 2	- 15
CO	10.05*	-	-	0.5*	17.5*
	4.91*	-	-	-	-
CO_2	5.12*	-	-	-	-

* Factory supplied data, with different gas measurement range settings than those used for the carbon dioxide and methane gas analysers.

Appendix K

Image analysis programs

This appendix contains the image analysis programs written for the austenitisation experimentation.

(K1) Measurement of pearlite true interlamellar spacing.

(i) PEARST2

(ii) PEARAN2

(K2) Measurement of initial cementite structures.

(i) CEMSTI

(ii) CEMANI

(K3) Measurement of austenitised structures with discrete martensite particles.

(i) STARTM3

(ii) ANALYM3

(K4) Measurement of austenitised structures with significant coalescence of martensite particles.

(i) STARTM2

(ii) ANALYM2

(K5) Measurement of cementite structures during austenitisation.

(i) CMNSEST

(ii) CMNSEAN

(K1) Measurement of pearlite true interlamellar spacing.

(i) PEARST2

Program comment "**Sets up spacing for pearlite structures. OK or CANCEL.**"
'
'This program sets up the columns to measure the true interlamellar spacings for pearlite 'structures.
'
'Setting up the data columns.
'
Data column clear 'clear data columns
Measure frame reset 'reset frame size to full screen
Data append 10000cal 'open 10,000x calibration file
Data close 'close 10,000x calibration file
'
Data column 1 count 'number of cementite lamellae
Data column 2 shape 'shape factor
'
Data formula 19.2/c1 sigmar
Data column 3 formula 'mean random pearlite interlamellar spacing
Data formula c3/2 sigmat
Data column 4 formula 'true pearlite interlamellar spacing
'
'This step opens a data file in which the measured variables can be stored.
'
Data new 'opens a new data file
'
'This step allows a file to be opened for measurement of the true interlamellar spacings for 'pearlite.
'
Program query "**Run pear structure analysis program PEARAN2" pearan2**
'

(ii) PEARAN2

Program comment "**Measures true interlamellar spacing. OK or CANCEL.**"
'
'This is a program designed to measure the true interlamellar spacing for pearlite.
'
'This step appends a data file to allow measurement variables to be stored.
'
Data append 'append a new data file
'
'This step measures the true pearlite interlamellar spacing.
'
Image read temp00.jpg 'allows the template image (15x1cm diameter circles) 'to be read

```
'
Colour detect black             'detects the dark template circles
Colour auto                     'automatically thresholds the template
Binary store load               'stores the image
'
Image read                      'allows the pearlite image to be read
'
Colour detect grey              'detects the white cementite lamellae
Colour threshold2 255           'set threshold 2
Colour histogram
Program comment "Set threshold2, then press OK"
Binary store and                'gives intersection of lamellae and template
'
Binary erode                    'erode to remove any small spots
Binary dilate                   'dilate to restore the size
Binary median                   'median to smooth the result
'
Sizer variable shape            'selects the sizer variable
Sizer lower 40                  'minimum shape factor
Sizer upper 100                 'maximum shape factor
Sizer edit                      'performs the sizer edit
Edit prepare                    'to eliminate the particles selected by the sizer function
'
Measure write enable            'enables the file write
Measure view enable             'enables the data viewing
Measure field                   'measures the martensite grains displayed
'
Measure view disable            'leaves the view off by default
'
```

(K2) Measurement of initial cementite structures.

(i) CEMSTI

Program comment "**Sets up Vv, SF, d, dn, for initial cem structures. OK or CANCEL.**"

```
'
'This is a program which sets up the columns to measure the volume fraction, shape factor,
'equivalent area diameter and cementite size distribution of the initial spheroidised
'structures.
'
'Setting up the data columns.
'
Data column clear                 'clear data columns
Measure frame reset               'reset frame size to full screen
Data append 5000xcal              'open 5000x calibration file
Data close                        'close 5000x calibration file
'
Data column 1 area                'total area of cementite particles (microns^2)
Data column 2 fraction            'volume fraction(%)
Data column 3 count               'number of cementite particles (frame intercepts as half)
Data column 4 shape               'average shape factor of cementite particles
'
Data column 5 count 0.25          'cementite particles less than 0.25 microns d
Data column 6 count 0.5           '0.25-0.5
Data column 7 count 0.75          '0.5-0.75
Data column 8 count 1.0           '0.75-1.0
Data column 9 count 1.25          1.0-1.25
Data column 10 count 1.5          1.25-1.5
Data column 11 count 1.75         1.5-1.75
Data column 12 count 2.0          1.75-2.0
Data column 13 count 2.25         '2.0-2.25
Data column 14 count 2.5          '2.25-2.5
Data column 15 count 2.75         '2.5-2.75
Data column 16 count 3.0          '2.75-3.0
Data column 17 count >3.0         'cementite particles greater than 3.0 microns d
'
Data formula c2/100.000 Vv
Data column 18 formula            'volume fraction of martensite
Data formula sqrt(4*(c1/c3)/3.1415) d
Data column 19 formula            'equivalent area diameter
'
Data formula (c5*100)/c3 %0.25
Data column 20 formula            '% of cementite particles less than 0.25 microns d
Data formula (c6*100)/c3 %0.25-0.5
Data column 21 formula            '% of cementite particles 0.25-0.5 microns d
Data formula (c7*100)/c3 %0.5-0.75
Data column 22 formula            '% of cementite particles 0.5-0.75 microns d
Data formula (c8*100)/c3 %0.75-1.0
Data column 23 formula            '% of cementite particles 0.75-1.0 microns d
```

Data formula (c9*100)/c3 %1.0-1.25
Data column 24 formula '% of cementite particles 1.0-1.25 microns d
Data formula (c10*100)/c3 %1.25-1.5
Data column 25 formula '% of cementite particles 1.25-1.5 microns d
Data formula (c11*100)/c3 %1.5-1.75
Data column 26 formula '% of cementite particles 1.5-1.75 microns d
Data formula (c12*100)/c3 %1.75-2.0
Data column 27 formula '% of cementite particles 1.75-2.0 microns d
Data formula (c13*100)/c3 %2.0-2.25
Data column 28 formula '% of cementite particles 2.0-2.25 microns d
Data formula (c14*100)/c3 %2.25-2.5
Data column 29 formula '% of cementite particles 2.25-2.5 microns d
Data formula (c15*100)/c3 %2.5-2.75
Data column 30 formula '% of cementite particles 2.5-2.75 microns d
Data formula (c16*100)/c3 %2.75-3.0
Data column 31 formula '% of cementite particles 2.75-3.0 microns d
Data formula (c17*100)/c3 %>3.0
Data column 32 formula '% of cementite particles >3.0 microns d
'
'This step opens a data file in which the measured variables can be stored.
'
Data new 'opens a new data file
'
'This step allows a file to be opened to measure the volume fraction, surface area to volume 'ratio, equivalent area diameter, average shape factor, number of grains per unit area, and 'number of grains per unit volume of martensite.
'
Program query "**Run initial cem structure analysis program CEMANI" cemani**
'

(ii) CEMANI

Program comment "**Measures Vv, SF, d, dn for initial cem structures. OK or CANCEL.**"
'
'This is a program which measures the volume fraction, shape factor, equivalent area 'diameter, and the cementite particle size distribution for the initial spheroidised structures.
'
'This step appends a data file to allow the measured variables to be stored.
'
Data append 'append a new data file
'
'This step measures the number of cementite particles and the average shape factor.
'
Image read 'allows an image to be read
'
Colour detect grey 'detects the white cementite particles
Colour threshold2 255 'set threshold 2
Colour histogram

Program comment "**Set threshold2, then press OK**"
'
Binary hole 'fills in the holes in the cementite particles
Binary erode 2 'erode to remove any small spots
Binary dilate 2 'dilate to restore the size
Binary median 2 'median to smooth the result
Binary store load 'to store this edited image
'
'Now delete the cementite particles intersecting the left and bottom frame.
'
Edit erase 'changes the editing mode to erase
Program comment "**Next, delete B, R particles, then press right mouse**"
Edit fill 'to fill the desired grains in
Binary store load 'to store this edited image
'
Measure write disable 'disables the file write
Measure view disable 'disables the data viewing
Measure field 'measures the cementite particles
Data column 3 protect 'protects cementite particle count
Data column 4 protect 'protects average shape factor
'
'This step measures the size distribution of the cementite particles.
'
Binary store retrieve 'to retrieve the previous edited image
Sizer variable area 'selects the sizer variable
Sizer lower 0 'minimum area
Sizer upper 0.04909 'maximum area
Sizer edit 'performs the sizer edit
Measure write disable 'disables the file write
Measure view disable 'disables the data viewing
Measure field 'measures the cementite particles
Data column 5 protect 'protects cementite particle count
'
Binary store retrieve 'to retrieve the previous edited image
Sizer variable area 'selects the sizer variable
Sizer lower 0.04909 'minimum area
Sizer upper 0.1963 'maximum area
Sizer edit 'performs the sizer edit
Measure write disable 'disable the file write
Measure view disable 'disable the data viewing
Measure field 'measure the cementite particles
Data column 6 protect 'protect cementite particle count
'
Binary store retrieve 'to retrieve the previous edited image
Sizer variable area 'selects the sizer variable
Sizer lower 0.1963 'minimum area
Sizer upper 0.4418 'maximum area
Sizer edit 'performs the sizer edit
Measure write disable 'disable the file write

```
Measure view disable                'disable the data viewing
Measure field                       'measure the cementite particles
Data column 7 protect               'protect cementite particle count
'
Binary store retrieve               'to retrieve the previous edited image
Sizer variable area                 'selects the sizer variable
Sizer lower 0.4418                  'minimum area
Sizer upper 0.7854                  'maximum area
Sizer edit                          'performs the sizer edit
Measure write disable               'disable the file write
Measure view disable                'disable the data viewing
Measure field                       'measure the cementite particles
Data column 8 protect               'protect cementite particle count
'
Binary store retrieve               'to retrieve the previous edited image
Sizer variable area                 'selects the sizer variable
Sizer lower 0.7854                  'minimum area
Sizer upper 1.227                   'maximum area
Sizer edit                          'performs the sizer edit
Measure write disable               'disable the file write
Measure view disable                'disable the data viewing
Measure field                       'measure the cementite particles
Data column 9 protect               'protect cementite particle count
'
Binary store retrieve               'to retrieve the previous edited image
Sizer variable area                 'selects the sizer variable
Sizer lower 1.227                   'minimum area
Sizer upper 1.767                   'maximum area
Sizer edit                          'performs the sizer edit
Measure write disable               'disable the file write
Measure view disable                'disable the data viewing
Measure field                       'measure the cementite particles
Data column 10 protect              'protect cementite particle count
'
Binary store retrieve               'to retrieve the previous edited image
Sizer variable area                 'selects the sizer variable
Sizer lower 1.767                   'minimum area
Sizer upper 2.405                   'maximum area
Sizer edit                          'performs the sizer edit
Measure write disable               'disable the file write
Measure view disable                'disable the data viewing
Measure field                       'measure the cementite particles
Data column 11 protect              'protect cementite particle count
'
Binary store retrieve               'to retrieve the previous edited image
Sizer variable area                 'selects the sizer variable
Sizer lower 2.405                   'minimum area
Sizer upper 3.142                   'maximum area
Sizer edit                          'performs the sizer edit
```

```
Measure write disable          'disable the file write
Measure view disable           'disable the data viewing
Measure field                  'measure the cementite particles
Data column 12 protect         'protect cementite particle count
'
Binary store retrieve          'to retrieve the previous edited image
Sizer variable area            'selects the sizer variable
Sizer lower 3.142              'minimum area
Sizer upper 3.976              'maximum area
Sizer edit                     'performs the sizer edit
Measure write disable          'disable the file write
Measure view disable           'disable the data viewing
Measure field                  'measure the cementite particles
Data column 13 protect         'protect cementite particle count
'
Binary store retrieve          'to retrieve the previous edited image
Sizer variable area            'selects the sizer variable
Sizer lower 3.976              'minimum area
Sizer upper 4.909              'maximum area
Sizer edit                     'performs the sizer edit
Measure write disable          'disable the file write
Measure view disable           'disable the data viewing
Measure field                  'measure the cementite particles
Data column 14 protect         'protect cementite particle count
'
Binary store retrieve          'to retrieve the previous edited image
Sizer variable area            'selects the sizer variable
Sizer lower 4.909              'minimum area
Sizer upper 5.94               'maximum area
Sizer edit                     'performs the sizer edit
Measure write disable          'disable the file write
Measure view disable           'disable the data viewing
Measure field                  'measure the cementite particles
Data column 15 protect         'protect cementite particle count
'
Binary store retrieve          'to retrieve the previous edited image
Sizer variable area            'selects the sizer variable
Sizer lower 5.94               'minimum area
Sizer upper 7.069              'maximum area
Sizer edit                     'performs the sizer edit
Measure write disable          'disable the file write
Measure view disable           'disable the data viewing
Measure field                  'measure the cementite particles
Data column 16 protect         'protect cementite particle count
'
Binary store retrieve          'to retrieve the previous edited image
Sizer variable area            'selects the sizer variable
Sizer lower 7.069              'minimum area
Sizer upper 0                  'maximum area
```

```
Sizer edit                      'performs the sizer edit
Measure write disable           'disables the file write
Measure view disable            'disables the data viewing
Measure field                   'measure the cementite particles
Data column 17 protect          'protect cementite particle count
'
'This step measures the total area and the volume fraction of cementite particles.
'
Colour detect grey              'detects the white cementite particles
Colour threshold2 255           'set threshold 2
Colour discriminate             'to show the histogram
'
Binary hole                     'fills in the holes in the cementite particles
Binary erode 2                  'erode to remove any small spots
Binary dilate 2                 'dilate to restore the size
Binary median 2                 'median to smooth the result
'
Measure write enable            'enables the file write
Measure view enable             'enables the data viewing
Measure field                   'measures the cementite particles
'
Data column * record            'releases column protection
Measure view disable            'leaves the view off by default
'
```

(K3) Measurement of austenitised structures with discrete martensite particles.

(i) STARTM3

Program comment "**Sets up Vv, Sv, d, SF, Na , Nv for M. OK or CANCEL.**"
'
'This is a program designed to set up the columns to measure the volume fraction, and the 'surface area to volume ratio of martensite.
'
'Setting up the data columns.
'

Data column clear	'clear data columns
Measure frame reset	'reset frame size to full screen
Data append 1000xcal	'open 1000x calibration file
Data close	'close 1000x calibration file
Data column 1 count	'number of martensite grains (frame intercepts as half)
Data column 2 area	'total area of martensite grains (microns^2)
Data column 3 shape	'average shape factor of martensite grains
Data column 4 fraction	'volume fraction(%)
Data column 5 count	'number of horizontal martensite grain boundary 'intersections

'

Data formula c4/100.000 Vv	
Data column 6 formula	'volume fraction of martensite
Data formula 2*(c5/0.142037) Sv	
Data column 7 formula	'surface area per unit volume for martensite grains
Data formula sqrt(4*(c2/c1)/3.1415) d	
Data column 8 formula	'equivalent area diameter
Data formula (c1/0.007285667) Na (/mm^2)	
Data column 9 formula	'number of martensite grains per unit area
Data formula (7.4022*((c9)^3)*c6) Nv (/mm^3)	
Data column 10 formula	'number of martensite grains per unit volume '(assuming spherical shape, log-normal distribution)

'
'This step opens a data file in which the measured variables can be stored.
'

Data new	'opens a new data file

'
'This step allows a file to be opened for measurement of the volume fraction, surface area to 'volume ratio, equivalent area diameter, average shape factor, number of grains per unit area, 'and number of grains per unit volume of martensite.
'
Program query "**Run martensite analysis program ANALYM3" analym3**
'

(ii) ANALYM3

Program comment "**Measures Vv, Sv, d, SF, Na, Nv for M. OK or CANCEL.**"
'
'This is a program designed to measure the volume fraction, surface area to volume ratio, 'grain size, shape factor, and the equivalent area diameter of martensite.
'
'This step appends a data file to allow the measured variables to be stored.
'
Data append 'appends a new data file
'
'This step counts the number of martensite grains appearing in the image. Grains intersecting 'the frame are counted as half by counting the bottom and right grains as one each, while the 'left and top grains are deleted.
'
Image read 'allows an image to be read
'
Colour detect black 'detects the dark martensite grains
Colour threshold2 255 'set threshold 2
Colour histogram
Program comment "Set threshold2, then press OK"
'
Binary erode 1 'erode to remove any small spots
Binary dilate 1 'dilate to restore the size
Binary median 'median to smooth the result
'
'Now delete the grains intersecting the left and bottom frame.
'
Edit erase 'changes the editing mode to erase
Program comment "**Next, delete B, R grains, then press right mouse**"
Edit fill 'to fill the desired grains in
'
Measure write disable 'disables the file write
Measure view disable 'disables the data viewing
Measure field 'measures the martensite grains displayed
Data column 1 protect 'protects martensite grain count
'
'This step measures the total area, the average shape factor, and the volume fraction of 'martensite grains of the image.
'
Edit clear 'clears the entire overlay
Colour detect black 'detects the dark martensite grains
Colour threshold2 255 'set threshold 2
Colour discriminate 'to show the histogram
'
Binary erode 1 'erode to remove any small spots
Binary dilate 1 'dilate to restore the size
Binary median 'median to smooth the result
'

```
Measure write disable          'disables the file write
Measure view disable           'disables the data viewing
Measure field                  'measures the martensite grains displayed
Data column 2 protect          'protects total area of martensite grains
Data column 3 protect          'protects average shape factor of martensite grains
Data column 4 protect          'protects volume fraction(%) of martensite grains
'
'This step measures the number of martensite grain boundary intersections with a horizontal
'grid.
'
Measure write disable          'disables the file write
Measure view disable           'disables the data viewing
Binary store load              'stores the image
'
Measure grid horizontal enable 'set up to draw a horizontal grid
Measure grid vertical disable  'ensures that no vertical grid is drawn
Measure grid height 35         'sets the grid spacing to 35 pixels
Measure grid draw              'draws the grid
Binary store load              'stores the grid
'
Colour detect black            'detects the dark martensite grains
Colour threshold2 255          'set threshold 2
Colour discriminate            'to show the histogram
'
Binary erode 1                 'erode to remove any small spots
Binary dilate 1                'dilate to restore the size
Binary median                  'median to smooth the result
'
Binary store and               'detects the lineal intercepts of the martensite grains
Binary conditional ends        'detects the grain boundary intersections
Measure write enable           'enables the file write
Measure view enable            'enable the data viewing
Measure field                  'measures the martensite grains displayed
Data column 5                  'protects the number of horizontal martensite grain
                               'boundary intersections
'
Data column * record           'releases column protection
Measure view disable           'leaves the view off by default
'
```

(K4) Measurement of austenitised structures with significant coalescence of martensite particles.

(i) STARTM2

Program comment "**Sets up Vv and Sv, for martensite. OK or CANCEL.**"
'
'This is a program designed to set up the columns to measure the volume fraction, and the 'surface area to volume ratio of martensite.
'
'Setting up the data columns.
'

Data column clear	'clear data columns
Measure frame reset	'reset frame size to full screen
Data append 1000xcal	'open 1000x calibration file
Data close	'close 1000x calibration file
Data column 1 fraction	'volume fraction(%)
Data column 2 count	'number of horizontal martensite grain boundary intersections

'
Data formula c1/100.000 Vv
Data column 3 formula 'volume fraction of martensite
Data formula 2*(c2/1420.37) Sv
Data column 4 formula 'surface area per unit volume for martensite grains
'
'This step opens a data file in which the measured variables can be stored.
'
Data new 'opens a new data file
'
'This step allows a file to be opened to measure the volume fraction, and surface area to 'volume ratio of martensite.
'
Program query "**Run martensite analysis program ANALYM2" analym2**
'

(ii) ANALYM2

Program comment "**Measures Vv and Sv for martensite. OK or CANCEL.**"
'
'This is a program designed to measure the volume fraction, surface area to volume ratio, 'grain size, factor, and the equivalent area diameter of martensite.
'
'This step appends a data file to allow measurement variables to be stored.
'
Data append 'appends a new data file
'
'This step measures the martensite volume fraction.
'
Image read 'allows an image to be read

```
Colour detect black                 'detects the dark martensite grains
Colour threshold2 255               'set threshold 2
Colour histogram
Program comment "Set threshold2, then press OK"
'
Binary erode 1                      'erode to remove any small spots
Binary dilate 1                     'dilate to restore the size
Binary median                       'median to smooth the result
'
Measure write disable               'disables the file write
Measure view disable                'disables the data viewing
Measure field                       'measures the martensite grains displayed
Data column 1 protect               'protects volume fraction(%)
'
'This step measures the number of martensite grain boundary intersections with a horizontal
'grid.
'
Measure write disable               'disables the file write
Measure view disable                'disables the data viewing
Binary store load                   'stores the image
'
Measure grid horizontal enable      'set up to draw a horizontal grid
Measure grid vertical disable       'ensures that no vertical grid is drawn
Measure grid height 35              'sets the grid spacing to 35 pixels
Measure grid draw                   'draws the grid
Binary store load                   'stores the grid
'
Colour detect black                 'detects the dark martensite grains
Colour threshold2 255               'set threshold 2
Colour discriminate                 'to show the histogram
'
Binary erode 1                      'erode to remove any small spots
Binary dilate 1                     'dilate to restore the size
Binary median                       'median to smooth the result
'
Binary store and                    'detects the lineal intercepts of the martensite grains
Binary conditional ends             'detects the grain boundary intersections
Measure write enable                'enables the file write
Measure view enable                 'enables the data viewing
Measure field                       'measure the martensite grains displayed
Data column 2 protect               'protects the number of horizontal martensite grain
boundary intersections
'
Data column * record                'releases column protection
Measure view disable                'leaves the view off by default
'
```

(K5) Measurement of cementite structures during austenitisation.

(i) CMNSEST

Program comment "**Sets up V_v, SF, d for cementite structures. OK or CANCEL.**"
'
'This is a program designed to set up the columns to measure the volume fraction, shape 'factor and equivalent area diameter of the cementite particles.
'
'Setting up the data columns
'
Data column clear 'clears data columns
Measure frame reset 'resets frame size to full screen
Data append 5000xcal 'open 5000x calibration file
Data close 'close 5000x calibration file
'
Data column 1 area 'total area of cementite particles (microns^2)
Data column 2 fraction 'volume fraction(%)
Data column 3 count 'number of cementite particles (frame intercepts as half)
Data column 4 shape 'average shape factor of cementite particles
'
Data formula c2/100.000 V_v
Data column 5 formula 'volume fraction of martensite
Data formula sqrt(4*(c1/c3)/3.1415) d
Data column 6 formula 'equivalent area diameter
'
'This step opens a data file in which the measured variables can be stored.
'
Data new 'opens a new data file
'
'This step allows a file to be opened to measure the volume fraction, shape factor and 'equivalent area diameter of the cementite particles.
'
Program query "**Run cem structure analysis program CMNSEAN" cmnsean**
'

(ii) CMNSEAN

Program comment "**Measures V_v, SF, d for cementite structures. OK or CANCEL.**"
'
'This is a program for measurement of the volume fraction, shape factor and equivalent area 'diameter of cementite particles.
'
'This step appends a data file to allow the measured variables to be stored.
'
Data append 'appends a new data file
'
'This step measures the number of cementite particles and the average shape factor.

```
'
Image read                          'allows an image to be read
'
Colour detect grey                  'detects the white cementite particles
Colour threshold2 255               'set threshold 2
Colour histogram
Program comment "Set threshold2, then press OK"
'
Binary hole                         'fills in the holes in the cementite particles
'
Sizer variable shape                'selects the sizer variable
Sizer lower 0
Sizer upper 100                     'excludes particles with shape factor above 100
Sizer edit                          'performs the sizer edit
Edit prepare                        'to eliminate the particles selected by the sizer function
'
Binary erode 2                      'erode to remove any small spots
Binary dilate 2                     'dilate to restore the size
Binary median 2                     'median to smooth the result
Binary store load                   'to store this edited image
'
'Now delete the cementite particles intersecting the left and bottom frame.
'
Edit erase                          'changes the editing mode to erase
Program comment "Next, delete B, R particles, then press right mouse"
Edit fill                           'to fill the desired grains in
'
Measure write disable               'disables the file write
Measure view disable                'disables the data viewing
Measure field                       'measures the cementite particles
Data column 3 protect               'protects cementite particle count
Data column 4 protect               'protects average shape factor
'
'This step measures the total area and the volume fraction of cementite particles of the image.
'
Binary store retrieve               'to retrieve the previous edited image
Sizer variable shape                'selects the sizer variable
Sizer lower 0                       'minimum shape factor
Sizer upper 100                     'excludes particles with shape factor above 100
Sizer edit                          'performs the sizer edit
Edit prepare                        'to eliminate the particles selected by the sizer function
'
Binary erode 2                      'erode to remove any small spots
Binary dilate 2                     'dilate to restore the size
Binary median 2                     'median to smooth the result
Binary store load                   'to store this edited image
'
Measure write enable                'enables the file write
Measure view enable                 'enables the data viewing
```

```
Measure field                   'measure the cementite particles
'
Data column * record            'releases the  column protection
Measure view disable            'leaves the view off by default
'
```

Appendix L

Papers published

This appendix contains the conference and journal papers published.

(i) IPENZ94
"Decarburisation understanding for improved automobile suspension spring performance"

(ii) IPENZ97a
"The influence of temperature and initial structure on the austenitisation of a high silicon spring steel"

(iii) IPENZ97b
"Decarburisation behaviour of high silicon spring steels"

(iv) IPENZ98a
"Variable decarburisation of a spring steel"

(v) IPENZ98b
"Monitoring spring steel decarburisation by sampling the heat treatment atmosphere"

(vi) IPENZ98c
"From go to whoa - experimental techniques for decarburising spring steels"

Appendix L-(i) IPENZ94

DECARBURISATION UNDERSTANDING FOR IMPROVED AUTOMOBILE SUSPENSION SPRING PERFORMANCE

C.A. MARDON[1]

1. Abstract

Automobile suspension spring steels utilise a high silicon content for reduced spring settlement during service. Unfortunately, a high silicon content has tended to facilitate surface decarburisation during manufacture of these steels, with a large proportion of suspension spring fatigue failures being attributable to this decarburisation. However, during decarburisation of SUP 7 spring steel specimens in a hydrogen/wet vapour atmosphere, decarburisation inhibition through the formation of a surface oxide layer was exhibited. Consequently, with a better understanding of the decarburisation processes occurring in spring steels, subsequent manufacture of these steels could be optimised for enhanced spring performance.

2. Introduction

2.1. Modern automobile suspension spring steels

Modern automobile suspension spring steels owe their development and implementation to the fuel crises of the 1970's, and the subsequent demand for more fuel efficient vehicles. This necessitated lighter automobiles, and was achieved, in part, by lowering the weight of the coil springs used for the suspensions of these vehicles. Automobile suspension springs are designed to avoid yielding under sustained loading; however, during repeated service loading, springs can deform plastically, thus exhibiting the phenomena of "sag" of suspension springs.

When attempts were made to reduce the weight of the springs, this phenomena of sag became more significant. Consequently, new steels utilising high carbon and high silicon contents were developed with improved sag resistance, thus achieving substantial spring weight reductions. One of the steels developed was the SUP 7 spring steel. The composition of this steel, by weight percent, is as follows:

Carbon: 0.55-0.65%; Silicon: 1.80-2.20%; Manganese: 0.70-1.0%; Phosphorus, Sulphur: Less than 0.035%.

2.2 Spring steel manufacture

It has been established that the higher the hardness of a spring steel, the better the sag resistance[(1)]; hence the higher carbon and silicon contents of the new spring steels. However, to avoid premature failure of these steels in service, a surface free from decarburisation (decarburisation involving the removal of carbon from the surface) is also required. Surface decarburisation occurs at various stages throughout spring manufacture, predominantly during the heating and shaping of the springs at high temperatures, and during the tempering operation.

Any decarburisation serves to reduce the fatigue life considerably, although the effect of a slight amount of decarburisation can be removed by a shotpeening operation[(2)] following the tempering operation. The addition of silicon to improve the sag resistance of SUP 7 spring steels was discovered to have a detrimental consequence, in that higher silicon spring steels are easily decarburised[(3)]. This arises from silicon increasing the activity of carbon, thus increasing the rate of decarburisation during spring manufacture.

1. Postgraduate student, Mechanical Engineering, University of Canterbury.

2.3. Silicon to decrease decarburisation of SUP 7 spring steels

The deleterious effect of silicon with regards to excessive surface decarburisation of SUP 7 spring steels has historically been considered a necessary and unavoidable evil. No real attempt has been made to examine the relevant mechanisms of decarburisation; instead, attempts to minimize decarburisation of these steels have focused on minimizing the heat treatment times, and on the shot peening operation following tempering.

However, it has recently been observed that during decarburisation experiments on SUP 7 spring steel[4] under certain conditions, the decarburisation of these steels was significantly inhibited, seemingly through the formation of a surface oxide layer. Although this is a well defined phenomena during the decarburisation of silicon steels containing 3 weight percent silicon and low carbon contents, parallel information on spring steels is lacking. Therefore, a better understanding and hence more accurate modelling of the mechanisms controlling decarburisation of spring steels is of significance. From this knowledge, rolling conditions in the steel mill, as well as the spring manufacturing conditions, could be optimised to reduce decarburisation of these steels. Furthermore, the wastage associated with the current practice of peeling bar stock prior to spring manufacture could be reduced, and the premature failure of the finished product due to the decarburisation arising from spring manufacture addressed.

3. Principles of decarburisation and oxide formation

3.1. Decarburisation of silicon steels

Decarburisation of silicon steels containing up to 3 weight percent silicon, and with low carbon contents, is usually accomplished on a commercial scale through a heat treatment in wet hydrogen over a temperature range of 700 to 1000^{o}C. This decarburisation occurs predominantly by the following two reactions[5]:

$$C + H_2O = CO + H_2 \quad (3.1)$$
$$C + 2H_2 = CH_4 \quad (3.2)$$

The rate of decarburisation is a function of the oxide film formation when iron or silicon reacts with water vapour. The formation of the various oxide films is influenced by the temperature of the atmosphere, the silicon content of the steel, and the water content of the wet vapour decarburising atmosphere. The partial pressure ratio of the water to the hydrogen of the wet vapour atmosphere, p_{H_2O}/p_{H_2}, is usually expressed in preference to the oxygen partial pressure.

3.2. Influence of silicon on decarburisation

One investigation[5] looked at the decarburisation of silicon sheet comprising silicon contents ranging from 0.4 to 2.9 weight percent silicon. With an experimental p_{H_2O}/p_{H_2} partial pressure ratio of 0.1, a SiO_2 surface oxide layer was formed. It was determined that two forms of the oxide layer occurred, depending on the silicon content of the steel. For silicon contents below approximately 2.0 weight percent silicon, the SiO_2 layer was thick, uneven and porous, whereas for the higher silicon contents, a thick, even and dense oxide layer formed.

The two different oxides resulted in two different decarburisation curves being observed. For materials with lower silicon contents, a non-linear decrease of carbon content with time was obtained, as shown by Figure 3.1. For higher silicon contents, a linear decrease of carbon content was obtained (Figure 3.2). The non-linear curve was linked to a higher degree of decarburisation, while a lower degree of decarburisation occurred with the linear process. In both cases, the rate of decarburisation was significantly lower than for uninhibited carbon diffusion in ferrite (the dashed curves of Figures 3.1 and 3.2), indicating the inhibiting influence of both SiO_2 structures on the decarburisation.

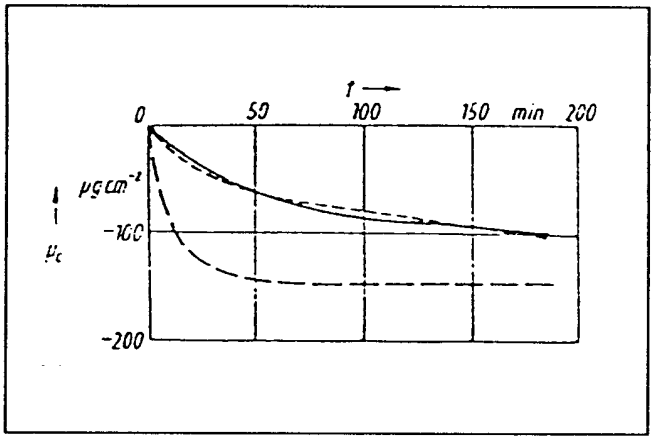

Figure 3.1 Non-linear decrease of carbon content with time[5].

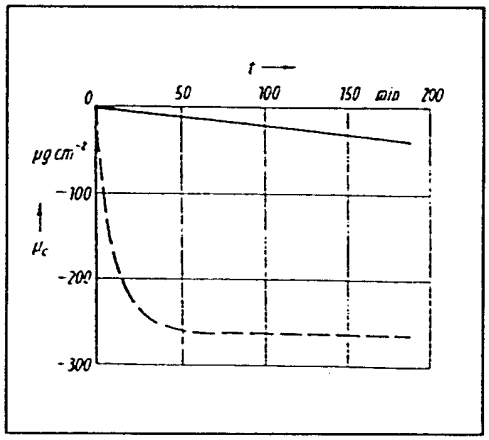

Figure 3.2 Linear decrease of carbon content with time[5].

3.3. Influence of p_{H_2O}/p_{H_2} ratio on oxide formation and decarburisation

A parallel study[6] investigated the decarburisation of 3 weight percent silicon steels at temperatures ranging from 700 to 1000°C in a hydrogen atmosphere containing various amounts of water vapour. Figure 3.3 illustrates the effect of water vapour content on the decarburisation rate for specimens heated at 800°C. From this figure, it is evident that the decarburisation rate increases with increasing water content (expressed in this instance as dew point). Figure 3.4 is for decarburisation at 1000°C. In this situation, the decarburisation rates at dew points of 0 and 10°C (p_{H_2O}/p_{H_2} = 0.006 and 0.012) are lower than those at 800°C. However, for dew points of 20 to 40°C (p_{H_2O}/p_{H_2} = 0.023 to 0.073), the decarburisation rates were greater than those at 800°C. From Figure 3.4, it can also be seen that the decarburisation rates for specimens at dew points of 30 and 40°C (p_{H_2O}/p_{H_2} = 0.042 and 0.073) are similar, suggesting that an optimum value of water content for maximum decarburisation exists at 1000°C.

An increasing decarburisation rate with increasing water vapour content and temperature (up to a limiting value) is apparently a function of the surface oxide formation. Depending on the experimental parameters, three chemical reactions were observed:

$$Si + 2H_2O = SiO_2 + 2H_2 \quad (3.3)$$

$$Fe + H_2O = FeO + H_2 \quad (3.4)$$

$$2Fe + SiO_2 + 2H_2O = Fe_2SiO_4 + 2H_2 \quad (3.5)$$

From a thermodynamic analysis, the relation between the phases in equilibrium, the p_{H_2O}/p_{H_2} partial pressure ratio, and the temperature, can be obtained, as shown in Figure 3.5. This thermodynamic analysis proved consistent with the experimental results, except for the formation of Fe_2SiO_4 at temperatures below 900°C. Thus, the type of oxide formed depended on both the p_{H_2O}/p_{H_2} ratio, and on the temperature. With respect to the decarburisation rate, formation of the compact SiO_2 surface oxide layer acted as a strong decarburisation inhibitor, whereas the decarburisation rate was not inhibited to the same degree by the non-protective Fe_2SiO_4 oxide.

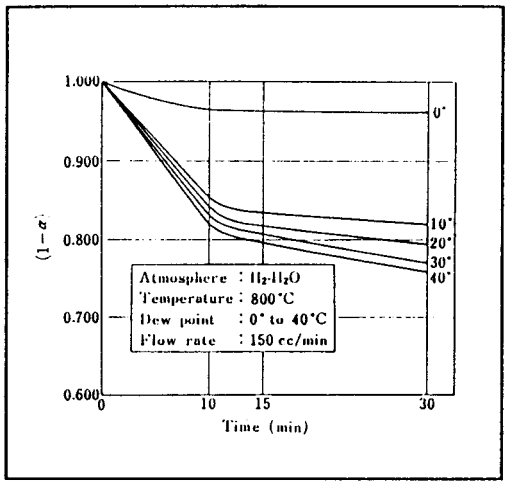

Figure 3.3 Relation between rate of decarburisation (1-α) and dew point in atmosphere of H_2-H_2O at 800°C[6].

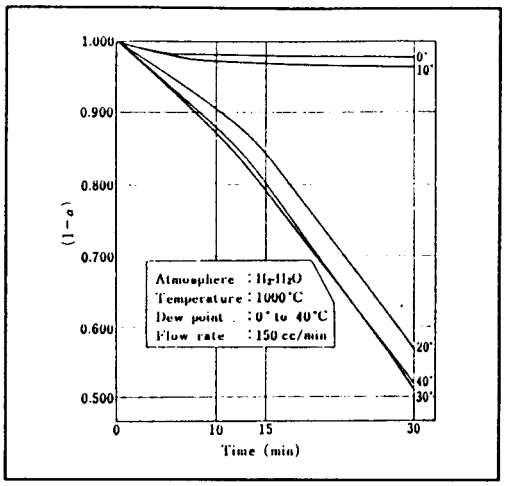

Figure 3.4 Relation between rate of decarburisation (1-α) and dew point in atmosphere of H_2-H_2O at 1000°C[6].

4. Experimental investigation

4.1 Experimental equipment

In order to simplify the decarburisation measurements, it was decided that initial decarburisation experimentation would be undertaken as close as possible to the Ac_3 temperature for the SUP 7 steel (the Ac_3 line being depicted in the left hand portion of the iron-carbon equilibrium diagram of Figure 4.1). At the Ac_3 temperature, decarburisation (with removal of carbon from the surface of test specimens), should result in an austenite (γ) to ferrite (α) transformation. Upon quenching, the austenite would transform to martensite, resulting in a decarburised layer of ferrite at the surface, with an interface separating the ferrite from the martensitic core.

As the rate of carbon diffusion in ferrite is considerably greater than in austenite, once carbon has diffused through the ferrite/austenite interface, it will be quickly transported through the ferrite layer to the surface. Consequently, the ferrite/martensite interface should be sharply defined (Figure 4.2), with the interface moving inwards with increasing decarburisation times.

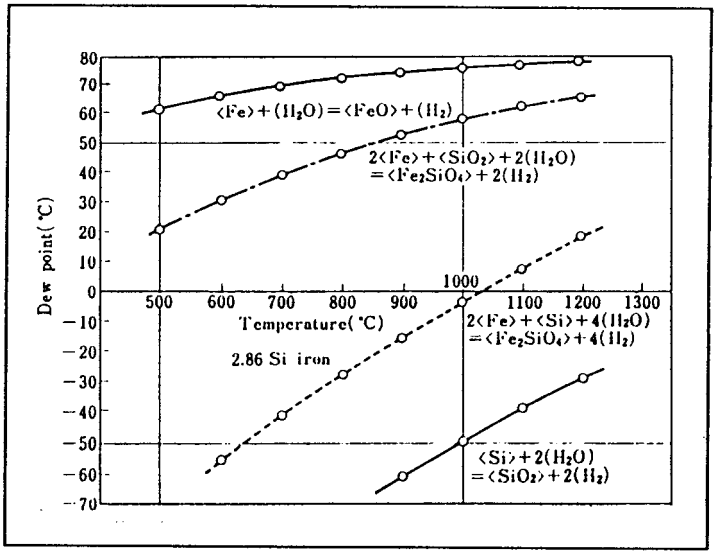

Figure 3.5 Relation between p_{H_2O}/p_{H_2} partial pressure ratio and temperature for formation of various oxides[6].

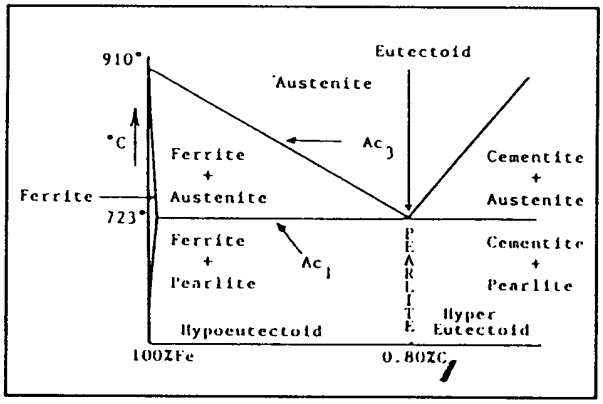

Figure 4.1 Ac_3 temperature for SUP 7 spring steel[7].

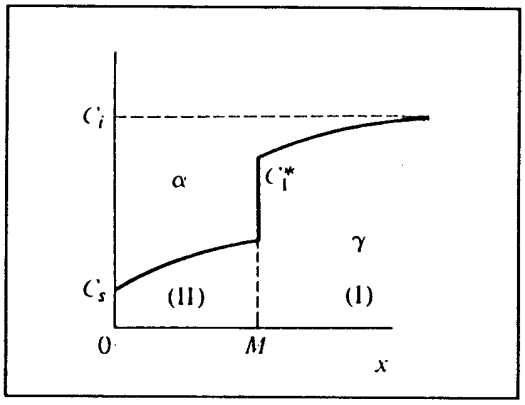

Figure 4.2 Carbon concentration profile arising from decarburisation at the Ac_3 temperature[8].

Given that only the compositional limits of the batch of SUP 7 steel supplied were known, an empirical formula[9] was used to determine the limiting values of the Ac_3 temperature. The two temperatures were calculated to be 797 and 817°C respectively. Consequently, 30 minute heat treatments were undertaken on specimens 14mm diameter by 12mm length at temperatures around the determined Ac_3 range. Microscopic preparation and investigation determined the Ac_3 temperature for this batch of SUP 7 spring steel to be 802±2°C.

4.2 Decarburisation experimentation

Preliminary decarburisation experiments were undertaken with the test rig illustrated in Figure 4.3, with the experimental programme being as listed in Table 4.1.

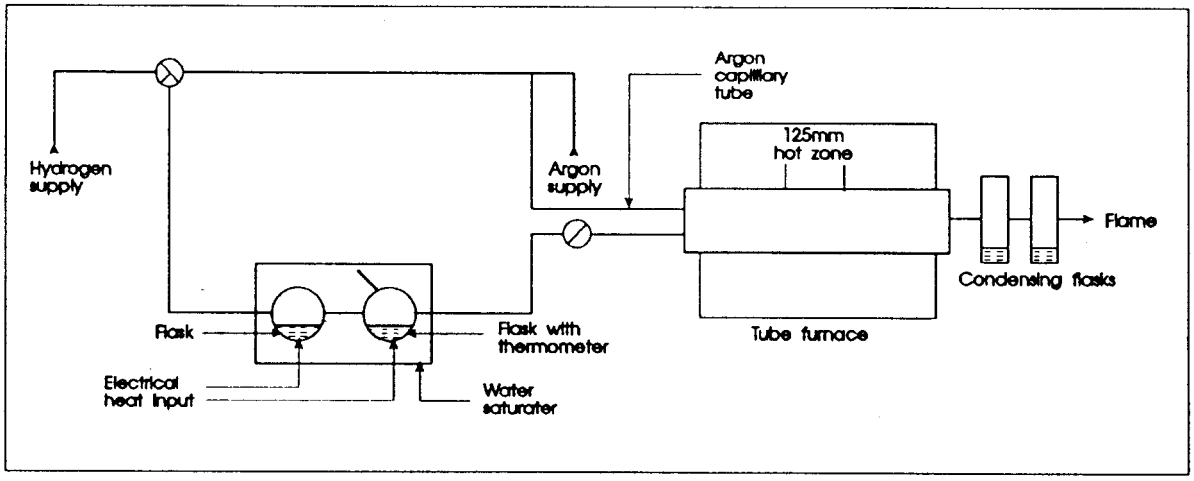

Figure 4.3 Schematic of experimental decarburisation rig.

Decarburisation Time (hours)	Decarburisation Temperature (^{o}C)	p_{H_2O}/p_{H_2} Ratio
1	800	0.15
2	800	0.15
4	800	0.06
4	800	0.15
4	800	0.22
12	800	0.15

Table 4.1 Experimental programme for preliminary decarburisation experiments.

With the above experimental programme, initial investigations pertaining to the effect of time and p_{H_20}/p_{H_2} ratio on the decarburisation were undertaken. Decarburisation experiments utilising the test rig (Figure 4.3) involved hydrogen being passed through the water saturater, which was maintained at the temperature required for specific p_{H_2O}/p_{H_2} ratios.

The test specimens used for the decarburisation experiments differ from the more conventionally shaped rectangular and cylindrical specimens, in that they possess the needle-like shape of Figure 4.4. The purpose of this shape is twofold. Firstly, through utilising a needle-like shape, different size test pieces can be effectively investigated using only one test specimen, with the length near the tip hopefully proving to be completely decarburizable. Secondly, by using a tapered test specimen, information on the effect of varying the cross-sectional area to volume ratios at different points on the test specimen can be obtained. This is of interest as the decarburisation process depends on the surface cross-sectional area exposed to the decarburising environment, while the amount of carbon to be removed depends on the volume of the test piece. Also, with the gradual taper of the test specimen, carbon diffusion should be predominantly one-dimensional (radially outwards of the test specimen), thus allowing different size cylindrical test specimens to be effectively approximated.

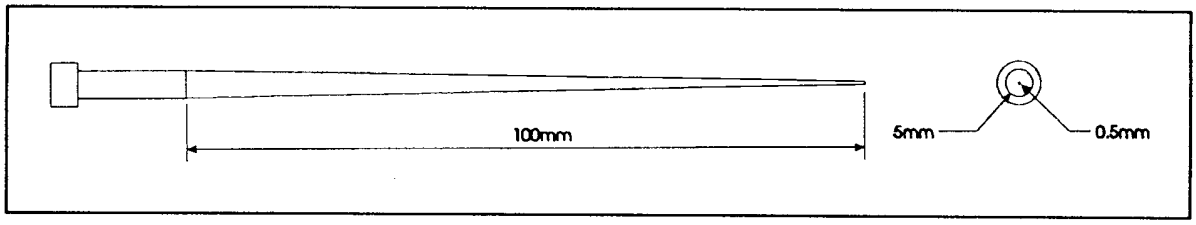

Figure 4.4 Needle-like decarburisation test specimen shape.

4.3 Macroscopic and microscopic examination

Upon completion of the experimental programme outlined in Table 4.1, each test specimen was sectioned into five approximately equal lengths, mounted, and polished. Subsequently, each section of the six test specimens was etched in 2 percent Nital, and investigated under both optical and scanning electron microscopes.

Figure 4.5, a photograph of the tip of the specimen decarburised for 1 hour, illustrates the transition along the test specimen from a fully decarburised to a partially decarburised cross-section. The darker outside regions of the section demonstrate the decarburised, almost carbon free, structure of ferrite, while the lighter core is that of martensite. Figure 4.6 shows the tip of the 12 hour test specimen. Complete decarburisation of this section is evident, demonstrating the effect of longer test durations on the decarburisation depth.

Figures 4.7 and 4.8 illustrate the decarburisation profiles for the 1 hour and 12 hour specimens near the large diameter end of the test specimens. For the 1 hour section, a uniform decarburisation depth is visible along its length. This contrasts with the 12 hour specimen, where the decarburisation profile is less well defined. Near the smaller end of the section, and along the right hand length in general, the decarburised depth is significantly greater than that of the 1 hour specimen. However, along the left hand side near the larger end, the depth of decarburisation varies considerably, and is actually less than that of the 1 hour specimen in places.

Illustrated in Figure 4.9 is a scanning electron microscope photograph of the oxide layer formed on the surface of the test specimens. Approximately 20 to 30 μm in thickness, the oxide layer is the central structure of the photograph. The upper third of this figure illustrates the ferrite grain structure of the decarburised zone, while the thin bright line underneath the oxide layer results from charging by the electron beam.

4.4 Decarburisation curves

Measurements of the decarburisation profiles at various locations along each section were undertaken via a Shadowgraph equipped with an accurate measuring table, yielding the decarburisation curves of Figures 4.10 through 4.13. The decarburisation depths plotted on the vertical axes of these figures refer to the depth of the observed ferrite layer. The decarburisation curves for each specimen commence at the diameter where incomplete decarburisation of the cross-sections was observed.

Exhibited in Figure 4.10 are the decarburisation curves for the 1, 2, 4, and 12 hour tests at a 0.15 p_{H_2O}/p_{H_2} ratio, with experimental data being plotted at various diameters along the test specimens. For the 1 and 2 hour tests, the decarburisation curves are reasonably constant and uniform along

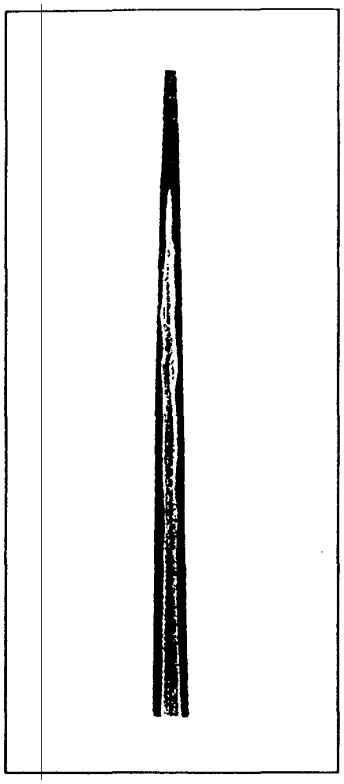

Figure 4.5 Decarburization at tip.
Magnification:X6
Test:1hr, $p_{H_2O}/p_{H_2}=0.15$

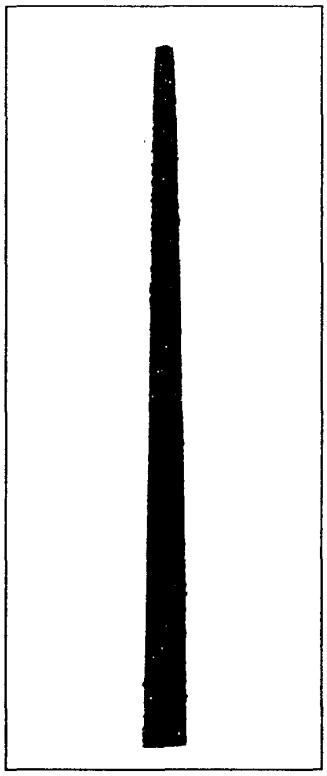

Figure 4.6 Decarburization at tip.
Magnification:X6
Test:12hr, $p_{H_2O}/p_{H_2}=0.15$

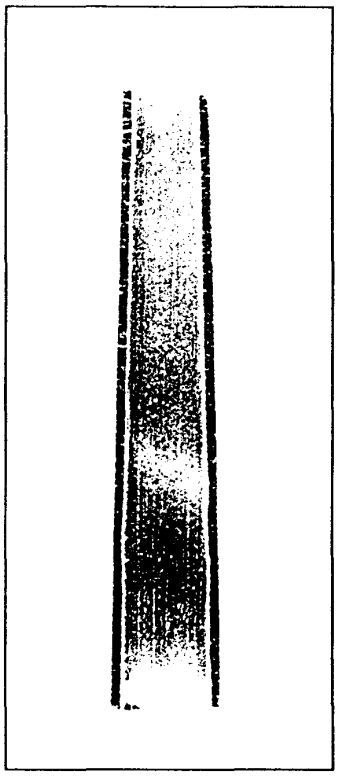

Figure 4.7 Decarburization at large end.
Magnification:X6
Test:2hr, $p_{H_2O}/p_{H_2}=0.15$

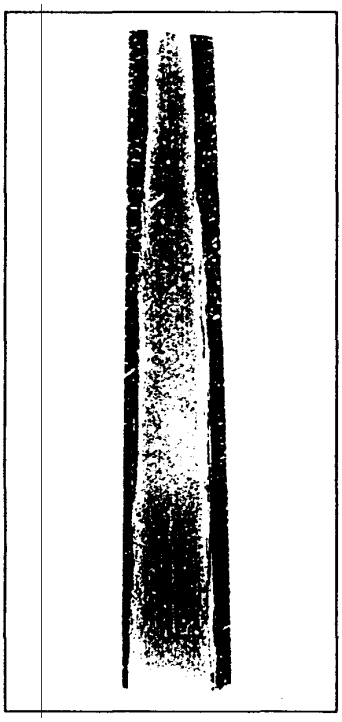

Figure 4.8 Decarburization at large end.
Magnification:X6
Test:12hr, $p_{H_2O}/p_{H_2}=0.15$

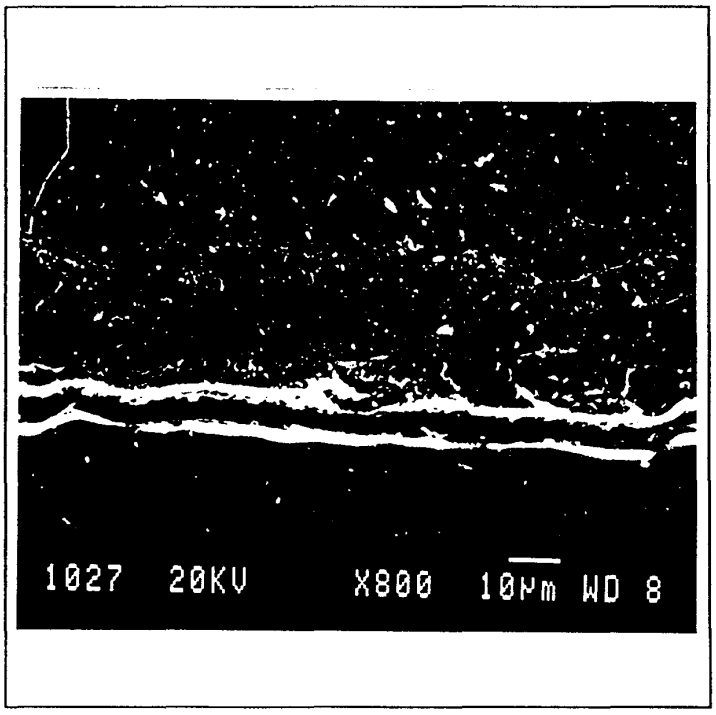

Figure 4.9 Scanning electron microscope photograph of surface oxide layer.

the test specimens. The increase in decarburisation depth of the 2 hour test is significant with respect to the 1 hour test.

For the 4 hour experiment, the profile of the curve was somewhat more inconsistent. For diameters from 1 to 3mm, the decarburisation depth is less than for either the 1 or 2 hour tests, with the curve being less well defined. From 3mm in diameter, the curve takes on a more uniform appearance, with the decarburisation depth being slightly greater than the 2 hour specimen. The situation for the 12 hour test is even more variable. Complete decarburisation occurred up to a diameter of 2.5mm, with the decarburisation depths varying significantly from this diameter.

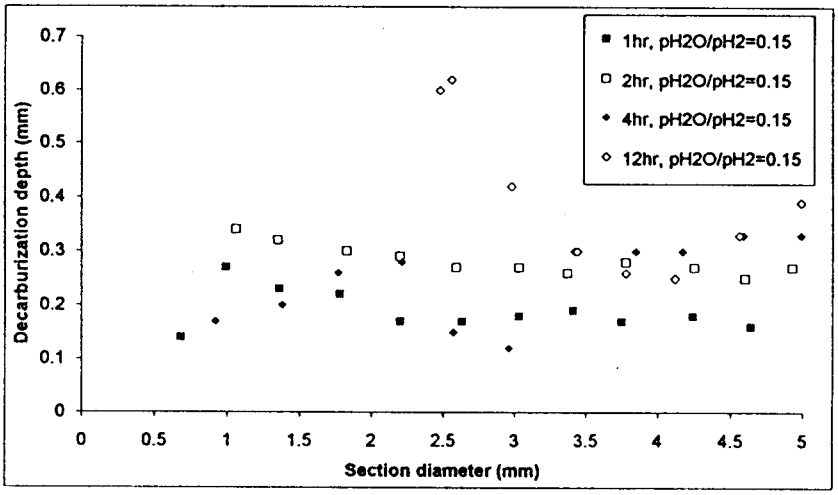

Figure 4.10 Decarburisation profiles for varying test durations at p_{H_2O}/p_{H_2}=0.15.

Figure 4.11 shows the decarburisation curves for the 1 and 12 hour tests. Also plotted are the decarburisation curves for uninhibited carbon diffusion in ferrite, assuming a diffusion coefficient of $8x10^{-7}cm^2/s$. These curves were determined by a first order approximation of the test specimens as cylindrical sections, given the finite nature of the test specimen size with respect to the decarburisation depths calculated.The linear portion of the two theoretical ferrite lines pertains to complete decarburisation at the relevant diameters. The curved section is indicative of increasing decarburisation depth with increasing diameter, up to a point where the test specimen diameter no longer influences the decarburisation depth (the horizontal lines of the theoretical ferrite profiles). Both the 1 and 12 hour curves suggest considerably greater decarburisation depths for pure iron relative to the high silicon SUP 7 spring steel, contrary to the observations that high silicon spring steels are easily decarburised.

It appears therefore that the decarburisation of the SUP 7 specimens tested has been significantly inhibited. This inhibition is considered to be a consequence of the surface oxide layer impeding the diffusion of carbon out of the specimens during the decarburisation experimentation.

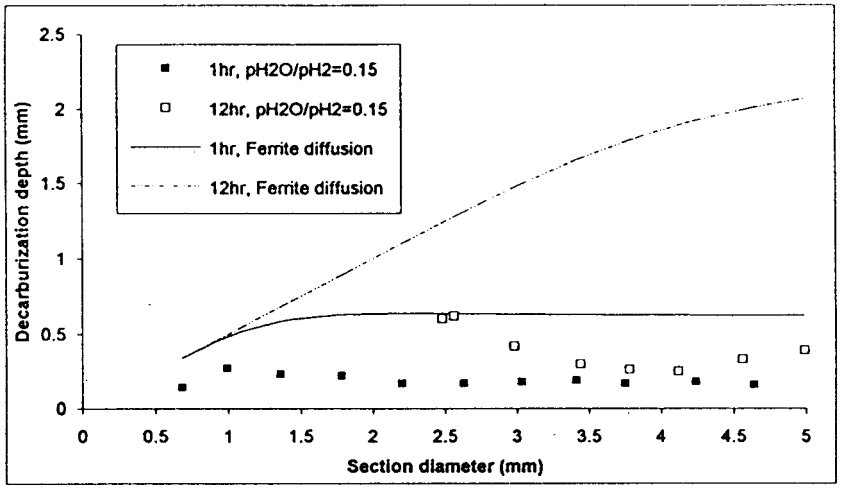

Figure 4.11 Comparison of experimental SUP 7 decarburisation profiles with those for theoretical carbon diffusion in ferrite.

Referring to the geometry of the test specimens, infinitesimal thick cross-sections along the length were taken to approximate cylindrical sections. For a cylinder, the volume of the specimen is proportional to its diameter squared, while the surface area is proportional to the diameter. Consequently, with increasing diameter along the test specimen, the ratio of volume to surface area increases.

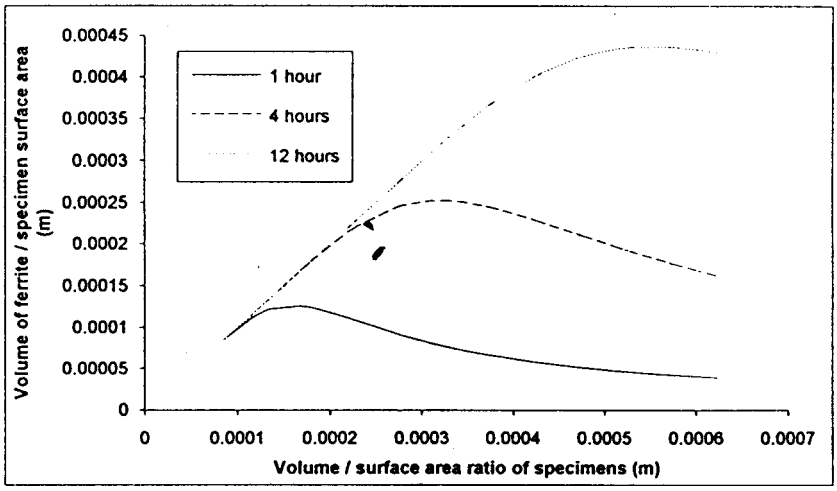

Figure 4.12 Ferrite profiles as a function of test specimen volume/surface area ratios for theoretical carbon diffusion in ferrite.

As the rate of decarburisation is a function of surface area, while the amount of carbon to be removed is dependent on the specimen volume, given the increasing volume to surface area ratio with increasing diameter, the theoretical increasing decarburisation depths of the ferrite curves that resulted were unexpected. However, it must be remembered that with increasing diameters, the surface area exposed to the decarburising atmosphere is also increasing. Upon investigation of Figure 4.12, which provides a plot of the volume of ferrite divided by the specimen surface area against the volume to surface area ratios of the specimens, the expected trend with increasing volume to surface area ratios on the carbon removal is indeed shown.

The increasing decarburisation depth trends were not observed for the experimental decarburisation tests of Figure 4.10, nor those of Figure 4.12. From this it is apparent that the surface oxide layer also influences the theoretical volume to area ratio trends. Figure 4.13 investigates the effect of p_{H_2O}/p_{H_2} ratios on the decarburisation curves for a 4 hour test duration.

Although the three curves have non-uniform profiles, the decarburisation depth does appear to increase with increasing p_{H_2O}/p_{H_2} ratios. However, none of the curves approached the theoretical curve for carbon diffusion in ferrite.

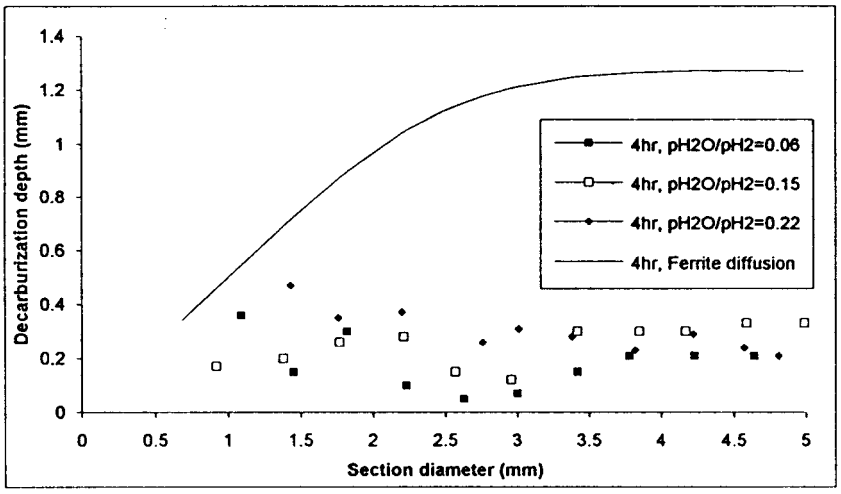

Figure 4.13 Decarburisation profiles for 4 hour experiments at various p_{H_2O}/p_{H_2} ratios.

5. Future research

From the initial decarburisation investigation, the decarburisation rate of SUP 7 spring steel appears to be substantially slower than for carbon diffusion in ferrite. With a better understanding of the decarburisation processes in SUP 7 spring steel, spring manufacturing production could be optimised to attain minimum decarburisation, and consequently, maximum spring performance. Thus, future research into this area is expected to involve:

(i) A comprehensive investigation of the effect of various p_{H_2O}/p_{H_2} ratios on the decarburisation of SUP 7 spring steel for times ranging from 30 minutes to 24 hours at 800^{o}C. Through a thermodynamic analysis, the p_{H_2O}/p_{H_2} range will be sufficient to encompass the relevant oxides predicted, so that the effect of oxide formation on decarburisation can be determined.

(ii) Decarburisation experiments over a range of temperatures up to 1000^{o}C, thus allowing determination of the effect of temperature on the decarburisation rate and oxide formation. Experimentation will be undertaken for specific decarburising times and p_{H_2O}/p_{H_2} ratios.

(iii) Decarburisation experiments in a typical spring manufacturing atmosphere, and in an optimal wet vapour atmosphere for minimal decarburisation, in order to facilitate a comparison.

6. Conclusion

Modern automobile suspension spring steels utilise a high silicon content for improved sag resistance during service. Concurrent to the improvement in sag resistance, high silicon spring steels have proved susceptible to surface decarburisation during spring manufacture. However, during experimentation in a decarburising atmosphere containing hydrogen and water vapour, decarburisation inhibition, relative to uninhibited carbon diffusion in ferrite, was observed. This inhibition is considered to be a consequence of the formation of a surface oxide layer on the test specimens, which prevents carbon diffusion out of the specimens. The decarburisation inhibition was determined to be dependent on the decarburisation duration, and on the p_{H_2O}/p_{H_2} ratio of the decarburising atmosphere. Through a better understanding of the decarburisation processes of

SUP 7 spring steels, automobile suspension spring manufacture could be optimised for enhanced spring performance.

7. Acknowledgements

I would gratefully like to acknowledge and thank New Zealand Steel for their financial support which made this paper possible. Furthermore, I would like to thank my supervisor, Dr. J.S. Smaill, and the Mechanical Engineering staff in the Engineering Department of the University of Canterbury for their support.

8. References

(1) "Parameters Affecting Sag Resistance in Spring Steels", Assefpour-Dezfuly, M.; Metallurgical Transactions A, Volume 20A, October 1989, 1951-1959.
(2) "Handbook of Heat Treatment of Steels", Prabhudev, K.H.; McGraw-Hill Publishing Company Limited, New Delhi, 1988.
(3) "Effect of Chemical Composition on Sag Resistance of Suspension Spring", Kawakami, H.; SAE paper 821028.
(4) Unpublished research, Bott, C.; Postgraduate Student, University of Canterbury, New Zealand.
(5) "About Oxidation and Decarburisation Behaviour of Fe-Si Alloys", Wiesner, U.; Neue Hutte, July 1986, 250-253.
(6) "On the Decarburisation of Silicon Steel Sheet", Yamazaki, T.; ISIJ Transactions, Volume 9, 1969, 66-75.
(7) "Engineering Materials", University of Canterbury, 1992.
(8) Transport Phenomena in Metallurgy", Geiger, G.H.; Addison-Wesley Publishing Company, California, 1973.
(9) "Empirical Formula for the calculation of some Transformation Temperatures", Andrews, K.W, JISI, July 1965, 721-727.

Appendix L-(ii) IPENZ97a

THE INFLUENCE OF TEMPERATURE AND INITIAL STRUCTURE ON THE AUSTENITISATION OF A HIGH SILICON SPRING STEEL

C. A. MARDON[1], J. S. SMAILL[2]

1 Abstract

Decarburisation that occurs during the manufacture of automobile suspension springs contributes to a high proportion of spring failures. During research into the decarburisation of a high silicon spring steel, the dissociation of the iron carbides and the partitioning of the silicon, manganese, and chromium alloying elements were investigated for various heat treatment temperatures. The information obtained will contribute to a better understanding of the decarburisation of such steels, allowing the spring manufacture to be optimised for enhanced spring performance.

2 Introduction

Modern automobile suspension spring steels owe their development to the fuel crises of the 1970's, and the subsequent demand for more fuel efficient vehicles. This necessitated lighter automobiles, and was achieved, in part, by the development of new higher strength steels which resulted in lighter automobile suspension coil springs. However, these steels with higher carbon and silicon contents were found to be more prone to surface decarburisation during the typical heat treatments used for the manufacture of suspension springs.

By lowering the hardness and consequently the fatigue behaviour of the spring surface, decarburisation can result in premature spring failures. During this research programme it has been observed[1] that the decarburisation of a high silicon spring steel in an atmosphere of moist hydrogen presented anomalous behaviour requiring further investigation.

Decarburisation involves carbon removal from the surface of the steel, with several different mechanisms contributing to the carbon transport through the steel to the surface The transport of carbon can occur in the steel by diffusion in the bulk, along dislocations and other defects, as well as along grain boundaries. The local carbon concentration in the steel is a function of the alloying element concentration, the phases that are present, the temperature with the associated solubility for these given phases, and the solubility product for the carbide precipitates in the presence of the given phases. With all of these factors influencing the decarburisation, an understanding of the decarburisation mechanisms for high silicon spring steels necessitates an investigation into the austenitisation of these steels. Based on equilibrium considerations, austenite formation will commence at the Ac_1 temperature for the steel. As the temperature increases above the Ac_1 value, the equilibrium austenite fraction will increase, with fully austenitic structures occurring at the Ac_3 temperature. This transformation is associated with the dissociation of the cementite by

1 Postgraduate Student, Department of Mechanical Engineering, University of Canterbury.

2 Senior Lecturer, Department of Mechanical Engineering, University of Canterbury

$$Fe_3C \Leftrightarrow 3Fe + C$$

and the modification of the ferrite (body centred cubic) phase to the austenite (face centred cubic) phase as a function of the carbon in solid solution.

In many steels, the transformation to austenite is rapid. This transformation requires less than one second for plain carbon steels[2], three seconds for chromium steels[3], and twenty seconds for complex steels with carbide forming elements[4]. The concurrent carbide dissolution in the austenite is found to proceed more slowly. However, Karmazin[5] illustrated that the austenite transformation is considerably retarded in steels containing increased silicon and manganese contents.

The rate of austenite formation is dependent on composition and the initial microstructure of the steel. Speich[6] investigated the austenite formation from pearlitic structures in 0.77 and 0.96wt.% C Fe-C steels, and a 0.96wt.% C Fe-Si-Mn alloy. He found that austenite was nucleated predominantly at carbides in the boundaries between the pearlite colonies, with the subsequent austenite growth controlled by carbon diffusion. On completion of the austenitisation, the remaining lamellar carbides are either dissolved or spheroidised, depending on the carbon content and the temperature. Nehrenberg[7] demonstrated that for various plain carbon and alloy steels heat treated within the Ac_1 to Ac_3 temperature range, the austenite growth is non-directional for structures that were initially pearlitic. This results in an approximately equiaxed grain structure.

Initial spheroidal carbide structures can be produced by either a high temperature transformation of inhomogeneous austenite[7], or by the tempering of martensite. There is a fundamental difference between the resultant spheroidised structures, with the former having an equiaxed microstructure with the majority of the carbides located within the ferrite grains, while the tempered martensite microstructure comprises an acicular ferritic structure, with the carbides located on the ferrite grain boundaries. For both types of microstructures[7], austenite started to grow from nuclei located on ferrite/carbide interfaces, with the austenite transformation confined to the initial ferrite grain boundaries. Therefore, the austenite grain structure depends on the prior ferrite grain structure.

This paper examines the austenitisation of a high silicon spring steel. Heat treatments were undertaken at temperatures ranging from just above the Ac_1 temperature to above the Ac_3 temperature for 15 minutes to 192 hours. Five initial structures, two pearlitic and three spheroidal cementite, were investigated. The kinetics of ferrite and cementite dissolution, and the concurrent austenite formation, are detailed to determine the influence of temperature and initial structure on the austenitisation of this steel. The redistribution of the alloying elements that occurs within the various phases and the subsequent influence on the austenitisation is also investigated.

3 Experimental investigation

3.1 Heat treatments

The austenitisation process was investigated for a spring steel, SUP7, with a composition, by weight percent, of 0.61%C, 1.95%Si, 0.79%Mn, and 0.19%Cr. Heat treatments were undertaken on 14mm diameter bar stock, which was held for 12hr at 900^{o}C to dissolve all the

carbides and form homogeneous austenite. Following quenching in water at ambient temperature, 14mm diameter by 10mm specimens were austenitised in a Nabertherm R7019 tube furnace with an inert argon atmosphere for 24hr at various temperatures, then water quenched, to determine the Ac_1 and Ac_3 transformation temperatures. This yielded an Ac_1 temperature of 745^{o}C and an Ac_3 temperature of 820^{o}C.

Five initial structures were prepared by heat treating 14mm diameter bar stock in the tube furnace with an inert argon atmosphere. Following austenitisation at 900^{o}C for 12hr, two specimens were furnace cooled in 20min to just above the Ac_3 temperature (to ensure that both structures had the same prior austenite grain size) before being air or furnace cooled through the transformation range to produce pearlitic structures with differing interlamellar spacings. The remaining three structures consisted of spheroidal carbides in a ferritic matrix. Of these, two were obtained by tempering martensite for 12hr and 96hr respectively, while the third resulted from air cooling and a subsequent intercritical heat treatment. Test specimens, 5mm diameter by 10mm, were machined from the heat treated bar stock, and austenitisation heat treatments undertaken in the tube furnace with an inert argon atmosphere for times ranging from 15min to 192hr at temperatures of 755^{o}C, 780^{o}C, 800^{o}C, 820^{o}C, and 840^{o}C.

	HEAT TREATMENT	**DESCRIPTION**
A	12hr at 900^{o}C, furnace cooled to 825^{o}C in 20min, air cooled.	**Air cooled**
B	12hr at 900^{o}C, furnace cooled to 825^{o}C in 20min, furnace cooled at 25^{o}C/hr to 600^{o}C, furnace turned off and cooled to ambient.	**Furnace cooled**
C	12hr at 900^{o}C, water quenched. Reheated for 12hr at 735^{o}C, air cooled.	**12hr tempered martensite**
D	12hr at 900^{o}C, water quenched. Reheated for 96hr at 735^{o}C, air cooled.	**96hr tempered martensite**
F	12hr at 900^{o}C, air cooled. Reheated for 6hr at 735^{o}C, furnace heated to 780^{o}C, furnace cooled as rapidly as possible to 740^{o}C, held 18hr at 740^{o}C, furnace cooled at 2^{o}C/hr to 700^{o}C, air cooled.	**Intercritical**

Table 1 Heat treatments used to produce the initial structures.

Following completion of each heat treatment, the specimens were quenched in water at 20^{o}C, with the austenite formed at the heat treatment temperature thus transformed into martensite. A one-to-one relationship between the fraction of austenite at the heat treatment temperature and the fraction of martensite following quenching was assumed. The martensite was then tempered at 250^{o}C for 1hr to achieve better contrast upon etching for subsequent image analysis. The specimens were mounted in bakelite, ground and polished, initially lightly etched in 2% Nital, then subsequently immersed in an etch comprising 21g sodium metabisulphite in 100ml H_2O to colour the martensite areas black.

3.2 Analysis

A Video Pro 32 colour image analyser connected to an Olympus BH2-MA-2 optical microscope via a JVC TK-870E video camera was used to measure the fraction of martensite and cementite present in each specimen. The martensite phase (austenite at the heat treatment temperature) was measured from images at a magnification of 1,000x. Twenty $7x10^{-3}mm^2$ fields were randomly selected for each specimen by positioning the microscope at a magnification of 50x, with the martensite volume fraction and equivalent area diameter measured at these locations. Computer printouts of images from a JEOL JSM-6100 scanning

electron microscope (SEM) of the spheroidal cementite phase were loaded via the video camera into the image analyser. Twelve randomly selected areas at a magnification of 5,000x were analysed and the volume fraction and average equivalent area diameter of the spheroidal cementite particles determined.

The SEM equipped with a LINK QX2000 energy dispersive X-ray analyser was used to measure the alloy element contents of the austentite and cementite phases using a cobalt standard, with an accelerating voltage of 20kV, an X-ray acquisition time of 100s, and a dead time of approximately 25%.

4 Results

4.1 Initial structures

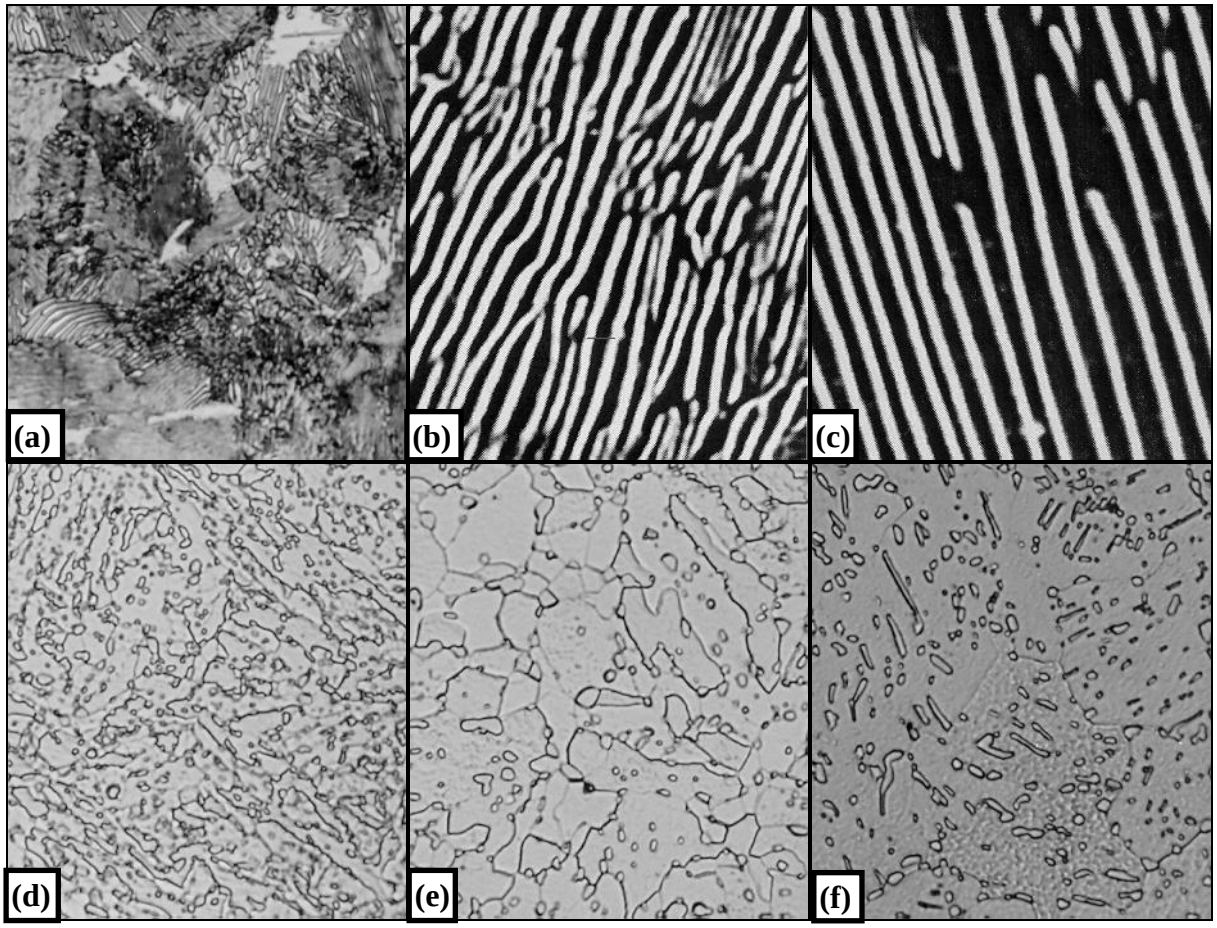

Figure 4.1 The five initial structures produced by: (a) air cooling (1,200x), (b) air cooling (10,000x), (c) furnace cooling (10,000x), (d) tempering martensite for 12hr at 735^{o}C (1,200x), (e) tempering martensite for 96hr at 735^{o}C (1,200x), and (f) an intercritical heat treatment (1,200x). 2% Nital etch.

The five initial microstructures are illustrated in Figure 4.1. The furnace cooled structure, Figure 4.1(c), had a coarser lamellar carbide structure than the air cooled structure, Figure 4.1(b), with a greater fraction of proeutectoid ferrite on the prior austenite grain boundaries. The two tempered martensite microstructures have an acicular ferrite structure with the majority of the carbides located on the ferrite grain boundaries. The 96hr tempered structure, Figure 4.1(e), had a coarser grain structure than that of the 12hr tempered structure, Figure

4.1(d), with the ferrite grains being more equiaxed than for the 12hr structure. The volume fraction of cementite is higher for the 12hr tempered structure, 12.8% versus 8.8%, while the 96hr structure has a greater average cementite size than the 12hr structure, with an equivalent area diameter of 1.14 microns versus 0.73 microns. The morphology of the structures produced by the intercritical heat, Figure 4.1(f), differed to that of the tempered martensite structures, with the ferrite grain shape being more equiaxed, and the majority of the cementite particles located within the ferrite grains.

4.2 Microstructural investigation

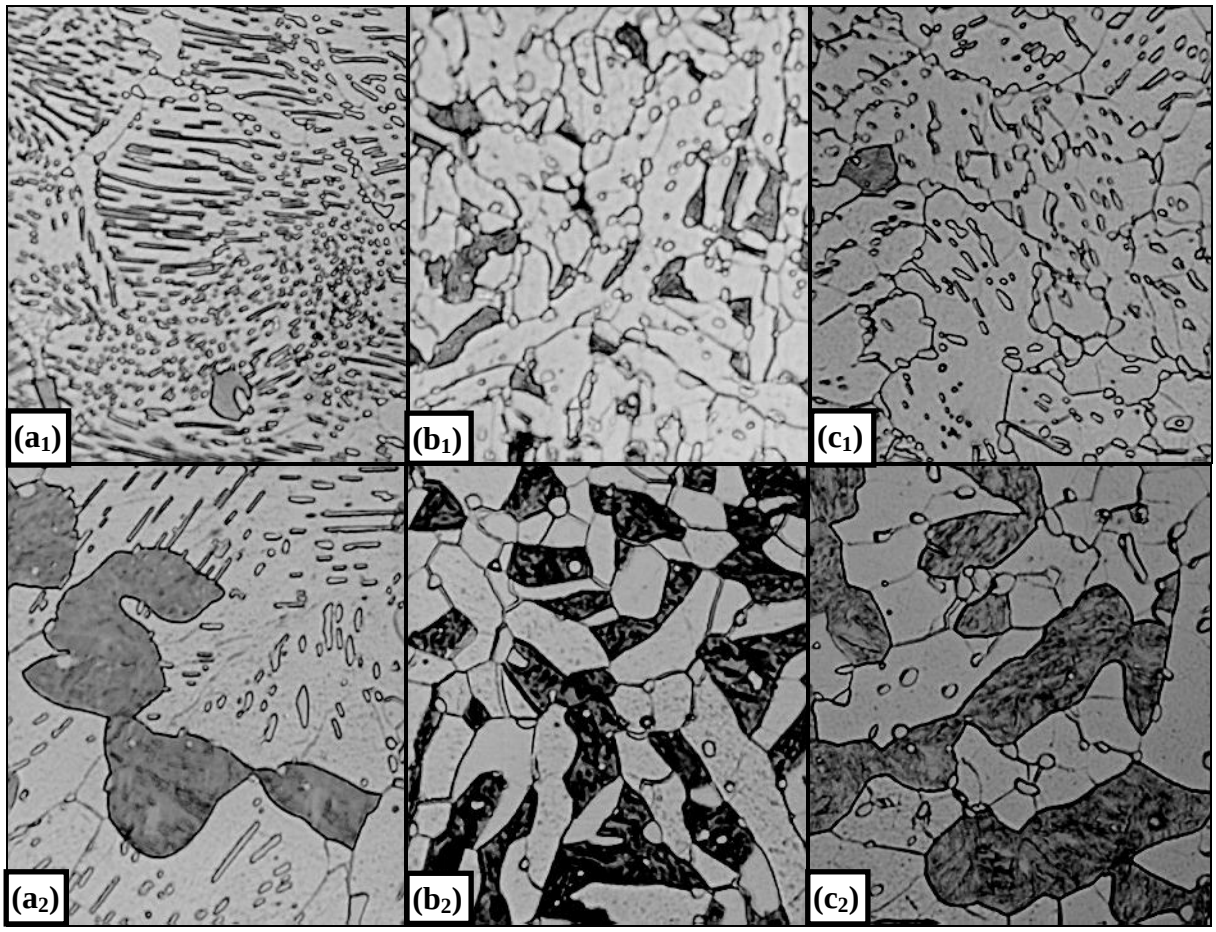

Figure 4.2 Microstructures obtained during austenitisation of pearlitic (B), tempered martensite (D) and intercritical (F) structures at 755°C (Ac_1 temperature plus 10°C) for 4hr (a_1, b_1, c_1), and 192hr (a_2, b_2, c_2). 1,200x magnification. 2% Nital etch.

Figure 4.2 illustrates the microstructures produced after austenitising the pearlitic, tempered martensite, and intercritical structures for 4hr and 192hr at 755°C (10°C above the Ac_1 temperature). After 4hr, significant austenite formation has occurred in the tempered martensite structure, b_1, but only the occasional austenite grain is evident in the pearlitic, a_1, and intercritical, c_1, structures. Austenite nucleation occurs at cementite particles located on ferrite grain boundary triple points for the tempered martensite and intercritical structures, and at the interface between ferrite grain boundaries and cementite particles for the pearlitic structure[6]. Considerable spheroidisation of the cementite occurred in the pearlitic structure.

After 192hr the transformation to the equilibrium microstructures is more advanced. A larger austenite volume fraction is observed for all three structures, a_2 to c_2, with coarsening of the austenite grains. Spheroidisation of the cementite from the pearlitic structure, a_2, has increased, although a reasonable number of elongated cementite particles remain. The presence of cementite particles in all three structures after 192hr is indicative of a three phase (austenite, ferrite, and cementite) region, instead of the austenite/ferrite dual phase region normally associated with heat treating at an intercritical temperature. The width of this three phase region (eutectoid gap) increases with increasing silicon and manganese contents[8]. For the steel used in these experiments this eutectoid gap appears to be about 35^{o}C, with some undissolved carbides present after 192hr at 780^{o}C.

The austenite transformation is more rapid at the Ac_3 temperature of 820^{o}C. After 15min the pearlitic microstructure is almost fully austenitic, Figure 4.3(a), with only some isolated ferrite particles present. The transformation is slower for the other two structures, with an appreciable fraction of ferrite remaining after 15min.

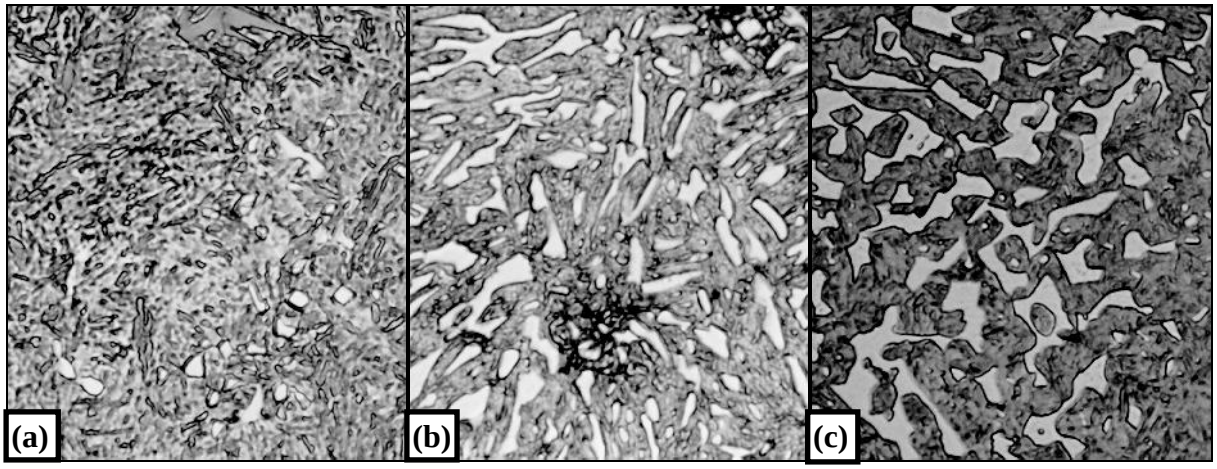

Figure 4.3 Microstructures obtained after austenitising for 15min at 820^{o}C (Ac_3 temperature) for (a) pearlitic (B), (b) tempered martensite (structure D), and (c) intercritical (F) initial structures. 1,200x magnification. 2% Nital etch.

4.3 Kinetics of austenite formation

The transformation of different initial structures to austenite at 755, 780 and 820^{o}C are illustrated in Figure 4.4. At 755^{o}C, Figure 4.4(a), a significant incubation time exists until austenite formation commences. Austenite formation is first observed after approximately 1hr for the tempered martensite structure, 2hr for the pearlitic structure, and 4hr for the intercritical structure. The tempered martensite structure transforms more rapidly, forming 24% austenite after 192hr compared with only 15% for the pearlitic structure. Although the intercritical structure exhibits a longer incubation period, once austenite nucleation occurs the austenite growth rate is faster than for other two structures, with 28% austenite present after 192hr.

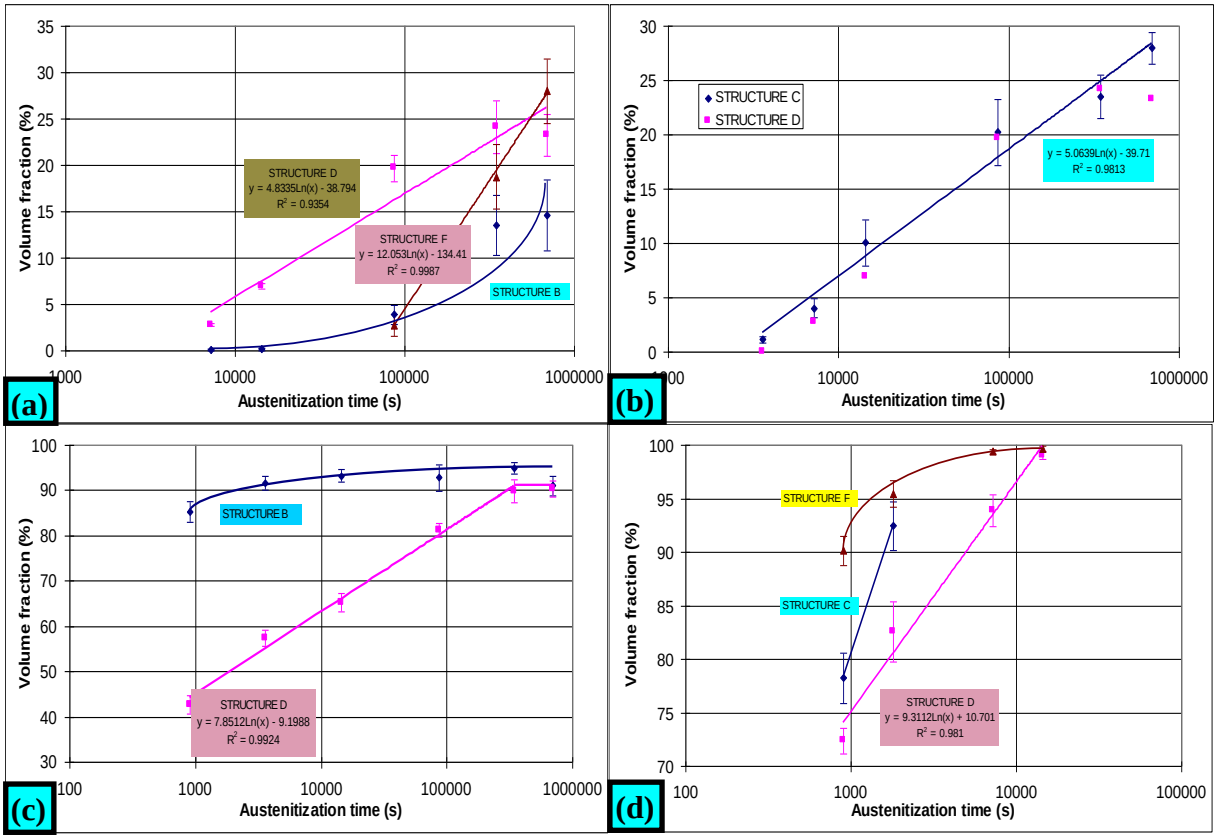

Figure 4.4 Change in austenite volume fraction for (a) pearlitic (B), tempered martensite (D) and intercritical (F) structures at 755°C, (b) tempered martensite (C & D) structures at 755°C, (c) pearlitic (B) and tempered martensite (D) structures at 780°C, and (d) tempered martensite (C & D) and intercritical (F) structures at 820°C.

The difference in both ferrite grain size and cementite particle size had no influence on the kinetics of austenitisation, Figure 4.4(b), of the tempered martensite structures at 755°C. The pearlitic structures also exhibited one line for the austenite growth, Figure 4.5(a), illustrating that the coarsening of the austenite grains is independent of the pearlite interlamellar spacing. However, the tempered martensite (D) structure was found to coarsen more rapidly than the finer (C) structure, as shown in Figure 4.5(b).

The change in cementite volume fraction during austenitisation at 755°C shows that the cementite dissolution for the tempered martensite structures is initially more rapid than that for the intercritical structure, Figure 4.6(a), with significant cementite dissolution for the intercritical structure not obvious until 24hr. However, the cementite volume fraction after 192hr is similar for all three structures, at approximately 3%. Figure 4.6(b) indicates that the coarsening kinetics for the average equivalent area cementite diameter are similar for both tempered martensite structures, and the intercritical structure. The two trend lines are parallel, with the separation due to the finer tempered martensite structure having a smaller initial average equivalent area diameter than the coarser tempered martensite and intercritical structures.

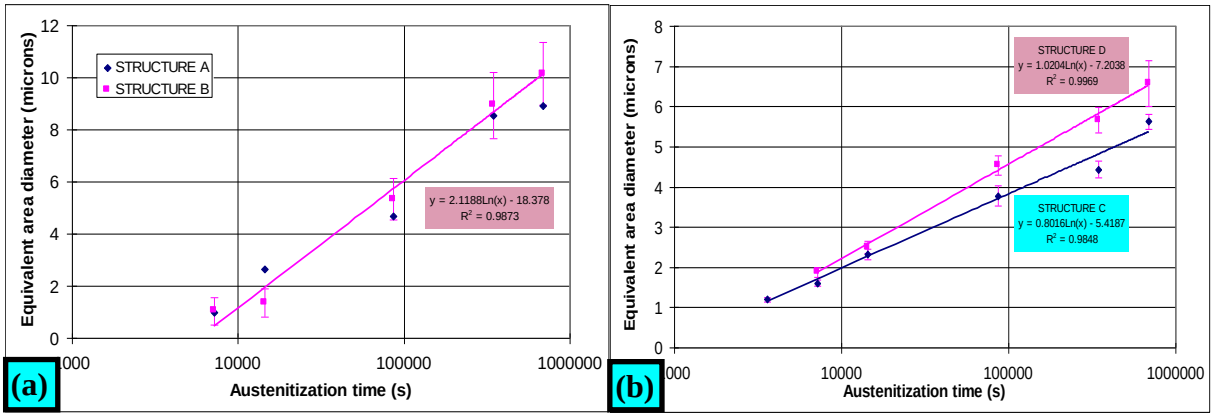

Figure 4.5 Change in austenite grain average equivalent area diameter during austenitisation of (a) pearlitic structures, and (b) tempered martensite structures.

Austenite formation at 780°C, Figure 4.4(c), is more rapid than at 755°C, with the pearlitic structure transforming to 85% austenite, and the tempered martensite structure to approximately half this volume, after 15min. The pearlitic structure now transforms more rapidly to austenite than the tempered martensite structure, which is in marked contrast to the situation at 755°C. Similarly, at the Ac_3 temperature of 820°C, the two pearlitic structures have transformed to 100% austenite after 15min, while the coarser tempered martensite structure (D) does not fully transform to austenite until 4 hours have elapsed, Figure 4.4(d). The finer tempered martensite structure (C) transforms more rapidly than the coarser structure, while the intercritical structure transforms at an intermediate rate between the pearlitic and tempered martensite structures.

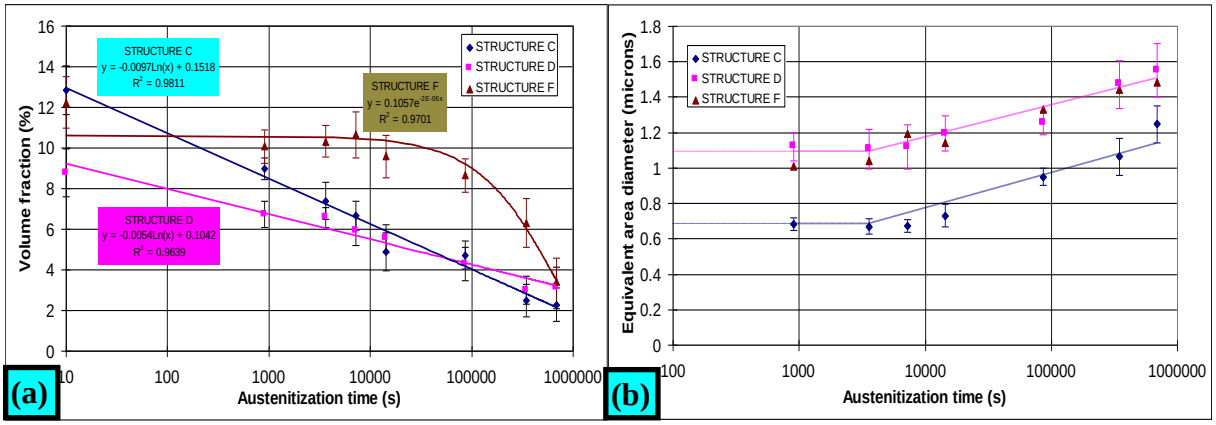

Figure 4.6 (a) Change in cementite volume fraction during austenitisation of tempered martensite (C & D) and intercritical (F) structures at 755°C, and (b) change in average equivalent area diameter of cementite during austenitisation of tempered martensite (C & D) and intercritical (F) structures at 755°C.

4.4 Alloy element partitioning

X-ray analysis results for 755°C, Figure 4.7(a) to (c), illustrate the partitioning of alloying elements that occurred between the austenite, ferrite, and cementite phases. For each phase, the silicon content of the tempered martensite and intercritical structures are similar. Relative to the bulk steel content of 1.95%Si, the austenite phase contains approximately 1.4%Si, ferrite 1.9%Si, and cementite 0.2%Si. These values remain constant throughout the austenitisation

process. From a bulk steel manganese content of 0.79%, both structures contain about 0.6%Mn in the ferrite. Differences exist between the two structures in the austenite and cementite phases, with the tempered martensite structure comprising 1.4% and 3.7%Mn in austenite and cementite respectively, relative to the lower contents of 1.2% and 3.1%Mn for the intercritical structure. Both have the bulk steel chromium content of 0.19% in the austenite and ferrite phases. In the cementite, the spheroidal cementite structure initially contains approximately 0.3% more Cr, 1.3% versus 1.0%, but after 192hr both structures contain 1.7%Cr.

During austenitisation at 820°C, Figure 4.7(d), the partitioning of alloying elements between the various phases is similar for both structures, although the ferrite silicon content is higher for the intercritical structure.

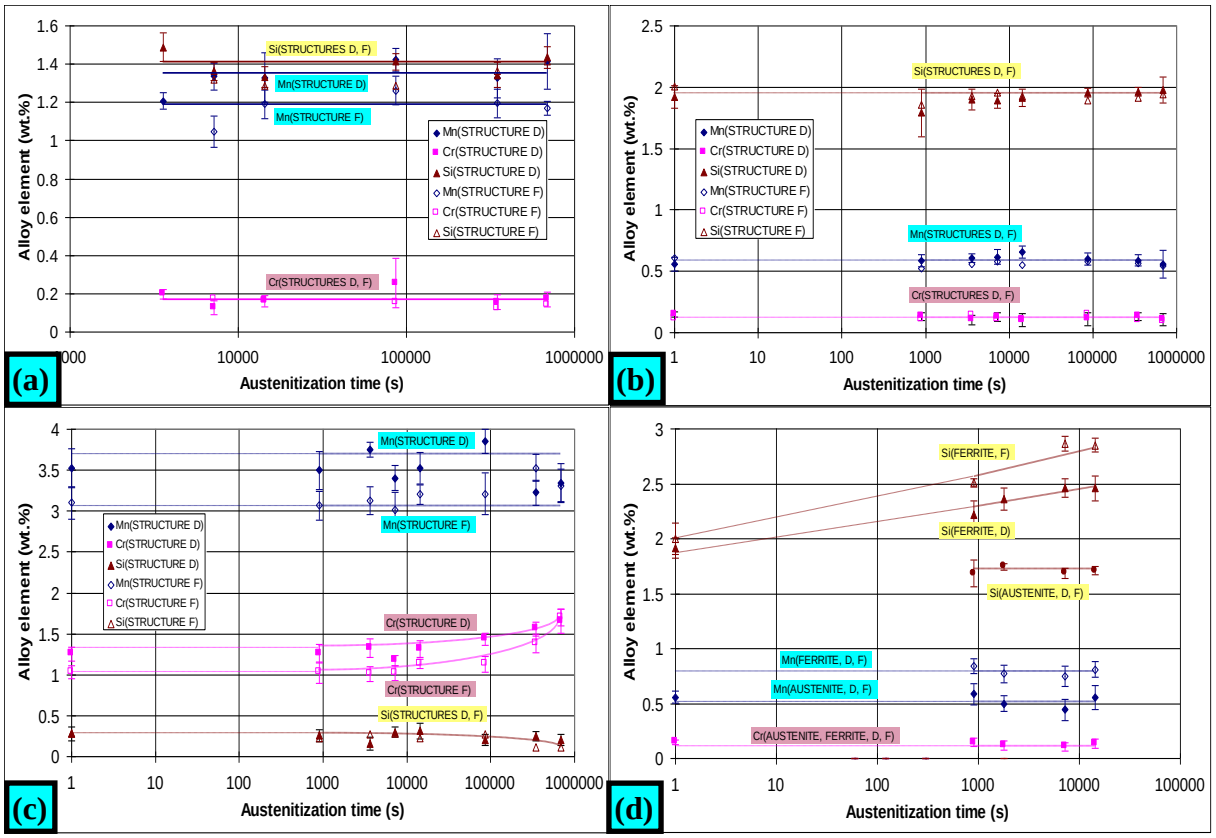

Figure 4.7 Phase alloy element concentrations during austenitisation of tempered martensite and intercritical structures. (a) Austenite at 755°C, (b) ferrite at 755°C, (c) cementite at 755°C, and (d) austenite and ferrite at 820°C.

5 Discussion

The kinetics, Figure 4.4, illustrate the long heat treatment times required for complete austenization. This is particularly evident at 755°C, where the austenite fraction for the pearlitic structures is just over half that of the tempered martensite and intercritical structures, indicating that equilibrium conditions were not achieved during these experiments. This contrasts with a pearlitic 0.96%C plain carbon steel which required approximately 15min[6] to complete the austenite transformation at 735°C (10°C above the Ac_1 temperature), while a pearlitic 0.96%C, 0.24%Si, 0.24%Mn steel required 400min at the same temperature.

The observed slower austenite formation is due to the increased Si and Mn concentrations.

Austenitisation commences with an austenite nodule nucleating at the ferrite/cementite boundary, Figure 5.1(a), and forming a shell around the cementite particle when it starts to dissociate. The subsequent growth of the austenite shell requires carbon diffusion from the dissociating cementite particle to the austenite/ferrite boundary, with the growth rate dependent on the carbon gradient across the austenite shell, Figure 5.1(b).

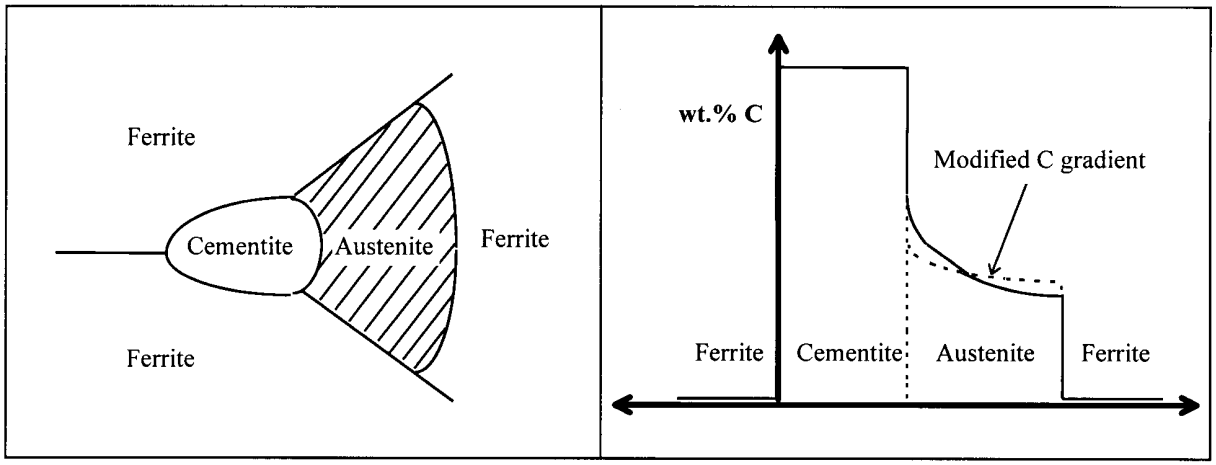

Figure 5.1 Schematic illustration of austenite growth. (a) austenite formation at a cementite particle, and (b) carbon concentration profile across the austenite growth area.

At the beginning of austenitisation, the austenite shell inherits the alloying element distribution of the initial structure[3]. Consequently, the higher Mn and Cr, and lower Si concentrations at the cementite/austenite boundary, are considered to result in a decrease in the carbon activity at this interface. At the austenite/ferrite boundary, lower Mn and Cr, but higher Si concentrations exist, raising the carbon activity at this interface. This serves to lower the driving force for carbon diffusion across the growing austenite grain (dashed line of Figure 5.1(b)), and hence reduces the rate of austenite formation.

The faster austenite formation of the tempered martensite structures at 755^{o}C compared to the pearlitic structures, Figure 4.4(a), is due to the considerably greater number of potential nucleation sites present. After 4hr, the tempered martensite structure has approximately 13,500 austenite grains per mm^2, compared with 400 grains per mm^2 for the pearlitic structure. The longer austenite incubation time for the intercritical structure arises because of the initial location of the majority of the cementite particles within the ferrite grains. As the energy required to nucleate austenite at cementite particles within a ferrite grain is greater than at a ferrite grain boundary[9], very few potential austenite nucleation sites exist for the intercritical structure, and so austenite formation is almost non-existent. However, after 4hr, considerable recrystallisation of this structure has occurred, Figure 4.2(b_1), with the majority of the cementite particles now being situated on the ferrite grain boundaries.

The rate of austenite formation then becomes more rapid than that of the tempered martensite structure, Figure 4.4(a). This more rapid austenite growth rate of the intercritical structure, once sufficient nucleation sites are available, is a consequence of the cementite particles initially being located within the ferrite grains. As the diffusion of alloying elements is greater along the ferrite grain boundaries than within the ferrite grains, the tempered martensite structure with the cementite particles located on the ferrite grain boundaries will involve a greater redistribution of alloying elements than the intercritical structure. This in turn lowers the

driving force for austenite growth, Figure 5.1, more in the tempered martensite structures. The alloy element partitioning results confirm this, with greater Mn and Cr concentrations in the cementite particles for the spheroidal cementite structures, Figure 4.7(c), and a higher Mn concentration in the austenite formed, Figure 4.7(a).

The coarseness of the pearlitic and tempered martensite structures at 755^{o}C, Figure 4.4(b), had no influence on the rate of austenite growth. The austenite grain coarsening of the pearlitic structures, Figure 4.5(a), were independent of interlamellar spacing. It should be noted that both structures were heat treated to produce the same prior grain size. The coarser austenite grain size in the tempered martensite structure (D), Figure 4.5(b), arises for the larger initial ferrite grain size. These results illustrate that the austenite grain shape is determined by the initial structure into which it grows. The pearlitic and intercritical structures with equiaxed initial grain structures yield equiaxed austenite growth at 755^{o}C, while the acicular ferrite structure of the tempered martensite structures result in an acicular austenite grain structure, Figure 4.2.

Austenitising at 780^{o}C resulted in a more rapid formation of austenite in the pearlitic structure relative to the tempered martensite structure, Figure 4.4(c), which is opposite to the situation at 755^{o}C. This suggests that the austenite growth rate is no longer controlled by the number of austenite nucleation sites, or by carbon diffusion through the austenite from the cementite particle to the austenite/ferrite interface, but now by an interface reaction at the cementite/austenite boundary. The pearlitic structure, with the lamellar cementite having a greater surface area to volume ratio than the spheroidal cementite of the tempered martensite structures, disintegrates more rapidly, yielding a greater austenite formation rate.

The same situation is evident at 820^{o}C, Figure 4.4(d), where the pearlitic structures transform more rapidly to austenite than the tempered martensite structures. The interface mechanism is further supported by the finer tempered martensite structure transforming more rapidly than the coarser structure.

6 Conclusion

The austenitisation processes in a high silicon steel at temperatures above the Ac_1 temperature for different types of initial structures was found to be considerably slower than for steels with lower silicon and manganese contents, and also strongly dependent on the initial structure. The partitioning of the alloying elements serves to lower the driving force for austenite growth once austenite is nucleated; the greater this partitioning, the lower the austenite growth rate.

Two different mechanisms of austenite growth were evident. At 755^{o}C, the austenite transformation was dependent on the number of nucleation sites, with the austenite growth rate controlled by the driving force for carbon diffusion across the austenite grains. However, for temperatures of 780^{o}C and above, a change to interface controlled austenite growth was observed.

7 Acknowledgments

I would like to gratefully acknowledge and thank BHP New Zealand Steel for their financial support which has made this paper possible. Furthermore, I would like to thank the Department of Mechanical Engineering staff at the University of Canterbury for their support.

8 References

1) Unpublished research, Bott, C.; Postgraduate student, University of Canterbury.
2) "A quantitative study of the formation of austenite and the solution of cementite at different austenitising temperatures for a 1.27% carbon steel", Molinder, G.; Acta Metallurgia, Volume 4, November 1956, 565-571.
3) "Effect of alloying elements on the formation of austenite and dissolution of cementite", Hillert, M.; Nilsson, K.; Torndahl, L. E.; Journal of The Iron and Steel Institute, January 1971, 49-66.
4) "The transformation to austenite in a fine grained tool steel", Dirnfeld, S. F.; Korevaar, B. M.; Van't Spijker, F.; Metallurgical Transactions, Volume 5, June 1974, 1437- 1444.
5) "Experimental study of the austenitisation process of hypereutectoid steel alloyed with small amounts of silicon, manganese and chromium, and with an initial structure of globular cementite in a ferrite matrix", Karmazin, L; Materials Science and Engineering, 1991, 71-77.
6) Formation of austenite from ferrite and ferrite-carbide aggregates", Speich, G. R.; Szirmae, A.; Transactions of the Metallurgical Society of AIME, Volume 245, May 1969, 1063-1074.
7) "The growth of austenite as related to prior structure", Nehrenberg, A. E.; Journal of Metals, Transactions AIME, Volume 188, January 1950, 162-174.
8) "Phase transformations of low-alloy steel at temperatures inside the eutectoid gap", Karmazin, L.; Materials Science and Engineering, 1988, 201-206.
9) "Formation of austenite in 1.5pct Mn steels", Garcia, C.I.; Deardo, A.J.; Metallurgical Transactions, Volume 12A, March 1981, 521-530.

Appendix L-(iii) IPENZ97b

DECARBURISATION BEHAVIOUR OF HIGH SILICON SPRING STEELS

CHRIS MARDON[1], JOHN SMAILL[2], LINCOLN SELL[3]

1 Abstract

"Engineering our nations future" demands new engineering materials, and improved performance from the existing materials. Of particular interest are automobile coil springs, which suffer from surface decarburisation during manufacture. This decarburisation is considered to be responsible for a high proportion of premature spring failures. Consequently, this paper investigates the decarburisation of four spring steels.

2 Introduction

Decarburisation of steel is a phenomena involving carbon removal which often occurs when the steel is heat treated. The extent of this decarburisation depends on the steel carbon and alloy content, the heat treatment time and temperature, and the atmosphere. Surface decarburisation occurs during the manufacture of automobile suspension coil springs when the bar stock is hot rolled in the steel mill, during the heating and hot shaping of the springs at high temperatures, and when the springs are tempered. Any decarburisation greatly reduces the fatigue life of the springs, with 0.19mm surface decarburisation reducing the fatigue life of a SUP6 spring to half that of the non-decarburised spring[1] . This reduction in fatigue life arises from the lower hardness and greater surface roughness of the decarburised layer.

The 1970's saw the development of new spring steels in response to the demand for more fuel efficient vehicles. This necessitated lighter automobiles, and was partly attained by reducing the weight of the suspension springs. However utilisation of lighter springs required the springs to operate at higher working stresses[2], which caused the phenomena of suspension spring sag to become more prevalent[3]. Consequently the new spring steels incorporated higher carbon and silicon contents which improved the sag resistance due to a finer carbide size and distribution[4] that more effectively resists the dislocation motion causing sag.

The surface decarburisation of high silicon spring steels has been investigated in limited detail, despite its effect on the fatigue and sag properties of automobile coil suspension springs. Instead attempts have focussed on minimising decarburisation of these steels by reducing the heat treatment temperatures and times. Current spring production techniques necessitate removal of the decarburised surface layer from the bar stock by a peeling operation following hot rolling in the steel mill, and shot peening of the springs following the tempering operation. This paper examines the decarburisation of four spring steels with silicon contents ranging from 1.03 to 3.57wt.%. Heat treatments were undertaken in an atmosphere of wet hydrogen at the steels' respective Ac_3 temperatures for 5min to 24hr. The decarburisation

1 Postgraduate Student, Department of Mechanical Engineering, University of Canterbury.
2 Senior Lecturer, Department of Mechanical Engineering, University of Canterbury.
3 Undergraduate Student, Department of Mechanical Engineering, University of Canterbury.

behaviour of the four steels is detailed, in conjunction with the influence of alloy content and oxidation on the decarburisation.

3 Experimental investigation

The decarburisation was investigated for four steels with the chemical analyses listed in Table 3.1. To obtain a uniform microstructure, 14 and 16mm diameter bar stock was austenitised in a Nabertherm R7019 tube furnace with an inert argon atmosphere for 12hr at 900^{o}C, then air cooled to produce pearlitic structures. 5mm diameter by 10mm test specimens were machined, austenitised in the tube furnace for 24hr at various temperatures, then water quenched to determine the Ac_3 transformation temperatures, Table 3.1.

Description	C (wt.%)	Si (wt.%)	Mn (wt.%)	Cr (wt.%)	V (wt.%)	Nb (wt.%)	Al (wt.%)	Cu (wt.%)	Ac_3 temp. (^{o}C)
1% Silicon	0.38	1.03	0.18	0.26	0.003	-	0.15	0.31	830
SUP7	0.60	1.94	0.77	0.19	0.005	-	0.033	0.01	820
SUP7NV	0.62	2.11	0.85	0.17	0.173	0.15	0.011	0.11	820
3% Silicon	0.47	3.57	0.77	0.26	0.015	-	0.073	0.35	945

Table 3.1 Composition and Ac_3 transformation temperatures of the four spring steels.

Specimens of 8mm diameter by 15mm with a ground surface finish were heat treated in an atmosphere of wet hydrogen comprising 5% water vapour, which was chosen to accelerate the decarburisation. Decarburisation occurred predominantly by reactions 3.1 and 3.2[5] . Times ranging from 5min to 24hr were investigated, with the specimens water quenched at the conclusion of testing. To simplify the decarburisation measurements, the heat treatments were undertaken at the respective Ac_3 temperatures of the four steels. Carbon removal at the Ac_3 temperature theoretically results in the formation of a surface ferrite layer on an initially austenitic structure. Consequently, the total decarburisation depth is the width of the ferrite layer which is easily measured. Once quenched, the specimens were mounted, sectioned, ground and polished to a final 1micron diamond finish, and etched in 2% Nital. Eight measurements of the free ferrite decarburisation depths were made at approximately equally spaced positions around the test specimen.

$$C_{(\text{in steel})} + H_2O_{(g)} = CO_{(g)} + H_{2(g)} \quad \text{- (3.1)}$$

$$C_{(\text{in steel})} + 2H_{2(g)} = CH_{4(g)} \quad \text{- (3.2)}$$

4 Results

Figure 4.1 illustrates the appearance of the SUP7, SUP7NV, and 3% Silicon steels decarburised for 24hr at their respective Ac_3 temperatures. Considerable decarburisation occurred in both the 1% Silicon and SUP7, Figures 4.1(a), steels, with a sharp interface separating the ferrite surface and austenite core. This interface was present after only 5min for both steels. The depth of this ferrite layer as a function of time, Figure 4.2, shows that the 1% Silicon steel decarburised more deeply than SUP7. The decarburisation behaviour of these two steels was modelled by a diffusion process, where the effective diffusion coefficient for carbon in ferrite is given by[6] :

$$D_{effective} = \frac{(C_i - 2/3C_B)}{2} \cdot \frac{x^2}{tC_B}, \quad \text{- (4.1)}$$

where $D_{effective}$ = effective carbon diffusion coefficient in ferrite (cm^2/s);
C_i = initial steel carbon content (wt.%);
C_B = saturation ferrite carbon content (wt.%);
x = free ferrite depth (cm); and
t = time (s).

C_B is approximately equal to 0.03 and 0.05wt.%Si respectively for 1% and 2% silicon, SUP7, steels[7]. The effective diffusion coefficients for carbon in ferrite at each heat treatment duration are listed in Table 4.1, with the 1% Silicon steel having a significantly higher mean effective diffusion coefficient than SUP7, $1x10^{-6}cm^2/s$ versus $0.4x10^{-6}cm^2/s$.

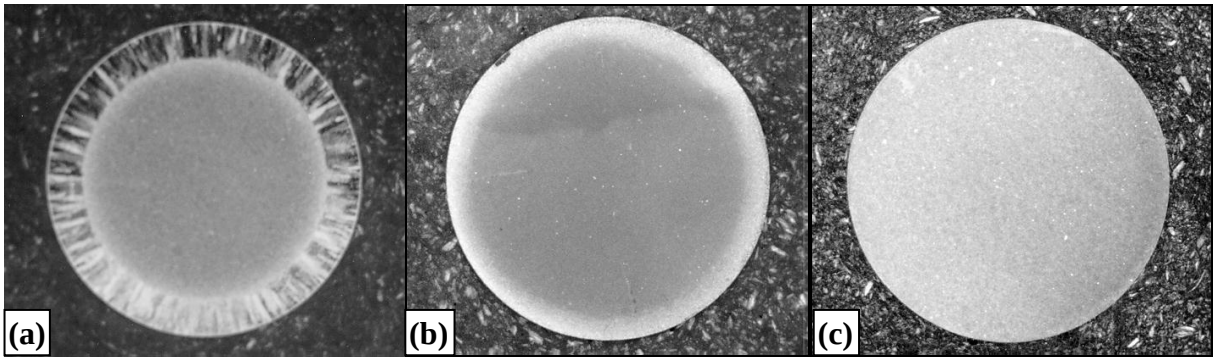

Figure 4.1 Decarburisation structures produced by 24hr heat treatments at the Ac_3 temperatures for (a) SUP7 at 820°C, (b) SUP7NV at 820°C, and (c) 3% Silicon at 945°C. 8x magnification. 2% Nital. p_{H2O}/p_{H2}=0.05.

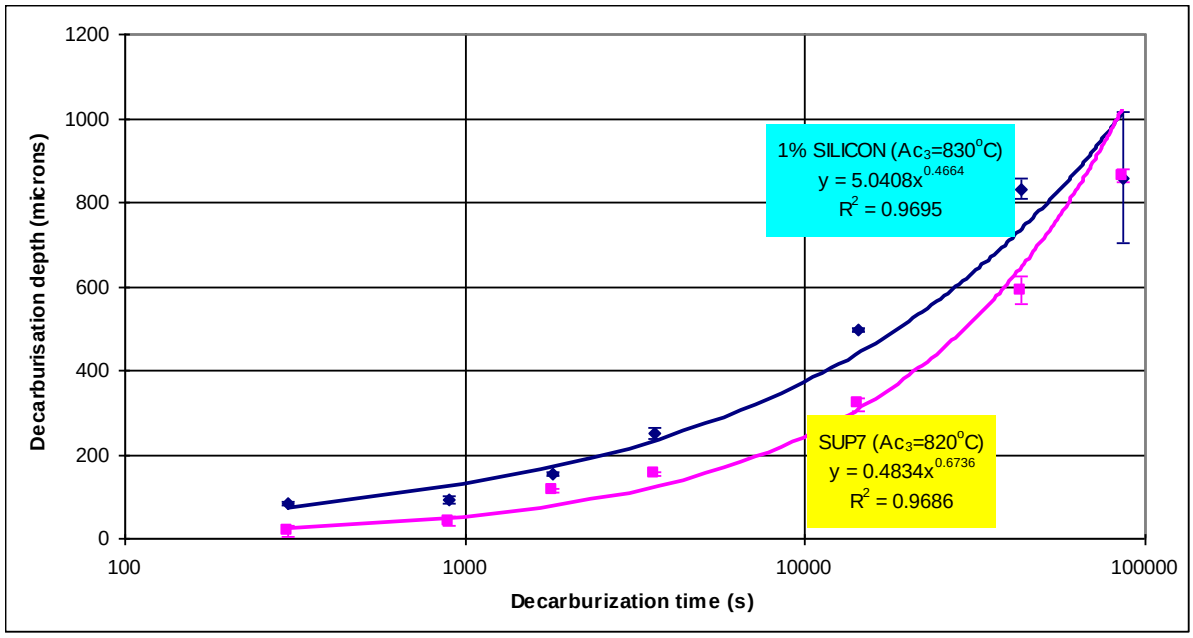

Figure 4.2 Free ferrite decarburisation depths for the 1% Silicon and SUP7 steels decarburised at their respective Ac_3 temperatures.

The decarburisation behaviour of SUP7NV, Figures 4.1(b), differs considerably from that of SUP7, with decarburisation occurring, but not the sharply defined ferrite/austenite structure of SUP7. A comparison of the decarburised microstructures of SUP7 and SUP7NV after 1hr is presented in Figure 4.3. SUP7, Figure 4.3(a), exhibits a sharp ferrite/austenite interface, with long ferrite columnar grains perpendicular to the surface, while SUP7NV has a significantly smaller ferrite region comprising equiaxed ferrite grains, Figure 4.3(b). The free ferrite and austenite regions of SUP7NV are also separated by a substantial mixed ferrite/austenite layer. The 3% Silicon steel exhibits an even more intriguing decarburisation behaviour, with no decarburisation despite heat treating for 24hr in wet hydrogen at 945^{o}C, Figure 4.1(c).

	$D_{effective}$ ($x10^{-6}cm^2/s$)							
DESCRIPTION	**5min**	**15min**	**30min**	**1hr**	**4hr**	**12hr**	**24hr**	**Mean $D_{effective}$ ($x10^{-6}cm^2/s$)**
1% Silicon	1.45	0.56	0.79	1.05	1.03	0.96	0.51	1.0
SUP7	0.06	0.11	0.43	0.39	0.42	0.49	0.52	0.4

Table 4.1 Effective ferrite carbon diffusion coefficients for 1% Silicon and SUP7 steels.

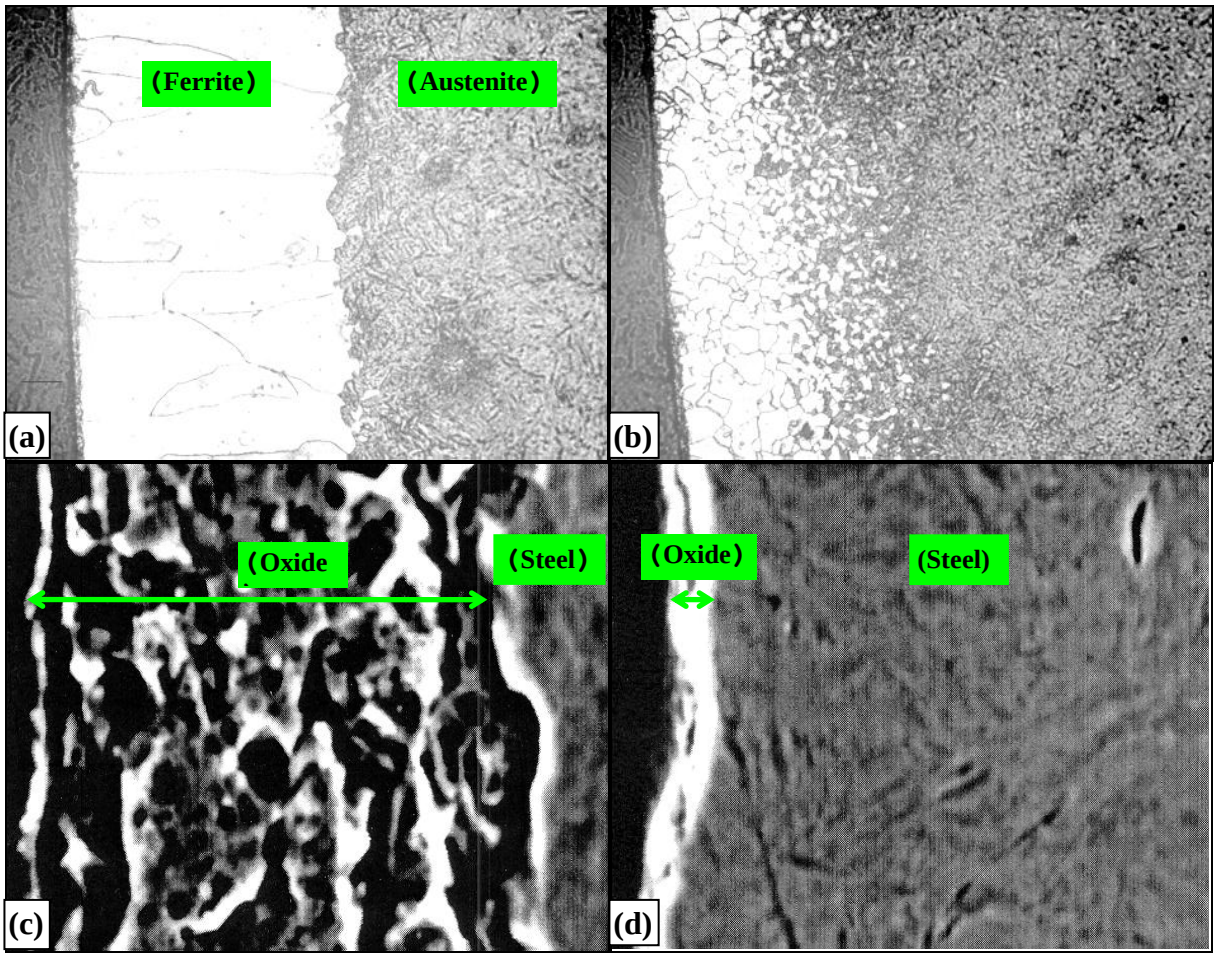

Figure 4.3 Decarburisation structures after 1hr heat treatments at the Ac_3 temperature of 820^{o}C for (a) SUP7, and (b) SUP7NV. 240x magnification. Oxidation structures after 24hr heat treatments at the Ac_3 temperature for (c) SUP7 at 820^{o}C, and (d) 3% Silicon at 945^{o}C. 5,000x magnification. 2% Nital. p_{H2O}/p_{H2}=0.05.

The surface oxide structures formed after decarburising for 24hr are illustrated in Figure 4.3. A relatively thick porous structure is evident for the 1% Silicon, SUP7, Figure 4.4(c), and SUP7NV steels, while a much thinner dense structure formed on the 3% Silicon steel, Figure 4.3(d). The 3% Silicon steel exhibited a bright metallic surface layer after being decarburised, while the other three steels had a dull grey surface.

5 Discussion

Of the four steels investigated, the 1% Silicon and SUP7 steels decarburised well with the formation of a uniform surface ferrite layer. Modelling of this decarburisation with a diffusion process yielded a mean effective diffusion coefficient for carbon in ferrite of $1x10^{-6}cm^2/s$ for the 1% Silicon steel, and $0.4x10^{-6}cm^2/s$ for SUP7. The higher alloy content of SUP7 relative to the 1% Silicon steel lowers the ferrite carbon diffusivity[8], while the thicker oxide structure results in longer diffusion paths for carbon. Consequently, decarburisation is impeded more for SUP7 than the 1% Silicon steel. Both values are considerably lower than the value of approximately $4x10^{-6}cm^2/s$ for Fe-C and Fe-C-Si steels between 820 to 830^oC[6].

Despite having similar alloy compositions, the decarburisation behaviour of SUP7 and SUP7NV differ, with SUP7NV decarburising to a lesser depth. This could be due to the higher vanadium and niobium contents of SUP7NV forming vanadium and niobium carbides which pin the surface ferrite grain boundaries formed during the carbon removal. This would prevent the formation of the long ferrite columnar grains growing directionally from the surface inward. The resulting equiaxed structure does not possess the direct path for carbon transport to the surface that the columnar structure does, effectively lowering the carbon diffusivity in ferrite. Consequently, decarburisation becomes more significant in the austenite, resulting in a mixed ferrite/austenite region separating the ferritic surface and austenitic core for SUP7NV. No decarburisation occurred for the 3% Silicon steel. Similar decarburisation behaviour occurs with Fe-Si steels due to a change in oxidation behaviour[5]. Below about 2wt.%Si, a thick porous oxide structure forms, but only impedes the decarburisation to a limited degree. However, at about 3wt.%Si, a thin dense oxide structure forms which strongly impedes the decarburisation. It appears that a thin dense oxide layer has formed on the 3% Silicon steel, preventing the decarburisation.

The intriguing feature of the decarburisation inhibition for the 3% Silicon steel is that although a silicon content of 2.5wt.% was found to be the optimum value for sag resistance[9], a silicon content of 2wt.% is used to reduce the decarburisation**.** However, an increase in silicon content from 1.94wt.% for SUP7 to 3.57wt.% for the 3% Silicon steel involved a change from a steel which decarburised easily to one that did not. This suggests some interesting possibilities for automobile coil suspension springs. Instead of utilising a silicon content lower than the optimum value for sag to reduce the decarburisation, the silicon content could instead be increased to somewhere between 2.5 and 3.57wt.% to eliminate the decarburisation. This would allow the spring manufacture to be streamlined, where the peeling of the bar stock and shot peening operations could be eliminated. With decarburisation less prevalent, greater heat treatment flexibility would be possible during spring manufacture.

To fully develop these possibilities however, it is necessary to obtain a more complete description of the decarburisation of high silicon spring steels. This involves decarburisation in atmospheres comprising different water contents over a range of temperatures, and for a variety of lamellar and spheroidal cementite initial structures.

6 Conclusion

The decarburisation behaviour was investigated for four high silicon spring steels ranging from 1.03 to 3.57wt.%Si that were heat treated at their respective Ac_3 temperatures in an atmosphere of wet hydrogen. The 1% Silicon and SUP7 steels decarburised with a surface ferrite columnar grain structure separated from the austenite core by a sharply defined interface. A mean effective diffusion coefficient for carbon in ferrite of approximately $1x10^{-6}$ and $0.4x10^{-6}cm^2/s$ were calculated for the 1% Silicon and SUP7 steels respectively. Both values are significantly lower than the coefficient of carbon diffusion in ferrite for Fe-C and Fe-Si-C steels, $4x10^{-6}cm^2/s$. This is attributable to the alloying content of the two steels, and the longer carbon diffusion paths through the porous surface oxide structures. Both factors were more prevalent in SUP7, with the higher alloy content and thicker oxide structure contributing to the lower mean effective diffusion coefficient of SUP7.

Reduced decarburisation occurred for SUP7NV, which is considered to be due to vanadium and niobium carbides pinning the ferrite grain boundaries, thus preventing the formation of a columnar grain structure and the subsequent direct path for carbon transport to the surface. No decarburisation occurred for the 3% silicon steel due to the formation of a thin dense surface oxide structure which prevented carbon removal. Further experimentation is necessary to more fully describe the decarburisation behaviour of the high silicon spring steels, with the potential outcome being superior automobile coil suspension springs.

7 Acknowledgments

I would like to gratefully acknowledge and thank BHP New Zealand Steel for their financial support which has made this paper possible. Furthermore, I would like to thank the Department of Mechanical Engineering staff at the University of Canterbury for their support.

8 References

1) "The effect of shot peening to decarburised steel plate, Sato, S.; Inoue, K.; Ohno, A.; Proceedings 1st International Conference on Shot Peening, September 1981, 303-312.
2) "Precipitation-strengthened spring steel for automobile suspensions, Yamamoto, et al; Journal of Heat Treating, Number 3, Volume 3, June 1984, 220-227.
3) "Spring steel hysteresis", Brownrigg, A.; Sritheran, T.; Materials Forum, Number 1, Volume 10, 1987, 58-63.
4) SAE Paper 800480, Toto, H.J.; Driscall, E.R.; Kary, J.J.; 1980.
5) "About oxidation and decarburisation behaviour of Fe-Si alloys", Wiesner, U.; Neue Hutte, July 1986, 250-253.
6) The diffusivity and solubility of carbon in alpha-iron", Smith, R.P.; Transactions of the Metallurgical Society of AIME, Volume 224, February 1962, 105-111.
7) "Alloy phase diagrams", ASM Handbook Volume 3, ASM International, Materials Park Ohio, 1990.
8) "Diffusion processes in iron alloys", Krishtal, M.A.; Israel Program for Scientific Translations, Jerusalem, 1970.
9) "Parameters affecting sag resistance in spring steels, Assefpour-Dezfuly, M.; Metallurgical Transactions A, Volume 20A, October 1989, 1951-1959.

Appendix L-(iv) IPENZ98a

VARIABLE DECARBURISATION OF A SPRING STEEL

CHRIS MARDON[1], JOHN SMAILL[2]

1 Abstract

Preliminary heat treatments of a spring steel yielded deep and uniform decarburisation. However, a more rigorous investigation often resulted in considerable variation in decarburisation, despite apparently similar experimental conditions. This paper reports the investigation undertaken into the variable decarburisation of this spring steel, and discusses the implications of these findings.

2 Introduction

The development of modern automobile suspension springs in the 1970's was a consequence of the fuel crises, and the subsequent demand for lighter and hence more fuel efficient vehicles. This was achieved, in part, by the development of higher strength steels which yielded lighter suspension springs. However, the increased carbon and silicon content of these steels increased the susceptibly to surface decarburisation during the heat treatments used to manufacture the springs.

Decarburisation of a steel involves carbon removal, and often occurs when the steel is heat treated. The surrounding atmosphere reacts with the carbon in the steel to remove carbon as a gaseous product. Surface decarburisation occurs during the manufacture of automobile suspension coil springs when the bar stock is hot rolled in the steel mill, during the heating and hot shaping of the springs at high temperatures, and when the springs are tempered. The decarburised surface has a lower hardness which reduces the fatigue life of the springs, with 0.19mm surface decarburisation reducing the fatigue life of a SUP6 spring to half that of the non-decarburised spring**(1)**.

Despite its effect on the performance of coil suspension springs, very few studies have been undertaken into the surface decarburisation of high silicon spring steels. A recent paper investigated the decarburisation of four different steels with silicon contents of 1.03 to 3.57wt.% in an atmosphere comprising hydrogen and five percent water vapour**(2)**. Both the 1 and 2wt.% silicon steels exhibited uniform decarburisation for the shortest test duration of five minutes. However, no decarburisation was observed for the 3.57wt.% silicon steel even after a 24hr heat treatment, due to the formation of a thin dense surface oxide structure which prevented carbon removal.

SUP7, comprising 2wt.% silicon, is commonly used for the coil springs of modern automobiles. Consequently this paper presents a more detailed investigation undertaken into the decarburisation of SUP7. Heat treatments were undertaken at the Ac_3 temperature in atmospheres of wet hydrogen with two different water contents. Several initial structures were decarburised for test duration's of 15min to 24hr. The decarburisation behaviour of SUP7 is summarised, with the influence of various experimental parameters quantified.

1 Postgraduate Student, Department of Mechanical Engineering, University of Canterbury.

2 Senior Lecturer, Department of Mechanical Engineering, University of Canterbury.

3 Experimental investigation

3.1 Heat treatments

Decarburisation heat treatments were undertaken for SUP7 which comprises, by weight percent, 0.60% carbon, 1.94% silicon, 0.77% manganese, and 0.19% chromium. Five different types of initial structures were produced by the heat treatment regimes undertaken on 14mm diameter bar stock, as detailed in Table 3.1. Two structures comprising lamellar carbides were produced by the air and furnace cooling heat treatments of Table 3.1, with the furnace cooled structure coarser than that of the air cooled structure. The remaining three structures consisted of spheroidal cementite particles in a ferritic matrix. The two tempered martensite structures have elongated ferrite grain structures, with the majority of the cementite particles located on the ferrite grain boundaries. The 96hr tempered martensite structure has coarser ferrite grains and cementite particles than the 12hr tempered martensite structure. The third spheroidal cementite structure produced by the intercritical heat treatment differs from the two tempered martensite structures in that the ferrite grains are equiaxed, with the cementite particles located within the ferrite grain boundaries. The initial microstructures for the furnace cooled, 96hr tempered martensite, and intercritical structures are illustrated in Figure 3.1.

Table 3.1 Heat treatments used to produce the initial structures.

	HEAT TREATMENT	**DESCRIPTION**
A	12hr at 900^{o}C, furnace cooled to 825^{o}C in 20min, air cooled.	**Air cooled**
B	12hr at 900^{o}C, furnace cooled to 825^{o}C in 20min, furnace cooled at 25^{o}C/hr to 600^{o}C, furnace turned off and cooled to ambient.	**Furnace cooled**
C	12hr at 900^{o}C, water quenched. Reheated for 12hr at 735^{o}C, air cooled.	**12hr tempered martensite**
D	12hr at 900^{o}C, water quenched. Reheated for 96hr at 735^{o}C, air cooled.	**96hr tempered martensite**
F	12hr at 900^{o}C, air cooled. Reheated for 6hr at 735^{o}C, furnace heated to 780^{o}C, furnace cooled as rapidly as possible to 740^{o}C, held 18hr at 740^{o}C, furnace cooled at 2^{o}C/hr to 700^{o}C, air cooled.	**Intercritical**

Test specimens 5mm diameter by 15mm, ground to a fine surface finish, were machined from the 14mm diameter bar stock. Decarburisation heat treatments were undertaken for test duration's of 15min to 24hr at the Ac_3 temperature of 820°C[(3)]. Holding at the Ac_3 temperature eventually yields a fully austenitic structure. Carbon removal then results in the formation of a surface ferrite layer, and since the carbon diffusion through ferrite is significantly faster than through austenite, a well defined ferrite/austenite interface is maintained throughout the heat treatment. Consequently, the total decarburisation depth is the width of the ferrite layer, which is easily measured.

The heat treatments were undertaken in a Nabertherm R7019 tube furnace using wet hydrogen atmospheres comprising 5 and 25% water vapour respectively with a hydrogen flow rate of 500cm^3/min. The test specimens were inserted into the cold end of the furnace, with the ambient air atmosphere removed by flushing with argon. Once an inert argon atmosphere was established, the test specimens were inserted into the hot zone and annealed in argon for:

i) An interval of time sufficient for the specimens to heat to temperature;
ii) An interval of time corresponding to the heating time, and the time required for the initial structure to transform to 95% austenite, which requires 2hr[3].

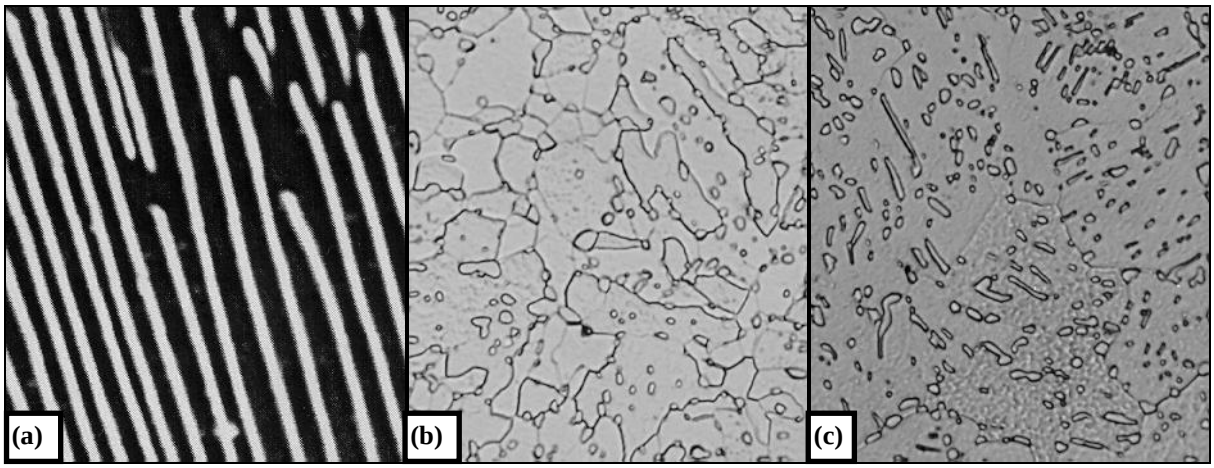

Figure 3.1 Initial structures produced by (a) furnace cooling, 10,000x, (b) tempering martensite for 96hr, 1,200x, and (c) an intercritical heat treatment, 1,200x. 2% Nital etch.

Following annealing in argon, the water/hydrogen decarburisation atmosphere was introduced. The heat treatment was concluded by removing the specimens from the hot zone and quenching them in water. Once quenched the specimens were mounted in bakelite, ground and polished, and etched in 2% Nital. Twelve measurements of the free ferrite decarburisation depths and oxidation layer thicknesses were made at approximately uniformly spaced locations around the test specimens. The width of the ferrite grains perpendicular to the surface of the decarburised ferrite layer was also measured.

3.2 Gas analysis

During the experimentation it became apparent that the amount of decarburisation occurring was dependent on the annealing duration in argon prior to introduction of the water/hydrogen atmosphere. Consequently further heat treatments were undertaken at 820°C on specimens with furnace cooled and 96hr tempered martensite initial structures in an atmosphere comprising hydrogen and 5% water vapour. With the test specimens in the cold end of the tube furnace, the water/hydrogen atmosphere was fully established before the specimens were inserted into the hot zone. This allowed the specimens to be exposed to the decarburisation atmosphere as they were heating. The exhaust gas leaving the tube furnace was continuously measured by carbon monoxide, carbon dioxide and methane infra-red gas analysers on the assumption that carbon removal occurred predominantly by reactions 3.1[4], 3.2[4] and 3.3[5].

$$C_{(\text{in steel})} + H_20_{(g)} = CO_{(g)} + H_{2(g)} \quad \text{-(3.1)}$$

$$C_{(\text{in steel})} + 2H_{2(g)} = CH_{4(g)} \quad \text{-(3.2)}$$

$$CO_{(g)} + H_20_{(g)} = CO_{2(g)} + H_{2(g)} \quad \text{-(3.3)}$$

The carbon monoxide, carbon dioxide and methane liberated over different time intervals was integrated to give the mass of carbon removed. Knowledge of the test specimen geometry then

allowed the free ferrite decarburisation depths to be calculated. These calculated values could then be compared to the values measured from the quenched specimens.

4 Results

Figure 4.1 illustrates the free ferrite decarburisation depths for furnace cooled structures as a function of time after heat treating in a hydrogen/5% water atmosphere, which equates to a p_{H_2O} / p_{H_2} ratio of 0.05. These results demonstrate that the amount of decarburisation was considerably less for specimens heated and austenitised for 2hr prior to the introduction of the decarburisation atmosphere compared with the specimens only heated before exposure to the decarburisation atmosphere. Only patchy decarburisation was evident after 4hr, compared with the uniform free ferrite layer which was present after 1hr for the specimens decarburised after heating without austenitisation. Figure 4.2 illustrates the microstructures of the specimens decarburised with heating, and with and without 2hr austenitisation. The decarburisation depths are less than that obtained for decarburisation of 8mm diameter by 15mm specimens[2], Figure 4.1, where uniform decarburisation was present after only 5min.

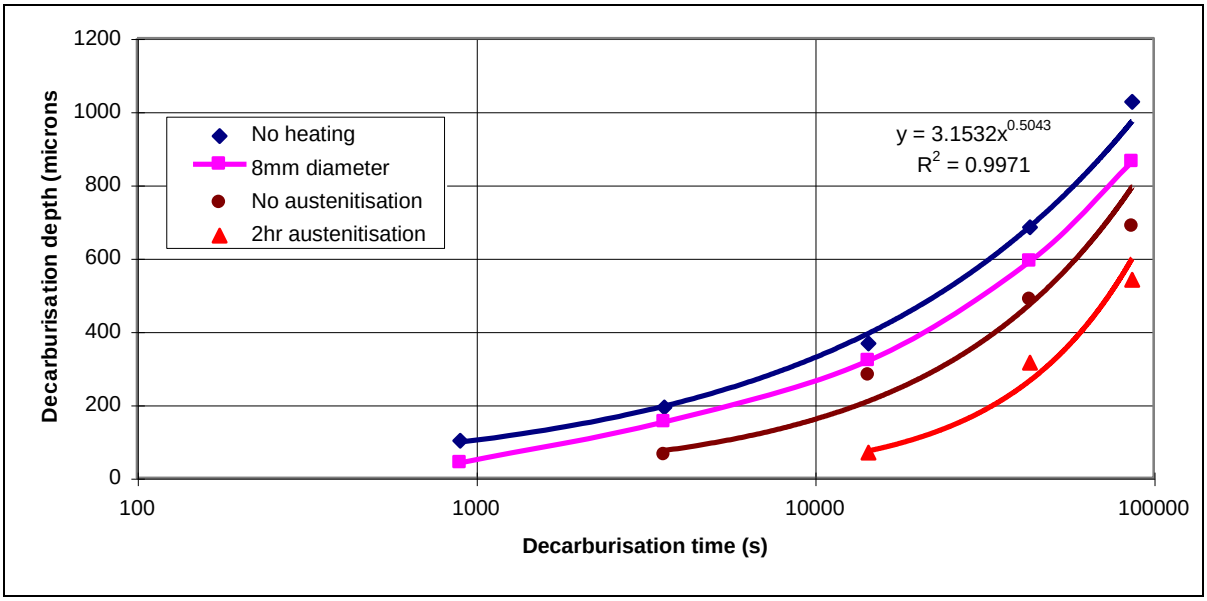

Figure 4.1 Free ferrite decarburisation depths for furnace cooled structures heat treated at 820°C, p_{H_2O} / p_{H_2} =0.05 with different heating and austenitisation durations.

Comparison of the free ferrite depths obtained after heating and 2hr austenitisation with different water contents illustrates that increasing the water content increases the amount of decarburisation, Figure 4.3. At a p_{H_2O} / p_{H_2} ratio of 0.25, uniform decarburisation is present after only 15min. Figure 4.3 also demonstrates that the different initial structures all exhibit identical decarburisation kinetics at a p_{H_2O} / p_{H_2} ratio of 0.25.

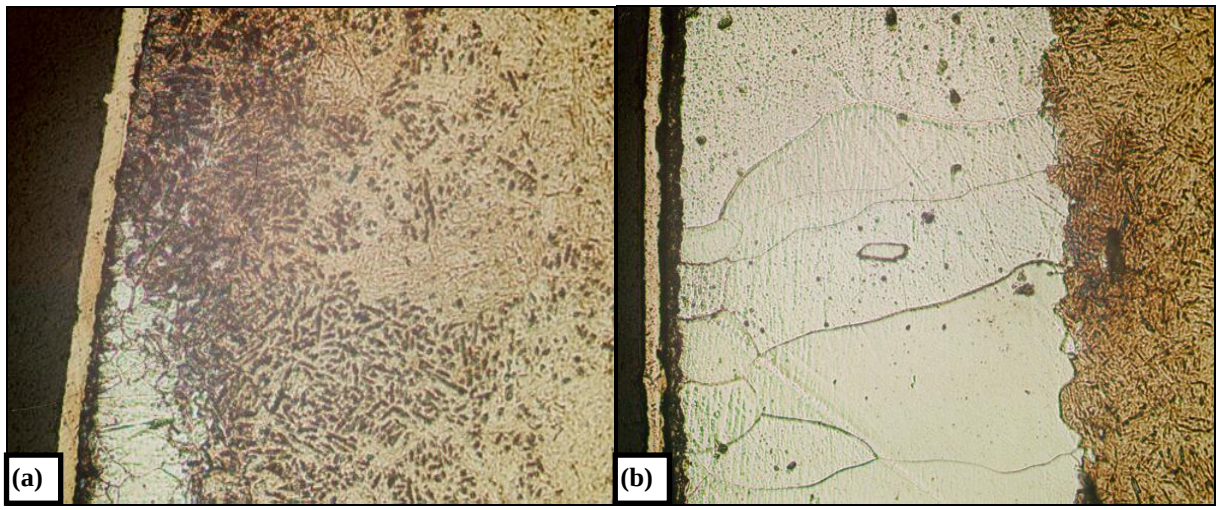

Figure 4.2 Decarburisation structures for 96hr tempered martensite initial structures after 4hr at 820°C, p_{H_2O} / p_{H_2} =0.05 for heating with (a) 2hr austenitisation, and (b) no austenitisation. x230 magnification. 2% Nital etch.

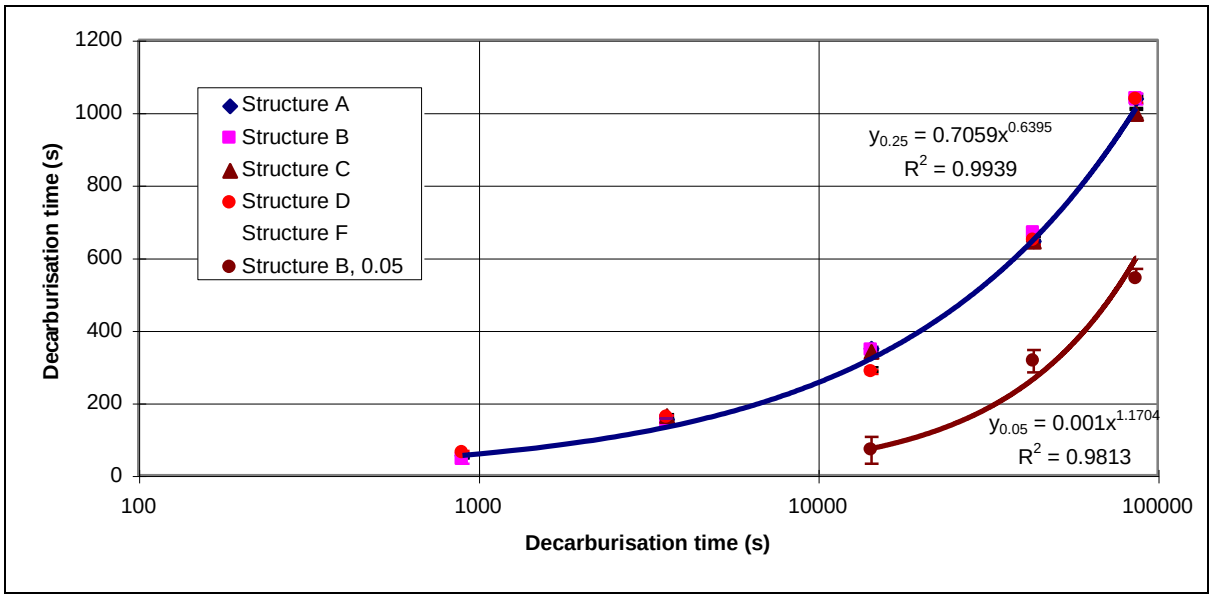

Figure 4.3 Free ferrite decarburisation depths of 820°C for p_{H_2O} / p_{H_2} =0.05 and 0.25 after heating and 2hr austenitisation in argon.

The growth in thickness of the surface oxide layers at 0.05 and 0.25 p_{H_2O} / p_{H_2} ratios as a function of time for furnace cooled structures is illustrated in Figure 4.4. The oxide thicknesses are greater at a p_{H_2O} / p_{H_2} ratio of 0.05 for no austenitisation than for 2hr austenitisation, and greater still for 2hr austenitisation at a 0.25 ratio. The width of the free ferrite columnar grains that formed perpendicular to the steel surface was measured[(6)], with the grain growth kinetics similar for furnace cooled structures at a p_{H_2O} / p_{H_2} ratio of 0.05 with and without 2hr austenitisation, and for 2hr austenitisation at a ratio of 0.25, as illustrated in Figure 4.5.

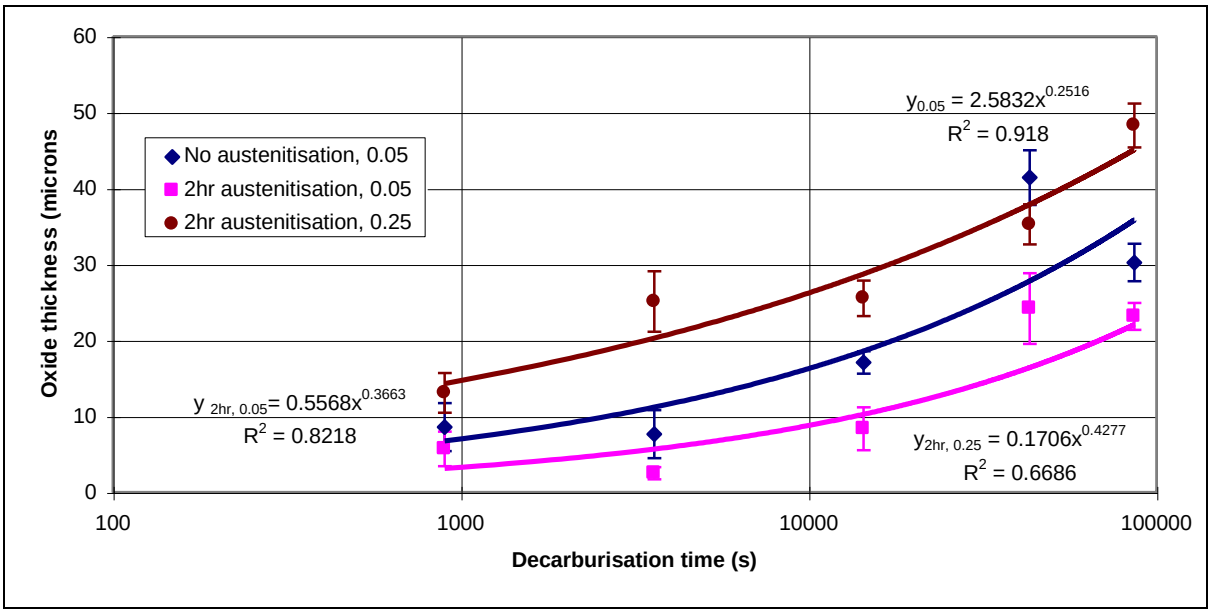

Figure 4.4 Oxidation kinetics for decarburisation of furnace cooled structures at 820°C with and without 2hr austenitisation at p_{H_2O} / p_{H_2}=0.05, and with 2hr austenitisation at p_{H_2O} / p_{H_2}=0.25.

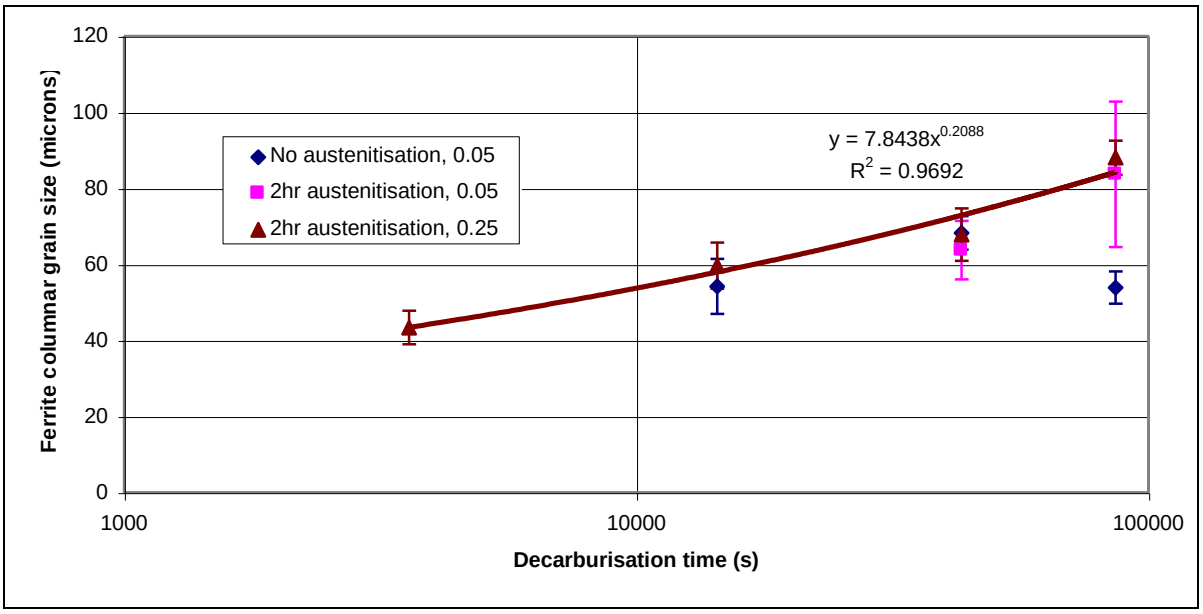

Figure 4.5 Free ferrite columnar grain growth kinetics of furnace cooled structures after decarburisation at 820°C with and without 2hr austenitisation at p_{H_2O} / p_{H_2}=0.05, and with 2hr austenitisation at p_{H_2O} / p_{H_2}=0.25.

The free ferrite decarburisation depths for the furnace cooled and 96hr tempered martensite test specimens inserted into the hot zone once the water/hydrogen atmosphere was established are also illustrated in Figure 4.1. This illustrates that the amount of decarburisation is greatest when the specimens are inserted into the decarburising atmosphere in the hot zone with no prior heating. The carbon monoxide and carbon dioxide concentrations measured by the infra-red gas analysers during the first 15min of decarburisation are illustrated in Figure 4.6. Small concentrations of methane were also expected, but were not detected due to the insufficient sensitivity of the methane gas analyser. The carbon monoxide content was approximately ten times that of the carbon dioxide content for the duration of the heat treatment, indicating that the predominant decarburisation reaction is that of equation 3.1.

Two carbon monoxide and carbon dioxide peaks were observed during the early stages of these heat treatments, with the first at approximately 41s and the second at 215s. The heating of a 5mm diameter by 15mm test specimen was measured by a thermocouple welded to the surface of the specimen. This showed that the first peak corresponded to a temperature of approximately 500°C, at a carbon monoxide content of 0.018 volume %. The carbon monoxide content then dropped to a minimum of 0.009 volume % after 83s at a temperature of 700°C. The second peak occurred at a temperature of 785°C and yielded a carbon monoxide content of 0.099 volume %. The carbon monoxide and carbon dioxide contents then decreased from this time onwards.

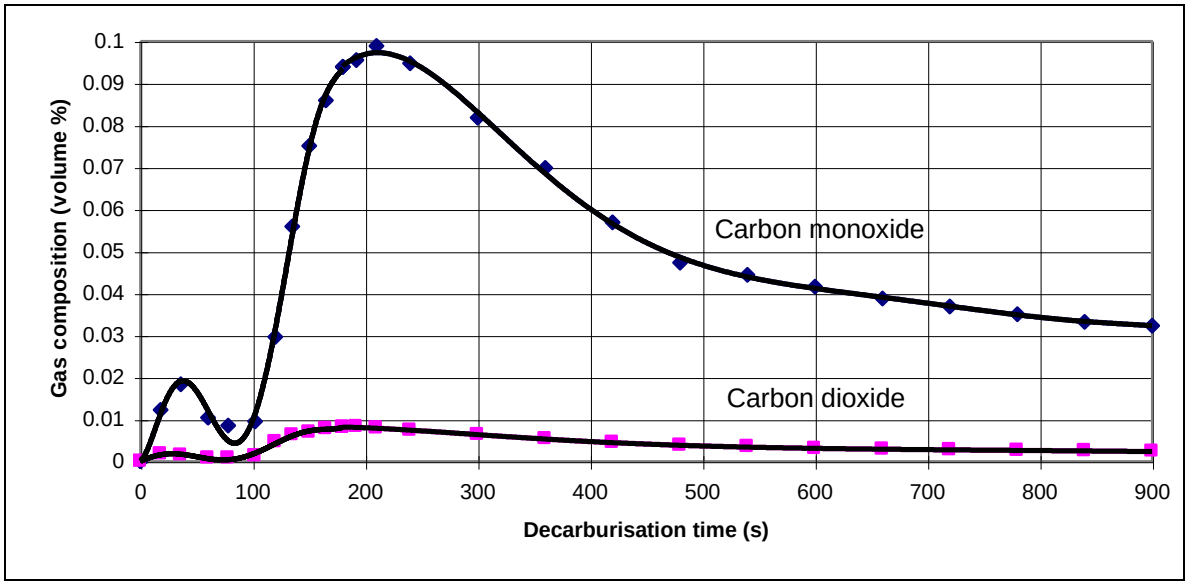

Figure 4.6 Carbon monoxide and carbon dioxide concentrations during the decarburisation of furnace cooled and 96hr tempered martensite structures at 820°C with no heating or austenitisation times, p_{H_2O} / p_{H_2}=0.05.

Excellent agreement between the measured decarburisation depths and those calculated from the carbon monoxide and carbon dioxide contents of the exhaust gas is displayed in Figure 4.7. The decarburisation depths calculated from the gas analysis data can also be compared with the decarburisation depths obtained for an effective diffusion coefficient of carbon in ferrite of $5x10^{-7}cm^2/s$, calculated from equation 4.1[7].

$$x = \sqrt{\frac{2t_d C_B D_{effective}}{(C_i - \frac{2}{3} C_B)}}, \qquad \text{-(4.1)}$$

where x = free ferrite decarburisation depth in cm;
t_d = decarburisation time in s;
C_B = saturation ferrite carbon content in wt.%;
C_i = initial carbon content of steel in wt.%;
$D_{effective}$ = effective carbon diffusion coefficient in ferrite in cm^2/s.

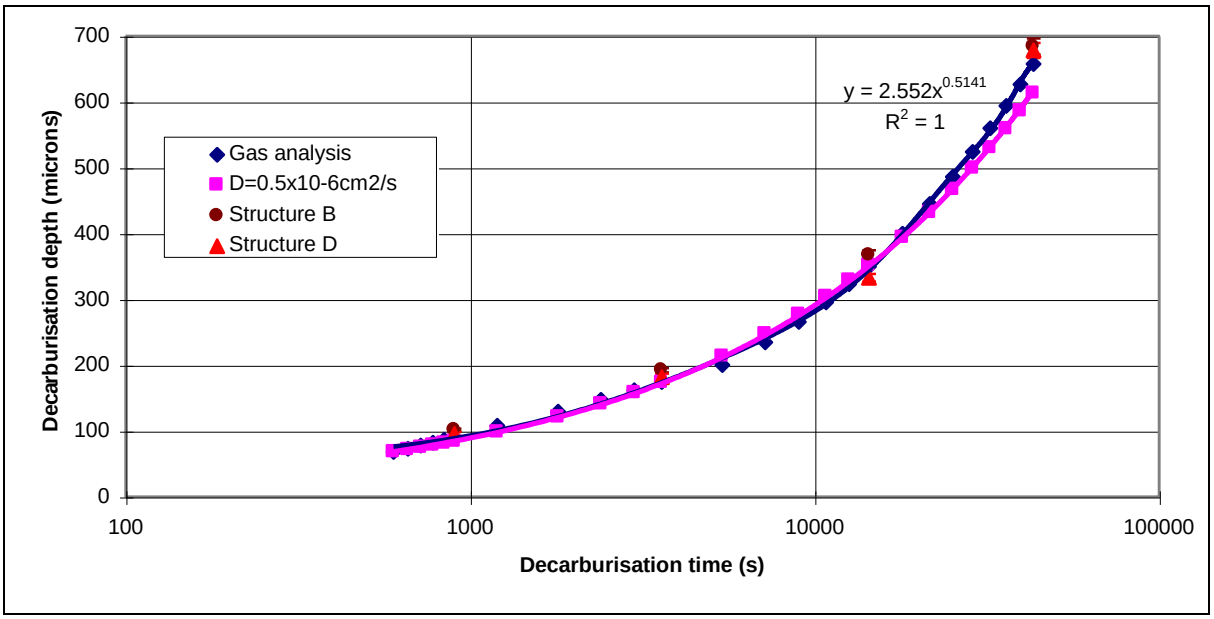

Figure 4.7 Comparison of measured decarburisation depths and those calculated from gas analysis during the decarburisation of furnace cooled and 96hr tempered martensite structures at 820°C with no heating or austenitisation times, p_{H_2O} / p_{H_2}=0.05.

The values of C_B and C_i are 0.60 and 0.05wt.%[2] respectively. Figure 4.7 demonstrates excellent agreement between the decarburisation depths calculated from the gas analysis data and those for an effective diffusion coefficient of $5x10^{-7}cm^2/s$ for the first 4hr of the heat treatment. However, the decarburisation depths are somewhat greater than that calculated from the effective diffusion coefficient of $5x10^{-7}cm^2/s$ for test duration's longer than 4hr.

5 Discussion

Upon inserting the test specimens into the hot zone of the furnace at 820°C, 558s elapse before the test specimens are heated to 815°C. A further period of time at the heat treatment temperature is required before different initial structures attain a fully austenitic structure, with the 96hr tempered martensite initial structure requiring approximately 2hr to transform to 95% austenite[3]. If the specimens are exposed to the decarburisation atmosphere while they are heating to temperature and transforming to the austenitic structure, carbon removal will accompany the heating and transformation processes. As different SUP7 initial structures vary

considerably in the time required for transformation at the Ac_3 temperature[3], meaningful comparisons between the specimens may be prevented.

Consequently, when designing the experimental program, it was decided that the specimens would be heated and austenitised in argon until the austenite transformation was predominantly complete before introducing the decarburisation atmosphere. This was to ensure that carbon removal only ever occurred from an austenitic structure. However, it has become apparent from this research that the longer the specimens are annealed in argon, the longer it takes for decarburisation initiation to occur. The deepest decarburisation was observed for the specimens exposed to the decarburisation atmosphere while they were heating.

The 8mm and 5mm diameter specimens were both heated for a similar duration prior to introduction of the decarburisation atmosphere, namely 900 and 810s respectively. However, the greater thermal inertia of the 8mm diameter specimens resulted in deeper decarburisation, since the same temperature attained by the 8mm diameter specimens after 900s is reached in approximately 360s by the 5mm diameter specimens. The 8mm diameter specimens were therefore exposed to the heat treatment atmosphere at a lower temperature, yielding the deeper decarburisation observed.

The argon used to flush the ambient atmosphere and then anneal the test specimens was passed through Labclear and Oxyclear gas filters to reduce the water and oxygen impurities to less than 50vppb. The 5mm diameter specimens that were annealed in argon exhibited no decarburisation, with no oxide structure visible at 1,000x magnification under the optical microscope. This would suggest that the water and oxygen contents in the argon atmosphere were reduced to a level sufficient to prevent any decarburisation or oxidation of SUP7 from occurring.

However, it is possible that minute concentrations of water vapour still remained in the argon atmosphere when the specimens were heated and austenitised. At low water concentrations, a thin dense SiO_2 layer can form. A 2.96wt.% silicon electrical steel annealed for 1hr at 850°C with a p_{H_2O} / p_{H_2} ratio of $1x10^{-3}$ formed a SiO_2 layer only 0.0225 μm thick[8], which is not observable under the optical microscope. Fast[9] found that a 2.0wt.% silicon electrical steel with an initial carbon content of 0.071wt.% decarburised to a final carbon content of 0.003wt.% at 900°C in pure hydrogen. However, no decarburisation was observed for a p_{H_2O} / p_{H_2} ratio of $3x10^{-5}$. As the p_{H_2O} / p_{H_2} ratio increased to $3x10^{-4}$ and $1x10^{-3}$, the final carbon contents were 0.033 and 0.010wt.% respectively.

A similar situation appears to be occurring here with the formation of a very thin dense SiO_2 layer during the heating and austenitising of the SUP7 specimens in argon. This layer, which was not visible under the optical or scanning electron microscopes, prevented the reaction of the heat treatment atmosphere with the steel, and hence the decarburisation of SUP7. However, decarburisation did commence at some stage for a p_{H_2O} / p_{H_2} ratio of 0.05; after 1hr for heating in argon, and after 4hr for heating with 2hr austenitisation. Once decarburisation began, the oxide became thick and porous, and decarburisation occurred readily. For this to happen, the heat treatment atmosphere had to be able to react with the bulk steel.

With a SiO_2 layer in contact with the bulk steel, decarburisation by the solid state reaction of equation 5.1 can occur[4].

$$C_{(\text{in steel})} + SiO_{2(s)} = SiO_{(g)} + CO_{(g)} \quad -(5.1)$$

Equation 5.1 gives a direct contribution to the decarburisation, and also facilitates the reaction between carbon and water, reaction 3.1, to form carbon monoxide by diminishing the blocking of the surface with SiO_2[9]. Eventually the SiO_2 layer became non-blocking, allowing reaction between the heat treatment atmosphere and the steel, and hence more rapid decarburisation. The greater delay of decarburisation initiation for the specimens heated and austenitised for 2hr compared with those only heated before exposure to the decarburisation atmosphere is attributable to a thicker SiO_2 layer forming during the 2hr austenitisation. This layer took longer to become non-blocking by the solid state reaction of equation 5.1. The earlier decarburisation initiation for a p_{H_2O} / p_{H_2} ratio of 0.25 compared to the 0.05 ratio with 2hr austenitisation, 15min versus 4hr, arose from the greater driving force of the higher water content facilitating a more rapid breakdown of the SiO_2 layer to a non-blocking structure.

Once the SiO_2 layer becomes non-blocking, oxygen can diffuse into the steel and react with silicon to precipitate SiO_2 within an iron rich structure[10]. More rapid growth of the oxide structure then occurred, as illustrated in Figure 4.4. The greater oxide thicknesses for heating but no austenitisation at a p_{H_2O} / p_{H_2} ratio of 0.05 compared with heating and 2hr austenitisation was due to the earlier breakdown of the impervious SiO_2 layer, and hence the earlier commencement of the growth of this layer. The oxide kinetics were even more rapid for heating and 2hr austenitisation at a p_{H_2O} / p_{H_2} ratio of 0.25 due to the earlier breakdown of the SiO_2 layer, and the higher water content supplying a greater oxygen flux.

The SiO_2 layer which formed during the decarburisation of specimens heated to temperature in the established decarburisation atmosphere is non-blocking, with decarburisation initiating at as low as 400°C. Modelling of the decarburisation as a diffusion process yielded an effective diffusion coefficient of $5x10^{-7}cm^2/s$ for carbon in ferrite, which is an order of magnitude lower than the value for carbon diffusion in pure ferrite, $5x10^{-6}cm^2/s$[6]. This is attributable to longer diffusion paths through the oxide, and reduced permeability of the surface for carbon.

This research indicates some interesting possibilities for the manufacture of automobile coil springs. Considerable decarburisation often occurs during the heat treatments used to produce these springs, presumably due to reaction of water vapour in the furnace atmosphere with the steel, effecting carbon removal. Current spring production techniques necessitate removal of the decarburised surface layer from the bar stock, by a peeling operation, following the hot rolling in the steel mill. The springs are then shot peened after being tempered to negate the effect of any decarburisation. It has been suggested[2] that increasing the silicon content of SUP7 to between 2.5 and 3.57wt.% would eliminate decarburisation during spring manufacture.

However, it appears that heating and annealing SUP7 in an atmosphere of argon with an appropriately low level of water results in the formation of an impervious SiO_2 layer, which then strongly impedes any decarburisation. This suggests the possibility of controlling the heat treatment environment to allow the formation of such an oxide layer early in the production of

the springs, thus preventing decarburisation. Consequently, the spring manufacture could be streamlined by perhaps allowing the peeling and shot peening operations to be eliminated. Less decarburisation would also allow greater heat treatment flexibility during spring manufacture.

6 Conclusion

The decarburisation of a SUP7 spring steel was investigated at the Ac_3 temperature of 820°C in atmospheres of wet hydrogen. Insertion of the test specimens into the hot zone of the furnace once the decarburisation atmosphere was established saw decarburisation commence at a specimen temperature of 400°C. The carbon monoxide and carbon dioxide concentrations as a function of time were measured, with two distinct peaks observed in these concentrations during heating of the specimens. The predominant decarburisation reaction was that of equation 3.1. A mean effective diffusion coefficient for carbon in ferrite of approximately $5x10^{-7}cm^2/s$ was calculated, being an order of magnitude lower than for reported carbon diffusion in pure ferrite due to the partial blocking effect of the SiO_2 oxide layer.

Heating of the specimens in argon before introducing the decarburisation atmosphere delayed the decarburisation initiation until 1hr, and reduced the free ferrite depths. Heating and then austenitising the specimens for 2hr in argon delayed decarburisation until 4hr, and further reduced the free ferrite kinetics. Delay of the decarburisation initiation was attributed to the formation of a thin impervious SiO_2 layer during the argon anneal due to the presence of minute levels of water vapour. This SiO_2 layer strongly inhibits carbon removal. The blocking effect of the SiO_2 layer was diminished by the solid state reaction of carbon with SiO_2, which eventually allowed decarburisation to occur. A 2hr austenitisation allowed the formation of a thicker SiO_2 layer, and hence a longer time to breakdown of the SiO_2 layer, delaying the decarburisation initiation. Increasing the p_{H_2O} / p_{H_2} ratio from 0.05 to 0.25 for heating and 2hr austenitisation in argon increased the driving force for breakdown of the SiO_2 layer, with decarburisation now observed after 15min.

The formation of this impervious SiO_2 layer early in the production of coil springs would possibly allow the elimination of some of the spring manufacture operations normally required to negate the effect of decarburisation, and hence improve the production of coil springs.

7 Acknowledgments

I gratefully acknowledge and thank BHP New Zealand Steel for their financial support which has made this paper possible. Furthermore, I would like to thank the Department of Mechanical Engineering staff at the University of Canterbury for their support.

8 References

1) "The effect of shot peening to decarburised steel plate", Sato, S.; Inoue, K.; Ohno, A.; Proceedings 1st International Conference on Shot Peening, September 1981, 303-312.
2) "Decarburisation behaviour of high silicon spring steels", Mardon, C.; Smaill, J.; Sell, L.; Proceedings IPENZ Annual Conference 1997, Volume 2, 269-271.

3) “The influence of temperature and initial structure on the austenitisation of a high silicon spring steel”, Mardon, C.; Smaill, J.; Proceedings IPENZ Annual Conference 1997, Volume 2, 263-268.
4) “On the decarburisation of silicon steel sheet”, Yamazaki, T.; Nippon Tekko Kyokai Transactions, Volume 9, 1969, 66-75.
5) “Ferrous physical metallurgy”, Sinha, A.K.; Butterworths, Boston, 1989.
6) “Factors affecting the final grain size of decarburised lamination steels”, Marder, A.R.; Metallurgical Transactions A, Volume 17A, August 1986, 1277-1285.
7) “The diffusivity and solubility of carbon in alpha-iron”, Smith, R.P.; Transactions of the Metallurgical Society of AIME, Volume 224, February 1962, 105-111.
8) “Transition from external to internal oxidation in iron-silicon alloy as a function of oxygen potential of the ambient atmosphere”, Ichido, T.; Morrito, N.; Scripta Metallurgica, Volume 10, 1976, 619-622.
9) “Decarburising and denitriding of ferrite-silicon steel”, Fast, J.D.; Brunning, H.A.C.M.; Z. Elektrochemie, Volume 63, Number 7, 1959, 765-772.
10) “Surface oxidation of non-oriented silicon-aluminium electrical steels during annealing”, Geiger, A.L.; Journal Applied Physics, Volume 49, Number 3, March 1978, 2040-2042.

Appendix L-(v) IPENZ98b

MONITORING SPRING STEEL DECARBURISATION BY SAMPLING THE HEAT TREATMENT ATMOSPHERE

CHRIS MARDON[1], JOHN SMAILL[2]

Abstract

Decarburisation of steels is commonly investigated by varying heat treatment durations under otherwise identical experimental conditions. However, detailed heat treatment regimes become lengthy since each test duration requires an individual specimen and subsequent microscopic examination. The experimentation necessary to investigate the decarburisation of spring steels was considerably reduced by sampling the heat treatment atmosphere instead. Both methods are compared, with the sampling technique yielding several advantages.

Introduction

Decarburisation (carbon removal) of a steel often occurs during heat treatments at elevated temperatures. Carbon in the steel reacts with the heat treatment atmosphere to form various gaseous products which facilitate carbon removal from the steel. Any decarburisation is often undesirable, with a lowering of the carbon content at the steel surface reducing the fatigue life. This applies to the production of automobile coil suspension springs, where decarburisation occurs during the heat treatments used in manufacturing the springs. The lower hardness of the decarburised surface greatly reduces the fatigue life of the springs, with 0.19mm decarburisation reduces the fatigue life of a SUP6 spring to half that of the non-decarburised spring[(1)].

Modern coil springs utilise higher silicon contents of around two weight percent to improve their hardness, and hence their fatigue life. However, these steels have also been found to decarburise more deeply than lower silicon steels[(2)]. Surprisingly, this phenomena has been investigated in limited detail, despite the tens of millions of coil springs produced annually, and the degraded performance of these springs with any decarburisation. However, recent studies[(3-5)] have shown that the decarburisation of springs steels varies considerably with silicon content of these steels, and with the heat treatment atmosphere used.

These heat treatments were undertaken by a relatively simple method. Test specimens were inserted into the hot zone of a tube furnace at the desired temperature and heat treatment atmosphere. Tests were undertaken for 15min to 24hr, and were concluded by quenching the specimens in water. Each specimen was mounted, polished and etched, with the decarburisation depths measured under a microscope. This method suffers from two serious limitations:

(1) Several test durations are required for each set of experimental parameters, with the heat treatment, specimen preparation and microscopic examination requirements becoming considerable for a range of steels that are heat treated at several temperatures, atmosphere compositions, and with different initial microstructures;
(2) The initial stages of the decarburisation kinetics cannot be investigated.

[1] Postgraduate Student, Department of Mechanical Engineering, University of Canterbury.
[2] Senior Lecturer, Department of Mechanical Engineering, University of Canterbury.

Consequently, experimental apparatus and techniques were developed for continuous sampling of the heat treatment atmosphere upon reaction with the test specimens. This allowed the amount of carbon removed from the steel to be determined, and hence calculation of the decarburisation depths. The methodology used to decarburise a SUP7 spring steel with continuous measurement of the heat treatment atmosphere, and the results obtained, are presented in this paper.

Experimental approach

SUP7 comprises, by weight percent, 0.60% carbon, 1.94% silicon, 0.77% manganese, and 0.19% chromium. 5mm diameter by 50mm SUP7 test specimens, machined to a ground surface finish, were inserted into the cold end of a Nabertherm R7019 tube furnace. The ambient atmosphere was removed from the tube furnace by flushing with argon purified to water and oxygen contents of less than 50vppb by passage through Labclear and Oxyclear gas filters. A 500cm^3/min hydrogen flow comprising less than 1vppm carbon monoxide, carbon dioxide and methane was bubbled through water held at the temperature required for the desired hydrogen water content, and into the tube furnace.

The gas flow was sampled at a point next to the test specimen in the furnace, with the reacted gas flowing through carbon monoxide, carbon dioxide, and methane infra-red gas analysers. Each analyser was calibrated using a calibration gas. Once the water/hydrogen atmosphere was fully established and had stabilised, the gas analysers were zeroed. The heat treatment commenced when the specimen was pushed into the hot zone, with the gas concentrations recorded by a three-pen chart recorder. 4hr heat treatments were undertaken, with the test being concluded by quenching the specimen in water. The decarburisation test rig is schematically illustrated in Figure 1. The heat treatments were undertaken at the Ac_3 temperature for SUP7 of 820°C[(6)], where carbon removal theoretically results in the formation of a surface ferrite layer from an initially austenitic structure.

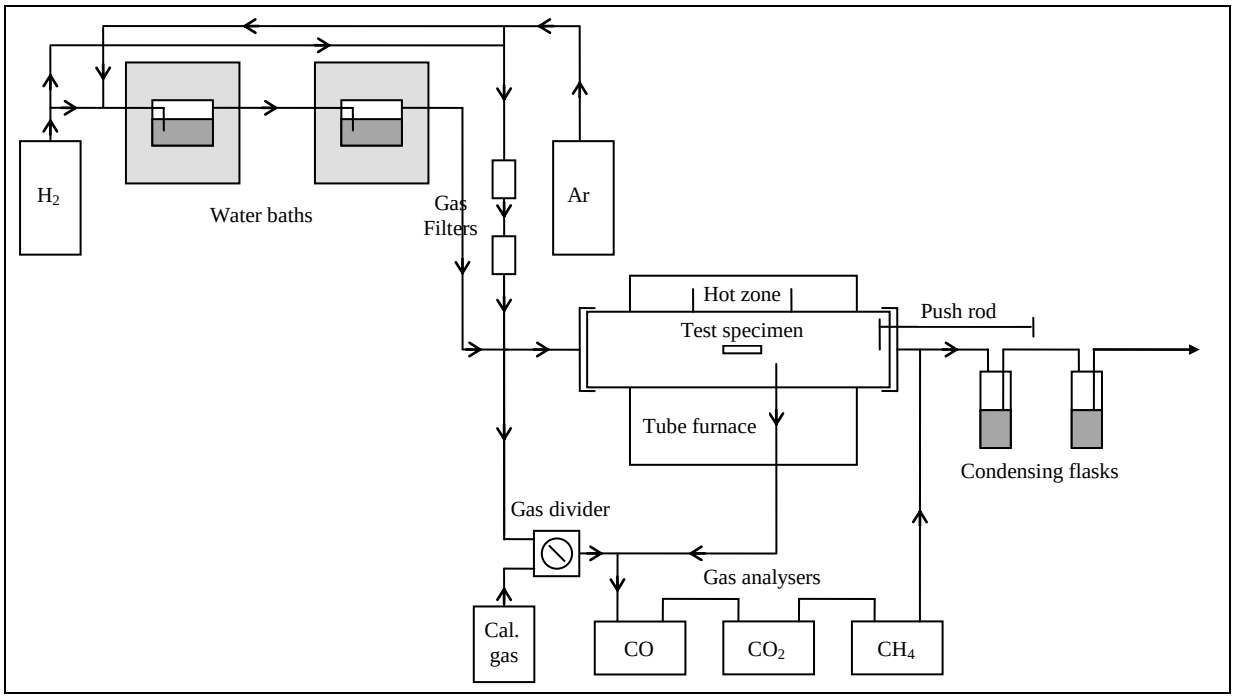

Figure 1 Schematic illustration of the decarburisation test rig.

Results

The pen-recorder profiles can be converted to gas concentrations by the calibration information for the gas analysers. Figure 2 illustrates the carbon monoxide and carbon dioxide contents measured during the first 15min of decarburisation for different initial structures in a hydrogen/5% water atmosphere, which equates to a p_{H_2O} / p_{H_2} ratio of 0.05. The gas concentrations for furnace cooled pearlitic structures decarburised at different p_{H_2O} / p_{H_2} ratios are illustrated in Figures 3 and 4.

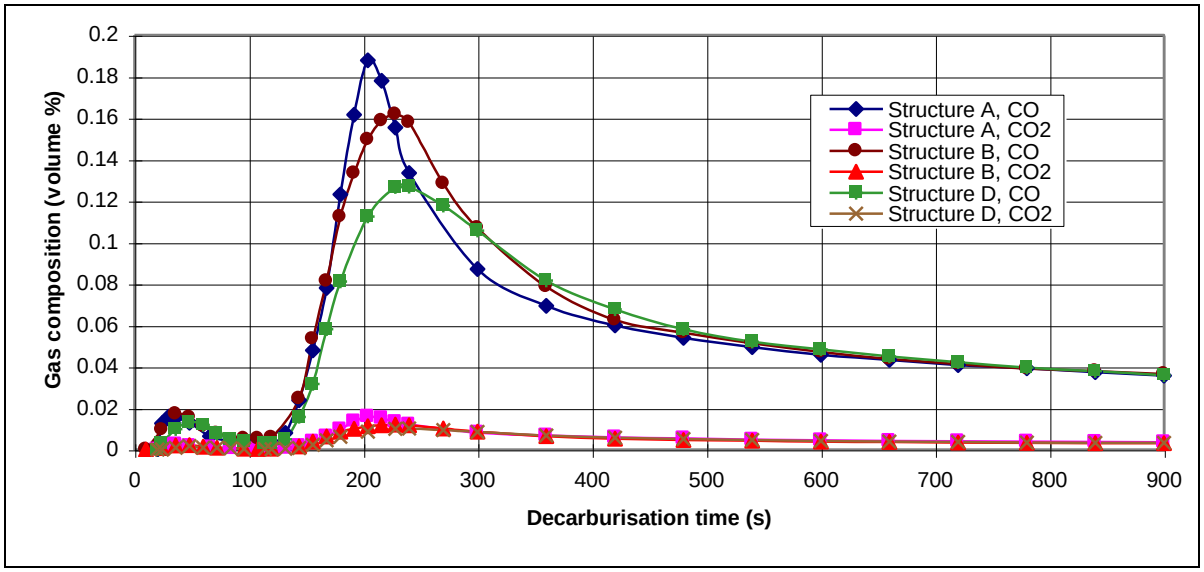

Figure 2 Carbon monoxide and carbon dioxide concentrations during the decarburisation of different initial structures at 820°C, p_{H_2O} / p_{H_2} =0.05.

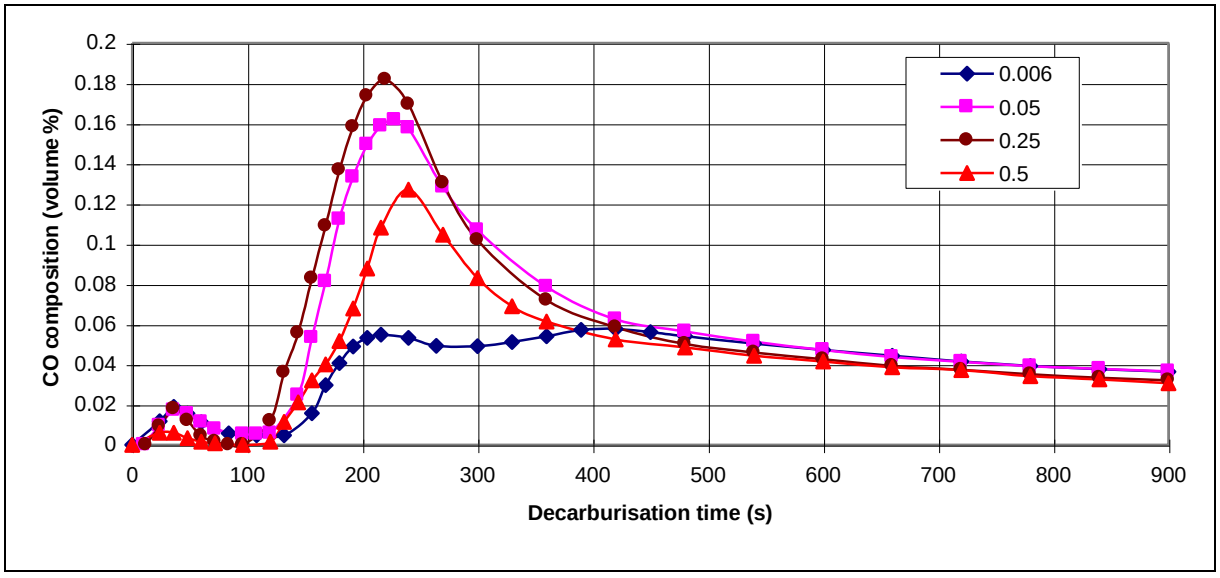

Figure 3 Carbon monoxide liberation during the decarburisation of furnace cooled pearlitic structures at 820°C with different p_{H_2O} / p_{H_2} ratios.

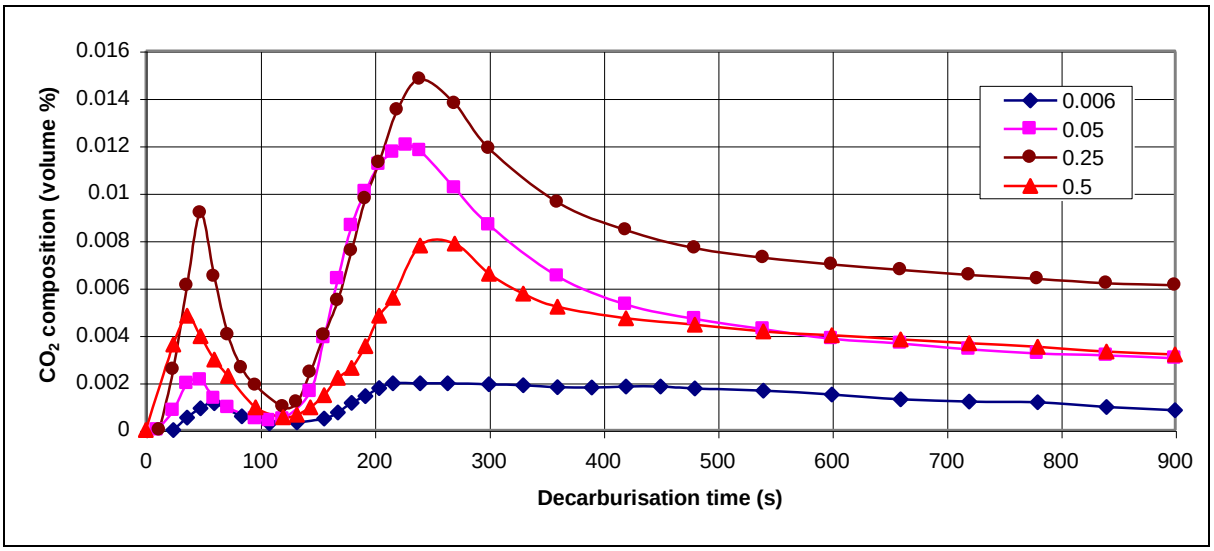

Figure 4 Carbon dioxide liberation during the decarburisation of furnace cooled pearlitic structures at 820°C with different p_{H_2O} / p_{H_2} ratios.

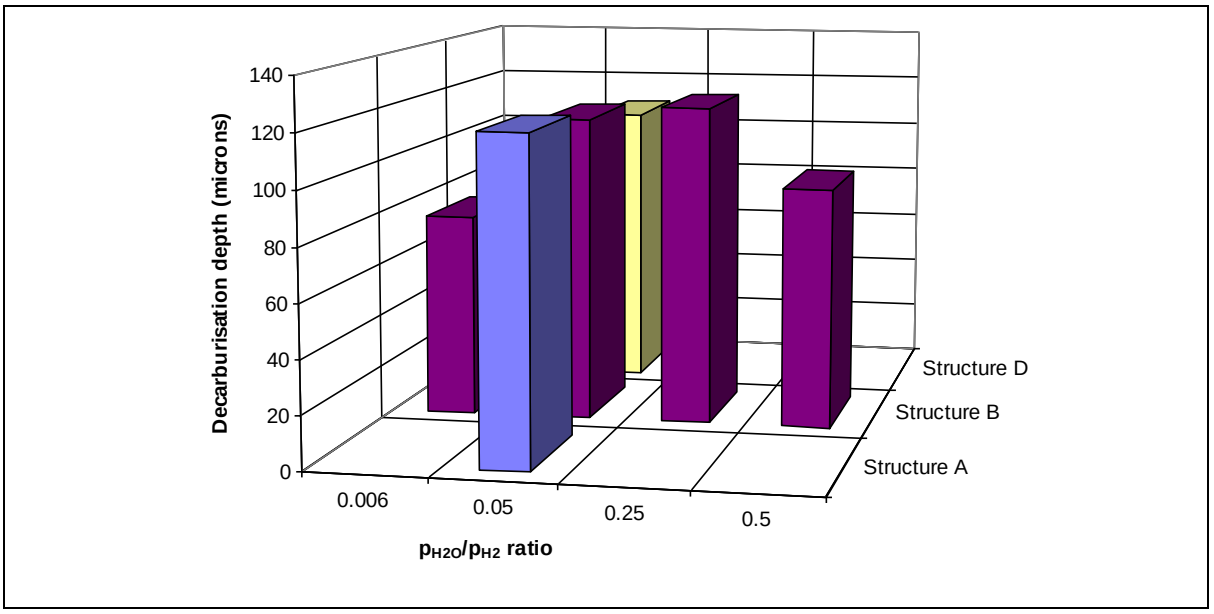

Figure 5 Free ferrite decarburisation depths calculated from the gas analysis data for different initial structures and p_{H_2O} / p_{H_2} ratios after 15min heat treatment at 820°C.

The predominant decarburisation reactions occurring appear to be[7-8]:

$C_{(in\ steel)}$	+	$H_2O_{(g)}$	=	$CO_{(g)}$	+	$H_{2(g)}$ -(1)
$CO_{(g)}$	+	$H_2O_{(g)}$	=	$CO_{2(g)}$	+	$H_{2(g)}$ -(2)

Polynomial curves were fitted to the gas analysis data, and integrated numerically to determine the average carbon monoxide and carbon dioxide gas compositions over the first

15min of decarburisation. This allowed the volume, and hence the mass, of carbon monoxide and carbon dioxide liberated to be calculated. From equations 1 and 2, every mole of carbon monoxide and carbon dioxide forming removed one mole of carbon from the steel. This allowed the amount of carbon removed from the steel to be calculated. The volume of steel over which carbon removal occurred was determined, and hence the free ferrite decarburisation depths. The decarburisation depths calculated for different initial structures and p_{H_2O} / p_{H_2} ratios after 15min heat treatment are illustrated in Figure 5.

Discussion

The carbon monoxide and carbon dioxide liberated during the decarburisation of different initial structures and at different p_{H_2O} / p_{H_2} ratios demonstrated several interesting characteristics. The finer air cooled pearlitic structure, Structure A, exhibited higher but narrower carbon monoxide and carbon dioxide peaks than the coarser furnace cooled structure, Structure B, as illustrated in Figure 2. The peaks for both pearlitic structures are higher and narrower than those of the 96hr tempered martensite spheroidal cementite structure, Structure D. However, after 15min, the carbon monoxide curves for the three initial structures were identical, as were the carbon dioxide curves. The calculated free ferrite depths of Figure 5 show that the air cooled pearlitic structure decarburised slightly more after 15min than the furnace cooled pearlitic and 96hr tempered martensite spheroidal cementite structures, to a free ferrite depth of 120 versus 116 and 109 μm respectively. These free ferrite depths are similar, and it would have been reasonable to assume that different initial microstructures exhibited similar decarburisation kinetics had these results been obtained from the heat treated microstructures alone. However, Figure 2 illustrates that there is a significant difference in the decarburisation behaviour of different initial structures during the early stages of the decarburisation process.

An increase in the p_{H_2O} / p_{H_2} ratio from 0.006 to 0.05 during the decarburisation of a furnace cooled pearlitic structure is accompanied by a change in the shape of the gas liberation curves, Figures 3 and 4, and considerably higher gas peaks. The height of the carbon monoxide and carbon dioxide peaks are higher again at a 0.25 p_{H_2O} / p_{H_2} ratio, before dropping considerably at a 0.50 ratio. This variation of the carbon release kinetics with time at different p_{H_2O} / p_{H_2} ratios, and for different initial structures, would not have been obtainable from measurement of the decarburised microstructures.

Significant reductions in heat treatment, specimen preparation, and microstructural investigation times are achieved when one heat treatment suffices for the description of the decarburisation kinetics for each combination of experimental parameters, instead of the several different duration heat treatments that are necessary when the decarburisation kinetics are obtained from the microstructures. It is also advantageous to be able to calculate the total amount of carbon removed instead of having to measure the decarburisation depths; especially at temperatures other than the Ac_3 value where partial ferrite/martensite decarburisation, which is much harder to estimate under an optical microscope, accompanies formation of a free ferrite layer. Good agreement between the decarburisation depths measured with the microscope, and those calculated from the gas analysis, have already been demonstrated[(5)].

Conclusion

An alternative to undertaking different duration heat treatments to describe the decarburisation kinetics of a SUP7 spring steel was investigated. This involved measuring the carbon monoxide and carbon dioxide contents of the reacted heat treatment atmosphere, from which the amount of carbon removed from the steel was calculated. Heat treatments were undertaken for different initial structures and water contents at 820°C. Definite advantages were obtained by sampling the reacted heat treatment atmosphere, including:

(1) Detection of the differences in carbon release kinetics during the early stages of decarburisation for various initial structures, where measurement of the free ferrite depths after 15min would have indicated no significant differences;
(2) Knowledge of the variation of the carbon removal kinetics as a function of specimen temperature and heat treatment time, which is not readily obtainable from a microstructural investigation;
(3) The ability to calculate the total amount of carbon removed from the steel, instead of having to measure decarburisation depths which are not so clearly defined at temperatures other than the Ac_3 value;
(4) A large reduction in the heat treatment and specimen preparation requirements due to only one specimen being required for each combination of experimental parameters.

Acknowledgments

I gratefully acknowledge and thank BHP New Zealand Steel for their financial support which has made this paper possible. Furthermore, I would like to thank the Department of Mechanical Engineering staff at the University of Canterbury for their support.

References

1) "The effect of shot peening to decarburised steel plate", Sato, S.; Inoue, K.; Ohno, A.; Proceedings 1st International Conference on Shot Peening, September 1981, 303-312.
2) "Effect of chemical composition on sag resistance of suspension spring", Kawakami, H.; SAE Paper 821028.
3) "Decarburisation understanding for improved automobile suspension spring performance", Mardon, C.; Proceedings IPENZ Annual Conference 1994, Volume 2, 311-316.
4) "The influence of temperature and initial structure on the austenitisation of a high silicon spring steel", Mardon, C.; Smaill, J.; Proceedings IPENZ Annual Conference 1997, Volume 2, 263-268.
5) "Variable decarburisation of a spring steel", Mardon, C.; Smaill, J.; to be published in 1998 IPENZ Annual Conference Proceedings.
6) "Decarburisation behaviour of high silicon spring steels", Mardon, C.; Smaill, J.; Sell, L.; Proceedings IPENZ Annual Conference 1997, Volume 2, 269-271.
7) "On the decarburisation of silicon steel sheet", Yamazaki, T.; Nippon Tekko Kyokai Transactions, Volume 9, 1969, 66-75.
8) "Ferrous physical metallurgy", Sinha, A.K.; Butterworths, Boston, 1989.

Appendix L-(vi) IPENZ98c

FROM GO TO WHOA - EXPERIMENTAL TECHNIQUES FOR DECARBURISING SPRING STEELS

CHRIS MARDON[1], JOHN SMAILL[2]

Abstract

From the development of a heat treatment rig to the final decarburisation results, various pieces of experimental apparatus, and the associated methodology, were used to decarburise spring steels. This paper outlines a few of the more interesting experimental features of a decarburisation program for spring steels, and some pertinent results.

Introduction

The steels used for modern automobile coil springs are susceptible to carbon removal during the heat treatments required for the production of these springs[(1)], with this decarburisation reducing the fatigue life of the springs[(2)]. However, difficulties have recently been experienced in decarburising a two percent silicon spring steel, SUP7[(3)], despite heat treating with a supposedly potent decarburising atmosphere of water and hydrogen. This apparent contradiction initiated a postgraduate research project. Suitable experimental apparatus, and the associated methodology, have been developed to facilitate an investigation into the decarburisation of spring steels comprising different silicon contents. Now that some interesting results have been obtained, it is pertinent to reflect on the experimental apparatus and techniques used, and the results obtained.

Heat treatment rig

At the commencement of this project, decarburisation heat treatments were undertaken with the existing experimental apparatus. This involved bubbling hydrogen into water contained within two conical flasks, and into the tube furnace to provide a water/hydrogen atmosphere. However, this apparatus gave limited control over the experimental parameters, so a more advanced test rig was developed, as illustrated schematically in Figure 1. The heat treatments were undertaken by inserting the test specimen into the cold end of the tube furnace, flushing the ambient atmosphere with argon purified to less than 50vppb water and oxygen, and then establishing the desired atmosphere. The water content of the atmosphere was controlled by the water bath temperature through which the hydrogen was bubbled. For this paper a 5% water/95% hydrogen atmosphere (giving p_{H_2O} / p_{H_2} ratio of 0.05) was used to effect the decarburisation. This corresponded to a water temperature of 32°C. Condensation in the plumbing between the water baths and the furnace was prevented by heating the plumbing with insulated silicon carbide heating wire. Once the heat treatment atmosphere was established, the specimen was pushed into the furnace hot zone. The reacted gas was sampled, and flowed through carbon monoxide, carbon dioxide and methane infra-red gas analysers, with the gas profiles recorded by a three-pen chart recorder. These analysers, which were calibrated using a range of gas concentrations obtained with the gas divider, the calibration gas, and the purified argon, allowed the amount of carbon removed from the steel to be determined. Each test specimen was quenched in water to conclude the heat treatment.

1 Postgraduate Student, Department of Mechanical Engineering, University of Canterbury.

2 Senior Lecturer, Department of Mechanical Engineering, University of Canterbury.

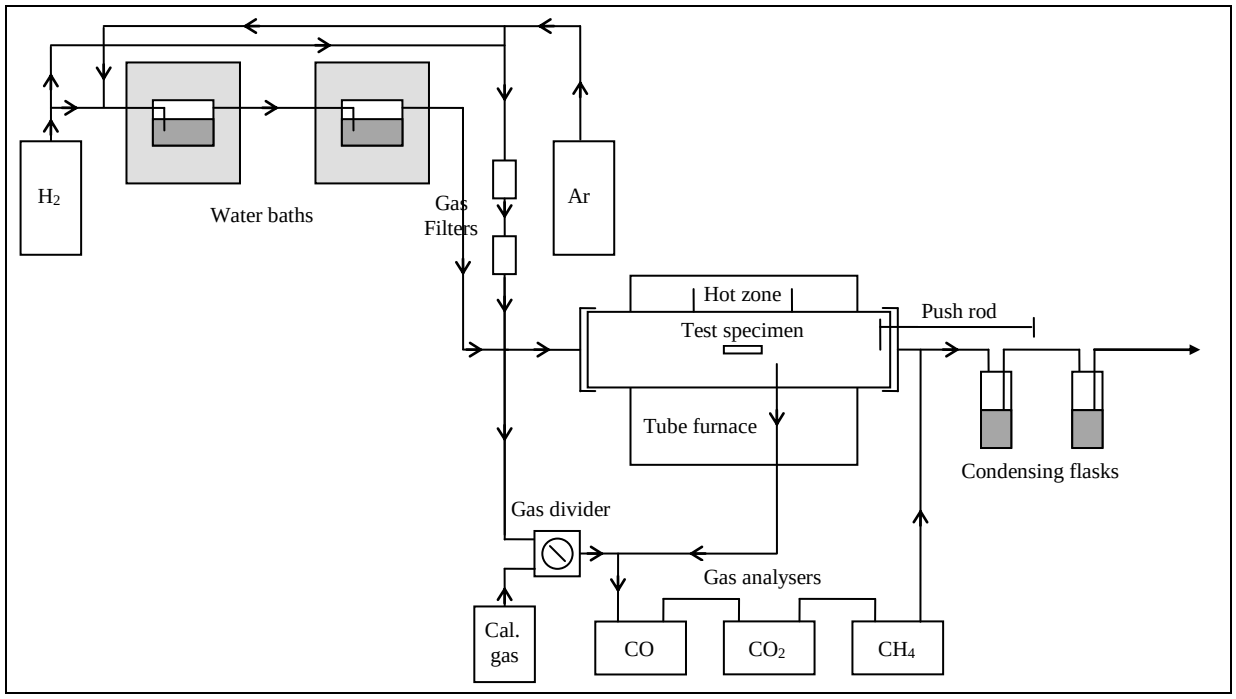

Figure 1 Schematic illustration of the heat treatment test rig.

Analytical techniques

To microscopically investigate the surface decarburisation and oxidation structures, it was necessary to plate a Nickel layer onto the heat treated test specimen in order to preserve edge flatness during polishing. An effective technique was developed involving deposition of a very thin Gold layer onto the specimens, followed by electroless Nickel plating in a suitable chemical solution maintained at approximately 85°C. An aluminium spacer in contact with the specimen allowing plating initiation. These specimens were then mounted in a low shrinkage transparent cold mounting compound, Epofix, and were polished and etched. The decarburised microstructures for SUP7 furnace cooled pearlitic structures at different temperatures are illustrated in Figure 2, with the Nickel, oxide and free ferrite layers evident. The ferrite and oxide layers were measured with the length function of an image analyser.

The carbon monoxide concentration profiles during the first 15min decarburisation of SUP7 furnace cooled pearlitic structures at various temperatures are illustrated in Figure 3. These profiles show the variation of the carbon removal kinetics during the early stages of the heat treatment, with the 5mm diameter by 50mm SUP7 test specimens requiring 558s to reach 815°C[(4)] when inserted into the hot zone maintained at 820°C. Similar shaped carbon dioxide profiles were observed, with the concentrations approximately an order of magnitude lower than the carbon monoxide values. Knowledge of the reaction chemistry, and the application of the appropriate thermodynamics, allowed the carbon removed from the steel, and hence the free ferrite depths, to be calculated[(4)] from these gas concentrations. Figure 4 illustrates the free ferrite depths calculated from the recorded gas concentrations after 15min decarburisation, along with the free ferrite depths measured from the 4hr microstructures.

The alloying element profiles were measured across the oxide, and into the free ferrite until the profiles had stabilised for each element, by using a scanning electron microscope equipped with energy dispersive spectroscopy. Analyses were made at 1µm intervals across the oxide,

with the electron beam, positioned by the spot mode, occupying a volume of approximately 1µm. Figure 5 illustrates the concentration profiles measured along the centreline of the oxide structure for a furnace cooled pearlitic structure decarburised at 820°C.

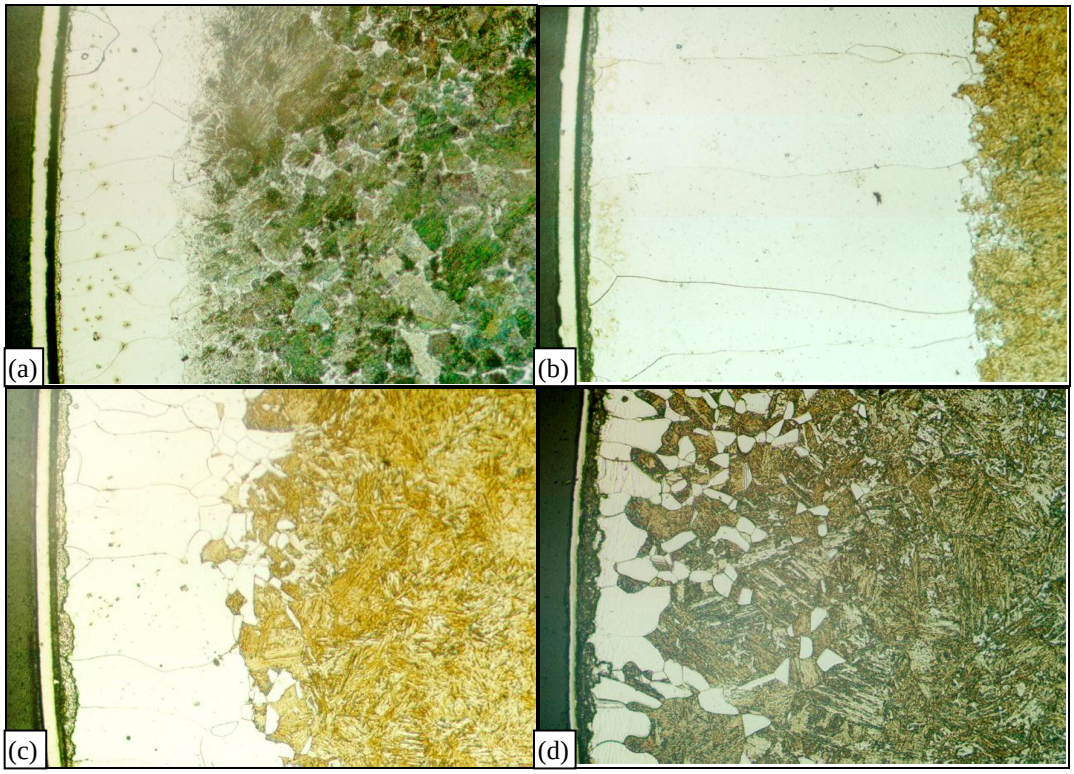

Figure 2 SUP7 microstructures after decarburisation of furnace cooled pearlitic structures with p_{H_2O} / p_{H_2} =0.05 at (a) 700°C, (b) 800°C, and (c) 900°C for 4hr, and (d) 900°C for 24hr. Etched in 2% Nital. 230x magnification.

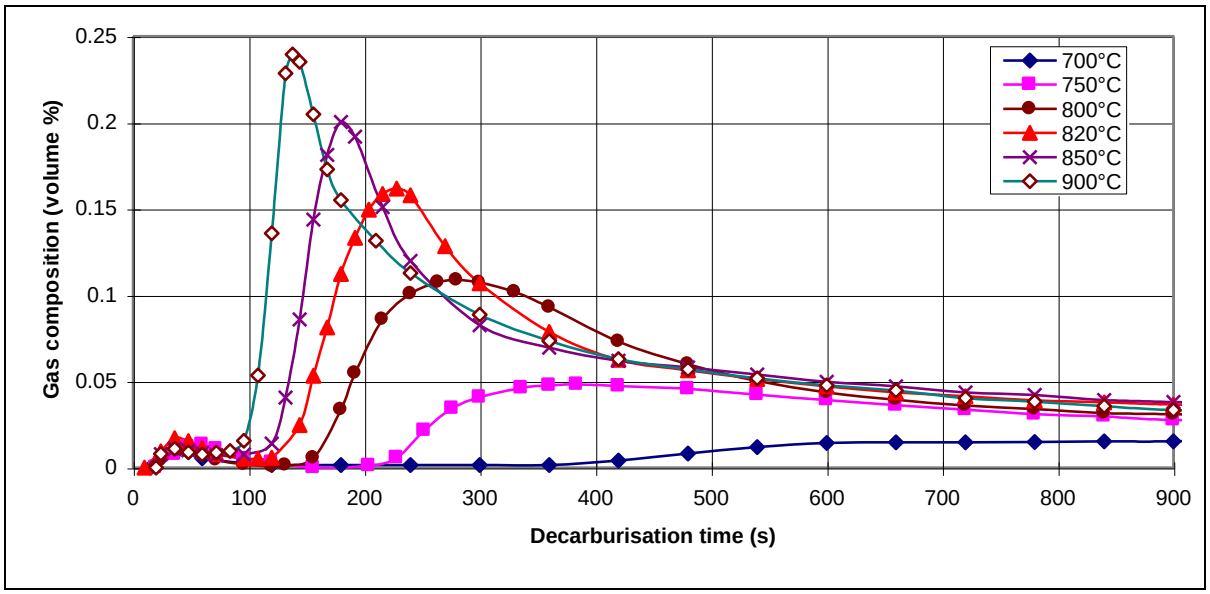

Figure 3 CO concentration profiles during the first 15min decarburisation of SUP7 furnace cooled structures at different temperatures with p_{H_2O} / p_{H_2} =0.05.

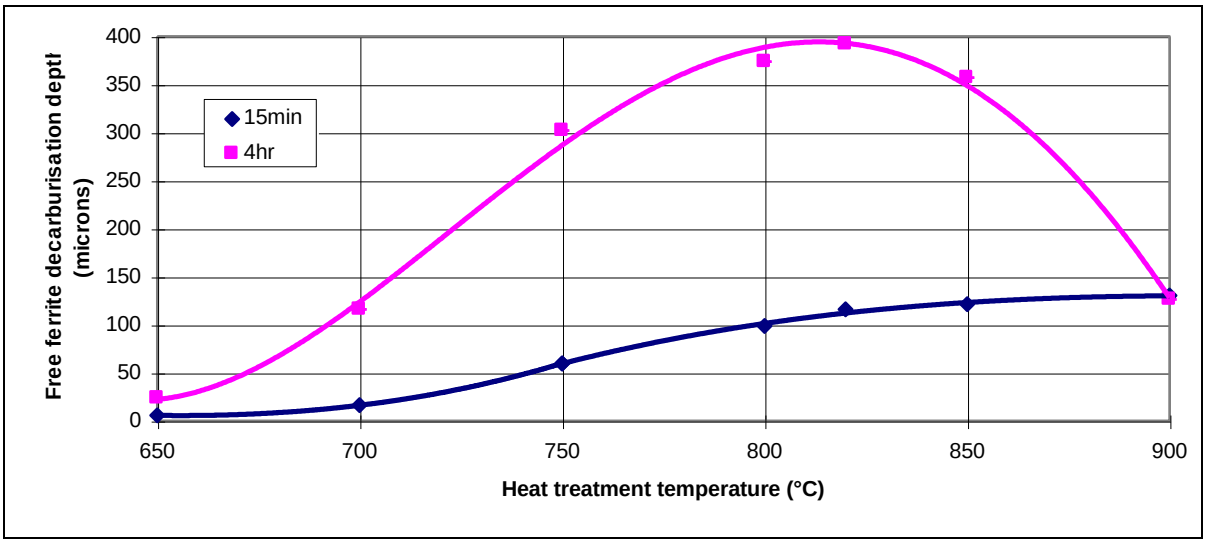

Figure 4 Influence of temperature on the free ferrite decarburisation depths for furnace cooled pearlitic structures heat treated with p_{H_2O}/p_{H_2} =0.05.

Experimental results

The decarburisation heat treatments undertaken at temperatures of 650 to 900°C with SUP7 (0.60wt.% carbon, 1.94wt.% silicon, 0.77wt.% manganese, 0.19wt.% chromium, 0.033wt.% aluminium) furnace cooled pearlitic test specimens illustrate the large temperature influence on the carbon release kinetics. At 650°C, carbon monoxide and carbon dioxide were barely detectable with the gas analysers. At 700°C, a peak carbon monoxide concentration of 0.015vol.% occurred after 900s, Figure 3. This was one-fifteenth the peak value of 0.239 vol.% for decarburisation at 900°C, which occurred after 138s. As the heat treatment temperature increased, the gas concentration peaks increased, but became more narrow.

The decarburised microstructures differ with temperature. At 700°C, a free ferrite case surrounds a pearlitic core, Figure 2a, while at 800°C, the free ferrite case sharply delineates a martensitic core, Figure 2b. The ferrite/martensite interface after 15min at 900°C was sharply defined. However, by 4hr this interface had started to break down, and was considerably more ragged than at 800°C, Figure 2c versus 2b. After 24hr the ferrite/martensite interface was almost non-existent, with martensite growth into the free ferrite, as illustrated in Figure 2d. This martensite growth extended to the surface in some places. The free ferrite depths after 15min, calculated from the carbon monoxide and carbon dioxide concentrations, increased from 6µm at 650°C to 130µm at 900°C, Figure 4. After 4hr, a free ferrite layer 24µm thick was measured from the 650°C microstructure. This increased to a maximum value of 392µm at 820°C. After 4hr at 900°C, the free ferrite depth was 126µm, before decreasing to only 53µm after 24hr.

The alloying element profile across the oxidation structure of a 4hr SUP7 furnace cooled pearlitic specimen at 820°C is illustrated in Figure 5, demonstrating the elevated silicon, manganese and aluminium concentrations relative to the bulk steel. The alloy concentrations fluctuated considerably, with peak silicon, manganese and aluminium concentrations of 7.9, 8.8 and 4.5wt.% respectively. The thermodynamics of a low carbon/2wt.% silicon steel predicts the formation of a SiO_2 oxide layer at 820°C with a p_{H_2O}/p_{H_2} ratio of 0.05[5]. The

highly elevated manganese and aluminium concentrations also suggest the presence of oxidation products involving manganese and aluminium. The iron concentrations of approximately 65 to 90wt.% across the oxide demonstrates that this structure is not purely oxide. Instead, the structure appears to comprise an iron matrix with oxide particles precipitated throughout.

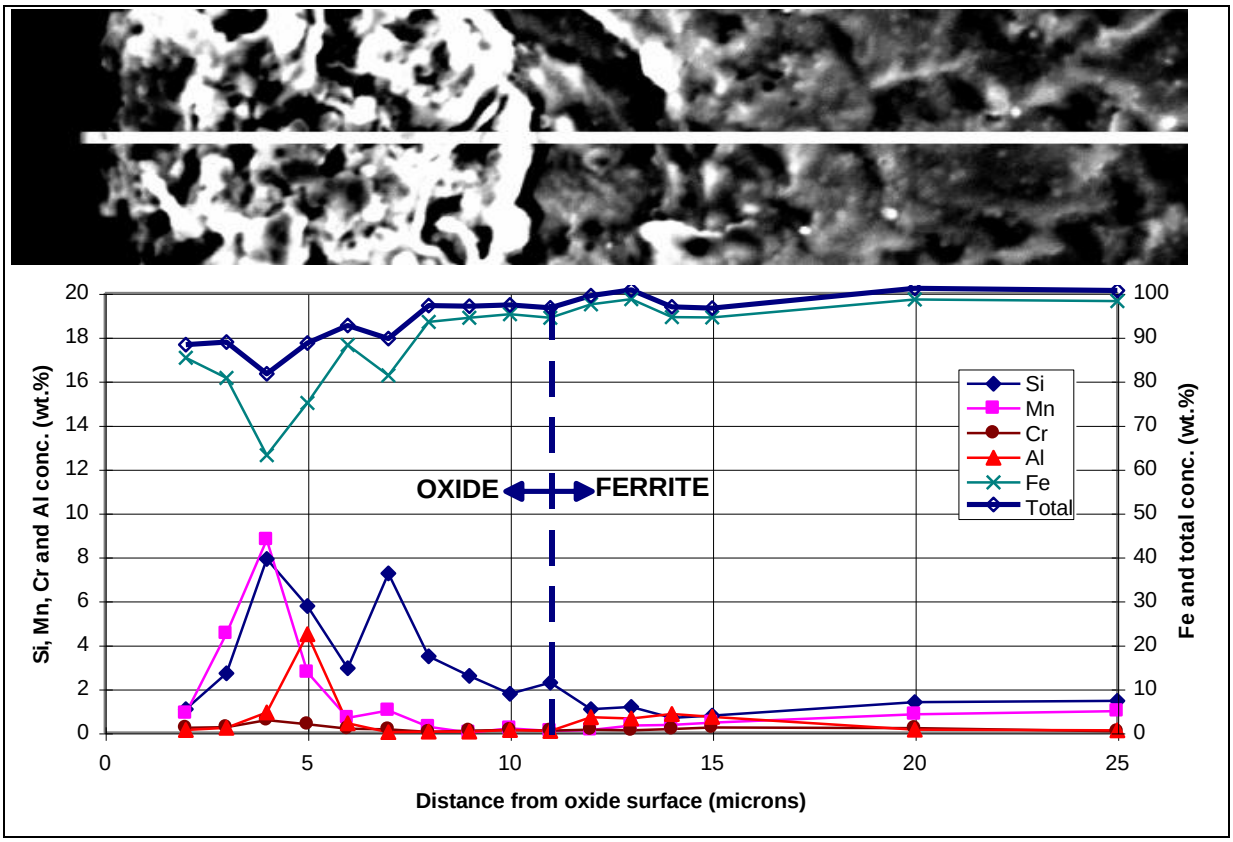

Figure 5 Alloying element concentration profiles for the oxide structure formed after 4hr decarburisation of a SUP7 furnace cooled pearlitic structure at 820°C, p_{H_2O} / p_{H_2} =0.05.

Discussion

The most interesting feature of this research was the decarburisation behaviour of SUP7 at 900°C. Carbon removal during the initial stages of the heat treatment yielded a uniform free ferrite surface layer similar to that forming at lower temperatures. However, upon prolonged holding, growth of austenite (martensite forms from austenite upon quenching) into the ferrite layer destroyed the uniform ferrite/austenite interface. It appears that at some stage during decarburisation at 900°C, carbon removal was strongly impeded. Presumably the surface oxide layer gradually changed from being porous, which allowed carbon removal, to being almost impervious to carbon removal. As a carbon concentration gradient existed across the ferrite/austenite interface, carbon was able to diffuse from the austenite to the ferrite. With carbon transport across the specimen surface inhibited, the ferrite carbon content increased sufficiently to allow austenite growth in the ferrite.

Earlier heat treatments were undertaken with SUP7, and with 1.01 and 3.57wt.% silicon steels comprising lower carbon and manganese contents than SUP7 in a hydrogen/5% water

atmosphere[6]. The 1.01% silicon and SUP7 steels decarburised deeply, although the increased silicon content of SUP7 yielded slower decarburisation kinetics than the 1.01% silicon steel. Increasing the silicon content to 3.57wt.% prevented any decarburisation from occurring, even after a 24hr heat treatment. This appeared to be due to the formation of a thin dense surface oxide structure preventing carbon removal. It was also demonstrated that the free ferrite initiation in SUP7 was retarded for several hours when the specimens were heated and annealed in argon prior to the heat treatment atmosphere being introduced[4]. It was suggested that an impervious SiO_2 layer formed during the supposedly pure argon anneal due to the presence of trace amounts of water vapour. Carbon removal was prevented until the SiO_2 layer broke down, with decarburisation then occurring readily.

Decarburisation occurs during the hot rolling of bar stock in the steel mill, with a peeling operation required to remove the decarburised surface layer prior to spring production. This research demonstrates the possibility of severely impeding SUP7 decarburisation by heat treating at temperatures in excess of 900°C. Alternatively, considerable decarburisation inhibition is achieved by increasing the silicon content of SUP7, and by annealing in a low water content atmosphere. Consequently, the peeling operation prior to spring production could be eliminated. Furthermore, carbon removal would also be inhibited during the heating, hot shaping, and tempering of the springs. The shot peening operation normally undertaken following tempering to negate the effect of the decarburised layer may no longer be necessary.

Conclusion

An investigation into the decarburisation of spring steels was undertaken. This necessitated the development of appropriate heat treatment apparatus and experimental techniques, with some interesting results obtained. Of particular interest was the inhibition of carbon removal upon prolonged holding of SUP7 at 900°C in a hydrogen/5% water atmosphere. This suggests another possibility for improving the automobile coil spring manufacturing processes.

Acknowledgments

I gratefully acknowledge and thank BHP New Zealand Steel for their financial support which has made this paper possible. Furthermore, I would like to thank the Department of Mechanical Engineering staff at the University of Canterbury for their support.

References

1) "Effect of chemical composition on sag resistance of suspension spring", Kawakami, H.; SAE Paper 821028.
2) "The effect of shot peening to decarburised steel plate", Sato, S.; Inoue, K.; Ohno, A.; Proceedings 1st International Conference on Shot Peening, September 1981, 303-312.
3) Unpublished research, Bott, C.; Postgraduate Student, University of Canterbury, New Zealand.
4) "Variable decarburisation of a spring steel", Mardon, C.; Smaill, J.; to be published in 1998 IPENZ Annual Conference Proceedings.
5) "About oxidation and decarburisation behaviour of Fe-Si alloys", Wiesner, U.; Neue Hutte, July 1986, 250-253.
6) "Decarburisation behaviour of high silicon spring steels", Mardon, C.; Smaill, J.; Sell, L.; Proceedings IPENZ Annual Conference 1997, Volume 2, 269-271.